

Quantum control of chemistry
by magnetic fields pp. 975 & 1006

Soil microbes restoring
degraded land p. 990

Comprehensive transcriptomic
cell atlas of the fruit fly p. 991

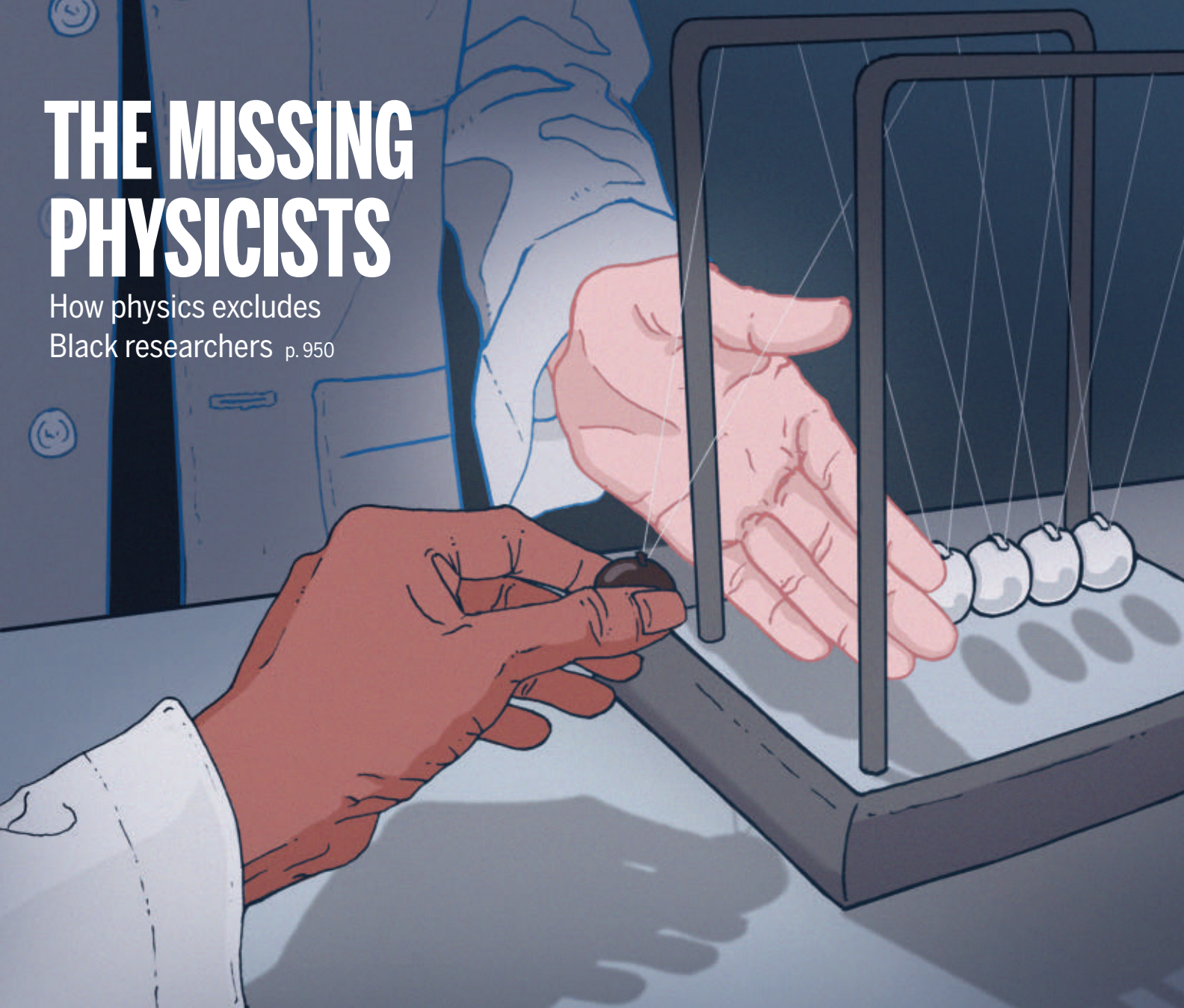
Science

\$15
4 MARCH 2022
SPECIAL ISSUE
science.org

 AAAS

THE MISSING PHYSICISTS

How physics excludes
Black researchers p. 950





Apply for our exciting research Prize!



\$25, 000 Grand Prize!
Get published in *Science*!

The *Science*-PINS Prize is a highly competitive international prize that honors scientists for their excellent contributions to neuromodulation research. For purposes of the Prize, neuromodulation is any form of alteration of nerve activity through the delivery of physical (electrical, magnetic, or optical) stimulation to targeted sites of the nervous system with implications for translational medicine.

For full details, judging criteria and eligibility requirements, visit:

www.science.org/pins

Submissions Open: 15 December 2021

Science
AAAS



Science
Translational
Medicine
AAAS

CONTENTS

4 MARCH 2022
VOLUME 375
ISSUE 6584

970

NEWS

IN BRIEF

940 News at a glance

IN DEPTH

942 War in Ukraine poses stark choices for scientists

As Ukrainian researchers hunker down or flee, backlash against Russian science builds
By R. Stone

943 Regulator halts assembly of fusion reactor

ITER must meet safety concerns before welding giant tokamak sections
By D. Clery

944 Mammoth mangrove bacterium has complex cell

"Eye-opening" discovery challenges evolutionary thinking on microbes
By E. Pennisi

945 New name won't fix all flaws in China Initiative, critics worry

Justice Department promises tighter focus on preventing espionage and no profiling of Chinese academics
By J. Mervis

946 Studies bolster pandemic origin in Wuhan animal market

Close scrutiny of earliest cases and samples from market suggests virus crossed over from animals sold there
By J. Cohen

948 U.N. panel warns of warming's toll and an 'adaptation gap'

Impact of climate change will be worst for the natural world and humanity's most vulnerable
By P. Voosen

949 China quietly plans a pivot from 'zero COVID'

Scientists are studying how to live with the virus while avoiding a crisis like in Hong Kong
By D. Normile

INSIGHTS

PERSPECTIVES

970 Anthropogenic influences on bee foraging

Efficient foraging is vital to bee fitness but is challenging in the Anthropocene
By D. Goulson and E. Nicholls



SPECIAL SECTION

Black physicists

INTRODUCTION

950 Can U.S. physics overcome its record of exclusion?

Data show white institutions falling short and Black colleges leading the way
By J. Mervis

FEATURES

952 The toll of white privilege

How the dominant culture in physics has discouraged diversity
By J. Mervis

956 Fix the system, not the students

Change requires building bridges, removing barriers
By J. Mervis

960 Black colleges can't do it all

At historically Black colleges and universities, tight funding threatens an extraordinary record of nurturing Black physicists
By J. Mervis

964 Called to teach

Black physics Ph.D.s are more than twice as likely as other groups to teach in high schools and community colleges. For many, it's a mission
By A. Smart

967 Michigan's surprising path to diversity

Black graduate students find a nurturing culture in its applied physics program
By J. Mervis

SEE ALSO

EDITORIAL p. 937 PODCAST

ON THE COVER

The Newton's cradle is often used to demonstrate the conservation of momentum and energy in U.S. college physics courses. But Black students are rare in those classes and, despite decades of efforts to increase Black representation in U.S. physics, the problem is

getting worse.

A special News section examines why, and ways of reversing the trend. See page 950. *Illustration: Nik Richard*



972 Addicted to dreaming

How does dopamine, the brain's pleasure signal, regulate the dream stage of sleep?

By E. Arrigoni and P. M. Fuller

RESEARCH ARTICLE p. 994

974 Forming roots from shoot

Uncovering the genes responsible for different types of roots will transform aspects of plant agriculture

By L. Shaar-Moshe and S. M. Brady

RESEARCH ARTICLE p. 993

975 Toward a coherent ultracold chemistry

Magnetic fields can be used to change chemical reaction rates by a factor of 100

By S. L. Cornish and J. M. Hutson

RESEARCH ARTICLE p. 1006

976 A new Hall for quantum protection

Long-range vacuum fluctuations break the integer quantum Hall topological protection

By A. Rubio

REPORT p. 1030

978 Catalyst coaxed to make branched α -olefins

Process conditions allow a titanium catalyst to add just two ethylene molecules to an α -olefin

By M. S. Rosen

REPORT p. 1021

POLICY FORUM**979 A role for funders in fostering China's research integrity**

Despite recent progress, challenges remain

By L. Tang

BOOKS ET AL.**982 Life-changing biology**

Genetically engineered genomes will disrupt the bioeconomy and rewrite human nature—are we ready?

By A. Woolfson

983 The lasting legacy of John von Neumann

A new biography seeks to acquaint readers with the once widely celebrated scientist

By D. Greenbaum and M. Gerstein

LETTERS**984 Greek roadless policy: A model for Europe**

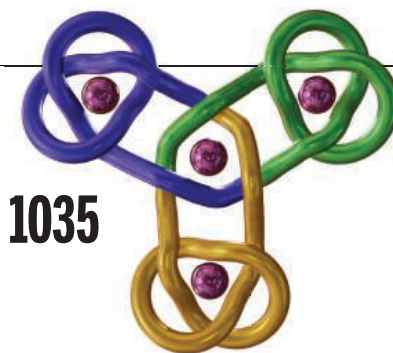
By V. Kati et al.

984 Iran's agricultural waste

By R. Akbari and M. Nasrollahzadeh

985 China's dams threaten the Sichuan taimen

By D. Tong



1035

RESEARCH**IN BRIEF**

987 From *Science* and other journals

REVIEW**990 Restoration ecology**

Soil microbiota as game-changers in restoration of degraded lands

O. Coban et al.

REVIEW SUMMARY; FOR FULL TEXT:
DOI.ORG/10.1126/SCIENCE.ABE0725

RESEARCH ARTICLES**991 Genetics**

Fly Cell Atlas: A single-nucleus transcriptomic atlas of the adult fruit fly

H. Li et al.

RESEARCH ARTICLE SUMMARY; FOR FULL TEXT:
DOI.ORG/10.1126/SCIENCE.ABK2432

992 Neurogenomics

A single-cell atlas of the normal and malformed human brain vasculature

E. A. Winkler et al.

RESEARCH ARTICLE SUMMARY; FOR FULL TEXT:
DOI.ORG/10.1126/SCIENCE.ABI7377

993 Plant science

A conserved superlocus regulates above- and belowground root initiation

M. Omary et al.

RESEARCH ARTICLE SUMMARY; FOR FULL TEXT:
DOI.ORG/10.1126/SCIENCE.ABF4368
PERSPECTIVE p. 974

994 Neuroscience

Rapid eye movement sleep is initiated by basolateral amygdala dopamine signaling in mice

E. Hasegawa et al.

PERSPECTIVE p. 972

1000 Synthetic genomics

Transcriptional neighborhoods regulate transcript isoform lengths and expression levels

A. N. Brooks et al.

1006 Ultracold chemistry

Control of reactive collisions by quantum interference

H. Son et al.

PERSPECTIVE p. 975

1011 Asteroids

Pebbles and sand on asteroid (162173) Ryugu: In situ observation and particles returned to Earth

S. Tachibana et al.

REPORTS**1017 Topological physics**

A synthetic monopole source of Kalb-Ramond field in diamond

M. Chen et al.

1021 Catalysis

Elongation and branching of α -olefins by two ethylene molecules

T. Dietel et al.

PERSPECTIVE p. 978

1025 Magnetism

Topological magnon band structure of emergent Landau levels in a skyrmion lattice

T. Weber et al.

1030 Quantum optics

Breakdown of the topological protection by cavity vacuum fields in the integer quantum Hall effect

F. Appugliese et al.

PERSPECTIVE p. 976

1035 Molecular knots

Vernier template synthesis of molecular knots

Z. Ashbridge et al.

1041 Coronavirus

Broad anti-SARS-CoV-2 antibody immunity induced by heterologous ChAdOx1/mRNA-1273 vaccination

C. I. Kaku et al.

1048 Coronavirus

Structures of the Omicron spike trimer with ACE2 and an anti-Omicron antibody

W. Yin et al.

1053 Epigenetics

Highly enriched BEND3 prevents the premature activation of bivalent genes during differentiation

J. Zhang et al.

DEPARTMENTS**937 Editorial**

Dismantle racism in science

By E. O. McGee

BLACK PHYSICISTS SECTION p. 950

939 Editorial

Biden doesn't get it

By H. H. Thorp

1062 Working Life

My writing journey

By Y. Tong

Science Careers1059

SCIENCE (ISSN 0036-8075) is published weekly on Friday, except last week in December, by the American Association for the Advancement of Science, 1200 New York Avenue, NW, Washington, DC 20005. Periodicals mail postage (publication No. 484460) paid at Washington, DC, and additional mailing offices. Copyright © 2022 by the American Association for the Advancement of Science. The title SCIENCE is a registered trademark of the AAAS. Domestic individual membership, including subscription (12 months): \$165 (\$74 allocated to subscription). Domestic institutional subscription (51 issues): \$2212; Foreign postage extra: Air assist delivery: \$98. First class, airmail, student, and emeritus rates on request. Canadian rates with GST available upon request. GST #125488122. Publications Mail Agreement Number 1069624. Printed in the U.S.A.

Change of address: Allow 4 weeks, giving old and new addresses and 8-digit account number. Postmaster: Send change of address to AAAS, P.O. Box 96178, Washington, DC 20090-6178. Single-copy sales: \$15 each plus shipping and handling available from backissues.science.org; bulk rate on request. Authorization to reproduce material for internal or personal use under circumstances not falling within the fair use provisions of the Copyright Act can be obtained through the Copyright Clearance Center (CCC), www.copyright.com. The identification code for Science is 0036-8075. Science is indexed in the Reader's Guide to Periodical Literature and in several specialized indexes.

Dismantle racism in science

William Shockley Jr. of Stanford University was an American physicist who jointly won the 1956 Nobel Prize in Physics for his role in inventing the transistor. Modern computing and communications would have been unthinkable without Shockley's work. But the Nobel laureate was also a proponent of eugenics and firmly committed to the racial inferiority of Black people. Shockley was not just a physicist who held racist views. He was part of a wider academic system that then, and now, perpetuates racial inequality. The persistence of this biased ecosystem means that dismantling it will require unrelenting tenacity by all of academia.

I've spent years studying how racism operates in science, technology, engineering, and mathematics (STEM) fields, especially in higher education institutions in the United States. Structural inequities perpetuate tendencies that discriminate against STEM faculty of color and stifle their progress. For example, institutions often expect these faculty to lead the charge when it comes to anti-racist efforts. They are approached to mentor students of color, to serve on diversity committees, and to speak on panels about diversity—activities that are tangential to their research. Although many people of color in STEM have a fervent desire to make their field and workplace more equitable, pressure to perform duties unrelated to their research creates a service burden that many of their white colleagues do not bear. By contrast, white faculty are busy advancing their research, thereby earning grants, joining collaborations, and publishing papers that bolster their careers. This imbalance disadvantages faculty of color in tenure and promotion decisions. People of color who do “make it” in STEM disciplines often do so while taking on a superhuman workload that is unfair and unsustainable.

Moreover, to function in the present biased ecosystem, underrepresented people of color are pressured to conform to a predominantly white male culture and are discouraged from bringing their authentic selves into the workplace. For example, STEM faculty of color are encouraged to remove any language about racial justice, including diversity, equity, and inclusion, in their grant proposals. Additionally, some alter their appearance, demeanor, and speech to assimilate into—and survive in—the mainstream STEM culture. This stress is a burden and humiliation that can take a psychological toll.

Because there are fewer people of color in university leadership positions, there are fewer leaders who are cognizant of these impediments. As a result, the barriers for people of color in STEM are rarely addressed because leaders' priorities are elsewhere.

To change the situation, the dominant culture needs to assume the burden of providing remedies. In the field of physics, for example, people of color are called upon to figure out how to “create change,” rather than those who benefit from the status quo. STEM ecosystems need to distribute this responsibility to everyone, especially to those faculty who hold the power and privilege to implement compelling and sustainable changes. Doing this involves the most influential people in efforts to innovate and restructure spaces in ways that support STEM equity.

Faculty of color across academia often take on students of color who are outside of their departments but who desperately need mentorship. Institutions need to recognize when faculty of color are functioning as de facto university leaders and reward these staff with the titles, compensation, and resources appropriate to the responsibilities they have assumed.

Higher education must also recruit more faculty of color. This is the most powerful way STEM departments can demonstrate that racial equity and diversity are a priority.

Students, faculty, and administrators who are women of color experience both raced and gendered forms

of abuse in academia. Hostile environments span from negative comments about their abilities, qualifications, and performance to sexual harassment. In my research, I have found that Black women have great difficulties convincing their professors and colleagues that they are worthy of belonging in STEM. Instead of creating programs to “fix” students, how about coaching STEM faculty and administrators on the toxicity associated with racially unwelcoming conditions and the particular effects it has on women of color? Having more women of color leadership in STEM academia would be a strong start.

Anti-racism work is hard work, but unless actions move beyond simply tossing about diversity and equity buzzwords, people of color will remain underrepresented in STEM fields. And the United States will continue to miss out on the STEM talent and innovation that exist within communities of color.

—Ebony Omotola McGee



Ebony Omotola McGee

is a professor of Education, Diversity, and STEM Education in the Department of Teaching and Learning at Peabody College, Vanderbilt University, Nashville, TN, USA.
ebony.mcgee@vanderbilt.edu

“...the barriers
for people
of color in STEM
are rarely
addressed...”

Rutgers University: R&D with Impact

Committed to research and development driven by
a relentless pursuit of excellence



\$907.9
million

Research grants and
sponsored programs

\$720
million

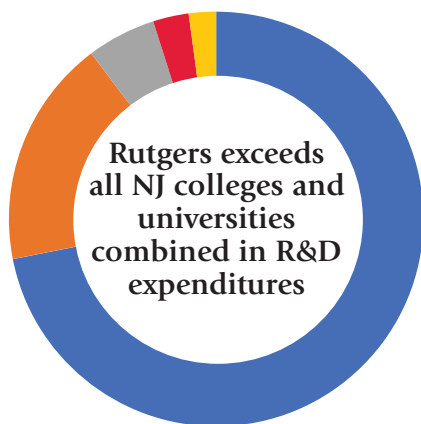
Research and development
expenditures

1187

Active technologies to
license and market

1000+

Companies partner with
Rutgers researchers



Top 5 Direct Federal Sponsors of Rutgers Research

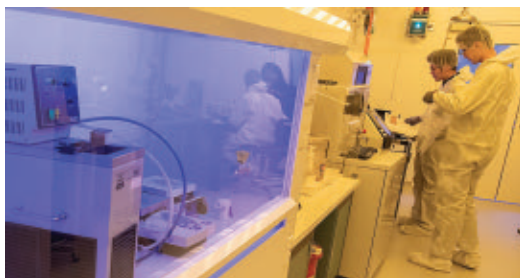
- National Institutes of Health \$229.7M
- National Science Foundation \$56.9M
- U.S. Health Resources and Services Administration \$17.2M
- U.S. Department of Education \$9M
- National Oceanic and Atmospheric Administration \$6.8M



Recent Outcomes with Global Impact

- Invented COVID-19 diagnostic tests and serving as COVID-19 vaccines clinical trials site
- Pioneering use of underwater gliders for hurricane intensity forecasting
- Lead authorship of Intergovernmental Panel on Climate Change Reports
- Invented clean manufacturing technology for polymers and other monomers
- Co-lead investigator of large-scale urban test site for next-gen Wi-Fi

Top 100
World's Most
Innovative
Universities —Reuters



RUTGERS
THE STATE UNIVERSITY
OF NEW JERSEY

*This is what **Excellence** looks like*
excellence.rutgers.edu

Annual data current as of January 2022

Biden doesn't get it

It has been a rough 2 weeks for the US science community. After 4 years of bludgeoning by the Trump administration, hope resurged a year ago as a new White House promised to value science. But there have been missteps, the most recent taking place on the heels of another blunder that many saw coming. Eric Lander, who just stepped down as President Biden's science adviser and director of the Office of Science and Technology Policy (OSTP), was a prominent research figure with a well-known record of bullying and callous actions. With the notable exception of the 500 Women Scientists organization, the scientific community was embarrassingly silent about Lander's nomination. Not surprisingly, he is out of the White House because of the same behavioral issues. And yet, in another tone deaf move, the administration just named Francis Collins, the recently retired director of the National Institutes of Health (NIH), as Lander's interim replacement as science adviser while asking Alondra Nelson, the OSTP's deputy director for science and society and an experienced administrator and scholar, to temporarily direct OSTP. Apparently, Biden doesn't think Nelson is capable of doing both jobs. I disagree and am not staying silent this time.

The decision to choose Collins for the presidential adviser aspect of the job may appear a strategic move to advance Biden's biomedical agenda, but the decision to keep Nelson out of this role reflects a chronic ill in America—inequity at the highest levels of leadership. Lander's vacated position and Nelson's presence at OSTP already presented a clear opportunity to put someone in the combined role who represents the future of American science.

Certainly, Francis Collins has been a major science policy figure in the US for many years. Through his dogged determination and political skill, he pushed the human genome project to completion and took the helm of the NIH, serving three presidents. Through his masterful abilities to engage with Congress, he reliably secured increases in NIH funding year after year. But the end of his tenure brought problems that weren't adequately resolved. He was unable to dismantle an outdated grant assessment process that reinforces a low funding rate for Black applicants. And NIH caved to political pressure around the China

Initiative, which sought to satisfy the Trump administration's anti-Asian tendencies by sending letters to universities to disrupt legitimate scientific collaborations with China.

At some point, the scientific community must stand up against anti-Asian racism and injustice in the funding of Black scientists, among other discrimination in the scientific enterprise. That time has to be now, and what is needed is a new cadre of scientific leaders in Washington, DC, who can build a scientific agenda where inclusion of individuals who reflect the diverse makeup, talents, and interests of society is prioritized. Appointing someone as the nation's science adviser—even on a temporary basis—who has already enjoyed the privilege of leading for many years sends a message that the White House doesn't

care, especially when so many new and diverse leaders are available. It's hard not to conclude that the administration has gotten what it needs out of science and has lost interest. Given the sluggish pace with which science appointments have been made by the administration, this latest arrangement may last for some time.

Alondra Nelson is one of the visionary leaders in American science today. She was the first Black professor to receive tenure in sociology at Columbia University, has held numerous challenging administrative roles, and currently occupies the Harold F. Linder Chair in the School of Social Science at the Institute for Advanced Study. When invited to join OSTP, Nelson stated that “as a Black woman researcher, I'm keenly aware of who has been missing from the room.” After 2 years of witnessing the scientific community succeed at developing vaccines to combat the pandemic but fail at getting full acceptance by the community, it's clear that Nelson has the expertise that is gravely needed for all of science.

It's time for the scientific community to commit to a vision of the future where young scientists can get a fair share of funding, where equity for women and people of color is prioritized over protecting processes that reinforce injustices of the scientific enterprise, and where leaders in Washington, DC, represent the future, not the past.

—H. Holden Thorp



H. Holden Thorp
Editor-in-Chief,
Science journals.
hthorp@aaas.org;
@hholdenthorp

“Lander's vacated position and Nelson's presence at OSTP already presented a clear opportunity...”

NEWS

“Fifty percent is a failing grade. It's an F. Someone with the resources of Facebook should be aiming for an A.”

Imran Ahmed of the Center for Countering Digital Hate, on its finding that Facebook is failing to label about half the posts that promote articles from publishers of climate misinformation.

IN BRIEF

Edited by
Jeffrey Brainard



Many schools that have mandated wearing masks are considering making them optional, following new U.S. government guidance.

COVID-19

CDC relaxes guidance on wearing masks in public

The often-acrimonious U.S. debate over wearing masks entered a new phase last week when the Centers for Disease Control and Prevention (CDC) loosened its guidance and suggested about 70% of the population could jettison them. The turnabout comes as the Omicron wave ebbs and scientists consider how to recalibrate public health precautions, given the mostly mild or moderate disease the virus variant causes in vaccinated people. CDC's new approach relies on regional COVID-19 hospital admission

rates, the percentage of hospital beds filled by those patients, and new cases per 100,000 people during the past week. Previously, case numbers had played the starring role. Some scientists praised the agency's change; others criticized it because the U.S. population includes many vulnerable people, like those with compromised immune systems, and children under age 5, for whom COVID-19 vaccines aren't yet available. State and local health authorities in the United States determine mask wearing rules but often turn to CDC for guidance.

Nobelists denied CRISPR patent

BIOTECHNOLOGY | The team that won a Nobel Prize for its groundbreaking creation of the CRISPR genome editor lost a key patent battle this week. An appeals board of the U.S. Patent and Trademark

Office ruled that a rival group led by the Broad Institute of MIT and Harvard convincingly showed it first “reduced to practice” the use of CRISPR as an editor of eukaryotic cells in October 2012. Nobel laureates Jennifer Doudna and Emmanuelle Charpentier and their colleagues first

described using CRISPR to edit specific DNA in 2012, but the group, known as the CVC, struggled to make it work in eukaryotic cells. The patents for CRISPR in eukaryotic cells represent a huge financial windfall because these are the foundation for human medicines. The CVC, which

lost an earlier patent battle over a similar claim, retains 40 other U.S. patents related to CRISPR and an intellectual property portfolio in 30 countries. A CVC representative said the team “is considering various options to challenge this decision.”

Panel to mull risky virus research

BIOSECURITY | In the wake of the coronavirus pandemic, the U.S. government is revisiting its oversight of “gain-of-function” studies that modify pathogens in ways that could make them more harmful to people. This week, the White House and National Institutes of Health asked the National Science Advisory Board for Biosecurity to review the scope and effectiveness of policies for research on “enhanced potential pandemic pathogens.” The assessment could examine whether controversial coronavirus experiments previously funded by the United States in China fall under that definition and should have received stricter scrutiny. The board will also look at existing policies on “dual-use research of concern” involving pathogens that could be misused to cause harm. Some board members cautioned against overly restrictive rules that could shut down research essential to fighting pandemics. But some critics have called existing policies too permissive. A report is due by December.

Subvariant proves no more severe

COVID-19 | BA.2, a more contagious version of the already highly infectious Omicron SARS-CoV-2 variant, does not make people sicker than the original Omicron, the World Health Organization (WHO) concluded last week, based on data from three countries where the subvariant has become dominant. Both a 19 February preprint from South Africa’s National Institute for Communicable Diseases and a 25 February report by the UK Health Security Agency showed no increase in the risk of hospitalization for people who carried BA.2, compared with those infected by the original Omicron variant, known as BA.1. And in a 22 February preprint, the Danish public health agency reported that reinfection by BA.2 did not lead to worse symptoms than an initial BA.1 infection, which were mild or moderate.

Edited gene’s effect persists

THERAPEUTICS | The first team to edit a disease gene by deploying CRISPR, the DNA scissors, within the body, reported this week that levels of a toxic protein stayed low for as long as 1 year, suggesting long-term benefits. In June 2021,

Intellia Therapeutics and Regeneron Pharmaceuticals announced that 1 month after receiving an injection of fat particles carrying messenger RNA for the CRISPR enzyme and a guide RNA sequence, six people with transthyretin amyloidosis, an inherited, progressive disease, had a drop in blood levels of a misfolded liver protein that can damage the heart and nerves. The companies said in a 28 February press release and webcast with investors that the reductions in levels—ranging from 41% to 93%, depending on the CRISPR dose—have remained stable in the six original participants and nine more, all treated between 2 and 12 months ago. The researchers do not know yet whether the patients’ neuropathy symptoms have improved.

Colonialism in fossil studies

RESEARCH ETHICS | Two basins—one in northeastern Brazil, the other in northern Mexico—have provided dozens of well-preserved fossils from the Jurassic and Cretaceous periods for research. But many journal articles about those finds, published during the past 3 decades, serve as glaring examples of what a new analysis calls “paleontological colonialism.” Examining about 200 such published studies, a team of scientists including ones from those countries found that approximately half the studies were led by foreign



Brazilian police seized fossils illegally offered for sale and presented them to a museum at a 2021 event.

researchers. Of those, half lacked any local researchers as co-authors or showed no evidence of any collaboration with them—even though Brazil and Mexico require such partnerships. Many publications did not state whether the authors obtained permits for fieldwork, and many of the specimens described in the papers had been illegally deposited in foreign collections, according to the study, published on 2 March in *Royal Society Open Science*.

Vaccine’s protection for kids dives

COVID-19 | Children ages 5 to 11 inoculated with the Pfizer COVID-19 vaccine lose most protection against infection by SARS-CoV-2 in as little as 1 month, although defense against hospitalization seems to persist, new evidence shows. The news disappointed public health specialists because the Pfizer vaccine is the only one authorized in the United States for that age group. The findings drew on New York state medical databases and compared more than 1 million vaccinated 5- to 17-year-olds with their unvaccinated peers. Among 5- to 11-year-olds who received two doses of Pfizer’s messenger RNA-based vaccine by the second half of December 2021, the vaccine’s effectiveness against infection dropped from 65% to 12% a month later; in teenagers vaccinated in that same period, the decline was smaller, from 76% to 56%, according to the analysis by researchers at the New York State Department of Health. The authors of the study, posted on 28 February as a preprint on medRxiv, suggest younger children may have lost more protection because they received smaller doses of the Pfizer vaccine than teenagers.

LGBTQ disclosure linked to papers

DIVERSITY | LGBTQ scientists who don’t disclose their sexual orientation in the workplace publish fewer papers than their peers, a study has found. Researchers surveyed 1745 academic scientists in 2016, 1093 of whom identified as a sexual minority, asking them questions about their publishing history and openness in the workplace. Based on the information each provided, straight men and openly gay or bisexual men published the most papers, whereas LGBTQ individuals whose colleagues weren’t aware of their sexual orientation published the fewest. The authors of the study, which appeared this week in *PLOS ONE*, say the publishing gap may reflect the challenges that LGBTQ individuals face when working in environments in which they’re not comfortable sharing their identity.



SCIENTIFIC COMMUNITY

War in Ukraine poses stark choices for scientists

As Ukrainian researchers hunker down or flee, backlash against Russian science builds

By **Richard Stone**

On 24 February, as Russian troops poured across the border in an unprovoked invasion of Ukraine, Sergei Mosyakin, director of the Institute of Botany in Kyiv, set out with a few key staff to secure the institute and its National Herbarium, which holds more than 2 million specimens representing the wealth of Ukraine's floral and fungal diversity. Several kilometers to the south, Fedor Danevich and six colleagues at the Institute for Nuclear Research had joined an online workshop for a multinational physics project in South Korea. The Zoom call included Russian physicists. "One said that he is sorry for the war," Danevich recalls. The other Russians kept silent.

In the weeks leading up to the invasion, many Ukrainian scientists had dismissed Russia's military buildup on their border as bluster. Now, their lives have been turned upside down as they make fateful decisions about whether to dig in or flee to other European nations that have stepped up to offer accommodations and job prospects.

As Russian forces bombarded and sought to encircle Kyiv, Mosyakin and some fellow

botanists hunkered down at home, while others took refuge with relatives in the countryside. Danevich says he intended to stay in Kyiv, but his son persuaded him to gather vulnerable family members and seek shelter in Budapest, Hungary. As *Science* went to press, they had made it as far as Romania.

Condemnation of the invasion has rained down on Russia from many quarters, and a rising chorus is calling on the West to sever ties with Russian scientists. "I'm sitting now with my 86-year-old mother, who is a prominent biochemist, listening to the sounds of battle some 20 kilometers to the west, and waiting for the next bombardment," says Maksym Strikha, a physicist and former top official in Ukraine's science ministry. "Could you imagine asking a Polish physicist, surrounded and bombed in Warsaw in September 1939, whether it would be fair to maintain scientific diplomacy with scientists in Nazi Germany?"

The repercussions in international science are already being felt. The European Space Agency (ESA) announced on 28 February that international sanctions against Russia and "the wider context" are likely to delay by at least 2 years the launch of a Mars rover, part of the ExoMars astrobiology mission

jointly sponsored by Russia and ESA. And the Massachusetts Institute of Technology (MIT) is pulling out of a key collaboration with a Russian university, the Skolkovo Institute of Science and Technology (Skoltech), which MIT had helped found.

Last week, as Russian troops crossed the border, Ukrainian scientists pleaded for more drastic steps. In an open letter posted on 27 February, the Council of Young Scientists at the Ministry of Education and Science of Ukraine called on the European Commission to "urgently suspend all kinds of international collaboration with Russian institutions," including ending Russian scientists' participation in Horizon Europe, the flagship research fund. They also urged that Russia be expelled from two premier international R&D ventures—the experimental ITER fusion reactor in France and the CERN particle physics research center in Switzerland.

For now, Russia remains part of Horizon Europe and other European funding schemes. And the nine-nation collaboration Danevich is involved in to examine the nature of the neutrino—the Advanced Mo-based Rare process Experiment (AMoRE) at South Korea's Yangyang Underground

PHOTO: GLEB GARANICH/REUTERS

Smoke and flames rose over Kyiv, Ukraine, during last week's Russian invasion.



Laboratory—is proceeding. In an email to collaborators, AMoRE's spokespeople described its leaders' "determination to carry out our program during this difficult period."

But the collateral damage to Russia's scientific enterprise is mounting. In addition to the effects on ExoMars and Skoltech, the United States imposed fresh sanctions on technology transfers to Russia, which the Russian space agency claimed could threaten operation of the International Space Station. After Germany's research ministry ordered a suspension of collaboration with Russia, the Max Planck Institute for Extraterrestrial Physics turned off the main instrument on Russia's Spektr-RG research satellite: the German-run eRosita x-ray survey telescope, meant to probe the universe's large-scale structure. And math societies in several countries announced last week they will not participate in the International Congress of Mathematicians, which was slated for St. Petersburg, Russia, in July but now plans to go virtual.

Within Russia itself, some scientists sought to show solidarity with Ukraine. More than 5400 Russian scientists and science journalists signed a letter calling the war "a step to nowhere" that will turn Russia into a pariah.

The invasion, the 24 February letter says, "means that we scientists will no longer be able to do our job normally: after all, conducting scientific research is unthinkable without cooperation with colleagues from other countries." Posted to the independent science news site TrV-Nauka, the letter is in

part an appeal to the international community "that any actions to punish Russia are weighted in such a way as to not punish the very people who object to what Russia is doing," says Mikhail Gelfand, a bioinformatics specialist who helps edit TrV-Nauka. (He notes that he is not speaking on behalf of his employer, Skoltech.) And climatologist Oleg Anisimov, head of Russia's delegation to the United Nations's Intergovernmental Panel on Climate Change, apologized for the invasion during a 27 February meeting, according to news reports.

Russian scientists may face peril for speaking out on Ukraine's behalf. The office of Russia's prosecutor general has declared that anyone caught providing assistance to a nation or organization acting against the Russian Federation could be charged with treason. Authorities have arrested hundreds of street protesters, including Skoltech professor Georgii Bazykin, a prominent evolutionary geneticist who was detained on 27 February after holding up a handwritten sign in downtown Moscow saying, "Stop the War Today." He was released pending trial. Bazykin later tweeted that his plight is a "minor inconvenience compared to what people of Ukraine face now, or what the world including Russia will face if [President Vladimir] Putin has his way."

In Europe, a number of institutions have offered refuge to Ukrainian scientists, some of whom have joined an exodus of more than 500,000 people from the besieged country. The Polish Young Academy, part of the Polish Academy of Sciences (PAN), has lined up scores of institutes and universities willing to host refugee scientists. "We want to find them jobs in their expertise," says Jacek Kolanowski of PAN's Institute of Bioorganic chemistry. So far, they've secured positions for a psychologist in Warsaw, a cancer researcher in Lublin, and a law professor in Poznań. In Germany, the Alexander von Humboldt Foundation's Philipp Schwartz-Initiative, which helps find succor for scholars at risk, has invited Ukrainian scientists to apply for funding with German partners. "Our lab in Berlin will support researchers who had to flee Ukraine," tweeted Matthias Rillig, an ecologist at the Free University of Berlin.

Many Ukrainian scientists have vowed to stay and defend their homeland. "Virtually the entire population has taken up arms," says Oleg Krishtal, a neurophysiologist with the Bogomoletz Institute of Physiology, who is sticking it out in Kyiv. Mosyakin says that although he is a mixture of at least four nationalities, "I am a Ukrainian, period." And most Ukrainians he knows "are not afraid to die for their native land." ■

FUSION

Regulator halts assembly of fusion reactor

ITER must meet safety concerns before welding giant tokamak sections

By Daniel Clery

France's nuclear regulator has ordered ITER, an international fusion energy project, to hold off assembling its doughnut-shaped reactor, called a tokamak. On 25 January, France's Nuclear Safety Authority (ASN) sent a letter halting work until ITER can respond to safety concerns. ITER staff say they intend to satisfy ASN so they can begin welding by July—and still open in 2025.

Fusing hydrogen isotopes under extreme temperatures generates energy. But no fusion reactor has produced more heat than it consumes. The \$25 billion ITER project is designed to demonstrate net energy output, but not until 2035.

One ASN concern is over the 1.5-meter-thick slab of concrete on which the reactor sits. ASN wants reassurance that the loads on the slab are within safety limits.

A second concern is protecting staff and the public from radiation. Thick concrete walls in the reactor building should stop high-energy neutrons produced during operation. But existing "radiological maps do not make it possible to demonstrate control of limiting exposure," ASN writes. ITER Director-General Bernard Bigot says most nuclear facilities only produce a 2D model of potential exposures. ASN wants more evidence that ITER's 3D model is as robust as the simpler one.

A third concern is over slight deformities discovered in two of the nine 11-meter-tall sections that will make up the tokamak. ITER staff developed a fix that would involve robotic and human welders, but ASN is not convinced. Bigot hopes ASN will be satisfied by tests of the welding system on a full-scale mockup.

Bigot says he understands ASN's desire to be careful with a machine that will be the first of its kind. "They want to understand very precisely the safety risks," Bigot says. "So it's not surprising they're taking a little more time." ■

BIOLOGY

Mammoth mangrove bacterium has complex cell

“Eye-opening” discovery challenges evolutionary thinking on microbes

By Elizabeth Pennisi

By definition, microbes are so small they can only be seen with a microscope. But a newly described bacterium living in Caribbean mangroves shatters that rule. Its threadlike single cell can be the length of a peanut—up to 2 centimeters long, 5000 times bigger than many other microbes. And whereas the genetic material of other bacteria floats freely within the cell, the huge genome of this giant is encased in a membrane, like that of more sophisticated cells including those in the human body.

Unveiled in a preprint posted bioRxiv last month, the organism drew astonished reactions. “Fantastic and eye-opening,” says Victor Nizet, a physician scientist at the University of California, San Diego, who studies infectious diseases. “When it comes to bacteria, I never say never, but this one for sure is pushing what we thought was the upper limit [of size] by 10-fold,” adds Verena Carvalho, a microbiologist at the University of Massachusetts, Amherst.

Aside from breaking size records, the bacterium, with its elaborate internal structure, “could be a missing link in the evolution of complex cells,” says Kazuhiro Takemoto, a computational biologist at the Kyushu Institute of Technology. Researchers have long thought that only eukaryotes, from yeast to most forms of multicellular life, package their DNA in a nucleus and compartmentalize various cell functions into vesicles called organelles.

When Olivier Gros, a marine biologist at the University of the French Antilles, Pointe-à-Pitre, came across the strange organism growing as thin filaments on decaying mangrove leaves in a local swamp a decade ago, he had no idea what it was. Not until 5 years later did he and colleagues examine its DNA and realize the filaments were actually bacteria. And they didn’t appreciate how special the microbes were until more recently, when Gros’s graduate student Jean-Marie Volland took up

the challenge of trying to characterize them.

Other microbes, such as slime molds and blue-green algae, form similar filaments, made up of many cells stacked together. But a variety of microscopy and staining methods made it clear the mangrove filaments were each just one enormous cell. This “was something we didn’t believe ... at first,” recalls Volland, now a marine biologist at Lawrence Berkeley National Laboratory.

The largest specimen of this new bacterium so far stretched 2 centimeters, but Carvalho thinks they could grow even bigger if not trampled, eaten, blown by wind, or washed away by a wave. Volland and his colleagues also found that each cell in-

giant sulfur-eating microbe roughly the size of a poppy seed off Namibia’s coast. Its cellular contents are squished up against its outer cell wall by a giant water- and nitrate-filled sac. The sac means the bacteria’s essential molecules only need to diffuse short distances because “only [along the edge] is the cell living,” says Carvalho, who worked on this group of bacteria.

The new mangrove bacterium also has a huge sac—presumably of water—that takes up 73% of its total volume. That similarity and a genetic analysis led the research team to place it in the same genus as most of the other microbial giants and propose calling it *Thiomargarita magnifica*.

“What an excellent name!” says Andrew Steen, a bioinformatician at the University of Tennessee, Knoxville, who studies how microorganisms affect geochemical cycles. “Reading about it makes me feel exactly the same way as when I hear about an enormous dinosaur.”

Its DNA proved extraordinary as well. When researchers at the Department of Energy Joint Genome Institute sequenced it, they found the genome was enormous, with 11 million bases harboring some 11,000 clearly distinguishable genes. Typically, bacterial genomes average about 4 million bases and about 3900 genes.

By labeling the DNA with fluorescent tags, Volland determined the bacterium’s genome was so big because it includes more than 500,000 copies of the same stretches of DNA. No one really knows why. Protein production factories called ribosomes nestled inside the DNA-filled sac as well, likely making the translation of a gene’s code into a protein more efficient. It’s yet another way *T. magnifica* defies preconceptions about bacteria, says Chris Greening, a microbiologist at Monash University, Clayton.

“All too often, bacteria are thought of as small, simple, ‘unevolved’ life forms—so-called ‘bags of proteins,’” Greening adds. “But this bacterium shows this couldn’t be much further from the truth.” ■



A new bacterium’s single-cell filaments are visible next to a dime.

cludes two membrane sacs, one of which contains all the cell’s DNA, like the nucleus of a eukaryotic cell.

“Perhaps it’s time to rethink our definition of eukaryote and prokaryote!” says Petra Levin, a microbiologist at Washington University in St. Louis.

The other sac may be the key to the microbe’s size. Microbiologists used to think bacteria had to be small, in part because they rely on diffusion, which only works over short distances, to carry out respiration, transport nutrients into and around the cell, and get rid of toxins. Eukaryotes, in contrast, actively transport molecules through molecular pumps and channels.

Then in 1999, researchers discovered a



Assistant Attorney General Matthew Olsen has renamed a controversial Department of Justice initiative that has prosecuted academic scientists.

SCIENCE AND SECURITY

New name won't fix all flaws in China Initiative, critics worry

Justice Department promises tighter focus on preventing espionage and no profiling of Chinese academics

By Jeffrey Mervis

University scientists and civil rights groups in the United States are offering qualified praise for the federal government's decision last week to rename and revise the China Initiative, a controversial, 3-year-old law enforcement campaign intended to prevent the Chinese government from stealing U.S.-funded technologies.

"Dropping the name is good," says Steven Pei, an electrical engineer at the University of Houston who has been a prominent advocate for reforming an initiative critics say has unfairly targeted U.S.-based scientists of Chinese origin and improperly subjected researchers who made paperwork errors to criminal prosecution. "But the real issue is how the new policy will be implemented."

Pei and other observers also worry the China Initiative has already done lasting damage to international research collaborations. The same suspicions that fed the initiative, they say, are driving Congress toward adopting tougher disclosure rules for U.S. researchers working with foreign partners and banning certain collaborations altogether.

Since its launch in 2018 under then-President Donald Trump, the China Initiative has resulted in criminal charges against some two dozen academic scientists, typically for failing to tell U.S. funding agencies about their financial ties to Chinese institutions. Most of the defendants were of Chinese origin. Although several pled guilty and were sentenced to prison terms, prosecutors dropped other cases and only one scientist, Harvard University chemist Charles Lieber, has been convicted by a jury.

Both that checkered record and sharp criticism from many quarters led to a review of the initiative by President Joe Biden's appointees at the Department of Justice (DOJ). Last week, Assistant Attorney General Matthew Olsen, who took over DOJ's national security division in November 2021, announced the initiative will now be called "a strategy for countering nation-state threats." The new name, Olsen explained during a 23 February speech at George Mason University, recognizes that the biggest danger to U.S. national security comes from foreign governments, not individuals or a particular ethnic group.

China stands at the top of that list, Olsen said, pointing to its ongoing cyber-

attacks and silencing of dissent as well as several explicit acts of economic espionage. He cited a recent speech by FBI Director Christopher Wray that described China's behavior as "more brazen and threatening than ever before."

In another change, Olsen said federal prosecutors will look more carefully at whether academic scientists accused of disclosure violations should face criminal charges. Science advocates have argued that most such lapses should be treated as a form of scientific misconduct and addressed with civil or administrative penalties. Olsen appeared to tacitly agree, referring to statements from academic leaders that DOJ's "pursuit of certain research grant fraud cases ... can lead to a chilling atmosphere ... that damages the country's scientific enterprise."

Olsen also acknowledged criticism from civil rights advocates that the Trump-era label had "fueled a narrative of intolerance and bias." But he did not apologize for any missteps that might have occurred, a silence that ranks many scientists.

"If you don't admit that you've done something wrong, then how can you prevent it from happening again?" asks Pei, a co-organizer of the nonprofit Asian Pacific American Justice Task Force, which has highlighted the plight of scientists it argues were unjustly prosecuted. Pei and others would like DOJ to conduct a blanket review of all pending cases. "That would go a long way toward winning back the trust of the Asian and scientific communities," Pei says.

In his speech, Olsen said the new strategy would be applied "going forward" and not used to review existing cases. Even so, the government has agreed to a 4-month delay in the case of physicist Zhengdong Cheng, a tenured professor who was fired by Texas A&M University, College Station, after the government accused him of defrauding NASA by not disclosing ties to China in a 2013 grant application. The trial of Cheng, who was detained for 1 year after his August 2020 arrest, was supposed to start on 4 April. But 2 days after Olsen's speech, Cheng's lawyer filed an unopposed motion for delay. It states the government and Cheng "have now entered into good-faith negotiations to resolve the prosecution ... so that justice may be done."

Olsen also promised to exercise greater oversight over FBI-conducted investigations. Michael German, a former FBI special agent now at New York University's Brennan Center for Justice, says the China Initia-

tive emboldened FBI agents to target anyone with ties to China rather than following the traditional practice of gathering evidence of wrongdoing before pursuing a full-blown investigation. “If your boss calls it the China Initiative, then you focus on anyone with connections to China,” German says.

That strategy backfired in the prosecution of Anming Hu, a mechanical engineering professor at the University of Tennessee, Knoxville, who was acquitted in September 2021 in a trial in which FBI agents admitted they had found no evidence of economic espionage. German hopes FBI will now put a priority on cases where it suspects espionage or the theft of intellectual property. Pei suggests using a simple metric for determining whether DOJ is following through on its reforms: “Fewer knocks on the doors of academic scientists by FBI agents.”

But Margaret Lewis, a China scholar and law professor at Seton Hall University, worries the new policy may do little to protect valuable collaborations with China given the abundant “anti-China rhetoric in Washington.” She notes that both the Senate and the House of Representatives have voted to prohibit any scientist supported by China’s foreign talents programs from receiving federal research dollars—a consensus that makes the ban likely to be included in a massive pending bill aimed at strengthening the ability of the United States to compete with China. If that happens, Lewis fears universities could create administrative “buffer zones” that discourage other kinds of interactions with China, in order to make sure that faculty don’t violate the ban.

That prospect troubles Peter Michelson, a physicist at Stanford University. Last year, he helped organize a faculty petition asking Attorney General Merrick Garland to end the China Initiative that has become a template for similar letters from many U.S. campuses. “I’m afraid that university administrators have become increasingly gutless in standing up to government research agencies because they are so dependent on federal funding,” he says. Chinese students—who represent a significant fraction of U.S. graduate students in many technical areas—are increasingly wary of coming to a country they believe doesn’t want them, Michelson adds. “This year [at Stanford] there was a significant drop in the number and quality of Chinese applicants to some of our graduate programs,” he says.

Such thorny issues are a big reason many scholars see DOJ’s announcement as only a first step. The name change “recognizes that our concerns were legitimate,” says John Yang, president of Advancing Justice-AAJC, an advocacy group. “But there is a lot more work to be done.” ■

COVID-19

Studies bolster pandemic origin in Wuhan animal market

Close scrutiny of earliest cases and samples from market suggests virus crossed over from animals sold there

By Jon Cohen

Three new studies offer one indisputable conclusion about the origin of SARS-CoV-2: Despite the passage of 2 years and the Chinese government’s lack of transparency, data that can shed light on the pandemic’s greatest mystery still exist. And although these new analyses don’t all reach the same conclusion for how COVID-19 was sparked, each undercuts the theory that the virus somehow escaped from the Wuhan Institute of Virology, long a focus of suspicions.

The studies examine different aspects of the viral spread at the Huanan Seafood Market in Wuhan, China, the city where the first cases were detected. Two international efforts build the case that SARS-CoV-2 jumped to people from infected animals—a zoonotic leap—at the market, likely twice, at the end of 2019. A third, largely Chinese effort details early signs of the coronavirus in environmental samples from the market. But it suggests the virus was imported there, perhaps from outside the country—a conclusion the University of Arizona’s Michael Worobey, an evolutionary biologist who is a corresponding author of the two international studies, calls “a huge disconnect.”

The studies were posted as preprints and are not peer reviewed, but scientists, biosecurity experts, journalists, and others are already intensely examining their details. “I have been brought closer to the zoonosis side with these preprints,” says Flo Débarre, an evolutionary biologist at the French national research agency, CNRS, who has followed the origin debate closely and not thrown her lot with either the natural-origin or the lab-leak camp. Evolutionary biologist William Hanage of Harvard University agrees these studies “will be taken as a blow” to the lab-leak hypothesis. “They substantially move the needle on the origins in the direction of the market,” Hanage says.

Skeptics of the natural-origin theory maintain the market cluster could merely be a superspreader event touched off when a person infected with a lab-escaped coronavirus visited it. But Worobey thinks further data could make that contention even less tenable. A more transparent analysis of the market’s genetic sampling data, in particular, might identify exactly which species of animals sold there carried the virus.

In one study, Worobey and colleagues describe two subtly different lineages of SARS-CoV-2 that were found in people and environmental samples at the Huanan Seafood Market in late 2019, which they take as a sign that the virus jumped

twice from animals to humans there. Their other study offers a geospatial analysis of the earliest human cases that pinpoints the market as the “epicenter” of SARS-CoV-2’s emergence, showing both lineages infected people who had links to the market or lived near it. It also connects the specific stalls at the market where live animals were sold to SARS-CoV-2-infected environmental samples. “Together,

these analyses provide dispositive evidence for the emergence of SARS-CoV-2 via the live wildlife trade and identify the Huanan market as the un-ambiguous epicenter of the COVID-19 pandemic,” they conclude.

Worobey and colleagues had hoped to release their preprints in the next week but sped up their plans, choosing a preprint server, Zenodo, that posts without any delays, when the Chinese study was posted on 25 February on the Research Square site. Led by George Gao of the Chinese Academy of Sciences and co-authored by 37 other scientists (one is from Canada), that research—which builds on data earlier leaked to the media but never officially published—offers the most detailed description yet of the environmental samples the Chinese Center for Disease Control and Prevention obtained at the Huanan Seafood Market between 1 January and 2 March 2020.

“I have been brought closer to the [natural-origin] side with these preprints.”

Flo Débarre, CNRS



New analyses build the case that COVID-19 originated at the Huanan Seafood Market in Wuhan, China.

In the new preprint, Gao and colleagues analyzed 1380 samples from 188 animals in the market and the environment, including sewer wells, the ground, feather removing machines, and “containers.” They found SARS-CoV-2 in 73 samples. But because all were from the environment, not the animals themselves, they assert that humans introduced the virus to the market. The authors call the market an “amplifier,” not the source, of SARS-CoV-2.

Hewing closely to government assertions on COVID-19’s origin, the preprint by Gao and colleagues notes studies that have reported evidence of SARS-CoV-2 in other countries before it surfaced in Wuhan, making no mention of critiques that attribute that evidence to contamination. It also floats a widely disputed theory that frozen food imported to China might have been the original source. (Authors of the paper, including Gao, did not respond to requests to discuss the work.)

The coronavirus lineage analysis from Worobey and colleagues refines an argument posited by Tulane University virologist Robert Garry last year. In data on the early human cases, Garry had identified two forms of SARS-CoV-2, differing by just two mutations, which he argued surfaced at different Wuhan markets in December

2019. The new work, which includes Garry as a co-author and cites evidence from the Gao study, reshapes that scenario significantly. It concludes that both lineages, dubbed A and B, originated at the Huanan Seafood Market and soon spread in nearby neighborhoods. B likely jumped from animals to humans in late November 2019, leading to the first detected case on 10 December, and lineage A a few weeks later, the group concludes. Either way, the team argues the almost simultaneous emergence of two lineages challenges the lab-origin thesis, as it would require two different viruses leaking at roughly the same time. (Gao and colleagues also found both SARS-CoV-2 lineages in environmental samples.)

The second preprint from the international team builds on a June 2021 Chinese-led study that spent 2 years documenting a tick fever disease in mammals for sale at specific stalls in the market. The new study pinpoints for the first time where species susceptible to SARS-CoV-2—including raccoon dogs, hedgehogs, badgers, red foxes, and bamboo rats—were sold and maps those sites to the positive environmental samples, including one from a “container” the authors believe was a cage. “To anyone who really grasps what is in all of those three papers, I think it’s very hard to dis-

miss that this is a very, very, very strong case that this pandemic started at that market,” Worobey says.

Others say the evidence is not definitive. “They are interesting studies, but I don’t think they close the case on what happened with the origins of the virus,” says Jesse Bloom, an evolutionary biologist at the Fred Hutchinson Cancer Research Center who has criticized colleagues for too blithely dismissing the lab-origin hypothesis. “I’m especially skeptical of the conclusion that there must have been two zoonotic jumps.”

He notes that in about 10% of human transmissions of SARS-CoV-2, the virus acquires two mutations, which means a second lineage could have emerged after the infection of the first human rather than after a second zoonotic jump. Worobey, Garry, and colleagues did a computer simulation that challenges Bloom’s assertion. They modeled many SARS-CoV-2 outbreaks, accounting for how the virus has been shown to mutate, and assessed each simulation’s results against the actual viruses sequenced from Wuhan COVID-19 cases through 23 January 2020. They found there was only a 3.6% chance that a single lineage of SARS-CoV-2 starting in one person could have produced the second lineage and the later known sequences.

The environmental samples from the Wuhan market that tested positive for SARS-CoV-2 might resolve the stalemate over the virus’ origin if they can reveal a specific animal source of the virus. “If you find a positive sample with, say, lots of raccoon dog DNA, you’ve got a hit” on the likely source of SARS-CoV-2, says evolutionary biologist David Robertson of the University of Glasgow, who co-authored the epicenter paper.

But the preprint by Gao and colleagues only notes that those samples contain DNA from many species without specifying which ones—other than humans. “The authors have already done the analysis, they have just not put all the results needed to interpret them in their paper,” says evolutionary biologist Andrew Rambaut of the University of Edinburgh, a co-author of both studies. “This will undoubtedly be fixed if the paper gets through peer review.”

Still, Worobey and his co-authors concede, even that evidence might not be enough to end this polarizing debate. “With the way that people have been able to just push aside any and all evidence that points away from a lab leak, I do fear that even if there were evidence from one of these samples that was full of red fox DNA and SARS-CoV-2 that people might say, ‘We still think it actually came from the handler of that red fox,’” Worobey says. ■



Increasing drought in the Middle East will jeopardize farming throughout the region.

CLIMATE CHANGE

U.N. panel warns of warming's toll and an 'adaptation gap'

Impact of climate change will be worst for the natural world and humanity's most vulnerable

By **Paul Voosen**

Over the past 70 years, humanity has made great strides on a number of metrics: increasing life expectancy, cutting hunger and disease, boosting education levels. But a prime engine of these gains—the burning of fossil fuels—now threatens to slow down global development, according to a report released this week by the United Nations's Intergovernmental Panel on Climate Change (IPCC).

With temperatures already 1.2°C warmer than in preindustrial times, some ecosystems are nearing a hard limit on their ability to adapt, including warm water coral reefs, coastal wetlands and rainforests, and the frigid mountain and polar realms, the report warns. And although humanity can adapt to warming more easily than the natural world, it needs to move faster, says Michael Oppenheimer, a climate scientist at Princeton University and one of 270 report co-authors. “We’re not keeping up. The rate of climate change is faster than our ability to figure out how to deal with climate change.”

The report is part of IPCC's sixth assessment of climate science, a process its volunteer scientists undertake every 7 to 8 years. A first report, released in August 2021, documented the evidence of climate change: rising seas, extreme heat, severe storms. The new report looks at its impacts on humans and nature—and our ability to adapt to it. (A third report, on reducing emissions, is due in April.)

The report recounts a familiar litany of present-day impacts. Half of the more than

4000 plant and animal species studied have shifted poleward or to higher elevations. Corals are bleaching, forests are burning, and marine heat waves are killing swaths of species. Yet the severity of the ecosystem impacts still surprised the report's authors, says Camille Parmesan, an ecologist at the University of Plymouth. Particularly alarming, she says, are the thawing of permafrost and drying of tropical peatlands, which are, in some years, turning these natural absorbers of carbon dioxide into emitters that could accelerate climate change. “We have an increased risk of irreversible impacts,” Parmesan says.

Humans aren't immune. Rising heat and humidity are increasing the number of days where outdoor exertion is nearly impossible and worsening pregnancy outcomes, the report finds. Disease vectors such as mosquitoes have benefited from longer warm seasons and expanding ranges. Worsening fires have increased smoke exposure and incidence of respiratory disease. “People are now suffering and dying from climate change,” says Kristie Ebi, a co-author and epidemiologist at the University of Washington, Seattle.

Drought has slowed the global growth in farming productivity, needed to feed growing populations. Ocean warming and acidification have damaged fisheries and shellfish aquaculture. Storm surge and flooding, worsened by rising seas, are damaging coastal cities. Although the influence of climate on migration and human conflict is murky, severe weather is already displacing populations. “It’s a red flag for the future,” says Brian O’Neill, director of the Joint Global Change Research Institute and a report co-author.

Across the board, the effects will get worse.

Even if global warming can be held to 2°C by later this century—which might be feasible if nations stick to emissions pledges made last year at the U.N. climate meeting in Glasgow, U.K.—up to 3 billion people could face water scarcity. Snowmelt for irrigation could decline by 20% in many river basins; ocean saltwater could displace fresh groundwater on small islands. Food insecurity will worsen, with malnutrition increasing in the global south. Exposure to dengue fever will grow.

No matter the scenario, 1 billion people will be exposed to chronic flooding from rising seas. If warming reaches 3°C or higher, it's possible that in some locations, sweating will no longer be enough to keep the human body from overheating. The Persian Gulf will be the first to reach that threshold, but “It’s going to become a problem in many places of the world, including, eventually, the United States,” Oppenheimer says.

The magnitude of the effects will depend heavily on underlying social conditions such as poverty, health, and governance, the report emphasizes. For example, O’Neill notes, the number of people forced into poverty over a span of 15 years by climate change could range from 10 million to 100 million depending on their vulnerability and that of their lands. Preparing for climate change, the report concludes, is not simply a matter of building seawalls or irrigation systems. “Equally important is improving living conditions across the world,” O’Neill says.

Most projects to adapt to this future are small, fragmented, and focused on near-term risks, the report finds. “There’s an adaptation gap,” Oppenheimer says. “Governments are paying much more lip service than actually doing a lot.” So far the adaptations mostly focus on water: levees and flood warning systems, coastal wetland restoration, soil moisture conservation for farming, and armoring of coastlines.

Bolstering access to health care or establishing heat emergency plans would also make societies more resilient. And the report calls for adaptations to preserve the natural world: restoring the diversity of forests, aiding the migration of species, and protecting more lands and waters to give species space to adapt.

Still the natural world will suffer. But for humanity, IPCC sees some hope, projecting that living conditions will continue to improve under many scenarios—just more slowly than they have in the past. “We’re trying not to jeopardize the progress we’ve made,” O’Neill says. “Though that can be hard to keep in mind when you look outside the window.” ■

COVID-19

China quietly plans a pivot from 'zero COVID'

Scientists are studying how to live with the virus while avoiding a crisis like in Hong Kong

By **Dennis Normile**

China's aggressive "zero COVID" strategy has served it remarkably well. The country has reported fewer than 154,000 cases and 5200 deaths from COVID-19 so far. But as the highly transmissible Omicron variant seeps into the country and the social and economic costs of the zero COVID policy mount, Chinese researchers are examining options for coexisting with the virus, as the rest of the world is doing. Some think that shift may soon begin.

It will be a momentous decision, and the country is sure to proceed cautiously. China wants to avoid COVID-19 outbreaks like the one now overwhelming Hong Kong, which reported more than 34,000 new COVID-19 infections and 87 deaths on 28 February alone. Models predict that toll will climb further.

Yanzhong Huang, a global health specialist at the Council on Foreign Relations, a U.S. think tank, says until recently he believed China might introduce more flexible measures as early as this month. Now, "It is very likely that Chinese leaders may wait till the dust settles" from the Hong Kong crisis, he says. Xi Chen, a public health scientist at the Yale School of Public Health, says China needs more time—up to 1 year—to further raise vaccination and booster coverage and bolster rural health care capabilities.

China's zero COVID policy has relied on mass testing, contact tracing, isolating the infected, restrictions on international and domestic travel, and lockdowns of entire cities. The system has helped China stamp out every outbreak so far, including several of the Omicron variant. But outbreaks are becoming more frequent and widespread. On 25 February, the National Health Commission reported 93 confirmed cases of local transmission in 10 provinces, despite the burdensome countermeasures. Shenzhen, which borders Hong Kong, recently closed museums, libraries, many parks, and beaches in response to an uptick in cases. Apartment compounds face lockdowns if

even one resident tests positive. Most people must get tested every 48 hours.

"The huge inconveniences and difficulties imposed upon people's livelihoods and lifestyles may be turning the wheels of the Chinese policy machinery to consider some kind of policy adjustment," China political analyst Chen Gang of the National University of Singapore (NUS) wrote in a February commentary for Channel News Asia. And COVID-19 countermeasures started to dent China's economic growth in the second half of 2021, says Xi Lu, an NUS specialist in Chinese economic policy. "All of the economic indices point to a continued decline," Xi says. "There will likely come a point when the costs [of zero COVID]

of 7.4 million followed its own zero COVID approach that eschewed citywide lockdowns. It worked relatively well through December 2021, but with the arrival of the Omicron variant, cases have soared. Although vaccination coverage overall is at 76%, only 46% of people in their 70s and 29% of those in their 80s were fully vaccinated. Many elderly were alarmed by early reports of side effects and felt confident in the city's ability to keep the virus at bay. Deaths are concentrated among those who shunned vaccination, says virologist Jin Dong-Yan of the University of Hong Kong (HKU). Unless stricter measures are introduced, 4.6 million Hong Kong residents will have been infected by mid-May, modeling by HKU researchers suggests. More than 3200 will have died.

China, too, will face a wave of infections during any transition. In places that lack community health clinics or general practitioners, even those with mild symptoms are likely to rush to hospitals, and "medical resources will quickly be exhausted," Xi says. Although the vaccination rate now tops 87%, and more than 550 million people have received boosters, vaccination of the elderly lags, especially in rural areas. And with many Chinese vaccines relying on inactivated virus rather than the messenger RNA technology common in the West, it's unclear how fast their

protection wanes or how well they will fare against new variants, says immunologist Rustum Antia of Emory University.

Given the high stakes, many predict China's leaders will proceed cautiously. Huang envisions steps such as reducing the length of quarantines and putting fewer contacts into isolation. Yale's Chen thinks China might first open up one city or region as a test case.

China's big leap may affect the rest of the world as well. Unleashing COVID-19 on a population of 1.4 billion means a lot of people "will be brewing the virus," says Gabriel Leung, HKU's dean of medicine. That will provide ample opportunity for new variants to emerge. "It's not just a national problem, it's actually a global issue," Leung says. ■

With reporting by Bian Huihui.

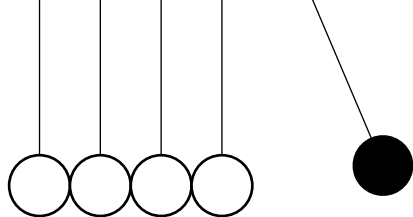


A temporary isolation facility for COVID-19 patients in Hong Kong, where cases and deaths have soared since December 2021.

outweigh the benefits," says Zhangkai Cheng, a respiratory specialist at Guangzhou Medical University. "Whether that point has arrived is up for debate."

The national government is already pushing back at what it considers unnecessary local restrictions. On 18 February, the National Development and Reform Commission told local governments to avoid arbitrary lockdowns and barred unauthorized closures of restaurants, supermarkets, tourist sites, and cinemas. The Chinese Center for Disease Control and Prevention is studying changes to existing control measures to "ensure normal international exchanges and economic development," its chief epidemiologist, Zunyou Wu, said on 15 February.

But the situation in Hong Kong shows why caution is needed. The semiautonomous city



CAN U.S. PHYSICS OVERCOME ITS RECORD OF EXCLUSION?

Data show white institutions falling short and Black colleges leading the way

By **Jeffrey Mervis**; Graphics by **Kelly Franklin**

In the 1990s, physics departments at U.S. universities faced an existential crisis. The number of undergraduate physics majors had plummeted by 25% over 10 years, prompting fears that many departments might disappear or be merged into other programs. Academic physicists scrambled for ways to attract more students, making lectures more interactive and updating the curriculum. The changes had the desired effect: The annual number of physics majors, the first rung in the career ladder, nearly tripled over the next 2 decades (see graphic 1).

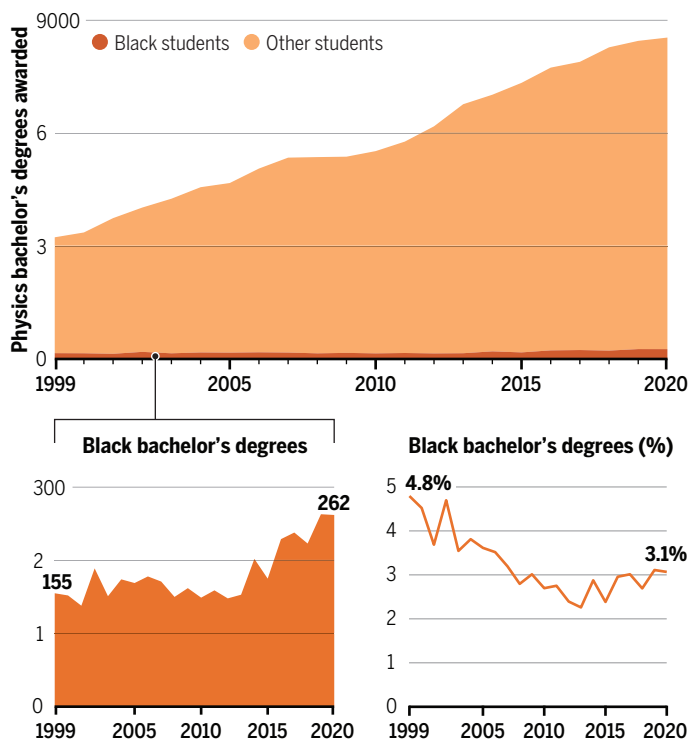
Black students, however, were left behind. In 2017, the American Institute of Physics (AIP) assembled a National Task Force to Elevate African American Representation in Undergraduate Physics & Astronomy (TEAM-UP), the discipline's first deep dive into the lack of diversity at the undergraduate level. The task force's 2020 report documented the crisis in dispiriting detail.

Data from the U.S. Department of Education show the percentage of undergraduate degrees awarded to Black students dropped from 4.8% in 1999 to 3.1% in 2020. Had the number of Black undergraduates earning physics degrees simply kept pace with the overall growth in the major, the current annual total would exceed 350. Instead, it was 262 in 2020.

As bad as those numbers are, they hide how rare Black students are on most U.S. campuses. Some 30% of the 853 U.S. departments awarding physics degrees did not graduate a single Black student between 1999 and 2020, and an additional 30% graduated just one or two (see graphic 2). In contrast, historically Black colleges and

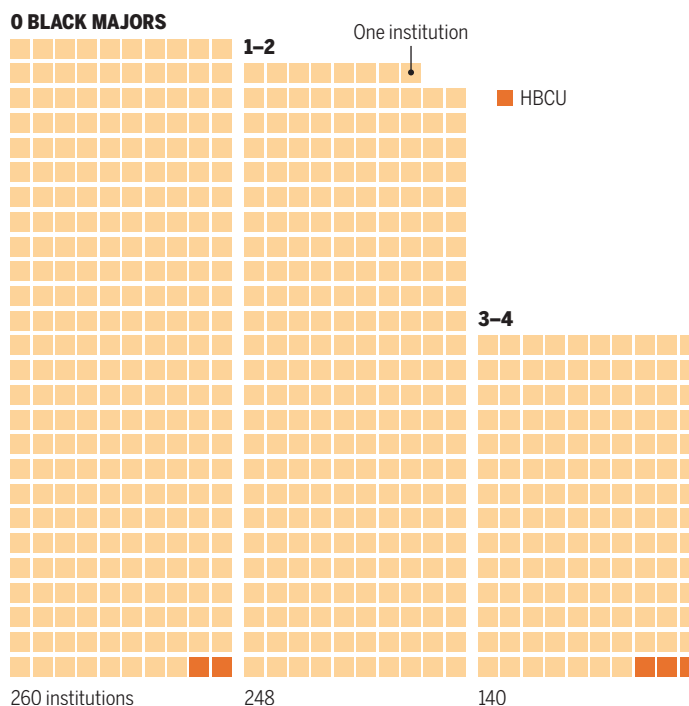
A rising tide, but not for Black students (1)

The number of U.S. undergraduate degrees in physics had tripled by 2020 compared with 1999. Although the absolute number of Black physics majors also rose, their share of the total plummeted.



Black majors rare at most U.S. campuses (2)

Some one-third of all U.S. physics departments graduated no Black physics majors between 1999 and 2020. Despite their small size, historically Black colleges and universities (HBCUs) far outpaced predominantly white institutions in awarding bachelor's degrees in physics to Black students.



CREDITS: (ILLUSTRATION) C. SMITH/SCIENCE; (DATA) NATIONAL CENTER FOR EDUCATION STATISTICS/INTEGRATED POSTSECONDARY EDUCATION DATA SYSTEM/COMPLETIONS 1999–2020 (2020 DATA ARE PROVISIONAL)

universities (HBCUs) lead the nation in graduating Black physics majors despite their relatively small size and limited resources.

The demographics at the graduate level are even more depressing. Black students made up less than 1% of Ph.D. recipients in physics in 2019 (see graphic 4). Over the past 2 decades, the absolute number of physics Ph.D.s awarded to Black students each year has remained essentially flat. In contrast, the number awarded to Hispanic students has increased substantially (see graphic 3).

The near invisibility of Black people has made it easier for the physics community to ignore their perspective. This special package, which draws from interviews of more than 50 Black scientists, seeks to rectify that situation and amplify their voices. They tell of battling systemic racism, which creates an uneven playing field, as well as pushing back against a culture that continues to question their ability and desire to do physics. They describe how that dominant culture in academic physics expects Black people to lead the way in correcting a problem not of their making. They talk about struggling to gain the same professional recognition, respect, and rewards that accrue to white physicists, and how working to improve diversity can jeopardize their own scientific careers. They also describe isolation and debilitating self-doubt, and their frustration and anger that decades of rhetorical support for improving diversity haven't translated into better demographics.

Especially poignant are the experiences of those who have broken through the double barriers of race and gender. In 1972, Willie Hobbs Moore became the first Black woman to earn a U.S. doctoral degree in physics. Exactly 50 years later, the total stands at only 150, according

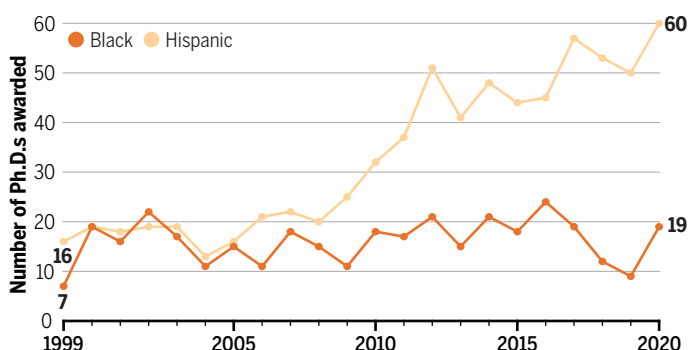
to a list (at aawip.org) compiled by physicist Jami Valentine Miller, a senior examiner with the U.S. Patent and Trademark Office. In 2007, she became the first Black woman to earn a Ph.D. in astrophysics from Johns Hopkins University. Many U.S. graduate physics departments have never handed a diploma to a Black woman.

Although Black scientists in other disciplines face similar barriers, this package examines physics because, as the TEAM-UP report notes, the community's record on diversity "is particularly depressing." The stories describe how the "priesthood," the white men who constitute a majority in the field, has stymied efforts to make meaningful change through a sense of white privilege (see p. 952), and how some universities are building a more welcoming environment by dismantling policies that disadvantage students from marginalized groups (see p. 956). One story examines the outsized role HBCUs have played in educating Black physics undergraduates, and how that role is threatened (see p. 960). Another shows how a graduate program at an elite, predominantly white institution has been more successful than its peers in training black Ph.D.s, using a model that was not intended to address diversity at all (see p. 967). The package also explores the disproportionate number of Black Ph.D. physicists who are drawn to teaching at the precollege and community college levels (see p. 964).

Together, these stories attempt to portray the Black experience in U.S. physics and identify institutions and programs that offer models for change. But there are no simple prescriptions. As the TEAM-UP report emphasizes, the physics community must first internalize how it got to this dismal point before it can make meaningful improvements in the culture. ■

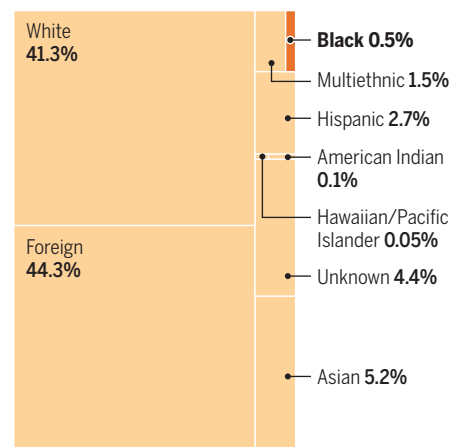
Growing gap with Hispanic students (3)

The number of U.S. physics Ph.D.s awarded to Hispanic students has tripled over the past 2 decades while remaining essentially flat for Black students.



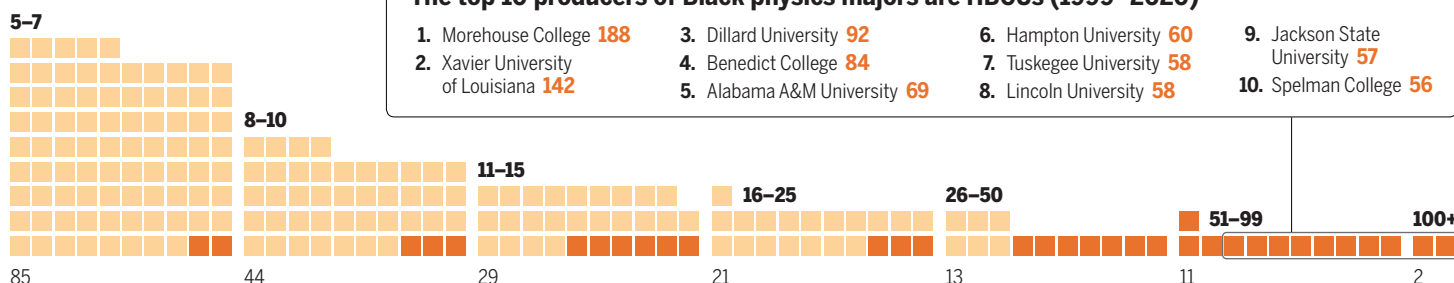
A dearth of Ph.D.s (4)

Black students are underrepresented by a factor of 10 in U.S. doctoral physics programs, which train mainly domestic white students and those from other countries.



The top 10 producers of Black physics majors are HBCUs (1999–2020)

- | | | | |
|--|---------------------------------|----------------------------------|---------------------------------------|
| 1. Morehouse College 188 | 3. Dillard University 92 | 6. Hampton University 60 | 9. Jackson State University 57 |
| 2. Xavier University of Louisiana 142 | 4. Benedict College 84 | 7. Tuskegee University 58 | 10. Spelman College 56 |
| 5. Alabama A&M University 69 | 8. Lincoln University 58 | | |





Physicist April Hodari has documented how the views of a white male "priesthood" shape the culture of U.S. physics.

THE TOLL OF WHITE PRIVILEGE



How the dominant culture in physics has discouraged diversity *By Jeffrey Mervis*

Apriel Hodari has spent many years studying how to improve training and reduce inequity in the scientific workforce. That research has brought her face to face with “the priesthood,” her name for the dominant white male culture in U.S. physics. White men, for example, hold 70% of the faculty positions at U.S. universities that grant physics Ph.D.s.

Hodari wondered whether there was a connection between the priesthood’s views on issues such as racism and sexism and the profession’s deplorable record on diversity. So in 2017, Hodari, a senior scientist at a California company that helps researchers obtain federal grants, and Melissa Dancy, a physics educator at the University of Colorado, Boulder, received support from the National Science Foundation to interview 27 white, male, academic physicists, from senior professors to graduate students.

What the researchers heard during those conversations didn’t surprise Hodari, who is one of only 150 Black women to earn a physics Ph.D. in the United States over the past 50 years. “Not me. Not my colleagues. Not my time. Not my field,” is how Dancy, who is white, summarized their thoughts on why U.S. physics lacks diversity during a presentation last year to a meeting of science education researchers.

Most of those in the small sample—chosen from those who volunteered to participate—voiced concerns about equity and diversity, Hodari and Dancy found. But they were

skeptical that racism and sexism were prevalent in physics. They also couldn’t think of any instances of racist or sexist behavior in their classrooms or labs. And to a man, they believed they were in no position to ease the harm such biases might have on the profession. “In other words, [any problem] is very far away from me,” Dancy reported, “and I have no responsibility for it.”

Hodari and Dancy believe their interviews also offer a peek into the corrosive impact of white privilege on physics. Scholars coined the term decades ago to describe how white people use their membership in a dominant group to assert political, cultural, and economic power over those outside that group.

White privilege allows physicists to “not pay attention to systemic racism because there aren’t any consequences,” Hodari says. She thinks it also explains why many of her colleagues “are completely clueless” about the harmful effects on their profession of attitudes and actions born of privilege and racism.

Black physicists don’t have the luxury of ignoring white privilege. Every one of the more than 50 Black scientists interviewed for this special package described experiences, beginning in their student years and extending into senior faculty positions, in which they were confronted with pernicious behavior associated with white privilege. Some episodes were blatantly racist—white people mocking their appearance or denigrating their intellect—whereas others were more subtle, such as

comments based on negative assumptions about their backgrounds or reasons for wanting to be a scientist.

Battling white privilege requires constant vigilance, and it can take a heavy toll. “I didn’t choose physics to clean up a mess I didn’t make ... [but] I’m bleeding so that people can learn about this toxic environment we face,” says Jessica Esquivel, an associate scientist at Fermi National Accelerator Laboratory (Fermilab) and an advocate for social justice and greater opportunities for Black girls in science. Esquivel, who identifies as an Afro-Latinx lesbian, says she’d rather be recognized for her work on the properties of the muon or neutrino physics. But her activism, she says ruefully, is often “the only thing [my colleagues] notice about me.”

White privilege must be fought on the individual and institutional levels, says Marta McNeese, chair of the physics department at Spelman College, an all-women historically Black college in Atlanta. “Removing barriers to participation isn’t enough,” says McNeese, who is Black. “If you have someone in your department who is toxic, you need to figure out how to protect students from them.”

ONE DAMAGING consequence of white privilege is what’s known as “the Black tax.” It stems from an assumption that Black faculty members, because they are the victims of racism, should do more than their white colleagues to promote diversity. That means spending more time recruiting and mentoring students from underrepresented groups,

more service on diversity committees, and more community outreach. The tax carries a double penalty because those extra efforts—which many Black physicists take on willingly and without compensation—are often discounted, if not ignored, when physicists come up for tenure and promotions.

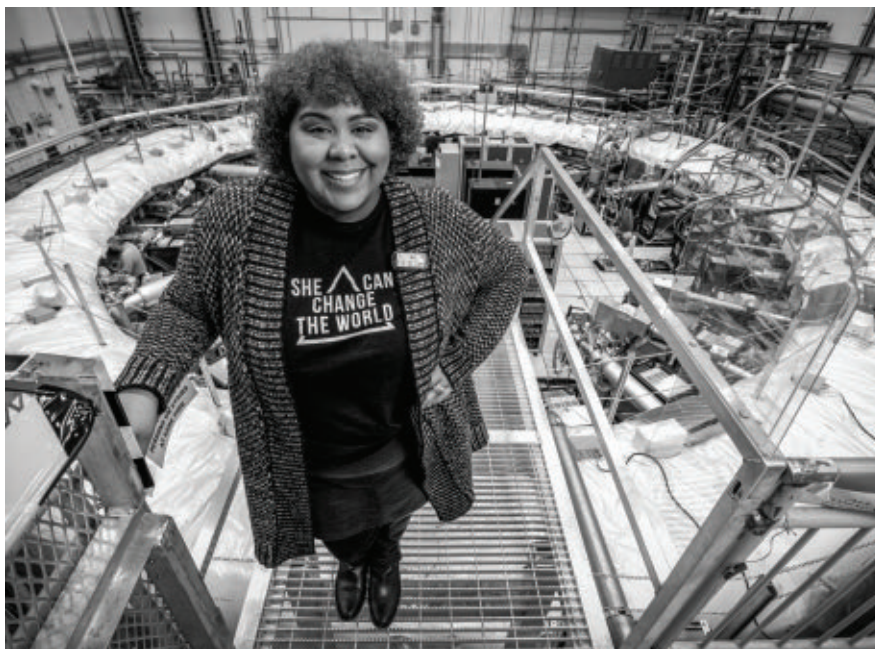
Physicist Adrienne Stiff-Roberts started to pay that tax in 2004 after coming to Duke University in North Carolina, where she says she became the “first—and still only” Black member of the physics department. The North Carolina native says she “knew that Duke had a reputation for not being a welcoming place for Black people,” a history that university officials have acknowledged. But she accepted the tenure-track position with the hope of improving the situation.

As Stiff-Roberts moved up the academic ladder, she poured her energy into fostering greater diversity by training graduate students, mentoring undergraduates, and running a Saturday morning academy for middle-school students. “You can get sucked into trying to make your institution a better place,” she says. But she also kept track of the toll such activities were taking on her research and turned down invitations that didn’t feel genuine. “Don’t ask me to do a lot of work that you don’t value,” Stiff-Roberts says. Instead, she says, “I decided that the best thing I can do is to succeed and become an existence proof.”

Computational cosmologist Brian Nord faces similar challenges at Fermilab, the U.S. government’s premier particle physics center. Along with Esquivel, Nord is part of a group of five Black lab employees who issued a 17-page “Change-Now” manifesto in June 2020, just days after Minneapolis police officer Derek Chauvin murdered George Floyd. In addition to demanding that Fermilab officials hire and retain more Black scientists and adopt policies to achieve social justice, the manifesto urged them to “listen to and do what Black employees say they need, and not make plans for us without us.”

Several months later, Fermilab’s director, Nigel Lockyer, who is white, asked Nord to lead efforts to hire and promote more minority scientists. “I want to build around Brian,” Lockyer said about Nord, who had recently been promoted to become the lab’s only tenured Black scientist. “I need somebody to be an attractor, if you will, so that a young Black scientist [looking for a job] would say, ‘Gee, I want to work with Brian.’”

The 39-year-old Nord says he is honored to receive such a vote of confidence and believes he has “demonstrated that I can lead on these issues.” But he thinks Lockyer’s approach falls far short of the necessary institutional commitment. In particular, Nord wonders why Lockyer decided to put all his eggs into one



Physicist Jessica Esquivel, who works on the Muon g-2 experiment at Fermi National Accelerator Laboratory, says battling white privilege can take a heavy toll.

basket—and one carried by a Black man.

“What if for some reason I had to leave?” Nord says. “Why not build upon the work of the entire cohort of Black scientists at the lab?” Nord is also worried about what happens if the lab’s demographics don’t improve. “Does it then become my fault?”

LOCKYER WON’T be around to see whether his strategy of asking Nord to lead Fermilab’s diversity effort succeeds, having announced his retirement in fall of 2021. But a similar effort at Stanford University 5 decades ago suggests expecting one Black leader to shoulder the burden can falter without sustained institutional support.

In the 1970s, Stanford administrators tacitly agreed to let Arthur Walker, a solar physicist recruited in 1974 as the first Black member of the department, take on the task of diversifying both graduate enrollment and the faculty ranks. “Art was a top scientist, and he brought in others [Black students and faculty],” recalls physicist Arthur Bienenstock, a white emeritus professor and special assistant to the Stanford president who served as the university’s first affirmative action officer in the early 1970s. “Looking back, I can’t say that I or anyone else did anything that was really effective.”

Walker, however, had an impact. In fact, Stanford often claimed that, from the early 1970s to 2000, it led the nation in awarding physics Ph.D.s to Black students. (The total is believed to be roughly two to three dozen, but *Science* could not confirm that because of

a lack of documentation.) The flow of Black graduate students had already begun to dry up, however, by the time Walker died of cancer in 2001. And since his death, Stanford’s track record is indistinguishable from that of other elite graduate physics programs.

Current and former white Stanford professors say one reason for the drop-off was their failure to recruit Black students. Robert Wagoner, who retired in 2012 after 40 years on the physics faculty, recalls “edicts” from department chairs to recruit at conferences they attended that attracted large numbers of students from marginalized groups. But Wagoner always came away empty-handed.

“Everybody wanted them,” he says about the students Stanford tried to recruit. “We did all we could. We’d call them and encourage them to come. But the pool was so tiny.”

Such explanations infuriate Roscoe Giles, a computer engineer at Boston University and longtime diversity advocate who in 1975 became the first Black student to earn a Stanford physics Ph.D. “It drives me crazy,” he says, “to hear people from elite places like Stanford say, ‘We can’t compete.’ It’s the opposite of what you hear them say the rest of the time about their ability to attract the most talented faculty and students.”

OTHER BLACK PHYSICISTS told *Science* they have had difficulty gaining institutional support for efforts to increase diversity—even when they volunteered to lead them. Physicist Kim Lewis, for example, says she worked hard to attract Black students and

faculty to the Rensselaer Polytechnic Institute (RPI), a predominantly white institution in upstate New York where she was a faculty member between 2006 and 2017. But she says senior administrators often pushed back against her efforts.

"I had been doing a lot of recruiting, on my own time," Lewis says, "and one day I realized that none of these students looked like me." Changing the demographics would require RPI to commit time and money, she concluded. "But whenever I tried to bring it up, the response was, 'We shouldn't need to make an extra effort to attract them. They should want to come. We're RPI.'"

In 2018, Lewis moved to Howard University, a historically Black college in Washington, D.C., where she is now a professor of physics and associate vice president of research. RPI's attitude toward recruiting a more diverse student body wasn't the only reason for the move, she says. Another factor was the way she was treated by RPI undergraduates.

"The students there can be brutal," she says. "They didn't like my hairstyle, they accused me of speaking Ebonics [rather than English], and they said I looked like a monkey standing in front of the class."

In contrast, she says, "At Howard I can take off my dean's hat and, for a few minutes, be an aunt," alluding to her approach to mentoring. "I couldn't do that at RPI."

Lewis says she chose not to file a formal complaint at RPI because, as a petite Black woman, she feared for her safety. "I have to walk around campus, and I just don't trust [the students]," she says she told a university official at the time. RPI declined requests from *Science* to address the issues Lewis raised.

The arrogance Lewis says she encountered at RPI is a common manifestation of white privilege in physics, Hodari says. "It's hard to empathize with the problems of marginalized populations when you think you're the smartest person in the room and have all the answers," she says.

Such smugness also hinders efforts to improve diversity, says Mary James, a physicist at Reed College and co-chair of an American Institute of Physics task force that issued a 2020 report on how to reverse the declining percentage of Black undergraduates majoring in physics. "It's hard for some physicists who think they are good at everything to say to themselves: 'Maybe what I've been doing for so long hasn't been effective,'" she says.

Another impediment to change, says James, who is Black, is that physicists can harbor condescending attitudes toward advice from experts in other fields. For example, physicists who pride themselves on making

decisions based on "hard data" may scoff at survey data from social scientists in which students describe deficiencies in their training, she says. "But qualitative data are data, too," James says. She and others think social scientists could help physicists address cultural, sociological, and institutional issues that might sabotage diversity initiatives.

EVEN MEMBERS of the priesthood who have embraced the value of diversity say change doesn't come easily. Keith Bechtol, a white cosmologist at the University of Wisconsin (UW), Madison, says he barely noticed the absence of Black students among the 18 physics majors in his graduating class at the College of William and Mary in 2007. And Bechtol thought little about having "maybe one Black man" among the 45 students in his graduate program at Stanford, where he earned his Ph.D. in 2012.

“

If you have someone
in your department
WHO IS TOXIC,
you need to figure out
how to protect
students from them.

MARTA MCNEESE,
SPELMAN COLLEGE

What finally opened his eyes to the corrosive effect of white privilege, he says, was his first teaching assignment at UW as an assistant professor in 2018. After asking students in his introductory physics class to write a paper on a physics Nobel laureate, he says, "I realized that I was perpetuating all these inequities by forcing them to write almost exclusively about white males."

Bechtol revised the assignment to allow students to write about any physicist. Then he began to devote one class period in the course to a discussion of diversity, equity, and inclusion. Last year, he won a departmental grant to fund research fellowships for a handful of undergraduates from groups traditionally underrepresented in physics.

He's hoping other faculty members will sign up to mentor those students, leading

to a more welcoming environment at UW. "We're not there yet," he admits. The top-tier research institution has no Black faculty in its 48-member physics department, he notes, and records show only two Black students earned undergraduate physics degrees in the 5 years from 2015 to 2019.

Advocates for greater diversity say many more white male physicists will have to follow Bechtol's lead if the field wants to reverse the declining participation by Black students. And Nord says the first step is a real commitment to change.

"At every place I've worked, I've witnessed promises unkept and seen racism in their committees," Nord told the leaders of the American Physical Society last year during a webinar on the value of diversity. "Most of my secure, senior colleagues—white men—encourage gradualism, and whiteness to me that 'change takes time.'"

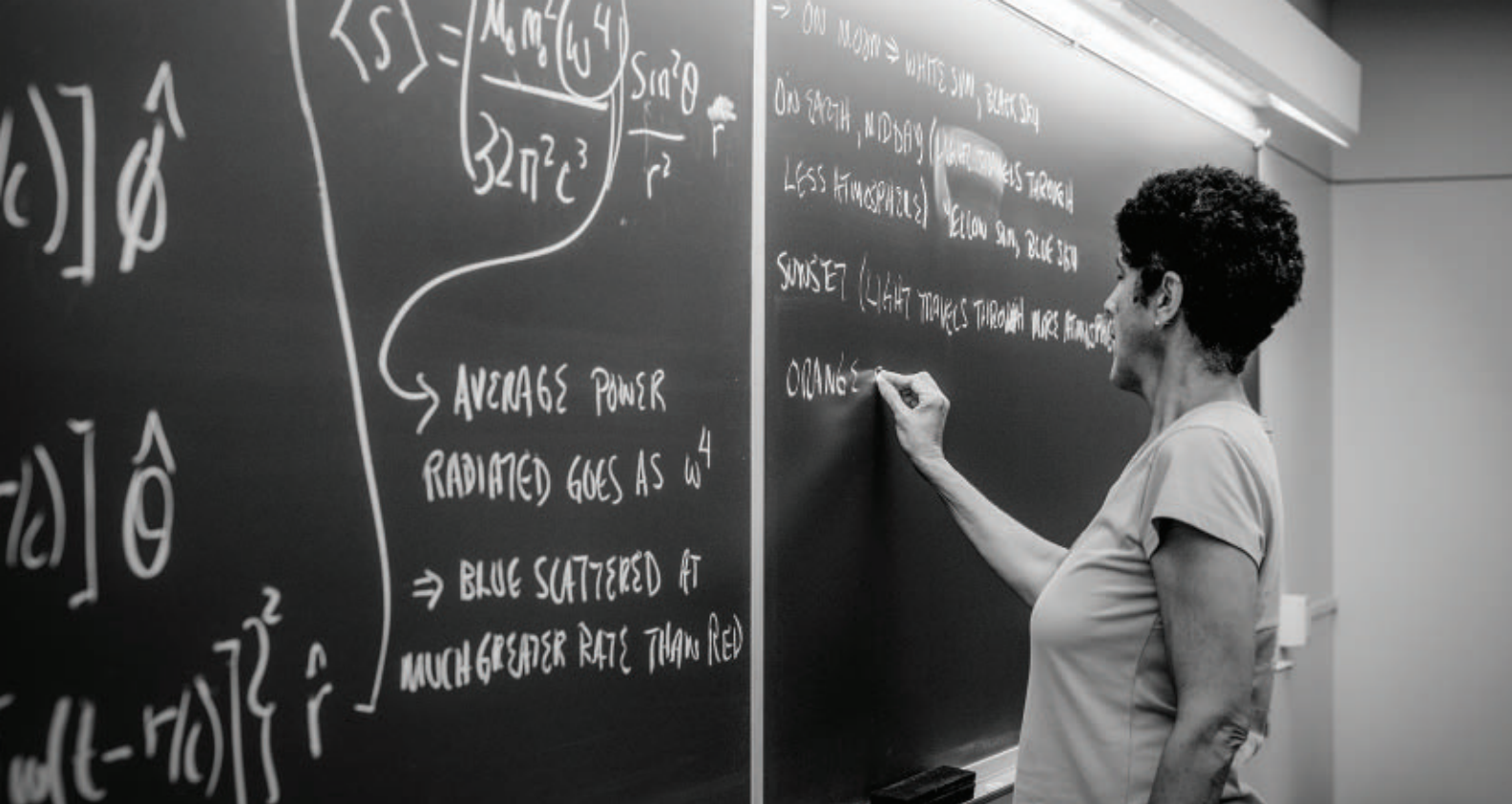
Any change must also be accompanied by greater accountability, Nord says. "Most of the talk I hear about helping people of color navigate the treacherous waters [in physics] amounts to suggestions on how to hop from one lily pad to another to avoid falling into deep water," Nord says. "But that's not enough. You also need to take the negative players out of the game by identifying and enforcing consequences for bad behavior." Those consequences, he says, could include preventing scientists and institutions from receiving federal research grants if they can't show progress in improving diversity, equity, and inclusion on their campuses.

Other diversity advocates, however, think such a punitive policy would be counterproductive. They want the federal government and other funders to use the carrot rather than the stick, offering additional support to institutions and departments that are doing the right thing.

Either way, diversity advocates agree that lasting change won't happen until the priesthood becomes fully engaged. Nadya Mason, a professor at the University of Illinois, Urbana-Champaign, says she is still waiting for that to happen.

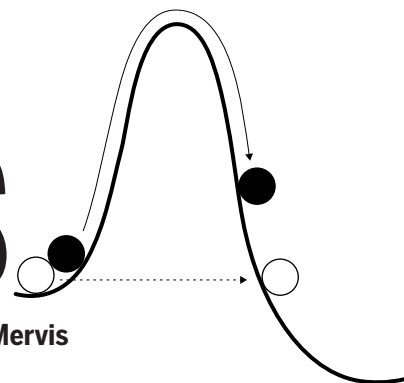
Mason, who is Black, recalls a senior white faculty member asking her for advice during a 2020 campus event on how to combat racism. "I don't know what to do. Can you help me?" he asked her.

"I told him that the point of the event was for whites to think about their actions," Mason says, "not to ask Black people what they think. I don't think he liked my answer. But until white people educate themselves, nothing will happen." ■



FIX THE SYSTEM, NOT THE STUDENTS

Change requires building bridges, removing barriers *By Jeffrey Mervis*



Physicist Mary James was a sophomore at Hampshire College in Massachusetts in 1974 when a professor encouraged her to apply for a prestigious internship at a world-class laboratory. Such competitive internships are often an essential step to becoming an academic scientist, which was her goal. But for a young Black woman from Chicago, the idea of spending 10 weeks at what is now called the SLAC National Linear Accelerator Laboratory in California seemed far-fetched.

"I had never been west of the Mississippi," she says. "And the brochure was so intimidating that I thought, 'This isn't even worth a stamp,'" James recalls. But her Hampshire professor kept pushing her

to apply, and the next year she did—and was accepted. Spending two summers at SLAC set her on the road to earning a Ph.D. from Stanford University and then to Reed College, where she's been a faculty member for 35 years.

Nearly a half-century later, James can still recall a lunch at SLAC that cemented her future. "A bunch of us students were sitting at the grown-ups' table," she says, "eavesdropping on a very lively conversation, when I had an epiphany: 'They are getting paid to do this! I hadn't realized you could make a living doing physics.'"

James also didn't realize that the internships were making her more acceptable to the white male "priesthood" that sets the discipline's culture (see p. 952). That culture, which has historically excluded people

who look like James, expects students to meet a certain standard. And rather than giving students the help they need, James and other Black physicists say, the priesthood too often decides that those students are unworthy of joining the profession.

That way of thinking is so common in physics that it even has a name. Diversity scholars call it the deficit model, and they say it's a major reason fewer than 4% of all undergraduate physics degrees awarded by U.S. institutions go to Black men and women. Sadly, that underrepresentation is getting worse: A 2020 report by the American Institute of Physics (AIP) found Black people now comprise a smaller slice of those degrees than they did 2 decades ago.

James was co-chair of AIP's National Task Force to Elevate African American Represen-



Reed College physicist Mary James co-chaired a 2020 American Institute of Physics report on improving recruitment and retention of Black physics majors.

tation in Undergraduate Physics & Astronomy (TEAM-UP), which wrote the report. It calls on physicists to reject the deficit model and replace it with something that assigns them primary responsibility for diversifying their profession. Black students “have the same drive, motivation, intellect, and capability to obtain physics and astronomy degrees as students of other races and ethnicities,” the report says. “[But] they are choosing majors that are perceived as being more supportive and/or rewarding.”

“Black students don’t need to be fixed,” James says, driving home the point. “We know that there are a robust number of African American students capable of doing physics because they are majoring in other STEM [science, technology, engineering, and math] fields. So instead of trying to change them, let’s talk about why they are turned off by the environment in physics and work to change that.”

THE TEAM-UP REPORT recommends several ways to improve that environment. One is for departments to help students develop what it calls a “physics identity”—the ability to see themselves as a future member of the profession. Another is for physics professors to abandon their traditional role as gatekeepers who only let the “best” students advance and instead find ways to attract and retain a more diverse group of students.

Students at historically Black colleges and universities (HBCUs, see p. 960) take that kind of nurturing for granted, says

Arlisa Richardson, who also served on the TEAM-UP task force. Richardson is a physics professor at Chandler-Gilbert Community College and an alumna of Grambling State University, an HBCU in Louisiana. “At Grambling, people were rooting for us and helping us deal with any problems,” says Richardson, who nearly dropped out of physics during graduate school at a predominantly white institution because of what she and a small cohort of other Black students regarded as a hostile learning environment. Richardson has spent the past decade at Chandler trying “to re-create the experience I had at Grambling,” she says, “by providing students with a welcoming environment, hands-on learning, clubs that are student-led, and free tutoring.”

Even before the TEAM-UP report, some academic physicists had begun to take similar steps. At Vanderbilt University, astrophysicist Keivan Stassun was moved to act by data showing Black undergraduates are being pushed out of the field they want to study.

“The percentage of incoming freshmen who express interest in astronomy [1%] is not different between majority and minority students,” says Stassun, who identifies as Hispanic and says he has “lived the life” of someone from an underrepresented group in science. “But 2 years later, 60% of all students have fallen away, while the rate is 90% for Black students. It’s a massive disparity from which we never recover.”

Similar attrition is occurring across the country, according to a recent decadal study

for astronomy and astrophysics by the National Academies of Sciences, Engineering, and Medicine (NASEM), in which Stassun took part. It reports that, among undergraduate students who say they intend to major in physics or astronomy, those from groups underrepresented in science are almost three times less likely to complete the degree than are white students.

Studies have shown research internships like the one James did at SLAC can help keep students engaged in physics. But some students who would benefit most from such an experience can’t participate, argues Sheila Kannappan, an astrophysicist at the University of North Carolina (UNC), Chapel Hill. Kannappan identifies as a woman of color—“I’m half-Indian, and I appear vaguely brown.” She is also the department’s associate chair for diversity, and once ran summer research internships at UNC funded by the National Science Foundation (NSF). But after several years, she realized NSF’s research experiences for undergraduates (REU) program wasn’t a great fit for her target audience of students from groups underrepresented in science.

“You had to be a superstar to get in,” Kannappan says. But many of the students she wanted to serve “don’t look good on paper—they don’t have 4.0 [grade point averages] and previous research experience. They may also need to work during the summer, or if they are transfer students from a community college, they may need to go to summer school” to catch up on prerequisite courses for their major.

Instead of trying to win another REU grant, Kannappan decided to create a 2-week paid boot camp just for UNC students, including those from marginalized groups. It teaches them computational skills applicable to any area of physics, and is supported by institutional funding and a supplement to her standard NSF research grant. Its short duration, she says, “still allows [students] to go home or take [other] classes.”

In fall of 2021, Kannappan also helped stand up a new peer mentoring program that pairs UNC graduate students in physics with undergraduate students in the department. “We understand that there are other things besides their coursework that affect someone’s ability to succeed in school,” says Zack Hall, who co-directs the program. All of the participants in the inaugural class—six mentees and five mentors—are from groups underrepresented in physics, says Hall, who is on track to become the first Black student to earn a physics Ph.D. from the university.



University of North Carolina, Chapel Hill, physics professor Sheila Kannappan (second from left) is flanked by graduate student Zack Hall (left), undergraduate Nathnael Kahassai (second from right), and graduate student Derrick Carr.

The program relies on volunteer mentors, and Hall says he's careful to make sure the 10 hours or so a week he spends coordinating their activities doesn't interfere with his work on lattice quantum chromodynamics. But Julieta Gruszko, a white assistant professor of physics at UNC, thinks such mentors should be compensated in order to recognize their value to strengthening the profession. So in 2020, when she negotiated her startup package, she included funding for a graduate student to work with individual students and organize public events to promote diversity.

Kannappan and Hall hope these and other efforts will ultimately help UNC improve its mediocre record of training Black physicists. Black students earned just seven of the 232 undergraduate physics degrees it awarded over the past decade, a rate slightly below the national average.

Similar efforts are still uncommon at other campuses around the United States, according to a 2020 AIP survey of 310 physics department chairs. Three out of four chairs identified "low enrollment or retention of historically underrepresented groups" as a major challenge. However, barely half of the department chairs listed "creating an inclusive learning environment"—exactly what the TEAM-UP report says is essential for improving retention rates and increasing diversity—as something they need to address. And fewer than two in five identified improving the department's "climate" as a priority.

PRODUCING MORE Black majors at the undergraduate level is only the first step in diversifying the profession. Such efforts will be for naught if they aren't sustained. Graduate training at predominantly white institutions poses its own set of challenges, because physics departments historically have only recruited from a small and homogeneous group of undergraduate schools and use entrance requirements that often put Black students at a disadvantage.

One increasingly popular alternative is for those departments to partner with institutions that serve large numbers of students from minority groups. Those arrangements, often called bridge programs, come in many flavors. But they share the goal of increasing the number of Black students earning graduate degrees in the natural sciences. Simultaneously, many departments have broadened their definition of a viable candidate.

In 2004, Stassun decided to combine those elements into a bridge program that has become a national model. Students apply to a master's degree program at Fisk University, an HBCU also located in Nashville, Tennessee, that feeds into a doctoral program at Vanderbilt. It caters to promising students with holes in their undergraduate education that need to be filled before they can begin a research-based doctoral training program.

Simultaneously, Vanderbilt reduced what Stassun calls an "overreliance on standardized test scores," in particular

the graduate record examination (GRE) in physics, to winnow the initial applicant pool. Studies have shown GRE scores are poor predictors of success in graduate school, and many minority students who are otherwise qualified do poorly on the exam, Stassun told a meeting last year of the Roundtable on Black Men and Women in Science, Engineering, and Medicine sponsored by NASEM.

The Fisk-Vanderbilt program puts more weight on factors such as perseverance, the ability to set long-term goals, leadership, and community engagement. Those qualities, Stassun says, don't penalize students of color and are also seen as better metrics for success.

Using those criteria helped Vanderbilt attract a more diverse pool of students. But that was only the first step toward producing more Black Ph.D.s in the natural sciences, Stassun explains. "The next challenge was building a sense of community." Vanderbilt's partnership with Fisk serves that role, he says, by giving minority students "1 to 3 years to capitalize on what Fisk has to offer."

And once students began their doctoral work at Vanderbilt, Stassun took on a third challenge: creating a more hospitable environment. That required creating mentoring networks that went beyond the traditional mentoring "dyad" between a graduate student and their adviser, he says.

"I can't be their only source of support," Stassun says. He says the broader mentor-

ing networks, which include faculty from other departments and peers, allow students to tap into “all the experiences they will need” to succeed.

The bridge program has made impressive strides in increasing diversity: Some 80% of the 150 students who have earned master’s and doctoral degrees identify as either Black or Hispanic, according to data compiled by the program, and more than half are women. Along the way, says Stassun, who stepped down as director of the program in 2015, Fisk has become the nation’s top producer of Black students with master’s degrees in physics and materials science. “And my lab has awarded more Ph.D.s in astrophysics to African Americans than any other lab in the country,” he says.

THE FISK-VANDERBILT bridge program has shown that pairing a minority-serving and a predominantly white institution can boost the flow of Black students into physics. A half-dozen major research universities have adopted variations of the model, and the American Physical Society is using the concept to build a nationwide network of graduate programs that have pledged to train more minority students. (Hall earned his master’s degree at California State University, Long Beach, under one such program, which he says “really bolstered my confidence.”)

But not every pairing has been successful. For example, the checkered history of the former Center for Integrated Space Weather Modeling (CISM) based at Boston University shows what can go wrong.

In addition to advancing research in the emerging field of space weather, CISM hoped to alter the field’s overwhelmingly white demographics. So the center partnered with Alabama A&M University (AAMU), an HBCU with a new graduate program in space physics. The plan was to have students earn a master’s degree from AAMU before pursuing doctoral work at that university or elsewhere. The center received 10 years of funding from NSF, which wanted to foster greater diversity in the discipline.

But AAMU’s program only graduated two Black students—Fana Mulu-Moore and Samaiyah Farid—over its decadelong affiliation with the center. And both women say the partnership was little help to their careers. In particular, they viewed themselves as tokens in a program they say only gave lip service to diversity.

“Sometimes it felt that they were just checking a box,” says Mulu-Moore, who spent 10 years trying to find her place in physics after also earning her Ph.D. from AAMU in 2009. “We were doing a lot of outreach to minority schools for CISM. But I don’t know of a single minority student who came through the CISM program and went into the field.”

Farid left the AAMU program after her master’s degree to work at the Harvard-Smithsonian Center for Astrophysics. She hoped it would be a springboard into space physics. But she says she was the only Black scientist there and was subject to racial taunts. After leaving that job and enrolling in a doctoral program at the Uni-

versity of New Hampshire (UNH), Farid said she experienced a similar sense of isolation and hostility toward her as a Black person. It was a “horrible experience,” she recalls. Although the department was a partner in CISM, Farid felt it offered her no additional support or guidance.

At the same time, her affiliation with the program has helped advance her career. She is now doing a postdoctoral fellowship at Yale University that is only available to astrophysics students who have gone through bridge programs at Vanderbilt, Columbia, and Ohio State universities.

Mulu-Moore now teaches at Aims Community College in Colorado. Last summer, after several years living a precarious existence as an adjunct, she was hired as the department’s only full-time faculty member. She relishes teaching first-generation college students who remind her of herself when she arrived in the United States 20 years ago from Ethiopia. “It’s a small, nurturing school, and I feel that I’ve found my niche,” she says. Along with engaging in extensive community outreach to broaden the pool, Mulu-Moore tries to connect her most promising students with the kind of high-quality summer internships that helped launch James’s career. One of those students is Carter Woodson, a biracial student who graduated from a rural West Virginia high school and has spent 10 years trying to acquire a college education, the cost of which is often beyond his means.

Woodson teaches and tutors at a local high school that Aims operates, a job that pays the tuition for his science courses and feeds his long-term ambition of becoming a science and math teacher. When Mulu-Moore told him about a 10-week, paid summer program run by the National Solar Observatory in conjunction with the University of Colorado, Boulder, he jumped at the chance. “I’ve always loved math,” he says, “and this sounds like the chance to do something really interesting.”

Mulu-Moore knows he’ll face stiff competition. “These internship programs are usually looking for students from the top universities,” she says. “But Carter checks all the boxes. He’s very smart, he’s a full-time student, and he’s absolutely determined to get a degree.”

To Mulu-Moore, Woodson is exactly the kind of student the U.S. physics community should be encouraging and welcoming. “He’s just as capable,” she says, “as somebody from an Ivy League school.” ■

“

Black students don’t need to be fixed. ... So instead of trying to change them, let’s talk about **WHY THEY ARE TURNED OFF** by the environment in physics and work to change that.

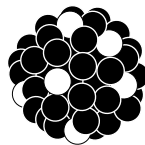
MARY JAMES,
REED COLLEGE

versity of New Hampshire (UNH), Farid said she experienced a similar sense of isolation and hostility toward her as a Black person. It was a “horrible experience,” she recalls. Although the department was a partner in CISM, Farid felt it offered her no additional support or guidance.

But Farid didn’t give up. After dropping out of UNH and taking a short respite, she resumed her doctoral studies at Vanderbilt under Stassun. Although Farid was too advanced to qualify for a master’s degree through the bridge program, she participated in many of its activities.

Looking back, Farid thinks her experiences at AAMU, UNH, and Vanderbilt show that a partnership between a predominantly white institution and a minority-serving institution is no panacea. “It defi-

BLACK COLLEGES CAN'T DO IT ALL



At historically Black colleges and universities, tight funding threatens an extraordinary record of nurturing Black physicists

By **Jeffrey Mervis**



Robert Dixon has spent more than 50 years mentoring physics students at historically Black colleges and universities.

CREDITS: (PHOTO) MATTHEW ODOM; (ILLUSTRATION) C. SMITH/SCIENCE

Historically Black colleges and universities (HBCUs) in the United States have had outsize success in launching Black students into physics. Although only 9% of all Black undergraduates attend the country's 100 HBCUs, those schools for decades have awarded the majority of physics degrees earned by Black students. HBCUs also claim all the slots on a top 10 list of schools graduating the most Black physicists, despite having departments that are much smaller and have less funding than those at predominantly white institutions (PWIs).

How do they do it? The key, say dozens of Black scientists who have worked at HBCUs or are knowledgeable about them, is that they provide a nurturing environment that addresses the academic, financial, emotional, and cultural needs of their students.

But HBCUs' ability to do so is threatened by declining overall enrollments over the past decade and the worsening of already serious financial constraints. In 2019, HBCUs garnered \$341 million in federal research funding, down 15% from 2001; over the same 2 decades, the amount going to all U.S. universities grew by 65%, to \$38 billion. The absolute number of Black students earning undergraduate physics degrees from HBCUs fell by half between 1996 and 2018, according to data from the American Institute of Physics (AIP). And HBCUs' share of all Black physics graduates, which stood above 50% in 2006, was only 28% in 2019. (Only one-third of HBCUs offer an undergraduate degree in physics.)

That shifting balance would matter less if the physics departments at the nation's research heavyweights—all PWIs—were doing a better job of deploying their large research budgets and hefty endowments to fill the pipeline with Black physicists. But even those with the best records are falling far short of what's needed to improve diversity.

The data for the Massachusetts Institute of Technology (MIT), one of the nation's leading universities, bear that out. Between 2012 and 2017, MIT awarded more undergraduate physics degrees to Black students—12—than any other PWI, according to AIP statistics. Even so, none of the 42 physics majors graduating from MIT in 2017 was Black. By comparison, eight Black students earned physics degrees that year from Morehouse College, an all-male HBCU in Atlanta.

That stark racial disparity is why Sylvester James Gates, an eminent theoretical physicist who is Black, views HBCUs as a precious resource for the community. "They are our intellectual lifeboats," Gates said last year

during an American Physical Society webinar on diversity that he chaired as APS president. "Investing in them is a bet on ourselves."

FOR HBCUs trying to build robust physics programs, Morehouse has long been an exemplar. A 2020 report from AIP's National Task Force to Elevate African American Representation in Undergraduate Physics & Astronomy (TEAM-UP) found the college produced 32 Black physics majors between 2012 and 2017, a dozen more than second place Alabama A&M University. A generation earlier, Morehouse had enjoyed similar success under Robert Dixon, a Black physicist who led its physics department from 1988 until 2004.

"Bob Dixon has probably trained more African American physics undergraduates than anyone else in the country," says Warren

“
Bob Dixon has
probably trained more
**AFRICAN AMERICAN
PHYSICS
UNDERGRADUATES**
than anyone
else in the country.

WARREN BUCK.
UNIVERSITY OF WASHINGTON, BOTHELL

Buck, a Black physicist and former chancellor of the University of Washington (UW), Bothell. "He's underrated because he doesn't look for glory. But he's very effective," adds Buck, a former chair of the physics department at Hampton University, an HBCU in Virginia.

Now 80 and semiretired, Dixon has worked as a faculty member and administrator at a half-dozen HBCUs over more than 5 decades. Arguably his greatest success came at Morehouse, where he earned an undergraduate degree in 1964 and then returned 2 decades later to join its faculty. Its small physics program was limping along, he says, and after becoming chair he realized the only way to build it up was "to look for grant opportunities."

His success in winning federal funding allowed him to grow the number of faculty from three to 11, offer scholarships, and hire

staff to plan a range of events that raised the department's campus profile. "We became a hub of activity," he says, "and it drew students into the program."

Nicholas Fuller was one of them. Raised in Trinidad and Tobago by a single mother who regarded a good education "as the only path to success," Fuller excelled at science in high school. When it was time to go to college, he chose Morehouse because it offered him a full scholarship. Dixon's approach to training the next generation of physicists also resonated with him.

"The level of nurturing is the key," says Fuller, who went on to earn a doctoral degree in applied physics at Columbia University and now directs global hybrid cloud services for IBM. "If you failed an exam, Dr. Dixon let you know that you still had a bright future. Without that support, students lose confidence in their ability to become a scientist or engineer, especially if they don't see many people in those jobs who look like them."

In 1996, Dixon won a \$7.3 million grant from a U.S. Department of Defense (DOD) program designed to strengthen undergraduate science at HBCUs. "DOD's original plan was to fund 20 schools," he recalls. "But I asked for all of the money, on the grounds that we had the best proposal."

Dixon used the money to create the Center for Excellence in Science, Engineering, and Mathematics (CESEM) at Morehouse. CESEM provided full scholarships and intensive academic and career guidance to 50 Morehouse freshmen seeking an undergraduate degree in the natural sciences, math, and engineering, including 17 in physics. Some 85% had earned degrees by the end of the grant, and upward of 80% chose to continue to a graduate science, technology, engineering, or math (STEM) program. Two hundred additional Morehouse STEM majors were able to take advantage of a subset of those activities.

The grant also supported a cohort of 50 ninth grade students from Atlanta public schools, providing academic and career counseling for the students, all of whom graduated, and professional development for their teachers. Although the program was not designed to be a recruiting device for Morehouse, some participants enrolled there and majored in science.

Yet Morehouse's success, like that of other physics departments at HBCUs, rested on a shaky foundation. In 2001, DOD officials declined to renew the 5-year grant that supported CESEM, and Dixon asked senior college administrators for internal funding to continue the program. But they turned him

down, he says, forcing him to shut the center and lay off its five-person administrative staff.

Without the scholarships and paid internships, students drifted into other fields. Over the next 2 years, Morehouse's annual production of Black physics majors plunged from six, a number that had sustained its top ranking, to zero. In 2004, after 16 years as department head, Dixon threw in the towel and took a job at Grambling State University, a Louisiana HBCU. "It was very disappointing that the college didn't give us a chance to continue what we were doing," he says. Physicist Walter Massey, Morehouse's president at the time, declined to comment.

However, Dixon had sown the seeds for the program to thrive again when, in 1997,

retired, said recently that seeing that initiative falter was one of his biggest regrets.

Even at the time, Rockward and his colleagues say, Georgia Tech didn't match the welcoming atmosphere of an HBCU. Rebuffed when they tried to join a study group, for example, the Black students converted a departmental storage room into a retreat they called "the Black Hole."

Moving to Morehouse required Rockward to make adjustments. "No startup package, and all I had to work with were undergraduates," he recalls. But he won a string of federal grants that included collaborations with colleagues at research-intensive universities, which provided internships for students to apply what they were learning in class.

One big attraction was the chance to replicate his success at Morehouse on a larger scale. "[Morgan State] had a strong record in the 1980s for graduating African Americans before things started to slide, and they were interested in reviving that tradition," he says.

Even better, Rockward says, school administrators had vowed that Morgan State would become a Tier 1 institution by 2030, a designation based on the amount of its external funding. Rockward hopes meeting that goal will catapult Morgan State into the ranks of Georgia Tech and other heavyweight physics programs at PWIs.

WARREN BUCK, former physics chair at Hampton, is another Dixon protégé who built a successful program at an HBCU by following his mentor's template—and by adding his own wrinkles. Buck was an undergraduate at Morgan State in 1966 when he met Dixon, then a new faculty member in his first academic job. "Bob convinced me I could do physics," Buck says.

He earned his Ph.D. from the College of William and Mary and joined the Hampton faculty in 1984. He expanded its physics department and also created a doctoral physics program, one of only five at an HBCU. Those efforts profited from the university's proximity to the Department of Energy's newly opened Thomas Jefferson National Accelerator Facility (JLab), home of the Continuous Electron Beam Accelerator Facility. Buck also won federal funding for a research center of excellence in nuclear and high energy physics, using the money to recruit faculty as well as to fund students to work with the world-class physicists at JLab. "I wanted to show that we could play with the big guys," he says.

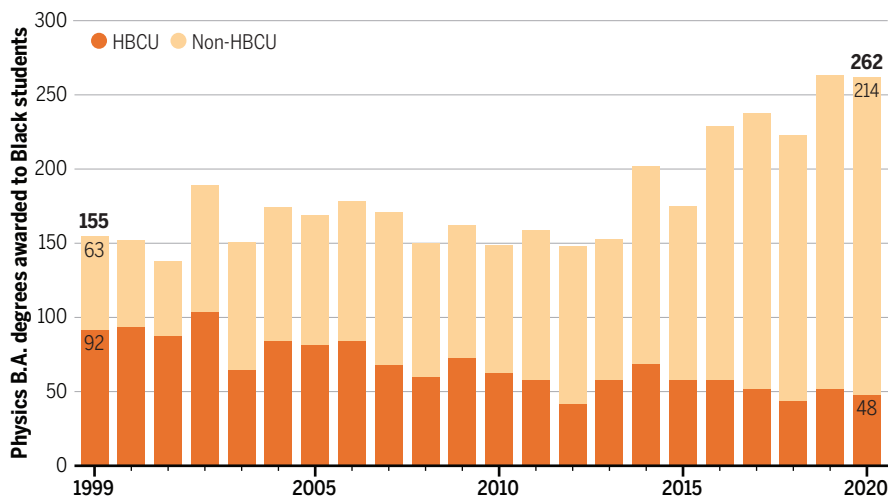
That approach appealed to Devin Walker, now an assistant professor at Dartmouth College. In 1994, Walker was a Black high school student in Memphis, Tennessee, with his sights set on MIT. "I had the grades, they had lots of resources, and I knew that smart kids went to MIT."

MIT accepted Walker—but didn't offer him a scholarship. So he sought out Buck during an event at Hampton, where Walker's siblings were enrolled. Walker's initiative—and resume—convinced Buck to offer him a full scholarship. In 2006, Walker became the first U.S.-born Black student to earn a physics Ph.D. at Harvard University, working under prominent particle physicist Howard Georgi, whom he had met during a JLab summer internship.

Despite Buck's success at Hampton—in 2001, five Black students earned physics Ph.D.s, an extraordinary feat the department repeated in 2002—he says the

Waning clout

Historically Black colleges and universities (HBCUs) once accounted for more than half of all U.S. physics degrees awarded to Black undergraduates. That share has now declined to less than one-fifth of the total.



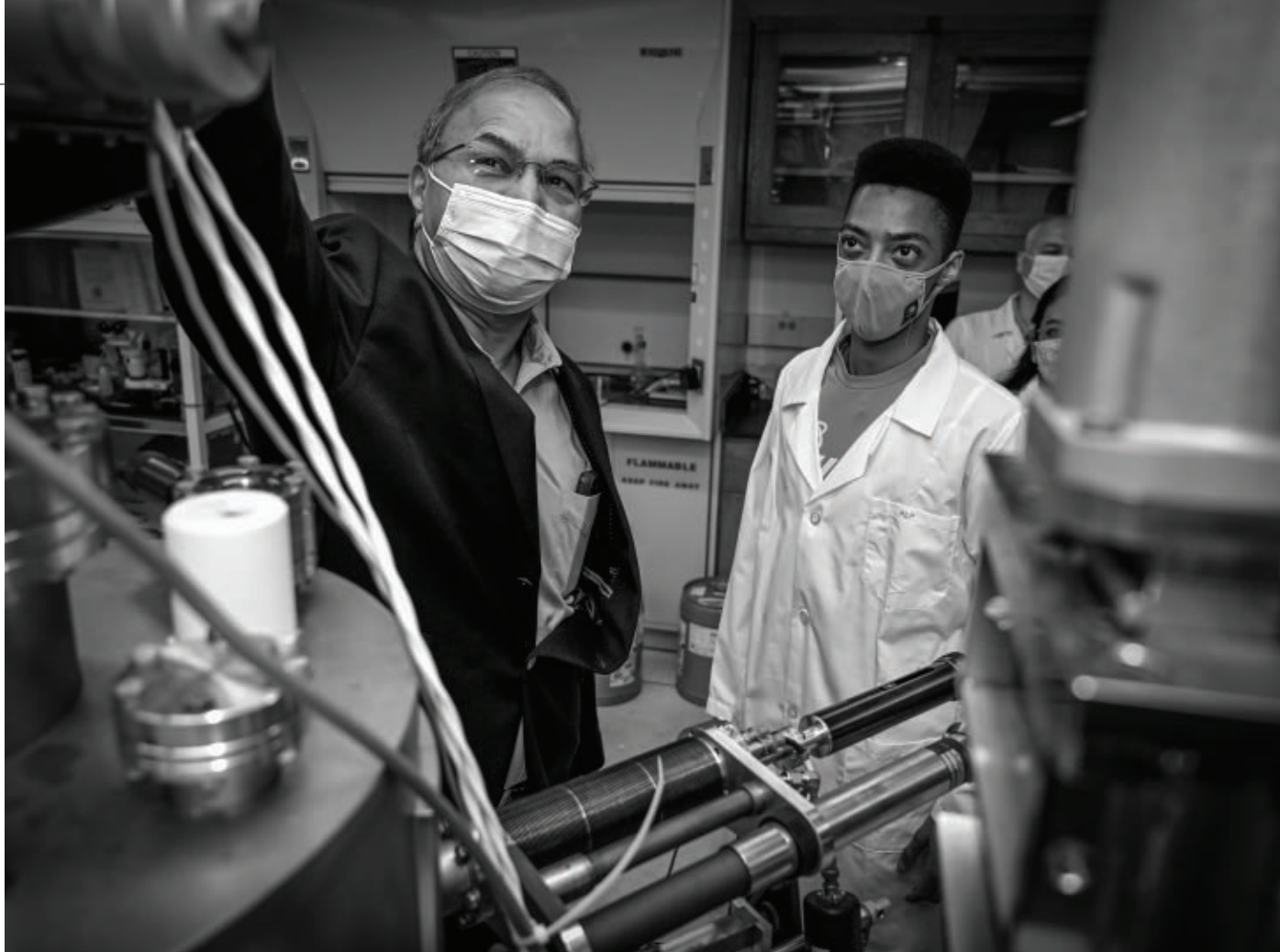
he recruited Willie Rockward, a Black physicist. Rockward had graduated from Grambling, where he was drawn into the field by the school's small but nurturing physics department. "Dr. [Odom] looked like me," Rockward says about the department's long-time chair, Thomas Odom Jr., one of several Black faculty members in the department. (Black science faculty are often in the minority at HBCUs as well.)

Rockward went on to earn his Ph.D. from the Georgia Institute of Technology (Georgia Tech), where he was part of a first ever cohort of five Black students recruited by physicist Henry Valk, a senior administrator. A few years later, Valk, who is white, recruited a second cohort of similar size. It was a short-lived attempt to diversify the physics department, and Valk, long since

In 2011, Rockward became department chair, giving him a chance to revamp a sequence of three calculus-based courses with notoriously high attrition rates. He reshuffled the instructors to match their strengths with the content of each course. Their success in retaining students led to larger graduating classes in physics, a virtuous cycle that made it easier to attract more majors.

Those and other moves helped Morehouse return to the top of the national rankings in producing Black physics majors. But eventually Rockward, like Dixon, felt that his efforts were not valued and that his career was stagnating. "I didn't get promoted to full professor," he says. "So I said, 'OK, that's your call.' And I started to look around."

In 2019, Rockward landed at Morgan State University, an HBCU in Baltimore.



At Morgan State University, a historically black university, physics professor Ramesh Budhani (left) works with undergraduate Don-Terry Veal Jr. in a spintronics lab.

school's senior administrators balked at supporting his vision for a more robust program. "Physics is expensive, and they didn't see its value," Buck says. Hampton officials declined to comment. But the online biography of its longtime president, William Harvey, emphasizes his concern for the bottom line by noting that "Dr. Harvey is an astute businessman who runs Hampton as a business for educational purposes."

Buck, who says he was "worn out and very frustrated" at Hampton, saw UW Bothell, an emerging 4-year college that caters to students from groups traditionally marginalized in science, as a chance to start over. Within a few years after he left to become UW Bothell's first chancellor in 1999, the flow of Black graduate students into physics at Hampton had dried up.

TOP U.S. RESEARCH universities have long relied on HBCUs to be the first rung on the academic ladder for Black physicists. The success enjoyed by Dixon, Rockward, and Buck shows how crucial federal research grants are to that role. But those dollars are in short supply at HBCUs. In 2019, for ex-

ample, North Carolina A&T State University led all HBCUs in winning federal research support, with \$22 million. In contrast, five PWIs received more than \$750 million each in federal research that year.

In competing for those funds, HBCU faculty are at a decided disadvantage compared with their peers at PWIs. Heavy teaching loads often leave them little time to do the preliminary work needed to win a federal grant, and few HBCUs have the institutional funds to supplement any grants to support student research.

In addition, the federal government prefers to back one-off experiments in education. "We don't make long-term, sustained investments in STEM education like we do for research projects," says physicist Claudia Rankins, former dean of science at Hampton who recently retired from the National Science Foundation after 2 decades of managing programs to broaden participation. "If you study some small particle, you can ... be funded for decades as long as you show progress. But if you are proposing to do something in STEM education, or institutional capacity building, you're fortunate to get 5 years of fund-

ing. And then you're expected to move onto something else."

The TEAM-UP report calls for U.S. physics departments to double the number of Black majors by 2030. Reaching that goal will require PWIs to boost their output, and collaborations with HBCUs are one obvious route to success. But Marta McNeese, chair of the physics department at Spelman College, an all-women HBCU in Atlanta, says those relationships will need to be genuine partnerships, not a check-the-box exercise.

"I've had people ask me to sign a letter of support [on a grant application], giving me 48 hours to sign, and telling me that all I need to do is send our students to their summer program," McNeese says. "They want to address diversity, equity, and inclusion, but they don't involve us in the planning."

The PWIs will also need to emulate the nurturing environment at HBCUs. "Our students are already stressed academically, politically, and economically," McNeese says. "The role of an HBCU today is to give students a place where they can be themselves." ■

CALLED TO TEACH

Black physics Ph.D.s are more than twice as likely as other groups to teach in high schools and community colleges. For many, it's a mission

By Ashley Smart

For years, Maritza Tavarez-Brown couldn't talk about the end of her astronomy career without tears. She'd wanted to be an astronomer since high school. But she struggled in her introductory physics classes at Yale University. At one point, she remembers, the department chair told her she should reconsider her major. Determined, she transferred to New York City's Hunter College, earned bachelor's and master's degrees in physics, and completed a Ph.D. on the properties of dark matter halos at the University of Michigan, Ann Arbor. She was offered a postdoc at the University of California, Berkeley, the kind of prestigious apprenticeship that could catapult her to an academic faculty position.

She turned it down. She and her husband had just relocated with their 5-year-old daughter to Seattle, and they decided moving to the San Francisco Bay Area wouldn't work for their family. That was more than 16 years ago, but Tavarez-Brown remembers it as if it were yesterday.

"I was devastated," recalls Tavarez-Brown, who is of Afro-Cuban descent. "In Spanish, we have this saying, 'You're work-

ing so hard that you're burning your eyelashes,'" she says. "I had done all this hard work, and now the thing that I was looking for ... I can't really do." Instead, she took a position as a long-term substitute physics teacher at Forest Ridge School of the Sacred Heart, a middle and high school for girls in nearby Bellevue, Washington.

Today, "Dr. T," as her students call her, is still at Forest Ridge, and she is part of a long but little-known tradition in U.S. science education: For decades, Black Ph.D. scientists have opted to teach outside the ivory tower in proportions higher than any other race or ethnicity. They are more than twice as likely as their non-Black peers to teach at 2-year colleges, high schools, or other precollege institutions, according to an analysis of the National Science Foundation's (NSF's) Survey of Doctorate Recipients. The disparity is present across a range of disciplines, but it has been especially pronounced in the physical sciences, where roughly one in 10 Black Ph.D. holders teaches outside of 4-year higher learning institutions—and where in some years Black Ph.D. holders have been more than three times as likely as the average to hold those jobs. These trends

date back at least to 1999, the first year NSF published the relevant data.

Education experts puzzle over the causes of the disparity. But for their part, Tavarez-Brown and other Black Ph.D. physicists who have made the leap say they are finding fulfillment on a career path that many science graduates never consider traveling. For the students they teach, their career choices mean a chance to learn from trained scientists—and to see new role models in science.

THE RELATIVE SURPLUS of Black Ph.D. scientists teaching in high schools and 2-year colleges has slipped under the radar of many researchers. Ebony McGee, an associate professor of diversity and science, technology, engineering, and math education at Vanderbilt University, calls it "extremely surprising." But she sees a possible explanation, pointing to evidence that many Black scientists and engineers flee the ivory tower because they find the environment constraining, marginalizing, and systemically racist. "What it sounds like to me is that the structures don't allow them to see themselves as authentically in [uni-



iversity] faculty positions as they do in community college or high school positions.”

A close look at the NSF data suggests additional factors may be at work. The data indicate Black scientists who obtain doctorates are no less likely to teach at 4-year higher learning institutions than Ph.D. scientists from other racial and ethnic groups. (The NSF data don’t show what fraction of those faculty are at research-intensive as opposed to teaching-intensive schools.) Rather, for reasons that remain unclear, the surfeit of Black doctorates opting to teach at high schools and 2-year colleges appears to be offset primarily by a deficit of Black doctorate holders working in private industry.

Kimberly Griffin, a professor of higher education, student affairs, and international education policy at the University of Maryland, College Park, cautions that it would be a mistake to assume that Black Ph.D. holders who opt for precollege and community college teaching careers are somehow settling. “This might be a very intentional choice,” Griffin says—“different than what they anticipated when they started [their Ph.D.], but still very intentional.”

VANESSA COHEN GIBBONS’S decision to pursue a teaching career was very much intentional. She realized toward the end of her Ph.D. that what she enjoyed more than crunching numbers and writing papers was talking to people. Both of her parents taught at community colleges, and she had an aunt and a cousin who taught at public schools. Plus, she had enjoyed the teaching she’d done as a graduate student—and she’d excelled at it, winning student teaching awards.

It wasn’t that she lacked the research credentials to pursue a university faculty position. Her dissertation was on the dynamics of merging black holes, an area that would soon become one of the hottest in physics, with the dramatic first detection of gravitational waves from such mergers. In the run-up to academic hiring season, her adviser had even helped arrange for her to give a series of symposia and public talks—which, she says, were “very well received.”

But Cohen Gibbons, who is Black, figured a high school teaching position would offer her a chance “to be much more than just somebody who’s delivering content”—to engage with students in areas such as social and emotional learning and social

Maritza Tavarez-Brown left behind a budding career in astronomy and found fulfillment as a teacher.

justice. So, just months before the academic hiring season began, she decided to apply exclusively for high school teaching jobs. Before long she had multiple offers. She accepted a position at the Garrison Forest School, a private, all-girls K-12 school in suburban Baltimore. (The high school teachers interviewed for this story all opted for private schools, noting, among other factors, that those jobs allowed them to bypass the time-consuming certification process many public schools require.)

Cohen Gibbons’s realization, years into her graduate studies, that an academic research career wasn’t for her is hardly unusual. Studies have repeatedly found that, in aggregate, students tend to lose interest in faculty positions over the course of their graduate careers. In a 2017 study that surveyed more than 850 U.S.-based Ph.D. students in physics, chemistry, engineering, computer science, and the life sciences, nearly one-third of students who entered their Ph.D. programs expressing an interest in academic research careers had cooled on the idea by the time they neared graduation. The drop-off appears to be especially steep for women from underrepresented racial and ethnic groups.

In focus group studies, these women are also more likely to credit “externally focused” values—such as a desire to mentor students or to solve health problems facing their communities—as motivating factors in their career choice. A study conducted by the American Institute of Physics similarly found that Black physics students were more likely than physics students of other ethnic groups to express a commitment to benefitting their community.

Griffin, who co-authored some of those studies, thinks those values—particularly a desire to give back through education—could help explain the disproportionate numbers of Black Ph.D. scientists opting for careers in K-12 and community college teaching. “I could see someone getting a [science] Ph.D. and using that as their pathway to fulfill this cultural commitment.”

Fana Mulu-Moore likely falls into that category. As a postdoctoral fellow studying solar physics at NASA’s Marshall Space Flight Center, she did a lot of outreach, speaking to and working with students at historically Black colleges and universities (HBCUs) in the southeast. Those interactions felt meaningful, she says. Meanwhile, she’d begun to feel burnt out by research, and she found it isolating being one of just a few Black women in her field. So in 2013, when Mulu-Moore took a year off to care

for her newborn child, she decided she would pursue teaching jobs. After a summer stint as a high school physics teacher, she landed at Aims Community College, a small school in Greeley, Colorado, about 1 hour's drive north of Denver. In the spring of 2021, she was promoted from an adjunct position to become the school's only full-time physics professor.

Mulu-Moore describes Aims as a small, nurturing community that reminds her of her own alma mater, Alabama A&M University, the HBCU where she earned both her bachelor's degree and her Ph.D. Its student body, like those of many community colleges, is diverse—roughly 40% students of color, many of them first generation students. “It’s a great place to make an impact,” she says.

mathematicians into secondary school teaching. Some high school administrators the committee interviewed speculated that Ph.D. scientists would be “overspecialized and overprepared for teaching secondary school students.” They also noted they could not match the pay Ph.D.s could earn outside the classroom. Still, the council concluded that if high schools could woo Ph.D. scientists into their classrooms—and provide them with the necessary pedagogical training—the rewards would be plentiful.

For Mark Hannum, a white physics teacher who serves as K-12 programs manager at the American Association of Physics Teachers and heads the science department at Thomas Jefferson High School for Science and Technology, an important advantage of having

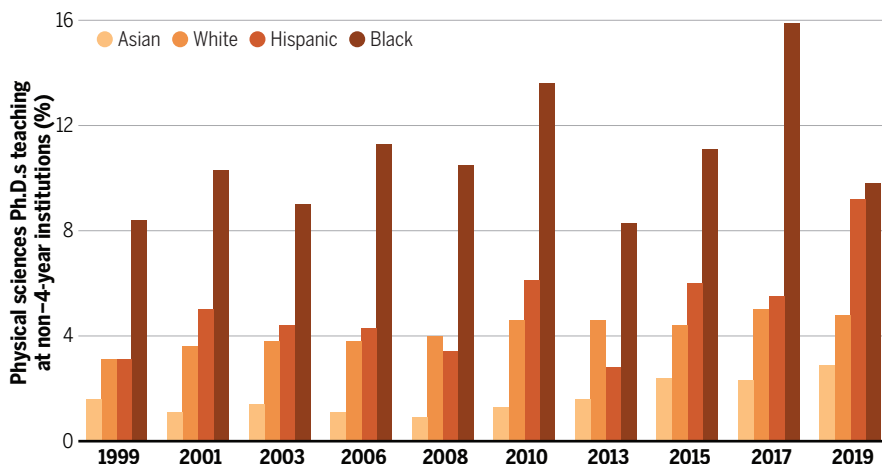
scientific process over content memorization, he says, and they bring a keen understanding of what it means to produce knowledge through experimentation.

The prospect of bringing research know-how into the classroom appealed to Angela Meyer. After finishing a Ph.D. in astronomy at Georgia State University, Meyer—a biracial Black woman—took a tenure-track faculty position at Florida Gulf Coast University, where she expected to help develop a new earth and space sciences major and launch a new observatory. But those plans never panned out. After a conversation with a cousin-in-law who taught biology at a private high school, Meyer figured a private school setting might offer her the opportunities she sought.

Meyer wound up at Culver Academies, a private boarding high school in northern Indiana. The job allowed her to pursue science without the constant pressure to write grants and publish. She developed a new astronomy curriculum, and she explored the use of classroom observatories—small, remote telescopes designed for educational use that can be controlled through the internet. One such observatory she’s worked with, a network of telescopes maintained by the Harvard-Smithsonian Center for Astrophysics, can be used for classroom projects on finding and characterizing exoplanets. “It’s not research at the level I was doing,” Meyer says. But it allows her to combine her passion for working with students with her passion for working with data. “Those are my two great loves.”

From the lab to the classroom

For decades, Black Ph.D.s in the physical sciences have opted to teach outside the ivory tower—largely at high schools and community colleges—in proportions higher than any other race or ethnicity.



TEACHERS WITH MULU-MOORE'S credentials are a boon to community colleges and high schools. According to a 2005 report from the American Association of Community Colleges, only about one-quarter of the science faculty at 2-year colleges hold doctorate degrees. In high schools, most physics, chemistry, and earth science teachers lack even an undergraduate degree in the discipline they teach, let alone a doctorate. According to recent data from the American Institute of Physics, just 27% of high school physics teachers hold a degree in physics, and about 4% have doctorates.

Two decades ago, the paucity of teachers trained in the sciences so troubled U.S. educators that the National Research Council convened a committee to explore the feasibility of recruiting more Ph.D. scientists and

trained researchers in the classroom is that, unlike many other science teachers, they think of themselves as scientists. Hannum, who has bachelor's and master's degrees in physics, counts himself among that group. Having a teacher who identifies as a scientist can profoundly impact the way the students see science, Hannum says. It gives them a role model—and all the better, he says, if that role model is someone who can broaden students' perceptions of who does science. To that end, he says, “having Black Ph.D.s working in schools is immensely valuable.”

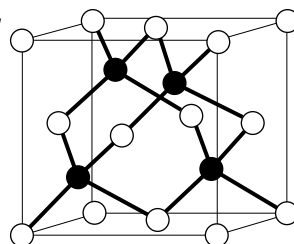
Having a scientific background can also affect how the teachers approach their work, Hannum says. “I think that mindset has subtle ramifications that spill over in a lot of ways.” For example, trained scientists are typically better prepared to emphasize the

AS FOR TAVAREZ-BROWN, she still feels twinges of regret. Once in a while, she'll pull out her doctoral thesis and thumb through the pages, reminding herself of the work that went into it: the weeks in New Mexico learning to analyze data from the Very Large Array; the weeks in the Netherlands learning to reduce data from the Westerbork Synthesis Radio Telescope. For her, an academic research career was always the prize. It stings to know that the goal has likely drifted permanently out of her reach.

But, like so many other Ph.D. physicists who have followed similar paths, she is ultimately at peace with the way things worked out. “To have a girl come up to you and be like, ‘I never thought I was good in science,’ or ‘I never thought I can do this and like it,’ ... honestly, you're not gonna get that being an astronomer,” she says. “I know I'm making an impact—right here, right now, for the future generation.” ■

Ashley Smart is associate director of the Knight Science Journalism Program at the Massachusetts Institute of Technology and a senior editor at *Undark* magazine.

MICHIGAN'S SURPRISING PATH TO DIVERSITY



Black graduate students find a nurturing culture in its applied physics program *By Jeffrey Mervis*

Roy Clarke missed the freewheeling atmosphere of the legendary Bell Telephone Laboratories after he left Bell to join the physics faculty at the University of Michigan (UM), Ann Arbor, in 1979. He realized that UM's graduate physics program, as is the case at most universities, operated within tight disciplinary silos that prescribed what students should learn and whom they studied with. "It limited the scope of the research you could do, and its impact," he says about an educational philosophy that he compares to the master-apprentice model of a medieval guild.

Rather than trying to change age-old practices, Clarke won approval for a new graduate program in applied physics (AP). And in making graduate physics training far more collaborative and interdisciplinary, Clarke unwittingly also found a formula to improve its racial, ethnic, and gender diversity. "We found that our approach attracted a lot of interest from students of color," he says.

That's a typical understatement by the white, Australian-born Clarke. Within a few decades of its 1987 debut, UM's AP program was producing roughly 10% of all Black students earning U.S. physics Ph.D.s each year, according to a 2017 study by Julie Posselt, an education researcher at the University of Southern California, who is white, and colleagues at UM. Black, Latino, and Native American students made up as much as one-third of the program's typical entering cohort compared with 5% nationally. And women

comprised one-third of a typical graduating class, twice the national average.

One factor behind those numbers, says Clarke, who stepped down as director in 2002 but maintains ties to the program, is that "we don't engage in the hand-to-hand combat" so common among graduate programs. Instead of winnowing out any student who is struggling, he says, "we make it clear that we expect people who come here to succeed."

What Clarke and his successors have done, the study notes, is discard the traditional playbook for graduate training in physics "that had implicitly created barriers to access and inclusion for underrepresented students." The new approach removes those barriers, Posselt explains, by "reconceptualizing the vision of the ideal student, empowering administrative staff to serve as cultural translators across racial and faculty-student boundaries, and creating a familylike climate." Meeting the needs of students needs to be a priority, she adds, not an afterthought.

SCIENCE SPOKE with eight alumni of UM's AP program to learn how those principles were implemented. One is Kim Lewis, now a professor of physics and associate research dean at Howard University, a historically Black institution in Washington, D.C.

In 1997, Lewis was a physics major at Dillard University, a historically black college and university (HBCU) in her hometown of New Orleans, when she first heard about UM's program. It checked most of her boxes for graduate school.

"I really still wanted to be an engineer," Lewis recalls, "so an applied physics program was very appealing. I also knew that I wanted to be an academic, and nobody would question my qualifications if I had graduated from Michigan."

But Lewis also wanted to go someplace where she felt comfortable—and Ann Arbor wasn't at the top of her list. "It would be the first time I had been in a school setting where the people did not look like me," says Lewis, who attended an all-Black high school. "It also meant being away from home."

It helped that four of the eight students in her class were Black, and that many had attended HBCUs. And Lewis says she was grateful to Clarke for setting up meetings that might lead to a lasting relationship. "You're about to be best friends," Clarke told Lewis when he introduced her to Adrienne Stiff-Roberts, who entered the program a year later. "And he was right."

After graduating with their Ph.D.s in 2004, both women have more than achieved the AP program's goal of preparing its students for success. Lewis spent 11 years on the faculty at the Rensselaer Polytechnic Institute before moving to Howard in 2018. Stiff-Roberts immediately joined the faculty at Duke University, where she is now a professor of computer and electrical engineering.

In addition to supporting students traditionally underrepresented in physics, Lewis says, the UM program has shattered the myth that a graduate physics program must sacrifice quality to achieve diversity. And she gives

Clarke a huge amount of credit for that.

“He’s a scholar, one of the best condensed matter physicists in the country,” says Lewis, who works in the same field. “He has great compassion for his students, but he’s never watered down the program.”

THE UNIVERSITY’S sterling reputation also attracted Mitaire Ojaruega. He entered the AP program in 2003 and soon benefited from another tenet of Clarke’s philosophy: ensuring staff and faculty work together to provide students with the help they need.

The 11th of 17 children, Ojaruega was born in the United States and spent much of his childhood in Nigeria. But he attended high school in Washington, D.C., and enrolled at the University of the District of Columbia (UDC). “It was a very safe environment, and the professors were very supportive, but it gives you a narrow view of the world,” he says about UDC, an HBCU that focuses on undergraduate teaching and has a tiny research budget. Summer internships at Northwestern University and UM “were my first exposure to the big leagues,” Ojaruega recalls, and he chose UM over other top-tier graduate physics programs after a professor promised “to make sure you graduate.”

Ojaruega benefited from that supportive environment, which he calls his “circle of trust,” after he initially failed his qualifying exams. That circle included Brad Orr, a white physicist who succeeded Clarke as director of the program. “Brad looked at my [undergraduate] transcript, saw that I hadn’t taken solid state physics, and suggested I sit in on those [undergraduate] classes I had missed,” Ojaruega recounts. Some students might have been too embarrassed to take a step back, he says, but he wasn’t. “And it helped a lot.”

“Michigan was hard as hell,” Ojaruega adds. “They didn’t babysit you. But they were invested in your success.”

Another key member of his circle was Charles Sutton, who served as a recruiter for the program from 2001 to 2015. Sutton, who is Black, didn’t fit the stereotype of a departmental program staffer: “I had gold chains, an earring, and the whole bit,” he says. He was also an unlikely mentor: He was younger than many of the graduate students, having just earned a communications degree from UM, and he held down a weekend gig as a DJ.

But Clarke regarded Sutton’s outgoing personality, along with his experiences growing up in Mississippi and as a student at an overwhelmingly white university, as valuable assets. When Clarke hired Sutton, “he told me to just be myself, and not change,” Sutton says. For the next 14 years,

Sutton became the “eyes and ears of the program,” as one UM professor told Posselt, serving as an intermediary to help students and faculty better understand one another.

Ojaruega had met Sutton at a recruitment fair and the two became good friends. “Sometimes I would pick him up at the library at 3 a.m.,” Sutton recalls. And after Ojaruega failed his qualifying exams, Sutton spoke up for his friend.

“I had heard that some faculty members wanted to let him go,” Sutton recalls, “so I went to professor Orr and told him, ‘I know how hard [Ojaruega] is working. And I can promise you he won’t let you down.’”

Sutton was right. Ojaruega passed his exams on the next try and sailed through the rest of his doctoral program, earning his degree in 2010. He has spent the past decade with the federal government and is now developing quantum sensor technology for the National Geospatial-Intelligence Agency within the Department of Defense.

“

Michigan was hard as hell. **THEY DIDN’T BABYSIT YOU.** But they also were invested in your success.

MITAIRE OJARUEGA,
DEPARTMENT OF DEFENSE

THE AP PROGRAM is an interdepartmental program, not a free-standing department with its own assigned faculty. That arrangement is a boon to the type of interdisciplinary projects that Clarke encourages, with students free to choose an adviser from across the university. But it can backfire if those faculty members don’t share the AP program’s passion for putting students’ welfare first.

That’s what happened to Bryan Ramson, who earned his undergraduate and master’s degrees from Howard. “I enjoyed being in the midst of high-achieving Black folks” and a predominantly Black faculty “committed to my success,” says Ramson, who is Black. That support evaporated, however, after he entered the AP program in 2011. Instead, Ramson says he went through “major culture shock” triggered by what he calls a “horrible”

environment in the university’s traditional physics department.

“Some of the professors there are really old-guard, and very resistant to teaching” in ways that recognize different learning styles, Ramson says. “My professors were not interested in my success; their focus was on the research.”

Sutton was there to reassure him that better times lay ahead. “It was the AP program staff, and Chuck in particular, who convinced me to stay whenever I would think about leaving,” Ramson says. He did, earning his Ph.D. in 2017. He’s doing a postdoc at Fermi National Accelerator Laboratory (Fermilab), where he began working as a graduate student in 2013.

Kelly Nash, a professor at the University of Texas, San Antonio (UTSA), battled that same “old-guard” culture—and lost. “It was traumatic for me from the very beginning,” says Nash, a Black physicist who entered the AP program in 2000 after graduating from

Dillard. The Ann Arbor campus was in turmoil as a lawsuit questioning the university’s use of race as a factor in admissions wended its way to the U.S. Supreme Court. In addition to being bombarded by the divisive rhetoric, Nash was also subject to pervasive racist stereotyping.


“I remember taking a quantum mechanics class with three or four other Black students,” Nash recalls, “and our professor pulled us aside one day early in the semester. ‘I just wanted you to know that you’re all going to struggle in this class because you come from HBCUs,’ he said. He was basically saying that we didn’t belong. My science identity was constantly under assault.”

Failing her qualifying exams turned out to be the final straw for Nash. “There was a huge debate about what should happen to me,” she says. “I had

never failed a course [at UM] and never been on academic probation. But I had to fight to [even] get my master’s degree.” She departed feeling “exhausted and demoralized.”

One year later she took another shot at graduate school and ended up at UTSA, which was starting a doctoral physics program. The fact that Latino students make up a majority of its undergraduate enrollment contributed to a welcoming environment that allowed her to thrive, she says.

“Being a new program, they may not have had preconceived notions about African American students,” she adds. And her productivity was undeniable. “By the time I graduated [in 2009], I had 13 papers,” she says. A few years later she returned as a faculty member, earning tenure in 2016 and becoming a full professor in 2020.



By putting students first, University of Michigan, Ann Arbor, physicist Roy Clarke achieved unprecedented diversity in the applied physics graduate program he created.

Undeterred—or perhaps driven—by their experiences at UM, both Ramson and Nash have spent years working to increase diversity in physics. Ramson co-directs Fermilab's long-running Saturday morning physics program for Chicago-area students and is a member of Change-Now, a collective of young Black physicists who are pushing Fermilab, the Department of Energy's leading high energy physics facility, to improve equity and social justice within the profession and in the community. Nash is involved in several programs to attract more women and people of color into science. For example, she has helped her university participate in a national program sponsored by the American Physical Society that finds spots for qualified students from underrepresented groups who have been passed over by other graduate physics programs.

UM'S AP PROGRAM has continued to evolve. Cagliyan Kurdak, a Turkish-born physicist who joined the department in 1998 and became the program's director in 2010, added a component for students who need to strengthen their academic background before diving into a doctoral program. Students from groups underrepresented in science receive 2 years of funding while they earn a master's degree, and over the years two-thirds have transitioned into a doctoral program, where their 80% completion rate is more than 20 percentage points higher than the national average. But Kurdak and his team can't rest on their laurels. "Creating conditions to support access and inclusion is not a one-time event, but an ongoing struggle," Posselt wrote in her 2017 study.

Posselt flagged two recurring challenges. One is what she calls the "negative racial climate" for many students of color at UM, a predominantly white institution. Those whom Posselt interviewed also spoke about a "negative feedback loop, in which poor representation of women and students of color raises red flags for prospective students ... and deters them from matriculating."

Posselt says the UM AP program has replaced those red flags with a welcome sign through its "commitment to diversity." Its interdisciplinary approach to science, flexible admissions criteria, and family atmosphere are baked into the AP program, agrees Sutton, who went to the White House as Clarke's guest when, in 2010, Clarke received the Presidential Award for Excellence in Science, Mathematics, and Engineering Mentoring.

"They just care so much about people," says Sutton, now a recruiter for Thermo Fisher Scientific in Atlanta, about his former colleagues. "And in the end, that is what has made them so successful. I hope the program lasts forever." ■

INSIGHTS

PERSPECTIVES

ANIMAL BEHAVIOR

Anthropogenic influences on bee foraging

Efficient foraging is vital to bee fitness but is challenging in the Anthropocene

By **Dave Goulson** and **Elizabeth Nicholls**

Bees are highly specialized insects, feeding almost exclusively on nectar and pollen from flowers, and in so doing contributing substantially to the pollination of wild plants and crops. Flying to and from patches of flowers is energetically costly, particularly for relatively large bees such as honey bees and bumble bees that live on a knife-edge in terms of balancing their energy intake.

Suboptimal foraging conditions can result in a net loss of energy over the course of a foraging trip. Bees have evolved numerous adaptations to efficiently locate and extract floral resources, including impressive learning, navigational, and communication abilities. These are key to their survival and successful reproduction, because the number of offspring that can be provisioned is determined by the food surplus adult bees can gather. However, these foraging adaptations can be affected by anthropogenic

factors, but there are opportunities to minimize negative effects.

The arrival of the Anthropocene has brought with it considerable challenges for wild bees. In particular, the spread of industrial agriculture has profoundly altered the landscape across large portions of the globe, often reducing the availability and diversity of floral resources. The most widely grown

School of Life Sciences, University of Sussex, Brighton, UK.
Email: d.goulson@sussex.ac.uk

A honey bee (*Apis mellifera*) collects pollen from a common sunflower (*Helianthus annuus*) and must then navigate back to its hive and communicate with others about this food source.

crops (cereals such as wheat, rice, and corn, comprising 79% of global crop area) are wind-pollinated, and hence provide minimal resources for pollinators. When grown in large monocultures, with extensive herbicide use to eliminate most weeds, the farmed landscape can be almost devoid of flowers. Although some crops such as canola, sunflowers, and many fruits and vegetables do require pollination and offer floral resources for bees, this situation also poses challenges. A field of canola, for example, can provide a glut of food for pollinators for a short period of perhaps 3 weeks, but very little before or afterward. A similar situation prevails in fruit orchards following the short blooming period. Honey bees may benefit from such highly clumped resources more than other bee species because they can recruit nestmates to this bounty by their waggle dance, have relatively long foraging ranges, and are able to store excess resources over the long term in their hive in the form of honey and bee bread. However, it has been repeatedly demonstrated that pollinator diversity is key to efficient pollination service delivery, and that relying on a single domesticated bee species can limit crop yields (1).

A further challenge for bees foraging in farmland is exposure to agrochemicals. Samples of honey commonly contain 10 or more pesticides in complex combinations, often including potent insecticides such as neonicotinoids (2). Bee exposure can occur in many ways, not just through feeding on treated crops, including contamination of wildflowers and woody plants in field margins and pollution of water sources. Neonicotinoids are neurotoxins, harming bees at concentrations commonly detected in the pollen and nectar of both treated crops and wildflowers (typical range 1 to 20 parts per billion). Sublethal effects include impaired navigation, which increases the frequency with which honey bees become lost when foraging (3). Neonicotinoids also impair learning of associations between scents and floral rewards, a vital skill that bees use to identify the most rewarding flowers. Exposure to neonicotinoids reduces the proportion of workers that bring back pollen to the nest, and the amount of pollen gathered per trip, perhaps by impairing motor skills needed in pollen collection (3). Other types of insecticide, such as sulfoxaflo, flupyradifurone, and even the herbicide glyphosate have also been found to have negative sublethal impacts on aspects of foraging behavior, memory, and learning

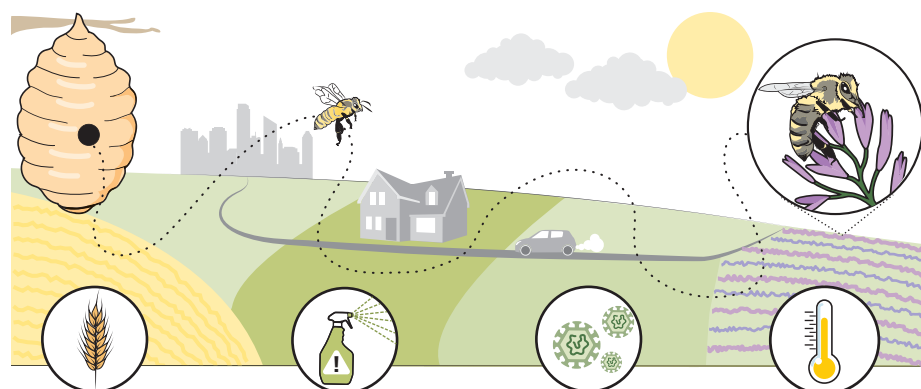
in various bee species (4) (see the figure).

These sublethal effects of pesticides on behavior are rarely evaluated by regulatory tests, which typically focus on short-term effects on bee mortality, yet sublethal effects on foraging efficiency could profoundly reduce colony and nesting success. For example, if foragers regularly become lost when foraging, a social bee nest may quickly weaken and die as worker numbers fall. For solitary bees, which must single-handedly collect all food resources to provision their individual nests, the impact of inefficient foraging on reproduction and population size is likely to be even more pronounced (3). Furthermore, pesticides are applied in formulations con-

food. For some solitary species with foraging ranges of less than 100 m, new developments such as buildings or roads can represent considerable barriers to foraging. Pollutants and the disturbance associated with industry and transport are likely to have an impact on bees, in terms of the availability of both food and suitable nesting sites. Bees have been found to avoid foraging in areas affected by turbulence from passing traffic (7), and diesel exhaust emissions degrade floral odors, rendering it harder for bees to use sensory cues to detect and recognize rewarding flowers (8). Contamination of pollen and nectar with particulate pollution can expose bees

Anthropogenic factors that affect bee foraging efficiency

Anthropogenic changes can affect the ability of bees to efficiently forage for food, which can reduce the survival of solitary and social bees.



Habitat fragmentation

Agriculture and/or urbanization cause bees to travel further from their nest to find food. This could especially affect smaller species or those exposed to pesticides and/or disease.

Exposure to pesticides and other chemicals

Pesticides can have sublethal effects on bee behavior that impair navigation, memory, and learning. So-called "inert" ingredients can also affect bee foraging.

Exposure to pollutants

Airborne pollutants affect the detection of floral odors and learning about floral rewards. They can also impair flight capacity and navigation.

Climate change

Higher temperatures and rising CO₂ affect floral traits, such as flower number, nectar production, and protein content of pollen, which influence bee foraging choices.

taining "inert" ingredients that are also not subject to regulatory tests. Recent studies reveal that surfactants used in "Roundup" (glyphosate-based herbicide) and "Amistar" (widely used fungicide based on azoxystrobin) are toxic to bumble bees (5). For example, the alcohol ethoxylate surfactants in Amistar cause gut damage, reducing appetite and foraging, and ultimately leading to 30% mortality in bumble bees (5).

Farming is not the only anthropogenic land use that has consequences for bees and their capacity to forage efficiently. Biodiverse, flower-rich natural and seminatural habitats may be destroyed or fragmented as a result of spreading urbanization, the building of factories, transport infrastructure, golf courses, and much more (6). Such habitat fragmentation means that bees often need to fly further to find

to a range of industrial pollutants, including metals such as manganese, copper, and lead, and these have been found to have various behavioral effects, including inducing foraging at an earlier age in honey bee workers and reducing the number of foraging trips made per bee (7).

Bees visiting flowers also risk infection with diseases, many of which are transmitted by shared contact with flower surfaces. Although a naturally occurring phenomenon to which bees have some behavioral adaptations, the threat to bee health has been greatly exacerbated by the transport of domesticated bees around the globe, leading to the introduction of diseases to which native bees have limited defenses. These emerging diseases can have profound effects on foraging ability and can alter floral preferences, as well as increasing mortality

(9). For example, infection with the parasite *Nosema ceranae*, which originated in Asia and is now common throughout the world, reduces honey bee foragers' homing ability.

If all this were not enough, climate change is likely to add further to the challenge of efficient foraging in bees. Being large and furry, bumble bees are adapted to cool, temperate climates and can overheat in warm weather, becoming unable to forage. In specialist bees that have a narrow range of food plants, the timing of emergence of bees and flowering may become uncoupled, and their offspring may lack the ability to digest and develop on alternative pollen sources (10). Rising CO₂ concentrations can reduce the protein content of pollen, while extreme climatic events such as heat waves, fires, and droughts are likely to alter the ability of plants to produce floral resources, and such effects will undoubtedly get worse in coming decades (10).

There are also likely to be other anthropogenic factors that affect bee foraging that are not yet recognized or properly researched. For example, electromagnetic radiation (radio waves, microwaves, and fields around high-voltage electricity lines) may plausibly interfere with the ability of bees to detect and use Earth's magnetic field for navigation, but robust experiments are lacking. Does particulate pollution block insect trachea? Are insects affected by other environmental pollutants, such as polychlorinated biphenyls (PCBs), polybrominated diphenyl ethers (PBDEs), or any of the approximately 144,000 different manufactured chemicals that enter the global environment (11)? Furthermore, very little is known about how these stressors interact (12). Are effects additive or synergistic? In bumble bees, for example, exposure to sublethal concentrations of the insecticide clothianidin has been shown to cause a temperature-dependent decrease in foraging duration (13). In honey bees, a recent study using flight mills has shown that nutritional stress combined with exposure to the pesticide flupyradifurone increased mortality and also increased flight velocity (14). These are just a few examples of the multitude of combined stressors bees are currently exposed to, and the pace of change is such that ecologists and ecotoxicologists cannot keep up with testing the impact of new formulations as they come to market.

There are opportunities to mitigate some of the pressures on bees. There is growing interest in planting bee-friendly flowers in gardens and other urban greenspaces, and in managing road verges to encourage wildflowers (despite risks associated with foraging in high traffic areas). Initiatives to reduce or eliminate pesticide use in urban areas,

such as the national ban on urban pesticide use in France, further enhance the value of urban areas for foraging bees. There is evidence to suggest that honey bee and bumble bee colonies may fare better in urban areas than in agricultural landscapes, thought to be due in part to the greater diversity and availability of floral resources throughout the year (6, 11). Increased public interest in bee declines has also led to a rise in urban beekeeping, with many businesses and hotels offering space for urban hives through a desire to help declining bee populations. However, increasing the number of managed hives does nothing to support wild bee populations, and actually raises concerns regarding competition with wild bees for floral resources and a potentially exacerbated risk of disease transmission at flowers.

Finding ways to support wild pollinators in farmland is an even greater challenge. Agri-environment schemes to support specific management for pollinators may enhance bee populations at a local scale but have not halted overall patterns of decline (15). The design and success of such schemes could be improved through a better understanding of the dietary needs and foraging behavior of bee species other than just honey bees and bumble bees, which currently benefit most from interventions such as wildflower strips. However, systemic change with a move toward regenerative farming practices—including use of legume cover crops, higher crop diversity, and reduced or eliminated pesticide use—are likely to be necessary to sustain the thriving and diverse wild pollinator community needed to provide a resilient pollination service for both crops and wildflowers. ■

REFERENCES AND NOTES

1. L. A. Garibaldi *et al.*, *Front. Ecol. Environ.* **12**, 439 (2014).
2. F. Sanchez-Bayo, K. Goka, *PLOS ONE* **9**, 94482 (2014).
3. T. J. Wood, D. Goulson, *Environ. Sci. Pollut. Res. Int.* **24**, 17285 (2017).
4. J. Hernández, A. J. Riveros, M. Amaya-Márquez, *J. Insect Conserv.* **25**, 683 (2021).
5. E. A. Straw, M. J. F. Brown, *Sci. Rep.* **11**, 21653 (2021).
6. K. C. R. Baldock, *Curr. Opin. Insect Sci.* **38**, 63 (2020).
7. B. B. Phillips *et al.*, *J. Appl. Ecol.* **58**, 1017 (2021).
8. R. D. Gilling, I. Lusebrink, E. Farthing, T. A. Newman, G. M. Poppy, *Sci. Rep.* **3**, 2779 (2013).
9. H. Koch, M. J. F. Brown, P. C. Stevenson, *Curr. Opin. Insect Sci.* **21**, 60 (2017).
10. C. C. Nicholson, P. A. Egan, *Glob. Change Biol.* **26**, 380 (2019).
11. D. Goulson, *Silent Earth* (HarperCollins, 2021).
12. H. Siviter *et al.*, *Nature* **596**, 389 (2021).
13. P. J. Kolano, M. Røyset Aarønes, K. Borgå, A. Nielsen, *J. Pollinat. Ecol.* **28**, 138 (2021).
14. L. Tong, J. C. Nieh, S. Tosi, *Chemosphere* **237**, 124408 (2019).
15. C. Geppert *et al.*, *J. Appl. Ecol.* **57**, 1818 (2020).

ACKNOWLEDGMENTS

E.N. is supported by a UK Research and Innovation Future Leaders Fellowship (MR/T021691/1).

NEUROSCIENCE

Addicted to dreaming

How does dopamine, the brain's pleasure signal, regulate the dream stage of sleep?

By Elda Arrigoni¹ and Patrick M. Fuller²

How human brains regulate sleep remains an enduring puzzle (1). How sleep subserves human dreaming—rapid eye movement (REM) sleep—is especially puzzling. There is considerable mechanistic understanding of the synaptic, cellular, and circuit bases of REM sleep (2, 3). However, despite pharmacological evidence that dopamine (DA) can potently modulate REM sleep, this neurotransmitter is conspicuously absent from most prevailing REM sleep circuit models. DA is historically associated with pleasure and addiction. On page 994 of this issue Hasegawa *et al.* (4) report that the release of DA in the basolateral amygdala (BLA), a brain structure associated with emotional processing, can trigger REM sleep in mice and also that selective manipulation of DA release within the BLA can trigger cataplexy, which occurs in the sleep disorder narcolepsy and manifests as a crippling pathologic intrusion of REM sleep into wakefulness that results in loss of postural motor control.

Although a role for DA has long been suggested in the regulation of sleep, including REM sleep, its precise contribution (and source) has remained enigmatic. An important clue emerged from a recent study in



Rapid eye movement (REM) sleep is a behavioral state that is conserved across the animal kingdom, yet the biological purpose it serves remains unknown.

10.1126/science.abn0185

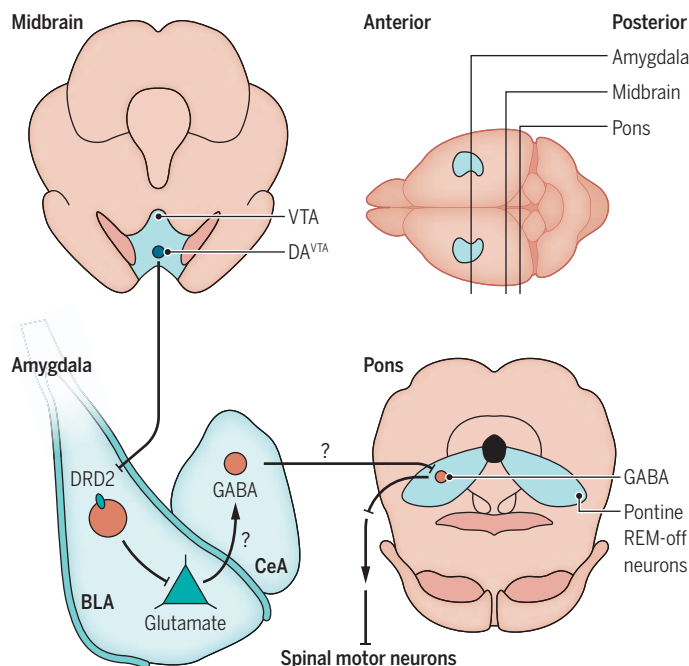
mice showing that DA neurons within the midbrain ventral tegmental area (VTA), a brain region long associated with reward and addiction, had higher firing rates during REM sleep and wakefulness than during non-REM (NREM) sleep and also increased their activity before NREM-to-REM transitions (5). Building on these important observations, Hasegawa *et al.* sought to understand if and how these “REM-on” dopaminergic VTA (DA^{VTA}) neurons might contribute to the regulation of REM sleep. To do so, they used a G protein-coupled receptor (GPCR) activation-based (GRAB) sensor for DA (GRAB_{DA}) to assess DA release at known postsynaptic targets of DA^{VTA} neurons, including the BLA, in mice.

The GRAB_{DA} tool permits precise temporal-spatial assessments of DA concentrations within the brain (6), even during complex behaviors. The authors could thus ascertain extracellular DA concentrations within the BLA and other brain regions as mice cycled through the stages of wakefulness, NREM sleep, and REM sleep. From these recordings, they determined that DA was transiently increased in both the BLA and the nucleus accumbens (NAc) preceding NREM-to-REM transitions. Subsequent photostimulation of DA^{VTA} terminals in the BLA but not in the NAc produced a rapid transition to REM sleep. The authors then acutely and selectively inhibited DA receptor D2 (DRD2)-expressing BLA neurons *in vivo* using an optogenetic tool (7), which triggered, albeit with some delay, an NREM-to-REM transition and increased total REM sleep time. Together, these findings reveal a central role for DA^{VTA} neurons, DA neurotransmission, and inhibition of DRD2-expressing BLA neurons in the regulation of REM sleep, including the triggering of REM sleep onset. These results therefore provide a cellular and circuit substrate for findings from previous studies showing that the pharmacological manipulation of brain DA (e.g., DA-depleted mice and the use of DRD2 agonists) can substantially alter REM sleep (8).

Can manipulation of DRD2 neurons in the BLA produce cataplexy in mice? Hasegawa

A putative circuit model of REM sleep

Dopamine neurons within the ventral tegmental area (DA^{VTA} neurons) project to and inhibit locally projecting basolateral amygdala (BLA) neurons that express DA receptor D2 (DRD2). This disinhibits the BLA efferent pathways, potentially including projections to the central amygdala nucleus (CeA). In this putative circuit model, activation of CeA γ -aminobutyric acid-specific (GABAergic) neurons could promote rapid eye movement (REM) sleep and cataplexy through projections to pontine and medullary cell populations.



et al. demonstrated that DA release into the BLA precedes cataplexy in narcoleptic mice (which are deficient in orexin, a neuropeptide expressed in cells of the lateral hypothalamus that regulates wakefulness and appetite). They also found that the surge of DA in the BLA—but not in other brain regions tested—was greater in the narcoleptic mouse model than in wild-type littermates. The authors then stimulated DA^{VTA} neurons in nonnarcoleptic mice, which express normal amounts of orexin, producing a transient increase in DA within the BLA and inducing cataplexy. Given the normal concentrations of orexin in these mice, this is a striking finding and one that may require a reconsideration of the prevailing neurobiological models of cataplexy in the context of narcolepsy because cataplexy is not known to occur spontaneously in orexin-competent animals, including humans.

Although the authors’ data firmly support a role for DA^{VTA} neurons in the control of REM sleep, how DRD2-expressing BLA neurons are functionally related or connected with cell groups located in the pontine and medullary brainstem, which were previously established to be necessary for the generation of REM sleep and REM paralysis, remains uncertain. Notably, BLA DRD2-expressing neurons do not appear to project beyond

the BLA itself. One possibility is that disinhibition of non-DRD2-expressing BLA neurons—which the authors suggest may occur after DA-induced inhibition of DRD2-expressing BLA neurons—could, in turn, activate inhibitory γ -aminobutyric acid-specific (GABAergic) neurons of the central amygdala nucleus (CeA) that normally serve to inhibit key pontine cell groups involved in REM motor control (9–11) (see the figure). It also remains unclear why the amount of DA released in the BLA by positive emotions (e.g., when mice are fed chocolate) is greatly amplified in orexin-deficient mice. The authors propose that this could be the result of disinhibition of DA^{VTA} input to the BLA or could result from plastic changes in the DA system—e.g., the number of aminergic neurons is increased in narcoleptic humans who are orexin deficient (12, 13).

Another remaining mystery is why drugs that increase extracellular DA (e.g., modafinil) and are used clinically to enhance wakefulness in people with disorders like idiopathic hypersomnia and narcolepsy do not have an effect

on cataplexy and REM sleep. Future studies should also examine the role of BLA DA signaling in shaping fundamental features of REM sleep, such as its homeostatic regulation, which is a process that remains incompletely understood. The study of Hasegawa *et al.* provides fresh insights into the control of both REM sleep and cataplexy by DA, and their findings raise the intriguing possibility that DRD2 BLA neurons could be a selective druggable target for treating debilitating symptoms in a wide range of REM sleep disorders, including cataplexy in narcolepsy and other disorders, such as Parkinson’s disease, in which DA signaling is disrupted. ■

REFERENCES AND NOTES

1. D. Kennedy, C. Norman, *Science* **309**, 75 (2005).
2. E. Arrigoni, M. C. Chen, P. M. Fuller, *J. Physiol.* **594**, 5391 (2016).
3. J. Peever, P. M. Fuller, *Curr. Biol.* **27**, R1237 (2017).
4. E. Hasegawa *et al.*, *Science* **375**, 994 (2022).
5. A. Eban-Rothschild, G. Rothschild, W. J. Giardino, J. R. Jones, L. de Lecea, *Nat. Neurosci.* **19**, 1356 (2016).
6. F. Sun *et al.*, *Cell* **174**, 481 (2018).
7. O. A. Masseck *et al.*, *Neuron* **81**, 1263 (2014).
8. K. Dziras *et al.*, *J. Neurosci.* **26**, 10577 (2006).
9. M. B. Snow *et al.*, *J. Neurosci.* **37**, 4007 (2017).
10. C. E. Mahoney, L. J. Agostinelli, J. N. K. Brooks, B. B. Lowell, T. E. Scammell, *J. Neurosci.* **37**, 3995 (2017).
11. E. Hasegawa *et al.*, *Proc. Natl. Acad. Sci. U.S.A.* **114**, E3526 (2017).
12. P. O. Valko *et al.*, *Ann. Neurol.* **74**, 794 (2013).
13. J. John *et al.*, *Ann. Neurol.* **74**, 786 (2013).

10.1126/science.abo1987

¹Department of Neurology, Beth Israel Deaconess Medical Center and Harvard Medical School, Boston, MA, USA.
²Department of Neurological Surgery, University of California, Davis School of Medicine, Davis, CA, USA.
 Email: earrigon@bidmc.harvard.edu; pmfuller@ucdavis.edu

PLANT BIOLOGY

Forming roots from shoot

Uncovering the genes responsible for different types of roots will transform aspects of plant agriculture

By **Lidor Shaar-Moshe**^{1,2} and
Siobhan M. Brady^{1,2}

Plants continuously elaborate their form through the production of new organs, including different types of roots. A primary root emerges from a seed, and lateral roots develop post-embryonically from the primary root axis. In addition, plants can generate a variety of shoot-borne roots. These are called adventitious roots (1) in dicotyledonous plants, such as tomato, or crown and brace roots (2) in monocotyledonous cereal crops, such as maize or sorghum. But the developmental mechanisms associated with shoot-borne root initiation as well as the conservation of this program with lateral and wound-induced roots are largely unknown. On page 993 of this issue, Omary *et al.* (3) report a conserved developmental pathway for shoot-borne roots across flowering plants and a conserved “superlocus” that regulates the initiation of specialized root types.

Lateral roots derive from pericycle cells that flank xylem cells (which transport water) within the root. By contrast, Omary *et al.* demonstrate that in tomato (*Solanum lycopersicum*), shoot-borne roots derive from cells located around the phloem (which transports nutrients), called the phloem parenchyma. Hormone (auxin and cytokinin) signaling contributes to the formation of a properly patterned root primordia, which includes the formation of a stem cell niche and asymmetric divisions of stem cells to produce root cell types. To determine how fields of hormone-responsive cells change through shoot-borne root primordia development, Omary *et al.* used hormone-response markers. Similarity in the cellular response fields

between lateral root and shoot-borne root primordia would demonstrate conserved mechanisms of root primordia. As the shoot-borne root primordia undergoes cell patterning, cells within the primordia respond to auxin or cytokinin or both. In tomato lateral root initiation, there is no overlap in the cytokinin- and auxin-responsive domains, similar to *Arabidopsis thaliana* (4). Thus, the cells and hormonal signaling that give rise to shoot-borne and lateral root primordia differ, suggesting that these two developmental programs are different.

Omary *et al.* carried out single-cell transcriptome profiling of shoot-borne root primordia over developmental time, which revealed a group of cells with an ephemeral cell identity. These cells share a transcriptional enrichment for root stem cell regulators, and a developmental trajectory analysis identified this cell group as a branch point for dif-

ferent identities. Thus, Omary *et al.* called them “transition stem cells”; they are the intermediary stage between phloem parenchyma cells and shoot-borne root primordia initial cells. This transitional state served as a platform to identify potential regulators, including a transcription factor belonging to the LATERAL ORGAN BOUNDARIES DOMAIN (LBD) family (5) that the authors named *SHOOTBORNE-ROOTLESS* (*SBRL*). They demonstrated that *SBRL* is necessary for shoot-borne root, but not lateral root, initiation in tomato. The function of *SBRL* orthologs was conserved in other dicotyledonous species, potato, and *A. thaliana* and likely conserved in sweet potato, white bean, and the monocot sorghum. Monocots and dicots had a most recent common ancestor ~150 million years ago. The identical function of this gene across such a long evolutionary time demonstrates substantial conservation.

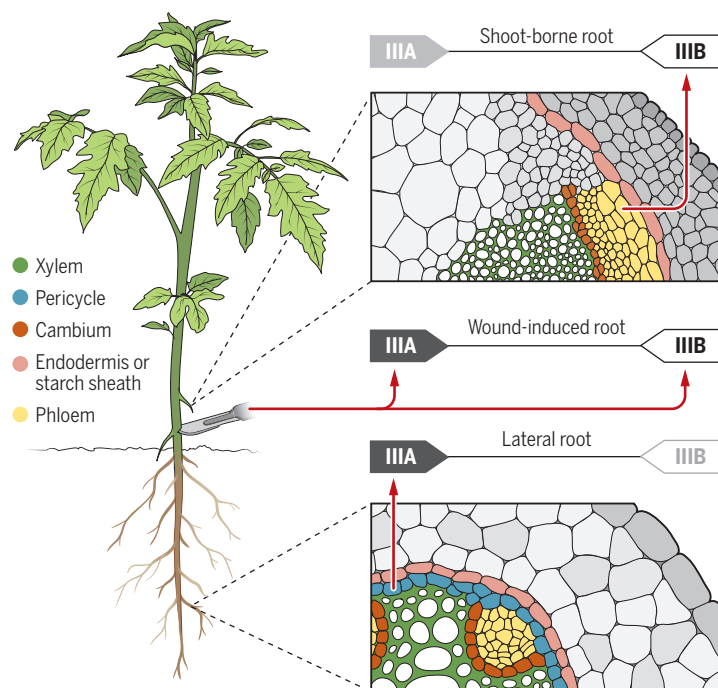
The analysis by Omary *et al.* of tomato *SBRL* and its orthologs indicated that shoot-borne and lateral root developmental programs are quite different. However, a phylogeny of LBD transcription factors demonstrated that *SBRL* belongs to subclass IIIB of LBD transcription factors. When assembling this phylogeny, the authors noted that a subclass IIIB gene was nearly always

located next to a closely related subclass IIIA gene, which they called an LBD superlocus, with conserved regulatory elements. Subclass IIIA genes are associated with lateral root initiation in maize and *A. thaliana* (6). Do subclass IIIA genes also regulate a transition stage in lateral root initiation? Omary *et al.* found that expression of a large proportion of a gene set that defines the transition state was induced in analogous stages of lateral root initiation. Mutation of the tomato subclass IIIA gene *BROTHER OF SBRL* (*BSBRL*) and its paralog *BSBRL2* reduced lateral root initiation, with no change to shoot-borne roots. Mutation of the *A. thaliana* subclass IIIA gene resulted in an equivalent phenotype. The local duplication that gives rise to these neighboring subclass IIIA and IIIB genes therefore allowed the evolution of two independent root-initiation programs from distinct parts of the plant body across diverse flowering plant species.

A third wound-induced root type is critical to agriculture

Formation of specialized root types

The LATERAL ORGAN BOUNDARIES DOMAIN (LBD) superlocus regulates root development by inducing a transition state. Lateral root initiation depends on expression of LBD IIIA genes in the xylem pole–pericycle. Shoot-borne root initiation depends on expression of LBD IIIB genes in phloem-associated cells. Both LBD IIIA and IIIB genes are required for initiation of wound-induced roots.



¹Department of Plant Biology, University of California, Davis, Davis, CA, USA.

²Genome Center, University of California, Davis, Davis, CA, USA. Email: lshaar@ucdavis.edu; sbrady@ucdavis.edu

and horticulture, as well as to the application of gene editing. Gardeners are familiar with the process of taking cuttings from plants to propagate a new plant asexually. Cuttings are the basis of the horticulture industry and involve the induction of roots from cut pieces of a plant stem that will eventually regenerate a whole plant. This is a form of asexual reproduction and is important for the propagation of flowering plants for which sexual reproduction can take years to decades. Gene editing in most species to improve plant performance in shorter times than traditional plant breeding approaches (7) requires transformation through the induction of root tissue (a wound-induced root) from a mass of undifferentiated cells called a callus and subsequent root initiation, followed by shoot initiation. Omary *et al.* showed that subclass IIIA and IIIB genes are also required for wound-induced root initiation (see the figure). Mutation of the subclass IIIB *SBRL* in potato interfered with root induction from callus. In tomato, simultaneous mutation of *SBRL* and the class IIIA *BSBRL* and *BSBRL2* genes resulted in an inability to form wound-induced, shoot-borne, and lateral roots.

Roots are incredibly important to plant survival owing to their roles in the transport of water and mineral nutrients and the provision of mechanical support. The discovery of this superlocus provides a beautiful example of how localized gene duplications produce a more complex plant form. The origin of cells that undergo the transition to a specialized root as well as the patterning events associated with generating the primordia can be distinct, but the IIIA and IIIB LBD transcription factors execute the same transitory state to produce different root types. Determining whether differences in class IIIA and IIIB transcription factor expression or activity underlie differences in the capacity for plant transformation or the production of cuttings will further strengthen the impact of the findings of Omary *et al.* The production of different root types is an important component of a plant's ability to successfully respond to stresses in their environment, including withstanding flooding and high wind. In the face of climate change, subclass IIIB transcription factors may become important target genes to manipulate and produce plants with an increased capacity to adapt to adverse weather conditions. ■

REFERENCES AND NOTES

1. B. Steffens, A. Rasmussen, *Plant Physiol.* **170**, 603 (2016).
2. A. N. Hostetler *et al.*, *Curr. Opin. Plant Biol.* **59**, 101985 (2021).
3. M. Omary *et al.*, *Science* **375**, eabf4368 (2022).
4. B. Müller, J. Sheen, *Nature* **453**, 1094 (2008).
5. A. S. Chandrabali *et al.*, *Mol. Biol. Evol.* **32**, 1996 (2015).
6. Y. Okushima *et al.*, *Plant Cell* **19**, 118 (2007).
7. R. A. Nasti, D. F. Voytas, *Proc. Natl. Acad. Sci. U.S.A.* **118**, e2004846117 (2021).

10.1126/science.abo2170

ULTRACOLD CHEMISTRY

Toward a coherent ultracold chemistry

Magnetic fields can be used to change chemical reaction rates by a factor of 100

By Simon L. Cornish¹ and Jeremy M. Hutson²

Collisions are fundamentally important to the study of atomic and molecular gases. For example, they dictate the lifetimes of ultracold samples and the efficiency of cooling by evaporation. Ultracold collisions are largely governed by quantum mechanics and are very sensitive to electromagnetic fields. Harnessing subtle interference effects, such as Feshbach resonances, has allowed the control of atomic collisions and revolutionized the study of atomic physics (1). Ramping an applied magnetic field across such a resonance is the key step in the formation of ultracold diatomic molecules (2). Opportunities for a broad range of scientific studies and applications will open up if molecular collisions can be controlled in the same way as atomic collisions. On page 1006 of this issue, Son *et al.* (3) used a magnetic Feshbach resonance to offer better-than-ever control over ultracold reactive collisions between sodium (Na) atoms and sodium-lithium (NaLi) molecules.

Ultracold molecule-molecule collisions have turned out to cause unexpectedly fast losses of molecules from the optical traps used to confine them (4–6). This loss happens even in systems in which two-body chemical reactions between the colliding species are not allowed (7). Most experiments have observed loss rates close to the so-called universal rate, at which all colliding pairs that reach short range are lost. The short-range loss is usually explained in terms of the formation of long-lived “complexes” during collisions (8). These complexes can be destroyed in a variety of ways, including by chemical reaction or absorption of light from the trapping laser (9). However, there is conflicting evidence on the lifetimes of the complexes and the mechanisms of their loss (5, 6, 10, 11).

Feshbach resonances occur at magnetic fields where a state of the collision complex has the same energy as the colliding

species. They have not yet been observed for molecule-molecule collisions, but atom-molecule collisions provide a simpler case for study. Son *et al.* have observed a resonance due to a long-lived state formed in a collision between ²³Na atoms and ²³Na⁶Li molecules. They have measured the rate of the reactive atom-molecule collision, NaLi+Na → Li+Na₂, in the vicinity of this resonance, reporting more than a factor of 100 variation as the magnetic field is tuned across the resonance.

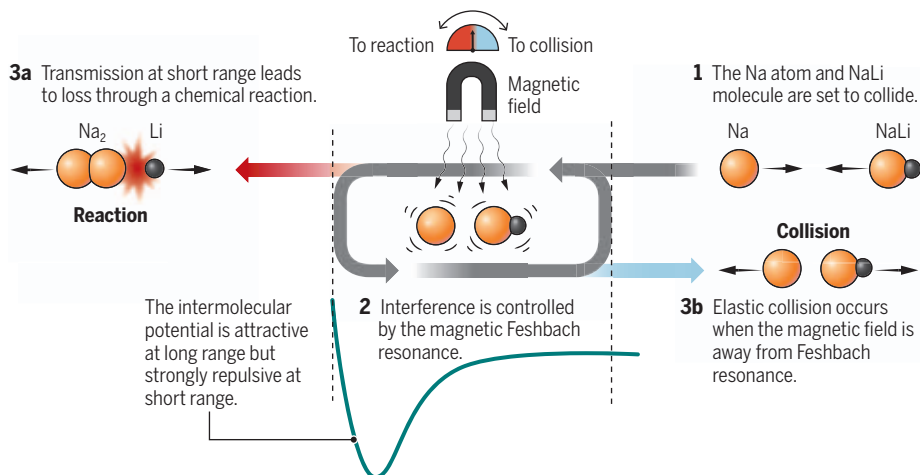
To understand the results reported by Son *et al.*, it is useful to consider a simple physical picture of ultracold molecular collisions. As atoms and molecules approach one another from afar, they experience an attractive van der Waals force. At ultracold temperatures, the colliding particles behave as matter waves—a consequence of wave-particle duality in quantum mechanics—and experience partial reflection from the attractive potential. As the colliding particles get closer to each other, the atom-molecule pair either remains in the initial state and is reflected off the repulsive core of the potential or is converted to a different state in which chemical reaction can occur (see the figure). If the colliding species are completely lost at short range, the overall loss rate is determined by the quantum reflection of the matter-wave from the attractive potential at long range. However, if the loss at short range is very small, the reflection from the short-range interaction may be followed by a second partial reflection from the attractive potential. This can continue ad infinitum, with multiple reflections back and forth within the molecular potential before the pair separates.

Son *et al.* sought to explain this behavior by adapting the existing model for the reflection of light inside a cavity with partially reflecting mirrors. The light wave escaping from such a cavity interferes with the wave originally reflected from the mirror where the light was first introduced. This interference can be either constructive or destructive depending on the spacing of the mirrors, leading to either enhanced or reduced overall reflection respectively. In the case of colliding particles,

¹Department of Physics, Durham University, South Road, Durham DH1 3LE, UK. ²Department of Chemistry, Durham University, South Road, Durham DH1 3LE, UK. Email: s.l.cornish@durham.ac.uk

Ultracold chemical reaction using a magnetic field

Multiple reflections within the intermolecular potential result in quantum interference that strongly affects the chemical reaction. Changing the magnetic field can tune the loss of NaLi molecules during collisions. Weak loss at short range leads to a large range of control in the overall loss rate.



treated as matter-waves, the presence of a magnetic Feshbach resonance allows the interference to be tuned with the applied magnetic field, akin to changing the spacing between the mirrors. This allows the probability of a reactive collision to be controlled.

The long-lived state of the complex formed during the collision that causes the resonance produces very little loss at short range. This is analogous to a highly reflecting inner mirror. The resulting high-contrast interference leads to large changes in the overall loss rate, from far below the universal rate to far above. Using a quantum mechanical scattering model based on an absorbing boundary condition at short range that is analogous to the optical cavity model, Son *et al.* estimated that only about 4% of the colliding pairs that reach short range are lost, which is far below the 100% loss at short range associated with the universal rate. The much lower loss at short range leads to a large variation in the reaction rate across the resonance. The authors contrast this resonance with a weaker one at a higher magnetic field, where the associated state of the complex is much shorter-lived, which results in a far smaller variation in the reaction rate across the resonance.

The authors show that ultracold collisions between Na and NaLi can be understood with relatively simple models. Their experiment provides an excellent testing ground for refining the understanding of ultracold chemistry. Looking to the future, tunable Feshbach resonances may ultimately form the basis of a coherent ultracold chemistry, in which bimolecular reactions are performed coherently across an

entire sample of molecules. Such a chemistry will allow polyatomic molecules to be built up from their constituent parts while maintaining them all in a single quantum state. This contrasts with the form of coherent control achieved with femtosecond lasers (12), in which coherence exists within a single molecule but not across the entire sample.

The ability to control ultracold molecular collisions will benefit many applications. For example, molecules with dipole moments offer fascinating opportunities to study quantum many-body physics in the presence of long-range interactions. This may help understand complex phenomena, such as superconductivity and exotic forms of magnetism. However, achieving this will undoubtedly require the ultracold chemistry to be under control. ■

REFERENCES AND NOTES

1. C. Chin, R. Grimm, P. Julienne, E. Tiesinga, *Rev. Mod. Phys.* **82**, 1225 (2010).
2. K.-K. Nietal., *Science* **322**, 231 (2008).
3. H. Son *et al.*, *Science* **375**, 1006 (2022).
4. P. D. Gregory *et al.*, *Nat. Commun.* **10**, 3104 (2019).
5. R. Bause *et al.*, *Phys. Rev. Res.* **3**, 033013 (2021).
6. P. Gersema *et al.*, *Phys. Rev. Lett.* **127**, 163401 (2021).
7. P. S. Zuchowski, J. M. Hutson, *Phys. Rev. A* **81**, 060703 (2010).
8. M. Mayle, G. Quémener, B. P. Ruzic, J. L. Bohn, *Phys. Rev. A* **87**, 012709 (2013).
9. A. Christianen, M. W. Zwielerlein, G. C. Groenenboom, T. Karman, *Phys. Rev. Lett.* **123**, 123402 (2019).
10. Y. Liu *et al.*, *Nat. Phys.* **16**, 1132 (2020).
11. P. D. Gregory, J. A. Blackmore, S. L. Bromley, S. L. Cornish, *Phys. Rev. Lett.* **124**, 163402 (2020).
12. C. Brif, R. Chakrabarti, H. Rabitz, *New J. Phys.* **12**, 075008 (2010).

ACKNOWLEDGMENTS

The authors acknowledge support from the UK Engineering and Physical Sciences Research Council (EPSRC) through grants EP/P01058X/1 and EP/P008275/1.

10.1126/science.abn1053

QUANTUM INFORMATION

A new Hall for quantum protection

Long-range vacuum fluctuations break the integer quantum Hall topological protection

By Angel Rubio^{1,2}

Cavitronics—a portmanteau of cavity and electronics—are devices with certain properties that can be controlled by the light waves bouncing inside the cavity in which the device sits. In quantum mechanical terms, this interaction between light and matter is done by the standing light waves inside the cavity known as vacuum field states. A major advantage of this setup for generating light-matter coupling is the ability to induce certain properties inside a material that otherwise require the use of a strong external electric or magnetic field (see the image). On page 1030 of this issue, Appugliese *et al.* (1) provide a special case of cavitronics. Their experimental setup modifies one of the most prominent quantum phenomena in materials, known as the quantum Hall effect (QHE). They found a drastic change in its Hall resistance, opening the path to designing materials functionalities by vacuum-field engineering.

When an electric current is passed through a conductor under the influence of a magnetic field, an electrical voltage perpendicular to the current is induced by the magnetic field. This is known as the Hall effect. However, this “sideways” voltage sometimes happens in steps rather than linearly as a function of the magnetic field (2, 3). This constitutes the QHE, namely a quantized version of the classical Hall effect (2), in which the Hall conductance exhibits steps, or Hall plateaus, at precisely integer and fractional multiples of the inverse of the quantum of resistance (4).

Whereas conventional resistance de-

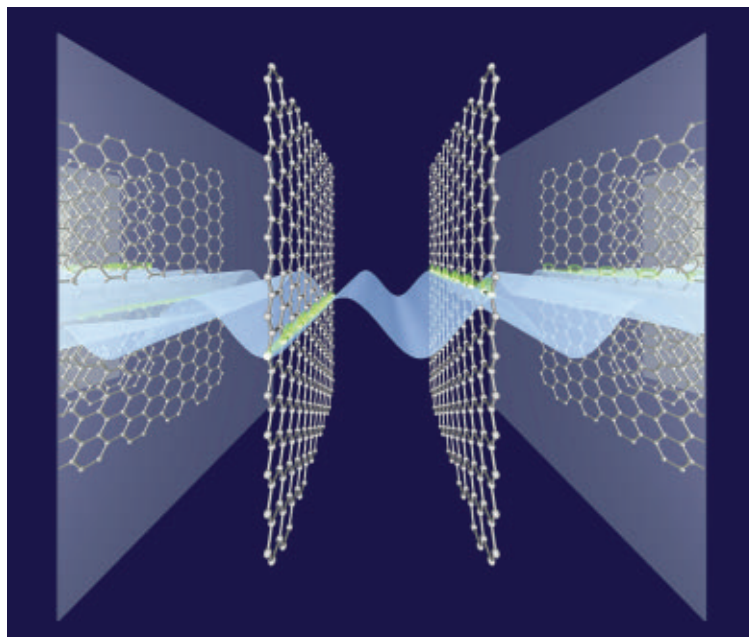
¹Max Planck Institute for the Structure and Dynamics of Matter and Center for Free-Electron Laser Science, Luruper Chaussee 149, 22761 Hamburg, Germany. ²Center for Computational Quantum Physics (CCQ), The Flatiron Institute, 162 Fifth Avenue, NY 10010, USA. Email: angel.rubio@mpsd.mpg.de

depends on the material's geometry and external factors, the quantum Hall resistance depends only on fundamental constants and can be reproduced with extraordinary precision. Not surprisingly, the QHE has become the primary standard of resistance metrology. The robustness of the QHE to structural defects, disorders, and other perturbations is a prominent manifestation of "topological protection," a desirable and advantageous property for many emerging quantum information applications. Without this protection, the quantum states of materials are subjected to changes caused by temperature-dependent scattering and dissipative processes. To protect certain quantum states from external disturbances, materials with specific symmetries can decouple some quantum states from interacting with the rest of the sample. Those are the so-called topological protected states, which are robust to external perturbations and have long lifetimes.

How robust can this topological quantum protection be, with respect to spatially long-range perturbations acting on the entire device? To answer this question, Appugliese *et al.* created a two-dimensional (2D) electron-gas device embedded in a splitting cavity resonator. Vacuum field states, which span the whole space inside the cavity, provide the sought spatially long-range interactions inside the device. This interaction creates new light-matter hybrid states, referred to as polaritonic states, with characteristics that neither the original material nor the cavity field state possesses. This hybridization effect is proportional to the strength of the light-matter coupling inside the cavity and can be better detected if the device is brought to a strong coupling regime (5–9), but this is often not the case as the light-matter coupling is generally weak. By confining the light field in a small region of space (the cavity), the probability of photon absorption and therefore the light-matter coupling strength, increases. Recent advances in cavity design have enabled the practical realization of this strong light-matter coupling regime (10).

The device created by Appugliese *et al.* realizes a strong light-matter coupling regime. Surprisingly, the authors observed that a

dark cavity, without external illumination, breaks the quantization of the Hall conductivity over a wide range of applied magnetic fields. They measured up to 11 integer Hall plateaus for the device outside the cavity. The shape of those plateaus is modified when immersed in the cavity, with especially strong changes for odd-numbered plateaus. The authors also found that the fractional Hall plateaus are much less af-



Cavitronics are devices whose properties can be controlled with the light waves, or vacuum field states, of the cavity. Researchers created a cavitronic device embedding a two-dimensional electron gas in a cavity where the quantized Hall conductivity is modified, paving the road for future design of materials for quantum technology applications.

ected by the cavity, which seems to be consistent with the observation that fractional plateaus couple weakly to light (3, 4). Those findings offer a new route to control quantum materials.

Why does the cavity modify the otherwise topologically protected integer quantum Hall conductivity in quantum Hall devices? To answer this, it is important to bring up the connection between topological protection and the physical path taken by the physical Hall current, which is localized at the edges of the device. The robustness of the QHE is linked to the physical separation of this edge current from the bulk of the sample. However, the vacuum field states of the cavity facilitate the hopping of electrons between the states carrying the edge current and the bulk states of the sample. This new coupling channel gives rise to the breakdown of the topological protection of the QHE. The microscopic process behind this coupling involves several intermediate states in which the defects in the sample play an important role (11). The demon-

stration that the cavity vacuum field states circumvent the QHE topological protection supports recent predictions about the cavity modification of the quantum Hall resistance in defect-free 2D devices (12) when the cavity field is larger than the external applied magnetic field.

Experimental and theoretical research on the control of materials by engineering cavity vacuum fields is destined to considerably accelerate and expand. Controlling the environment surrounding a material inside a cavity can alter its properties, enabling the design of quantum materials and phenomena (7). Recent theoretical predictions for a material's quantum phenomena mediated by cavity photons include photon-mediated superconductivity, ferroelectricity, and magnetism, as well as the control of many-body interactions and topological phenomena in multilayer 2D materials. These are among the lines of research that may soon come under the umbrella of "cavity materials engineering," which can be used to induce specific functional properties, such as superconductivity, in materials. For example, it may be possible to control, in twisted bilayer graphene and transition metal

dichalcogenides, the low-energy scales of their moiré electronic bands and electron-correlated phases with engineered cavity vacuum field states to create new exotic states of matter (13, 14), increasing the impressive portfolio of materials phenomena in 2D heterostructures. ■

REFERENCES AND NOTES

1. F. Appugliese *et al.*, *Science* **375**, 1030 (2022).
2. K. Klitzing, G. Dorda, M. Pepper, *Phys. Rev. Lett.* **45**, 494 (1980).
3. I. V. Kukushkint *et al.*, *Nature* **415**, 409 (2002).
4. H. L. Stormer, D. C. Tsui, A. C. Gossard, *Rev. Mod. Phys.* **71**, S298 (1999).
5. C. Genet, J. Faist, T. W. Ebbesen, *Phys. Today* **42**, (2021).
6. F. J. Garcia-Vidal, C. Ciuti, T. W. Ebbesen, *Science* **373**, eabd0336 (2021).
7. H. Hübener *et al.*, *Nat. Mater.* **20**, 438 (2021).
8. A. Frisk Kockum *et al.*, *Nat. Rev. Phys.* **1**, 19 (2019).
9. P. Forn-Díaz *et al.*, *Rev. Mod. Phys.* **91**, 025005 (2019).
10. G. L. Paravicini-Bagliani *et al.*, *Nat. Phys.* **15**, 186 (2019).
11. C. Ciuti, *Phys. Rev. B* **104**, 155307 (2021).
12. V. Rokaj, M. Penz, M. A. Sentef, M. Ruggenthaler, A. Rubio, *arXiv* 2109.15075v1 (2021).
13. L. Balents, C. R. Dean, D. K. Efetov, A. F. Young, *Nat. Phys.* **16**, 725 (2020).
14. D. M. Kennes *et al.*, *Nat. Phys.* **17**, 155 (2021).

CATALYSIS

Catalyst coaxed to make branched α -olefins

Process conditions allow a titanium catalyst to add just two ethylene molecules to an α -olefin

By **Mari S. Rosen**

Linear and branched α -olefins are an important class of chemicals that are used for making polyolefins, detergents, plasticizers, and lubricants, as well as other products, and are made in quantities that exceed 3.2 million tonnes per year (1). These α -olefins, which have been produced on an industrial scale for almost a century (2), are typically made in processes that generate a broad distribution of products. More recently, on-purpose technologies have been developed to synthesize particular linear α -olefins. By contrast, branched α -olefins are produced in non-selective processes such as fluid catalytic cracking and oligomerization of olefins with acid-based or transition metal catalysts (3, 4). On page 1021 of this issue, Dietel *et al.* (5) now add to the collection of on-purpose α -olefin technologies with their report of a method for selectively synthesizing branched α -olefins.

On-purpose technologies for linear α -olefin synthesis first appeared with the report of ethylene dimerization to make 1-butene in 1960 (see the figure) (6). Later advances include ethylene trimerization to produce 1-hexene in 1989 (7) and ethylene tetramerization to produce 1-octene in 2004 (8). The importance of these processes is reflected in their subsequent commercialization, and all three are practiced on an industrial scale today (9, 10).

The impressive selectivities of the titanium- and chromium-based catalysts used for selective ethylene oligomerization have been attributed to a mechanism that uses metallacycle intermediates (7, 11). Notably, the catalyst designed by Dietel *et al.* instead makes use of more traditional transition metal-based ethylene polymerization catalysts, which typically operate through a Cossee-Arlman mechanism, to produce a Schulz-Flory distribution of polymers of different lengths (9). Polymer molecular weight is not only defined by catalyst fea-

tures such as transition metal and ligand choice but also by process parameters such as ethylene concentration and reaction temperature (12).

The system reported by Dietel *et al.* uses a titanium-based catalyst with aminopyridinato and imidazolidiniminato ligands that, under typical olefin polymerization conditions, produces a Schulz-Flory distribution of low-molecular weight oligomers. However, by selecting process conditions that feature a very low concentration of ethylene and a high concentration of an

and one α -olefin, and 1-butene. Notably, no polymer by-products were observed that could lead to fouling issues and that plague many ethylene tetramerization catalyst systems (9).

This excellent selectivity does not come with any sacrifices in catalyst activity, with turnover frequencies reported to be as high as 2.3×10^6 per hour. Based on the catalyst and product amounts in the provided examples, this rate can be converted to a catalyst activity of 2.1×10^6 grams of product per gram of titanium per hour,

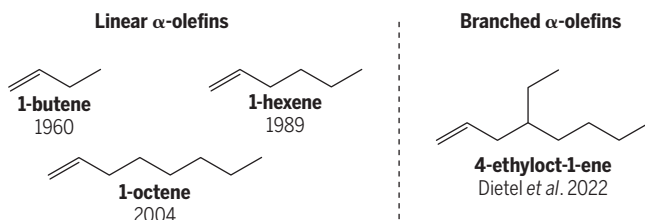
which is a comparable activity to top-performing chromium-based ethylene trimerization and tetramerization catalysts (8, 13). Dietel *et al.* also demonstrate the versatility of the catalyst system by successfully performing this trimerization reaction with linear α -olefins from 1-pentene to 1-hexadecene and also with non-aliphatic and cyclic α -olefins like styrene and norbornene.

This work enables the selective synthesis of a broad range of branched α -olefins and undoubtedly will spur additional research in this area. Ultimately, the system described by Dietel *et al.* demonstrates

the power of combining both judicious catalyst design along with careful choice of process conditions to make an otherwise conventional catalyst perform useful reactions. New products are likely to be developed that take advantage of the availability of pure branched α -olefins. ■

On-purpose oligomerization

The synthesis of α -olefins usually forms a broad product distribution, but several selective routes for linear α -olefins have been developed. Dietel *et al.* now report that a titanium catalyst run under olefin-rich conditions is highly selective for producing branched α -olefins.



α -olefin, the authors produced a branched α -olefin trimer product that incorporates two ethylene molecules and one α -olefin (see the figure).

The combination of catalyst and process conditions described by Dietel *et al.* results in up to an impressive 74 mole % selectivity of the desired branched α -olefin product. This selectivity is excellent given that, until this report, it had been thought that a metallacycle mechanism would be needed to explain a selective olefin trimerization (7, 11). Important to achieving the high selectivity in this work are key attributes of the catalyst: It terminates the growing chain readily, and, as a good α -olefin incorporator, it has a high probability for including any α -olefins present in the growing oligomer chain. When such a catalyst is combined with a reaction environment that is rich in α -olefins and lean in ethylene, the selective synthesis of a branched α -olefin product results. The side products of this reaction include a branched species with an internal olefin, an α -olefin tetramer product made from three ethylenes

REFERENCES AND NOTES

1. P.-A. R. Breuil, L. Magna, H. Olivier-Bourbigou, *Catal. Lett.* **145**, 173 (2015).
2. C. P. Nicholas, *Appl. Catal. A Gen.* **543**, 82 (2017).
3. Y. V. Kissin, *Catal. Rev., Sci. Eng.* **43**, 85 (2011).
4. A. Forestière, H. Olivier-Bourbigou, L. Saussine, *Oil Gas Sci. Technol.* **64**, 649 (2009).
5. T. Dietel, F. Lukas, W. P. Kretschmer, R. Kempe, *Science* **375**, 1021 (2022).
6. K. Ziegler, H. Martin, US Patent 2,943,125 (1960).
7. J. R. Briggs, *J. Chem. Soc. Chem. Commun.* **1989**, 674 (1989).
8. A. Bollmann *et al.*, *J. Am. Chem. Soc.* **126**, 14712 (2004).
9. O. L. Sydora, *Organometallics* **38**, 997 (2019).
10. D. S. McGuinness, *Chem. Rev.* **111**, 2321 (2011).
11. T. Agapie, S. J. Schofer, J. A. Labinger, J. E. Bercaw, *J. Am. Chem. Soc.* **126**, 1304 (2004).
12. M. C. Baier, M. A. Zuideweld, S. Mecking, *Angew. Chem. Int. Ed.* **53**, 9722 (2014).
13. S. Kuhlmann *et al.*, *J. Catal.* **262**, 83 (2009).

A role for funders in fostering China's research integrity

Despite recent progress, challenges remain

By Li Tang

Given its sheer scale and growth, China's scientific research and development (R&D) enterprise can have tremendous effects across the global scientific community in terms of both research quality and research integrity (1, 2). Although issues of research funding and integrity arise in countries around the globe, they are particularly salient in China given the major role of government funding in supporting research and the alarming number of scientific publications by authors affiliated with Chinese institutions that have been retracted. With its pivoting position in knowledge production, the Chinese science grant system is taking a greater role in curbing scientific misconduct and fostering research integrity. Despite this, several barriers remain.

The Chinese science grant system plays a major role in supporting basic research, including a huge amount of false science as evidenced by journal retractions. Unlike many counterparts in other countries, many Chinese universities and research institutes are often reluctant to initiate and publicize misconduct investigations. As an emerging science power, Chinese attention toward spotting and stopping misconduct is a rather recent phenomenon. With its voluminous history of print publications, it takes quite a while for the Chinese government and scientific community to process and prioritize certain misconducts to investigate, punish, and deter.

PROGRESS

Policy formulation

The Chinese scientific community has taken proactive stances against academic misconduct and toward fostering responsible research. A series of policy documents, initiatives, and codes on research integrity, which often involve the science grant system, were issued, revised, and adopted across different

sectors over the past 3 years. For example, in 2019 the Ministry of Science and Technology (MOST), the Central Propaganda Department, the Ministry of Education (MOE), the National Health Commission (NHC), the National Natural Science Foundation of China (NSFC), the Chinese Academy of Social Sciences (CASS), the Ministry of Finance (MOF), and 13 other central agencies jointly issued *The Rules for the Investigation and Handling of Research Integrity Cases (Trial)*. Focusing on research grants management, the revised version of *Measures for Investigation and Handling of Scientific Research Misconduct in National Natural Science Foundation of China* became effective from 1 January 2021. The most recent and prominent change is demonstrated in the *Law on Scientific and Technological Progress of the People's Republic of China* effective on 1 January 2022. This marks the first time that Chinese law (instead of past agency regulation or measures) has prohibited individuals and organizations from buying research papers, grant proposals, and laboratory experiments. In a departure from its 2007 version, research integrity (pinyin, “keyan chengxin”) appeared in six articles of the latest law promoting science, technology, and innovation, laying legal foundation of research integrity cultivation.

Implementation

In addition to issuing regulations and codes, the enforcement efforts of the Chinese science grant system in curbing misconduct are evident. For example, the NSFC, China's largest funder of basic research, has adopted an integrated approach to crack down on funding-related misconduct. They limit the number of proposals an individual can submit per, for example, a given time, competition, or agency; restrict the number of supporting representative research publications that can be submitted; use plagiarism-detection software for grant proposals; publicize investigation results on confirmed misconduct of both unfunded grant applications and awarded grants; release names of proposal reviewers; and earmark grants for research integrity studies.

The NSFC is not the only agency demon-

strating a strong commitment to research integrity. In June 2021, the NHC launched a special column on its official website, providing education and training on research integrity for medical researchers and practitioners and publicizing misconduct investigation results. Within 7 months (June to December 2021), the NHC released 310 investigation results involving more than 850 researchers with confirmed research misconduct, with punishments ranging from admonishment to disqualification of career promotions and grant applications in given years to suspension and debarment. CASS, the statutory agency overseeing integrity in social and humanities research, launched its official website of research integrity in March 2021. The National Research Integrity Information Management System is in operation and has been compiling information from grantees (affiliations) on proven misconducts, punitive actions, and integrity construction.

Evaluation

Progress is also underway in how funding proposals are evaluated and performance of awarded grants is assessed, to counteract the detrimental effects of excessive pursuit of publishing in international journals. Research evaluation practices that prioritized tallying articles published in international journals have partially contributed to excessive low-quality articles and false science, which is detrimental to science globally. Encouraging publications in domestic journals, decoupling cash bonuses from publications included in the Science Citation Index (SCI), and shifting emphasis in faculty recruitment selection to teaching and training students are gradually taking place in Chinese elite universities and research institutes. In the merit-review phase of awarded grants, Chinese major administrative apparatus and funding agencies such as MOST, MOE, and NSFC have adopted a one-vote veto of “scientific misconduct” in their funding and talent-rewarding decisions.

CHALLENGES

The science grant system still faces five barriers that must be dealt with in its ongoing mission of research integrity reform.

Dual absence of victim and complainant

The damage of research misconduct, although affecting the entire scientific enterprise, is diffused and obscure for specific individuals or groups. Potential direct victims bearing the cost of the violation could be the general taxpayers or grantee's substitutes (the would-be awardees), who often either do not care or are not aware of this cost. Insiders may remain silent because of con-

School of International Relations and Public Affairs,
Fudan University, Shanghai, 200433, China.
Email: litang@fudan.edu.cn

cern about the burden of proof of hard evidence and possible retaliation by fraudsters. This dual absence of victim and complainant signals a low probability of being caught and encourages intentional deviant behavior (3).

Limited sanction tools of funding agencies

Being public organizations, major Chinese science funding agencies such as MOST, NSFC, and MOE have their hands tied with multiple tasks. Curbing misconduct is still in its nascent phase in China. Given the lag of legal authorization and specific measures for punishment, misconduct investigators and funding agencies often use discretionary power to enforce punishments if legal authorization has not been granted. But there is potential risk in doing so. There were some types of fraudulent actions that are not explicitly prohibited on the legal level. Except for explicitly stated limited tools of heightening the scrutiny of grant applications, terminating research funding, retrieving allocated funding, publicizing misconduct investigation, and circulating criticism within their jurisdiction, funding agencies have no direct influence on fraudsters' salaries, employment, and career development. In the ongoing battle against misconduct, the potential questioning of the legality of available policy tools and punishment actions makes science grant agencies reluctant to exercise penalties.

Dilemma of collective punishment

Chinese scholars and practitioners remain split on the legitimacy and effectiveness of collective punishment on principal investigators (PIs), affiliated institutions, and team members. Opponents contend that it is unfair for PIs or affiliated organizations to shoulder the responsibility of others' misbehavior. They believe that an increasing phenomenon of blended or braided funding across different sectors and countries makes collective punishment even more challenging and unrealistic. The supporters, however, argue that credit and responsibility are inseparable from the fault of omission. They hold that responsibility is the price of honor, and liability should not be limited to fraudsters per se. Through collective punishment, the funding agencies could reclaim their monetary losses, remind senior researchers to safeguard the integrity of joint knowledge production, and alert affiliations and research managers of their oversight and education responsibilities.

Enforcement difficulties

Difficulty of enforcement is a universal challenge in sanctioning infractions, including for misconduct investigations in the Chinese science grant system. Inundated with mount-

ing grant applications, short-staffed public funding agencies are inclined to support innovative research proposals rather than to oversee, investigate, and sanction funding-related misconducts that demand time, financial support, and human resources. Over the period of 2011 to 2020, NSFC funding applications grew at an average annual rate of 9.0%, in sharp contrast to a 3.7% growth rate in the number of in-service personnel at NSFC to handle this increasing workload over the same period. In 2020, the NSFC alone received 281,200 grant applications and funded 45,700 proposals. In the same year, the NSFC initiated 525 misconduct investigations after preliminary review; 165 respondents and eight affiliated organizations were sanctioned to various extents (4).

research paradigms toward team science, interdisciplinary integration, and collaboration involving people of disparate backgrounds.

ACTIONS

These five predicaments are inextricably intertwined and represent great challenges facing the Chinese science grant system to curb misconduct, cultivate integrity, and promote responsible research and innovation. How can funding agencies address or ameliorate these issues? I propose the following suggestions.

Classifying gradients of misconducts and degrees of sanctions

Chinese funding agencies need to achieve consensus and draft measures to decide



Lack of consensus

The progress of research misconduct sanctions and integrity cultivation are imbedded in and thus affected by the national and local cultural, economic, and political systems to which they are oriented. Funding agencies, research managers, and university research ethics committees agree on the direction of the path, but both the pace of development and extent to which institutions can devote resources to the mission remains debatable. Within the Chinese science grant system, different agencies and awardee organizations have not reached an agreement on the demarcation line between research ethics and integrity, questionable research practices and research misconducts, and the punitive scope and severity for principals and accessories involved in proven misconducts. This issue is further compounded by shifting scientific

the gradients of misconducts and degrees of sanctions. Bold policy cannot go far without well-crafted design and solid implementation. Institutionalizing anti-misconduct reform, including classifying misbehavior and sanctions for handling alleged misconducts, can help, at least to some extent, to maintain standards even when political focus or media attention wane, to reduce contrived randomness of enforcement when combined with due process and procedural justice for handling alleged misconducts (5), and to make curbing grant-relevant misconducts consistent, manageable, and sustainable across different agencies. Classification needs to take the "first forgive then get tough" principle into consideration (2). To what extent and for how long the limited nonretrospective rule can be applied must be clarified on

the basis of experts' inputs. This seemingly weak countermeasure may be practical when dealing with the alarming stock of past misconducts and rising retractions of Chinese articles, which could be an artifact of better global oversight or a growing caution toward Chinese contributed knowledge production evidenced by shorter retraction time (6, 7).

Strengthening gatekeeping

As the engine of basic research and stewardship of public funds, the quality of peer review, anonymous correspondence review, or panel review of grant applications plays a critical role in selection excellence and upholding research integrity. Hometown-based favoritism, rent-seeking, and other nonmerit factors are non-negligible in the Chinese science system (8–10). The RCC (responsibility, credibility, contribution) principle has been recently proposed and trialed by the NSFC (11). However, to be effective in gatekeeping misbehavior, RCC has to be applied in tandem with fair artificial intelligence algorithms to assist grant proposal distribution to a sufficient number of trustworthy and qualified experts.

Proper incentivizing

Detecting, disclosing, and sanctioning socially deviant behavior can be particularly difficult in Asian cultures that value collectivism and organizational loyalty. To recoup public money misused on fraudulent research, proper incentives need to be adopted for misconduct whistleblowers, expert panels of misconduct investigations, punitive enforcers, and other stakeholders in grant-relevant research activities. Some countries have adopted an appropriate division of recovered grants [for example, in the US case of Thomas vs. Duke University, the court decided the amount of money that Duke is to pay back to the federal government (recovered grant) given its violation of the False Claims Act]. In China, people are rewarded for whistleblowing in some fields such as environmental protection, food and drug safety, and so on. The negative consequences of money for publication may be also applicable to misconduct whistleblowers. Therefore, compensation en masse can be applicable in the science grant system in the future, letting the valid whistleblowers reap the benefits of recovered grants to compensate the risk of retaliation for revealing grant-related frauds. Funding agencies must reward whistleblowers wisely and vigilantly to avoid perverse incentives or bounties that risk glaring instances of alleged misconduct in the pursuit of fortune. Proper incentives should be extended to research managers

and supporting staff for outstanding work in research integrity cultivation.

Enhancing transparency

Research funded by public money should be available to scientific peers and the public. Chinese funding agencies have made noticeable improvements in transparency aspects, such as NSFC publicizing abstracts of funded proposals and funded research outputs and the National Office for Philosophy and Social Sciences (NOPSS) publishing selected funded research output. NSFC, NOPSS, and more recently NHC regularly disclose grant debarments and investigation results.

More can be done. To reduce funding fragmentation and duplicate awards across different agencies (12), the long-called-for integrated funding platform can be extended beyond MOST with awarded projects, research data, and findings of public funded research accessible to the scientific community. The decision by multiple agencies to no longer publicize the names of awardees of prestigious talent programs has raised some concerns within and beyond national borders. More transparency not only reduces reinventing the wheel in public funding and encourages competitive ideas (13) but also alleviates the cost of oversight and deters potential misconduct.

Extending integrity education and training

It has been increasingly accepted in the Chinese scientific community that integrity education and training outweigh misconduct sanctioning when factoring in effectiveness, efficiency, and equity into consideration. Such education and training need to be more extensive and specialized in the science grant system.

The Matthew effect of research resources (“the rich get richer”) combined with the inevitable rise of team science and division of labor calls for team-oriented rather than individual-oriented ethics and integrity training and education (14). Such collaborative education and training should be extended not only to PIs who manage large laboratories and contribute to substantial numbers of publications but also to earlier career researchers, data analysts, and supporting technicians who work in large research teams to be aware of data cross-checking and collaborators' knowledge validation.

In addition, the Chinese science grant system needs to tailor research ethics and academic integrity education considering the differences between natural sciences and social sciences; the latter has been long sidelined in research integrity cultivation. In the evidence-based or evidence-informed

policy-making era, the quality and integrity of social science studies impacts are the same as if not greater than the natural sciences. Extensive and specialized education modules can be set as mandatory before researchers submit grant applications or awardees sign a contract, as well as before midterm assessments for all team members.

AGENDA FOR TOMORROW

Research integrity is the cornerstone of the science, technology, and innovation system. The Chinese science grant system alone is insufficient to reduce funding-relevant research fraud. In tandem with carefully optimistic and patient objectives, reinforcing research integrity must be advanced in alignment with China's ongoing reform of science and technology evaluation. It must be systematic and involve orchestrated efforts of different stakeholders across the whole spectrum of scientific exploration, within and beyond national boundaries. For example, Chinese funding agencies can initiate and engage with other stakeholders to participate in and organize global academic conferences and practitioner workshops such as the World Conferences of Research Integrity, Asian and Pacific Rim Research Integrity Network, and so on to share best practices (15). Through people-to-people and agency-to-agency exchanges such as the Integrity Ambassador Program, Chinese funding agencies can strengthen their collaboration with their international counterparts, sending out and inviting in experts to learn from each other to foster research integrity and promote responsible and innovative research. ■

REFERENCES AND NOTES

1. National Science Board, National Science Foundation, *Science and Engineering Indicators 2020: The State of U.S. Science and Engineering*; <https://ncses.nsf.gov/pubs/nsb20201>.
2. L. Tang, *Nature* **575**, 589 (2019).
3. E. A. Fong et al., *J. Law Med. Ethics* **48**, 331 (2020).
4. NSFC, NSFC Annual Reports (accessed 2 October 2021); www.nsf.gov.cn/csc/20345/20290/index.html.
5. C. Hood, O. James, B. G. Peters, C. Scott, Eds., *Controlling Modern Government: Variety, Commonality and Change* (Edward Elgar Press, 2004).
6. J. Brainard, *Science* **362**, 390 (2018).
7. L. Tang et al., *Sci. Eng. Ethics* **26**, 1681 (2020).
8. Y. Xie, *Science* **355**, 1022 (2017).
9. R. Fisman et al., *Polit. Econ.* **126**, 1134 (2018).
10. Y. Shi, Y. Rao, *Science* **329**, 1128 (2010).
11. G. Chen et al., *Bull. Chin. Acad. Sci.* **36**, 1427 (2021).
12. Y. Sun, C. Cao, *Science* **345**, 1006 (2014).
13. S. Feigenbaum, D. M. Levy, *Rationality Soc.* **8**, 261 (1996).
14. J. Walsh et al., *Res. Policy* **48**, 444 (2019).
15. D. Moher et al., *PLOS Biol.* **18**, e3000737 (2020).

ACKNOWLEDGMENTS

The research is partially funded by the Ministry of Education (17YJAZH075) and the National Natural Science Foundation of China (L2024009). I thank the four anonymous reviewers for their insightful comments. The views expressed here are those of the author and do not reflect the positions of the funders.

10.1126/science.abm7992



A farmer carries freshly harvested genetically modified cauliflower in Panchkhal, Nepal, in 2020.

BOOKS *et al.*

SYNTHETIC BIOLOGY

Life-changing biology

Genetically engineered genomes will disrupt the bioeconomy and rewrite human nature—are we ready?

By **Adrian Woolfson**

When interviewed in 1958 by *The Paris Review*, Ernest Hemingway confessed to having rewritten the ending of *A Farewell to Arms* a total of 39 times. The writer Raymond Chandler, on the other hand, adopted a different approach. He encouraged authors to “throw up” into their typewriters every morning and “clean up” at noon.

The strategy adopted by evolution by natural selection in authoring the genomes of living things has, by necessity, been more aligned with the latter approach than the former. While allowing individual letters in the genetic text to be edited, and facilitating the deletion, insertion, recombination, and duplication of more substantial genomic regions, evolution precludes throwing the entire folio away and starting again from scratch. Synthetic biology practitioners, however, are not necessarily bound by such constraints.

In their engaging and energetic new book, *The Genesis Machine*, Amy Webb and Andrew Hessel outline an optimistic manifesto for synthetic biology whereby “new biological circuits” and

“programmable cells” will, if they are right, eventually upend traditional methods for building genomes. They assert that we are rapidly approaching a time when it will be possible to design and artificially synthesize the genomes of living things, including those of humans, from first principles.

The release of genomes from the constraints of evolution and the ability to prespecify genetic configurations are, the authors argue, likely to transform human nature and that of all living things. At a minimum, they may eliminate the “bad genes” underlying straightforward genetic diseases and remove some of the anguish and uncertainty of human reproduction. They will also establish the foundations of a biologically inspired industrial revolution and initiate a disruptive new bioeconomy.



The Genesis Machine
Amy Webb
and Andrew Hessel
PublicAffairs, 2022. 368 pp.

DNA sequences might one day replace existing information storage technologies, the authors speculate. Meanwhile, the synthetic production of protein drugs by cells in the body, while having a beneficial effect on clinical medicine, may adversely affect the current biopharmaceutical industry. And genomically rewritten crops, while helping to achieve global food security, may restructure the agricultural industry.

Although existing biofoundries and related methods of DNA assembly have en-

abled the construction and recoding of simple genomes such as that of the bacterium *Escherichia coli* (1), the realization of the type of “genesis machine” envisaged by the authors—an entity capable of synthesizing the genomes of complex organisms from scratch—has remained elusive. A “DNA typewriter” will be required to achieve this goal. However, given that genome reading technologies have advanced to the point that human genomes can now be sequenced inexpensively within hours, it is not unreasonable to assume that genome writing technologies will follow suit.

Even more challenging and time-consuming than DNA writing is the debugging that synthetic genomes will likely require. Efficient genome writing will need to be tightly coupled to quality control.

It is one thing to have the ability to write genomes and another to know what to say. In this regard, databases of DNA sequences derived from natural organisms will help elucidate the principles necessary for effective genome authorship. The success with which machine learning enabled the artificial intelligence program AlphaFold to predict the unknown structures of proteins (2) vindicates this type of approach.

Biowarfare and the unpredictability of the ecological impact of bioengineering aside, and regardless of whether we will eventually be forced to choose between extinction or reengineering in order to survive, the issue of who will determine genome authorship, and how it will be deployed and regulated, is nontrivial. The power to control the essential substance of human nature may be a willing handmaiden of totalitarian agendas.

Ethical constructs, furthermore, are more fluid than we might like. The authors reference China’s national DNA drive to “collect, sequence, and store its citizens’ genetic data” and its prioritization of synthetic biology in a quest for “global science and tech hegemony.”

It appears, however, that governmental agencies have largely ignored the strategic implications of synthetic biology. Without greater attention to this topic, we risk being blindsided by the “great transformation of life” that is already underway. ■

REFERENCES AND NOTES

1. J. Fredens *et al.*, *Nature* **569**, 514 (2019).
2. J. Jumper *et al.*, *Nature* **596**, 583 (2021).

ACKNOWLEDGMENTS

A.W. is a cofounder of Replay Holdings LLC, which maintains interests in gene therapy, genome engineering, and genome writing.

The reviewer is at Replay Holdings LLC, San Diego, CA, USA, and author of *Life Without Genes* (HarperCollins, 2000). Email: adrianwoolfson@yahoo.com

10.1126/science.abm9852

SCIENCE LIVES

The lasting legacy of John von Neumann

A new biography seeks to reacquaint readers with the once widely celebrated scientist

By **Dov Greenbaum**^{1,2} and **Mark Gerstein**²

John von Neumann, often referred to by his peers as Johnny, was a Hungarian American polymath and prodigious academic who made vital contributions to numerous fields of study during the first half of the 20th century. In 2022, however, von Neumann could be the smartest person most people have never heard of. To wit, Google Trends shows that his online popularity last year was almost an order of magnitude less than that of Alan Turing, a contemporary in computing; Erwin Schrödinger, a predecessor in quantum mechanics; and Stephen Wolfram, a successor in the world of automata.

This remarkable scholar was not always uncelebrated. “When he died, aged just fifty-three, von Neumann was as famous as it is possible for a mathematician to be,” writes Ananyo Bhattacharya in *The Man from the Future*, which examines the tremendous impact von Neumann had on various scientific disciplines in eight exceptional chapters.

Bhattacharya observes that von Newman “constantly sought new practical fields to which he could apply his mathematical genius, and he seemed to choose each one with an unerring sense of its potential to revolutionize human affairs.” His research and insights were as invaluable to the emerging military-industrial complex as they were to IBM, and his adherents ranged from hardcore “cold warriors” to groundbreaking computer engineers to radical innovators working on artificial life. At the end of his life, as he lay dying in a hospital, he was surrounded by the secretary of defense; the deputy secretary of defense; the secretaries of the air force, army, and navy; and the chiefs of staff. He left the hospital briefly in a wheelchair to accept the Medal of Freedom from President Eisenhower, notes

Bhattacharya. “We need you,” the president informed him.

The book sketches the natural progression of von Neumann’s academic development, demonstrating how his early work with David Hilbert in Göttingen provided the mathematical foundation for his later work on matrix mechanics and formalizing computers and algorithms and how the degree he earned in chemical engineering from ETH Zurich—a compromise with his banker father, who considered engineering a more financially prudent educational pursuit than mathematics—may have steered him toward more applied pursuits, such as bomb-making



Von Neumann receives the Medal of Freedom from President Eisenhower in 1956.

and computer engineering. Meanwhile, his work in digital computing led von Neumann to a late-in-life interest in artificial life, automata, and the brain.

Compared with his other pursuits, von Neumann’s path to game theory was not as obvious. It is, nonetheless, where he made some of his greatest contributions. “A half-dozen Nobel laureates are reckoned to have been influenced by the work,” notes Bhattacharya.

Apart from game theory, von Neumann is perhaps best known today for his work in computing. His incomplete *First Draft of a Report on the EDVAC* (the electronic discrete variable automatic computer) has become the “most influential document in the history of computing,” describing what we now intuit as the necessary components of a computer:

**The Man from the Future:
The Visionary Life
of John von Neumann**
Ananyo Bhattacharya
Norton, 2022. 368 pp.



a processing unit, a control unit, random access memory, mass storage, and input and output methods.

This report was not without controversy. Von Neumann appears to have scooped the efforts of John W. Mauchly and J. Presper Eckert, other early pioneers in the field. More than a mere academic slight, the battle over the invention of the modern computer became “the longest trial in the history of the federal court system.” Ultimately, however, the courts ruled, as von Neumann had intended, that the basic ideas of the digital computer were left to the public domain.

The reader learns much about math and physics in this biography, including the differences between the matrix and wave interpretations of quantum mechanics, Gödel’s incompleteness theorems, and the mathematics that underlies the Turing machine. In contrast, we learn sparingly little about von Neumann’s personal life: for example, that he had an interesting custody agreement with his first wife (his daughter, Marina, was to live

with her mother until she reached “the age of reason,” at which point she would live with her father in order to “receive the benefit of his genius”), that he enjoyed partying, and that he “showed signs of obsessive-compulsive disorder.” “A drawer could not be opened unless it was pushed in and out seven times,” according to his second wife. “The same with a light switch, which also had to be flipped seven times before you could let it stay.”

Many of von Neumann’s prescient ideas still play an immeasurable role in modern life more than half a century after his death. Reacquainting modern readers with “the most famous scientist in America after Einstein,” *The Man from the Future* calls attention to a conundrum: Why has von Neumann so largely faded from contemporary view? ■

10.1126/science.abn7018

The reviewers are at ¹Zvi Meitar Institute for Legal Implications of Emerging Technologies, Radzyner Law School, Reichman University, Herzliya, Israel; and ²Computational Biology and Bioinformatics, Yale University, New Haven, CT, USA. Email: dov.greenbaum@aya.yale.edu



LETTERS

Greece has banned the construction of new roads in some of its mountainous areas, a policy that can proactively protect vulnerable habitats and species.

Edited by Jennifer Sills

Greek roadless policy: A model for Europe

On 18 January 2022, the Greek government banned road construction in six Natura 2000 roadless mountainous areas, triggering a broader national roadless policy (1). Road sprawl is a key catalyst of land use change, which is the greatest threat to biodiversity worldwide (2). For years, scientists have called for halting infrastructure expansion, including roads, to protect biodiversity (3–6), with little success. Greece's policy should serve as a model for the EU.

Europe is the most road-fragmented continent (4). However, the EU has not yet passed legislation to protect its natural ecosystems from new road construction, as the United States did for its forests in 2001 (5, 6). In 2011, the EU set a goal to eliminate new land conversion to artificial land by 2050 (known as the “no net land take” milestone) (7), but the target was not legally binding. In the years since, land conversion to artificial land, soil imperviousness, landscape fragmentation, and land use change have increased, and terrestrial biodiversity has continued to decline (8). The EU's 2030 Biodiversity Strategy commits to legally protect a minimum

of 30% of the EU's land area but does not address road fragmentation (9). The plan will allocate billions of euros for planting trees and restoring degraded environments but leave natural ecosystems vulnerable to new roads and land-consuming projects. This conflict is particularly pronounced in biodiversity-rich European countries such as Spain and Greece, which are facing a rapid expansion of renewable energy infrastructures in ecologically sensitive zones (10, 11).

Europe is a densely populated continent that still holds large tracts of natural unfragmented lands (12). The EU should adopt a roadless policy (5) similar to the Greek legislation. Roadless areas should be integrated into the criteria for expansion, interconnection, and strict protection of parts of the Natura 2000 network, and roadless areas should be considered proactive restoration targets (9). The Greek model could provide an efficient, straightforward, and cost-effective approach to tackle both climate change and the biodiversity crisis in the EU.

Vassiliki Kati^{1,2*}, Nuria Selva^{2,3} Per Sjögren-Gulve²

¹University of Ioannina, Department of Biological Applications and Technology, GR-45110 Ioannina, Greece. ²Society for Conservation Biology Europe Section, FR-75013 Paris, France. ³Institute of Nature Conservation, Polish Academy of Sciences, 31-120 Kraków, Poland.

*Corresponding author. E-mail: vkati@uoi.gr

REFERENCES AND NOTES

1. Biodiversity Conservation Lab, University of Ioannina, “Roadless” (2022); <https://bc.lab.uoi.gr/en/research/projects/roadless/>.
2. S. Díaz *et al.*, *Science* **366**, eaax3100 (2019).
3. W. F. Laurance *et al.*, *Nature* **513**, 229 (2014).
4. P. L. Ibisch *et al.*, *Science* **354**, 1423 (2016).
5. V. Kati *et al.*, *Biol. Conserv.* **252**, 108828 (2020).
6. N. Selva *et al.*, *Environ. Manage.* **48**, 865 (2011).
7. European Union, “Science for environmental policy. Future brief: No net land take by 2050?” (2016); https://ec.europa.eu/environment/integration/research/newsalert/pdf/no_net_land_take_by_2050_FB14_en.pdf.
8. European Environmental Agency, “The European environment-state and outlook 2020: Knowledge for transition to a sustainable Europe” (2019); www.eea.europa.eu/soer/2020.
9. European Commission, “EU Biodiversity Strategy for 2030” (2020); https://ec.europa.eu/environment/nature/biodiversity/strategy/index_en.htm.
10. D. Serrano *et al.*, *Science* **370**, 1282 (2020).
11. V. Kati *et al.*, *Sci. Tot. Environ.* **768**, 144471 (2021).
12. European Environmental Agency, “Landscape fragmentation pressure and trends in Europe” (2021); www.eea.europa.eu/data-and-maps/indicators/mobility-and-urbanisation-pressure-on-ecosystems-2/assessment.

10.1126/science.abo2014

Iran's agricultural waste

Global agricultural waste poses a serious threat to food security (1). Each year, Iran wastes 35 million tons of food in different harvesting stages (2), 25 times more than the annual agricultural waste produced by developed countries (3). The wasted products in Iran could feed 15

million people annually (3). The value of the wasted food is equal to the value of half of the country's oil revenue (4). By wasting food, Iran is also wasting the 300 million liters of fuel and the 13.7 billion cubic meters of water that were required to produce it (1). Because of drought conditions and a climate with three times the global average evaporation rate (1), Iran devotes 90% of its water consumption to agriculture. Iran must mitigate food waste for the sake of food security, water sustainability, and human safety (1).

Iran's inadequate farming practices contribute to food waste. Farmers lack necessary knowledge about the benefits of modern agricultural techniques (2) and productive cultivation patterns (5). Because of rising and unregulated prices (6), many farmers cannot afford modern agricultural equipment (3), packing techniques, warehousing systems, or refrigeration rooms (1).

Some waste occurs because crops are not purchased, transported (1, 2, 4, 5), or distributed efficiently (5, 7). Products such as watermelons, tomatoes, and apples are particularly vulnerable to weaknesses in the supply chain (7). Insufficient government oversight allows interference by middlemen (5, 7), which can lead to the production of more supply than demand and the excess produce, such as oranges (7), going to waste.

Consumers also contribute to waste. Government subsidies on some products incentivize buying more food than one can eat (1). A range of factors influence how likely consumers are to let food go to waste (8), and current government policies do not take this information into account.

Iran's government could reduce agricultural waste by improving farming standards and providing better incentives. Legislation should be passed to manage import and export of crops (4, 5), guarantee purchase of products from farmers (3), reduce transaction costs (1), and provide agricultural insurance (3). Farmers should receive more support to fight pests and plant diseases, modernize farming equipment (6), provide efficient cold storage of raw products (7), and develop new methods of warehousing such as dynamic and smart atmosphere control systems, advanced ventilation, and online control (1). Small farmers should receive financial support for setting aside cultivation to prevent production that is in excess of consumption (9). The government should invest in the development of new technologies for protecting and harvesting agricultural

products more safely. Some agricultural waste should be used as organic fertilizer, clean fuels, and bio(nano)materials (10). Beyond government, broad national mass media coverage should emphasize the proper consumption of agricultural products. Finally, nongovernmental organizations should spearhead campaigns to encourage food-waste reduction.

Reza Akbari¹ and Mahmoud Nasrollahzadeh^{2*}

¹Department of Chemistry, Faculty of Science, Gonbad Kavous University, Gonbad, Iran.

²Department of Chemistry, Faculty of Science, University of Qom, Qom, Iran.

*Corresponding author.

Email: mahmoudnasr81@gmail.com

REFERENCES AND NOTES

1. A. Mirmajidi-Hashjtjin *et al.*, "Post-harvest loss reduction: Most important strategic approach in enhancement of food security," Ministry of Agriculture, Jihad, Agricultural Research, Education, and Extension Organization (2016); <http://fipak.areeo.ac.ir/site/catalogue/18823032> [in Farsi].
2. "Management and processing of agricultural waste in Iran is necessary," *Science News Agency* (2021); <https://isfahan.sinapress.ir/news/115076> [in Farsi].
3. "35% of agricultural products are turned into waste," *Donya-e-eqtasad* (2020); www.donya-e-eqtasad.com/fa/tiny/news-3707031 [in Farsi].
4. M. R. Jamshidi, "Why hasn't an agriculture reduction research institute been established?," *Food Security Scout News Station* (2020); <http://iwo.ir/j09rn> [in Farsi].
5. "When the wages of their labors are destroyed by this waste," *Iranian Students News Agency* (2020); www.isna.ir/news/99091510891/ [in Farsi].
6. "Farmers cannot afford to use up-to-date equipment," *Donya-e-eqtasad* (2020); www.donya-e-eqtasad.com/fa/tiny/news-3682985 [in Farsi].
7. M. Naji, "Thirty percent of waste in the cycle of production and distribution of agricultural products," *Broadcasting News Agency of the Islamic Republic of Iran* (2021); www.iribnews.ir/00CzMf [in Farsi].
8. J. Aschemann-Witzel, *Sci. Transl. Med.* **352**, 408 (2016).
9. "The need to use the correct consumption pattern to reduce agricultural waste," *Iranian Students News Agency* (2013); www.isna.ir/news/92070603338/ [in Farsi].
10. C. Xu, M. Nasrollahzadeh, M. Selva, Z. Issaabadi, R. Luque, *Chem. Soc. Rev.* **48**, 4791 (2019).

10.1126/science.abn9765

China's dams threaten the Sichuan taimen

The Sichuan taimen (*Hucho bleekeri*), a glacial relict and freshwater salmonid fish endemic to the Yangtze River (1), has been categorized as Critically Endangered on the Red List of the International Union for Conservation of Nature (2) and is listed as an endangered species on China's Species Red List (3). There are currently between 2000 and 2500 Sichuan taimen individuals, and the population is likely to decrease by more than 20% over the next two generations (2, 4). The species' decline is the result of

habitat loss, overfishing, pollution, and climate change (2, 5–7). The planned construction of the Barra dam now threatens to destroy the Sichuan taimen's last refuge (8, 9).

China has decided to invest a sum equivalent to about US\$63.4 billion in hydropower along the Yangtze River (10), where the Sichuan taimen lives. Four massive dams are planned to help China decrease its reliance on fossil fuel energy (10). Hydropower projects have already reduced the habitats of these fish from 5000 km² in the 1960s to less than 100 km² (11). The Barra hydropower station will destroy the four remaining Sichuan taimen spawning sites (8). Without these important habitats, the species may die out.

A survivor of the quaternary glacial period, the Sichuan taimen is a valuable genetic resource with scientific value for studying animal geography, paleoecology, and climate change (11, 12). To protect the Sichuan taimen, the Chinese government should understand the risks of its extinction and should designate the spawning sites as natural reserves. The construction of the Barra hydropower station should stop until a sustainable path forward for the Sichuan taimen is found. Meanwhile, China should implement scientific management and protection policies to minimize habitat fragmentation and illegal fishing in the Yangtze River.

Di Tong

College of Environmental and Resource Sciences, Zhejiang University, Hangzhou 310058, China, and Zhejiang Provincial Key Laboratory of Agricultural Resources and Environment, Zhejiang University, Hangzhou 310058, China.
E-mail: tongdi@hnu.edu.cn

REFERENCES AND NOTES

1. K. Wang *et al.*, *J. Appl. Ichthyol.* **32**, 343 (2016).
2. Z. Song, "Hucho bleekeri (errata version published in 2020)," The IUCN Red List of Threatened Species (2012); www.iucnredlist.org/species/13151680/174797529.
3. Y. Wang *et al.*, *Mar. Genom.* **4**, 221 (2011).
4. P. S. Rand, *Arch. Polish Fish.* **21**, 119 (2013).
5. G. Tong *et al.*, *Aquaculture* **529**, 735680 (2020).
6. Y. Chen *et al.*, *Dev. Compar. Immunol.* **116**, 103934 (2021).
7. M. Hu, Y. Wang, L. Cao, B. Xiong, *Environ. Biol. Fish.* **82**, 385 (2008).
8. L. Hu, "The 8.15-billion-yuan project threatens Sichuan taimen, a giant panda in the water," *Thepaper.net* (2021); https://m.thepaper.cn/baijiahao_16083356 [in Chinese].
9. "Critically endangered Sichuan taimen crisis: The last homes may be destroyed by a hydropower station," *Baidu* (2018); <https://baijiahao.baidu.com/s?id=1619645349684424461&wfr=spider&for=pc> [in Chinese].
10. J. Qiu, *Science* **336**, 288 (2012).
11. Y. Zhang, P. Luan, G. Ren, G. Hu, J. Yin, *Ecol. Evol.* **10**, 1390 (2020).
12. Y. Chen *et al.*, *Conserv. Genet. Resour.* **12**, 157 (2020).

10.1126/science.abo0354



Research at the intersection of the social and life sciences

Unconventional. Interdisciplinary. Bold.

The **NOMIS & Science Young Explorer Award** recognizes and rewards early-career M.D., Ph.D., or M.D./Ph.D. scientists that perform research at the intersection of the social and life sciences. Essays written by these bold researchers on their recent work are judged for clarity, scientific quality, creativity, and demonstration of cross-disciplinary approaches to address fundamental questions.

A cash prize of up to 15 000 USD will be awarded to essay winners, and their engaging essays will be published in *Science*. Winners will also be invited to share their work and forward-looking perspective with leading scientists in their respective fields at an award ceremony as well as a meeting of the NOMIS Board of Directors to consider future funding.

Apply by May 15, 2022
at www.science.org/nomis



RESEARCH

IN SCIENCE JOURNALS

Edited by
Michael Funk

KIDNEY DISEASE

Fingering FANCD2 in tubular repair

The transition from acute kidney injury, characterized by intrinsic repair, to incomplete repair and chronic damage has been difficult to study. Gupta *et al.* modeled the transition from intrinsic to incomplete repair using human kidney organoids. A single exposure to cisplatin resulted in intrinsic repair, with preserved tubular architecture and up-regulation of genes associated with homology-directed repair, including Fanconi anemia complementation group D2 (*FANCD2*). However, with repeated cisplatin exposure, *FANCD2* and *RAD51* recombinase (*RAD51*) were down-regulated, leading to incomplete repair. The DNA ligase IV inhibitor SCR7 increased *FANCD2*-mediated repair and ameliorated progression to chronic injury in the organoids, suggesting that targeting the *FANCD2*/*RAD51* pathway may have the potential to treat kidney disease. —MN *Sci. Transl. Med.* **14**, eabj4772 (2022).

Fluorescence microscopy image of proximal tubules in a kidney organoid that have been immunostained to detect DNA damage markers (green)

SYNTHETIC GENOMICS

Predicting effects from genomic changes

Genetic modifications of organisms can create artificial, synthetic genomes. Such changes are forecast to be useful for understanding the principles

of how genomic context affects cellular function. However, the effects of most drastic genomic movements are unknown, never having been observed in nature. Brooks *et al.* examined a line of yeast that are easily induced to move genes within the genome to determine how the context of

genes affects their expression. Examining 612 genetic changes, the authors found differences in the length and content of transcripts, which indicates that the local genetic environment is important for transcription. From these experiments, the authors were able to determine specific

rules affecting transcription, resulting in predictable changes within the genome. —LMZ
Science, abg0162, this issue p. 1000

TOPOLOGICAL PHYSICS

A monopole set in diamond

Magnetic monopoles, hypothetical sources of magnetic field in three-dimensional space, have not been observed as elementary particles. However, synthetic monopoles can be engineered in ultra-cold systems. Going a step further, Chen *et al.* used the quantum levels of a nitrogen vacancy center in diamond to observe the effects of a synthetic tensor monopole: the generalization of the magnetic monopole to four dimensions. The researchers modulated an applied microwave pulse to measure the “magnetic” field emanating from the tensor monopole and its topological charge. —JS

Science, abe6437, this issue p. 1017

MOLECULAR KNOTS

Opportune mismatches

The typical approach to making molecular knots is to use metal ions to orient ligand strands in mutually overlapping arrangements. Ashbridge *et al.* added a Vernier templating technique to expand the size and complexity of accessible knots. Specifically, they introduced a mismatch between the numbers of coordination sites on the ligands and on the metal ions, resulting in an assembly comprising the lowest common multiple of sites. A 3:4 stoichiometry produced a 378-atom trefoil-of-trefoils after ring closure by olefin metathesis. —JSY

Science, abm9247, this issue p. 1035

EPIGENETICS

Safeguarding stem cells

Bivalent genes co-occupied by the epigenetic markers histone 3 trimethyllysine 4 (H3K4me3) and 27 (H3K27me3) were first

observed in embryonic stem cells (ESCs). Gene bivalency has been widely thought to be a priming mechanism to facilitate gene induction kinetics during differentiation. However, loss of H3K4me3 at bivalent promoters by deleting the methyltransferase Mll2 has little effect on gene induction kinetics. Zhang *et al.* report that the protein BEND3 is required for optimal H3K27me3 occupancy at hundreds of bivalent promoters, and deletion of the *Bend3* gene in ESC causes premature activation of bivalent genes and the failure of differentiation. The authors propose BEND3-mediated Polycomb stabilization as a mechanism to prevent premature activation and to safeguard the differentiation process. —DJ

Science, abm0730, this issue p. 1053

ASTEROIDS

Obtaining and returning samples of Ryugu

The Hayabusa2 mission investigated the nearby carbonaceous asteroid Ryugu and collected samples for return to Earth. Tachibana *et al.* describe Hayabusa2's second sample collection, which picked up material that was excavated from Ryugu's subsurface by an earlier impact experiment. By analyzing footage from both touchdown events, the authors determined the morphological properties of small pebbles on the asteroid. After the sample return capsule was opened on Earth, they found that



A small pebble returned from the asteroid Ryugu to Earth by the Hayabusa2 mission

the chambers contained pebbles with properties consistent with the touchdown locations, indicating that they are representative samples of Ryugu's surface and subsurface. —KTS

Science, abj8624, this issue p. 1011

CORONAVIRUS

Omicron's defenses and vulnerabilities

The Omicron variant of severe acute respiratory syndrome coronavirus 2 quickly became dominant across the world partly because of its ability to evade existing immune defenses. Yin *et al.* provide structural data showing how the Omicron spike protein maintains and even strengthens binding to the human ACE2 receptor, whereas binding to most existing therapeutic antibodies is inhibited. JMB2002, an antibody that has completed phase 1 clinical trials, effectively neutralizes Omicron as well as variants Alpha, Beta, and Gamma, but not Delta. A structure shows the basis for this breadth. —VV

Science, abn8863, this issue p. 1048

QUANTUM SIMULATION

Time crystal in quantum computer

One of the most promising applications of quantum computers is to simulate quantum phenomena that are difficult to efficiently simulate using classical computers. A time crystal is a unique quantum phase of matter that repeats in time and never reaches thermal equilibrium. Frey and Rachel used a state-of-the-art quantum computer involving 57 qubits to realize this state, and their experiments show that the true dynamics of a discrete time crystal appear in the quantum computer. This study highlights the power of a quantum computer to explore quantum phenomena for sizeable quantum systems. —RO

Sci. Adv. 10.1126/sciadv.abm7652 (2022).

IN OTHER JOURNALS

Edited by **Caroline Ash**
and **Jesse Smith**



PLANT ECOLOGY

Island seed dispersal

Madagascar's large fruit eaters, including elephant birds and giant lemurs, went extinct about 1000 years ago. As a result, seed dispersal for some large-fruited plant species is inefficient. The modern distributions of some plant species may therefore reflect past distributions of extinct animals. Méndez *et al.* examined the roles of environmental conditions and extinct and extant frugivores on the occurrences of 190 palm species in Madagascar. Living frugivores, including birds and lemurs, had the strongest influence on palm composition across the island. However, palm distributions still showed a small but distinct signature of extinct megafauna dispersal. —BEL *Ecography* 10.1111/ecog.05885 (2022).

Extinct giant lemurs helped distribute the fruit of extant palm trees in Madagascar.

SOCIOLOGY

Developing infant brains by reducing poverty

The Baby's First Years study is a randomized controlled trial that investigates whether

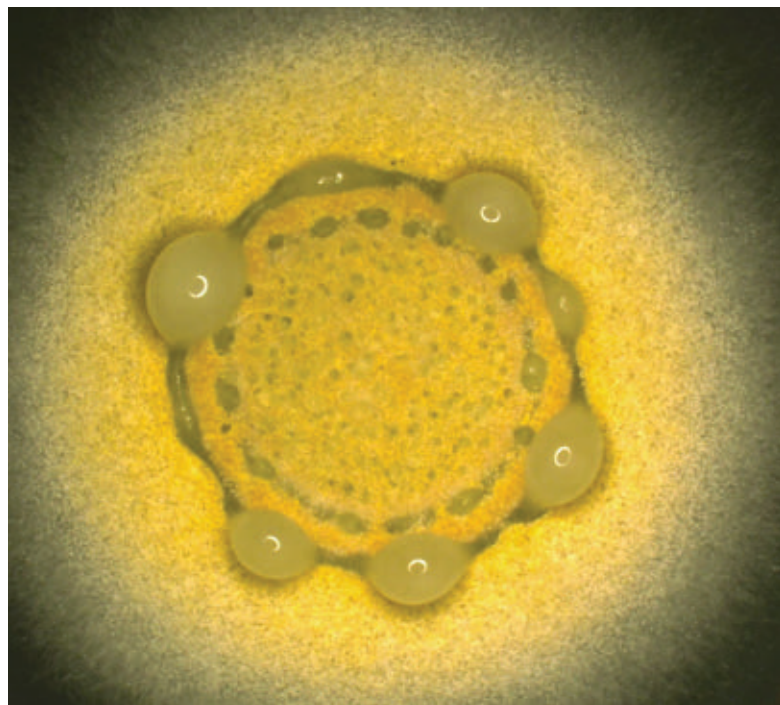
poverty reduction can cause noticeable changes in children's early brain development. After giving either \$333 per month or \$20 per month to 1000 low-income mothers from four different metro areas

SYMBIOSIS

Personalized fungal detox

Bacteria in the wild use a slew of small molecules to help them earn a living. Phenazines are redox-active bacterial products that are widespread in the environment and are harmful to fungi but not to all bacteria. Dahlstrom and Newman found in crop-land soils that the bacterium *Paraburkholderia edwinii* protected cohabiting *Aspergillus* fungi from the toxic effects of phenazine-1-carboxylic acid (PCA). Aggregates of bacteria within a colony of *Aspergillus* soaked up the PCA, whereas the fungus promoted acidic reducing conditions that limited the toxicity of the sequestered PCA. Aggregation in *P. edwinii* is regulated by the transcriptional repressor HrcA, which is found in many bacteria with fungal partners. HrcA could be as important in establishing interkingdom microbial communities on coral reefs or in the human gut as it is in the rhizosphere. —CA *Curr. Biol.* **32**, 275 (2021).

The fungus *Aspergillus* finds refuge from toxins within colonies of the bacterium *Paraburkholderia edwinii*.



in the United States, the study reports statistically significant differences in the electroencephalography brain scans of 1-year-old infants from the two groups. The study is ongoing and will follow these families to determine whether the observed differences between the two groups will persist and lead to cognitive and behavioral differences later on. —YY

Proc. Natl. Acad. Sci. U.S.A. **119**, e2115649119 (2022).

OBESITY

Unfolding the sequelae of obesity

Obesity and type 2 diabetes are increasingly common worldwide and are associated with numerous health complications. Given the complexity of these metabolic illnesses, it is not surprising that multiple signaling pathways are involved and the connections are not always straightforward. For example, activation of the unfolded protein response can be protective or detrimental depending on the degree and duration of activation. Madhavan *et al.* have untangled some of the

complexities of the unfolded protein response signaling in mouse models, then attempted to deflect the response using a small-molecule compound. The treatment improved glucose metabolism and reduced the accumulation of fat in the animals' livers, indicating its potential for therapeutic applications. —YN

Nat. Commun. **13**, 608 (2022).

CANCER IMMUNOLOGY

Sweet spot for TCR

The T cell receptor (TCR) is a complex on the surface of T lymphocytes that participates in the activation of antitumor T cell immune responses. During acute infections, high-affinity interactions with pathogen antigens trigger T cell expansion, but in cancer, TCR affinity to tumor self-antigens may be low. Shakiba *et al.* examined how different TCR signal strengths affected the ability of a subset of T cells called CD8⁺ T cells to control tumors in mice. Weak TCR–tumor antigen interactions led to ineffective cancer cell killing, whereas strong TCR–tumor antigen engagement drove T cells into a nonfunctional state.

However, immunogenic tumor neoantigens from human melanoma and lung cancer mostly have intermediate TCR affinity. Subsequent fine-tuning of the TCR signal to the intermediate “sweet spot” improved the ability of T cells to elicit tumor cell clearance and may provide avenues for improved cancer immunotherapies. —PNK

J. Exp. Med. **219**, e20201966 (2022).

MACHINE LEARNING

Exploring organophosphorus ligands

Machine learning (ML) has become a mainstream tool in the development of numerous algorithms for virtual chemical space exploration and is increasingly being applied to more and more complex chemical systems. Gensch *et al.* present a comprehensive ML-based discovery platform to study the property space of organophosphorous (III) ligands (actively used in homogeneous catalysis), which was able to predict 190 physicochemical descriptors for more than 300,000 new ligands. Their platform could be used for the inverse design

of homogeneous catalysts and could be adapted to other classes of ligands in the future. —YS

J. Am. Chem. Soc. **144**, 1205 (2022).

GENDER GAP

The manly art of self-promotion

Gender wage gaps may have roots in men being more self-promoting than women. Exley and Kessler had more than 4000 adults perform tasks and then rate their subjective performance on a scale. Men judged their math and science performance more favorably than did equally performing women regardless of whether participants were first told how they actually scored and if they were first told that the self-evaluations were to be shared with potential employers or kept private. Men and women rated performance similarly for other participants and for themselves on a test of verbal skills. Similar gaps were seen in more than 10,000 middle- and high-school-aged participants. —BW

Q. J. Econ. <https://doi.org/10.1093/qje/qjac003> (2022).

ALSO IN *SCIENCE* JOURNALS

Edited by Michael Funk

GENETICS

Cell type diversity in a whole fly

The fruit fly *Drosophila melanogaster* has served as a premier model organism for discovering fundamental and evolutionarily conserved biological mechanisms. Combining recent advances in single-cell sequencing with powerful fly genetic tools holds great promise for making further discoveries. Li *et al.* present a single-cell atlas of the entire adult fruit fly that includes 580,000 cells and more than 250 annotated cell types. Cells from the head and body recapitulated cell types from 15 dissected tissues. In-depth analyses revealed rare cell types, cell-type-specific gene signatures, and sexual dimorphism. This atlas provides a resource for the *Drosophila* community to study genetic perturbations and diseases at single-cell resolution. —BAP

Science, abk2432, this issue p. 991

NEUROGENOMICS

Mapping the brain's blood vessels

Cerebrovascular diseases are a leading cause of death and disability, but our understanding of the cellular and molecular constituents of normal and diseased human cerebrovasculature is incomplete. Winkler *et al.* generated a cellular-resolution atlas of the adult human cerebrovasculature. The authors used spatial transcriptomics to reveal the geographical organization of an unexpectedly diverse array of molecularly defined cell types within the human brain. They then explored the cellular and molecular alterations that occur in arteriovenous malformations, a leading cause of stroke in young people. A specialized subtype of peripheral monocyte plays a role in destabilizing the cerebrovasculature, and the

authors identified candidate targets for therapeutic intervention. —STS

Science, abi7377, this issue p. 992

PLANT SCIENCE

Getting to the root of root development

Plants have the useful ability to grow new pieces on an as-needed basis. Omary *et al.* analyzed the developmental programs that control root development in the tomato plant (see the Perspective by Shaar-Moshe and Brady). Underground, lateral roots are initiated from pericycle tissue of the primary root and branch off from the main root column. Lateral roots can also develop above ground, initiated off of the aboveground shoot. These shoot-borne roots grow from cells associated with the phloem that take on a stem-cell-like state regulated by the transcription factor *SHOOTBORNE ROOTLESS (SBRL)*. Although belowground lateral roots and aboveground shoot-borne roots differ in details, their development shares a suite of transcription factors that regulate a transitional cellular state. —PJH

Science, abf4368, this issue p. 993;
see also abo2170, p. 974

NEUROSCIENCE

Dopamine and the gating of REM sleep

Sleep is composed of rapid eye movement (REM) and non-REM sleep, and REM sleep usually appears after periods of non-REM sleep. However, we do not understand the mechanisms by which the brain cycles between these states. Using fiber photometry, Hasegawa *et al.* found increases in dopamine activation before non-REM to REM transitions but not before non-REM to wake transitions in the basolateral amygdala (see

the Perspective by Arrigoni and Fuller). This effect was mediated by dopamine receptor D2-expressing neurons in the amygdala. Artificially activating these neurons induced a transition from non-REM to REM sleep and cataplectic states in awake mice. —PRS

Science, abl6618, this issue p. 994;
see also abo1987, p. 972

ULTRACOLD CHEMISTRY

Magnetic control of chemistry

There is a considerable interest in realizing control of molecular reactions at ultracold temperatures because of unprecedented opportunities in the ultimate quantum regime. Son *et al.* discovered an ideal system, a sodium atom and a sodium–lithium molecule, in which the combination of Feshbach resonances and low short-range loss probability allows for the significant suppression or enhancement of reactive collisions controlled by external magnetic fields (see the Perspective by Cornish and Hutson). This work presents a method for manipulating the reactivity of ultracold molecules that is qualitatively different from previous experiments. At the same time, this method is highly dependent on the distinctive short-range properties offered by the sodium/sodium–lithium complex and is subject to further testing in other systems. —YS

Science, abl7257, this issue p. 1006;
see also abn1053, p. 975

CATALYSIS

Ethylene extensions

Ethylene is the most common building block of plastics, but it is often mixed with longer carbon chains during polymerization to tune material properties. Selective preparation of particular longer, terminal olefins is therefore an area of active

research. Dietel *et al.* report that a titanium catalyst with optimized nitrogen-coordinating ligands can add two equivalents of ethylene to a terminal olefin, extending the main chain by two carbons while also appending an ethyl branch (see the Perspective by Rosen). The authors attribute the selectivity to unusually rapid β -hydride elimination. —JSY

Science, abm5281, this issue p. 1021;
see also abo1265, p. 978

MAGNETISM

Magnons in a skyrmion lattice

Electrons in two-dimensional solids placed in an external magnetic field fill the so-called Landau energy levels. In materials with a nontrivial spin texture, spin excitations (magnons) may have an analogous energy-level structure. However, showing this effect in an experiment is tricky. Weber *et al.* used inelastic neutron scattering and numerical simulations to demonstrate this effect in the skyrmion lattice phase of the material manganese monosilicide. —JS

Science, abe4441, this issue p. 1025

QUANTUM OPTICS

Harnessing vacuum fluctuations

Vacuums are not simply empty voids but rather volumes teeming with electromagnetic vacuum fluctuations. Although energy conservation forbids any process that could extract energy from such states, Appugliese *et al.* show that the enhancement of vacuum field fluctuations in subwavelength split-ring resonators affects the quantum Hall electron transport in high-mobility two-dimensional electron gases (see the Perspective by Rubio). Both the longitudinal and transverse values of the resistance depart greatly from their quantized

values despite the topological protection offered by the quantum Hall effect. These results suggest that vacuum fluctuations could be engineered to optoelectronically control electronic systems without the need for illumination. —ISO

Science, abt5818, this issue p. 1030;
see also abn5990, p. 976

CORONAVIRUS

Enhancing the immune response

Many lives have been saved by the vaccines that were rapidly developed against severe acute respiratory syndrome coronavirus 2. As the pandemic continues, we are faced with waning vaccine-induced immunity and variants of the virus that partly evade this immunity, so there are questions regarding boosting strategies. Kaku *et al.* examined the immunity induced by either prime and boost with the adenoviral vectored vaccine ChAdOx1 or prime with ChAdOx1 and boost with a messenger RNA (mRNA) vaccine. Whereas ChAdOx1 expresses wild-type viral spike, the mRNA vaccines express spike stabilized in the prefusion conformation. Boosting with the mRNA vaccine focuses the response on epitopes in the prefusion conformation and results in overall higher neutralizing activity and increased breadth against variants of concern. —VV

Science, abn2688, this issue p. 1041

IMMUNOLOGY

A brake on lymphocyte activation

Stimulation of antigen receptors leads to the formation of a protein complex called CBM on the scaffolding protein CARD11 and ultimately promotes T or B cell activation. The ability of CARD11 to recruit its binding partners to the CBM complex is regulated by multiple phosphorylation events.

Kutzner *et al.* identified an inhibitory phosphorylation site that restrained antigen receptor-induced formation of the CBM complex and lymphocyte activation. This phosphorylation event prevented T cell activation without co-receptor stimulation and sensitized B cell lymphomas to inhibitors used to treat this cancer type. —WW

Sci. Signal. **15**, eabk308 (2022).

INNATE LYMPHOID CELLS

Friendly competition in the liver

Hepatotropic viruses such as hepatitis B virus (HBV) can cause chronic liver disease in part by generating antiviral effector T cells that subsequently contribute to collateral tissue damage. Using intravital microscopy in mouse models of HBV infection, Fumagalli *et al.* demonstrate that group 1 innate lymphoid cells (ILCs), comprising natural killer cells and ILC1s, interact closely with HBV-specific CD8⁺ T cells in the liver and protect against liver damage caused by effector T cells. Rather than directly killing nearby CD8⁺ T cells, group 1 ILCs limited effector T cell responses by competing for local interleukin-2 required for their proliferation. These results provide insight into cross-talk between liver lymphocyte populations and identify a regulatory function for group 1 ILCs in constraining antiviral T cell responses. —CO

Sci. Immunol. **7**, eabi6112 (2022).

ANIMAL BEHAVIOR

Human impacts on bee foraging

Bees are important pollinators that have evolved numerous learning, navigation, and communication abilities that allow them to forage for food. However, human activity can have a substantial influence on foraging by bees, affecting

their survival. In a Perspective, Goulson and Nicholls discuss the anthropogenic effects on bee foraging, including the use of neurotoxic pesticides, diverse influences of urbanization, and emerging concerns such as electromagnetic radiation and particulate pollution. Combinations of these stressors may synergistically affect bee behavior, affecting their ability to thrive. Although mitigations in urban spaces have shown some improvements in bee foraging, mitigations in farmland pose a much greater challenge. —GKA

Science, abn0185, this issue p. 970

RESTORATION ECOLOGY

Microbes repairing degraded soils

Soils worldwide have become increasingly degraded by human activities, especially in drylands. Land degradation negatively affects soil hydrological functioning and thereby the ecosystem services that soil provides. Soil microbes may play an important part in the restoration of degraded soils, positively influencing moisture content and other physical features of soil. Coban *et al.* reviewed recent work on soil hydraulic properties, potential groups of microorganisms for hydrological soil restoration based on their resilience in dry soils, and future strategies for long-term restoration of degraded lands. —AMS

Science, abe0725, this issue p. 990

REVIEW SUMMARY

RESTORATION ECOLOGY

Soil microbiota as game-changers in restoration of degraded lands

Oksana Coban*, Gerlinde B. De Deyn, Martine van der Ploeg

BACKGROUND: Soil, the living skin of Earth, provides ecosystem services critical for life: Soil acts as a filter and store of water, provides a growing medium that supplies plants and heterotrophs with water and nutrients, offers habitat for a large diversity of organisms, and is the source of most of our antibiotics. Humanity is increasingly challenged by the combination of climate change, population growth, and land degradation, including carbon loss, biodiversity decline, and erosion. In particular, land degradation reduces soil hydrological functioning and thereby several other ecosystem services. Such impacts occur through alterations of hydraulic functioning, infiltration and soil moisture storage, carbon cycling, biological activity, transport of nutrients and contaminants, and plant growth. Impacts of global environmental change and associated soil degradation need to be understood and reversed as biodiversity, food production, climate regulation, and people's livelihoods are increasingly affected by soil

ecosystem degradation. The interplay between soil biota and soil hydrological functioning plays an essential role in many biogeochemical cycles, including the water and carbon cycles. Microorganisms dominate soil life and perform an array of vital soil functions by regulating nutrient cycling, decomposing organic matter, defining soil structure, suppressing plant diseases, and supporting plant productivity. The presence of microorganisms and their activity can affect soil structure and hydraulic properties in multiple ways. Case studies indicate the potential of microorganisms as game-changers toward the restoration of soil functioning. However, the role of soil microbiota in forming and sustaining soils has historically been overlooked.

ADVANCES: It has been proposed that microbial communities not only are an indicator of ecosystem health and restoration level but also can be manipulated to enhance the recovery of degraded ecosystems. In the past

decade, there have been an increasing number of studies suggesting the use of microorganisms as ecosystem mediators, particularly to enhance crop production and to engineer microorganisms for dryland restoration. Most current experimental approaches focus on monitoring changes in the microbial community that can be correlated with land restoration; however, microorganisms are also facilitators of ecosystem change, not just followers. We review how microorganisms can help address different types of land degradation, with a focus on physical soil loss and transformation, loss of soil chemical properties, and contamination. We discuss potentially the most valuable groups of microorganisms for soil restoration (namely, plant growth-promoting rhizobacteria, nitrogen-fixing bacteria, and mycorrhizal fungi), emphasizing drylands and advances in plant-microbe interaction studies. We review known effects of microorganisms on soil physical and, specifically, hydraulic properties at pore scale and discuss future strategies for the long-term restoration of degraded lands. We also identify the methodological challenges that have so far hampered progress in understanding soil biophysical processes.

OUTLOOK: Microorganisms can play the leading role in restoring degraded lands, improving soil hydraulic properties such as infiltration and water retention and reducing soil hydrophobicity, which together can facilitate ecosystem restoration. We advocate for research on mechanisms to restore degraded soils with the use of microorganisms. Given the critical role of freshwater availability to terrestrial life and the paucity of studies on hydrological restoration, we especially advocate for research on the hydrological restoration of degraded soil using microorganisms. We propose that microorganisms can improve soil hydraulic properties such as infiltration and water retention and reduce soil hydrophobicity. Along with new organic matter derived from microbes, this will promote plant growth and facilitate further ecosystem restoration. Such a restoration strategy requires collaboration across the research fields of microbiology and soil hydrology, of which there has been very little to date. Understanding the dynamics of soil microbes and connected hydrological processes would create the foundation for restoration practices that can return resilience to the soil ecosystem. ■

Department of Environmental Sciences, Wageningen University & Research, Wageningen, Netherlands.
*Corresponding author. Email: coban.oksana@gmail.com
Cite this article as O. Coban *et al.*, *Science* **375**, eabe0725 (2022). DOI: [10.1126/science.abe0725](https://doi.org/10.1126/science.abe0725)



READ THE FULL ARTICLE AT
<https://doi.org/10.1126/science.abe0725>



Degraded land in Libya. In degraded lands, a decrease in soil nutrients and organic matter, deterioration of soil structure, increase in salinity, water deficiency, and physical instability can be observed.

REVIEW

RESTORATION ECOLOGY

Soil microbiota as game-changers in restoration of degraded lands

Oksana Coban*, Gerlinde B. De Deyn, Martine van der Ploeg

Land degradation reduces soil functioning and, consequently, the services that soil provides. Soil hydrological functions are critical to combat soil degradation and promote soil restoration. Soil microorganisms affect soil hydrology, but the role of soil microbiota in forming and sustaining soil is not well explored. Case studies indicate the potential of soil microorganisms as game-changers in restoring soil functions. We review the state of the art of microorganism use in land restoration technology, the groups of microorganisms with the greatest potential for soil restoration, knowledge of the effect of microorganisms on soil physical properties, and proposed strategies for the long-term restoration of degraded lands. We also emphasize the need to advance the emerging research field of biophysical landscape interactions to support soil-plant ecosystem restoration practices.

Soil, the living skin of Earth, provides ecosystem services critical for life: It acts as a filter and store of water, provides a growing medium that supplies plants and heterotrophs with water and nutrients, offers habitat for a large diversity of organisms, and is the source of most antibiotics (1). Many of these services are created by soil life, which interacts with the complex biological, chemical, and physical dimensions of soil. When soil life disappears or degrades as a result of environmental disturbances, ecosystem services are also affected. The combination of climate change, human population growth, and soil degradation—including carbon loss, biodiversity decline, pollution, and erosion—represents an increasing challenge to humanity (2). At present, one-third of all global land surfaces are degraded to some extent (3), and 24 billion metric tons of fertile soil are lost every year (4). It is estimated that 50 million people may be displaced in the next decade as a consequence (4). Therefore, urgent efforts are needed to find solutions to restore well-functioning living topsoil in the coming years.

Soil water represents only 0.05% of the global freshwater stocks, yet it is essential in supporting terrestrial life. The crucial role of soil moisture in the Earth system and in global environmental change is well studied (5, 6). Global environmental change and unsustainable land management can irreversibly reduce soil moisture retention properties (7, 8) and so can affect all life that depends on soil moisture. Moreover, short and extreme weather fluctuations can be as influential as gradual climate change in driving change in ecosystems (9). In addition, land degradation has a

negative impact on soil hydrological functions. Soil hydraulic functions include rainfall infiltration and storage of soil moisture, which in return provide water to the soil-plant-microbial and faunal ecosystem components. The interplay between soil biology and soil hydrological functioning performs an essential role in the hydrological cycle: Biophysical interactions regulate the water flux to the atmosphere through evapotranspiration, while the influx is dependent on adequate water supply from the atmosphere to the soil. Biophysical landscape interactions are those biotic and abiotic processes that influence the evolution of the landscape over time (10). Those interactions influence soil properties, which can lead to a shift in soil moisture regime attributable to, for example, the formation of soil crusts (8). Such regime shifts are different from common hysteresis effects associated with repeated wetting and drying of the soil (11); they are associated with an actual physical change of soil pore connectivity and structure (8).

Changes in land management or climate can lead to a sudden shift in an ecosystem from one stable state to another (8, 9, 12, 13). The concept of alternative stable states was proposed as a way to understand system behavior in ecology (14) and physics (15). The transition between states is a consequence of nonlinear feedbacks initiated by “disruptive” perturbation (16)—for example, from a healthy ecosystem to a collapsed one, or from one type of ecosystem to another. For soil ecosystems, evidence for the occurrence of alternative stable states is scarce (7), but it can be expected that soil-degrading processes such as intense droughts, erosion, and landslides can trigger or at least contribute to state shifts and collapse. The actual mechanism of such changes would likely include drought-induced posi-

tive feedbacks among erosion, loss of organic matter, and reduction of soil water retention (7, 17). Whether such shifts lead to irreversible changes in soil moisture availability remains debated; for some ecosystems, these altered trajectories may be reversible on human time scales.

A healthy soil ecosystem sustains itself, biological productivity, and environmental quality within a landscape and promotes plant and soil biota health (18). These coupled components of the soil ecosystem are affected by land use and landscape position. In turn, differences in microbehavior in the soil ecosystem driven by the interplay of heterogeneous soil and flora and fauna dynamics affect emergent soil characteristics locally and across the landscape and determine soil resilience. The role of microbiota in forming and sustaining landscapes has been historically overlooked. In recent years, new field observations have given rise to the concept of “biophysical landscape interactions,” which implies that the physical mechanisms of soil functioning should be reevaluated to include biotic processes (8).

Microorganisms dominate soil life and perform an array of vital soil functions by regulating nutrient cycling, decomposing organic matter, suppressing soil-borne plant diseases, defining soil structure, and supporting plant productivity. Hence, soil microorganisms are facilitators of soil ecosystem change. On the other hand, microbial community structure and diversity can also be used as indicators of soil health (19), and research so far has mainly focused on how microbial communities respond to environmental change (20). In an opinion paper on restoration ecology published 13 years ago, it was proposed that microbial communities are not just indicators of change but also underpin the recovery of degraded ecosystems when managed well to promote the restoration process and system health (21). Since then, an increasing number of studies have explored how microorganisms can be used as ecosystem mediators (22), particularly to enhance crop production (23, 24) and to engineer dryland restoration (25). These studies indicate the potential of microorganisms to be game-changers in restoring soil functions.

To move this new research field of microbial soil restoration forward, we discuss a number of factors that need to be considered and describe the state of the art in the field. Furthermore, we discuss the groups of microorganisms that have potential in land restoration along with their effects on soil properties. We explore hydrological restoration from local to landscape scale and identify how soil microbes and microbe-plant interactions improve and sustain soil hydrological functioning and thus are necessary to ecosystem resilience and health.

Department of Environmental Sciences, Wageningen University & Research, Wageningen, Netherlands.

*Corresponding author. Email: coban.oksana@gmail.com

Groups of microorganisms used in restoring degraded lands

Restoration of degraded ecosystems can be slow and unsuccessful if conditions are unfavorable for the development of soil biota (26). Because soil biota is an important driver of plant community development (27, 28), the successful restoration of terrestrial ecosystems may depend on the manipulation of soil organisms (27). With respect to their impact on plant growth, nutrient cycling, and soil structure, three main groups of beneficial microorganisms can be distinguished: plant growth-promoting rhizobacteria (PGPR), nitrogen-fixing bacteria, and arbuscular mycorrhizal fungi (AMF) together with ectomycorrhizal fungi (EMF). As a possible fourth group, cyanobacteria in biological soil crusts (BSCs) are able to increase soil nutrient availability by fixing nitrogen and improving soil structure at the surface (29, 30). Examples of beneficial microorganisms as remediation agents are shown in Fig. 1.

PGPR are loosely defined as soil bacteria that colonize the plant roots and enhance plant growth. Enhancement can occur in a direct or indirect way, and only some of the mechanisms involved have been characterized so far (31). Among direct mechanisms are nitrogen fixation, solubilization of minerals (e.g., phosphorus) and enhancement of their uptake by plants, synthesis of phytohormones, and chelation of metals to make them available to plant roots. The addition of PGPR has also been shown to increase crop yield by protecting plants from pests, parasites, or diseases (32).

Agricultural yields are often limited by N availability, and the natural N input into the biosphere is mostly provided by biological N fixation by bacteria and archaea. Nitrogen-fixing organisms or diazotrophs can be free-living or exist in a symbiotic relationship with their host plant (33). Among different forms

of association, symbioses in which rhizobacteria live within root nodules are the most efficient in terms of making N available to the plant. Root nodule symbioses between leguminous crops and rhizobia result in particularly high rates of N fixation (50 to 465 kg N ha⁻¹ year⁻¹) and can occur in nearly all cropping systems (34). The world's main cereal crops (rice, wheat, and maize) do not associate with rhizobia, and associative N fixation in cereals is often considered insignificant in comparison to nodulated symbiotic N-fixing plants (35). Manipulating bacteria to increase biological N fixation in nonleguminous plants has been a long-standing pursuit (36), but the expansion of symbiotic associative N fixation to other crops has been hindered by poor understanding of the genetic requirements that allow the host plant to associate with and benefit from diazotrophs (37). Technological advances during the past two decades, including next-generation sequencing, gene editing, and synthetic biology, enable genetic manipulation of plants and microbes at an unprecedented scale. However, it is expected that the development of nodulation in non-nodulating crops will still take a few decades (33, 38).

EMF form symbiotic structures with the roots of woody plants and drive the nutrient cycle in forest ecosystems. In addition to nutrient supply, EMF have been shown to enhance water transfer between plants through their hyphal network, thereby increasing plant survival during drought periods (39). AMF form symbioses with the roots of ~80% of vascular plant species, helping them to acquire soil nutrients (especially phosphorus) in return for plant carbohydrates (40). In some cases, AMF provide most of the plant's phosphorus needs, and all its phosphorus uptake may be of hyphal origin (41). Phosphorus is needed for all major metabolic processes (photosynthesis, respiration, energy transfer), and seed

formation and root strength depend on it. Associations between AMF and bacteria are important in the symbiosis with the plant roots because of the critical role they play in mycorrhizal functions (42, 43). Disentangling the very complex ecological roles of AMF requires a collaborative effort involving physiologists, molecular biologists, and ecologists. Recent advances in molecular genetics are helping to decipher the morphological, physiological, and genetic characteristics of AMF and to understand the molecular mechanisms of symbiosis among AMF, bacteria, and plants (44). Stable isotope probing (SIP), for example, makes it possible to study the interrelated effects of structure and function of the symbiont organisms (45, 46).

Plant-microbe interactions

Plants in natural environments coexist with a wide variety of microbes (archaea, bacteria, fungi, viruses, and protists), collectively called the microbiome. The microbiome is vital to plant growth, productivity, and plant overall condition (47). The interactions can be pathogenic, commensal, or beneficial, depending on such factors as plant species, soil type, and environmental conditions (31). Plant-microbiome engineering aims to direct the interactions toward increasing crop yield. The understanding of plant-microbiome interactions remains rudimentary (31), but it has become clear that there is considerable scope for manipulation. In recent years, research into the application of microorganisms as biocontrol, biostimulant, and bioremediation agents has expanded (48–50). In agriculture, the primary research foci are product reliability and consistency (48). Better understanding of the mechanisms of plant-microbial interactions is key to increasing the benefits to be gained from their exploitation (51).

Major developments in plant-microbe interactions have occurred in recent years thanks to advances in techniques for genomic studies and the increased availability of genomic information (52, 53). Such developments provide a basis for exploring plant-microbe interactions across chemical, molecular, metagenomic, and exometabolomic scales (54). For example, progress is being made toward large-scale microbial isolation and the synthetic production of communities (55). Next-generation sequencing techniques provide a necessary basis for the preparation of bacterial isolates that are further inoculated in germ-free plants. Systematic microbiota culture collections can be used in microbiota reconstitution experiments with germ-free plants to investigate the principles underlying community assembly and to identify microbiota-mediated functions important for plant health (56). Furthermore, novel methods of exometabolomics can help to unravel the mechanisms underlying

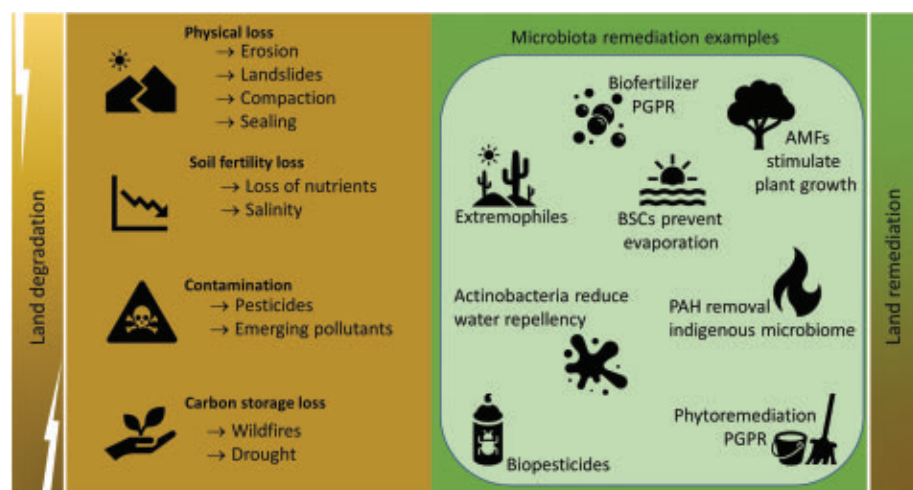


Fig. 1. Land degradation types and examples of beneficial microorganisms acting as remediation agents.

the ability of plants to actively shape their microbiomes through insight into the molecular mechanisms of microbial-induced plant-specialized metabolism (57,58). In field situations, the microbiota present in the soil acts as the main pool from which plants can select their rhizosphere or root microbiome. Hence, soil management and its impact on the soil microbiome remain of critical importance for engineering root microbiota. On the other hand, the agricultural environment and the genotypes of the cultivated plants have an impact on individual microbial genotypes (59). This suggests that manipulation of plants and cropping systems is the key to sustainable biocontrol. When the biology underpinning plant-microbe interactions is well understood, inoculation with individual bacterial isolates can also be effective (60). Further protection for plants is provided by the initial soil microbiome acting against pathogen invasion or by promoting plant resistance and crop productivity (61). This provides a basis for engineering root microbiota and for greater understanding of the functions of root and soil microbiota in plant growth and health.

Choice of microorganisms for dryland restoration

Many studies have focused on the resilience of microbial communities in dry soils and on the effects of soil degradation on a microbial community structure (62, 63). These studies can help in selecting the most promising candidate species for degraded land restoration.

Several species of algae have been shown to promote soil hydrological properties by breaking water repellency and improving water retention (64, 65). In studies of the response to desiccation, fungi showed higher resistance than bacteria to changes in water availability (63, 66), enabled by hyphae that may traverse air-filled soil pores to access nutrients and water. In bacterial communities, survival strategies for dry conditions have long been examined by testing physiological responses (67, 68). More recently, next-generation sequencing techniques have helped to further explore trends in abundances of major taxonomic groups as a function of soil moisture conditions (62, 63, 69). In the context of differences between arid and non-arid environments, or differential responses to desiccation stress, bacterial abundances vary in response to different moisture levels in three main ways:

1) With decreasing soil humidity, there is an increase in abundances of Cyanobacteria (69–71) and monoderm bacteria (i.e., prokaryotic cells surrounded by a single membrane) (68, 72); this latter group includes Actinobacteria (69, 73), Chloroflexi (62, 73), and Firmicutes (70, 73, 74). All of these bacterial taxa possess multiple mechanisms that help them withstand harsh environments including desiccation for extended periods, namely

a thick peptidoglycan layer (75) and an ability to produce resting stages (e.g., endospores) (76).

2) Some of the terrestrial diderm bacteria [phyla such as Acidobacteria (62, 69) and Verrucomicrobia (62, 69)] follow the opposite pattern: Their abundances decline during dry-out and increase with rewetting. An exception is the class Chloracidobacteria of Acidobacteria that is distinct from this group (69, 77).

3) Other diderm phyla (e.g., Proteobacteria, Planctomycetes, Bacteroidetes) do not show a consistent response to aridity. Their abundances in dry soil have been reported to increase in some studies and to decrease in others (62, 69, 70, 74).

Each of the three possible responses (increase, decline, no change) was also found in ribosomal synthesis of these phyla (63, 74), a response that usually serves as a proxy for potential activity, although rRNA concentration and growth rate are not always simply related (78).

Different bacterial species can produce either hydrophilizing or hydrophobizing substances as a part of extracellular polymeric substances (EPSs) (79) and thereby affect soil hydrophobicity and water infiltration. Hydrophilizing properties were found for *Bacillus sphaericus* of the Firmicutes phylum (79). Furthermore, some Actinobacteria and Proteobacteria are able to degrade waxes and thereby reduce water repellency (80, 81). This indicates a promising potential use of these bacteria to improve soil wettability and break down hydrophobicity.

All of these findings suggest the possible application in arid environments of either monoderm bacteria (Actinobacteria, Chloroflexi, Firmicutes) and Cyanobacteria or the generalists that expose drought-resistant patterns (e.g., fungi, algae, Proteobacteria). Recently, fungi have been shown to facilitate colonization of dry soil by bacteria (82), and therefore studies investigating co-inoculations of bacteria and fungi are also of interest.

Types of land degradation and the state of the art of microbe use in land restoration

Land degradation is the loss of the intrinsic physical, chemical, or biological soil characteristics by natural or anthropogenic processes, resulting in a reduction or eradication of vital ecosystem functions (83). Land degradation estimations at the global scale are complex and vary between studies (Fig. 2). Because no formal classification of land degradation exists, we propose three principal and interconnected processes of degradation (84):

1) The physical loss or physical transformation of soils (e.g., associated with erosion, landslides, drought, severe fires, soil compaction, and sealing);

2) The loss of soil chemical properties, such as decline in fertility and organic carbon content

due to acidification, salinization, or nutrient deficiency; and

3) Soil contamination.

Microorganisms can promote soil restoration in each of these cases. Here, we discuss each of the three degradation types with special emphasis on driving causes most commonly associated with global environmental change, namely drought, fire, and soil salinization (Fig. 3).

Physical loss of soil

Physical land degradation can affect soil at all latitudes and on all continents. One driving cause is the increased frequency and severity of drought. Drylands already cover an estimated one-third of Earth's terrestrial surface (85) and are expected to increase in size as a result of climate change and human activities (86). In drylands, strong winds and ultraviolet radiation lead to decreases in soil nutrients and organic matter, deterioration of soil structure, and increases in salinity, water deficiency, and physical instability (87). Under such stresses, plants suffer from a number of biochemical, morphological, and physiological modifications that suppress their growth and productivity (88). PGPR found in dry environments are well adapted to extreme environmental conditions such as drought, heat, and high salinity, providing essential nutrients from soil or through N fixation and enhancing plant tolerance to abiotic and biotic stresses (89). PGPR in drylands possess unique traits, including a stronger expression of genes related to dormancy and osmoregulation as well as a weaker expression of genes regulating nutrient cycling and catabolism (89). They are also capable of increasing the soluble sugars content and chlorophyll content in the leaves, which enable drought stress tolerance in plants (90). Highly desiccation-tolerant PGPR, such as Actinobacteria, produce the sugar trehalose, which increases their abiotic stress tolerance and at the same time symbiotically protects plants against drought by induction of their stress-response genes (91). Over the past decade, there has been increased interest in the development of biofertilizers based on desert PGPR that can promote plant tolerance against abiotic stress in drylands (88, 89). Inoculating soil in degraded drylands with biological crusts can contribute to the recovery of ecosystem functions at the landscape scale, such as erosion resistance by improving soil stability and nutrient cycling. Using living inoculum has shown to be more effective in drylands than replacing topsoil or organic carbon additions (92).

Low-severity fires, such as grassland fires or prescribed fires for landscape management, enhance soil properties by reducing surface flow and erosion and increasing soil organic matter and nutrient content (93). In contrast, wildfires greatly change soil physical properties

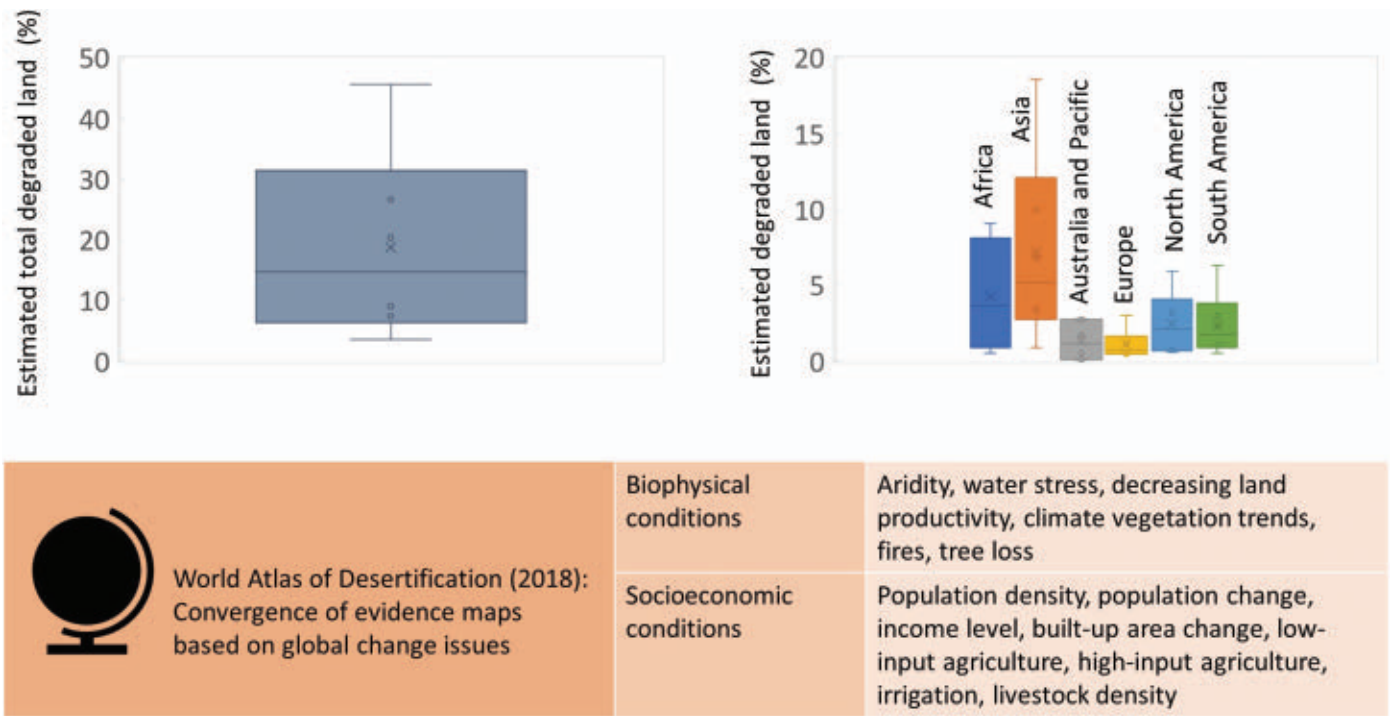


Fig. 2. Development of land degradation estimations. Top left: Total estimated land degradation. Top right: Estimated land degradation per continent. These graphs are based on data from Gibbs and Salmon (2015) and IPBES (2018) (177, 178); Antarctica is excluded in both panels. Variations between these estimations have not led to a conclusive estimate of spatial coverage and severity of land degradation at the global scale (179). For this reason, IPBES (2018) uses a convergence-of-evidence approach based on global change issues.

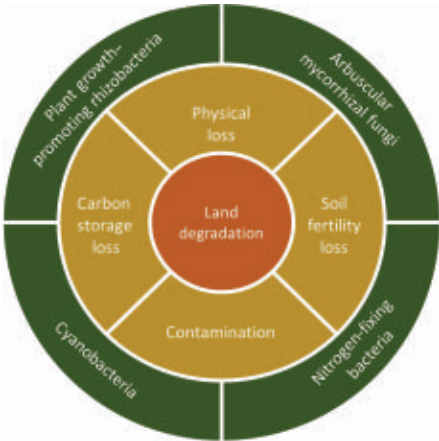


Fig. 3. Main types of land degradation and main types of useful bacteria.

(altered pore size, water repellency, stability of aggregates), biological composition (vegetation loss, changes in microbial communities), and chemical properties (increase in organic carbon due to combustion, volatilization of nitrogen and phosphorus), with detrimental effects (94, 95). Burned soil may become hydrophobic as a result of accumulation of hydrophobic substances on the soil surface after burning of organic materials (96). Moreover, the exposed soil is much more vulnerable to wind (97) and water (96) erosion during the first few years

following wildfires. Loss of topsoil due to erosion is the primary risk of failure for forest replanting. Another consequence of the wildfires is the formation of hazardous organic compounds such as polycyclic aromatic hydrocarbons (PAHs) as a result of combustion processes of the plant biomass (98). Soil microorganisms play an important role in soil function recovery after fire. PGPR have been shown to enhance nutrient availability and promote plant growth in fire-impacted soil (99, 100). The inoculation of soil with ectomycorrhizal fungi in burned forest also stimulates plant growth (101), making them attractive for assisted forest regeneration in fire-damaged soils. Alternatively, the growth of locally indigenous soil microorganisms can be stimulated with organic matter, oxygen, specific plant species, or other stimulating factors through so-called biostimulation (102). Biostimulation enhances the natural biodegradation potential of the indigenous microbial community and has been shown to be a most promising strategy for PAH removal from burned forest soil (103) and from contaminated soil (104). To combat hydrophobicity of soils, wax-degrading Actinobacteria have successfully been used to reduce water repellency, either via Actinobacteria inoculation in soil (105) or when still present in soil via their biostimulation (106), which is a more practical and economical approach.

Loss of soil fertility
Since the Green Revolution in the 1950s and 1960s, agricultural production has increased worldwide with the aim of feeding an increasing world population. Global food demand will rise by another 70% in the coming decades, emphasizing the need for intensive crop production (107). The intensive cultivation of crops can lead to the exhaustion of soil organic matter and soil nutrient reserves, resulting in soil degradation (108). Driven by increased understanding of the role of microorganisms in soil health and crop productivity, the use of agronomic practices to restore soil fertility through organic matter addition, microbial N fixation, and nutrient recycling (i.e., regenerative agriculture) is also increasing rapidly. Such practices include no-tillage, rotating crops and growing cover crops, returning crop residue into the soil, using biofertilizers or biopesticides, and applying organic fertilizers such as manure, biochar, and compost (109). It has been shown that biofertilizers (i.e., inocula of fungi and bacteria) can be combined with organic fertilizers to reduce the need for chemical fertilizers and to use soil resources more efficiently (110). As for the biopesticides, these are less toxic than abiotic pesticides, reducing environmental pollution, and can be more effective than chemical pesticides in the long term (110). Soil organic matter, biopesticides, and biofertilizers provide

a foundation to achieve food security for the growing population and restore soil fertility (48). Indeed, next to soil chemical and soil physical parameters, microbial soil indicators have been used as a proxy to measure soil fertility and soil health levels more generally (19).

Remediation of saline soils

Each year, around 1 to 2% of fertile soils are being degraded worldwide as a consequence of salinity (111), and about 20% of irrigated land is currently already affected by salinization (112). Soil salinity can be due to cations such as sodium (Na^+) and anions such as chloride (Cl^-), among others. Exposure to salinity increases the concentrations of Na^+ and Cl^- ions and decreases the availability of other ions such as potassium (K^+) to plants. Sodium ions not only cause plant cell injury but also degrade soil structure. By contrast, K^+ is essential to plant cells as a major inorganic nutrient and an osmotic regulator (113). Along with ionic imbalance, long-term salinity reduces the ability of plants to extract water from the soil, making the salt and drought problems of plants closely related (113). Salinity occurs in agricultural soils in the arid and semi-arid regions of the world, but also in some coastal regions (e.g., the Netherlands) as a result of rising seawater level. Consequently, interest in salinity-tolerant plants and sustainable methods for the bioremediation of saline soils is also growing (111).

Biological remediation by the application of salt-tolerant, or halophilic, PGPR and AMF is a sustainable alternative to conventional physical and chemical treatments of saline soil (111, 114, 115). Halophilic PGPR can remediate saline soils directly via improving nutrient status, soil structure, organic matter, pH, electrical conductivity, and deposition of ionic salts in soil (116). These PGPR are increasingly seen as an efficient tool to mitigate salinity stress in plants through mechanisms stimulating multidirectional physiological, biochemical, and molecular responses. In particular, inoculation with halophilic PGPR and AMF increases K^+/Na^+ ratios, which are beneficial in maintaining ionic homeostasis in the cytoplasm or Na^+ efflux from plants (114, 115). Lately, the application of halophilic PGPRs from the rhizosphere of halophilic plant species has been actively explored as a means to stimulate plant growth and increase the salt tolerance of nonhalophytic crops (111, 117). Recent studies on the underlying mechanisms have shown that halophilic PGPR can modify the expression in plants of several genes responsible for the amelioration of salinity stress (118, 119). The connection among plant stress responses, signaling molecules, and microbiome assembly can be used to modify the phytomicrobiome for the benefit of stressed

plants and can be explored further for the development of stress-resilient “smart agriculture” (120–122).

Soil contamination

Soil can become contaminated by chemicals originating from various sources, including agricultural and industrial activities, dumping waste, and urbanization. Soil pollution can produce negative agricultural, industrial, urban, and environmental effects such as reduced soil fertility, water pollution, reduced plant growth, and modified soil biodiversity. These can cause subsequent soil erosion and degradation, ultimately changing the whole ecosystem (123). Information about the global extent of soil pollution is lacking, as only some countries undertake national surveys of soil pollution (124). However, the information that is available is cause for concern. For example, China has categorized 16% of all its soils as polluted (125). Among physical, chemical, and biological approaches for remediation, interest in the latter has amplified in recent years as societies turn to sustainable and green solutions to solve environmental problems (126). Bioremediation of contaminated soils refers to the degradation of pollutants through microbial metabolic activities by mostly indigenous microorganisms (102). PGPR also have an indirect positive impact on removal of contaminants by plants (phytoremediation)—for example, by stimulating plant growth and increasing contaminant bioavailability—and this role can be manipulated to improve the efficacy of phytoremediation (127). Microbe-assisted phytoremediation has shown to be efficient in restoring sites contaminated by heavy metals, pesticides, and hydrocarbons (128). This biotechnology can kick-start further recovery of degraded ecosystems, leading to much faster biodiversity restoration (128). For example, inoculation of contaminated soil with fungi when reintroducing vegetation not only enhances the extraction of heavy metals from the polluted soils but also enables the plants to establish themselves on degraded soil and thereby improve soil quality and health (129, 130).

The effects of remediation on the restoration of biodiversity remains to be explored further. For example, one recent study considers how the composition and structure of fungi after phytoremediation are driven by the plant species present (131). A wide variety of microorganisms and metabolites that can degrade pollutants are still largely unexplored, and better understanding of their metabolism will enable their use in bioremediation. Recently, the potential of extremophiles that survive in environments with high concentrations of metals, radionuclides, or other pollutants has been explored (132, 133). Next-generation sequencing approaches can help to discover microbial diversity and metabolic functions that

predict the presence and extent of contamination, characterize the process of natural attenuation by unculturable microbes, and clarify the impact of biostimulation on microbial communities (134).

Effects of microorganisms on soil physical properties

Microbes affect soil structure by direct and indirect processes, including (i) moving primary particles along cell or hyphal surfaces; (ii) adhering particles together by their secretions, such as EPSs; (iii) enmeshing and binding aggregates by fungal hyphae and actinomycete filaments; and (iv) producing hydrophobic compounds that coat pore walls, particularly in fungi. A major factor in soil structure formation and stabilization is the soil organic matter, which increases soil aggregation. Microbes, including their remains or necromass, can make up more than half of soil organic carbon (135, 136), highlighting the role of microbes along with macroorganisms and plants in strongly related soil physical properties, such as porosity and aggregate stability.

Soil aggregates support root growth, resistance to erosion, carbon storage, and water-holding capacity (137), and a well-aggregated soil structure is fundamental to ensure healthy functioning of soil (43). Bacteria and fungi excrete mucilages that play important roles in soil microaggregate stabilization by gluing soil particles together (110, 137). They also take part in macroaggregate stabilization by entangling particles within the hyphae network and through production of EPSs (110, 137). Also, AMF are known to produce glomalin-like proteins that play an important role in soil stabilization, carbon storage, and soil aggregate stability and thereby decrease soil susceptibility to erosion (138). Although the role of bacteria and fungi in soil aggregate formation and stability is established, experimental studies on the application of microorganisms for soil structure improvement are scarce (139, 140).

Effects of microorganisms on soil hydraulic properties

Aggregate stability, soil structure, organic matter, and microtopography are all attributes associated with soil hydraulic properties. Microorganisms affect soil hydraulic properties at the pore scale in multiple ways (Fig. 4): by biofilm formation, EPS excretion, exudation of binding agents (e.g., glomalin-like proteins), particle enmeshment by fungi, production of water-repellent compounds, and alteration of soil surface microtopography.

Biofilms are aggregations of microorganisms whose cells adhere to each other or to a surface, often embedded within a self-produced matrix of EPS (141). Biofilms can form as a response to an environmental stress, enabling

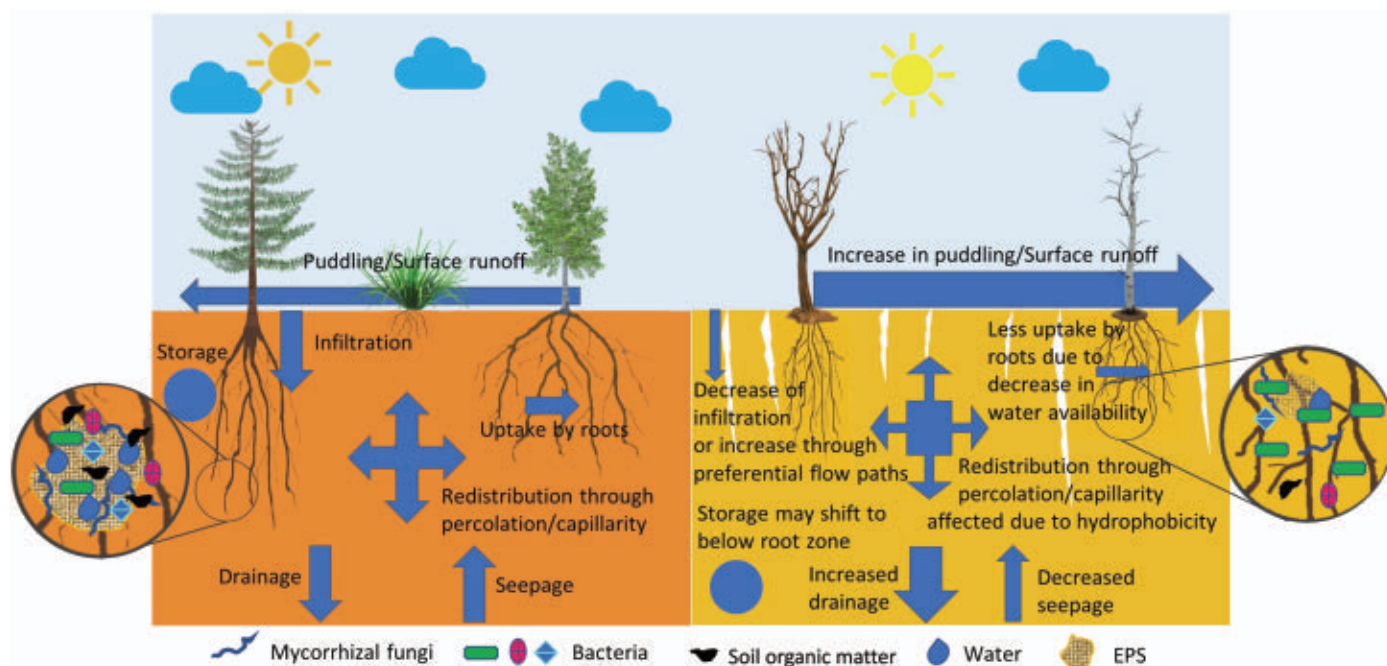


Fig. 4. Comparison of healthy and degraded land. Left: Hydrological fluxes in healthy soil. Right: Possible changes in soil hydrological fluxes as a result of soil degradation. Microbial processes are circled. Degraded land is experiencing a decline in microbial diversity as well as reduced amounts of extracellular polymeric substances (EPSs) and soil organic matter (SOM) that lead to a decrease in water-holding capacity and other hydrological changes, as shown here.

the cells to remain in a favorable niche and form mutualistic relationships (141). The key mechanism for changing soil hydraulic properties with biofilms is bioclogging, which is one of two main applications of a new branch of geotechnical engineering called microbial geotechnology (142, 143). It aims for a manipulated partial clogging of porous media by microorganisms and their by-products, in order to reduce soil porosity and hydraulic conductivity. Another application, biocementation, uses microorganisms to improve the engineering properties of soils and is beneficial for increasing soil strength and stiffness.

Bacterial EPS formation can improve soil water retention and reduce desiccation (144–146). EPS improves soil water-holding capacity in three different ways. First, certain polysaccharides (e.g., xanthan, dextran, scleroglucan) are a component of EPS and are known for their hydrophilic properties. By formation of clay- or sand-polysaccharide associations with soil microorganisms, a general increase in water-holding capacity may be observed (146, 147). In particular, a creation of hydrated microenvironments via production of alginate as an important component of EPS that decrease desiccation stress was shown for *Pseudomonas* (148). Second, EPS promotes the formation of soil aggregates and thereby soil water retention as the small intra-aggregate spaces hold water firmly (149, 150). Third, EPS modifies soil surface water repellency, causing an increase in the number of hydrophobic micropores that inhibit water evaporation (149, 151, 152).

A better understanding of the role of biofilms in soil hydraulic properties requires more studies, following a standardized methodology (Box 1).

Microorganisms are also able to produce substances other than EPSs to protect them in dry conditions. In bacteria, such compounds include disaccharide trehalose, which is responsible for osmotic stress response, and a polysaccharide α -glycan that increases desiccation tolerance in bacteria (91, 153). Microbial activity affects soil micro- and macroporosity via the exudation of binding agents and particle enmeshment by fungi that promote aggregate formation (154). Glomalin-related soil proteins, soil particle gluing agents that are produced by AMF, also improve soil moisture retention properties by increasing aggregate stability (155, 156).

Soil water repellency or hydrophobicity occurs when hydrophobic organic compounds accumulate at the soil surface. Those compounds can be derived from plant leaves and roots as well as from microorganisms. Examples of hydrophobic microbe-derived compounds are ergosterol and glomalin-related soil proteins (157). Fungal hyphae and bacterial excreta promote aggregate stability but at the same time can increase soil water repellency (158). On the other hand, some bacterial species have hydrophilizing properties, or have ability to degrade waxes, and thereby reduce hydrophobicity (80, 81).

BSCs in arid and semi-arid environments develop when communities of extremely drought-

resistant microorganisms dominated by cyanobacteria colonize the soil surface (159). They influence soil hydrology because they alter soil properties. Although there is abundant literature on the effects of BSCs on soil water repellency and infiltration, reports are contradictory. Some authors observed lower infiltration rates and higher runoff for soils with BSCs, relative to soils with low levels or no microbial cover (159, 160); others report positive effects (161) or no effects at all (162). These discrepancies can be attributed to methodological approaches, rainfall characteristics, soil factors, and/or natural variations of the BSC composition on crust functioning (160, 163). Because infiltration rates are controlled by soil surface structure, the rough surface microtopography of BSCs, characteristic for semi-arid cool and cold drylands, increases water infiltration and reduces runoff. On the other hand, BSCs in hyper-arid warm regions tend to be smooth and flat because of the absence of frost heaving, thereby reducing water infiltration and increasing runoff. Mixed effects are observed in arid regions (164, 165).

Conclusions and future prospects

Ecosystems vary greatly in the degree to which they are able to recover naturally from human disturbance. Conservation efforts have increasingly focused on active or natural restoration of degraded ecosystems in order to restore ecosystem services and biodiversity (166). In some cases, only minor interventions such as removing human disturbances (e.g., fire,

Box 1. Methodological challenges.

Although a number of studies have explored the role of biofilms in soil physical processes, most of these studies face methodological issues. Methodological needs are summarized below.

Setting proper scientific controls

In studies (142, 180, 181) investigating effects of a microorganism on soil hydraulic properties, the control group did not include all of the constituents of the media that had been used along with the microorganism in the treatment group. Considering that soil additives have been shown to affect soil hydrology (182), a lack of the proper negative control prohibits distinguishing effects of the tested microorganism from the effects of media.

Combining microbiological and hydrological methodologies

For measurements of soil hydrophysical properties that may take weeks, the laboratory needs to be temperature- and humidity-controlled. Low temperature is important for minimizing microbial growth that could alter hydraulic parameters while these measurements take place. Although some studies use elevated temperature settings for stimulation of evaporation in order to reduce the required duration of the experiment (180), use of lower-humidity settings is recommended over increasing temperature in such experiments (181).

Standardizing the hydrological methodology

Standardization of methodological procedures is vital for cross-comparison of data from different experiments, consistency between replicates, and minimizing risk of procedural bias. Soil compaction has been shown to affect bacterial abundances in inoculated soil (142) and also strongly affects soil hydraulic properties via changes of bulk density (183). For soil sterilization, double sterilization or gamma-radiation appear to be most efficient (184, 185), although their alteration of soil chemical and physical properties should be considered (186). Also, a temperature dependence of water retention curves for various types of soils has been shown (187), and comparisons between different studies would be facilitated by the use of low temperature (as explained above).

Monitoring of microbial growth

Hydrological methodologies require a substantial amount of time (e.g., several days or even weeks), and microbial growth should be evaluated and reported. A study (181) showed that carbon deficit assessment demonstrated more consistent results than cell counting, a method used in most similar experiments (64, 142); therefore, careful consideration should be given to the choice of monitoring method. How microbial abundance affects soil hydraulic properties remains to be tested.

Microorganism addition to a sterilized, not living soil

"Proof of concept" studies evaluating the effect of a single microorganism in sterilized soil are useful for early investigational stages (65, 180, 181). The next step for such studies should be focused on approaches to enrich a microorganism in field soil and investigation of the effects of such enrichment on the entire microbial community.

Finding suitable microorganism(s)

Reports on enhancement of soil hydraulic properties after incubation with microorganisms are scarce in the current literature. Effects on soil hydraulic properties of only a few bacterial species (142, 180, 181), fungi (188), and algae (64, 65) have been reported. In addition to these, several studies on arid and semi-arid land restoration using biological crusts are available (71, 161, 189). We also suggest exploring the synergistic effects of consortia of microorganisms that can provide additional benefits for improving soil quality by means of, for example, N fixation and soil structure formation.

grazing) are sufficient to facilitate unassisted recovery. For severely degraded ecosystems, in particular when soil hydrology is affected (167), greater efforts may be needed to accelerate and influence the successional trajectory of recovery. Given the spread of land use and change by humans globally, we need approaches that return healthy soil ecosystems in more timely and steady trajectories than are achieved with the methods that are currently

available (168). In agricultural systems, land use and management strategies critically affect the rate and trajectory of recovery (168). Agricultural practices such as reduced tillage, crop rotation, organic amendments, and reduced fertilizer use where there was overuse can help prevent disruption of beneficial plant root symbioses, such as with N-fixing bacteria and mycorrhizal fungi, and entire microbial communities.

Although beneficial soil-borne organisms are already naturally present, the aim in soil restoration is to enhance their abundance and activity by either inoculation or enhancement of their growth. Direct injections of bacteria together with growth substrates into the soil has disadvantages, such as clogging of the soil pore spaces and higher concentrations of organisms and substrates near the injection points (169). Furthermore, a single microbial species is not likely to adapt and survive in all soil environments (170) and thus geographical differences in microbial soil composition should be considered (171). Furthermore, commercially available PGPR may affect the native microbial population, unlike indigenous bacteria that are well adapted to the local environment (100). Instead, a strategy more likely to be successful is to introduce microorganisms as a part of a healthy soil inoculum as an aid to plant community reestablishment, especially in conditions where the topsoil has been replaced (26, 110, 172).

Another way to stimulate the establishment of healthy soil microbiomes in degraded soils is through amendments with (noncontaminated) sewage sludge (173) or another organic substrate that matches the needs of the degraded soil. Given the risks to human health from pathogenic microbes of such organic materials as manure and sewage biosolids (174), alternative approaches to enhance soil quality are needed. Novel amendments are currently being developed that are free of such risks and are still able to enhance soil hydraulic properties, while at the same time stimulating microbial growth and increasing soil organic matter content (175). The long-term effects of these amendments on soil properties and on entire microbial communities remain to be studied. Before upscaling such approaches, detailed and systematic studies are needed in which a particular microorganism is enriched in living soil and its long-term effects on soil properties and soil microbial communities are tracked; such studies are entirely lacking at present.

Given the critical role of freshwater availability in terrestrial life and the paucity of studies on hydrological restoration, we especially advocate for research on the hydrological restoration of degraded soil using microorganisms. We propose that microorganisms can improve soil hydraulic properties such as water infiltration and water retention and reduce soil hydrophobicity. Along with new organic matter derived from microbes, this will promote plant growth and facilitate further ecosystem restoration. Such a restoration strategy requires collaboration across the research fields of soil microbiology and soil hydrology, of which there has been very little to date (176). Understanding the interaction between soil microbial and hydrological dynamics will create the

foundation for restoration practices that can return resilience to the soil-plant ecosystem.

REFERENCES AND NOTES

- J. Clardy, M. A. Fischbach, C. R. Currie, The natural history of antibiotics. *Curr. Biol.* **19**, R437–R441 (2009). doi: [10.1016/j.cub.2009.04.001](https://doi.org/10.1016/j.cub.2009.04.001); pmid: 19515346
- G. Schwilch *et al.*, Operationalizing ecosystem services for the mitigation of soil threats: A proposed framework. *Ecol. Indic.* **67**, 586–597 (2016). doi: [10.1016/j.ecolind.2016.03.016](https://doi.org/10.1016/j.ecolind.2016.03.016)
- M. Cherlet, C. Hutchinson, J. Reynolds, J. Hill, S. Sommer, G. von Maltitz, Eds., *World Atlas of Desertification* (Publication Office of the European Union, Luxembourg, 2018).
- United Nations Convention to Combat Desertification, *The Global Land Outlook* (ed. 1, 2017); www.unccd.int/actions/global-land-outlook-glo.
- J. K. Green *et al.*, Large influence of soil moisture on long-term terrestrial carbon uptake. *Nature* **565**, 476–479 (2019). doi: [10.1038/s41586-018-0848-x](https://doi.org/10.1038/s41586-018-0848-x); pmid: 30675043
- S. I. Seneviratne *et al.*, Investigating soil moisture-climate interactions in a changing climate: A review. *Earth Sci. Rev.* **99**, 125–161 (2010). doi: [10.1016/j.earscirev.2010.02.004](https://doi.org/10.1016/j.earscirev.2010.02.004)
- D. A. Robinson *et al.*, Experimental evidence for drought induced alternative stable states of soil moisture. *Sci. Rep.* **6**, 20018 (2016). doi: [10.1038/srep20018](https://doi.org/10.1038/srep20018); pmid: 26804897
- D. A. Robinson *et al.*, Global environmental changes impact soil hydraulic functions through biophysical feedbacks. *Global Change Biol.* **25**, 1895–1904 (2019). doi: [10.1111/gcb.14626](https://doi.org/10.1111/gcb.14626); pmid: 30900360
- R. M. B. Harris *et al.*, Biological responses to the press and pulse of climate trends and extreme events. *Nat. Clim. Change* **8**, 579–587 (2018). doi: [10.1038/s41558-018-0187-9](https://doi.org/10.1038/s41558-018-0187-9)
- M. J. van der Ploeg, J. E. M. Baartman, D. A. Robinson, Biophysical landscape interactions: Bridging disciplines and scale with connectivity. *Land Degrad. Dev.* **29**, 1167–1175 (2018). doi: [10.1002/ldr.2820](https://doi.org/10.1002/ldr.2820)
- J. H. Dane, R. J. Lenhard, in *Encyclopedia of Soils in the Environment*, D. Hillel, Ed. (Academic Press, 2005), pp. 231–237.
- N. G. McDowell *et al.*, Predicting Chronic Climate-Driven Disturbances and Their Mitigation. *Trends Ecol. Evol.* **33**, 15–27 (2018). doi: [10.1016/j.tree.2017.10.002](https://doi.org/10.1016/j.tree.2017.10.002); pmid: 29146414
- M. Reichstein *et al.*, Climate extremes and the carbon cycle. *Nature* **500**, 287–295 (2013). doi: [10.1038/nature12350](https://doi.org/10.1038/nature12350); pmid: 23955228
- C. S. Holling, Resilience and Stability of Ecological Systems. *Annu. Rev. Ecol. Syst.* **4**, 1–23 (1973). doi: [10.1146/annurev.es.04.110173.000245](https://doi.org/10.1146/annurev.es.04.110173.000245)
- J. M. Porr, J. Masoliver, K. Lindenberg, Bistability driven by dichotomous noise. *Phys. Rev. A* **44**, 4866–4875 (1991). doi: [10.1103/PhysRevA.44.4866](https://doi.org/10.1103/PhysRevA.44.4866); pmid: 9906538
- M. Scheffer *et al.*, Anticipating critical transitions. *Science* **338**, 344–348 (2012). doi: [10.1126/science.1225244](https://doi.org/10.1126/science.1225244); pmid: 23087241
- R. D. Bardgett, T. Caruso, Soil microbial community responses to climate extremes: Resistance, resilience and transitions to alternative states. *Philos. Trans. R. Soc. London Ser. B* **375**, 20190112 (2020). doi: [10.1098/rstb.2019.0112](https://doi.org/10.1098/rstb.2019.0112); pmid: 31983338
- E. K. Bünemann *et al.*, Soil quality – A critical review. *Soil Biol. Biochem.* **120**, 105–125 (2018). doi: [10.1016/j.soilbio.2018.01.030](https://doi.org/10.1016/j.soilbio.2018.01.030)
- N. Fierer, S. A. Wood, C. P. Bueno de Mesquita, How microbes can, and cannot, be used to assess soil health. *Soil Biol. Biochem.* **153**, 108111 (2021). doi: [10.1016/j.soilbio.2020.108111](https://doi.org/10.1016/j.soilbio.2020.108111)
- J. P. Schimel, Life in Dry Soils: Effects of Drought on Soil Microbial Communities and Processes. *Annu. Rev. Ecol. Syst.* **49**, 409–432 (2018). doi: [10.1146/annurev-ecolsys-110617-062614](https://doi.org/10.1146/annurev-ecolsys-110617-062614)
- J. Harris, Soil microbial communities and restoration ecology: Facilitators or followers? *Science* **325**, 573–574 (2009). doi: [10.1126/science.1172975](https://doi.org/10.1126/science.1172975); pmid: 19644111
- E. K. Hall *et al.*, Understanding how microbiomes influence the systems they inhabit. *Nat. Microbiol.* **3**, 977–982 (2018). doi: [10.1038/s41564-018-0201-z](https://doi.org/10.1038/s41564-018-0201-z); pmid: 30143799
- P. Trivedi, P. M. Schenk, M. D. Wallenstein, B. K. Singh, Tiny Microbes, Big Yields: Enhancing food crop production with biological solutions. *Microb. Biotechnol.* **10**, 999–1003 (2017). doi: [10.1111/1751-7915.12804](https://doi.org/10.1111/1751-7915.12804); pmid: 28840959
- I. Saha, S. Datta, D. Biswas, Exploring the Role of Bacterial Extracellular Polymeric Substances for Sustainable Development in Agriculture. *Curr. Microbiol.* **77**, 3224–3239 (2020). doi: [10.1007/s00284-020-02169-y](https://doi.org/10.1007/s00284-020-02169-y); pmid: 32876713
- F. T. Maestre, R. Solé, B. K. Singh, Microbial biotechnology as a tool to restore degraded drylands. *Microb. Biotechnol.* **10**, 1250–1253 (2017). doi: [10.1111/1751-7915.12832](https://doi.org/10.1111/1751-7915.12832); pmid: 28834240
- E. R. J. Wubs, W. H. van der Putten, M. Bosch, T. M. Bezemer, Soil inoculation steers restoration of terrestrial ecosystems. *Nat. Plants* **2**, 16107 (2016). doi: [10.1038/nplants.2016.107](https://doi.org/10.1038/nplants.2016.107); pmid: 27398907
- J. A. Lau, J. T. Lennon, Evolutionary ecology of plant-microbe interactions: Soil microbial structure alters selection on plant traits. *New Phytol.* **192**, 215–224 (2011). doi: [10.1111/j.1469-8137.2011.03790.x](https://doi.org/10.1111/j.1469-8137.2011.03790.x); pmid: 21658184
- W. H. van der Putten *et al.*, Plant-soil feedbacks: The past, the present and future challenges. *J. Ecol.* **101**, 265–276 (2013). doi: [10.1111/1365-2745.12054](https://doi.org/10.1111/1365-2745.12054)
- X. Peng, M. A. Bruns, Development of a nitrogen-fixing cyanobacterial consortium for surface stabilization of agricultural soils. *J. Appl. Phycol.* **31**, 1047–1056 (2019). doi: [10.1007/s10811-018-1597-9](https://doi.org/10.1007/s10811-018-1597-9)
- J. S. Singh, V. C. Pandey, D. P. Singh, Efficient soil microorganisms: A new dimension for sustainable agriculture and environmental development. *Agric. Ecosyst. Environ.* **140**, 339–353 (2011). doi: [10.1016/j.agee.2011.01.017](https://doi.org/10.1016/j.agee.2011.01.017)
- L. Quiza, M. St-Arnaud, E. Yergeau, Harnessing phytomicrobiome signaling for rhizosphere microbiome engineering. *Front. Plant Sci.* **6**, 507 (2015). doi: [10.3389/fpls.2015.00507](https://doi.org/10.3389/fpls.2015.00507); pmid: 26236319
- R. Backer *et al.*, Plant growth-promoting rhizobacteria: Context, mechanisms of action, and roadmap to commercialization of biostimulants for sustainable agriculture. *Front. Plant Sci.* **9**, 1473 (2018). doi: [10.3389/fpls.2018.01473](https://doi.org/10.3389/fpls.2018.01473); pmid: 30405652
- V. C. S. Pankiewicz, T. B. Irving, L. G. S. Maia, J. M. Ané, Are we there yet? The long walk towards the development of efficient symbiotic associations between nitrogen-fixing bacteria and non-leguminous crops. *BMC Biol.* **17**, 99 (2019). doi: [10.1186/s12915-019-0710-0](https://doi.org/10.1186/s12915-019-0710-0); pmid: 31796086
- F. Stagnari, A. Maggio, A. Galieni, M. Pisante, Multiple benefits of legumes for agriculture sustainability: An overview. *Chem. Biol. Technol. Agric.* **4**, 1–13 (2017). doi: [10.1186/s40538-016-0085-1](https://doi.org/10.1186/s40538-016-0085-1)
- C. Franche, K. Lindström, C. Elmerich, Nitrogen-fixing bacteria associated with leguminous and non-leguminous plants. *Plant Soil* **321**, 35–59 (2009). doi: [10.1007/s11104-008-9833-8](https://doi.org/10.1007/s11104-008-9833-8)
- M. Charpentier, G. Oldroyd, How close are we to nitrogen-fixing cereals? *Curr. Opin. Plant Biol.* **13**, 556–564 (2010). doi: [10.1016/j.pbi.2010.08.003](https://doi.org/10.1016/j.pbi.2010.08.003); pmid: 20817544
- G. E. D. Oldroyd, O. Leyser, A plant's diet, surviving in a variable nutrient environment. *Science* **368**, eaab0196 (2020). doi: [10.1126/science.aba0196](https://doi.org/10.1126/science.aba0196); pmid: 32241923
- M. Bueno Batista, R. Dixon, Manipulating nitrogen regulation in diazotrophic bacteria for agronomic benefit. *Biochem. Soc. Trans.* **47**, 603–614 (2019). doi: [10.1042/BST20180342](https://doi.org/10.1042/BST20180342); pmid: 30936245
- I. Prieto *et al.*, Species-specific roles of ectomycorrhizal fungi in facilitating interplant transfer of hydraulically redistributed water between *Pinus halepensis* saplings and seedlings. *Plant Soil* **406**, 15–27 (2016). doi: [10.1007/s11104-016-2860-y](https://doi.org/10.1007/s11104-016-2860-y)
- A. Schüßler, D. Schwarzott, C. Walker, A new fungal phylum, the Glomeromycota: Phylogeny and evolution. *Mycol. Res.* **105**, 1413–1421 (2001). doi: [10.1017/S0959756201005196](https://doi.org/10.1017/S0959756201005196)
- S. E. Smith, F. A. Smith, I. Jakobsen, Mycorrhizal fungi can dominate phosphate supply to plants irrespective of growth responses. *Plant Physiol.* **133**, 16–20 (2003). doi: [10.1104/pp.103.024380](https://doi.org/10.1104/pp.103.024380); pmid: 12970469
- P. Bonfante, I.-A. Anca, Plants, mycorrhizal fungi, and bacteria: A network of interactions. *Annu. Rev. Microbiol.* **63**, 363–383 (2009). doi: [10.1146/annurev.micro.091208.073504](https://doi.org/10.1146/annurev.micro.091208.073504); pmid: 19514845
- J. M. Barea, R. Azcón, C. Azcón-Aguilar, in *Microorganisms in Soils: Roles in Genesis and Functions*, A. Varma, F. Buscot, Eds. (Springer, 2005), pp. 195–212.
- M. A. Hassani, P. Durán, S. Hacquard, Microbial interactions within the plant holobiont. *Microbiome* **6**, 58 (2018). doi: [10.1186/s40168-018-0445-0](https://doi.org/10.1186/s40168-018-0445-0); pmid: 29587885
- J. Zhou *et al.*, Different Arbuscular Mycorrhizal Fungi Cocolonizing on a Single Plant Root System Recruit Distinct Microbiomes. *mSystems* **5**, e00929-20 (2020). doi: [10.1128/mSystems.00929-20](https://doi.org/10.1128/mSystems.00929-20); pmid: 33323417
- E. T. Kiers *et al.*, Reciprocal rewards stabilize cooperation in the mycorrhizal symbiosis. *Science* **333**, 880–882 (2011). doi: [10.1126/science.1208473](https://doi.org/10.1126/science.1208473); pmid: 21836016
- M. Buée, W. de Boer, F. Martin, L. van Overbeek, E. Jurkevitch, The rhizosphere zoo: An overview of plant-associated communities of microorganisms, including phages, bacteria, archaea, and fungi, and of some of their structuring factors. *Plant Soil* **321**, 189–212 (2009). doi: [10.1007/s11104-009-9991-3](https://doi.org/10.1007/s11104-009-9991-3)
- J. J. Parnell *et al.*, From the lab to the farm: An industrial perspective of plant beneficial microorganisms. *Front. Plant Sci.* **7**, 1110 (2016). doi: [10.3389/fpls.2016.01110](https://doi.org/10.3389/fpls.2016.01110); pmid: 27540383
- J. Köhl, R. Kolnaar, W. J. Ravensberg, Mode of Action of Microbial Biological Control Agents Against Plant Diseases: Relevance Beyond Efficacy. *Front. Plant Sci.* **10**, 845 (2019). doi: [10.3389/fpls.2019.00845](https://doi.org/10.3389/fpls.2019.00845); pmid: 31379891
- M. R. Griffin, in *Advances in Endophytic Research*, V. C. Verma, A. C. Gange, Eds. (Springer, 2014), pp. 257–282.
- J. A. Vorholt, Microbial life in the phyllosphere. *Nat. Rev. Microbiol.* **10**, 828–840 (2012). doi: [10.1038/nrmicro2910](https://doi.org/10.1038/nrmicro2910); pmid: 23154261
- J. Imam, P. K. Singh, P. Shukla, Plant microbe interactions in post genomic era: Perspectives and applications. *Front. Microbiol.* **7**, 1488 (2016). doi: [10.3389/fmicb.2016.01488](https://doi.org/10.3389/fmicb.2016.01488); pmid: 27725809
- C. Knief, Analysis of plant microbe interactions in the era of next generation sequencing technologies. *Front. Plant Sci.* **5**, 216 (2014). doi: [10.3389/fpls.2014.00216](https://doi.org/10.3389/fpls.2014.00216); pmid: 24904612
- R. P. Jacoby, S. Kopriva, Metabolic niches in the rhizosphere microbiome: New tools and approaches to analyse metabolic mechanisms of plant-microbe nutrient exchange. *J. Exp. Bot.* **70**, 1087–1094 (2019). doi: [10.1093/jxb/ery438](https://doi.org/10.1093/jxb/ery438); pmid: 30576534
- Y. Bai *et al.*, Functional overlap of the Arabidopsis leaf and root microbiota. *Nature* **528**, 364–369 (2015). doi: [10.1038/nature16192](https://doi.org/10.1038/nature16192); pmid: 26633631
- S. Pfeilmeier *et al.*, The plant NADPH oxidase RBOHD is required for microbiota homeostasis in leaves. *Nat. Microbiol.* **6**, 852–864 (2021). doi: [10.1038/s41564-021-00929-5](https://doi.org/10.1038/s41564-021-00929-5); pmid: 34194036
- A. C. Huang *et al.*, A specialized metabolic network selectively modulates *Arabidopsis* root microbiota. *Science* **364**, eaau6389 (2019). doi: [10.1126/science.aau6389](https://doi.org/10.1126/science.aau6389); pmid: 31073042
- K. Zhulina *et al.*, Dynamic root exudate chemistry and microbial substrate preferences drive patterns in rhizosphere microbial community assembly. *Nat. Microbiol.* **3**, 470–480 (2018). doi: [10.1038/s41564-018-0129-3](https://doi.org/10.1038/s41564-018-0129-3); pmid: 29556109
- T. H. Mauchline *et al.*, An analysis of *Pseudomonas* genomic diversity in take-all infected wheat fields reveals the lasting impact of wheat cultivars on the soil microbiota. *Environ. Microbiol.* **17**, 4764–4778 (2015). doi: [10.1111/1462-2920.13038](https://doi.org/10.1111/1462-2920.13038); pmid: 26337499
- H. Matsumoto *et al.*, Bacterial seed endophyte shapes disease resistance in rice. *Nat. Plants* **7**, 60–72 (2021). doi: [10.1038/s41477-020-00826-5](https://doi.org/10.1038/s41477-020-00826-5); pmid: 33398157
- Z. Wei *et al.*, Initial soil microbiome composition and functioning predetermine future plant health. *Sci. Adv.* **5**, eaaw0759 (2019). doi: [10.1126/sciadv.aaw0759](https://doi.org/10.1126/sciadv.aaw0759); pmid: 31579818
- F. T. Maestre *et al.*, Increasing aridity reduces soil microbial diversity and abundance in global drylands. *Proc. Natl. Acad. Sci. U.S.A.* **112**, 15684–15689 (2015). doi: [10.1073/pnas.1516684112](https://doi.org/10.1073/pnas.1516684112); pmid: 26647180
- R. L. Barnard, C. A. Osborne, M. K. Firestone, Responses of soil bacterial and fungal communities to extreme desiccation and rewetting. *ISME J.* **7**, 2229–2241 (2013). doi: [10.1038/ismej.2013.104](https://doi.org/10.1038/ismej.2013.104); pmid: 23823489
- S. R. Ragusa, D. S. de Zoysa, P. Rengasamy, The effect of microorganisms, salinity and turbidity on hydraulic conductivity of irrigation channel soil. *Irrig. Sci.* **15**, 159–166 (1994). doi: [10.1007/BF00193683](https://doi.org/10.1007/BF00193683)
- L. Lichner *et al.*, Algae influence the hydrophysical parameters of a sandy soil. *Catena* **108**, 58–68 (2013). doi: [10.1016/j.catena.2012.02.016](https://doi.org/10.1016/j.catena.2012.02.016)
- F. T. de Vries *et al.*, Land use alters the resistance and resilience of soil food webs to drought. *Nat. Clim. Change* **2**, 276–280 (2012). doi: [10.1038/nclimate1368](https://doi.org/10.1038/nclimate1368)
- R. F. Harris, in *Water Potential Relations in Soil Microbiology*, J. Parr, W. Gardner, L. Elliot, Eds. (Soil Science Society of America, Madison, WI, 1981), pp. 23–95.
- E. Uhlirová, D. Elhottová, J. Triska, H. Santrúcková, Physiology and microbial community structure in soil at extreme water content. *Folia Microbiol.* **50**, 161–166 (2005). doi: [10.1007/BF02931466](https://doi.org/10.1007/BF02931466); pmid: 16110922
- N. Fierer *et al.*, Cross-biome metagenomic analyses of soil microbial communities and their functional attributes. *Proc. Natl. Acad. Sci. U.S.A.* **109**, 21390–21395 (2012). doi: [10.1073/pnas.1215210110](https://doi.org/10.1073/pnas.1215210110); pmid: 23236140

70. A. Šťovíček, M. Kim, D. Or, O. Gillor, Microbial community response to hydration-desiccation cycles in desert soil. *Sci. Rep.* **7**, 45735 (2017). doi: [10.1038/srep45735](https://doi.org/10.1038/srep45735); pmid: [28383531](https://pubmed.ncbi.nlm.nih.gov/28383531/)
71. S. Chamizo, Y. Cantón, I. Miralles, F. Domingo, Biological soil crust development affects physicochemical characteristics of soil surface in semiarid ecosystems. *Soil Biol. Biochem.* **49**, 96–105 (2012). doi: [10.1016/j.soilbio.2012.02.017](https://doi.org/10.1016/j.soilbio.2012.02.017)
72. D. M. Griffin, Water and Microbial Stress. *Adv. Microb. Ecol.* **5**, 91–136 (1981). doi: [10.1007/978-1-4615-8306-6_3](https://doi.org/10.1007/978-1-4615-8306-6_3)
73. M. Hernández *et al.*, Structure, function and resilience to desiccation of methanogenic microbial communities in temporarily inundated soils of the Amazon rainforest (Cunía Reserve, Rondonia). *Environ. Microbiol.* **21**, 1702–1717 (2019). doi: [10.1111/1462-2920.14535](https://doi.org/10.1111/1462-2920.14535); pmid: [30680883](https://pubmed.ncbi.nlm.nih.gov/30680883/)
74. A. Reim *et al.*, Response of Methanogenic Microbial Communities to Desiccation Stress in Flooded and Rain-Fed Paddy Soil from Thailand. *Front. Microbiol.* **8**, 785 (2017). doi: [10.3389/fmicb.2017.00785](https://doi.org/10.3389/fmicb.2017.00785); pmid: [28529503](https://pubmed.ncbi.nlm.nih.gov/28529503/)
75. F. U. Battistuzzi, S. B. Hedges, A major clade of prokaryotes with ancient adaptations to life on land. *Mol. Biol. Evol.* **26**, 335–343 (2009). doi: [10.1093/molbev/msn247](https://doi.org/10.1093/molbev/msn247); pmid: [18988685](https://pubmed.ncbi.nlm.nih.gov/18988685/)
76. W. L. Nicholson, N. Munakata, G. Horneck, H. J. Melosh, P. Setlow, Resistance of *Bacillus* endospores to extreme terrestrial and extraterrestrial environments. *Microbiol. Mol. Biol. Rev.* **64**, 548–572 (2000). doi: [10.1128/MMBR.64.3.548-572.2000](https://doi.org/10.1128/MMBR.64.3.548-572.2000); pmid: [10974126](https://pubmed.ncbi.nlm.nih.gov/10974126/)
77. R. T. Jones *et al.*, A comprehensive survey of soil acidobacterial diversity using pyrosequencing and clone library analyses. *ISME J.* **3**, 442–453 (2009). doi: [10.1038/ismej.2008.127](https://doi.org/10.1038/ismej.2008.127); pmid: [19129864](https://pubmed.ncbi.nlm.nih.gov/19129864/)
78. S. J. Blazewicz, R. L. Barnard, R. A. Daly, M. K. Firestone, Evaluating rRNA as an indicator of microbial activity in environmental communities: Limitations and uses. *ISME J.* **7**, 2061–2068 (2013). doi: [10.1038/ismej.2013.102](https://doi.org/10.1038/ismej.2013.102); \pmid: [23823491](https://pubmed.ncbi.nlm.nih.gov/23823491/)
79. G. E. Schaumann *et al.*, Influence of biofilms on the water repellency of urban soil samples. *Hydrol. Processes* **21**, 2276–2284 (2007). doi: [10.1002/hyp.6746](https://doi.org/10.1002/hyp.6746)
80. M. M. Roper, The isolation and characterisation of bacteria with the potential to degrade waxes that cause water repellency in sandy soils. *Soil Res.* **42**, 427–434 (2004). doi: [10.1071/SR03153](https://doi.org/10.1071/SR03153)
81. F. McKenna, K. A. El-Tarabily, S. Petrie, C. Chen, B. Dell, Application of actinomycetes to soil to ameliorate water repellency. *Leit. Appl. Microbiol.* **35**, 107–112 (2002). doi: [10.1046/j.1472-765X.2002.01136.x](https://doi.org/10.1046/j.1472-765X.2002.01136.x); pmid: [12100583](https://pubmed.ncbi.nlm.nih.gov/12100583/)
82. A. Worrich *et al.*, Mycelium-mediated transfer of water and nutrients stimulates bacterial activity in dry and oligotrophic environments. *Nat. Commun.* **8**, 15472 (2017). doi: [10.1038/ncomms15472](https://doi.org/10.1038/ncomms15472); pmid: [28589950](https://pubmed.ncbi.nlm.nih.gov/28589950/)
83. L. Montanarella, in *Climate and Land Degradation*, M. V. K. Sivakumar, N. Ndiang'ui, Eds. (Springer, 2007), pp. 83–104.
84. A. Cook, K. Ljung, R. Watkins, in *Encyclopedia of Environmental Health* (Elsevier, 2019), pp. 546–553.
85. UN Decade for Deserts and the Fight against Desertification, “Why Now?” (2010); www.un.org/en/events/desertification_decade/whynow.shtml.
86. P. Reich, S. Numbem, R. Almaraz, H. Eswaran, Land resource stresses and desertification in Africa. *Agro Sci.* **2**, (2004). doi: [10.4314/as.v2i2.1484](https://doi.org/10.4314/as.v2i2.1484)
87. A. S. Ayangbenro, O. O. Babalola, Reclamation of arid and semi-arid soils: The role of plant growth-promoting archaea and bacteria. *Curr. Plant Biol.* **25**, 100173 (2021). doi: [10.1016/j.cpb.2020.100173](https://doi.org/10.1016/j.cpb.2020.100173)
88. D. Daffonchio, H. Hirt, G. Berg, in *Principles of Plant-Microbe Interactions: Microbes for Sustainable Agriculture*, B. Lugtenberg, Ed. (Springer, 2015), pp. 265–276.
89. W. Alsharif, M. M. Saad, H. Hirt, Desert Microbes for Boosting Sustainable Agriculture in Extreme Environments. *Front. Microbiol.* **11**, 1666 (2020). doi: [10.3389/fmicb.2020.01666](https://doi.org/10.3389/fmicb.2020.01666); pmid: [32793155](https://pubmed.ncbi.nlm.nih.gov/32793155/)
90. C. Chen *et al.*, Pantoea alhagi, a novel endophytic bacterium with ability to improve growth and drought tolerance in wheat. *Sci. Rep.* **7**, 41564 (2017). doi: [10.1038/srep41564](https://doi.org/10.1038/srep41564); pmid: [28128318](https://pubmed.ncbi.nlm.nih.gov/28128318/)
91. J. I. Vilchez, C. García-Fontana, D. Román-Naranjo, J. González-López, M. Manzanera, Plant Drought Tolerance Enhancement by Trehalose Production of Desiccation-Tolerant Microorganisms. *Front. Microbiol.* **7**, 1577 (2016). doi: [10.3389/fmicb.2016.01577](https://doi.org/10.3389/fmicb.2016.01577); pmid: [27746776](https://pubmed.ncbi.nlm.nih.gov/27746776/)
92. L. P. Chiquoine, S. R. Abella, M. A. Bowker, Rapidly restoring biological soil crusts and ecosystem functions in a severely disturbed desert ecosystem. *Ecol. Appl.* **26**, 1260–1272 (2016). doi: [10.1002/15-0973](https://doi.org/10.1002/15-0973); pmid: [27509763](https://pubmed.ncbi.nlm.nih.gov/27509763/)
93. M. Alcañiz, L. Outeiro, M. Francos, X. Úbeda, Effects of prescribed fires on soil properties: A review. *Sci. Total Environ.* **613–614**, 944–957 (2018). doi: [10.1016/j.scitotenv.2017.09.144](https://doi.org/10.1016/j.scitotenv.2017.09.144); pmid: [28946382](https://pubmed.ncbi.nlm.nih.gov/28946382/)
94. G. Certini, Effects of fire on properties of forest soils: A review. *Oecologia* **143**, 1–10 (2005). doi: [10.1007/s00442-004-1788-8](https://doi.org/10.1007/s00442-004-1788-8); pmid: [15688212](https://pubmed.ncbi.nlm.nih.gov/15688212/)
95. S. H. Doerr, A. Cerdà, Fire effects on soil system functioning: New insights and future challenges. *Int. J. Wildland Fire* **14**, 339 (2005). doi: [10.1071/WF05094](https://doi.org/10.1071/WF05094)
96. L. F. DeBano, The role of fire and soil heating on water repellency in wildland environments: A review. *J. Hydrol.* **231–232**, 195–206 (2000). doi: [10.1016/S0022-1694\(00\)00194-3](https://doi.org/10.1016/S0022-1694(00)00194-3)
97. S. Ravi, P. D’Odorico, T. M. Zobeck, T. M. Over, The effect of fire-induced soil hydrophobicity on wind erosion in a semiarid grassland: Experimental observations and theoretical framework. *Geomorphology* **105**, 80–86 (2009). doi: [10.1016/j.geomorph.2007.12.010](https://doi.org/10.1016/j.geomorph.2007.12.010)
98. E. J. Kim, J. E. Oh, Y. S. Chang, Effects of forest fire on the level and distribution of PCDD/Fs and PAHs in soil. *Sci. Total Environ.* **311**, 177–189 (2003). doi: [10.1016/S0048-9697\(03\)00095-0](https://doi.org/10.1016/S0048-9697(03)00095-0); pmid: [12826391](https://pubmed.ncbi.nlm.nih.gov/12826391/)
99. A. M. Aguirre-Monroy, J. C. Santana-Martínez, J. Dussán, Lysinibacillus sphaericus as a nutrient enhancer during fire-impacted soil reclamation. *Appl. Environ. Soil Sci.* **2019**, 1–8 (2019). doi: [10.1155/2019/3075153](https://doi.org/10.1155/2019/3075153)
100. P. Radhapriya, A. Ramachandran, P. Palani, Indigenous plant growth-promoting bacteria enhance plant growth, biomass, and nutrient uptake in degraded forest plants. *3 Biotech.* **8**, 154 (2018). doi: [10.1007/s13205-018-1179-1](https://doi.org/10.1007/s13205-018-1179-1)
101. N. R. Sousa, A. R. Franco, M. A. Ramos, R. S. Oliveira, P. M. L. Castro, Reforestation of burned stands: The effect of ectomycorrhizal fungi on Pinus pinaster establishment. *Soil Biol. Biochem.* **43**, 2115–2120 (2011). doi: [10.1016/j.soilbio.2011.06.013](https://doi.org/10.1016/j.soilbio.2011.06.013)
102. I. G. Sales da Silva *et al.*, Soil Bioremediation: Overview of Technologies and Trends. *Energies* **13**, 4664 (2020). doi: [10.3390/en13184664](https://doi.org/10.3390/en13184664)
103. M. Andreoli, S. Lampis, P. Brignoli, G. Vallini, Bioaugmentation and biostimulation as strategies for the bioremediation of a burned woodland soil contaminated by toxic hydrocarbons: A comparative study. *J. Environ. Manage.* **153**, 121–131 (2015). doi: [10.1016/j.jenvman.2015.02.007](https://doi.org/10.1016/j.jenvman.2015.02.007); pmid: [25688477](https://pubmed.ncbi.nlm.nih.gov/25688477/)
104. N. Haleyr *et al.*, Influence of bioaugmentation and biostimulation on PAH degradation in aged contaminated soils: Response and dynamics of the bacterial community. *J. Environ. Manage.* **238**, 49–58 (2019). doi: [10.1016/j.jenvman.2019.02.115](https://doi.org/10.1016/j.jenvman.2019.02.115); pmid: [30844545](https://pubmed.ncbi.nlm.nih.gov/30844545/)
105. M. Roper, Potential for remediation of water repellent soils by inoculation with wax-degrading bacteria in south-western Australia. *Biologia* **61**, S358–S362 (2007). doi: [10.2478/s11756-006-0189-3](https://doi.org/10.2478/s11756-006-0189-3)
106. M. M. Roper, Managing soils to enhance the potential for bioremediation of water repellency. *Soil Res.* **43**, 803 (2005). doi: [10.1071/SR05061](https://doi.org/10.1071/SR05061)
107. H. C. J. Godfray *et al.*, Food security: The challenge of feeding 9 billion people. *Science* **327**, 812–818 (2010). doi: [10.1126/science.1185383](https://doi.org/10.1126/science.1185383); pmid: [20110467](https://pubmed.ncbi.nlm.nih.gov/20110467/)
108. R. Kraaijvanger, T. Veldkamp, Grain Productivity, Fertilizer Response and Nutrient Balance of Farming Systems in Tigray, Ethiopia: A Multi-Perspective View in Relation to Soil Fertility Degradation. *Land Degrad. Dev.* **26**, 701–710 (2015). doi: [10.1002/ldr.2330](https://doi.org/10.1002/ldr.2330)
109. V. S. Bharti, M. L. Dotaniya, S. P. Shukla, V. K. Yadav, in *Agro-Environmental Sustainability, Volume 1: Managing Crop Health*, J. S. Singh, G. Seneviratne, Eds. (Springer, 2017), pp. 81–111.
110. M. I. Rashid *et al.*, Bacteria and fungi can contribute to nutrients bioavailability and aggregate formation in degraded soils. *Microbiol. Res.* **183**, 26–41 (2016). doi: [10.1016/j.jmires.2015.11.007](https://doi.org/10.1016/j.jmires.2015.11.007); pmid: [26805616](https://pubmed.ncbi.nlm.nih.gov/26805616/)
111. H. Etesami, G. A. Beattie, Mining halophytes for plant growth-promoting halotolerant bacteria to enhance the salinity tolerance of non-halophytic crops. *Front. Microbiol.* **9**, 148 (2018). doi: [10.3389/fmicb.2018.00148](https://doi.org/10.3389/fmicb.2018.00148); pmid: [29472908](https://pubmed.ncbi.nlm.nih.gov/29472908/)
112. R. Munns, M. Tester, Mechanisms of salinity tolerance. *Annu. Rev. Plant Biol.* **59**, 651–681 (2008). doi: [10.1146/annurev.arplant.59.032607.092911](https://doi.org/10.1146/annurev.arplant.59.032607.092911); pmid: [18444910](https://pubmed.ncbi.nlm.nih.gov/18444910/)
113. H. Bothe, Arbuscular mycorrhiza and salt tolerance of plants. *Symbiosis* **58**, 7–16 (2012). doi: [10.1007/s13199-012-0196-9](https://doi.org/10.1007/s13199-012-0196-9)
114. N. Kumar Arora *et al.*, Halo-tolerant plant growth promoting rhizobacteria for improving productivity and remediation of saline soils. *J. Adv. Res.* **26**, 69–82 (2020). doi: [10.1016/j.jare.2020.07.003](https://doi.org/10.1016/j.jare.2020.07.003); pmid: [33133684](https://pubmed.ncbi.nlm.nih.gov/33133684/)
115. M. Chandrasekaran, S. Boughattas, S. Hu, S. H. Oh, T. Sa, A meta-analysis of arbuscular mycorrhizal effects on plants grown under salt stress. *Mycorrhiza* **24**, 611–625 (2014). doi: [10.1007/s00572-014-0582-7](https://doi.org/10.1007/s00572-014-0582-7); pmid: [24770494](https://pubmed.ncbi.nlm.nih.gov/24770494/)
116. S. Arora, M. Vanza, in *Bioremediation of Salt Affected Soils: An Indian Perspective*, S. Arora, A. K. Singh, Y. P. Singh, Eds. (Springer, 2017), pp. 87–100.
117. S. Ullah, A. Bano, Isolation of plant-growth-promoting rhizobacteria from rhizospheric soil of halophytes and their impact on maize (*Zea mays* L.) under induced soil salinity. *Can. J. Microbiol.* **61**, 307–313 (2015). doi: [10.1139/cjm-2014-0668](https://doi.org/10.1139/cjm-2014-0668); pmid: [25776270](https://pubmed.ncbi.nlm.nih.gov/25776270/)
118. I. Pinedo, T. Ledger, M. Greve, M. J. Poupin, Burkholderia phytofirmans PsJN induces long-term metabolic and transcriptional changes involved in Arabidopsis thaliana salt tolerance. *Front. Plant Sci.* **6**, 466 (2015). doi: [10.3389/fpls.2015.00466](https://doi.org/10.3389/fpls.2015.00466); pmid: [26157451](https://pubmed.ncbi.nlm.nih.gov/26157451/)
119. H. Yasmin *et al.*, Halotolerant rhizobacteria Pseudomonas pseudoalcaligenes and Bacillus subtilis mediate systemic tolerance in hydroponically grown soybean (Glycine max L.) against salinity stress. *PLOS ONE* **15**, e0231348 (2020). doi: [10.1371/journal.pone.0231348](https://doi.org/10.1371/journal.pone.0231348); pmid: [32298338](https://pubmed.ncbi.nlm.nih.gov/32298338/)
120. P. A. Rodriguez *et al.*, Systems Biology of Plant-Microbiome Interactions. *Mol. Plant* **12**, 804–821 (2019). doi: [10.1016/j.molp.2019.05.006](https://doi.org/10.1016/j.molp.2019.05.006); pmid: [31128275](https://pubmed.ncbi.nlm.nih.gov/31128275/)
121. V. Tripathi, P. Kumar, P. Tripathi, A. Kishore, M. Kamle, Eds., *Microbial Genomics in Sustainable Agroecosystems, Volume 2* (Springer, 2019). doi: [10.1007/978-981-32-9860-6](https://doi.org/10.1007/978-981-32-9860-6)
122. R. Porcel, R. Aroca, J. M. Ruiz-Lozano, Salinity stress alleviation using arbuscular mycorrhizal fungi. A review. *Agron. Sustain. Dev.* **32**, 181–200 (2012). doi: [10.1007/s13593-011-0029-x](https://doi.org/10.1007/s13593-011-0029-x)
123. M. C. Hernandez-Soriano, Ed., *Environmental Risk Assessment of Soil Contamination* (InTech, 2014).
124. D. Hou, Y. S. Ok, Soil pollution - speed up global mapping. *Nature* **566**, 455 (2019). doi: [10.1038/d41586-019-00669-x](https://doi.org/10.1038/d41586-019-00669-x); pmid: [30809065](https://pubmed.ncbi.nlm.nih.gov/30809065/)
125. Food and Agriculture Organization of the United Nations, “Report sounds alarm on soil pollution” (2018); www.fao.org/news/story/en/item/1126971/icode/.
126. P. Singh *et al.*, in *Abatement of Environmental Pollutants: Trends and Strategies*, P. Singh, A. Kumar, A. Borthakur, Eds. (Elsevier, 2019), pp. 1–23.
127. J. L. Wood, W. Liu, C. Tang, A. E. Franks, Microorganisms in heavy metal bioremediation: Strategies for applying microbial-community engineering to remediate soils. *AIMS Bioeng.* **3**, 211–229 (2016). doi: [10.3934/bioeng.2016.2.211](https://doi.org/10.3934/bioeng.2016.2.211)
128. A. A. Juwarkar, Microbe-Assisted Phytoremediation for Restoration of Biodiversity of Degraded Lands: A Sustainable Solution. *Proc. Natl. Acad. Sci. India B* **82**, 313–318 (2012). doi: [10.1007/s40011-012-0098-x](https://doi.org/10.1007/s40011-012-0098-x)
129. O. Akhtar, R. Mishra, H. K. Kehri, Arbuscular Mycorrhizal Association Contributes to Cr Accumulation and Tolerance in Plants Growing on Cr Contaminated Soils. *Proc. Natl. Acad. Sci. India B* **89**, 63–70 (2017). doi: [10.1007/s40011-017-0914-4](https://doi.org/10.1007/s40011-017-0914-4)
130. O. Akhtar, H. K. Kehri, I. Zoomi, Arbuscular mycorrhiza and Aspergillus terreus inoculation along with compost amendment enhance the phytoremediation of Cr-rich technosol by *Solanum lycopersicum* under field conditions. *Ecotoxicol. Environ. Saf.* **201**, 110869 (2020). doi: [10.1016/j.ecoenv.2020.110869](https://doi.org/10.1016/j.ecoenv.2020.110869); pmid: [32585490](https://pubmed.ncbi.nlm.nih.gov/32585490/)
131. M. Gil-Martínez *et al.*, Soil fungal diversity and functionality are driven by plant species used in phytoremediation. *Soil Biol. Biochem.* **153**, 108102 (2021). doi: [10.1016/j.soilbio.2020.108102](https://doi.org/10.1016/j.soilbio.2020.108102)
132. M. Figueroa *et al.*, Synthesis and Antibacterial Activity of Metal(loid) Nanostructures by Environmental Multi-Metal (loid) Resistant Bacteria and Metal(loid)-Reducing Flavoproteins. *Front. Microbiol.* **9**, 959 (2018). doi: [10.3389/fmicb.2018.00959](https://doi.org/10.3389/fmicb.2018.00959); pmid: [29869640](https://pubmed.ncbi.nlm.nih.gov/29869640/)
133. C. R. Marques, Extremophilic microfactories: Applications in metal and radionuclide bioremediation. *Front. Microbiol.* **9**, 1191 (2018). doi: [10.3389/fmicb.2018.01191](https://doi.org/10.3389/fmicb.2018.01191); pmid: [29910794](https://pubmed.ncbi.nlm.nih.gov/29910794/)
134. S. M. Techtman, T. C. Hazen, Metagenomic applications in environmental monitoring and bioremediation. *J. Ind. Microbiol. Biotechnol.* **43**, 1345–1354 (2016). doi: [10.1007/s10295-016-1809-8](https://doi.org/10.1007/s10295-016-1809-8); pmid: [27558781](https://pubmed.ncbi.nlm.nih.gov/27558781/)
135. C. Liang, W. Amelung, J. Lehmann, M. Kästner, Quantitative assessment of microbial necromass contribution to soil organic matter. *Global Change Biol.* **25**, 3578–3590 (2019). doi: [10.1111/gcb.14781](https://doi.org/10.1111/gcb.14781); pmid: [31365780](https://pubmed.ncbi.nlm.nih.gov/31365780/)

136. C. M. Kallenbach, S. D. Frey, A. S. Grandy, Direct evidence for microbial-derived soil organic matter formation and its ecophysiological controls. *Nat. Commun.* **7**, 13630 (2016). doi: [10.1038/ncomms13630](https://doi.org/10.1038/ncomms13630); pmid: 27892466
137. J. Six, H. Bossuyt, S. Degryze, K. Denef, A history of research on the link between (micro)aggregates, soil biota, and soil organic matter dynamics. *Soil Tillage Res.* **79**, 7–31 (2004). doi: [10.1016/j.still.2004.03.008](https://doi.org/10.1016/j.still.2004.03.008)
138. M. C. Rillig, Arbuscular mycorrhizae, glomalin, and soil aggregation. *Can. J. Soil Sci.* **84**, 355–363 (2004). doi: [10.4141/S04-003](https://doi.org/10.4141/S04-003)
139. N. Requena, E. Perez-Solis, C. Azcón-Aguilar, P. Jeffries, J.-M. Barea, Management of indigenous plant-microbe symbioses aids restoration of desertified ecosystems. *Appl. Environ. Microbiol.* **67**, 495–498 (2001). doi: [10.1128/AEM.67.2.495-498.2001](https://doi.org/10.1128/AEM.67.2.495-498.2001); pmid: 11157208
140. A. Medina, R. Azcón, Effectiveness of the application of arbuscular mycorrhiza fungi and organic amendments to improve soil quality and plant performance under stress conditions. *J. Soil Sci. Plant Nutr.* **10**, 354–372 (2010). doi: [10.4067/S0718-95162010000100009](https://doi.org/10.4067/S0718-95162010000100009)
141. K. K. Jefferson, What drives bacteria to produce a biofilm? *FEMS Microbiol. Lett.* **236**, 163–173 (2004). doi: [10.1111/j.1574-6968.2004.tb09643.x](https://doi.org/10.1111/j.1574-6968.2004.tb09643.x); pmid: 15251193
142. M. L. Dennis, J. P. Turner, Hydraulic Conductivity of Compacted Soil Treated with Biofilm. *J. Geotech. Geoenviron. Eng.* **124**, 120–127 (1998). doi: [10.1061/\(ASCE\)1090-0241\(1998\)124:2\(120\)](https://doi.org/10.1061/(ASCE)1090-0241(1998)124:2(120))
143. V. Ivanov, J. Chu, Applications of microorganisms to geotechnical engineering for bioclogging and biocementation of soil in situ. *Rev. Environ. Sci. Biotechnol.* **7**, 139–153 (2008). doi: [10.1007/s1157-007-9126-3](https://doi.org/10.1007/s1157-007-9126-3)
144. C. Chenu, Clay- or sand-polysaccharide associations as models for the interface between micro-organisms and soil: Water related properties and microstructure. *Geoderma* **56**, 143–156 (1993). doi: [10.1016/0016-7061\(93\)90106-U](https://doi.org/10.1016/0016-7061(93)90106-U)
145. E. B. Roberson, M. K. Firestone, Relationship between desiccation and exopolysaccharide production in a soil *Pseudomonas* sp. *Appl. Environ. Microbiol.* **58**, 1284–1291 (1992). doi: [10.1128/aem.58.4.1284-1291.1992](https://doi.org/10.1128/aem.58.4.1284-1291.1992); pmid: 16348695
146. D. Or, S. Phutane, A. Dechesne, Extracellular Polymeric Substances Affecting Pore-Scale Hydrologic Conditions for Bacterial Activity in Unsaturated Soils. *Vadose Zone J.* **6**, 298–305 (2007). doi: [10.2136/vzj2006.0080](https://doi.org/10.2136/vzj2006.0080)
147. L. J. Henao, K. Mazeau, Molecular modelling studies of clay-exopolysaccharide complexes: Soil aggregation and water retention phenomena. *Mater. Sci. Eng. C* **29**, 2326–2332 (2009). doi: [10.1016/j.msec.2009.06.001](https://doi.org/10.1016/j.msec.2009.06.001)
148. W. S. Chang *et al.*, Alginate production by *Pseudomonas putida* creates a hydrated microenvironment and contributes to biofilm architecture and stress tolerance under water-limiting conditions. *J. Bacteriol.* **189**, 8290–8299 (2007). doi: [10.1128/JB.00727-07](https://doi.org/10.1128/JB.00727-07)
149. Y. S. Guo *et al.*, Bacterial extracellular polymeric substances amplify water content variability at the pore scale. *Front. Environ. Sci.* **6**, 93 (2018). doi: [10.3389/fevs.2018.00093](https://doi.org/10.3389/fevs.2018.00093)
150. D. Or, B. F. Smets, J. M. Wraith, A. Dechesne, S. P. Friedman, Physical constraints affecting bacterial habitats and activity in unsaturated porous media - a review. *Adv. Water Resour.* **30**, 1505–1527 (2007). doi: [10.1016/j.advwatres.2006.05.025](https://doi.org/10.1016/j.advwatres.2006.05.025)
151. B. C. Cruz *et al.*, Pore-scale water dynamics during drying and the impacts of structure and surface wettability. *Water Resour. Res.* **53**, 5585–5600 (2017). doi: [10.1002/2016WR019862](https://doi.org/10.1002/2016WR019862)
152. D. B. George *et al.*, The effects of microbiotic soil crusts on soil water loss. *Arid Land Res. Manage.* **17**, 113–125 (2003). doi: [10.1080/15324980301558](https://doi.org/10.1080/15324980301558)
153. S. D. Woodcock *et al.*, Trehalose and α -glucan mediate distinct abiotic stress responses in *Pseudomonas aeruginosa*. *PLoS Genet.* **17**, e1009524 (2021). doi: [10.1371/journal.pgen.1009524](https://doi.org/10.1371/journal.pgen.1009524); pmid: 33872310
154. J. R. Helliwell, A. J. Miller, W. R. Whalley, S. J. Mooney, C. J. Sturrock, Quantifying the impact of microbes on soil structural development and behaviour in wet soils. *Soil Biol. Biochem.* **74**, 138–147 (2014). doi: [10.1016/j.soilbio.2014.03.009](https://doi.org/10.1016/j.soilbio.2014.03.009)
155. S. F. Wright, A. Upadhyaya, A survey of soils for aggregate stability and glomalin, a glycoprotein produced by hyphae of arbuscular mycorrhizal fungi. *Plant Soil* **198**, 97–107 (1998). doi: [10.1023/A:1004347701584](https://doi.org/10.1023/A:1004347701584)
156. Q. S. Wu *et al.*, Spatial distribution of glomalin-related soil protein and its relationships with root mycorrhization, soil aggregates, carbohydrates, activity of protease and β -glucosidase in the rhizosphere of *Citrus unshiu*. *Soil Biol. Biochem.* **45**, 181–183 (2012). doi: [10.1016/j.soilbio.2011.10.002](https://doi.org/10.1016/j.soilbio.2011.10.002)
157. I. M. Young, D. S. Feeney, A. G. O'Donnell, K. W. T. Goulding, Fungi in century old managed soils could hold key to the development of soil water repellency. *Soil Biol. Biochem.* **45**, 125–127 (2012). doi: [10.1016/j.soilbio.2011.10.007](https://doi.org/10.1016/j.soilbio.2011.10.007)
158. W. Zheng, E. K. Morris, A. Lehmann, M. C. Rillig, Interplay of soil water repellency, soil aggregation and organic carbon. A meta-analysis. *Geoderma* **283**, 39–47 (2016). doi: [10.1016/j.geoderma.2016.07.025](https://doi.org/10.1016/j.geoderma.2016.07.025)
159. O. Malam Issa, C. Défarge, J. Trichet, C. Valentin, J. L. Rajot, Microbiotic soil crusts in the Sahel of Western Niger and their influence on soil porosity and water dynamics. *Catena* **77**, 48–55 (2009). doi: [10.1016/j.catena.2008.12.013](https://doi.org/10.1016/j.catena.2008.12.013)
160. A. Yair, in *Biological Soil Crusts: Structure, Function, and Management*, J. Belnap, O. L. Lange, Eds. (Springer, 2001), pp. 303–314.
161. S. Chamizo, Y. Cantón, E. Rodríguez-Caballero, F. Domingo, Biocrusts positively affect the soil water balance in semiarid ecosystems. *Ecohydrology* **9**, 1208–1221 (2016). doi: [10.1002/eco.1719](https://doi.org/10.1002/eco.1719)
162. D. J. Eldridge, M. E. Tozer, S. Slangen, Soil hydrology is independent of microphytic crust cover: Further evidence from a wooded semiarid Australian rangeland. *Arid Soil Res. Rehabil.* **11**, 113–126 (1997). doi: [10.1080/15324989709381465](https://doi.org/10.1080/15324989709381465)
163. S. D. Warren, in *Biological Soil Crusts and Hydrology in North American Deserts*, J. Belnap, O. L. Lange, Eds. (Springer, 2001), pp. 327–337.
164. J. Belnap, The potential roles of biological soil crusts in dryland hydrologic cycles. *Hydrol. Processes* **20**, 3159–3178 (2006). doi: [10.1002/hyp.6325](https://doi.org/10.1002/hyp.6325)
165. J. Belnap, R. Rosentreter, S. Leonard, J. Kaltenecker, J. Williams, D. Eldridge, “Biological soil crusts: Ecology and management” (US Department of the Interior, 2001).
166. R. L. Chazdon, Beyond deforestation: Restoring forests and ecosystem services on degraded lands. *Science* **320**, 1458–1460 (2008). doi: [10.1126/science.1155365](https://doi.org/10.1126/science.1155365)
167. J. K. Zimmerman, T. M. Aide, A. E. Lugo, in *Old Fields: Dynamics and Restoration of Abandoned Farmland*, V. A. Cramer, R. J. Hobbs, Eds. (Island, 2007), pp. 51–74.
168. K. D. Holl, T. M. Aide, When and where to actively restore ecosystems? *For. Ecol. Manage.* **261**, 1558–1563 (2011). doi: [10.1016/j.foreco.2010.07.004](https://doi.org/10.1016/j.foreco.2010.07.004)
169. V. S. Whiffin, L. A. van Paassen, M. P. Harkes, Microbial carbonate precipitation as a soil improvement technique. *Geomicrobiol. J.* **24**, 417–423 (2007). doi: [10.1080/01490450701436505](https://doi.org/10.1080/01490450701436505)
170. J. S. Singh, Microbes: The chief ecological engineers in reinstating equilibrium in degraded ecosystems. *Agric. Ecosyst. Environ.* **203**, 80–82 (2015). doi: [10.1016/j.agee.2015.01.026](https://doi.org/10.1016/j.agee.2015.01.026)
171. B. Roncero-Ramos *et al.*, Polyphasic evaluation of key cyanobacteria in biocrusts from the most arid region in Europe. *PeerJ* **7**, e6169 (2019). doi: [10.7717/peerj.6169](https://doi.org/10.7717/peerj.6169); pmid: 30627491
172. V. Carbaljo, B. den Braber, W. H. van der Putten, G. B. De Deyn, Enhancement of late successional plants on ex-arable land by soil inoculations. *PLOS ONE* **6**, e21943 (2011). doi: [10.1371/journal.pone.0021943](https://doi.org/10.1371/journal.pone.0021943); pmid: 21760929
173. M. Curci *et al.*, Short-Term Effects of Sewage Sludge Compost Amendment on Semiarid Soil. *Soil Syst.* **4**, 48 (2020). doi: [10.3390/soilsystems4030048](https://doi.org/10.3390/soilsystems4030048)
174. M. J. Goss, A. Tubeileh, D. Goorahoo, A Review of the Use of Organic Amendments and the Risk to Human Health. *Adv. Agron.* **120**, 275–379 (2013). doi: [10.1016%2FB978-0-12-407686-0.00005-1](https://doi.org/10.1016%2FB978-0-12-407686-0.00005-1)
175. C. M. Kallenbach, R. T. Conant, F. Calderón, M. D. Wallenstein, A novel soil amendment for enhancing soil moisture retention and soil carbon in drought-prone soils. *Geoderma* **337**, 256–265 (2019). doi: [10.1016/j.geoderma.2018.09.027](https://doi.org/10.1016/j.geoderma.2018.09.027)
176. J. T. DeJong *et al.*, Soil engineering in vivo: Harnessing natural biogeochemical systems for sustainable, multi-functional engineering solutions. *J. R. Soc. Interface* **8**, 1–15 (2011). doi: [10.1098/rsif.2010.0270](https://doi.org/10.1098/rsif.2010.0270); pmid: 20829246
177. H. K. Gibbs, J. M. Salmon, Mapping the world's degraded lands. *Appl. Geogr.* **57**, 12–21 (2015). doi: [10.1016/j.apgeog.2014.11.024](https://doi.org/10.1016/j.apgeog.2014.11.024)
178. Intergovernmental Science-Policy Platform on Biodiversity and Ecosystem Services, The IPBES Assessment Report on Land Degradation and Restoration (2018). doi: [10.5281/zenodo.3237393](https://doi.org/10.5281/zenodo.3237393)
179. S. D. Prince, in *The End of Desertification? Disputing Environmental Change in the Drylands*, R. Behnke, M. Mortimore, Eds. (Springer, 2016), pp. 225–263.
180. W. Zheng *et al.*, Plant Growth-Promoting Rhizobacteria (PGPR) Reduce Evaporation and Increase Soil Water Retention. *Water Resour. Res.* **54**, 3673–3687 (2018). doi: [10.1029/2018WR026566](https://doi.org/10.1029/2018WR026566)
181. E. Volk, S. C. Iden, A. Furman, W. Durner, R. Rosenzweig, Biofilm effect on soil hydraulic properties: Experimental investigation using soil-grown real biofilm. *Water Resour. Res.* **52**, 5813–5828 (2016). doi: [10.1002/2016WR018866](https://doi.org/10.1002/2016WR018866)
182. M. O. Omundi *et al.*, Quantification of biochar effects on soil hydrological properties using meta-analysis of literature data. *Geoderma* **274**, 28–34 (2016). doi: [10.1016/j.geoderma.2016.03.029](https://doi.org/10.1016/j.geoderma.2016.03.029)
183. D. Dec, J. Dörner, O. Becker-Fazekas, R. Horn, Effect of bulk density on hydraulic properties of homogenized and structured soils. *Rev. Cienc. Suelo Nutr. Veg.* **8**, 1–13 (2008).
184. J. T. Trevors, Sterilization and inhibition of microbial activity in soil. *J. Microbiol. Methods* **26**, 53–59 (1996). doi: [10.1016/0167-7012\(96\)00843-3](https://doi.org/10.1016/0167-7012(96)00843-3)
185. N. P. McNamara, H. I. J. Black, N. A. Beresford, N. R. Parekh, Effects of acute gamma irradiation on chemical, physical and biological properties of soils. *Appl. Soil Ecol.* **24**, 117–132 (2003). doi: [10.1016/S0929-1393\(03\)00073-8](https://doi.org/10.1016/S0929-1393(03)00073-8)
186. A. E. Berns *et al.*, Effect of gamma-sterilization and autoclaving on soil organic matter structure as studied by solid state NMR, UV and fluorescence spectroscopy. *Eur. J. Soil Sci.* **59**, 540–550 (2008). doi: [10.1111/j.1365-2389.2008.01016.x](https://doi.org/10.1111/j.1365-2389.2008.01016.x)
187. J. Bachmann, R. Horton, S. A. Grant, R. van der Ploeg, Temperature Dependence of Water Retention Curves for Wettable and Water-Repellent Soils. *Soil Sci. Soc. Am. J.* **66**, 44–52 (2002). doi: [10.2136/sssaj2002.4400](https://doi.org/10.2136/sssaj2002.4400)
188. K. Seki, T. Miyazaki, M. Nakano, Effects of microorganisms on hydraulic conductivity decrease in infiltration. *Eur. J. Soil Sci.* **49**, 231–236 (1998). doi: [10.1046/j.1365-2389.1998.00152.x](https://doi.org/10.1046/j.1365-2389.1998.00152.x)
189. G. Colica *et al.*, Microbial secreted exopolysaccharides affect the hydrological behavior of induced biological soil crusts in desert sandy soils. *Soil Biol. Biochem.* **68**, 62–70 (2014). doi: [10.1016/j.soilbio.2013.09.017](https://doi.org/10.1016/j.soilbio.2013.09.017)

ACKNOWLEDGMENTS

O.C. acknowledges support from the NWO Open Mind grant, G.B.D.D. thanks FoodShot Global for their support through the GroundBreaker Prize, and all authors thank A. Van Dijk for valuable comments and English proofreading. **Author contributions:** Conceptualization: O.C., M.v.d.P., G.B.D.D. Visualization: O.C., M.v.d.P. Funding acquisition: M.v.d.P., G.B.D.D. Writing—original draft: O.C., M.v.d.P., G.B.D.D. Writing—review and editing: O.C., M.v.d.P., G.B.D.D. **Competing interests:** The authors declare that they have no competing interests.

10.1126/science.abe0725

RESEARCH ARTICLE SUMMARY

GENETICS

Fly Cell Atlas: A single-nucleus transcriptomic atlas of the adult fruit fly

Hongjie Li[†], Jasper Janssens[†], Maxime De Waegeneer, Sai Saroja Kolluru, Kristofer Davie, Vincent Gardeux, Wouter Saelens, Fabrice P. A. David, Maria Brbić, Katina Spanier, Jure Leskovec, Colleen N. McLaughlin, Qijing Xie, Robert C. Jones, Katja Brueckner, Jiwon Shim, Sudhir Gopal Tattikota, Frank Schnorrrer, Katja Rust, Todd G. Nystul, Zita Carvalho-Santos, Carlos Ribeiro, Soumitra Pal, Sharvani Mahadevaraju, Teresa M. Przytycka, Aaron M. Allen, Stephen F. Goodwin, Cameron W. Berry, Margaret T. Fuller, Helen White-Cooper, Erika L. Matunis, Stephen DiNardo, Anthony Galenza, Lucy Erin O'Brien, Julian A. T. Dow, FCA Consortium, Heinrich Jasper, Brian Oliver, Norbert Perrimon*, Bart Deplancke*, Stephen R. Quake*, Liqun Luo*, Stein Aerts*

INTRODUCTION: *Drosophila melanogaster* has had a fruitful history in biological research because it has contributed to many key discoveries in genetics, development, and neurobiology. The fruit fly genome contains ~14,000 protein-coding genes, ~63% of which have human orthologs. Single-cell RNA-sequencing has recently been applied to multiple *Drosophila* tissues and developmental stages. However, these data have been generated by different laboratories on different genetic backgrounds with different dissociation protocols and sequencing platforms, which has hindered the systematic comparison of gene expression across cells and tissues.

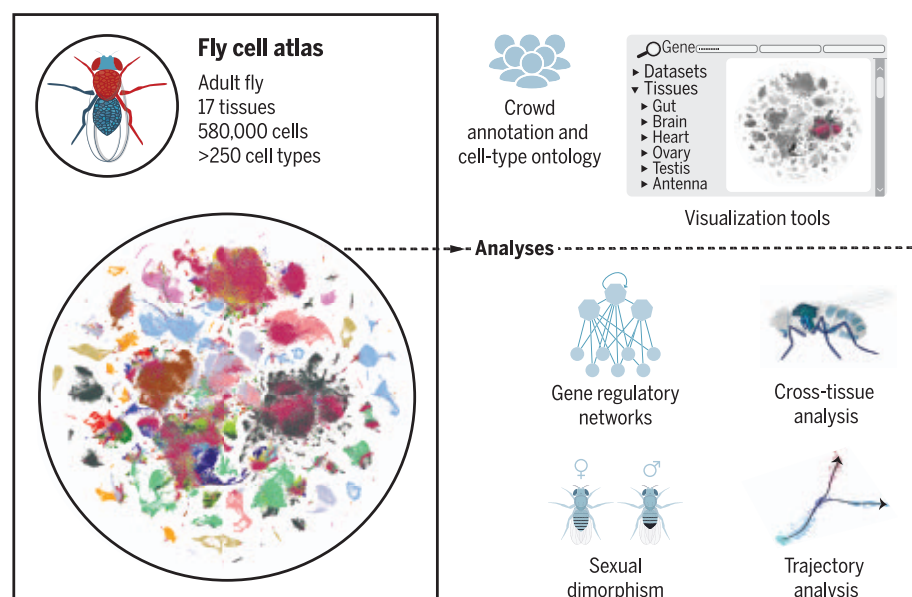
RATIONALE: We aimed to establish a cell atlas for the entire adult *Drosophila* with the same genetic background, dissociation protocol, and

sequencing platform to (i) obtain a comprehensive categorization of cell types, (ii) integrate single-cell transcriptome data with existing knowledge about gene expression and cell types, (iii) systematically compare gene expression across the entire organism and between males and females, and (iv) identify cell type-specific markers across the entire organism. We chose single-nucleus RNA-sequencing (snRNA-seq) to circumvent the difficulties of dissociating cells that are embedded in the cuticle (e.g., sensory neurons) or that are multinucleated (e.g., muscle cells). We took two complementary strategies: sequencing nuclei from dissected tissues to know the identity of the tissue source and sequencing nuclei from the entire head and body to ensure that all cells are sampled. Experts from 40 laboratories participated in

crowd annotation to assign transcriptomic cell types with the best knowledge available.

RESULTS: We sequenced 570,000 cells using droplet-based 10x Genomics from 15 dissected tissues as well as whole heads and bodies, separately in females and males. We also sequenced 10,000 cells from dissected tissues using the plate-based Smart-seq2 platform, providing deeper coverage per cell. We developed reproducible analysis pipelines using NextFlow and implemented a distributed cell-type annotation system with controlled vocabularies in SCoPe. Crowd-based annotations of transcriptomes from dissected tissues identified 17 main cell categories and 251 detailed cell types linked to FlyBase ontologies. Many of these cell types are characterized for the first time, either because they emerged only after increasing cell coverage or because they reside in tissues that had not been previously subjected to scRNA-seq. The excellent correspondence of transcriptomic clusters from whole body and dissected tissues allowed us to transfer annotations and identify a few cuticular cell types not detected in individual tissues. Cross-tissue analysis revealed location-specific subdivisions of muscle cells and heterogeneity within blood cells. We then determined cell type-specific marker genes and transcription factors with different specificity levels, enabling the construction of gene regulatory networks. Finally, we explored sexual dimorphism, finding a link between sex-biased expression and the presence of *doublesex*, and investigated tissue dynamics through trajectory analyses.

CONCLUSION: Our Fly Cell Atlas (FCA) constitutes a valuable resource for the *Drosophila* community as a reference for studies of gene function at single-cell resolution. All the FCA data are freely available for further analysis through multiple portals and can be downloaded for custom analyses using other single-cell tools. The ability to annotate cell types by sequencing the entire head and body will facilitate the use of *Drosophila* in the study of biological processes and in modeling human diseases at a whole-organism level with cell-type resolution. All data with annotations can be accessed from www.flycellatlas.org, which provides links to SCoPe, ASAP, and cellxgene portals. ■



Tabula *Drosophilae*. In this single-cell atlas of the adult fruit fly, 580,000 cells were sequenced and >250 cell types were annotated. They are from 15 individually dissected sexed tissues as well as the entire head and body. All data are freely available for visualization and download, with featured analyses shown at the bottom right.

The list of author affiliations is available in the full article online.

*Corresponding author. Email: perrimon@genetics.med.harvard.edu (N.P.); bart.deplancke@epfl.ch (B.D.); steve@quake-lab.org (S.R.Q.); lluo@stanford.edu (L.L.); stein.aerts@kuleuven.be (S.A.)

[†]These authors contributed equally to this work.

Cite this article as H. Li *et al.*, *Science* **375**, eabk2432 (2022). DOI: 10.1126/science.abk2432

S READ THE FULL ARTICLE AT
<https://doi.org/10.1126/science.abk2432>

RESEARCH ARTICLE

GENETICS

Fly Cell Atlas: A single-nucleus transcriptomic atlas of the adult fruit fly

Hongjie Li^{1,2,3,†}, Jasper Janssens^{4,5,†}, Maxime De Waegeneer^{4,5}, Sai Saroja Kolluru^{6,7,8}, Kristofer Davie⁴, Vincent Gedeux^{9,10}, Wouter Saelens^{9,10}, Fabrice P. A. David^{9,10,11}, Maria Brbić^{12,8}, Katina Spanier^{4,5}, Jure Leskovec^{12,8}, Colleen N. McLaughlin¹, Qijing Xie¹, Robert C. Jones^{6,7,8}, Katja Brueckner^{13,†}, Jiwon Shim¹⁴, Sudhir Gopal Tattikota^{15,16}, Frank Schnorfer¹⁷, Katja Rust^{18,19}, Todd G. Nystul¹⁹, Zita Carvalho-Santos²⁰, Carlos Ribeiro²⁰, Soumitra Pal²¹, Sharvani Mahadevaraju²², Teresa M. Przytycka²¹, Aaron M. Allen²³, Stephen F. Goodwin²³, Cameron W. Berry²⁴, Margaret T. Fuller²⁴, Helen White-Cooper²⁵, Erika L. Matunis²⁶, Stephen DiNardo^{27,28}, Anthony Galenza²⁹, Lucy Erin O'Brien²⁹, Julian A. T. Dow³⁰, FCA Consortium[§], Heinrich Jasper³¹, Brian Oliver²², Norbert Perrimon^{15,16,*}, Bart Deplancke^{9,10,*}, Stephen R. Quake^{6,7,8,*}, Liqun Luo^{1,*}, Stein Aerts^{4,5,*}

For more than 100 years, the fruit fly *Drosophila melanogaster* has been one of the most studied model organisms. Here, we present a single-cell atlas of the adult fly, Tabula *Drosophilae*, that includes 580,000 nuclei from 15 individually dissected sexed tissues as well as the entire head and body, annotated to >250 distinct cell types. We provide an in-depth analysis of cell type-related gene signatures and transcription factor markers, as well as sexual dimorphism, across the whole animal. Analysis of common cell types between tissues, such as blood and muscle cells, reveals rare cell types and tissue-specific subtypes. This atlas provides a valuable resource for the *Drosophila* community and serves as a reference to study genetic perturbations and disease models at single-cell resolution.

D*rosophila melanogaster* has had a fruitful history in biological research, dating back to the experiments of Thomas Hunt Morgan more than a century ago (1), and has been at the basis of many key biological discoveries. The highly collaborative nature of the *Drosophila* community contributed to many of these successes and led to the development of essential research resources, including a high-quality genome (2), a large collection of genetic and molecular tools, and important databases such as Flybase (3), FlyMine (4), FlyLight (5), VirtualFlyBrain (6), and ModERN (7). The fly genome contains about 17,000 genes, including 13,968 protein-coding genes of which ~63% have human orthologs. Studies such as ModENCODE (8) and FlyAtlas (9) explored expression patterns in different tissues but lacked

cell-type resolution. Recent advances in single-cell technologies have enabled the transcriptomic profiling of thousands of cells at once, facilitating the creation of tissue-wide atlases. Several studies have already applied single-cell RNA sequencing (scRNA-seq) to multiple *Drosophila* tissues and developmental stages (10). However, these data were generated by different laboratories on different genetic backgrounds with different dissociation protocols and sequencing platforms, which has hindered the systematic comparison of gene expression across cells and tissues.

Here, we present a single-cell transcriptomic atlas of the entire adult *Drosophila*, with male and female samples separately analyzed, using a uniform genotype and a unified single-nucleus RNA-seq (snRNA-seq) platform (11) with two

sequencing strategies: droplet-based 10x Genomics (12) and plate-based Smart-seq2 (13). The resulting Tabula *Drosophilae*, the first dataset within the Fly Cell Atlas (FCA) Consortium, contains more than 580,000 cells, resulting in >250 distinct cell types annotated by >100 experts from 40 laboratories. This atlas reports cellular signatures for each tissue, providing the entire *Drosophila* community a reference for studies that probe the effects of genetic perturbations and disease models at single-cell resolution. All data and annotations can be accessed through multiple visualization and analysis portals from <https://flycellatlas.org> (figs. S1 to S3).

Sampling single cells across the entire adult fly

We used a unified snRNA-seq platform for all samples because it is difficult to isolate intact cells from many adult *Drosophila* tissues, especially cuticular ones (e.g., antenna, wing) and adipocyte-enriched ones (e.g., fat body). In addition, snRNA-seq can be applied to large multinucleated cells (e.g., muscle) and facilitates (frozen) tissue collection from different laboratories. Finally, 70 to 90% of transcriptomic information is preserved from snRNA-seq compared with scRNA-seq of the same fly cell types (11).

To achieve a comprehensive sampling, we used two complementary strategies. First, we dissected 12 individual tissues from both males and females as well as three sex-specific tissues (Fig. 1A). For tissues that are localized across the body (fat body, oenocytes, and trachea) and cannot be directly dissected, we used specific GAL4 lines driving nuclear-green fluorescent protein (GFP) to label and collect nuclei using fluorescence-activated cell sorting (FACS). In addition, two rare cell types were sequenced only with Smart-seq2: insulin-producing cells and corpora cardiaca cells. Second, we sorted and profiled nuclei from the entire head and body, aiming to detect cell types not covered by the selected tissues. In total, we obtained 580,000 high-quality nuclei: 570,000 from 10x Genomics and 10,000 from Smart-seq2 (Fig. 1A).

¹Howard Hughes Medical Institute, Department of Biology, Stanford University, Stanford, CA 94305, USA. ²Huffington Center on Aging, Baylor College of Medicine, Houston, TX 77030, USA.

³Department of Molecular and Human Genetics, Baylor College of Medicine, Houston, TX 77030, USA. ⁴VIB-KU Leuven Center for Brain and Disease Research, KU Leuven, 3000 Leuven, Belgium.

⁵Laboratory of Computational Biology, Department of Human Genetics, KU Leuven, Leuven 3000, Belgium. ⁶Department of Bioengineering, Stanford University, Stanford, CA, USA. ⁷Department of Applied Physics, Stanford University, Stanford, CA, USA. ⁸Chan Zuckerberg Biohub, San Francisco CA, USA. ⁹Laboratory of Systems Biology and Genetics, Institute of Bioengineering, School of Life Sciences, Ecole Polytechnique Fédérale de Lausanne (EPFL), CH-1015 Lausanne, Switzerland. ¹⁰Swiss Institute of Bioinformatics, CH-1015 Lausanne, Switzerland. ¹¹Bioinformatics

Competence Center, EPFL, Switzerland. ¹²Department of Computer Science, Stanford University, Stanford, CA 94305, USA. ¹³Department of Cell and Tissue Biology, University of California, San Francisco, CA 94143, USA. ¹⁴Department of Life Science, College of Natural Science, Hanyang University, 04763 Seoul, Republic of Korea. ¹⁵Department of Genetics, Blavatnik Institute, Harvard Medical School, Boston, MA 02115, USA. ¹⁶Howard Hughes Medical Institute, Harvard Medical School, Boston, MA, USA. ¹⁷Aix-Marseille University, CNRS, IBDM (UMR 7288), Turing Centre for Living Systems, 13009 Marseille, France. ¹⁸Institute of Physiology and Pathophysiology, Department of Molecular Cell Physiology, Philipps-University, Marburg, Germany. ¹⁹Department of Anatomy, University of California, San Francisco, CA 94143, USA. ²⁰Behavior and Metabolism Laboratory, Champalimaud Research, Champalimaud Centre for the Unknown, Lisbon, Portugal.

²¹National Center of Biotechnology Information, National Library of Medicine, National Institutes of Health, Bethesda, MD 20894, USA. ²²Laboratory of Cellular and Developmental Biology, National Institute of Diabetes and Kidney Digestive Diseases, National Institutes of Health, Bethesda, MD 20892, USA. ²³Centre for Neural Circuits and Behaviour, University of Oxford, Oxford OX1 3SR, UK. ²⁴Department of Developmental Biology and Genetics, Stanford University School of Medicine, Stanford, CA 94305, USA. ²⁵Molecular Biosciences Division, Cardiff University, Cardiff CF10 3AX, UK. ²⁶Department of Cell Biology, Johns Hopkins University School of Medicine, Baltimore, MD 21205, USA. ²⁷Perelman School of Medicine, The University of Pennsylvania, Philadelphia, PA 19104, USA. ²⁸The Penn Institute for Regenerative Medicine, Philadelphia, PA 19104, USA. ²⁹Department of Molecular and Cellular Physiology, Stanford University School of Medicine, Stanford, CA 94305, USA. ³⁰Institute of Molecular, Cell and Systems Biology, College of Medical, Veterinary and Life Sciences, University of Glasgow, Glasgow G12 8QQ, UK.

³¹Immunology Discovery, Genentech, Inc., South San Francisco, CA 94080, USA.

*Corresponding author. Email: perrimon@genetics.med.harvard.edu (N.P.); bart.deplancke@epfl.ch (B.D.); steve@quake-lab.org (S.R.Q.); lluo@stanford.edu (L.L.); stein.aerts@kuleuven.be (S.A.)

†These authors contributed equally to this work. ‡Deceased. §FCA Consortium authors and affiliations are listed at the end of this paper.

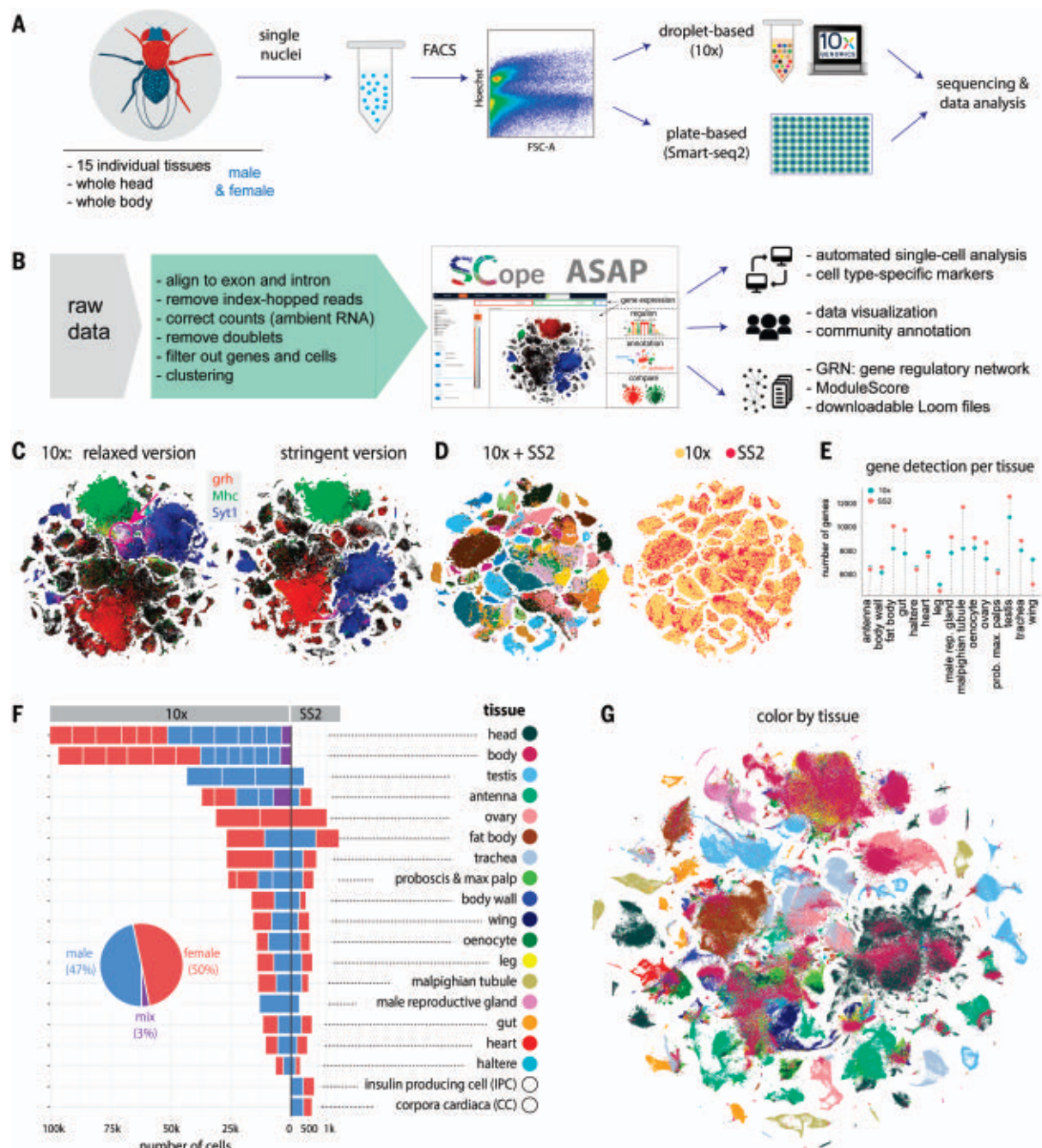


Fig. 1. Overview of the FCA. (A) Experimental platform of snRNA-seq using 10x Genomics and Smart-seq2. (B) Data analysis pipeline and data visualization using SScope (17) and ASAP (18). (C) Two versions of 10x datasets: Relaxed and Stringent. *t*-distributed stochastic neighbor embedding (tSNE) colors are based on gene expression: *grh* (epithelia, red), *Mhc* (muscle, green), and *Syt1* (neuron, blue). The red arrow denotes an artifactual cluster with coexpression of all three markers in the Relaxed dataset. (D) tSNE visualization of cells from the Stringent 10x dataset and Smart-seq2 (SS2) cells. 10x cells

are from individual tissues. Integrated data are colored by tissue (left) and platform (right). (E) Tissue-level comparison of the number of detected genes between 10x and Smart-seq2 platforms. (F) Number of cells for each tissue by 10x and Smart-seq2. Male and female cells are indicated. Mixed cells are from pilot experiments where flies were not sexed. Different batches are separated by vertical white lines. (G) All 10x cells from the Stringent dataset clustered together; cells are colored by tissue type. Tissue names and colors are indexed as in (F).

To analyze the 10x Genomics data in a reproducible manner, we used the automated VSN pipeline (14) (methods and table S1), which takes the raw sequencing data as input and performs preprocessing (e.g., normalization, doublet removal, batch-effect correction)

to produce LoomX-formatted files with expression data, embeddings, and clusterings (Fig. 1B and fig. S4). A presumed artifactual cluster showed expression of nearly all genes, so we added an additional preprocessing step that models and subtracts ambient RNA sig-

nals (15) to remove this cluster, resulting in a Stringent dataset of 510,000 cells (see methods and Fig. 1C). However, because adjusting the gene expression values per cell can introduce other biases (e.g., overcorrection, removal of nondoublet cells), we also retained the original

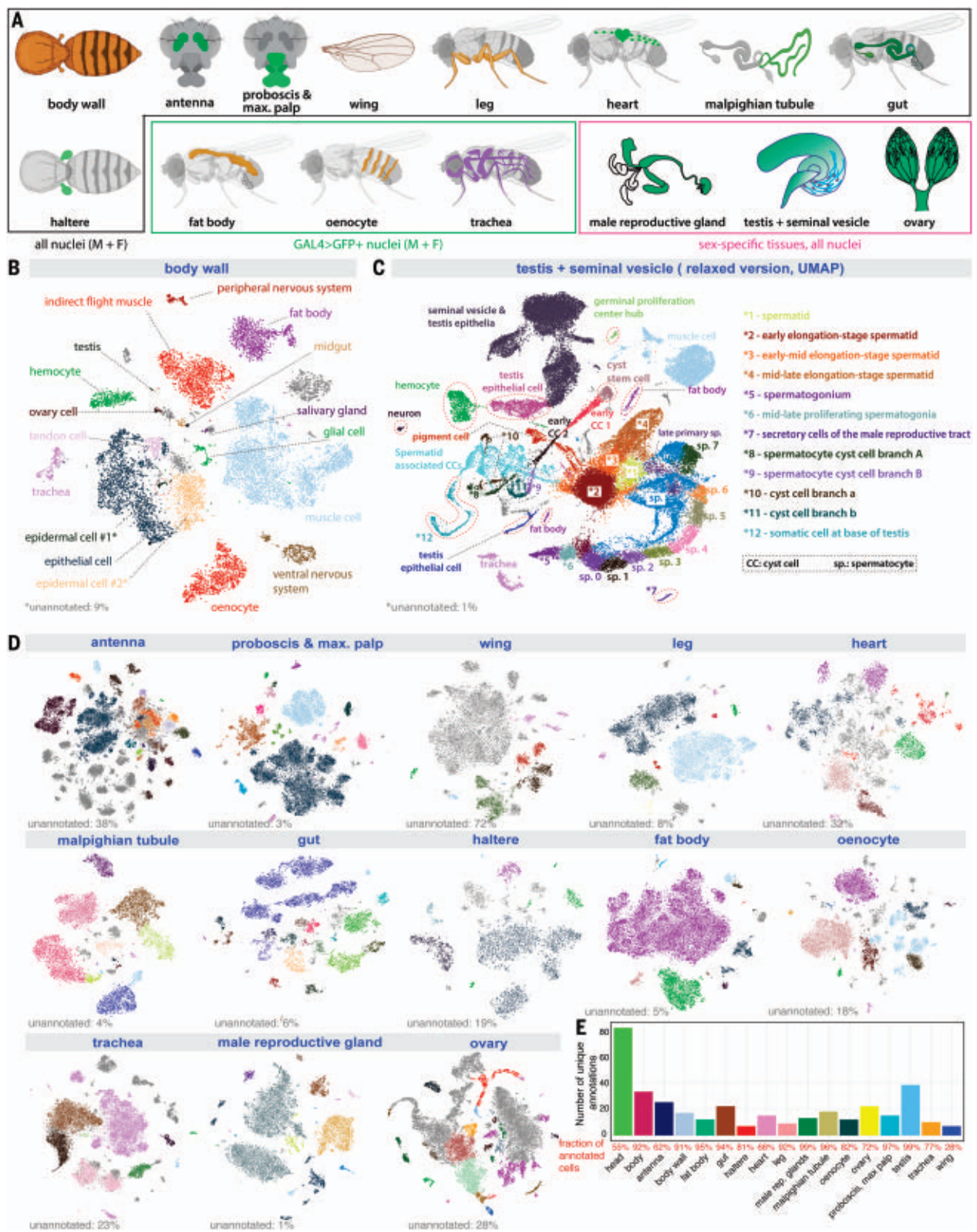


Fig. 2. Cell-type annotation for dissected tissues. (A) Illustration of 15 individual tissues: Twelve are sequenced separately from males and females and three are sex-specific. Fat body, oenocyte, and tracheal nuclei were labeled using a tissue-specific GAL4 driving UAS–nuclear-GFP. (B) tSNE plot with annotations for the body wall from the Stringent 10x dataset. *1, epidermal cells of the abdominal posterior compartment; *2, epidermal cells specialized in

antimicrobial response. (C) Uniform manifold approximation and projection (UMAP) plot with annotations for the testis from the Relaxed 10x dataset. (D) tSNE plots of the other 13 tissues from the Stringent 10x dataset. Detailed annotations are in figs. S6 to S18. (E) Number of unique annotations for each tissue. Fractions of annotated cells over all analyzed cells from the Relaxed dataset are indicated in red.

Relaxed dataset of 570,000 cells. In the analyses below, unless mentioned otherwise (e.g., Fig. 2C), the Stringent dataset was used.

Cells from 10x Genomics and Smart-seq2 were well integrated after batch correction using Harmony (16) (Fig. 1D). Smart-seq2 yielded a higher number of detected genes for most tissues (Fig. 1E) because cells were sequenced to a higher depth. We analyzed each tissue separately, combining the male and female runs, which yielded between 6500 (haltere) and 100,000 (head) cells and a median of 16,500 cells per tissue for 10x and between 263 (male reproductive gland) and 1349 (fat body) cells and a median of 534 cells per tissue for Smart-seq2 (Fig. 1F). We obtained similar numbers of male and female cells for non-sex-specific tissues with, on average, 1895 unique molecular identifiers (UMIs) and 828 genes per cell (fig. S5). Next, all cells were combined in a meta-analysis, showing tissue-specific clusters like the germline cells of the testis and ovary and shared clusters of common cell types (Fig. 1G and figs. S24 and S25).

Crowd-based cell-type annotation by tissue experts

Experts from 40 laboratories collaborated on cell-type annotation for 15 individual tissues, including 12 tissues for both sexes (antenna, body wall, fat body, haltere, heart, gut, leg, Malpighian tubule, oenocyte, proboscis with maxillary palp, trachea, and wing) and three sex-specific tissues (male reproductive gland, testis, and ovary) (Fig. 2A). We developed a consensus-voting strategy within the SCoPe web application (<https://flycellatlas.org/scope>) (17), where curators annotated clusters at multiple resolutions (ranging from 0.8 to 8; fig. S6A), with additional analysis performed in ASAP (<https://flycellatlas.org/asap>) (18). To ensure that cell-type annotations are consistent with previous literature and databases and to allow posteriori computational analyses at different anatomical resolutions, we used Flybase anatomy ontology terms (19).

Because some cell types are annotated at low resolutions and others at high resolutions, we collapsed all annotations across resolutions and retained the annotation with the highest number of up votes. All initial annotations were performed on the Relaxed dataset and were then exported to the Stringent dataset, where field experts verified the accuracy of the annotation transfer (Fig. 2, A to E, and figs. S6 to S18). Overall, we annotated 251 cell types in the Stringent dataset (262 cell types if combining Relaxed and Stringent datasets; table S2), with a median of 15 cell types per tissue.

Our dataset provides a single-cell transcriptomic profile for several adult tissues not profiled previously, including the haltere, heart, leg, Malpighian tubule, proboscis, maxillary

palp, trachea, and wing (figs. S6 to S18). In these tissues, all major expected cell types were identified. In the proboscis and maxillary palp (fig. S7, A and B), we could annotate gustatory and olfactory receptor neurons, mechanosensory neurons, and several glial clusters. All seven olfactory receptors expressed in the maxillary palp were detected. In the wing (fig. S8), we could identify four different neuronal types—gustatory receptor neurons, pheromone-sensing neurons, nociceptive neurons, and mechanosensory neurons—as well as three glial clusters. In the leg (fig. S9), we could distinguish gustatory receptor neurons from two clusters of mechanosensory neurons. In the heart (fig. S10), we found a large proportion of resident hemocytes and muscle cells, with cardiac cells marked by the genes *Hand* and *tinman* constituting a small proportion. In the Malpighian tubule (fig. S11), 15 cell types were identified, including the different principal cells of the stellate and main segments. In the haltere (fig. S13), we identified two clusters of neurons, three clusters of glial cells, and a large population of epithelial cells. In some tissues, cell types formed a big cluster instead of being split into distinct populations. In these cases, we identified genes or pathways that showed a gradient or compartmentalized expression. For example, in the fat body (figs. S14 and S19), the main fat body cells formed one big cluster, but our metabolic pathway enrichment analysis performed through ASAP (18) revealed that fatty acid biosynthesis and degradation are in fact compartmentalized, highlighting possible fat body cell heterogeneity in metabolic capacities.

Our crowd annotations with tissue experts also revealed cell types that had not been profiled previously, such as multinucleated muscle cells (Fig. 2B) and two distinct types of nuclei among the main cells in the male accessory gland (fig. S17), a cell type that was previously thought to be uniform. The high number of nuclei analyzed allowed identification of rare cell types. For example, in the testis (Fig. 2C), we identified 25 distinct cell types, covering all expected cell types, including very rare cells, such as germinal proliferation center hub cells (79 nuclei in the Relaxed version, out of 44,621 total testis nuclei).

Next, we compared the distribution of cells between 10x and Smart-seq2 and found a good match based on a coclustering analysis (figs. S20 and S21). Because Smart-seq2 cells only account for a small fraction, our previous annotations focused on 10x cells. The cell-matched coclustering analysis allowed us to transfer annotations from 10x to Smart-seq2 datasets (fig. S20E), using cluster-specific markers as validation (fig. S20F). We also identified genes that were specifically detected using Smart-seq2 thanks to its higher gene detection rate (Fig. 1E and fig. S20G). In summary, the high-

throughput 10x datasets form the basis for identifying cell types, whereas the Smart-seq2 datasets facilitate the detection of lowly expressed genes and enable future exploration of cell-specific isoform information.

Correspondence between dissected tissues and whole head and body

To generate a complete atlas of the fly, we next performed snRNA-seq experiments on whole-head and whole-body samples. Whole-body single-cell experiments were previously performed on less complex animals (20, 21). Full head and body sequencing provides a practical means to assess the impact of mutations or to track disease mechanisms, without having to focus on specific tissues. In addition, it could yield cell types that are not covered by any of the targeted tissue dissections.

In the head, we annotated 81 mostly neuronal cell types (Fig. 3A and fig. S22). In the body, we annotated the top 33 most abundant cell classes, including epithelia, muscle, and ventral nerve cord and peripheral neurons, followed by fat cells, oenocytes, germ line cells, glia, and tracheal cells (Fig. 3B and fig. S23). Many of these cell classes can be further divided into cell types for further annotation (see Fig. 2 and figs. S6 to S18).

Next, we examined how well the head and body samples covered the cell types from the dissected tissues. We analyzed head, body, and tissue samples together, with most of the selected tissues clustering together with the body. We also detected head- and body-enriched clusters (Fig. 3C). One body-specific cluster contained cuticle cells, likely from connective tissue (Fig. 3D). Others were relatively rare cell types in their respective tissues, such as adult stem cells. Conversely, most tissue clusters contained body cells, with only a small number being completely specific to dissected tissues. Because tissue-specific clusters were mostly observed in tissues with high cell coverage, such as the testis and Malpighian tubule, we anticipated that these clusters would also be identified in the body upon sampling a larger number of cells.

For the head, the antenna and proboscis with maxillary palp were dissected for tissue sequencing. Cell types from those two tissues largely overlapped with head cells. Many other cell types, such as central brain cells, including Kenyon cells (*ey*, *pvt*) and lamina glia (*repo*, *Optix*), were only detected in the head sample.

To compare our data with existing datasets, we integrated our head snRNA-seq dataset (“head” hereafter) with published brain scRNA-seq data (“brain” hereafter) (17, 22–24) (Fig. 3E). Head-specific clusters made up 20% of the cells, including the antennae, photoreceptors, muscle, cone cells, and cuticular cell types, whereas the other 80% were present in clusters containing both head- and brain-derived

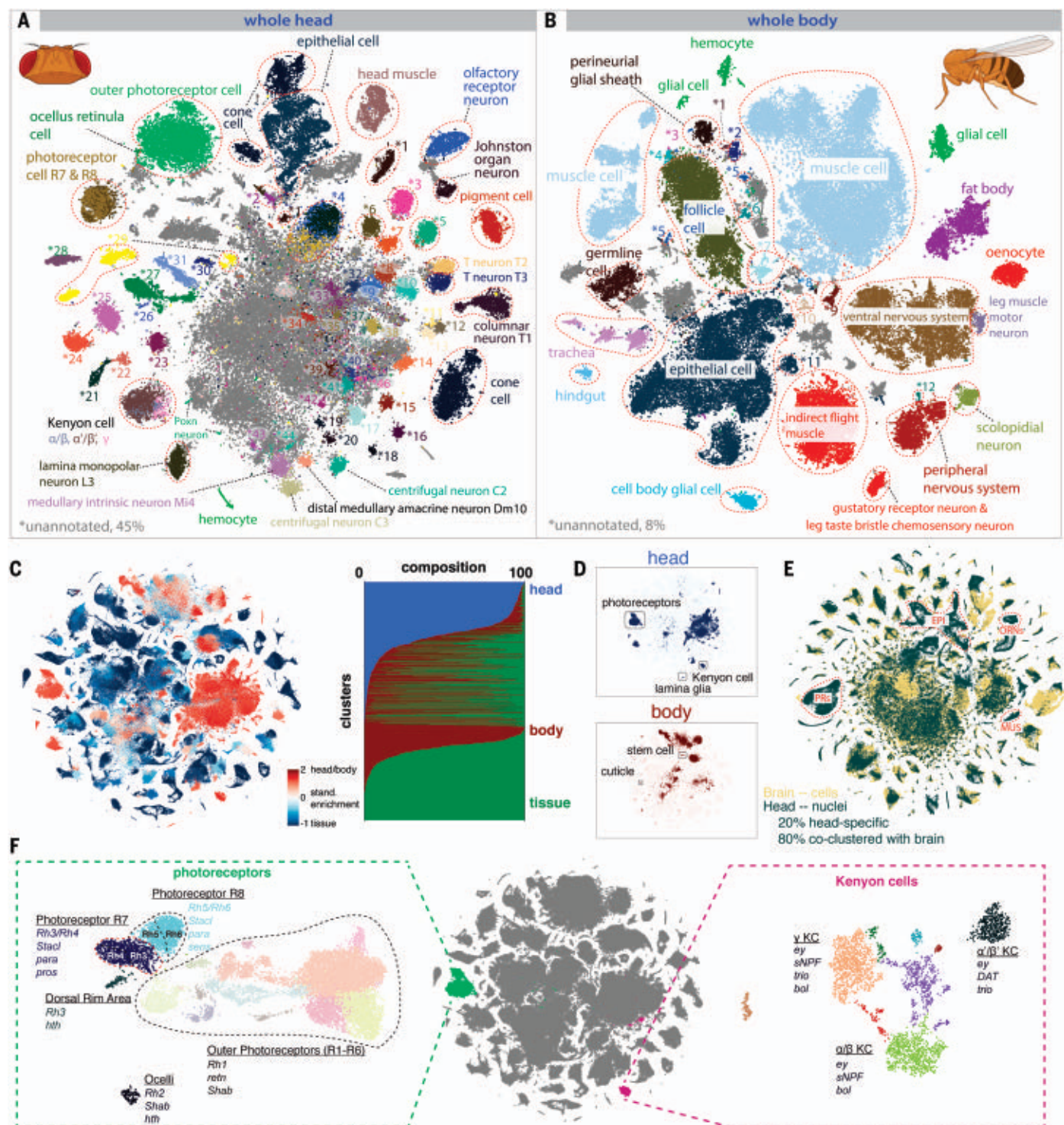


Fig. 3. Whole-head and whole-body sequencing leads to full coverage of the entire fly. (A) tSNE of the whole-head sample with 81 annotated clusters. See fig. S22 for full cell types. Many cells in the middle (gray) are unannotated, most of which are central brain neurons. (B) tSNE of the whole-body sample with 33 annotated clusters, many of which can be further divided into subclusters. Cells in gray are unannotated. See fig. S23 for full cell types. (C) tSNE of the entire dataset colored by standardized tissue enrichment, leading to the identification of head- and body-specific clusters, is shown on the left. Stacked bar plot showing tissue composition (head, body, or dissected tissues) for different

clusters at Leiden resolution 50 are shown on the right. (D) Examples of head- and body-specific clusters. (E) Integration of a brain scRNA-seq dataset with the head snRNA-seq for label transfer. Outlined are example clusters revealed by the head snRNA-seq dataset but not by the brain scRNA-seq datasets, including epithelial cells (EPI), photoreceptors (PRs), olfactory receptor neurons (ORNs), and muscle cells (MUS). (F) Subclustering analysis reveals types of photoreceptors, including inner and outer photoreceptors, with the inner photoreceptors further splitting into R7 and R8 types, and mushroom body Kenyon cells comprising three distinct types: α/β , α'/β' , and γ .

cells covering the neuronal and glial cell types of the brain. This coclustering across genotypes and protocols underscores the quality and utility of our snRNA-seq data compared with that of scRNA-seq data. Next, we used machine-learning models to predict annotations per cluster, followed by manual curation (22). Given the high number of neuron types, additional subclustering was performed on each cluster, identifying subtypes of peptidergic neurons (*dimm*, *Pdf*) and olfactory projection neurons based on *oaz*, *c15*, and *kn*. Finally, we identified many cell types in the optic lobe, including lamina (e.g., L1 to L5), medulla (e.g., Mi1, Mi15), lobula (e.g., LC), and lobula plate (e.g., LPLC). Using *acj6* and *SoxN*, we identified the T4/T5 neurons of the optic lobe that split in T4/T5a-b and T4/T5c-d subtypes by subclustering. A big clump of neurons remained unannotated (Fig. 3A), indicating that our dataset cannot resolve the complexity of the central brain, which may contain hundreds to thousands of neuron types.

Subclustering in the combined dataset separated inner and outer photoreceptors from the dorsal rim area and ocellar photoreceptors, with the inner photoreceptors further splitting into R7 and R8 types, each with *pale* and *yellow* types based on *rhodopsin* expression (Fig. 3F). Additionally, Kenyon cells were split into three types: α/β , α'/β' , and γ (17). These cases highlight the resolution in our dataset and the potential of using subclustering to discover rare cell types.

Cross-tissue analyses allow comparison of cell types by location

Using the whole-body and whole-head sequencing data, we assigned cells to major cell classes (e.g., epithelial cells, neurons, muscle cells, hemocytes), which allowed us to compare common classes across tissues (Fig. 4, A to C, and figs. S24 and S25). First, we compared blood cells across tissues by selecting all *Hml*-positive cells, a known marker for hemocytes (Fig. 4D). Combining hemocytes across tissues revealed a major group of plasmatocytes, the most common hemocyte type (~56%), crystal cells (1.5%; *PPO1*, *PPO2*), and several unknown types (fig. S26, A and B). Looking deeper into the plasmatocytes, we uncovered gradients based on the expression of *Pxn*, *LysX*, *Tep4*, *trtl*, and *Nplp2* that can be linked to maturation and plasticity, with *Pxn*-positive cells showing the highest *Hml* expression, whereas *Tep4*, *trtl*, and *Nplp2* are prohemocyte markers (25). Furthermore, different antimicrobial peptide families such as the Attacins and Cecropins were expressed in different subgroups, indicating specialization. Finally, expression of acetylcholine receptors was specific for a subset of hemocytes, relating to the cholinergic anti-inflammatory pathway as described in humans and mice (26). Lamellocytes were not

observed in adults as previously suggested (27). On the contrary, an unknown hemocyte type expressed *Antp* and *kn* (43 cells, 0.5%) reminiscent of the posterior signaling center in the lymph gland, an organization center previously thought to be absent in the adult (28, 29) (fig. S26B). These findings highlight the value of performing a whole organism-level single-cell analysis and constitute a foundation for investigating the fly immune system in greater detail.

Second, we compared the muscle cells of the different tissues (Fig. 4E and fig. S26, C and D). Muscle cells are syncytia—individual cells containing many nuclei—and to our knowledge have not been profiled by single-cell sequencing before our study. With snRNA-seq, we recovered all known muscle cell types, with specific enrichment in the body, body wall, and leg. This comprehensive view of the fly muscular system highlights a separation of visceral, skeletal, and indirect flight muscle based on the expression of different troponins. Specifically, we discovered gradients of *dysf* and *fhn* in the indirect flight muscle, which may indicate regional differences in these very large cells (>1000 nuclei) (fig. S26E). We identified four types of visceral muscle in the gut based on expression of the *AstC*, *Ms*, *Dh31*, and *CCAP* neuropeptide receptors, indicating potential modulators for muscle contraction (30). *Ms* and *Dh31* have been described to function in spatially restricted domains (30–32), suggesting similar domains for *AstC* and *CCAP*. All visceral muscle cells are enriched for the receptor of *Pdf*, a neuropeptide involved in circadian rhythms, pointing toward a function in muscle contraction as well (33).

Transcription factors and cell-type specificity

Our data allow the comparison of gene expression across the entire fly. Clustering cell types showed the germline cells as the most distinct group, followed by neurons (figs. S27 to S32). We calculated marker genes for every cell type using the whole FCA data as background, with 14,240 genes found as a marker for at least one cell type and a median of 638 markers per cell type [minimum: visceral muscle (94); maximum: spermatocyte (7736)]. Notably, markers specific for cell types in a tissue were not always specific in the whole body (fig. S33).

Next, we calculated the tau score of tissue specificity (34) for all predicted transcription factors (TFs) (3) and identified 500 TFs with a score >0.85, indicating a high specificity for one or very few cell types (Fig. 5A and table S3). Of these TFs, 127 were “CGs” (computed genes), indicating that their functions are poorly studied. We found that the male germline stands out in showing expression of a great number of cell type-specific TFs. This may be related to the broad activation of many genes in late spermatocytes, as discussed below.

Similar analysis across broad cell types (Fig. 5, B and C) identified 156 TFs with high tau scores, for example, the known regulators *grh* for epithelial cells and *repo* for glia, as well as 24 uncharacterized genes. Network visualization shows the grouping of central nervous system (CNS) neurons and sensory organ cells, including many sensory neurons, with shared pan-neuronal factors such as *onecut* and *scrt* but with each cluster having a distinct set of TFs, such as *ey*, *scro*, and *dati* for CNS neurons and *lz* and *glass* (*gl*) for sensory neurons.

In addition to the specificity of TF expression, we predicted gene regulatory networks based on coexpression and motif enrichment using SCENIC (31). Because of the stochasticity of this network inference method, we ran SCENIC 100 times, ranking predicted target genes by their recurrence. This approach selected 6112 “regulons” for 583 specific TFs across all tissues, whereby each regulon consists of the TF, its enriched motif, and the set of target genes that are predicted in at least 5 out of 100 runs. In fat cells, our analysis predicted a regulon for *sugarbabe* (*sug*), a sugar-sensitive TF necessary for the induction of lipogenesis (32). In photoreceptors, the analysis identified a *gl* regulon, with key photoreceptor markers such as *Arr1*, *eya*, and multiple rhodopsins as predicted target genes (Fig. 5, D and E) (33). The SCENIC predictions for all cell types are available through SCoPe (<https://flycellatlas.org/scope>).

A comparative analysis of genes across broad cell types or tissues (Fig. 5F and fig. S34) identified common genes and specifically expressed genes, such as a shared set of 555 housekeeping genes that are expressed in all tissues. The testis has the highest number of specifically expressed genes consistent with previous reports (34), followed by the Malpighian tubule and male reproductive glands (fig. S34). These tissue-specific genes seemed to be evolutionarily “younger” based on GenTree age compared with the set of commonly expressed genes that are all present in the common ancestor. This suggests that natural selection works on the tissue specialization level, with the strongest selection on testis, male reproductive tract, and Malpighian tubules (35). In addition, this analysis allowed an estimation of transcriptomic similarity or difference measured by the number of shared distinct genes. For example, the two flight appendages, the haltere and wing, share a set of 16 specifically expressed genes, reflecting the evolutionary origin of halteres as a modified wing (36) (fig. S34).

Analysis of sex-biased expression and sex-specialized tissues

To study sex-related differences, we compared male- and female-derived nuclei for all common tissues (fig. S35) and found *roX1/2* and *Yp1/2/3* as the top male- and female-specific genes, respectively. Notably, a large fraction

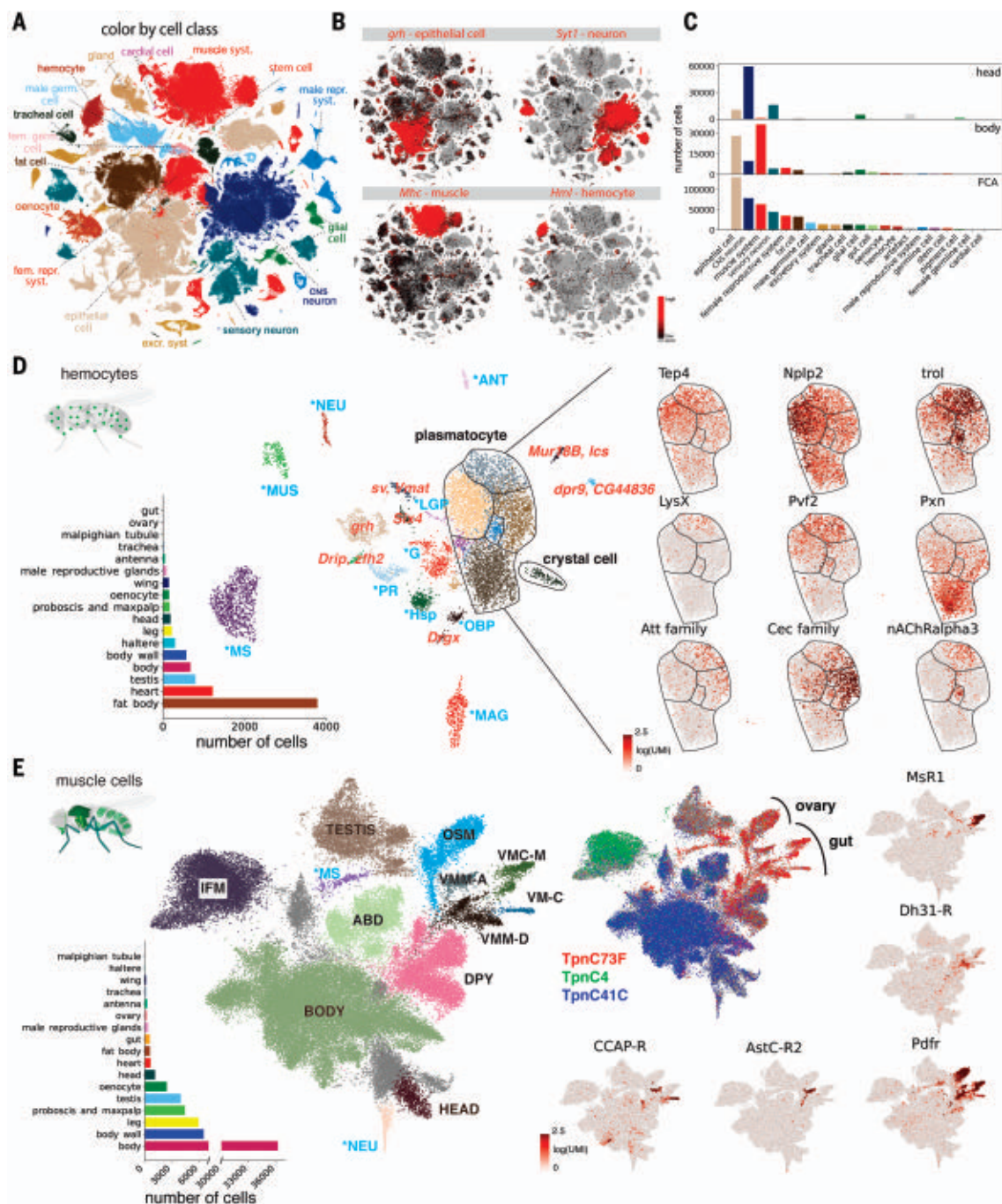
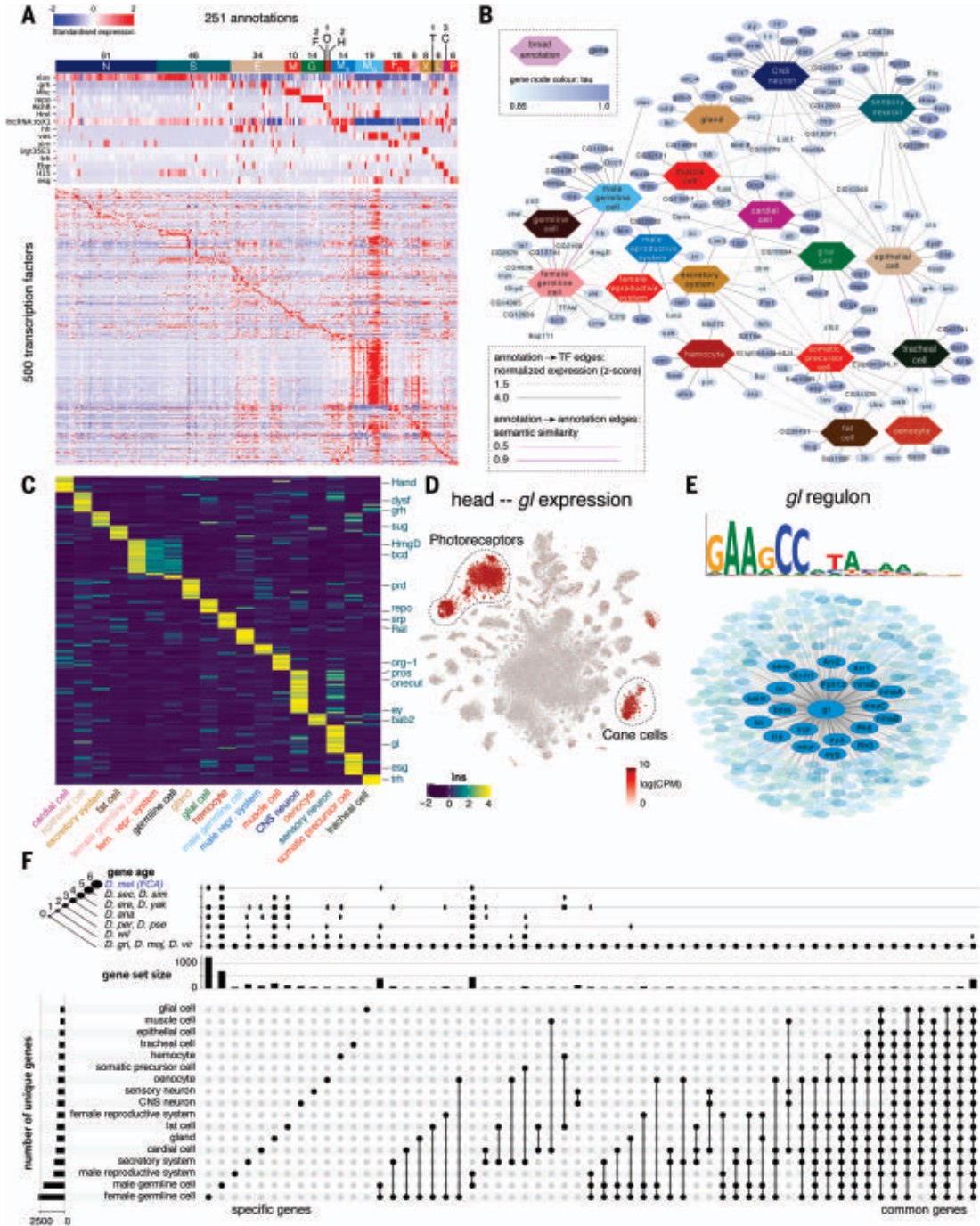


Fig. 4. Cross-tissue analyses of common cell classes. (A) Overview of main cell classes identified throughout the fly cell atlas. Male repr. syst. and fem. repr. syst., male and female reproductive system; male germ. cell and fem. germ. cell, male and female germline cells. (B) tSNE plots showing expression of four markers in four common cell classes. (C) Composition of whole-head and whole-body samples, showing a shift from neurons to epithelial and muscle cells. Composition of the entire FCA shows enrichment for rarer cell classes compared with the whole-body sample. (D) Cross-tissue analysis of hemocytes reveals different cell states of plasmatocytes. Annotations marked in blue are hemocytes containing markers of different cell types, including lymph gland posterior signaling center (LGP), muscle (MUS), antenna (ANT), neurons (NEU), photoreceptor (PR), male accessory glands (MAG), glia (G), male testis and spermatocyte (MS), odorant-binding proteins (OBP), and heat-shock proteins (Hsp). Other abbreviations show top marker gene(s) in

red. Plasmatocytes and crystal cells are indicated. On the right are genes showing compartmentalized expression patterns within the plasmatocyte cluster. (E) Cross-tissue analysis of muscle cells reveals subdivision of the visceral muscle cells based on neuropeptide receptors. Annotations marked in blue are muscle cells containing markers of different cell types, including neuron (NEU) and male testis and spermatocyte (MS). Muscle cells from three body parts are indicated: head muscle (HEAD), body muscle (BODY), and testis muscle (TESTIS). Other annotated muscle types include indirect flight muscle (IFM), ovarian sheath muscle (OSM), abdominal visceral muscle (ABD), *dpy* expressing muscle (DPY), visceral muscle of the midgut *AstC-R2* (VMM-A), visceral muscle of the crop *MsR1* (VMC-M), visceral muscle of the midgut *Dh31-R* (VMM-D), and visceral muscle *CCAP-R* (VM-C). *Pdfr* is expressed in all visceral muscle cells, including the ovarian sheath muscle; the other four receptor genes (*AstC-R2*, *MsR1*, *Dh31-R*, *CCAP-R*) are expressed in different gut visceral muscle types.

Fig. 5. TF pleiotropy versus cell-type specificity.

(A) Heatmap showing the expression of key marker genes and distinctive TF profiles for each of the annotated cell types. TFs were selected based on tau score. Cell types were grouped based on hierarchical terms: CNS neurons (N), sensory organ cells (S), epithelial cells (E), muscle cells (M), glia (G), fat cells (F), oenocytes (O), hemocytes (H), (fe)male reproductive system and germline (MR, MG, FR, FG), excretory system (X), tracheal cell (T), gland (L), cardiac cell (C), and somatic precursor cell (P). (B) A network analysis of TFs and cell classes based on similarity of ontology terms, reveals specific and shared TFs across the individual tissues. (C) Heatmap showing the expression of specific TFs per cell class. Factors from the literature are highlighted. (D) *Glass* is specifically expressed in photoreceptors and cone cells in the head. (E) Overview of the *Glass* regulon of 444 target genes, highlighting known photoreceptor marker genes. (F) Gene expression comparison across broad cell types. Only sets with more than 10 genes are shown. The left bar graph shows the number of uniquely expressed genes for each tissue. The top bar graph shows the gene age in branches, ranging from the common ancestor to *D. melanogaster*-specific genes (<http://gentree.ioz.ac.cn>). See fig. S34 for a tissue-based comparison.



of genes with male-enriched expression were uncharacterized (37). The primary sex-determination pathway in somatic cells leads to sex-specific splicing of *doublesex* (*dsx*) to encode female- or male-specific TFs (38) (Fig. 6A). Consistent with this, we found *dsx* expression in a largely non-sex-specific pattern, whereas many other genes showed sex-biased expression (Fig. 6B). Next, we performed differential expression between sexes for all cell types. Notably, cell types tended to show either high female or male bias, but not both (Fig. 6, B and C). We

found strong female bias in the excretory system, including the principal and stellate cells of the Malpighian tubule and in the pericardial nephrocytes (Fig. 6C). Female-biased genes (i.e., *Ics* and *whe*) were differentially expressed under high-salt conditions, suggesting sex-bias in nephric ion transport. Across cell types, sex-biased expression strongly correlated with *dsx* expression (Fig. 6D) (39), consistent with the role of *Dsx* as a key regulator. Among all tissues in the adult fly, those best characterized that have ongoing cellular dif-

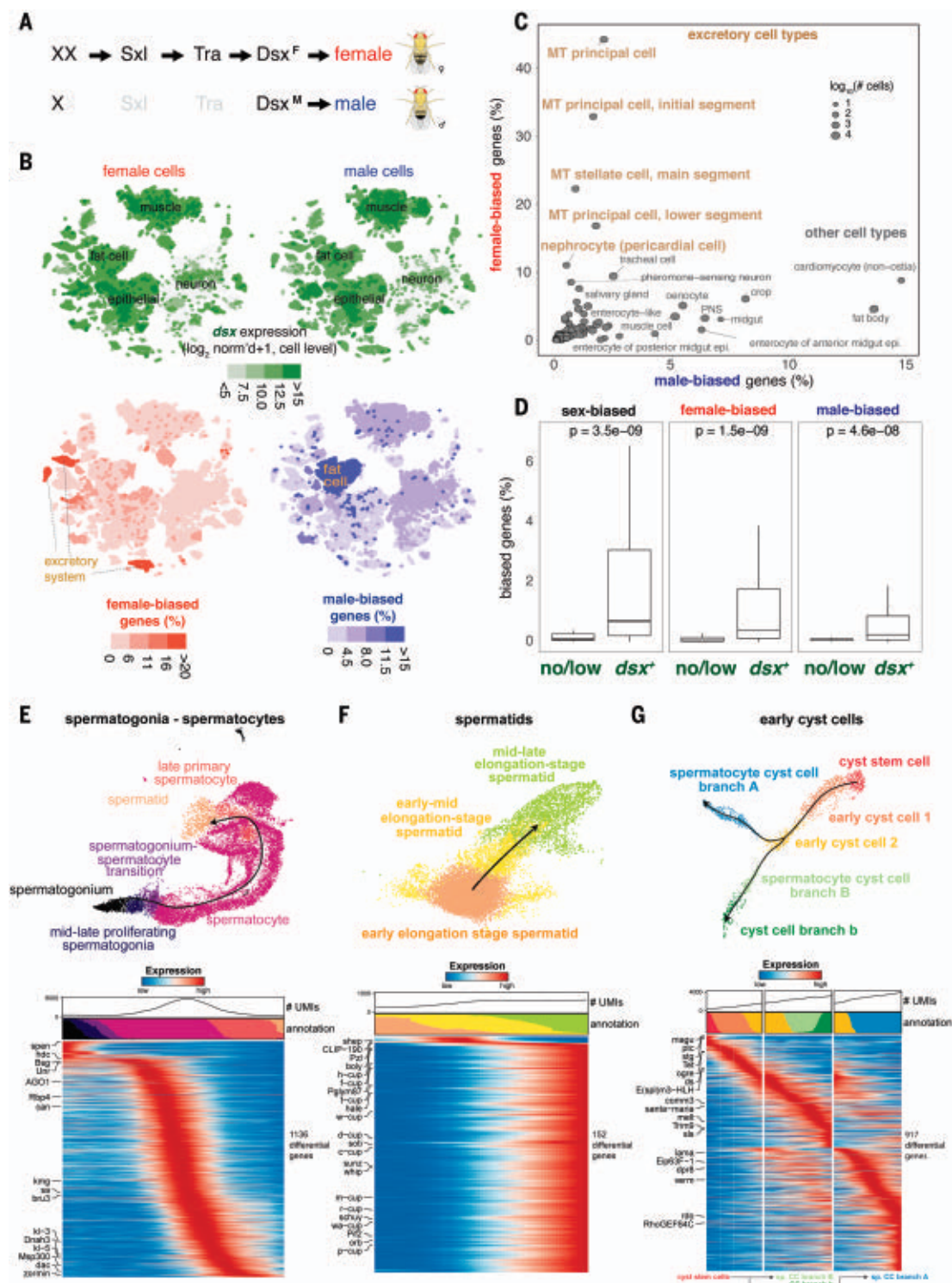
ferentiation are the gut, ovaries, and testis. Trajectory analysis has been performed on the gut and ovary stem cell lineages in previous studies (40–42), and our FCA data on gut and ovary accurately coclustered with these published datasets (figs. S36 and S37). Therefore, we focused on the testis plus seminal vesicle as a case study. The testis has two populations of stem cells, the somatic cyst stem cells (CySCs) that produce cell types with supporting roles essential to spermatogenesis, and the germline stem cells (GSCs) that produce haploid

Fig. 6. Sex-biased expression and trajectory analysis of testis cell lineages. (A) Simplified sex-determination pathway.

Sex-chromosome karyotype (XX) activates Sex-lethal (Sxl), which regulates transformer (Tra), resulting in a female *Dsx*^F isoform (Dsx^F). In XY (or XO) flies, Sxl and Tra are inactive (light gray) and the male-specific *Dsx*^M is produced.

(B) *dsx* expression and female- and male-biased expression projected onto tSNE plots of all female (top left) and male (top right) cells except reproductive tissue cells (tables S4 and S5). Female-biased (bottom left) and male-biased (bottom right) expression measured as the percentage of genes in the cluster showing biased expression in favor of the respective sex (table S6) are also shown. The percentage values were computed for each annotated cluster, and those cluster-level values were projected onto the individual cells in the corresponding clusters. For all four tSNE plots, values outside the scale in the heatmap key are represented by the closest extreme color (> and < signs in the scale).

(C) Scatter plot of female- and male-bias values across non-reproductive cell clusters defined as percentage of sex-biased genes (at least twofold change with false discovery rate <0.05 based on the Wilcoxon test and Benjamini-Hochberg correction) in the cluster (table S6). Data point size indicates cell numbers per cluster (key). Selected clusters are labeled, with those from excretory cells highlighted (brown). MT, Malpighian tubule. (D) Box plots showing the relationship between *dsx* gene expression and sex-biased expression (table S5). Clusters (B) were partitioned into the set of clusters with *dsx* expression (*dsx*⁺) or not (*no/low dsx*) using *dsx* expression in germ cells as an expression cutoff. Each box shows hinges at first and third quartiles and median in the middle. The upper whisker extends from the upper hinge to the largest value no further than 1.5 times the interquartile range (IQR) from the hinge (where the IQR is the distance between the first and third quartiles). The lower whisker extends from the hinge to the smallest value, at most 1.5 times the IQR of the hinge. Outliers are not shown. *p* values are based on the Wilcoxon test. (E to G) Trajectory of testis subsets. We used slingshot to infer a possibly branching trajectory for spermatogonia-spermatocytes (E), spermatids (F), and early cyst cells (G). Shown are the trajectories on a UMAP (top) and the expression patterns of the strongest differentially expressed genes, together with the smoothed proportions of annotated cells and average number of UMIs along the trajectory (bottom).



sperm (Fig. 2C). The main testis analysis (Fig. 2C) revealed transitions from GSCs and proliferating spermatogonia to spermatocytes, then to maturing spermatids, and finally to late elongation stage spermatids.

We further performed trajectory inference on spermatocytes and spermatids separately (Fig. 6, E and F). As expected, the spermatocyte stage featured a continuous increase in the number of genes being transcribed (Fig. 6E), with many of the strongly up-regulated genes (*kmg*, *Rbp4*, *fzo*, *can*, *sa*, and, for later spermatocytes, Y-linked fertility factors *kl-3* and *kl-5*) not substantially expressed in any other cell type. Late spermatocytes, however, showed expression of marker genes from many other cell types like somatic cells (*Upd1*, *eya*), epithelial cells (*grh*), muscle (*Mhc*), or hemocytes (*Hml*) (Fig. 5A), although their expression level was lower than in their marked cell type. Early spermatids are in transcriptional quiescence, as can be seen by a very low number of nuclear transcripts (Fig. 6F; low UMI), followed by a burst of new transcription in elongating spermatids, including many *cup* genes. In the somatic cyst cell lineage, we found CySCs expressing the cell cycle marker *string* that were transitioning into postmitotic (no *string* expression) early cyst cells and branching into two related clusters of cyst cells likely associated with spermatocytes (Fig. 6G).

Discussion

Recent technological developments have enabled single-cell transcriptomic atlases of *Caenorhabditis elegans* (21) and selected tissues in mice and humans (43–46). Here, we provide a single-cell transcriptomic map of the entire adult *D. melanogaster*, a premier model organism for studies of fundamental and evolutionarily conserved biological mechanisms. The FCA provides a resource for the *Drosophila* community as a reference for studies of gene function at single-cell resolution.

A key challenge in large-scale cell atlas projects is the definition of cell types. We addressed this using a consensus-based voting system across multiple resolutions. An FCA cell type is thus defined as a transcriptomic cluster detected at any clustering resolution that could be separated by the expression of known marker genes from other clusters. Further, all annotations were manually curated by tissue experts, leading to a high-confidence dataset with more than 250 annotated cell types. We note differences in annotation depth for different cell groups, with some cell types only linked to broad classes (e.g., epithelial cell), in contrast to other, more detailed cell types (e.g., different olfactory receptor neurons). We also note that although many marker genes are useful in identifying cell types, some marker-gene expression was not congruent with cluster expression. This can be caused by discrepancies

between mRNA and expression or by mistakes that were made in the literature. These examples highlight the need for and the opportunities presented by Tabula *Drosophila* to serve as the basis for future validation.

We have generated lists of marker genes per cell type with different levels of specificity, ranging from the tissue-wide to the animal-wide level. This distinctive level of precision presents a blueprint for future integration with other data modalities such as single-cell assay for transposase-accessible chromatin (ATAC)-seq (47) and spatial omics and for generating cell-type reporter lines to study new cellular functions. Furthermore, the large number of uncharacterized genes that show cell-type specific, sex-biased, or trajectory-dependent expression provides the foundation for many follow-up studies. Our analysis also presents several technical novelties, including the use of reproducible Nextflow pipelines (VSN, <https://github.com/vib-singlecell-nf>), the availability of raw and processed datasets for users to explore, and the development of a crowd-annotation platform with voting, comments, and references through SCoPe (<https://flycellatlas.org/scope>), linked to an online analysis platform in ASAP (<https://asap.epfl.ch/fca>). These elements may inspire future atlas projects. Given the work in other model organisms, we also envision a use for the FCA data in cross-species studies. Furthermore, Tabula *Drosophila* is fully linked to existing *Drosophila* databases by a common vocabulary, benefitting its use and integration in future projects. Finally, all FCA data are freely available for further analysis through multiple portals and can be downloaded for custom analysis using other single-cell tools (fig. S1; links available on www.flycellatlas.org).

Materials and methods summary

For most samples, 5-day-old adult *w¹¹¹⁸* flies were used for both male and female tissues except sex-specific tissues. We estimated the required tissue number based on three factors: total cell number in each tissue, targeted cell number, and recovery rate. Fly tissues were dissected by different dissection labs, flash-frozen using liquid nitrogen, stored at -80°C , and then processed using the same platform. The snRNA-seq was largely adapted from our recently published protocol (17). All libraries were sequenced using Illumina NovaSeq 6000.

Before read alignment, the raw FASTQ files from 10x Genomics were processed with the index-hopping-filter software. A Cell Ranger (version 3.1.0) index was built from a pre-mRNA GTF from the Flybase version r6.31. To ensure reproducibility of the 10x Genomics data processing, all the analyses from raw counts to final processed files were performed using the Nextflow VSN-Pipelines. Two versions of the processed data were generated: Relaxed and Stringent. For most analyses, we

focused on the Stringent dataset, which should be used as a default for new users. Leiden clustering was performed for a wide range of resolutions, and large clusters were subclustered. Crowd annotation by tissue experts was performed across all cluster resolutions in SCoPe, using terms from the FBbt ontology. ASAP was used to perform more specific analyses. Loom and H5AD files are available for download, visualization in SCoPe and cellxgene, and detailed analyses in ASAP.

10x Genomics and Smart-seq2 data were integrated using Harmony. For brain-head data integration, annotations were added using computational approaches, and all annotations were then manually curated in jamborees. For common cell analyses, hemocytes and muscle cells were extracted from different tissues, and harmony was used to remove batch effects. Cell type-specific TFs were identified using the tau factor, and TF regulons were predicted using SCENIC. For the sex-bias analysis, sex-specific cells were removed, and about 270,000 cells from 176 annotated clusters were used to calculate male- and female-bias genes for each cluster. Trajectory analyses of the testes were performed using slingshot. The strongest differentially expressed genes along the trajectories were calculated and shown using heatmaps.

Detailed descriptions of all experimental protocols and analyses are provided in the supplementary materials.

REFERENCES AND NOTES

1. T. H. Morgan, Sex limited inheritance in *Drosophila*. *Science* **32**, 120–122 (1910). doi: [10.1126/science.32.812.120](https://doi.org/10.1126/science.32.812.120); pmid: [17759620](https://pubmed.ncbi.nlm.nih.gov/17759620/)
2. M. D. Adams et al., The genome sequence of *Drosophila melanogaster*. *Science* **287**, 2185–2195 (2000). doi: [10.1126/science.287.5461.2185](https://doi.org/10.1126/science.287.5461.2185); pmid: [10731132](https://pubmed.ncbi.nlm.nih.gov/10731132/)
3. A. Larkin et al., FlyBase: Updates to the *Drosophila melanogaster* knowledge base. *Nucleic Acids Res.* **49**, D899–D907 (2021). doi: [10.1093/nar/gkaa1026](https://doi.org/10.1093/nar/gkaa1026); pmid: [33219682](https://pubmed.ncbi.nlm.nih.gov/33219682/)
4. R. Lyne et al., FlyMine: An integrated database for *Drosophila* and *Anopheles* genomics. *Genome Biol.* **8**, R129 (2007). doi: [10.1186/gb-2007-8-7-r129](https://doi.org/10.1186/gb-2007-8-7-r129); pmid: [17615057](https://pubmed.ncbi.nlm.nih.gov/17615057/)
5. A. Jenett et al., A GAL4-driver line resource for *Drosophila* neurobiology. *Cell Rep.* **2**, 991–1001 (2012). doi: [10.1016/j.celrep.2012.09.011](https://doi.org/10.1016/j.celrep.2012.09.011); pmid: [23063364](https://pubmed.ncbi.nlm.nih.gov/23063364/)
6. N. Milyshev et al., The Virtual Fly Brain browser and query interface. *Bioinformatics* **28**, 411–415 (2012). doi: [10.1093/bioinformatics/btr677](https://doi.org/10.1093/bioinformatics/btr677); pmid: [22180411](https://pubmed.ncbi.nlm.nih.gov/22180411/)
7. M. M. Kudron et al., The ModERN Resource: Genome-wide binding profiles for hundreds of *Drosophila* and *Caenorhabditis elegans* transcription factors. *Genetics* **208**, 937–949 (2018). doi: [10.1534/genetics.117.300657](https://doi.org/10.1534/genetics.117.300657); pmid: [29284660](https://pubmed.ncbi.nlm.nih.gov/29284660/)
8. S. Roy et al., Identification of functional elements and regulatory circuits by *Drosophila* modENCODE. *Science* **330**, 1787–1797 (2010). doi: [10.1126/science.1198374](https://doi.org/10.1126/science.1198374); pmid: [21179774](https://pubmed.ncbi.nlm.nih.gov/21179774/)
9. V. R. Chintapalli, J. Wang, J. A. T. Dow, Using FlyAtlas to identify better *Drosophila melanogaster* models of human disease. *Nat. Genet.* **39**, 715–720 (2007). doi: [10.1038/ng2049](https://doi.org/10.1038/ng2049); pmid: [17534367](https://pubmed.ncbi.nlm.nih.gov/17534367/)
10. H. Li, Single-cell RNA sequencing in *Drosophila*: Technologies and applications. *Wiley Interdiscip. Rev. Dev. Biol.* **10**, e396 (2021). doi: [10.1002/wdev.396](https://doi.org/10.1002/wdev.396); pmid: [32940008](https://pubmed.ncbi.nlm.nih.gov/32940008/)
11. C. N. McLaughlin et al., Single-cell transcriptomes of developing and adult olfactory receptor neurons in *Drosophila*. *eLife* **10**, e63856 (2021). doi: [10.7554/eLife.63856](https://doi.org/10.7554/eLife.63856); pmid: [33555999](https://pubmed.ncbi.nlm.nih.gov/33555999/)
12. G. X. Y. Zheng et al., Massively parallel digital transcriptional profiling of single cells. *Nat. Commun.* **8**, 14049 (2017). doi: [10.1038/ncomms14049](https://doi.org/10.1038/ncomms14049); pmid: [28091601](https://pubmed.ncbi.nlm.nih.gov/28091601/)

13. S. Picelli *et al.*, Smart-seq2 for sensitive full-length transcriptome profiling in single cells. *Nat. Methods* **10**, 1096–1098 (2013). doi: [10.1038/nmeth.2639](https://doi.org/10.1038/nmeth.2639); pmid: 24056875
14. M. De Waegeneer, C. C. Flerin, K. Davie, G. Hulselmans, vib-single-cell-nf/vsn-pipelines: v0.26.0. *Zenodo* (2021); <https://doi.org/10.5281/zenodo.5055627>.
15. S. Yang *et al.*, Decontamination of ambient RNA in single-cell RNA-seq with DecontX. *Genome Biol.* **21**, 57 (2020). doi: [10.1186/s13059-020-1950-6](https://doi.org/10.1186/s13059-020-1950-6); pmid: 32138770
16. I. Korsunsky *et al.*, Fast, sensitive and accurate integration of single-cell data with Harmony. *Nat. Methods* **16**, 1289–1296 (2019). doi: [10.1038/s41592-019-0619-0](https://doi.org/10.1038/s41592-019-0619-0); pmid: 31740819
17. K. Davie *et al.*, A single-cell transcriptome atlas of the aging *Drosophila* brain. *Cell* **174**, 982–998.e20 (2018). doi: [10.1016/j.cell.2018.05.057](https://doi.org/10.1016/j.cell.2018.05.057); pmid: 29909982
18. F. P. A. David, M. Litovchenko, B. Deplancke, V. Gardeux, ASAP 2020 update: An open, scalable and interactive web-based portal for (single-cell) omics analyses. *Nucleic Acids Res.* **48**, W403–W414 (2020). doi: [10.1093/nar/gkaa412](https://doi.org/10.1093/nar/gkaa412); pmid: 32449934
19. M. Costa, S. Reeve, G. Grumblin, D. Osumi-Sutherland, The *Drosophila* anatomy ontology. *J. Biomed. Semantics* **4**, 32 (2013). doi: [10.1186/2041-1480-4-32](https://doi.org/10.1186/2041-1480-4-32); pmid: 24139062
20. S. Levy *et al.*, A stony coral cell atlas illuminates the molecular and cellular basis of coral symbiosis, calcification, and immunity. *Cell* **184**, 2973–2987.e18 (2021). doi: [10.1016/j.cell.2021.04.005](https://doi.org/10.1016/j.cell.2021.04.005); pmid: 33945788
21. J. Cao *et al.*, Comprehensive single-cell transcriptomic profiling of a multicellular organism. *Science* **357**, 661–667 (2017). doi: [10.1126/science.aam8940](https://doi.org/10.1126/science.aam8940); pmid: 28818938
22. M. N. Özel *et al.*, Neuronal diversity and convergence in a visual system developmental atlas. *Nature* **589**, 88–95 (2021). doi: [10.1038/s41586-020-2879-3](https://doi.org/10.1038/s41586-020-2879-3); pmid: 33149298
23. H. Li *et al.*, Classifying *Drosophila* olfactory projection neuron subtypes by single-cell RNA sequencing. *Cell* **171**, 1206–1220.e22 (2017). doi: [10.1016/j.cell.2017.10.019](https://doi.org/10.1016/j.cell.2017.10.019); pmid: 29149607
24. Y. Z. Kurmangaliyev, J. Yoo, J. Valdes-Aleman, P. Sanfilippo, S. L. Zipursky, Transcriptional programs of circuit assembly in the *Drosophila* visual system. *Neuron* **108**, 1045–1057.e6 (2020). doi: [10.1016/j.neuron.2020.10.006](https://doi.org/10.1016/j.neuron.2020.10.006); pmid: 33125872
25. B. Cho *et al.*, Single-cell transcriptome maps of myeloid blood cell lineages in *Drosophila*. *Nat. Commun.* **11**, 4483 (2020). doi: [10.1038/s41467-020-18135-y](https://doi.org/10.1038/s41467-020-18135-y); pmid: 32909993
26. V. A. Pavlov, K. J. Tracey, The cholinergic anti-inflammatory pathway. *Brain Behav. Immun.* **19**, 493–499 (2005). doi: [10.1016/j.bbi.2005.03.015](https://doi.org/10.1016/j.bbi.2005.03.015); pmid: 15922555
27. P. Sanchez Bosch *et al.*, Adult *Drosophila* lack hematopoiesis but rely on a blood cell reservoir at the respiratory epithelia to relay infection signals to surrounding tissues. *Dev. Cell* **51**, 787–803.e5 (2019). doi: [10.1016/j.devcel.2019.10.017](https://doi.org/10.1016/j.devcel.2019.10.017); pmid: 31735669
28. J. Krzemien *et al.*, Control of blood cell homeostasis in *Drosophila* larvae by the posterior signalling centre. *Nature* **446**, 325–328 (2007). doi: [10.1038/nature05650](https://doi.org/10.1038/nature05650); pmid: 17361184
29. L. Mandal, J. A. Martinez-Agosto, C. J. Evans, V. Hartenstein, U. Banerjee, A. Hedgehog- and Antennapedia-dependent niche maintains *Drosophila* haematopoietic precursors. *Nature* **446**, 320–324 (2007). doi: [10.1038/nature05585](https://doi.org/10.1038/nature05585); pmid: 17361183
30. R. J. Svitter *et al.*, Expression and functional characterization of a *Drosophila* neuropeptide precursor with homology to mammalian preprotachykinin A. *J. Biol. Chem.* **275**, 23273–23280 (2000). doi: [10.1074/jbc.M002875200](https://doi.org/10.1074/jbc.M002875200); pmid: 10801863
31. S. Aibar *et al.*, SCENIC: Single-cell regulatory network inference and clustering. *Nat. Methods* **14**, 1083–1086 (2017). doi: [10.1038/nmeth.4463](https://doi.org/10.1038/nmeth.4463); pmid: 28991892
32. J. Mattila, V. Hietakangas, Regulation of carbohydrate energy metabolism in *Drosophila melanogaster*. *Genetics* **207**, 1231–1253 (2017). pmid: 29203701
33. K. Moses, M. C. Ellis, G. M. Rubin, The glass gene encodes a zinc-finger protein required by *Drosophila* photoreceptor cells. *Nature* **340**, 531–536 (1989). doi: [10.1038/340531a0](https://doi.org/10.1038/340531a0); pmid: 2770860
34. H. Kaessmann, Origins, evolution, and phenotypic impact of new genes. *Genome Res.* **20**, 1313–1326 (2010). doi: [10.1101/gr.101386.109](https://doi.org/10.1101/gr.101386.109); pmid: 20651121
35. Y. Shao *et al.*, GenTree, an integrated resource for analyzing the evolution and function of primate-specific coding genes. *Genome Res.* **29**, 682–696 (2019). doi: [10.1101/gr.238733.118](https://doi.org/10.1101/gr.238733.118); pmid: 30862647
36. E. B. Lewis, A gene complex controlling segmentation in *Drosophila*. *Nature* **276**, 565–570 (1978). doi: [10.1038/276565a0](https://doi.org/10.1038/276565a0); pmid: 103000
37. J. Andrews *et al.*, Gene discovery using computational and microarray analysis of transcription in the *Drosophila melanogaster* testis. *Genome Res.* **10**, 2030–2043 (2000). doi: [10.1101/gr.159800](https://doi.org/10.1101/gr.159800); pmid: 11116097
38. H. K. Salz, J. W. Erickson, Sex determination in *Drosophila*: The view from the top. *Fly* **4**, 60–70 (2010). doi: [10.4161/fly.4.1.11277](https://doi.org/10.4161/fly.4.1.11277); pmid: 20160499
39. E. Clough *et al.*, Sex- and tissue-specific functions of *Drosophila* doublesex transcription factor target genes. *Dev. Cell* **31**, 761–773 (2014). doi: [10.1016/j.devcel.2014.11.021](https://doi.org/10.1016/j.devcel.2014.11.021); pmid: 25535918
40. R.-J. Hung *et al.*, A cell atlas of the adult *Drosophila* midgut. *Proc. Natl. Acad. Sci. U.S.A.* **117**, 1514–1523 (2020). doi: [10.1073/pnas.1916820117](https://doi.org/10.1073/pnas.1916820117); pmid: 31915294
41. K. Rust *et al.*, A single-cell atlas and lineage analysis of the adult *Drosophila* ovary. *Nat. Commun.* **11**, 5628 (2020). doi: [10.1038/s41467-020-19361-0](https://doi.org/10.1038/s41467-020-19361-0); pmid: 33159074
42. A. Jevitt *et al.*, A single-cell atlas of adult *Drosophila* ovary identifies transcriptional programs and somatic cell lineage regulating oogenesis. *PLOS Biol.* **18**, e3000538 (2020). doi: [10.1371/journal.pbio.3000538](https://doi.org/10.1371/journal.pbio.3000538); pmid: 32339165
43. Tabula Muris Consortium, Single-cell transcriptomics of 20 mouse organs creates a *Tabula Muris*. *Nature* **562**, 367–372 (2018). doi: [10.1038/s41586-018-0590-4](https://doi.org/10.1038/s41586-018-0590-4); pmid: 30283141
44. X. Han *et al.*, Mapping the mouse cell atlas by microwell-seq. *Cell* **173**, 1307 (2018). doi: [10.1016/j.cell.2018.05.012](https://doi.org/10.1016/j.cell.2018.05.012); pmid: 29775597
45. J. Cao *et al.*, A human cell atlas of fetal gene expression. *Science* **370**, eaba7721 (2020). doi: [10.1126/science.aba7721](https://doi.org/10.1126/science.aba7721); pmid: 33184181
46. X. Han *et al.*, Construction of a human cell landscape at single-cell level. *Nature* **581**, 303–309 (2020). doi: [10.1038/s41586-020-2157-4](https://doi.org/10.1038/s41586-020-2157-4); pmid: 32214235
47. J. Janssens *et al.*, Decoding gene regulation in the fly brain. *Nature* **601**, 630–636 (2022). doi: [10.1038/s41586-021-04262-z](https://doi.org/10.1038/s41586-021-04262-z); pmid: 34987221

ACKNOWLEDGMENTS

We thank the fly community for the enthusiastic support for this project and W. Burkholder, C. Murphy, and K. Vogelaers for coordinating FCA and all Jamboree meetings. **Funding:** The sequencing was supported by the Chan Zuckerberg Biohub (S.R.Q.), Genentech Inc. (H.J.), National Institutes of Health intramural 1ZIAIDK015600 (B.O.), national funds through the FCT in the framework of the financing of the Norma Transitória DL 57/2016 (Z.C.-S.), Wu Tsai Neurosciences Institute at Stanford (S.R.Q. and L.L.) and the Howard Hughes Medical Institute and a National Institutes of Health grant (L.L.). Computational work was supported by the KU Leuven and the Flemish Supercomputer Center (VSC) (S.A.) and EPFL (B.D.). FCA Consortium funding is provided in the supplementary materials. **Author contributions:** All byline authors are members of the FCA Consortium. See FCA Consortium contribution list in the supplementary materials.

Competing interests: H.J., N. S. Katheder, and X. T. Cai are employees of Genentech, Inc. The other authors declare no competing interests. **Data and materials availability:** All data are available for user-friendly querying at <https://flycellatlas.org/scope> and for custom analyses at <https://flycellatlas.org/asap>. For each tissue, a cellgene portal is also available (www.flycellatlas.org). Raw data and count matrices can be downloaded from ArrayExpress (accession number E-MTAB-10519 for 10x, and E-MTAB-10628 for Smart-seq2; the same accession numbers are available at EBI Single Cell Expression Atlas at www.ebi.ac.uk/gxa/sc). Files with expression data, clustering, embeddings, and annotation can be downloaded for each tissue, or all data combined, in h5ad and LoomX formats from www.flycellatlas.org. Three supplementary figures describe how to access and explore FCA data: fig. S1 for summary of data availability and figs. S2 and S3 for how to use Scope and ASAP. We also include a video tutorial for using Scope (www.youtube.com/watch?v=yNETQvASJYM&t=349s). Analysis codes are at GitHub (<https://github.com/flycellatlas>). Dataset access is as follows: GSE107451 (scRNA-seq adult fly brain), GSE120537 (scRNA-seq adult fly gut), and GSE136162, GSE146040, and GSE131971 (scRNA-seq adult ovary). The neural network is from (22) (see appendix 1).

FCA Consortium authors (alphabetically by last name)

Stein Aerts^{4,5}, Devika Agarwal³², Yasir Ahmed-Braimah³³, Aaron M. Allen²³, Michelle Arbeitman³⁴, Majd M. Ariss³⁵, Jordan Augsburger¹³, Kumar Ayush¹², Catherine C. Baker³⁶, Torsten Banisch³⁷, Cameron W. Berry²⁴, Katja Birker³⁸, Rolf Bodmer³⁸, Benjamin Bolival³⁶, Susanna E. Brantley³⁶, Maria Brbic^{42,8}, Julie A. Brill^{39,76}, Nora C. Brown⁴⁰, Katja Brueckner^{13,1}, Norene A. Buehner⁴⁰, Xiaoyu Tracy Cai³¹, Rita Cardoso-Figueiredo²⁰,

Zita Carvalho-Santos²⁰, Fernando Casares⁴¹, Amy Chang⁴², Thomas R. Clandinin⁴³, Sheela Crasta^{6,7,8}, Fabrice P. A. David^{9,10}, Kristofer Davies⁴, Bart Deplancke^{9,10}, Claude Desplan⁴⁴, Angela M. Detweiler⁸, Darshan B. Dhakan²⁰, Stephen DiNardo^{27,28}, Erika Donà⁴⁵, Julian A. T. Dow³⁰, Stefanie Engert⁴², Swann Flöckh^{4,5}, Margaret T. Fuller²⁴, Anthony Galenza²⁹, Vincent Gardeux^{9,10}, Nancy George⁴⁶, Amanda J. González-Segarra⁴², Stephen F. Goodwin²³, Andrew K. Groves^{47,48}, Samantha Gumbin²⁹, Yammeng Guo^{49,50}, Devon E. Harris³⁹, Yael Heifetz⁵¹, Stephen L. Holtz⁵², Felix Horns⁵³, Bruno Hudry⁵⁴, Ruel-Jun Hung¹⁵, Yuh Nung Jan^{49,50}, Jasper Janssens^{4,5}, Heinrich Jasper³¹, Jacob S. Jaszczak^{49,50}, Gregory S. X. E. Jefferis⁴⁵, Robert C. Jones^{5,7,8}, Jim Karkanias⁸, Timothy L. Karr⁵⁵, Nadja Sandra Katheder³¹, James Kezos³⁸, Anna A. Kim^{29,56,57}, Seung K. Kim^{24,58}, Lutz Kockel²⁴, Sai Saroja Kolluru^{6,7,8}, Nikolaos Konstantinides²⁹, Thomas B. Kornberg⁶⁰, Henry M. Krause⁶¹, Andrew Thomas Labott²⁹, Meghan Laturney⁴², Ruth Lehmann^{62,1}, Sarah Leinwand⁴², Jure Leskovec^{12,8}, Hongjie Li^{1,2,3}, Jiefu Li¹, Joshua Shing Shun Li¹⁵, Kai Li^{49,50}, Lijing Li^{49,50}, Tun Li^{49,50}, Maria Litovchenko^{9,10}, Han-Hsuan Liu^{49,50}, Yifang Liu¹⁵, Tzu-Chiao Lu², Liquan Luo¹, Sharvani Mahadevaraju²², Jonathan Manning⁶³, Anjeli Mase¹³, Mikaela Matera-Vatnick⁴⁰, Neza Reis Matias³⁶, Erika L. Matunis²⁶, Caitlin E. McDonough-Goldstein^{64,77}, Aaron McGeevers⁸, Alex D. McLachlan⁶⁵, Colleen N. McLaughlin¹, Paola Moreno-Roman²⁹, Norma Nefz⁶⁶, Megan Neville²³, Sang Ngo²⁹, Tanja Nielsen³⁸, Todd G. Nystul¹⁹, Caitlin E. O'Brien^{49,50}, Lucy Erin O'Brien²⁹, Brian Oliver²², David Osumi-Sutherland⁶⁶, Mehmet Neset Özal⁶⁷, Soumitra Pal²¹, Irene Papatheodorou⁴⁶, Norbert Perrimon^{15,16}, Maja Petkovic^{49,50}, Clare Pilgrim⁶⁸, Angela Oliveira Pisco⁸, Teresa M. Przytycka²¹, Stephen R. Quake^{6,7,8}, Carolina Reissenman⁴⁰, Carlos Ribeiro²⁰, Katja Rust^{13,19}, Wouter Saels^{9,10}, Erin Nicole Sanders²⁹, Gilberto dos Santos⁶⁹, Frank Schnorrer¹⁷, Kristin Scott⁴², Aparna Sherlekar²⁹, Jiwon Shim¹⁴, Phil Shiu⁴², David Sims³², Rene V. Sit⁴, Majia Slaidina^{7,8}, Harold E. Smith⁷¹, Katina Spanier^{4,5}, Gabriella Sterne⁴², Yu-Han Su²⁹, Daniel Sutton⁷², Marco Tamayo³⁸, Michelle Tan⁸, Ibrahim Tastekin²⁰, Sudhir Gopal Tattikotla^{15,16}, Christoph Treiber⁷³, David Vacek¹, Georg Vogler³⁸, Scott Waddell⁷³, Maxime De Waegeneer^{4,5}, Wanpeng Wang⁶⁰, Helen White-Cooper²⁵, Rachel I. Wilson⁵², Mariana F. Wolflner⁴⁰, Yiu-Cheung E. Wong³⁶, Anthony Xie¹, Qijing Xie¹, Jun Xu¹⁵, Shinya Yamamoto^{47,74}, Jia Yan⁸, Zepeng Yao⁴², Kazuki Yoda²⁹, Ruijun Zhu^{49,50}, Robert P. Zinzen⁷⁵.

¹Howard Hughes Medical Institute, Department of Biology, Stanford University, Stanford, CA 94305, USA. ²Huffington Center on Aging, Baylor College of Medicine, Houston, TX 77030, USA.

³Department of Molecular and Human Genetics, Baylor College of Medicine, Houston, TX 77030, USA. ⁴VIB-KU Leuven Center for Brain and Disease Research, KU Leuven, 3000 Leuven, Belgium.

⁵Laboratory of Computational Biology, Department of Human Genetics, KU Leuven, 3000 Leuven, Belgium. ⁶Department of Bioengineering, Stanford University, Stanford, CA, USA. ⁷Department of Applied Physics, Stanford University, Stanford, CA, USA. ⁸Chan Zuckerberg Biohub, San Francisco CA, USA. ⁹Laboratory of Systems Biology and Genetics, Institute of Bioengineering, School of Life Sciences, Ecole Polytechnique Fédérale de Lausanne (EPFL), CH-1015 Lausanne, Switzerland. ¹⁰Swiss Institute of Bioinformatics, CH-1015 Lausanne, Switzerland. ¹¹Bioinformatics Competence Center, EPFL, Switzerland. ¹²Department of Computer Science, Stanford University, Stanford, CA 94305, USA. ¹³Department of Cell and Tissue Biology, University of California, San Francisco, CA 94143, USA. ¹⁴Department of Life Science, College of Natural Science, Hanyang University, 04763 Seoul, Republic of Korea. ¹⁵Department of Genetics, Blavatnik Institute, Harvard Medical School, Boston, MA 02115, USA. ¹⁶Howard Hughes Medical Institute, Harvard Medical School, Boston, MA, USA. ¹⁷Aix-Marseille University, CNRS, IBDM (UMR 7288), Turing Centre for Living Systems, 13009 Marseille, France.

¹⁸Institute of Physiology and Pathophysiology, Department of Molecular Cell Physiology, Philipps-University, Marburg, Germany. ¹⁹Department of Anatomy, University of California, San Francisco, CA 94143, USA. ²⁰Behavior and Metabolism Laboratory, Champalimaud Research, Champalimaud Centre for the Unknown, Lisbon, Portugal. ²¹National Center of Biotechnology Information, National Library of Medicine, National Institutes of Health, Bethesda, MD 20894, USA. ²²Laboratory of Cellular and Developmental Biology, National Institute of Diabetes and Kidney and Digestive Diseases, National Institutes of Health, Bethesda, MD 20892, USA. ²³Centre for Neural Circuits and Behaviour, University of Oxford, Oxford OX1 3SR, UK. ²⁴Department of Developmental Biology and Genetics, Stanford University School of Medicine, Stanford, CA 94305, USA. ²⁵Molecular Biosciences Division, Cardiff University, Cardiff CF10 3AX, UK. ²⁶Department of Cell Biology, Johns Hopkins University School of Medicine, Baltimore, MD 21205, USA. ²⁷Perelman School of Medicine, The University of

Pennsylvania, Philadelphia, PA 19104, USA. ²⁸The Penn Institute for Regenerative Medicine, Philadelphia, PA 19104, USA. ²⁹Department of Molecular and Cellular Physiology, Stanford University School of Medicine, Stanford, CA 94305, USA. ³⁰Institute of Molecular, Cell and Systems Biology, College of Medical, Veterinary and Life Sciences, University of Glasgow, Glasgow G12 8QQ, UK. ³¹Immunology Discovery, Genentech, Inc., South San Francisco, CA 94080, USA. ³²MRC Weatherall Institute of Molecular Medicine, University of Oxford, John Radcliffe Hospital, Headington, Oxford OX3 9DS, UK. ³³Department of Biology, Syracuse University, Syracuse, NY 13244 USA. ³⁴Biomedical Sciences Department, Florida State University, Tallahassee, FL, USA. ³⁵Department of Genetics, Harvard Medical School, Boston, MA, USA. ³⁶Department of Developmental Biology, Stanford University School of Medicine, Stanford, CA 94305, USA. ³⁷Skirball Institute and HHMI, New York University Langone Medical Center, New York City, NY 10016, USA. ³⁸Development, Aging and Regeneration Program, Sanford Burnham Prebys Medical Discovery Institute, La Jolla, CA 92037, USA. ³⁹Cell Biology Program, The Hospital for Sick Children (SickKids), Toronto, ON M5G 0A4, Canada. ⁴⁰Department of Molecular Biology and Genetics, Cornell University, Ithaca, NY 14853, USA. ⁴¹CABD (Andalusian Centre for Developmental Biology), CSIC-UPO-JA. Seville 41013, Spain. ⁴²Department of Molecular and Cell Biology, University of California, Berkeley, Berkeley, CA 94720, USA. ⁴³Department of Neurobiology, Stanford University, Stanford, CA 94305, USA. ⁴⁴Department of Biology, New York University, New York, New York 10003, USA. ⁴⁵Neurobiology Division, MRC Laboratory of Molecular Biology, Cambridge CB2 0QH, UK. ⁴⁶European Molecular Biology Laboratory, European Bioinformatics Institute, EMBL-EBI, Wellcome Trust Genome Campus, Hinxton CB10 1SD, UK. ⁴⁷Department of Molecular and Human Genetics, Baylor College of Medicine, Houston, TX 77030, USA. ⁴⁸Department of Neuroscience, Baylor College of Medicine, Houston, TX 77030, USA. ⁴⁹Department of Physiology, Department

of Biochemistry and Biophysics, University of California at San Francisco, San Francisco, CA, USA. ⁵⁰Howard Hughes Medical Institute, San Francisco, CA, USA. ⁵¹The Hebrew University of Jerusalem, Jerusalem, Israel. ⁵²Department of Neurobiology, Harvard Medical School, Boston, MA 02115, USA. ⁵³Department of Bioengineering and Biophysics Graduate Program, Stanford University, Stanford, CA 94305, USA. ⁵⁴Université Côte d'Azur, CNRS, INSERM, iBV, France. ⁵⁵Biodesign Institute, Arizona State University, Tempe, AZ 85281, USA. ⁵⁶University of California, Santa Barbara, CA 93106, USA. ⁵⁷Uppsala University, Sweden. ⁵⁸Department of Medicine, Stanford University School of Medicine, Stanford, CA 94305, USA. ⁵⁹Institut Jacques Monod, Centre National de la Recherche Scientifique-UMR 7592, Université Paris Diderot, Paris, France. ⁶⁰Cardiovascular Research Institute, University of California, San Francisco, CA 94143, USA. ⁶¹Donnelly Centre for Cellular and Biomolecular Research, Department of Molecular Genetics, University of Toronto, Toronto, ON M5S 3E1, Canada. ⁶²Skirball Institute, Department of Cell Biology and HHMI, New York University Langone Medical Center, New York City, NY 10016. ⁶³European Molecular Biology Laboratory, European Bioinformatics Institute, EMBL-EBI, Wellcome Trust Genome Campus, Hinxton CB10 1SD, UK. ⁶⁴Department of Biology, Syracuse University, Syracuse, NY, USA. ⁶⁵Department of Physiology, Development and Neuroscience, University of Cambridge, Downing Street, Cambridge CB2 3DY, UK. ⁶⁶European Bioinformatics Institute (EMBL/EBI), Wellcome Trust Genome Campus, Cambridge, UK. ⁶⁷Department of Biology, New York University, New York, NY 10003, USA. ⁶⁸Department of Physiology, Development and Neuroscience, University of Cambridge, Cambridge CB2 3DY, UK. ⁶⁹The Biological Laboratories, Harvard University, 16 Divinity Avenue, Cambridge, MA 02138, USA. ⁷⁰Skirball Institute, Faculty of Medicine, New York University, New York, NY 10016. ⁷¹Genomics Core, National Institute of Diabetes and Digestive and Kidney Diseases, US National Institutes of Health, Bethesda, MD, USA.

⁷²Graduate Program in Genetics and Genomics, Department of Molecular and Human Genetics, Baylor College of Medicine, Houston, TX 77030 USA. ⁷³Centre for Neural Circuits and Behaviour, University of Oxford, Tinsley Building, Mansfield Road, Oxford OX1 3TA, UK. ⁷⁴Jan and Dan Duncan Neurological Research Institute, Texas Children's Hospital, Houston, TX 77030, USA. ⁷⁵Laboratory for Systems Biology of Neural Tissue Differentiation, Berlin Institute for Medical Systems Biology (BIMSB), Max Delbrueck Centre for Molecular Medicine (MDC) in the Helmholtz Association, Robert-Roessle-Strasse 12, 13125 Berlin, Germany. ⁷⁶Department of Molecular Genetics, University of Toronto, Toronto, ON M5S 1A8, Canada. ⁷⁷Department of Evolutionary Biology, University of Vienna, Vienna, Austria.

†Deceased.

‡Present address: Whitehead Institute and Department of Biology, MIT, Boston, MA, USA.

§Present address: University of Bergen, Faculty of Medicine, Bergen, Norway.

SUPPLEMENTARY MATERIALS

science.org/doi/10.1126/science.abk2432

FCA Consortium Contributions

Materials and Methods

FCA Consortium Funding

Figs. S1 to S37

Tables S1 to S6

References (48–58)

MDAR Reproducibility Checklist

5 July 2021; accepted 19 January 2022
10.1126/science.abk2432

RESEARCH ARTICLE SUMMARY

NEUROGENOMICS

A single-cell atlas of the normal and malformed human brain vasculature

Ethan A. Winkler[†], Chang N. Kim[†], Jayden M. Ross, Joseph H. Garcia, Eugene Gil, Irene Oh, Lindsay Q. Chen, David Wu, Joshua S. Catapano, Kunal Raygor, Kazim Narsinh, Helen Kim, Shantel Weinsheimer, Daniel L. Cooke, Brian P. Walcott, Michael T. Lawton, Nalin Gupta, Berislav V. Zlokovic, Edward F. Chang, Adib A. Abila*, Daniel A. Lim*, Tomasz J. Nowakowski*

INTRODUCTION: The cerebrovasculature delivers nourishment and regulates blood-brain molecular exchanges that are necessary for neurologic function. Coordinated communications between multiple cell types—including endothelium, pericytes, smooth muscle cells, and perivascular fibroblasts—provides the basis for the functional specialization of arteries, capillaries, and veins. Cellular dysfunction results in cerebrovascular diseases, a leading cause of death and disability. However, we currently lack a comprehensive atlas of cerebrovascular cells in the human brain. Further understanding of disease mechanisms and therapeutic strategies requires a deeper knowledge of cerebrovascular cells in humans.

RATIONALE: To provide a human cerebrovascular cell atlas, we used single-cell mRNA sequencing (scRNA-seq), using dissociated vascular cells isolated from the adult human brain and arteriovenous malformations (AVMs), a cerebrovascular disease of arteriovenous patterning in which patients are prone to bleeding and stroke. Using marker genes identified from single-cell transcriptomes, we characterized

spatial distributions of cerebrovascular cell states with multiplexed fluorescent in situ hybridization and immunostaining. Joint comparative analyses between scRNA-seq datasets systematically profiled patterns of aberrant gene expression in AVMs. To investigate potential relevance of these findings, we performed in silico analyses to catalog dysregulated cell-to-cell interactions and to resolve cell states enriched in advanced stages of AVMs that bled. Predictions were validated with immunostaining and functional assays in cell culture.

RESULTS: By performing scRNA-seq on 181,388 individual cells, we identified more than 40 transcriptomically defined cell states of vascular, immune, and neighboring glial or neuronal cells from the human adult cerebrovasculature and AVMs. Iterative analyses of single-cell gene expression profiles revealed endothelial molecular signatures underlying arteriovenous phenotypic changes called zonations. Our study uncovered an expanded diversity of perivascular cells in human but not mouse brain, including a molecular marker of pericytes, transcriptional variation within smooth muscle

cells and perivascular fibroblasts, and the presence of smooth muscle-like cells known as fibromyocytes. In AVMs, our data suggested a loss of normal zonation among endothelial cells. Moreover, we observed the emergence of a distinct transcriptomic state that corresponded to the nidus, which was characterized by heightened angiogenic potential and immune cell cross-talk. In addition, we characterized the cellular ontology of the cerebrovasculature-derived immune cell response and identified infiltration of distinct immune cell states, such as *GPNMB*⁺ monocytes, which contribute to depletion of stabilizing smooth muscle cells in AVMs that bled.

CONCLUSION: Our single-cell atlas highlights the transcriptomic heterogeneity underlying cell function and interaction in the human cerebrovasculature and defines molecular and cellular perturbations in AVMs, a leading cause of stroke in young people. The identified interplay between vascular and immune cells may aid the development of therapeutics that target angiogenic and inflammatory programs in vascular malformations. More broadly, this cell atlas should inform future studies in other human diseases to accelerate mechanistic understanding and therapeutic targeting of the human cerebrovasculature and its diseases. ■

The list of author affiliations is available in the full article online.

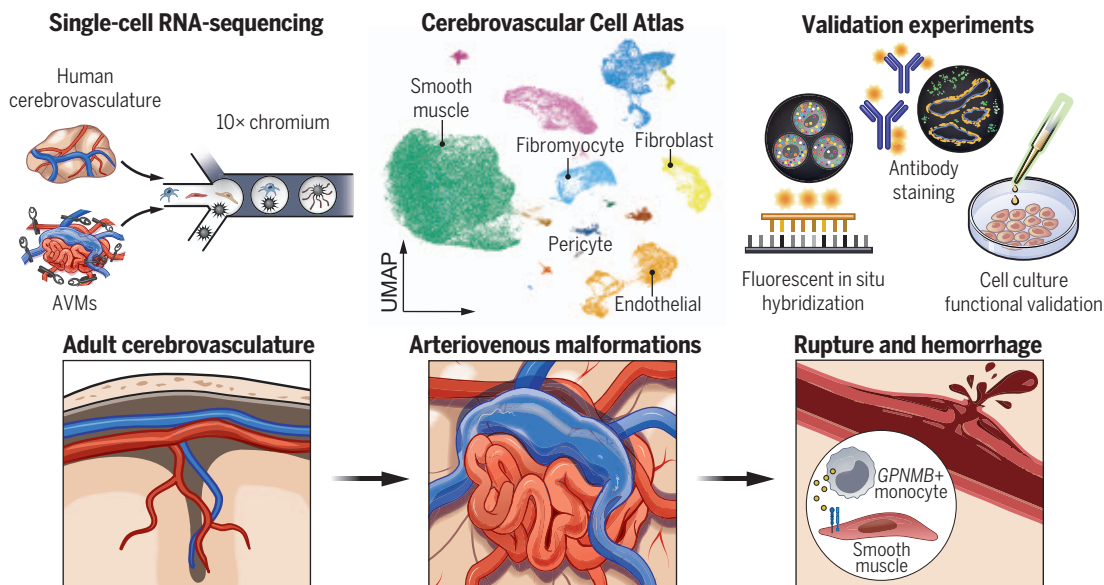
*Corresponding author. Email: adib.abila@ucsf.edu (A.A.A.); daniel.lim@ucsf.edu (D.A.L.); tomasz.j.nowakowski@gmail.com (T.J.N.)

[†]These authors contributed equally to this work.

Cite this article as E. A. Winkler et al., *Science* 375, eabi7377 (2022). DOI: 10.1126/science.abi7377

S READ THE FULL ARTICLE AT
<https://doi.org/10.1126/science.abi7377>

The adult human cerebrovascular cell atlas. We used scRNA-seq to assemble a cerebrovascular cell atlas from the adult human brain and AVMs. Findings were then experimentally validated. Comparative analyses revealed endothelial molecular transformations and heightened immune cell response in AVMs. Using this cell atlas, we identified immune cell states implicated in AVM rupture and brain hemorrhage.



RESEARCH ARTICLE

NEUROGENOMICS

A single-cell atlas of the normal and malformed human brain vasculature

Ethan A. Winkler^{1,2,3,4,†}, Chang N. Kim^{2,3,5,6,†}, Jayden M. Ross^{1,2,3,5,6}, Joseph H. Garcia¹, Eugene Gil^{1,2}, Irene Oh⁷, Lindsay Q. Chen⁷, David Wu^{1,2}, Joshua S. Catapano⁴, Kunal Raygor¹, Kazim Narsinh⁸, Helen Kim⁹, Shantel Weinsheimer⁹, Daniel L. Cooke^{3,8}, Brian P. Walcott¹⁰, Michael T. Lawton⁴, Nalin Gupta¹, Berislav V. Zlokovic^{11,12}, Edward F. Chang^{1,3}, Adib A. Abila^{1,3,*}, Daniel A. Lim^{1,2,3,13,*}, Tomasz J. Nowakowski^{1,2,3,5,6,14,*}

Cerebrovascular diseases are a leading cause of death and neurologic disability. Further understanding of disease mechanisms and therapeutic strategies requires a deeper knowledge of cerebrovascular cells in humans. We profiled transcriptomes of 181,388 cells to define a cell atlas of the adult human cerebrovasculature, including endothelial cell molecular signatures with arteriovenous segmentation and expanded perivascular cell diversity. By leveraging this reference, we investigated cellular and molecular perturbations in brain arteriovenous malformations, which are a leading cause of stroke in young people, and identified pathologic endothelial transformations with abnormal vascular patterning and the ontology of vascularly derived inflammation. We illustrate the interplay between vascular and immune cells that contributes to brain hemorrhage and catalog opportunities for targeting angiogenic and inflammatory programs in vascular malformations.

The cerebrovasculature comprises an uninterrupted, arborized network of vascular conduits through which circulating blood flows (1–3). It is tasked with ensuring delivery of oxygen, energy metabolites, and other nutrients to the brain while removing by-products of brain metabolism or preventing entry of circulating toxins (1, 3). Interruptions in cerebral blood flow or structural compromise and hemorrhage lead to stroke, which is a leading cause of death and disability worldwide (4, 5).

Like other vascular beds, the cerebrovasculature has functionally distinct, contiguous

segments identified as arteries, arterioles, capillaries, venules, and veins hierarchically organized along an “arteriovenous axis” (1, 6, 7). Cell composition varies with these transitions, and each cerebral vessel is composed of endothelial cells, pericytes, smooth muscle cells (SMCs), and/or perivascular fibroblast-like cells (referred to hereafter as perivascular fibroblasts) (1, 7, 8). Coordinated molecular interactions between vascular cells and surrounding neurons, glia, and perivascular immune cells endow the cerebrovasculature with medically relevant, specialized properties. The blood-brain barrier in capillaries, for example, provides a basis for brain immune privilege and serves as an obstacle to pharmacologic treatment of brain diseases (3, 6, 9–11).

Single-cell mRNA-sequencing (scRNA-seq) in mice has suggested additional cell variation and provided a molecular basis for arteriovenous phenotypic changes known as “zonations” (7, 12–14). Because of biases in cell isolation, existing human brain cell atlas studies have overlooked the cerebrovasculature, and its cellular heterogeneity has been largely unexplored in humans (15, 16). Neurologic diseases, such as stroke or Alzheimer’s disease, or brain aging show a predilection for select arteriovenous segments (12, 17–19). Thus, large-scale single-cell profiling of the human cerebrovasculature should provide a translational reference to better understand molecular underpinnings of selective cell vulnerabilities and patterns of aberrant gene expression in human cerebrovascular disease.

Cellular and molecular profiles of the adult human cerebrovasculature

To profile cells of the cerebrovasculature, we obtained normal cerebral cortex tissue from patients undergoing tailored lobectomies for epilepsy (table S1). Large arteries and veins were microdissected, and smaller vessels (arterioles, capillaries, and venules) were isolated by use of established methods (Fig. 1A and fig. S1A) (20–22). We processed for scRNA-seq dissociated cells from five individuals using the 10X Genomics Chromium platform and generated high-quality transcriptomes from 74,535 cells (fig. S1, B to E). We performed graph-based Leiden clustering, and clusters were annotated with differentially expressed genes to identify 15 major cell populations, each with a distinct set of enriched genes and present in multiple individuals (Fig. 1, B to D; fig. S1, F and G; and table S2).

On the basis of previously described gene expression patterns, we identified the major vascular cell classes: endothelial cells (*CLDN5*), pericytes (*KCNJ8*), SMCs (*MYH11*), and perivascular fibroblasts (*DCN*) (Fig. 1, B and C, and table S2) (7, 23, 24). Using our scRNA-seq analysis to inform probe design, we spatially resolved vascular cell diversity in the adult human cerebral cortex with multiplexed spatial transcriptomics (Fig. 2, A to D, and fig. S2, A to F). Consistent with known variations of the human cerebrovasculature, the spatial distribution of cerebrovascular cells revealed reduced vascular cell densities in the white matter (fig. S2A) (25). Cerebrovascular cell classes were organized in known vascular cytoarchitectural structures such as arteries, capillaries, and veins (Fig. 2D). Thus, we define cell classes across the major subdivisions of the cerebrovasculature by intersecting multiplexed spatial transcriptomics with cell-specific markers defined from scRNA-seq.

Endothelial diversity and arteriovenous zonation in humans

Endothelial cells compose the inner, blood-facing lining of the cerebrovasculature (1, 3). Identified by expression of *CLDN5* and *PECAMI*, endothelial cells composed six clusters (Fig. 1, E and F). Using a previously annotated cell atlas of mouse endothelial cells (13), we found that gene expression signatures corresponding to four arteriovenous segments—arteries, capillaries, venules, and veins—consistently mapped onto distinct clusters in our dataset (Fig. 1, F and G; fig. S3, A to H; and table S3). We also identified three clusters of endothelial cells within the arterial zonation (Fig. 1, E and F, and fig. S3D), including a cluster enriched for *TXNIP*, a regulator of glucose metabolism and oxidative stress (26), likely representing a metabolic state of arterial endothelial cells. By visualizing the spatial position of endothelial arteriovenous zonation

¹Department of Neurological Surgery, University of California, San Francisco, CA, USA. ²Eli and Edythe Broad Center for Regeneration Medicine and Stem Cell Research, University of California, San Francisco, CA, USA. ³Weill Institute for Neurosciences, University of California, San Francisco, CA, USA. ⁴Department of Neurosurgery, Barrow Neurological Institute, Phoenix, AZ, USA. ⁵Department of Anatomy, University of California, San Francisco, CA, USA. ⁶Department of Psychiatry and Behavioral Sciences, University of California, San Francisco, CA, USA. ⁷Rebus Biosystems, Santa Clara, CA, USA. ⁸Department of Radiology and Biomedical Imaging, University of California, San Francisco, CA, USA. ⁹Center for Cerebrovascular Research, Department of Anesthesia and Perioperative Care, University of California, San Francisco, CA, USA. ¹⁰Department of Neurosurgery, NorthShore University HealthSystem, Evanston, IL, USA. ¹¹Department of Physiology and Neuroscience, Keck School of Medicine, University of Southern California, Los Angeles, CA, USA. ¹²Zilkha Neurogenetic Institute, Keck School of Medicine, University of Southern California, Los Angeles, CA, USA. ¹³San Francisco Veterans Affairs Medical Center, San Francisco, CA, USA. ¹⁴Chan Zuckerberg Biohub, San Francisco, CA, USA.

*Corresponding author. Email: adib.abila@ucsf.edu (A.A.A.); daniel.lim@ucsf.edu (D.A.L.); tomasz.j.nowakowski@gmail.com (T.J.N.)

†These authors contributed equally to this work.

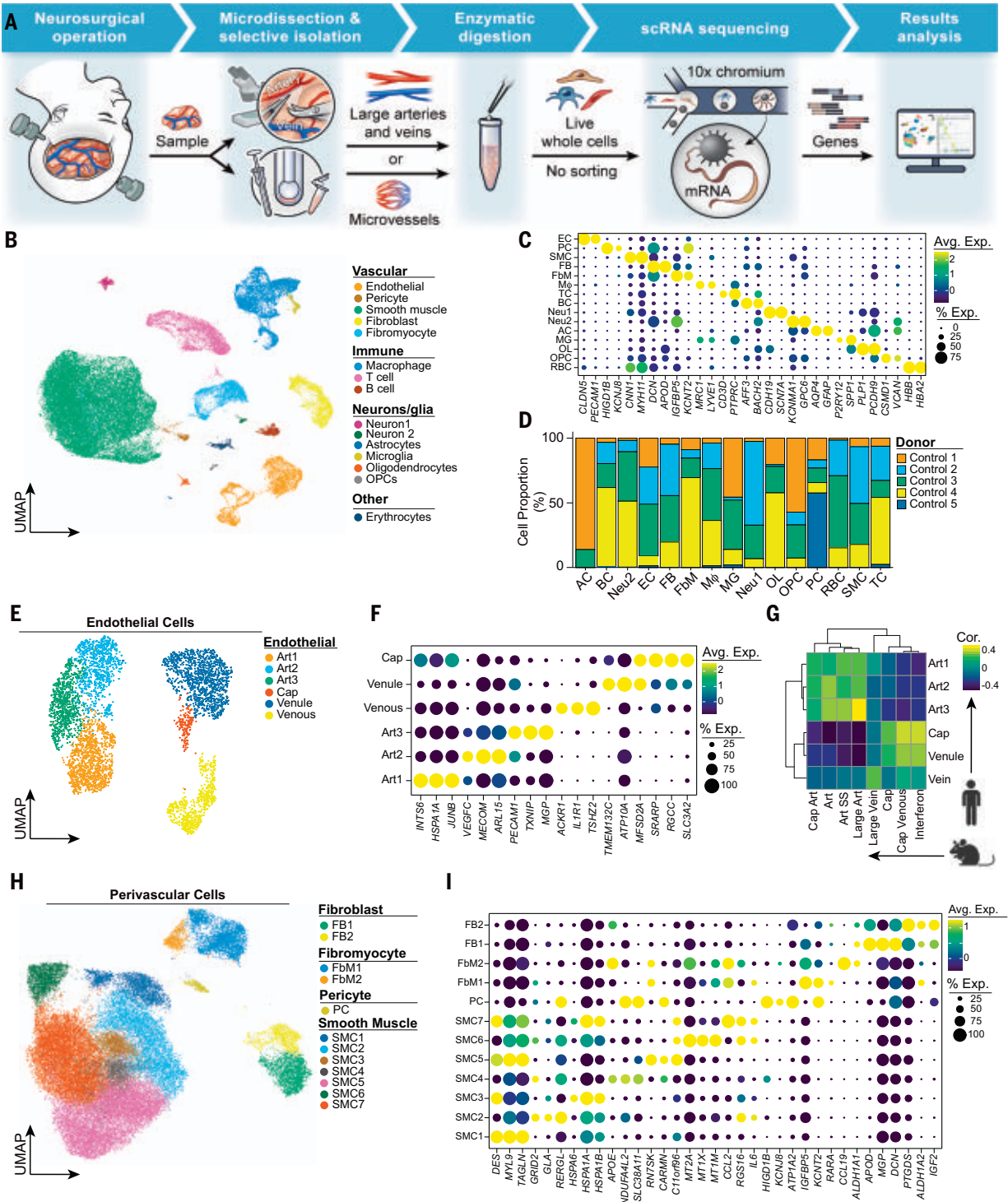


Fig. 1. Cells of the human cerebrovasculature. (A) Isolation and cell sampling from human cerebral cortex. scRNA, single cell mRNA. (B) UMAP visualization showing cell states from control adult cerebrovasculature ($n = 5$ donors). (C) Dot plot showing expression of cell state markers. EC, endothelial cell; PC, pericyte; SMC, smooth muscle cell; FB, perivascular fibroblast; FbM, fibromyocyte; Mφ, macrophage; TC, T cell; BC, B cell; Neu, neuron; AC, astrocyte; MG, microglia; OL, oligodendrocyte; OPC, oligodendrocyte precursor cell; and RBC, erythrocyte. (D) Bar graph showing cell state proportion by donor. Number of cells sequenced by donor: control 1, 6033 cells; control 2, 25,730 cells; control 3, 22,816 cells;

control 4, 19,302 cells; and control 5, 654 cells. (E) UMAP visualization of endothelial cell states. Art, arterial; Cap, capillary. (F) Dot plot showing expression of endothelial cell state markers. (G) Correlation matrix of gene expression profiles between mouse and human cerebrovascular endothelial cell states. Mouse data obtained from a previously published database (13). Art, arterial; Cap, capillary; SS, shear stress. (H) UMAP visualization of perivascular cell states. FB, perivascular fibroblast; FbM, fibromyocyte; PC, pericyte; and SMC, smooth muscle cell. (I) Dot plot showing expression of perivascular cell state markers.

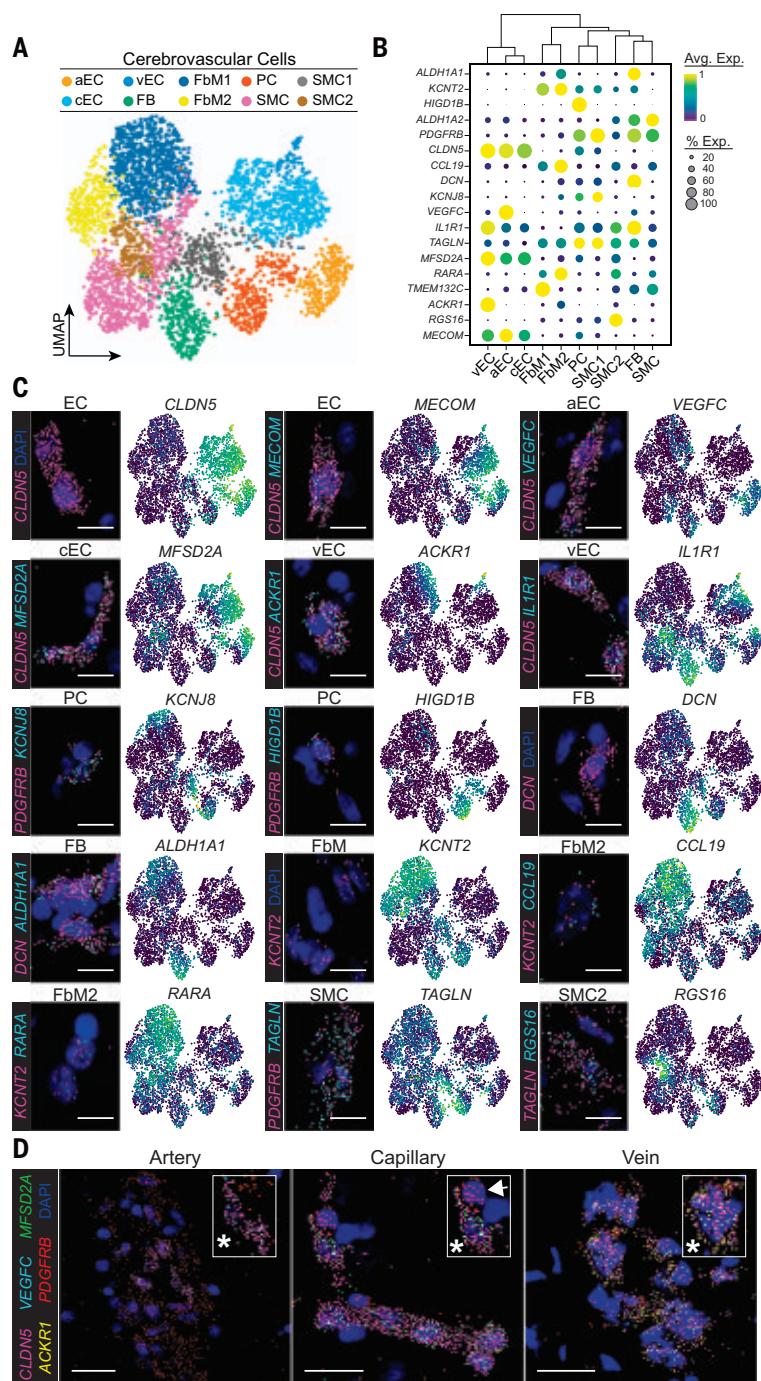


Fig. 2. Spatial RNA analysis resolves the cells of the human cerebrovasculature. (A) UMAP visualization of spatially defined cerebrovascular cell gene expression profiles identified by means of multiplexed, iterative single-molecule fluorescent in situ hybridization (smFISH). RNA molecules were quantified and assigned to cells through automated spot detection and nuclei segmentation. aEC, arterial endothelial cell; cEC, capillary endothelial cell; vEC, venous endothelial cell; FbM, fibromyocyte; PC, pericyte; and SMC, smooth muscle cell. (B) Dot plot showing expression of cell state markers. (C) Representative high-magnification microscopy images of merged smFISH and expression distribution of cell state markers projected on UMAP embeddings from (A). DAPI (blue) stains are cell nuclei. Scale bar, 10 μ m. (D) Representative merged smFISH images showing cellular expression of *CLDN5* (magenta, endothelial cells), *VEGFC* (cyan, arterial endothelial cells), *MFSD2A* (green, capillary endothelial cells), *ACKR1* (yellow, venous endothelial cells), and *PDGFRB* (red, mural cells). DAPI (blue) stains are cell nuclei. (Left) Artery. Asterisk indicates endothelial cell coexpressing *CLDN5* (magenta) and *VEGFC* (cyan). Scale bar, 20 μ m. (Middle) Capillary. Asterisk indicates endothelial cell coexpressing *CLDN5* (magenta) and *MFSD2A* (green); arrow indicates *PDGFRB*-expressing pericyte (red). Scale bar, 15 μ m. (Right) Vein. Asterisk indicates endothelial cell coexpressing *CLDN5* (magenta) and *ACKR1* (yellow). Scale bar, 15 μ m.

markers and relationships with surrounding vascular cells, we confirmed *VEGFC*⁺, *MFSD2A*⁺, and *ACKR1*⁺ endothelium in arteries, capillaries, and veins, respectively (Fig. 2D) (7, 12, 13). Thus, our human vascular cell dataset captures the conserved distinctions of endothelial arteriovenous zonations in humans.

Diversity and distinction of brain perivascular cells

In addition to endothelial cells, we identified the major perivascular cell classes in the brain: pericytes, SMCs, and perivascular fibroblasts (Fig. 1, H and I; fig. S4, A to C; and table S2) (1, 7, 8). Our data serve as a reference for transcriptomic-based perivascular cell definitions on the basis of correlated patterns of gene expression variation (cell identity scores), as opposed to a handful of marker genes with partially overlapping patterns of expression (fig. S4, D to F) (8, 27, 28).

Pericytes are found in capillaries, venules, and some arterioles and induce and maintain the blood-brain barrier (20, 29, 30). Although previously identified pericyte markers, such as *ABCC9* and *KCNJ8*, together captured all putative pericyte clusters (Fig. 2, H and I; fig. S4G; and table S3) (7, 28), variations in their expression limited use of any single gene as a pan-pericyte marker. We therefore sought to nominate an alternative marker to capture a larger proportion of transcriptomically defined pericytes. Specifically, we identified that *HIGD1B* mRNA is highly enriched in pericytes and detected in 91.7% of pericytes (91.7% of cells, $\log_2FC = 3.10$, $P_{adj} < 0.01$) (Fig. 1I, fig. S4G, and table S2). We confirmed *HIGD1B* expression in *PDGFRB*⁺ or *KCNJ8*⁺ pericytes (Fig. 2, B and C).

SMCs are contractile cells in arteries, veins, and most arterioles (7, 31, 32). We selected these cells on the basis of expression of pan-SMC markers *CNN1*, *TAGLN*, and *MYH11* (Fig. 1, C and I, and fig. S3A). Iterative analysis of SMC transcriptional variation suggested that additional axes of variation may exist (Fig. 1, H and I, and table S3). For example, one cluster was enriched for metallothioneins *MTIX*, *MT2A*, *MT1M*, *MT1E*, and *MT1A*, which modulate SMC proliferation and migration (Fig. 1I and fig. S5A) (33). Additional transcriptional variation included the perivascular cell chemokine ligand *CCL2*, which coordinates brain response to systemic infection (Fig. 1I and fig. S5A) (34), and *RGS16*, which regulates sphingosine-1-phosphate signaling implicated in SMC proliferation (Figs. 1I and 2, B and C) (35). Thus, SMCs may represent a spectrum of transcriptional states, and future studies will be necessary to identify their functional roles.

Fibroblasts loosely adhere to arteries, arterioles, venules, and veins within the perivascular space, express extracellular matrix proteins, and provide structural support (7, 23, 36). We

identified two clusters of *DCN*⁺ and *APOD*⁺ perivascular fibroblasts (Fig. 1, H and I). None of the perivascular fibroblasts expressed markers of other brain fibroblasts—such as those in the meninges, which were surgically excluded in this study (37)—and *DCN*⁺ perivascular fibroblasts were visually confirmed to be associated with the cerebrovasculature (fig. S5B). Thus, our data confirm the presence of perivascular fibroblasts in the adult human brain.

Fibromyocytes in the human cerebrovasculature

Two cell clusters were not explained by known brain perivascular cell identities (Fig. 1, H and I, and fig. S4, D to F). We annotated these clusters as “fibromyocytes” on the basis of lower expression of contractile proteins (*TAGLN* and *ACTA2*) and higher expression of fibroblast (*DCN* and *LUM*) and macrophage (*LGALS3*) genes as described in peripheral arteries, such as the aorta and cervical internal carotid artery (38–40). No expression of the smooth muscle transcription factor *MYOCD* was detected, which suggests that fibromyocytes are distinct from SMCs (fig. S5C) (41). Differential gene expression identified *IGFBP5*, *KCNT2*, and *CCL19* to be more specific to fibromyocytes (fig. S5C and table S2), and we validated *KCNT2*⁺ and *CCL19*⁺ fibromyocytes in the human cerebral cortex (Fig. 2, A to C). Not identified in prior mouse cell atlases (7, 23, 24), our results demonstrate the presence of fibromyocytes in the human cerebrovasculature.

Fibromyocytes are thought to arise from SMCs in peripheral vascular beds (42). We therefore performed RNA velocity analysis, which infers transcriptomic trajectories according to the relative abundance of exonic and intronic reads (43). On the basis of inferred relationships of informatically predicted splicing dynamics, this analysis predicted that SMCs enriched for *CARMN*, a long noncoding RNA (lncRNA) associated with mesodermal differentiation (44), may give rise to fibromyocytes through the up-regulation of marker genes, such as *LGALS3*, *KCNT2*, and *IGFBP5* (fig. S5, D and E). However, in the absence of direct evidence of lineage tracing, we cannot conclusively demonstrate that such a relationship exists.

Retinoic acid signaling regulates smooth-muscle-to-fibromyocyte transitions in the periphery (39). However, prior human brain cell atlases have not documented nonmeningeal sources of retinoic acid (fig. S5F). Investigation of retinoic acid synthetic enzyme and receptor gene expression identified enrichment in brain fibromyocyte clusters and perivascular fibroblasts (Fig. 1I and fig. S5, G and H). We spatially confirmed *ALDH1A1* and *RARA* expression in *DCN*⁺ perivascular fibroblasts and *CCL19*⁺ fibromyocytes, respectively (Fig. 2, B and C). Thus, fibromyocytes and perivascular fibro-

blasts may be endogenous sources of retinoic acid in the adult human brain.

Deconstructing the dysplastic cerebrovasculature in arteriovenous malformations

To showcase the utility of our dataset, we generated a scRNA-seq dataset from arteriovenous malformation (AVM) samples (45). We obtained intraoperative, angiographically confirmed human brain AVMs from five patients (table S1). Using analogous dissection and scRNA-seq techniques (Fig. 3A), we generated high-quality whole-cell transcriptomes from 106,853 cells and identified 11 major cell populations (Fig. 3, B and C, and fig. S6, A to D). Each cell population was identified in multiple specimens, except for astrocytes and choroid plexus (Fig. 3C and fig. S6E). We spatially confirmed *CLDN5*⁺ endothelial cells, *TAGLN*⁺ SMCs, *CCL19*⁺ fibromyocytes, and *COL1A2*⁺ perivascular fibroblasts in AVMs (Fig. 3D). To identify endothelial and perivascular cell molecular changes in AVMs, we coembedded control and AVM scRNA-seq datasets (Fig. 3E and fig. S7A), identified differentially expressed genes (Fig. 3F; fig. S7, D to H; and table S4), and performed iterative clustering in each vascular cell class (Fig. 3E; figs. S8, A to E, and S9, A to C; and table S5). Thus, we define cell composition and cell-specific patterns of aberrant gene expression within AVMs.

Endothelial aberrancy in brain AVMs

AVMs arise from pathologic molecular changes in endothelial cells (46, 47). This catalyzes direct connections to form between arteries and veins without intervening capillaries and results in tortuous, dysmorphic tangles of blood vessels referred to as the “nidus” (45). Joint analysis of control and AVM datasets revealed that endothelial subsets were enriched for arterial and venous but not venular or capillary transcriptional identity scores in AVMs (Fig. 3, E and G, and fig. S9, D to G). Endothelial cell clusters with suppressed venule and capillary cell identities [nidus 1 (Nd1) and nidus 2 (Nd2)] showed greatest differential gene expression (Fig. 3H and table S6). RNA velocity analysis identified a consensus molecular trajectory from Nd1 to Nd2 (Fig. 3I and fig. S9H) and predicted a progressive up-regulation of *PLVAP*, a marker of fenestrated endothelium normally confined to developmental angiogenesis, the brain’s circumventricular organs and choroid plexus, and *PGF*, a potent stimulator of brain angiogenesis (Fig. 3I) (13, 30, 48, 49). Gene set enrichment analysis (GSEA) confirmed pathogenic cascades, such as angiogenesis, inflammation, and epithelial-to-mesenchymal transition, enriched in AVM Nd2 endothelium (Fig. 3J and table S7) (50–52). Control capillary endothelial cells robustly expressed blood-brain barrier nutrient trans-

porters, including *MFSD2A*, *SLC16A1*, and *SLC38A5* (Fig. 3K). By contrast, AVM Nd2 endothelial suppressed nutrient transporter expression and up-regulated pro-inflammatory (*CCL14*), pro-angiogenic (*PGF* and *STC1*), and pro-permeability (*PLVAP* and *ANGPT2*) genes (Fig. 3, K and L). Additionally, we confirmed the localization of Nd2 endothelial cells in the AVM nidus (Fig. 3M).

To characterize how pathologic endothelial gene expression may influence cell-to-cell communication networks, we used an in silico algorithm to predict reciprocal ligand-receptor interactions (53). The assembled interactome identified Nd2 as the strongest contributor to abnormal cell communications in AVMs (fig. S10A). Dysregulated communication pathways included established pathogenic cascades, such as angiopoietin, vascular endothelial growth factor, and transforming growth factor- β (TGF- β) signaling (54–56) as well as previously unrecognized immune activating and angiogenic communication networks in AVMs, such as *CD99*, *SPPI1*, and *CALCR* (fig. S10, B to F). Thus, aberrant nidus endothelial gene expression is predicted to result in pathologic cell-to-cell communication networks within AVMs.

Immune cell microenvironment and cerebrovascular-derived inflammation

Inflammation is hypothesized to play a role in the formation of AVMs (45, 52). Iterative analysis of the immune cell populations associated with the cerebrovasculature identified 17 immune cell clusters in coembedded cell populations (Fig. 4, A and B, and fig. S11, A and B). Nine clusters comprised myeloid cells, including vessel-associated microglia, conventional dendritic cells (cDCs), three perivascular macrophage (pvM ϕ) subpopulations, and three monocyte (Mo) subpopulations. In addition, we computationally separated myeloid cells with evidence of ex vivo activation (ExV) (Fig. 4, A and B, and fig. S11C) (57). Eight clusters comprised lymphoid cells, including CD4⁺ T cells, two CD8⁺ T cell subpopulations, regulatory T cells (T_{reg} cells), B cells, natural killer (NK) cells, plasmacytoid dendritic cells (pDCs), and a population of dividing lymphocytes (Div) composed of T_{reg} cells (Fig. 4, A and B). Resident pvM ϕ s were the most abundant immune cell population, composing 31.2% and 28.3% of immune cells in controls and AVMs, respectively (Fig. 4C). Greater than 90% of circulating immune cells, such as CD8⁺ T cells, were confined within the resting cerebrovasculature but infiltrated into the perivascular space or adjacent brain in AVMs ($P < 0.01$) (fig. S11, D and E).

Myeloid immune cells were more abundant and expressed gene signatures suggestive of activation in AVMs (Fig. 4, D to G, and fig. S11F), and we cataloged dysregulated immune cell communication networks

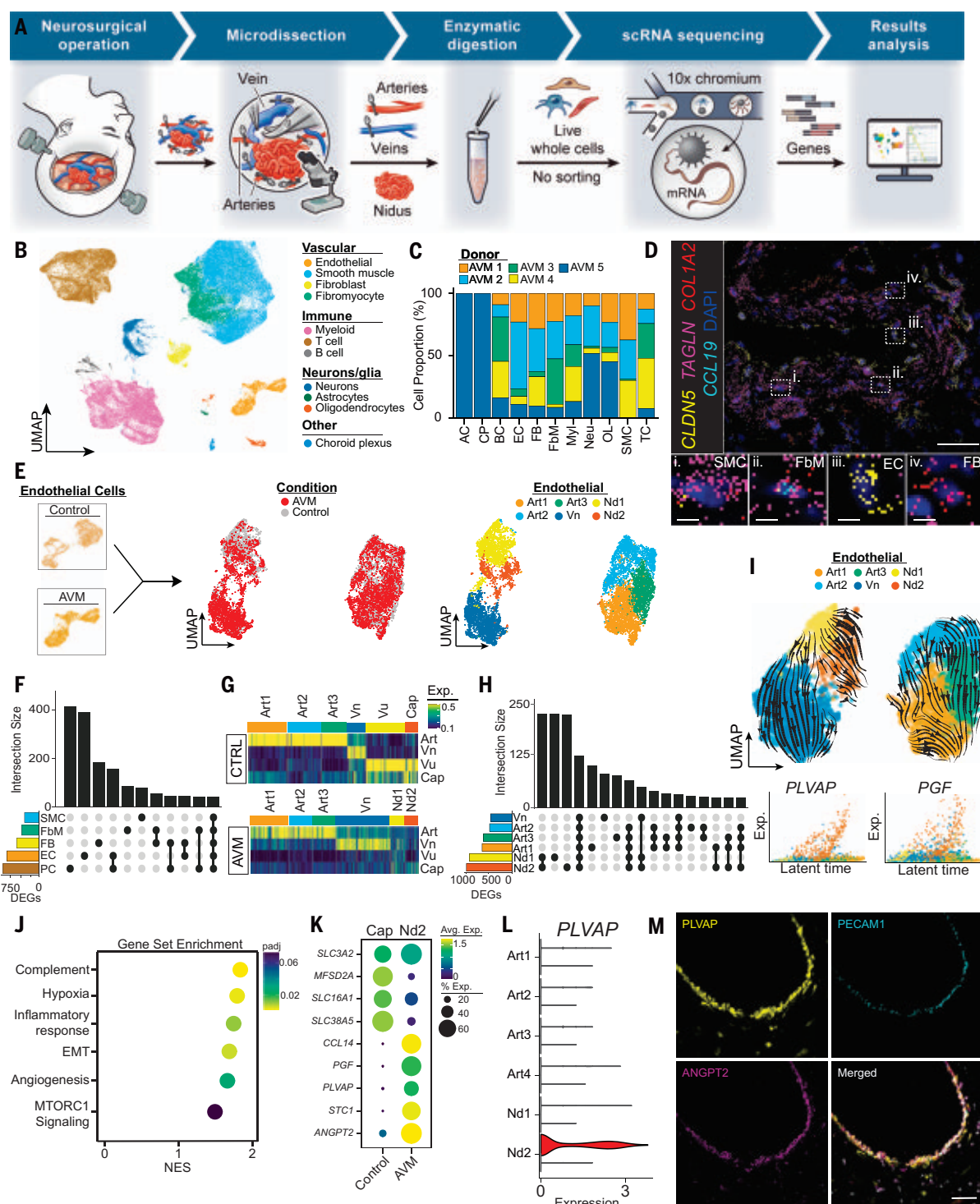


Fig. 3. Cellular aberrancy in the malformed cerebrovasculature. (A) Isolation and cell sampling from human brain AVMs. scRNA, single-cell mRNA. (B) UMAP visualization showing cell states from AVMs ($n = 5$ donors). (C) Bar graph showing cell state proportion by donor. Number of cells sequenced by donor are AVM1, 26,122 cells; AVM2, 28,868 cells; AVM3, 14,541 cells; AVM4, 26,660 cells; and AVM5, 10,662 cells. EC, endothelial cell; SMC, smooth muscle cell; FB, perivascular fibroblast; FbM, fibromyocyte; Myl, myeloid cells; TC, T cell; BC, B cell; Neu, neuron; AC, astrocyte; MG, microglia; OL, oligodendrocyte; and CP, choroid plexus. (D) Representative microscopy image of single-molecule fluorescent in situ hybridization showing expression of *CLDN5* [yellow, endothelial cells (EC)], *TAGLN*

[magenta, smooth muscle cells (SMC)], *COL1A2* [red, perivascular fibroblasts (FB)], and *CCL19* [cyan, fibromyocytes (FbM)]. DAPI (blue) stains are cell nuclei. Boxes highlight representative cells. Scale bar, 50 μm . (i) *TAGLN*⁺ smooth muscle cell. (ii) *CCL19*⁺ and *TAGLN*⁺ fibromyocyte. (iii) *CLDN5*⁺ endothelial cell. (iv) *COL1A2*⁺ perivascular fibroblast. Scale bars, insets, 5 μm . (E) (Left) Schematic describing computational pipeline. Endothelial cells (orange) are identified in silico by marker expression, coembedded for downstream analytics, and iteratively clustered. An identical workflow was applied to perivascular cells (fig. S7). (Middle) UMAP visualization of coembedded endothelial cell states in control (gray) and AVMs (red). (Right) UMAP visualization of iteratively clustered endothelial cell

states. Art, arterial; Cap, capillary; Vn, venous; and Nd, nidus. **(F)** Upset plot of DEGs (horizontal bars) by cell class. Number of DEGs exclusive to one cell class (black circles) or shared between multiple cell classes (linked black circles). Vertical bars show the number of genes per intersection. **(G)** Heatmap visualization of arteriovenous transcriptional identity in control (top, CTRL) and AVM (bottom) endothelial cell states. Art, arterial; Cap, capillary; Vu, venule; Vn, venous; Nd, nidus. Exp., expression; blue, low expression; and yellow, high expression. **(H)** Upset plot showing intersections of DEGs in AVM endothelial cell states compared with controls. **(I)** UMAP visualization of AVM endothelial cell RNA velocity reveals two divergent trajectories from Nd1

(yellow). Up-regulation of *PLVAP* and *PGF* occurs with endothelial Nd1-to-Nd2 transitions. Exp., expression. **(J)** Gene set enrichment analysis of DEGs in AVM endothelial Nd2. P_{adj} , false discovery rate adjusted P value; NES, normalized enrichment score. **(K)** Dot plot showing top marker gene expression for control capillary and AVM Nd2 endothelial cells. Avg. Exp., average expression; Exp., expression **(L)** Violin plot of *PLVAP* expression showing specificity to AVM Nd2. **(M)** Representative confocal microscopy analysis of *PLVAP* (yellow) and *ANGPT2* (magenta) expression in PECAM1⁺ endothelial cells (cyan) in AVM nidus. Vessel shown in cross section. Colocalization of fluorescence results in white coloration. Scale bar, 50 μ m.

(fig. S11G). Vessel-associated CD11c⁺ antigen-presenting cells are potent activators of brain CD4⁺ T cell responses in situ (58, 59). scRNA-seq confirmed that vessel-associated CD11c⁺ cells were composed of myeloid cells, including cDCs, pM ϕ s, and some microglia, and we identified a heterogeneous spatial distribution of vessel-associated antigen-presenting myeloid cells in the AVM nidus (Fig. 4F). Discrete areas appeared to have a greater number of IBA1⁺P2RY12[−] macrophages or IBA1⁺P2RY12⁺ microglia, for example (Fig. 4, F and G). A pronounced perivascular myeloid cell response was observed, and IBA1⁺P2RY12[−] macrophages were found at greater distances from the adjacent vasculature consistent with infiltration in AVMs ($P < 0.01$) (Fig. 4G). Thus, there are diverse cellular and spatially heterogeneous cerebrovascular inflammatory responses within AVMs.

Vascular immune cell cross-talk with brain hemorrhage

Hemorrhagic stroke is a devastating consequence of AVMs (60). We therefore sought to identify deleterious cell states associated with AVM rupture. We used scMappR to deconvolute cellular heterogeneity and to compute cell-specific gene expression signatures from AVM bulk RNA-seq ($n = 39$ AVMs; ruptured, 26 AVMs; unruptured, 13 AVMs) (Fig. 5A and table S1) (61). We first identified 871 differentially expressed genes (DEGs) associated with AVM rupture enriched in vascular developmental pathways (such as blood vessel development and morphogenesis) and inflammatory processes (such as cell recruitment) (fig. S12, A and B, and table S8). Using our scRNA-seq dataset, in silico cell abundance deconvolution resolved probable alterations in cell proportions (Fig. 5B). A subpopulation of *AIF1*⁺ (encodes IBA1)—*P2RY12*[−] monocytes, identified as *GPNMB*⁺ Mo3 monocytes—was over-represented in ruptured AVMs ($P < 0.01$) and expressed gene signatures consistent with activation (Fig. 5, B to D, and fig. S12, C and D). Thus, distinct infiltrating immune cell states become enriched with AVM rupture.

Inflammation leads to a loss of vessel integrity, and SMCs contribute to brain hemorrhage when depleted (52, 62–64). In silico abundance of *GPNMB*⁺ monocytes and SMCs correlated

negatively in ruptured AVMs [correlation coefficient (r) = -0.43 , $P < 0.05$]. We therefore investigated whether *GPNMB*⁺ monocytes contribute to SMC death. Coculture of isolated *GPNMB*⁺ monocytes from ruptured AVM patients with primary brain vascular SMCs (VSMCs) increased apoptotic cleaved caspase-3⁺ VSMCs ($P < 0.01$) (Fig. 5E). Cell-to-cell communication analysis identified *SPPI* [which encodes osteopontin (OPN)] as the greatest dysregulated outgoing signaling pathway from *GPNMB*⁺ monocytes in AVMs (Fig. 5F). The ligand OPN is predicted and previously shown to interact with CD44 and integrin receptors on SMCs (65). Soluble OPN induced a 2.7-fold increase in VSMC apoptosis, which was ameliorated by pretreatment with neutralizing CD44 antibody, an integrin inhibitor, or a combination of both ($P < 0.01$) (Fig. 5G). Thus, *GPNMB*⁺ monocytes contribute to SMC depletion and are associated with AVM rupture and brain hemorrhage.

Discussion

We present a cell-resolution atlas that describes the transcriptomic heterogeneity underlying cell function and interaction in the human adult cerebrovasculature. We identified conservation of endothelial molecular zonations essential to arteriovenous phenotypic change and expanded cellular diversity of brain perivascular cells, including fibromyocytes not previously identified in the cerebrovasculature (7, 23, 24). SMCs are predicted to transform into fibromyocytes, but this will require validation with fate-tracing methods. Fibromyocytes and perivascular fibroblasts may produce retinoic acid in the adult human brain. Retinoic acid signaling contributes to cortical vascular development and modulates smooth muscle plasticity and fibromyocyte speciation in other vascular beds (39, 66, 67). However, the functional relevance of these findings in the adult cerebrovasculature warrants further investigation.

This atlas has many implications for neuroscience and clinical medicine. To exemplify its utility, we defined cellular and gene expression changes in AVMs, a leading cause of stroke in young people, and identified pathologic endothelial molecular transformations, spatially localized to the AVM nidus. Some

molecular changes are shared with immature embryonic endothelium or angiogenic tip cells, but other developmental or angiogenic transcriptional programs are notably absent or altered (14, 30, 68, 69). We also describe the cellular ontology and communication networks of cerebrovascular-derived inflammation. The interplay between vascular and immune cells, such as *GPNMB*⁺ monocytes and SMCs, induced pathological changes associated with brain hemorrhage. Consequently, our findings may guide the development of future therapies.

We recognize that this atlas represents only a first step toward a comprehensive census of the human cerebrovasculature. Limitations in unintended biases of cell capture or isolation and random sampling, such as relative proportions of small and large vessels from each individual, may alter relative cell proportions and require further validation in spatially resolved datasets. Additional work will also be needed to ascertain distinctions between cell types and cell states, such as transient or metabolic variations. Nonetheless, our results should inform future studies in other brain regions or cerebrovascular diseases to accelerate mechanistic understanding and therapeutic targeting of the human cerebrovasculature.

Materials and methods

Ethics statement and tissue acquisition

Human brain tissue specimens and clinical data were obtained from the University of California San Francisco with protocols approved from the institutional review board and ethics committee (IRB 10-01318 and 10-02012). All tissues were acquired from patients undergoing neurosurgical operations and written informed consent was obtained prior to the procedure permitting collection of tissue specimens for the purposes of research. Normal cerebral cortex was obtained as part of a neurosurgical operation to reach deep seated lesions causing epilepsy and uninvolved in the pathology. All specimens were >2 cm from any radiographic abnormality on magnetic resonance imaging, showed no abnormalities on routine electrocorticography, and were histologically normal on a rapid hematoxylin and eosin stain. Diagnosis of human brain AVMs

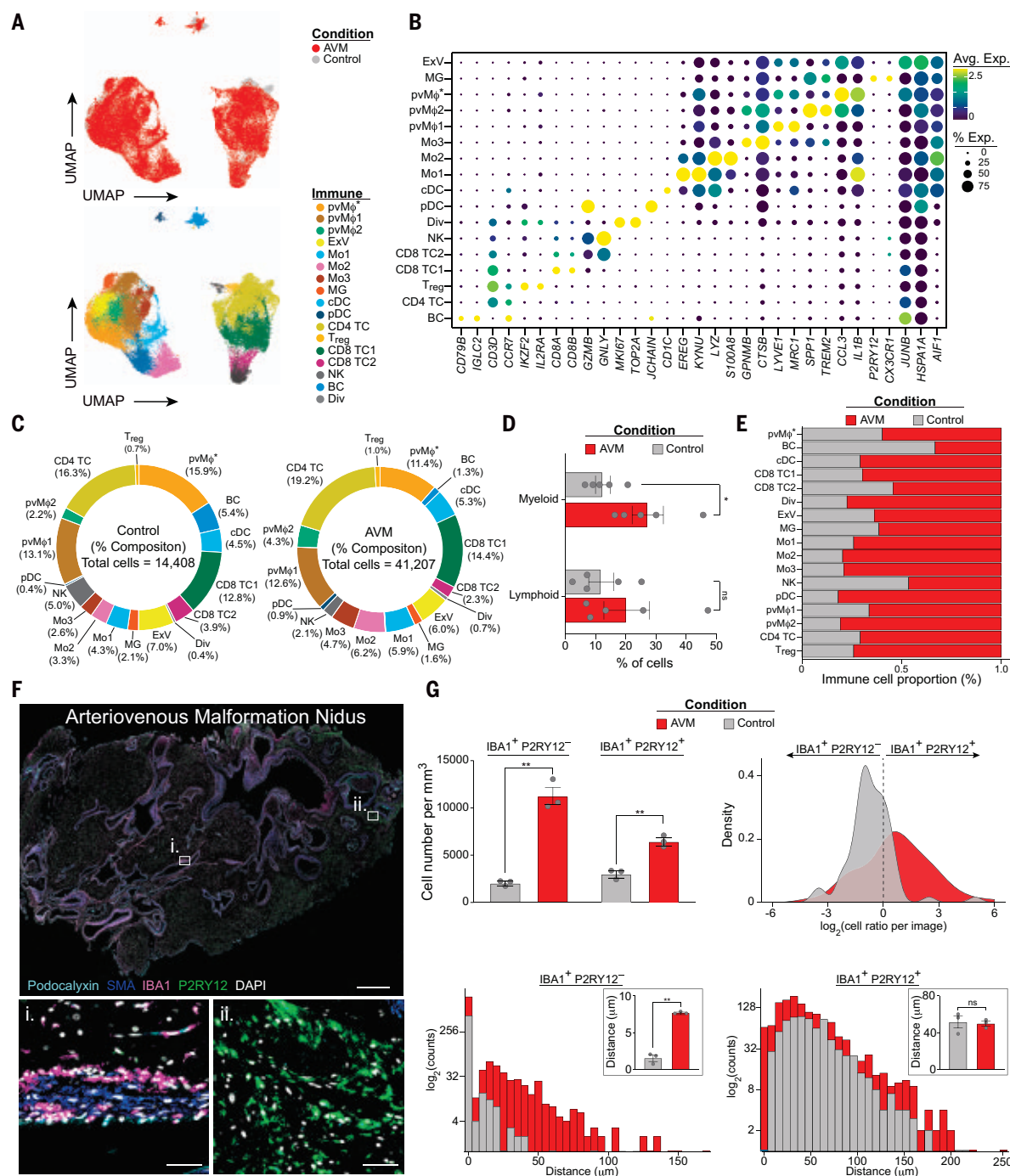


Fig. 4. Cerebrovascular inflammation with malformation. (A) UMAP visualizations of coembedded immune cells states in control cerebrovasculature and brain AVMs ($n = 5$ donors per condition). (Top) Colored by condition. Control, gray; AVM, red. (Bottom) Colored by cell state. pvMφ perivascular macrophage; pvMφ*, activated perivascular macrophage; Mo, monocyte; MG, microglia; ExV, ex vivo activated myeloid cells; cDC, conventional dendritic cells; pDC, plasmacytoid dendritic cells; CD8 TC, CD8⁺ T cells; CD4 TC, CD4⁺ T cells; T_{reg}, regulatory T cells; NK, natural killer cells; BC, B cells; and Div, dividing immune cells. (B) Dot plot showing expression of immune cell markers. (C) Pie charts showing immune cell state proportions in (left) controls and (right) AVMs. (D) Bar graph with individual data points showing the proportion of myeloid and lymphoid immune cells captured in AVMs (red) and controls (gray). $n = 5$ donors per condition, mean \pm SEM,

two-tailed t test. * $P < 0.05$; ns, not significant. (E) Bar graph of relative immune cell state proportions normalized to total cells sequenced in AVMs (red) and controls (gray). (F) Representative confocal microscopy analysis of endothelial cells [cyan, podocalyxin (PODOXL)], smooth muscle cells [blue, α smooth muscle actin (SMA)], macrophages [magenta, ionized calcium binding adaptor molecule 1 (IBA1) encoded by the gene *AIF1* in (B)], and microglia [green, purinergic receptor P2RY12 (P2RY12)]. Scale bar, 1 mm. (i) Layered ameiboid perivascular macrophages. (ii) Perivascular microglial response. Scale bars, insets, 50 μ m. (G) Quantification of (top left) abundance, (top right) cell ratio per image, and (bottom) perivascular distance of IBA1⁺P2RY12⁻ macrophages and IBA1⁺P2RY12⁺ microglia ($n = 3$ donors per condition; three nonadjacent sections per donor; 8 to 10 images per section). Mean \pm SEM, two-tailed t test. ** $P < 0.01$; ns, not significant.

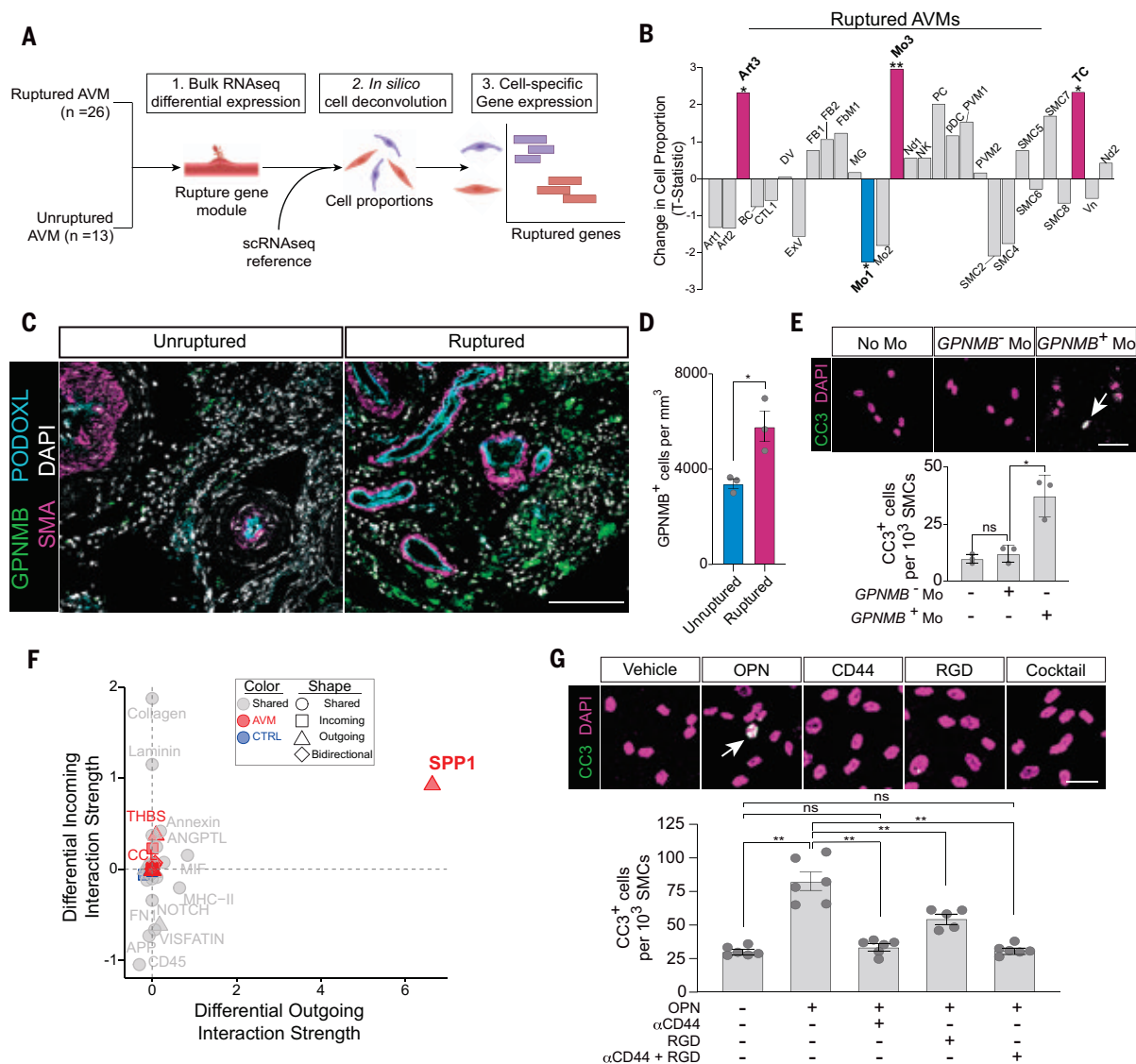


Fig. 5. Cell states implicated in brain AVM rupture. (A) Cellular deconvolution and cell-specific differential expression analysis of bulk RNA-seq from ruptured and unruptured brain AVM. (B) Bar graph of change in cell proportion *t* statistic in ruptured AVMs. Purple, increased cell abundance; blue, decreased cell abundance. **P* < 0.05; ***P* < 0.01. (C) Representative confocal microscopy imaging showing GPNMB⁺ monocytes (green), endothelial cells [cyan, podocalyxin (PODOXL)], and smooth muscle cells [magenta, α-smooth muscle actin (SMA)] in unruptured and ruptured AVMs. Scale bar, 100 μm. (D) Quantification of GPNMB⁺ monocytes in unruptured (blue) and ruptured (purple) AVMs (*n* = 3 donors per condition; three nonadjacent sections per donor; 8 to 10 random images per section). Mean ± SEM, two-tailed *t* test. **P* < 0.05. (E) (Top) Confocal microscopy analysis of cleaved caspase-3⁺ (green, CC3) human primary SMCs after coculture with GPNMB⁺ and GPNMB[−] monocytes isolated from ruptured AVMs. DAPI (magenta) stains are cell nuclei. White, colocalization of CC3 and DAPI; arrow, CC3⁺ cell.

Scale bar, 20 μm. (Bottom) Quantification of CC3⁺ smooth muscle cells (*n* = 3 independent cultures per condition). Mo, monocytes. Mean ± SEM, ANOVA with Tukey post hoc test. **P* < 0.05; ns, not statistically significant. (F) Scatterplot of dysregulated cell communication pathways in AVM GPNMB⁺ monocytes (Mo3) relative to controls by scRNA-seq. Red, up-regulated in AVM; blue, up-regulated in control; gray, shared between conditions; triangle, outgoing network; square, incoming network; and diamond, outgoing and incoming network. (G) (Top) Confocal microscopy analysis of cleaved caspase-3⁺ (green, CC3) human primary smooth muscle cells treated with osteopontin (OPN, encoded by *SPP1*) and CD44-neutralizing antibody, RGD integrin inhibitor, or inhibitor cocktail. DAPI (magenta) stains are cell nuclei. White, colocalization of CC3 and DAPI; arrow, CC3⁺ cell. Scale bar, 20 μm. (Bottom) Quantification of CC3⁺ smooth muscle cells (*n* = 5 to 6 independent cultures per condition). Mo, monocytes. Mean ± SEM, ANOVA with Tukey post hoc test. ***P* < 0.01; ns, not statistically significant.

were angiographically confirmed preoperatively, and fresh tissues were acquired as part of planned surgical resection. For scRNA-seq, only unruptured brain AVMs were enrolled into the study. Specimen orientation was main-

tained to ensure coverage of arteriovenous axis with surgical clips of different sizes with aide of intraoperative fluorescent angiography. All tissues were acquired in close collaboration with neurosurgeons trained in tissue isolation

techniques to minimize tissue disruption such as avoidance of electrocautery. For bulk sequencing experiments, we utilized snap-frozen ruptured and unruptured AVM specimens as part of our biorepository. Patient demographic

information for all tissues utilized is summarized in table S1.

Isolation of cerebrovascular specimens

No differences in vascular isolation methods were applied between normal cerebral cortex or AVM tissues. Tissue specimens were placed in chilled preoxygenated Dulbecco's modified Eagle medium (DMEM, Fisher Scientific, Waltham, MA, catalog number: MT10017CV) and transported to the laboratory on ice. All tissue handling was performed with autoclave-sterilized equipment within a class II biological safety cabinet. Large arteries and veins were selectively isolated under $5\times$ magnification with a Leica MZ75 dissecting microscope (Leica Microsystems, Wetzlar, Germany) with two #5/45 Dumont micro-forceps (Fine Science Tools, Foster City, CA, catalog number: 11251-35). Under $5\times$ magnification, the lumen of each vessel was longitudinally opened with a #15 scalpel blade (Fine Science Tools) or flushed with DMEM. The large vessels were placed in an Eppendorf LoBind 5-ml tube (Eppendorf North America, Enfield, CT, catalog number: 0030122348) and kept on ice in chilled oxygenated DMEM. Following removal of all visible vasculature, the microvasculature was isolated using dextran gradient centrifugation followed by cell-strainer filtration (20–22). More specifically, tissue was cut into ~1- to 2-mm pieces with a scalpel and gently homogenized in a Dounce homogenizer containing oxygenated pre-chilled DMEM with 1% bovine serum albumin (BSA) (Sigma Aldrich, St. Louis, MO, catalog number: A9418). The homogenate was mixed in 18% dextran solution (MW: ~70,000 Da; Sigma-Aldrich, catalog number: 31390) at a volume ratio of 1:1 and centrifuged at 6000g for 20 min at 4°C. This resulted in a microvascular pellet and floating vascular-depleted brain. The floating vessel-depleted brain was gently aspirated and discarded. The vascular pellet resuspended in DMEM with 1% BSA and passed through a 40- μ m cell strainer (Fisher Scientific, catalog number: 08-771-1) to remove circulating cells or other debris. Microvascular fragments remain trapped on top of the cell strainer and were subsequently collected by inverting with cell strainer and washing with prechilled oxygenated DMEM. A small aliquot was visualized at $10\times$ magnification to confirm both purity and yield with brightfield microscopy. The microvascular fragments were pelleted by centrifugation at 500g for 5 min. The supernatant was aspirated and then pooled with the microdissected arteries and veins from the same individual in prechilled oxygenated DMEM. These pooled preparations are referred to as isolated vascular preparations for subsequent steps and maintained in chilled oxygenated media on ice and immediately processed to create single-cell suspensions.

Generation of vascular single-cell suspensions

Isolated vascular preparations were incubated for 45 min in 0.2% collagenase type 2 (Worthington Biochemical Corporation, Lakewood, NJ, catalog number: LS004176) diluted in preoxygenated DMEM at 37°C with gentle agitation in an Eppendorf LoBind 5-ml tube (Eppendorf North America). Cell suspensions were filtered through a sterile 40- μ m cell strainer (Fisher Scientific) to isolate undigested debris. Cells contained within the flowthrough were collected by centrifugation at 500g at 5 min and the supernatant carefully aspirated. To lyse any residual erythrocytes, the cell pellet was resuspended in Gibco ACK lysing buffer (Fisher Scientific, catalog number: A1049201) for 3 min at room temperature. Cells were then collected by centrifugation at 500g at 5 min and washed three times with sterile RNase-free phosphate buffered saline (PBS) (Sigma-Aldrich, catalog number: D8537-500ml) containing 0.04% BSA. Cells were pelleted with centrifugation at 500g for 5 min and resuspended in PBS with 0.04% BSA. To confirm cell viability and yield, a 10- μ l aliquot of the cell suspension was mixed 1:1 with 0.4% trypan blue (Thermo Fisher Scientific, catalog number: T10282) to stain non-viable cells. Cells were then counted on a hemocytometer.

scRNA-seq

All scRNA-seq experiments were performed on freshly isolated, whole cells as described above. Droplet-based scRNA-seq was performed with 10X Genomics Chromium Single Cell 3 prime reagent kits v3 as described by the manufacturer (10X Genomics, Pleasanton, CA, product code: 1000092; $n = 5$ normal cortex samples and $n = 5$ AVMs). Based on hemocytometer counts, single cells were loaded onto chromium chips with a capture target of 15,000 cells per sample. When cell yield was sufficient, two reactions per individual were performed. Libraries were prepared following the provided manufacturer's protocol. Quality of prepared sequencing libraries were confirmed by electrophoretic analysis on an Agilent 4200 TapeStation System (Agilent Technologies, Santa Clara, CA). Libraries were sequenced with an Illumina NovaSeq 6000 (Illumina, San Diego, CA) with a targeted sequencing depth of 50,000 reads per cell.

Bulk RNA sequencing

Undigested, isolated vascular tissues from ruptured and unruptured AVMs were obtained from the operating room, snap frozen in liquid nitrogen and stored at -80°C . Snap frozen tissues were embedded in Optical Cutting Temperature Compound (Sakura Finetek USA, Torrance, CA, catalog number: 4583) and cryosectioned at a thickness of 20 μ m. Tissue scrolls were collected in RNAase free Eppendorf LoBind-1.5 ml microcentrifuge tubes

(Eppendorf North America, catalog number: 022431021). DNA/RNA Shield reagent (Zymo Research, Irvine, CA, catalog number: R1100) was added. Tissues were mechanically homogenized with a Squisher-Single homogenizer (Zymo Research, catalog number: H1001) and subsequently digested with proteinase K (Zymo Research, catalog number: R1057). Total RNA was isolated from the homogenized tissues with the Quick-RNA Miniprep Plus Kit as instructed by the manufacturer (Zymo Research, catalog number: R1057). The purified RNA was quantified with a NanoDrop (Thermo Fisher Scientific) and integrity confirmed with an Agilent 4200 TapeStation System (Agilent Technologies, Inc.). Ribosomal RNA was depleted using the NEBNext rRNA Depletion Kit as instructed by the manufacturer (New England Biolabs, Ipswich, MA, catalog number: E6310X), and sequencing libraries prepared with the SEQuoia Complete Stranded RNA Library Prep Kit (BioRad Laboratories, Hercules, CA, catalog number: 17005710). Sequencing library quality was confirmed on an Agilent 4200 TapeStation System (Agilent Technologies, Inc) and quantified with a Qubit dsDNA high sensitivity assay kit (Thermo Fisher Scientific). Libraries were sequenced in batch with an Illumina NovaSeq 6000 sequencer (Illumina) with targeted read depth of at least 5×10^7 reads per sample.

Rebus Esper spatial omics platform

Spatially resolved, multiplexed in situ RNA detection and analysis was performed using the automated Rebus Esper spatial omics platform (Rebus Biosystems, Santa Clara, CA). By intersecting a list of known or candidate cell type markers generated by scRNA-seq, suitability for probe design, including gene length and relative abundance, and design constraints for compatibility with the Rebus Esper spatial omics platform using proprietary software, we generated the following gene probe panel: *MECOM*, *RGS16*, *RARA*, *MFS2A*, *TAGLN*, *IL1R1*, *VEGFC*, *KCNJ8*, *DCN*, *TMEM132C*, *CCL19*, *CLDN5*, *PDGFRB*, *HIGD1B*, *KCNT2*, *ALDH1A2*, and *ALDH1A1*. Experiments and analyses using the Rebus Esper spatial omics platform were performed as previously described (70).

Immunofluorescent staining of tissues and cerebrovascular fragments

Formalin-fixed paraffin-embedded tissue sections were cut at a thickness of 6 μ m, deparaffinized with xylene, and rehydrated to distilled water with serial ethanol washes. For immunostaining of isolated vessel fragments, cerebrovascular vessel isolation was performed as described above and immersion fixed in 4% paraformaldehyde overnight at 4°C. For antigen retrieval, all specimens were incubated with pH 9 Tris-EDTA buffer at 97°C for 15 min. Tissue sections were then blocked with PBS

containing 0.2% gelatin, 1% donkey serum, and 1% triton for 1 hour at room temperature and incubated in the following primary antibodies overnight at 4°C. Primary antibodies included: podocalyxin (1:100, R&D Systems, Minneapolis, MN, catalog number: AF1658), alpha smooth muscle actin clone 1A4 (1:100, Dako North America, Inc. Carpinteria, CA, catalog number: M085129), P2RY12 (1:500, Sigma Aldrich, catalog number: HPA014518), IBA1 (1:500, Synaptic Systems, Goettingen, Germany, catalog number: 234004), PECAM1 (1:50, Agilent Technologies, catalog number: M0882329), PLVAP (1:100, Sigma Aldrich, catalog number: HPA002279), angiopoietin-2 (1:100, R&D systems, catalog number: AF623), PDGFRB (28E1) (1:100, Cell Signaling Technology, catalog number: 3169S), GPNMB (1:100, R&D systems, catalog number: AF2550), and CD8 clone C8/144B (1:100, Dako North America, catalog number: M710301). Sections were washed with PBS containing 1% Triton and incubated with fluorescent dye-conjugated secondary antibodies for 2 hours at room temperature. Alexa Fluor 488-conjugated donkey anti-mouse secondary antibody (1:500, Thermo Scientific, catalog number: A32766), Alexa Fluor 546-conjugated donkey anti-rabbit secondary antibody (1:500, Thermo Fisher, catalog number: A10040), and Alexa Fluor 647-conjugated donkey anti-goat secondary antibodies (1:500, Thermo Fisher, catalog number: A32787) were used to detect mouse, rabbit, and goat primary antibodies, respectively. Sections were washed and autofluorescence quenched by incubating with 1% Sudan Black (Sigma Aldrich, catalog number: 199664) for 10 min at room temperature. Slides were mounted with 4-prime,6-diamidino-2-phenylindole (DAPI)-containing Fluoromount-G (SouthernBiotech, Birmingham, AL, catalog number: 0100-20). All imaging was performed with a Leica TCS SP8 X confocal microscope with a 20X objective (Leica Microsystems).

Fluorescence-activated cell sorting (FACS)

To isolate circulating GPNMB⁺ and GPNMB⁻ monocytes, 10 ml of whole blood was collected in standard 5-ml EDTA-containing vacutainer blood collection tubes obtained from adult patients with acutely ruptured AVMs. Cells were subsequently centrifuged at 500g for 5 min and erythrocytes were then lysed with incubation in Gibco ACK lysing buffer (Fisher Scientific, catalog number: A1049201). The resulting cell suspension was filtered through a sterile 40-μm filter to remove debris and washed with PBS containing 0.04% BSA. Cell suspensions were then resuspended in FACS staining buffer (Thermo Fisher Scientific, catalog number: 00-4222-26). Cells were blocked to prevent non-specific staining, and cells were stained with Alexa Fluor 647-conjugated mouse anti-human CD45 monoclonal anti-

body clone HI30 (1.25 ng/μl, Thermo Fisher Scientific, catalog number: 51-0459-42), FITC-conjugated mouse anti-human CD11b monoclonal antibody clone ICRF44 (5.0 ng/μl, Thermo Fisher Scientific, catalog number: 11-0118-42), and PE-conjugated mouse anti-human GPNMB monoclonal antibody clone HOST5DS (1.25 ng/μl, Thermo Fisher Scientific, catalog number: 12-9838-42) for 30 min at room temperature. Cells were subsequently isolated by FACS with a BD FACSaria II Flow Cytometer (BD Biosciences, Franklin Lakes, NJ). Viable CD45⁺CD11b⁺GPNMB⁺ cells and CD45⁺CD11b⁺GPNMB⁻ cells were separately collected for subsequent coculture experiments.

Cell culture

All cell culture experiments utilized primary human brain vascular smooth muscle cells (VSMCs, ScienCell Research Laboratories, Carlsbad, CA, catalog number: 1100). Cells were cultured in SMC media in 5% CO₂ at 37°C. Early passage (P3, P4) cultures were used in the present study. Primary VSMCs were plated in equal number for all conditions. VSMCs were grown on 96-well tissue culture plates pre-coated with collagen. For coculture experiments, CD45⁺CD11b⁺GPNMB⁺ or CD45⁺CD11b⁺GPNMB⁻ cells were immediately cocultured with VSMCs following FACS isolation at an approximate ratio of 1:1 (71). Monocytes and VSMCs were cocultured for 24 hours and then subsequently fixed with 4% paraformaldehyde for subsequent immunostaining. For osteopontin (OPN, encoded by *SPPT*) treatment studies, cells were pretreated with vehicle control or anti-human CD44 neutralizing monoclonal antibody (10 μg/ml, Thermo Fisher Scientific, catalog number: MA4400), RGD peptide to inhibit integrin receptors (10 μM, Sigma Aldrich, catalog number: A8052), or both in combination for 30 min as previously described (65). Cultures were then subsequently treated with OPN (200 ng/ml, Sigma Aldrich, catalog number: SRP3131) for 6 hours. The cell culture media was changed and cells were then fixed with 4% paraformaldehyde for subsequent immunostaining.

Cell culture immunostaining

Paraformaldehyde fixed cells were blocked with PBS containing 0.2% gelatin, 1% donkey serum, and 0.1% triton for 1 hour at room temperature and incubated in primary antibodies overnight at 4°C. Primary antibodies included: alpha smooth muscle actin clone 1A4 (1:100, Dako North America, Carpinteria, CA, catalog number: M085129) and cleaved caspase-3 (1:300, Cell Signaling, catalog number: 9661S). Alexa Fluor 488-conjugated donkey anti-mouse secondary antibody (1:500, Thermo Scientific, catalog number: A32766) and Alexa Fluor 546-conjugated donkey anti-rabbit secondary

antibody (1:500, Thermo Fisher, catalog number: A10040) were used to detect mouse and rabbit primary antibodies, respectively. Cells were washed and nuclei stained with DAPI. All imaging was performed with a Leica TCS SP8 X confocal microscope with a 20X objective (Leica Microsystems, Inc.).

Tissue and cell culture image analysis

For all quantitative imaging experiments, a tile-scan image was generated encompassing the tissue section or cell culture well with 10- to 12-μm z-stack and maximum projection z-stack images were reconstructed. For all tissue studies, 8 to 10 randomly selected fields in three non-adjacent tissue sections per tissue specimen were analyzed as previously described (20). Tissues from three donors per condition were used for all analyses. For quantification of IBA1⁺, P2RY12⁺, and CD8⁺ immune cells, cell bodies were counted with the NIH ImageJ multipoint tool and expressed as number of positive cells per cubic millimeter of tissue. For immune cell distance analysis, the distance between cell bodies and abluminal vascular wall was measured using the NIH ImageJ length measurement tool. For coculture experiments, three independent cultures were analyzed per condition. For OPN experiments, 5 to 6 independent cultures were analyzed per condition. Cleaved caspase-3⁺ cells were counted with the NIH ImageJ multipoint tool, normalized to total cell number, and expressed per 1000 SMCs.

Single-cell RNA-sequencing analysis

Salmon Alevin 1.3.0 was used to create a cell by gene matrix for spliced and unspliced counts using the annotation from GENCODE 34 for GRCh38 (72, 73). Solo was used for doublet detection and removal and enriched softmax values in clusters were used as additional criteria for another round of doublet filtering (74). A minimum of 1000 genes and 40% mitochondrial cutoff were used to remove low quality cells from all datasets. The SCTransform workflow was used for count normalization (75). Principal component analysis was computed on the residuals for input into Harmony for batch correction (76). Control immune cells were not batch corrected due to inability to resolve rare cell types after correction. The parameters of Harmony were set to use the top 30 principal components. Uniform manifold approximation and projection (UMAP) embeddings and neighbors for Leiden clustering used the batch corrected embeddings (77, 78). RNA velocity analysis was done using the scVelo package (79). HGNC labels replaced all corresponding Ensembl gene ID and non HGNC annotated gene IDs were left in the matrix as Ensembl gene IDs. Latent time from scVelo was computed to order the cells. RNA velocity analysis was performed on batch

corrected embeddings. dittoSeq was used for color-blind friendly plotting (80). CellChat was used to infer cell communication analysis (53). scMappR was used to deconvolute gene expression between bulk gene expression datasets using the AVM perivascular, endothelial, and immune cell types as the reference (61). Correlations between mouse and human endothelial cell types were calculated on the space of shared orthologous marker genes of clusters. fgsea was used to look for enriched hallmark pathways from differential expressed endothelial genes (81). The *t* statistic for cell type proportions was based on deconvolution output from scMappR. All marker genes were using a Wilcoxon rank-sum test with a minimum of 0.5 average log fold-change cutoff and filtering for genes with <0.05 FDR with Bonferroni correction. UCell was used for the cell type identity score and utilized the top 30 genes of the cluster (82). More specifically, gene lists were generated using a Wilcoxon rank sum test and filtered for statistical significance (FDR < 0.01) for the top 30 genes. For endothelial cells, this list was also intersected with published mouse datasets based on their specificity after aggregating into four different subclasses: artery, capillary, venule, and vein (13). Genes used for UCell scoring for each cell type are listed in table S10.

Spatial transcriptomic analysis

The RNA spot table was log-normalized and scaled before PCA. The top 10 components were used for UMAP and neighbor analysis for Leiden clustering using the scanpy package.

Bulk tissue RNA-sequencing analysis

Salmon 1.3.0 was used to pseudo-align all ruptured and unruptured bulk AVM samples (83). The output of Salmon was used to generate counts using tximport (84). edgeR was used to compute differential gene expression between ruptured and unruptured samples using the exact test (85). Genes with a false discovery rate (FDR)-adjusted *q* value < 0.05 were considered to be differentially expressed.

Statistical analysis

For all immunostaining and cell culture experiments, statistical analysis was performed with Student's *t* test for two-way comparisons and one-way analysis of variance (ANOVA) with post hoc Tukey tests for comparisons of three or more groups using GraphPad Prism. Data are presented as mean ± standard error of the mean unless otherwise indicated with individual data points shown.

Schematics

Schematic cartoons in Fig. 5A were created with BioRender.com.

REFERENCES AND NOTES

- S. Schaeffer, C. Iadecola, Revisiting the neurovascular unit. *Nat. Neurosci.* **24**, 1198–1209 (2021). doi: [10.1038/s41593-021-00904-7](https://doi.org/10.1038/s41593-021-00904-7); pmid: [34354283](https://pubmed.ncbi.nlm.nih.gov/34354283/)
- M. D. Sweeney, K. Kisler, A. Montagne, A. W. Toga, B. V. Zlokovic, The role of brain vasculature in neurodegenerative disorders. *Nat. Neurosci.* **21**, 1318–1331 (2018). doi: [10.1038/s41593-018-0234-x](https://doi.org/10.1038/s41593-018-0234-x); pmid: [30250261](https://pubmed.ncbi.nlm.nih.gov/30250261/)
- M. D. Sweeney, Z. Zhao, A. Montagne, A. R. Nelson, B. V. Zlokovic, Blood-brain barrier: From physiology to disease and back. *Physiol. Rev.* **99**, 21–78 (2019). doi: [10.1152/physrev.00050.2017](https://doi.org/10.1152/physrev.00050.2017); pmid: [30280653](https://pubmed.ncbi.nlm.nih.gov/30280653/)
- GBD 2016 Lifetime Risk of Stroke Collaborators, Global, regional, and country-specific lifetime risks of stroke, 1990 and 2016. *N. Engl. J. Med.* **379**, 2429–2437 (2018). doi: [10.1056/NEJMoal804492](https://doi.org/10.1056/NEJMoal804492); pmid: [30575491](https://pubmed.ncbi.nlm.nih.gov/30575491/)
- GBD 2016 Stroke Collaborators, Global, regional, and national burden of stroke, 1990–2016: A systematic analysis for the Global Burden of Disease Study 2016. *Lancet Neurol.* **18**, 439–458 (2019). doi: [10.1016/S1474-4422\(19\)30034-1](https://doi.org/10.1016/S1474-4422(19)30034-1); pmid: [30871944](https://pubmed.ncbi.nlm.nih.gov/30871944/)
- R. Daneman, A. Prat, The blood-brain barrier. *Cold Spring Harb. Perspect. Biol.* **7**, a020412 (2015). doi: [10.1101/cshperspect.a020412](https://doi.org/10.1101/cshperspect.a020412); pmid: [25561720](https://pubmed.ncbi.nlm.nih.gov/25561720/)
- M. Vanlandewijck et al., A molecular atlas of cell types and zonation in the brain vasculature. *Nature* **554**, 475–480 (2018). doi: [10.1038/nature25739](https://doi.org/10.1038/nature25739); pmid: [29443965](https://pubmed.ncbi.nlm.nih.gov/29443965/)
- J. M. Ross et al., The expanding cell diversity of the brain vasculature. *Front. Physiol.* **11**, 600767 (2020). doi: [10.3389/fphys.2020.600767](https://doi.org/10.3389/fphys.2020.600767); pmid: [33343397](https://pubmed.ncbi.nlm.nih.gov/33343397/)
- J. V. Forrester, P. G. McMenamin, S. J. Dando, CNS infection and immune privilege. *Nat. Rev. Neurosci.* **19**, 655–671 (2018). doi: [10.1038/s41583-018-0070-8](https://doi.org/10.1038/s41583-018-0070-8); pmid: [30310148](https://pubmed.ncbi.nlm.nih.gov/30310148/)
- W. M. Pardridge, Blood-brain barrier and delivery of protein and gene therapeutics to brain. *Front. Aging Neurosci.* **11**, 373 (2020). doi: [10.3389/fnagi.2019.00373](https://doi.org/10.3389/fnagi.2019.00373); pmid: [31998120](https://pubmed.ncbi.nlm.nih.gov/31998120/)
- Z. Zhao, A. R. Nelson, C. Betsholtz, B. V. Zlokovic, Establishment and dysfunction of the blood-brain barrier. *Cell* **163**, 1064–1078 (2015). doi: [10.1016/j.cell.2015.10.067](https://doi.org/10.1016/j.cell.2015.10.067); pmid: [26590417](https://pubmed.ncbi.nlm.nih.gov/26590417/)
- M. B. Chen et al., Brain endothelial cells are exquisite sensors of age-related circulatory cues. *Cell Rep.* **30**, 4418–4432.e4 (2020). doi: [10.1016/j.celrep.2020.03.012](https://doi.org/10.1016/j.celrep.2020.03.012); pmid: [32234477](https://pubmed.ncbi.nlm.nih.gov/32234477/)
- J. Kalucka et al., Single-cell transcriptome atlas of murine endothelial cells. *Cell* **180**, 764–779.e20 (2020). doi: [10.1016/j.cell.2020.01.015](https://doi.org/10.1016/j.cell.2020.01.015); pmid: [32059779](https://pubmed.ncbi.nlm.nih.gov/32059779/)
- M. F. Sabbagh et al., Transcriptional and epigenomic landscapes of CNS and non-CNS vascular endothelial cells. *eLife* **7**, e36187 (2018). doi: [10.7554/eLife.36187](https://doi.org/10.7554/eLife.36187); pmid: [30188322](https://pubmed.ncbi.nlm.nih.gov/30188322/)
- R. D. Hodge et al., Conserved cell types with divergent features in human versus mouse cortex. *Nature* **573**, 61–68 (2019). doi: [10.1038/s41586-019-1506-7](https://doi.org/10.1038/s41586-019-1506-7); pmid: [31435019](https://pubmed.ncbi.nlm.nih.gov/31435019/)
- T. J. Nowakowski et al., Spatiotemporal gene expression trajectories reveal developmental hierarchies of the human cortex. *Science* **358**, 1318–1323 (2017). doi: [10.1126/science.aap8809](https://doi.org/10.1126/science.aap8809); pmid: [29217575](https://pubmed.ncbi.nlm.nih.gov/29217575/)
- A. Montagne et al., APOE4 leads to blood-brain barrier dysfunction predicting cognitive decline. *Nature* **581**, 71–76 (2020). doi: [10.1038/s41586-020-2247-3](https://doi.org/10.1038/s41586-020-2247-3); pmid: [32376954](https://pubmed.ncbi.nlm.nih.gov/32376954/)
- D. A. Nation et al., Blood-brain barrier breakdown is an early biomarker of human cognitive dysfunction. *Nat. Med.* **25**, 270–276 (2019). doi: [10.1038/s41591-018-0297-y](https://doi.org/10.1038/s41591-018-0297-y); pmid: [30643288](https://pubmed.ncbi.nlm.nih.gov/30643288/)
- J. Ratelade et al., Reducing hypermuscularization of the transitional segment between arterioles and capillaries protects against spontaneous intracerebral hemorrhage. *Circulation* **141**, 2078–2094 (2020). doi: [10.1161/CIRCULATIONAHA.119.040963](https://doi.org/10.1161/CIRCULATIONAHA.119.040963); pmid: [32183562](https://pubmed.ncbi.nlm.nih.gov/32183562/)
- R. D. Bell et al., Pericytes control key neurovascular functions and neuronal phenotype in the adult brain and during brain aging. *Neuron* **68**, 409–427 (2010). doi: [10.1016/j.neuron.2010.09.043](https://doi.org/10.1016/j.neuron.2010.09.043); pmid: [21040844](https://pubmed.ncbi.nlm.nih.gov/21040844/)
- E. A. Winkler, J. D. Sengillo, R. D. Bell, J. Wang, B. V. Zlokovic, Blood-spinal cord barrier pericyte reductions contribute to increased capillary permeability. *J. Cereb. Blood Flow Metab.* **32**, 1841–1852 (2012). doi: [10.1038/jcbfm.2012.113](https://doi.org/10.1038/jcbfm.2012.113); pmid: [22850407](https://pubmed.ncbi.nlm.nih.gov/22850407/)
- Z. Zhao et al., Central role for PICALM in amyloid- β blood-brain barrier transcytosis and clearance. *Nat. Neurosci.* **18**, 978–987 (2015). doi: [10.1038/nn.4025](https://doi.org/10.1038/nn.4025); pmid: [26005850](https://pubmed.ncbi.nlm.nih.gov/26005850/)
- A. Saunders et al., Molecular diversity and specializations among the cells of the adult mouse brain. *Cell* **174**, 1015–1030.e16 (2018). doi: [10.1016/j.cell.2018.07.028](https://doi.org/10.1016/j.cell.2018.07.028); pmid: [30096299](https://pubmed.ncbi.nlm.nih.gov/30096299/)
- A. Zeisel et al., Molecular architecture of the mouse nervous system. *Cell* **174**, 999–1014.e22 (2018). doi: [10.1016/j.cell.2018.06.021](https://doi.org/10.1016/j.cell.2018.06.021); pmid: [30096314](https://pubmed.ncbi.nlm.nih.gov/30096314/)
- T. Kubíková, P. Kočová, P. Tomášek, K. Witter, Z. Tónar, Numerical and length densities of microvessels in the human brain: Correlation with preferential orientation of microvessels in the cerebral cortex, subcortical grey matter and white matter, pons and cerebellum. *J. Chem. Neuroanat.* **88**, 22–32 (2018). doi: [10.1016/j.jchemneu.2017.11.005](https://doi.org/10.1016/j.jchemneu.2017.11.005); pmid: [29113946](https://pubmed.ncbi.nlm.nih.gov/29113946/)
- X. Li et al., Thioredoxin-interacting protein promotes high-glucose-induced macrovascular endothelial dysfunction. *Biochem. Biophys. Res. Commun.* **493**, 291–297 (2017). doi: [10.1016/j.bbrc.2017.09.028](https://doi.org/10.1016/j.bbrc.2017.09.028); pmid: [28890350](https://pubmed.ncbi.nlm.nih.gov/28890350/)
- A. Armulik, G. Genové, C. Betsholtz, Pericytes: Developmental, physiological, and pathological perspectives, problems, and promises. *Dev. Cell* **21**, 193–215 (2011). doi: [10.1016/j.devcel.2011.07.001](https://doi.org/10.1016/j.devcel.2011.07.001); pmid: [21839917](https://pubmed.ncbi.nlm.nih.gov/21839917/)
- L. He et al., Analysis of the brain mural cell transcriptome. *Sci. Rep.* **6**, 35108 (2016). doi: [10.1038/srep35108](https://doi.org/10.1038/srep35108); pmid: [27725773](https://pubmed.ncbi.nlm.nih.gov/27725773/)
- A. Armulik et al., Pericytes regulate the blood-brain barrier. *Nature* **468**, 557–561 (2010). doi: [10.1038/nature09522](https://doi.org/10.1038/nature09522); pmid: [20944627](https://pubmed.ncbi.nlm.nih.gov/20944627/)
- R. Daneman, L. Zhou, A. A. Kebede, B. A. Barres, Pericytes are required for blood-brain barrier integrity during embryogenesis. *Nature* **468**, 562–566 (2010). doi: [10.1038/nature09513](https://doi.org/10.1038/nature09513); pmid: [20944625](https://pubmed.ncbi.nlm.nih.gov/20944625/)
- R. A. Hill et al., Regional blood flow in the normal and ischemic brain is controlled by arteriolar smooth muscle cell contractility and not by capillary pericytes. *Neuron* **87**, 95–110 (2015). doi: [10.1016/j.neuron.2015.06.001](https://doi.org/10.1016/j.neuron.2015.06.001); pmid: [26119027](https://pubmed.ncbi.nlm.nih.gov/26119027/)
- L. C. D. Smyth et al., Markers for human brain pericytes and smooth muscle cells. *J. Chem. Neuroanat.* **92**, 48–60 (2018). doi: [10.1016/j.jchemneu.2018.06.001](https://doi.org/10.1016/j.jchemneu.2018.06.001); pmid: [29885791](https://pubmed.ncbi.nlm.nih.gov/29885791/)
- S. Zbinden et al., Metallothionein enhances angiogenesis and arteriogenesis by modulating smooth muscle cell and macrophage function. *Arterioscler. Thromb. Vasc. Biol.* **30**, 477–482 (2010). doi: [10.1161/ATVBAHA.109.200949](https://doi.org/10.1161/ATVBAHA.109.200949); pmid: [20056912](https://pubmed.ncbi.nlm.nih.gov/20056912/)
- L. Duan et al., PDGFR β cells rapidly relay inflammatory signal from the circulatory system to neurons via chemokine CCL2. *Neuron* **100**, 183–200.e8 (2018). doi: [10.1016/j.neuron.2018.08.030](https://doi.org/10.1016/j.neuron.2018.08.030); pmid: [30269986](https://pubmed.ncbi.nlm.nih.gov/30269986/)
- M. C. Hendriks-Balk et al., Sphingosine-1-phosphate regulates RGS2 and RGS16 mRNA expression in vascular smooth muscle cells. *Eur. J. Pharmacol.* **606**, 25–31 (2009). doi: [10.1016/j.ejphar.2009.01.018](https://doi.org/10.1016/j.ejphar.2009.01.018); pmid: [19374869](https://pubmed.ncbi.nlm.nih.gov/19374869/)
- A. M. Rajan, R. C. Ma, K. M. Kocha, D. J. Zhang, P. Huang, Dual function of perivascular fibroblasts in vascular stabilization in zebrafish. *PLoS Genet.* **16**, e1008800 (2020). doi: [10.1371/journal.pgen.1008800](https://doi.org/10.1371/journal.pgen.1008800); pmid: [33104690](https://pubmed.ncbi.nlm.nih.gov/33104690/)
- J. DeSisto et al., Single-cell transcriptomic analyses of the developing meninges reveal meningeal fibroblast diversity and function. *Dev. Cell* **54**, 43–59.e4 (2020). doi: [10.1016/j.devcel.2020.06.009](https://doi.org/10.1016/j.devcel.2020.06.009); pmid: [32634398](https://pubmed.ncbi.nlm.nih.gov/32634398/)
- Y. Li et al., Single-cell transcriptome analysis reveals dynamic cell populations and differential gene expression patterns in control and aneurysmal human aortic tissue. *Circulation* **142**, 1374–1388 (2020). doi: [10.1161/CIRCULATIONAHA.120.046528](https://doi.org/10.1161/CIRCULATIONAHA.120.046528); pmid: [33017217](https://pubmed.ncbi.nlm.nih.gov/33017217/)
- H. Pan et al., Single-cell genomics reveals a novel cell state during smooth muscle cell phenotypic switching and potential therapeutic targets for atherosclerosis in mouse and human. *Circulation* **142**, 2060–2075 (2020). doi: [10.1161/CIRCULATIONAHA.120.048378](https://doi.org/10.1161/CIRCULATIONAHA.120.048378); pmid: [32962412](https://pubmed.ncbi.nlm.nih.gov/32962412/)
- R. C. Wirka et al., Atheroprotective roles of smooth muscle cell phenotypic modulation and the TCF21 disease gene as revealed by single-cell analysis. *Nat. Med.* **25**, 1280–1289 (2019). doi: [10.1038/s41591-019-0512-5](https://doi.org/10.1038/s41591-019-0512-5); pmid: [31359001](https://pubmed.ncbi.nlm.nih.gov/31359001/)
- X. Long, R. D. Bell, W. T. Gerthoffer, B. V. Zlokovic, J. M. Miano, Myocardin is sufficient for a smooth muscle-like contractile phenotype. *Arterioscler. Thromb. Vasc. Biol.* **28**, 1505–1510 (2008). doi: [10.1161/ATVBAHA.108.166066](https://doi.org/10.1161/ATVBAHA.108.166066); pmid: [18451334](https://pubmed.ncbi.nlm.nih.gov/18451334/)
- L. S. Shankman et al., KLF4-dependent phenotypic modulation of smooth muscle cells has a key role in atherosclerotic plaque pathogenesis. *Nat. Med.* **21**, 628–637 (2015). doi: [10.1038/nm.3866](https://doi.org/10.1038/nm.3866); pmid: [25985364](https://pubmed.ncbi.nlm.nih.gov/25985364/)
- G. La Manno et al., RNA velocity of single cells. *Nature* **560**, 494–498 (2018). doi: [10.1038/s41586-018-0414-6](https://doi.org/10.1038/s41586-018-0414-6); pmid: [30089906](https://pubmed.ncbi.nlm.nih.gov/30089906/)
- S. Qunzain et al., CARMEN, a human super enhancer-associated long noncoding RNA controlling cardiac specification, differentiation and homeostasis. *J. Mol. Cell. Cardiol.* **89**, 98–112 (2015). doi: [10.1016/j.jmcc.2015.09.016](https://doi.org/10.1016/j.jmcc.2015.09.016); pmid: [26423156](https://pubmed.ncbi.nlm.nih.gov/26423156/)

45. M. T. Lawton *et al.*, Brain arteriovenous malformations. *Nat. Rev. Dis. Primers* **1**, 15008 (2015). doi: [10.1038/nrdp.2015.8](https://doi.org/10.1038/nrdp.2015.8); pmid: 27188382
46. J. E. Fish *et al.*, Somatic gain of KRAS function in the endothelium is sufficient to cause vascular malformations that require MEK but not PI3K signaling. *Circ. Res.* **127**, 727–743 (2020). doi: [10.1161/CIRCRESAHA.119.316500](https://doi.org/10.1161/CIRCRESAHA.119.316500); pmid: 32552404
47. P. A. Murphy *et al.*, Constitutively active Notch4 receptor elicits brain arteriovenous malformations through enlargement of capillary-like vessels. *Proc. Natl. Acad. Sci. U.S.A.* **111**, 18007–18012 (2014). doi: [10.1073/pnas.1415316111](https://doi.org/10.1073/pnas.1415316111); pmid: 25468970
48. H. Jiang *et al.*, MCH neurons regulate permeability of the median eminence barrier. *Neuron* **107**, 306–319.e9 (2020). doi: [10.1016/j.neuron.2020.04.020](https://doi.org/10.1016/j.neuron.2020.04.020); pmid: 32407670
49. E. I. Gaál *et al.*, Comparison of vascular growth factors in the murine brain reveals placenta growth factor as prime candidate for CNS revascularization. *Blood* **122**, 658–665 (2013). doi: [10.1182/blood-2012-07-441527](https://doi.org/10.1182/blood-2012-07-441527); pmid: 23803710
50. M. N. Jabbour *et al.*, Aberrant angiogenic characteristics of human brain arteriovenous malformation endothelial cells. *Neurosurgery* **64**, 139–148 (2009). doi: [10.1227/01.NEU.0000334417.56742.24](https://doi.org/10.1227/01.NEU.0000334417.56742.24); pmid: 19145162
51. L. D. Shoemaker, A. K. McCormick, B. M. Allen, S. D. Chang, Evidence for endothelial-to-mesenchymal transition in human brain arteriovenous malformations. *Clin. Transl. Med.* **10**, e99 (2020). doi: [10.1002/ctm2.99](https://doi.org/10.1002/ctm2.99); pmid: 32564509
52. R. Wright *et al.*, Histopathology of brain AVMs part II: Inflammation in arteriovenous malformation of the brain. *Acta Neurochir.* **162**, 1741–1747 (2020). doi: [10.1007/s00701-020-04328-3](https://doi.org/10.1007/s00701-020-04328-3); pmid: 32306161
53. S. Jin *et al.*, Inference and analysis of cell-cell communication using CellChat. *Nat. Commun.* **12**, 1088 (2021). doi: [10.1038/s41467-021-21246-9](https://doi.org/10.1038/s41467-021-21246-9); pmid: 33597522
54. A. M. Crist *et al.*, Angiopoietin-2 inhibition rescues arteriovenous malformation in a Smad4 hereditary hemorrhagic telangiectasia mouse model. *Circulation* **139**, 2049–2063 (2019). doi: [10.1161/CIRCULATIONAHA.118.036952](https://doi.org/10.1161/CIRCULATIONAHA.118.036952); pmid: 30744395
55. Y. Hwan Kim *et al.*, Overexpression of activin receptor-like kinase 1 in endothelial cells suppresses development of arteriovenous malformations in mouse models of hereditary hemorrhagic telangiectasia. *Circ. Res.* **127**, 1122–1137 (2020). doi: [10.1161/CIRCRESAHA.119.316267](https://doi.org/10.1161/CIRCRESAHA.119.316267); pmid: 32762495
56. W. Zhu *et al.*, Soluble FLT1 gene therapy alleviates brain arteriovenous malformation severity. *Stroke* **48**, 1420–1423 (2017). doi: [10.1161/STROKEAHA.116.015713](https://doi.org/10.1161/STROKEAHA.116.015713); pmid: 28325846
57. S. E. Marsh *et al.*, Single cell sequencing reveals glial specific responses to tissue processing and enzymatic dissociation in mice and humans. *bioRxiv* 408542 [Preprint] (2020). doi: [10.1101/2020.12.03.408542](https://doi.org/10.1101/2020.12.03.408542)
58. E. J. McMahon, S. L. Bailey, C. V. Castenada, H. Waldner, S. D. Miller, Epitope spreading initiates in the CNS in two mouse models of multiple sclerosis. *Nat. Med.* **11**, 335–339 (2005). doi: [10.1038/nm1202](https://doi.org/10.1038/nm1202); pmid: 15735651
59. C. Proding *et al.*, CD11c-expressing cells reside in the juxtavascular parenchyma and extend processes into the glia limitans of the mouse nervous system. *Acta Neuropathol.* **121**, 445–458 (2011). doi: [10.1007/s00401-010-0774-y](https://doi.org/10.1007/s00401-010-0774-y); pmid: 21076838
60. M. Majumdar, L. A. Tan, M. Chen, Critical assessment of the morbidity associated with ruptured cerebral arteriovenous malformations. *J. Neurointerv. Surg.* **8**, 163–167 (2016). doi: [10.1136/neurintsurg-2014-011517](https://doi.org/10.1136/neurintsurg-2014-011517); pmid: 25568227
61. D. J. Sokolowski *et al.*, Single-cell mapper (scMapPR): Using scRNA-seq to infer the cell-type specificities of differentially expressed genes. *NAR Genom. Bioinform.* **3**, lqab011 (2021). doi: [10.1093/nargab/lqab011](https://doi.org/10.1093/nargab/lqab011); pmid: 33655208
62. R. N. Munji *et al.*, Profiling the mouse brain endothelial transcriptome in health and disease models reveals a core blood-brain barrier dysfunction module. *Nat. Neurosci.* **22**, 1892–1902 (2019). doi: [10.1038/s41593-019-0497-x](https://doi.org/10.1038/s41593-019-0497-x); pmid: 31611708
63. W. Chen *et al.*, Reduced mural cell coverage and impaired vessel integrity after angiogenic stimulation in the Akt1-deficient brain. *Arterioscler. Thromb. Vasc. Biol.* **33**, 305–310 (2013). doi: [10.1161/ATVBAHA.112.300485](https://doi.org/10.1161/ATVBAHA.112.300485); pmid: 23241407
64. J. Frösen, A. Joutel, Smooth muscle cells of intracranial vessels: From development to disease. *Cardiovasc. Res.* **114**, 501–512 (2018). doi: [10.1093/cvr/cvy002](https://doi.org/10.1093/cvr/cvy002); pmid: 29351598
65. Y. H. Zheng *et al.*, Osteopontin stimulates autophagy via integrin/CD44 and p38 MAPK signaling pathways in vascular smooth muscle cells. *J. Cell. Physiol.* **227**, 127–135 (2012). doi: [10.1002/jcp.22709](https://doi.org/10.1002/jcp.22709); pmid: 21374592
66. S. Bonney *et al.*, Diverse functions of retinoic acid in brain vascular development. *J. Neurosci.* **36**, 7786–7801 (2016). doi: [10.1523/JNEUROSCI.3952-15.2016](https://doi.org/10.1523/JNEUROSCI.3952-15.2016); pmid: 27445154
67. S. Mishra, Y. Choe, S. J. Pleasure, J. A. Siegenthaler, Cerebrovascular defects in *Foxc1* mutants correlate with aberrant WNT and VEGF-A pathways downstream of retinoic acid from the meninges. *Dev. Biol.* **420**, 148–165 (2016). doi: [10.1016/j.ydbio.2016.09.019](https://doi.org/10.1016/j.ydbio.2016.09.019); pmid: 27671872
68. R. del Toro *et al.*, Identification and functional analysis of endothelial tip cell-enriched genes. *Blood* **116**, 4025–4033 (2010). doi: [10.1182/blood-2010-02-270819](https://doi.org/10.1182/blood-2010-02-270819); pmid: 20705756
69. M. Hupe *et al.*, Gene expression profiles of brain endothelial cells during embryonic development at bulk and single-cell levels. *Sci. Signal.* **10**, eaag2476 (2017). doi: [10.1126/scisignal.aag2476](https://doi.org/10.1126/scisignal.aag2476); pmid: 28698213
70. A. Bhaduri *et al.*, An atlas of cortical arealization identifies dynamic molecular signatures. *Nature* **598**, 200–204 (2021). doi: [10.1038/s41586-021-03910-8](https://doi.org/10.1038/s41586-021-03910-8); pmid: 34616070
71. J. J. Boyle, D. E. Bowyer, P. L. Weissberg, M. R. Bennett, Human blood-derived macrophages induce apoptosis in human plaque-derived vascular smooth muscle cells by Fas-ligand/Fas interactions. *Arterioscler. Thromb. Vasc. Biol.* **21**, 1402–1407 (2001). doi: [10.1161/hq0901.094279](https://doi.org/10.1161/hq0901.094279); pmid: 11557663
72. C. Sonesson, A. Srivastava, R. Patro, M. B. Stadler, Preprocessing choices affect RNA velocity results for droplet scRNA-seq data. *PLOS Comput. Biol.* **17**, e1008585 (2021). doi: [10.1371/journal.pcbi.1008585](https://doi.org/10.1371/journal.pcbi.1008585); pmid: 33428615
73. A. Srivastava, L. Malik, T. Smith, I. Sudbery, R. Patro, Alevin efficiently estimates accurate gene abundances from dscRNA-seq data. *Genome Biol.* **20**, 65 (2019). doi: [10.1186/s13059-019-1670-y](https://doi.org/10.1186/s13059-019-1670-y); pmid: 30917859
74. N. J. Bernstein *et al.*, Solo: Doublet identification in single-cell RNA-seq via semi-supervised deep learning. *Cell Syst.* **11**, 95–101.e5 (2020). doi: [10.1016/j.cels.2020.05.010](https://doi.org/10.1016/j.cels.2020.05.010); pmid: 32592658
75. C. Hafemeister, R. Satija, Normalization and variance stabilization of single-cell RNA-seq data using regularized negative binomial regression. *Genome Biol.* **20**, 296 (2019). doi: [10.1186/s13059-019-1874-1](https://doi.org/10.1186/s13059-019-1874-1); pmid: 31870423
76. I. Korsunsky *et al.*, Fast, sensitive and accurate integration of single-cell data with Harmony. *Nat. Methods* **16**, 1289–1296 (2019). doi: [10.1038/s41592-019-0619-0](https://doi.org/10.1038/s41592-019-0619-0); pmid: 31740819
77. E. Becht *et al.*, Dimensionality reduction for visualizing single-cell data using UMAP. *Nat. Biotechnol.* **37**, 38–44 (2018). doi: [10.1038/nbt.4314](https://doi.org/10.1038/nbt.4314); pmid: 30531897
78. V. A. Traag, L. Waltman, N. J. van Eck, From Louvain to Leiden: Guaranteeing well-connected communities. *Sci. Rep.* **9**, 5233 (2019). doi: [10.1038/s41598-019-41695-z](https://doi.org/10.1038/s41598-019-41695-z); pmid: 30914743
79. V. Bergen, M. Lange, S. Peidli, F. A. Wolf, F. J. Theis, Generalizing RNA velocity to transient cell states through dynamical modeling. *Nat. Biotechnol.* **38**, 1408–1414 (2020). doi: [10.1038/s41587-020-0591-3](https://doi.org/10.1038/s41587-020-0591-3); pmid: 32747759
80. D. G. Buniis, J. Andrews, G. K. Fragiadakis, T. D. Burt, M. Sirota, dittoSeq: Universal user-friendly single-cell and bulk RNA sequencing visualization toolkit. *Bioinformatics* **36**, 5535–5536 (2020). doi: [10.1093/bioinformatics/btaa1011](https://doi.org/10.1093/bioinformatics/btaa1011); pmid: 33313640
81. G. Korotkevich *et al.*, Fast gene set enrichment analysis. *bioRxiv* 060012 [Preprint] (2021). doi: [10.1101/060012](https://doi.org/10.1101/060012)
82. M. Andreatta, S. J. Carmona, UCell: Robust and scalable single-cell gene signature scoring. *Comput. Struct. Biotechnol. J.* **19**, 3796–3798 (2021). doi: [10.1016/j.csbj.2021.06.043](https://doi.org/10.1016/j.csbj.2021.06.043); pmid: 34285779
83. R. Patro, G. Duggal, M. I. Love, R. A. Izarrry, C. Kingsford, Salmon provides fast and bias-aware quantification of transcript expression. *Nat. Methods* **14**, 417–419 (2017). doi: [10.1038/nmeth.4197](https://doi.org/10.1038/nmeth.4197); pmid: 28263959
84. C. Sonesson, M. I. Love, M. D. Robinson, Differential analyses for RNA-seq: Transcript-level estimates improve gene-level inferences. *F1000Res.* **4**, 1521 (2015). doi: [10.12688/f1000research.7563.1](https://doi.org/10.12688/f1000research.7563.1); pmid: 26925227
85. M. D. Robinson, D. J. McCarthy, G. K. Smyth, edgeR: A Bioconductor package for differential expression analysis of digital gene expression data. *Bioinformatics* **26**, 139–140 (2010). doi: [10.1093/bioinformatics/btp616](https://doi.org/10.1093/bioinformatics/btp616); pmid: 19910308
86. C. Kim, Single cell atlas of the normal and malformed human brain vasculature, version 1, *Zenodo* (2022). doi: [10.5281/zenodo.5826205](https://doi.org/10.5281/zenodo.5826205)

ACKNOWLEDGMENTS

The authors acknowledge K. Probst and N. Srivassanti for creating schematics for the summary page figure and Figs. 1 and 3. **Funding:** This work was supported by National Institutes of Health grant U54NS065705 (E.A.W., H.K., and S.W.); National Institutes of Health grant ROINS034949 (H.K.); National Institutes of Health grant ROINS099268 (H.K.); National Institutes of Health grant ROIEB012031 (K.N.); National Institutes of Health grant ROINS034467 (B.V.Z.); National Institutes of Health grant SPO1AG052350 (B.V.Z.); National Institutes of Health grant ROINS112357 (D.A.L.); National Institutes of Health grant F32CA228372 (E.A.W.); National Institutes of Health grant U01MH115747 (T.J.N.); Brain Aneurysm Foundation grant (E.A.W.); Veterans Affairs Merit award (D.A.L.); and gifts from the William K. Bowes Jr Foundation, the Shurl and Kay Curci Foundation, and Schmidt Futures (T.J.N.). **Author contributions:** Conceptualization: E.A.W., C.N.K., D.L.C., M.T.L., B.V.Z., A.A.A., D.A.L., and T.J.N. Methodology: E.A.W., C.N.K., I.O., L.Q.C., and T.J.N. Formal analysis: E.A.W., C.N.K., J.M.R., I.O., L.Q.C., and T.J.N. Investigation: E.A.W., C.N.K., J.M.R., J.H.G., E.G., I.O., L.Q.C., D.W., J.S.C., K.R., and K.N. Visualization: E.A.W., J.M.R., and C.N.K. Resources: A.A.A., E.F.C., M.T.L., and N.G. Funding acquisition: E.A.W., H.K., B.P.W., N.G., and T.J.N. Project administration: E.A.W., H.K., S.W., D.A.L., and T.J.N. Supervision: A.A.A., D.A.L., and T.J.N. Writing, original draft: E.A.W., C.N.K., T.N., and D.A.L. Writing, review and editing: E.A.W., C.N.K., J.S.C., K.R., K.N., H.K., D.L.C., M.T.L., N.G., B.V.Z., D.A.L., and T.J.N. **Competing interests:** The authors declare that they have no competing interests. **Data and materials availability:** Data are available to explore with an interactive cell viewer: <https://adult-brain-vasc.cells.ucsc.edu>. Sequencing data have been deposited at dbGAP phs002624.v2.p1. All code is available at <https://github.com/cnk113/vascular-analysis> and (86). All other data are available in the main text or the supplementary materials.

SUPPLEMENTARY MATERIALS

science.org/doi/10.1126/science.abi7377
Figs. S1 to S12
Tables S1 to S10
MDAR Reproducibility Checklist

29 March 2021; resubmitted 23 September 2021
Accepted 19 January 2022
[10.1126/science.abi7377](https://doi.org/10.1126/science.abi7377)

RESEARCH ARTICLE SUMMARY

PLANT SCIENCE

A conserved superlocus regulates above- and belowground root initiation

Moutasem Omary[†], Naama Gil-Yarom[†], Chen Yahav, Evyatar Steiner, Anat Hendelman, Idan Efroni*

INTRODUCTION: Plants continuously adjust their body plans to adapt to the local environment by forming new organs in different developmental contexts. Underground, lateral roots initiate from designated cells in the pericycle of the main root. Aboveground, plants generate shoot-borne roots, bypassing the embryonic root-shoot lineage separation. Shoot-borne roots commonly form in response to stimuli such as flooding or wounding, but many plants also initiate these roots as part of their normal development. Indeed, fossil record evidence suggests that growth by shoot-bearing roots is an ancestral trait of flowering plants (angiosperms). However, the ontogeny of shoot-borne roots and its relationship to the initiation of lateral and wound-induced roots are unclear.

RATIONALE: Tomato (*Solanum lycopersicum*) is a vine that readily generates many roots from its stem as part of its normal development, making it an attractive model system with which to study shoot-borne root initiation. Here, we characterized the ontogeny of tomato shoot-borne roots at single-cell resolution. We used these data to identify a key regulator of shoot-borne root initiation and applied genetic and molecular characterization to multiple angiosperm species to test the functional and

regulatory conservation of shoot-borne and lateral root initiation programs.

RESULTS: To identify the origin of shoot-borne roots, we generated tomatoes carrying fluorescent reporters for early root initiation transcriptional responses. Using these, we show that tomato shoot-borne roots initiate from a small population of primary phloem-associated cells. We isolated these rare cells for single-cell mRNA-sequencing profiling, along with three other time points of shoot-borne root development. This analysis uncovered the existence of a transition state unique to the earliest stage of root meristem initiation. Trajectory reconstruction indicated that cells in this state were the progenitors of the new root stem cells and cap tissues.

The transition state was characterized by the expression of a *LATERAL ORGAN BOUNDARIES DOMAIN (LBD)* transcription factor that we named *SHOOT BORNE ROOTLESS (SBRL)* because loss of function of this gene resulted in plants lacking shoot-borne roots. High-resolution phylogenetic analysis of the *SBRL* family revealed that it belongs to an angiosperm-specific gene clade (subclass IIIB). We show that members of this clade had shoot-borne root-specific expression or function in multiple species (potato, *Arabidopsis*, sweet

potato, white beans, and sorghum). Further, previously identified regulators of shoot-borne root initiation in maize and rice were also classified as subclass IIIB genes, indicating that the shoot-borne root-specific function of this gene is deeply conserved.

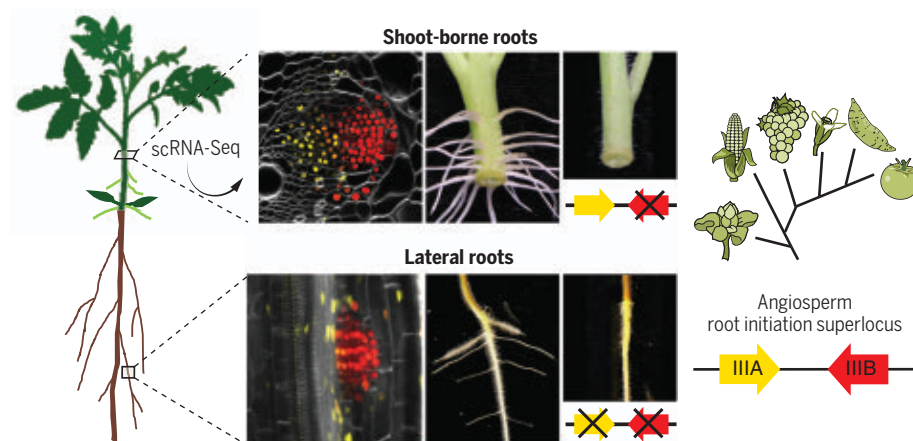
Comparative genomics identified that subclass IIIB genes are part of a conserved superlocus containing genes of the sister clade, subclass IIIA. Although subclass IIIA genes did not play a role in shoot-borne root initiation, we show that they control the initiation of underground lateral roots in multiple plant species. Similar to the function of subclass IIIB in shoot-borne roots, the expression of subclass IIIA genes was transient and correlated with the expression of transition state markers, suggesting a common mechanism for root meristem initiation.

Apart from naturally occurring shoot-borne roots, plants also form wound-induced roots. Genetic analysis identified at least two classes of these roots: The first is derived from stems and regulated by the subclass IIIB gene *SBRL*, and the second is derived from hypocotyl wound tissue and regulated by a subclass IIIA gene.

The conserved root-type-specific function of subclass IIIA and IIIB genes suggested that their regulatory program may be ancient. Indeed, the superlocus had a high level of noncoding sequence conservation, and tomato regulatory sequences were sufficient to drive transient shoot-borne- and lateral-root-specific expression even when used in the distant *Arabidopsis*.

Finally, to test whether this family regulates the initiation of all root types, we generated a tomato loss-of-function mutant for all three subclass IIIA/IIIB genes found in this species. These triple mutants lacked shoot-borne, lateral, and wound-induced roots, producing only a single barren embryonic root.

CONCLUSION: We conclude that root meristem formation initiates through a common transition state associated with deeply conserved subclass IIIA and IIIB genes. These genes control the initiation of different root types, with subclass IIIB playing a nonredundant role in shoot-borne root initiation and subclass IIIA acting in the initiation of lateral and some wound-induced roots. The appearance of a superlocus of subclass IIIA and IIIB genes in early angiosperm allowed specialization in the genetic regulation of different root types, enabling the plant's complex developmental response to varied environments. ■



Conserved regulation of root initiation. The initiation of tomato shoot-borne and lateral roots varies in developmental and hormonal dynamics. However, single-cell RNA-sequencing (scRNA-Seq) of shoot-borne roots revealed that they share a common transition state. An angiosperm-specific superlocus of transition-state-expressed genes governs root initiation, with the two superlocus members (subclass IIIA and IIIB genes) having conserved root-type-specific activity.

The list of author affiliations is available in the full article online.

*Corresponding author. Email: idan.efroni@mail.huji.ac.il

[†]These authors contributed equally to this work.

Cite this article as M. Omary et al., *Science* 375, eabf4368 (2022). DOI: 10.1126/science.abf4368

S READ THE FULL ARTICLE AT
<https://doi.org/10.1126/science.abf4368>

RESEARCH ARTICLE

PLANT SCIENCE

A conserved superlocus regulates above- and belowground root initiation

Moutasem Omary^{1†}, Naama Gil-Yarom^{1†}, Chen Yahav¹, Evyatar Steiner², Anat Hendelman³, Idan Efroni^{1*}

Plants continuously form new organs in different developmental contexts in response to environmental cues. Underground lateral roots initiate from prepatterned cells in the main root, but cells can also bypass the root-shoot trajectory separation and generate shoot-borne roots through an unknown mechanism. We mapped tomato (*Solanum lycopersicum*) shoot-borne root development at single-cell resolution and showed that these roots initiate from phloem-associated cells through a unique transition state. This state requires the activity of a transcription factor that we named *SHOOTBORNE ROOTLESS* (*SBRL*). Evolutionary analysis reveals that *SBRL*'s function and cis regulation are conserved in angiosperms and that it arose as an ancient duplication, with paralogs controlling wound-induced and lateral root initiation. We propose that the activation of a common transition state by context-specific regulators underlies the plasticity of plant root systems.

The body of vascular plants is divided into the root and shoot. Roots are formed through the activity of root meristems, which contain tissue-specific stem cells, or initials, arranged around slowly dividing quiescent cells and protected by the root cap (1). The primary root meristem is formed from the basal part of the embryo (2). After embryogenesis, lateral root meristems initiate from the pluripotent pericycle tissue of the primary root (3). Lateral root initiation is patterned by a periodic oscillatory mechanism that integrates auxin responses, root growth rates, localized cell wall modifications, and chemical signals to prime specific pericycle cells (4–9). Although the root-shoot lineages separate early during embryogenesis, most plants can also initiate shoot-borne roots to form multiple independent root systems. Reflecting the conceptual separation between the lineages, these roots are commonly referred to as “adventitious,” meaning “in the wrong place” (10). However, shoot-borne roots arise as part of the normal development of many plants, and according to the fossil record, root-bearing shoots were the dominant body plan of early angiosperms (11). Botanists distinguish between adventitious roots such as those induced by wounds and naturally occurring shoot-borne roots (12); however, little is known about the initiation of these roots, their tissue

of origin is disputed, and the ontogenetic relationships among shoot-borne, lateral, and wound-induced roots are unclear (13, 14).

Two plant hormones, auxin and cytokinin, play a key role in root initiation. Auxin response is activated in lateral root meristem progenitors, whereas response to cytokinin marks their flanking cells (15, 16). Auxin triggers multiple downstream processes, including promotion of cell growth and mitotic cell division, through the activation of *LATERAL ORGAN BOUNDARIES DOMAIN* (*LBD*) transcription factors (17). Other auxin-induced transcription factors, such as members of the *PLETHORA/AINTEGUMENTA* family (18), are required for the establishment of proper cell division patterns and, at later stages, for the acquisition of specific cell fates (19, 20).

Scarce evidence from monocots, in which shoot-borne roots form the bulk of the root system, suggests that similar genes may play a role in both shoot-borne and lateral root initiation. In maize and rice, shoot-borne root initiation requires the auxin-induced *LBD* transcription factors *ROOTLESS CONCERNING CROWN AND SEMINAL ROOT* (*RTCS*) and *CROWN ROOTLESS1* (*CRL1*), respectively (21–23), as well as the *PLETHORA/AINTEGUMENTA* (*PLT*) family protein *CRL5* (24). Not all gene families are shared between root types, however, because the *WUSCHEL*-like *WOX11* is specifically required for shoot-borne root development (25). The common model plant *Arabidopsis thaliana* lacks stem elongation and only rarely produces shoot-borne roots from its hypocotyl. Thus, to study dicot shoot-borne root initiation at high resolution, we turned to tomato (*Solanum lycopersicum*), a vine that naturally generates a large num-

ber of roots from easily accessible stems (Fig. 1, A to J).

Shoot-borne roots initiate from phloem-associated cells

Under our growth conditions, shoot-borne roots were observed on the first tomato internode 7 days after cessation of internode elongation (fig. S1, A and B). Roots continuously initiated from young internodes, forming a developmental gradient such that older internodes had more developed roots (Fig. 1, B to J). Anatomically, the stem is composed of an external epidermal layer, several layers of large cortex cells, and a layer of elongated starch-sheath cells containing starch granules. Internal to these is the vasculature tissue, the phloem with embedded phloem fibers (or pericyclic fibers), sieve cells, and accompanying companion cells. Further internal to the phloem are the cambium and xylem layers surrounding the stem pith (Fig. 1A and fig. S1, C to E). Shoot-borne roots formed at the vasculature tissue region and were preferentially located at the edge of vascular bundles (fig. S1, F and G). To study events before the activation of cellular proliferation, we generated a tomato carrying a dual-color transcriptional reporter for auxin (*DR5*) (26) and cytokinin (*TCSn*) (27) response (*DR5:mScarlet-NLS TCSn:mNeonGreen-NLS*). Before root meristem initiation, we observed sporadic expression of *TCSn* in the distal region of the phloem (Fig. 1K). In ~4-week-old plants, immediately after the cessation of internode elongation, root initiation events, which were marked by the induction of both auxin and cytokinin signaling in a group of 21 ± 4.4 cells, were observed in enlarged primary phloem parenchyma cells (Fig. 1L and fig. S1H). Subsequently, the expression of auxin and cytokinin response reporters separated into two domains, resembling a mature meristem, although regions of overlap remained (Fig. 1, M to P, and fig. S1I). We observed similar dynamics in tomatoes carrying the sensitive auxin response marker *pIAA* (*motif*) (28) (fig. S1, J to N). These events were used to define five stages of shoot-borne root formation: (i) *TCS* induction, (ii) *DR5/TCS* coexpression, (iii) expression domain expansion, (iv) primordia entry into cortex, and (v) *DR5/TCS* domain separation and mature meristem (Fig. 1, K to P). In *Arabidopsis*, a transient overlap of the auxin-cytokinin response was reported to occur during embryonic root meristem initiation (29) but not during lateral root initiation (15, 16). These hormonal dynamics were conserved in tomato, with initial lateral root cells marked by auxin response and flanked by cytokinin response-expressing cells (Fig. 1, Q to V), whereas in the tomato embryo, both auxin and cytokinin responses overlapped at the basal part, followed by domain separation (fig. S2, A to E). Overall, this shows that shoot-borne roots initiate from differentiated primary phloem parenchyma cells

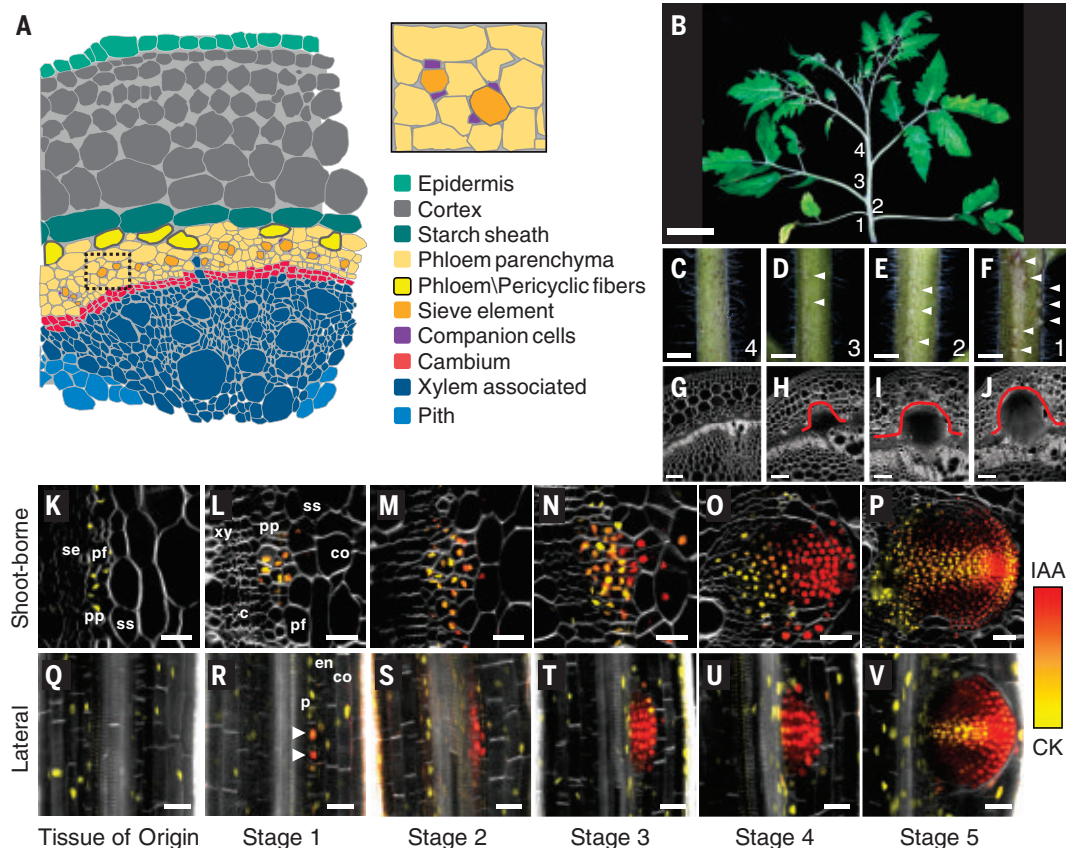
¹The Institute of Plant Science and Genetics in Agriculture, Faculty of Agriculture, The Hebrew University of Jerusalem, Rehovot, Israel. ²Department of Plant Sciences, Weizmann Institute of Science, Rehovot, Israel. ³Cold Spring Harbor Laboratory, Cold Spring Harbor, NY, USA.

*Corresponding author. Email: idan.efroni@mail.huji.ac.il

†These authors contributed equally to this work.

Fig. 1. Shoot-borne and lateral root formation in tomato.

(A) Two-dimensional illustration of the different cell types in the tomato stem and their spatial organization. Inset shows a magnification of the phloem region. (B) Eight-week-old tomato plant. (C to J) Close-up [(C) to (F)] and confocal images of cross-sections [(G) to (J)] of numbered internodes of the plant in (B) from young [(C) and (G)] to old [(F) and (J)]. Arrowheads in (D) to (F) indicate initiating shoot-borne roots. Red lines in (H) to (J) mark the root primordia. (K to V) Confocal images of *DR5::mScarlet-NLS TCSn::mNeonGreen-NLS* plants showing auxin (red) and cytokinin (yellow) responses at the different stages of shoot-borne [(K) to (P)] or lateral [(Q) to (V)] root development at corresponding developmental stages. Scale bars: (B), 5 cm; (C) to (F), 1 cm; (G) to (J), 50 μ m; and (K) to (V), 25 μ m. c, cambium; xy, xylem; pp, phloem parenchyma; pf, phloem/pericyclic fibers; se, sieve element; co, cortex; ss, starch sheath; p, pericycle; en-endodermis.



with an initiation program that distinguishes it from lateral roots.

Single-cell profiling reveals transitional cell state

To follow the trajectories of phloem parenchyma cells as they form root meristems, we generated single-cell mRNA-sequencing profiles of stage 1, 3 and 5 root meristems and from phloem-associated tissue of origin before root initiation. To isolate these very rare tissues, we staged and microdissected individual initiation events under a microscope, followed by cell disassociation and sorting based on hormonal response reporters using fluorescence-activated cell sorting (FACS; TCSn for tissue of origin, DR5 for root meristems; Figs. 1, K to P, and 2A). After quality control, we obtained 3087 cells (893, 621, 445, and 1128 cells from the tissue of origin at stages 1, 3, and 5, respectively; mean unique molecular identifiers/cell = 5680; mean genes/cell = 2843).

Louvain clustering (30) of the combined data from all stages identified 13 clusters (Fig. 2B and fig. S3A). To annotate these, we applied the index of cell identity (ICI) method, based on the published expression profiles of seven tomato root tissues (31, 32). Using 1669 identified marker genes (mean 273 markers/tissue;

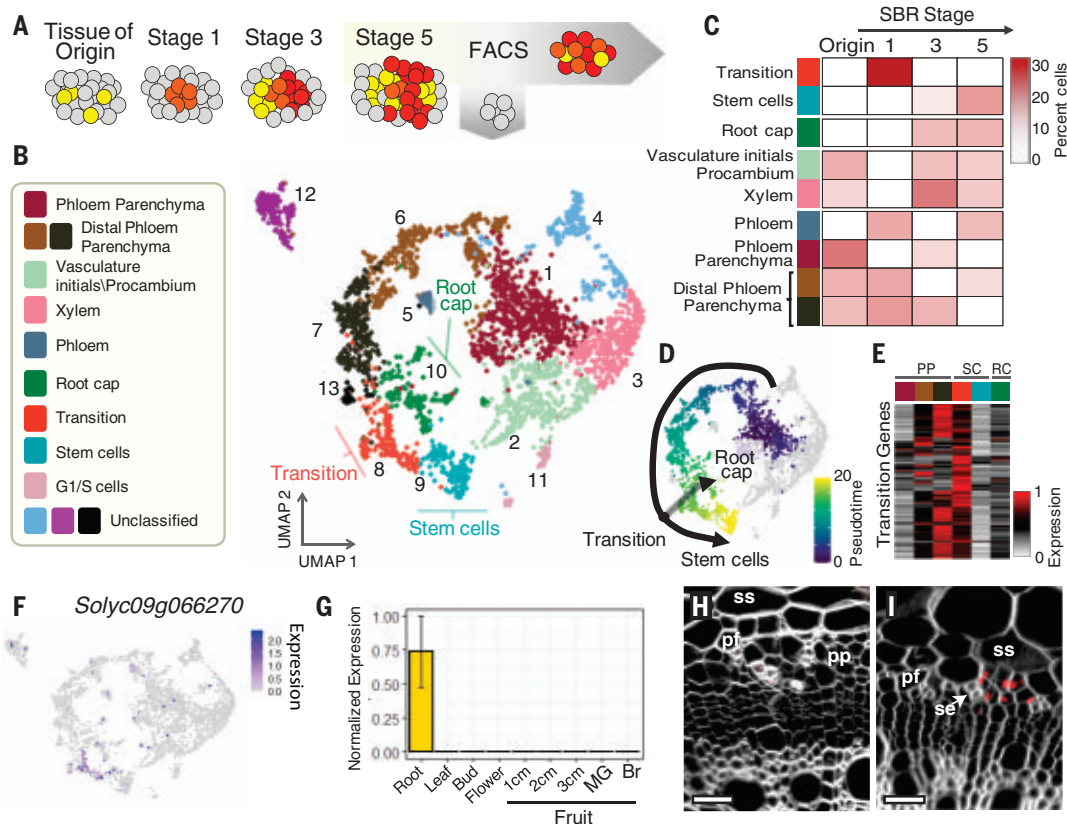
table S1), we obtained significant ICI classifications for 1861 cells [false discovery rate (FDR) < 0.05; fig. S3, B and C], identifying the xylem, phloem, stem cells, root cap, and vasculature initial clusters (clusters 3, 5, 8, 9, 10, and 2, respectively). A large number of cells were classified as root cortex parenchyma (clusters 1, 6, and 7), a tissue found in mature roots but absent from our microdissected tissues. Because these cells were enriched in the tissue of origin and stage 1 sorts (fig. S3A), we reasoned that they likely represented the morphologically similar phloem-associated parenchyma cells. To verify this, we generated a transcriptional reporter for *Solyc04g078650*, a tomato ortholog of the *Arabidopsis* *WOX4*, the expression of which was enriched in parenchyma clusters (fig. S3D; table S2), and that was previously reported to be expressed in tomato vasculature (33). Expression of *SIWOX4::mScarlet-NLS* was enriched in phloem parenchyma, and in situ hybridization revealed expression in phloem parenchyma and fibers (fig. S3, E to J). Among the *SIWOX4*-expressing parenchyma cells, cluster 6 specifically had mixed endodermis identity and was most abundant in stage 1 sort, which is enriched for distal phloem cells (Fig. 1K and fig. S3A). Although this root-specific tissue is not found in stems, this finding suggests the

existence of multiple identities or cell states within the parenchyma tissue (fig. S3C). Cluster 11 consisted of cells from multiple and mixed identities. Common to these cells was high expression of *G₁/S phase-associated cyclin A* genes, suggesting that the cluster represents cells at this distinct stage of the cell cycle (fig. S3K).

Gene Ontology (GO) term analyses for the clusters' markers (FDR < 0.01; mean 969 markers/cluster; table S2), based either on annotation of tomato or of likely *Arabidopsis* orthologs, were consistent with the ICI identity assignments showing enrichment of phloem histogenesis terms. Markers for phloem parenchyma and distal phloem clusters were enriched for photosynthesis terms (figs. S4 and S5). Indeed, light can penetrate these external tissues and chloroplasts are found in distal phloem cells (fig. S1D). DNA replication and ribosome biogenesis terms were enriched in stem cells (figs. S4 and S5). Current annotation of shoot identities is sparse, and three clusters (12, 4, and 13) had ICI scores consistent with general vascular identity but could not be reliably assigned to a previously described cell type.

Root-specific identities such as root cap and procambium were only found from stage 3 onward, indicating that cells only differentiate at

Fig. 2. Single-cell transcriptomics of shoot-borne root initiation. (A) Single-cell profiling experimental design. (B) Uniform manifold approximation and projection (UMAP) of cells from shoot-borne root development. (C) Composition of cell identities in each of the four stages expressed as a percentage of cells. (D) Trajectory of early stage identities. (E) Expression of transition genes along the phloem parenchyma to root trajectory. (F and G) Expression of *Solyc09g066270* from the single-cell data (F) and in the tomato expression atlas (36) (G). (H and I) Confocal images of *pSBRL::mScarlet-NLS-SBRLterm* in vascular tissue (H) and at stage 1 root meristems (I). Scale bars in (H) and (I), 25 μ m.



later stages of meristem initiation. By contrast, one-third of stage 1 cells were classified as phloem parenchyma or phloem, confirming that shoot-borne roots arise from this tissue (Fig. 2C). Two clusters (8 and 9) were classified as stem cells and were enriched for the expression of several root stem cell regulators (fig. S6). One of the stem cell clusters was only found in stage 1, where it made up ~30% of the cells. A monocle3 (34) trajectory analysis identified this cluster as a branching point between root cap and the stem cells (clusters 9 and 10, respectively; Fig. 2D), suggesting that this ephemeral cell identity, which we named “transition,” represents progenitors of the new shoot-borne root meristem. GO term enrichment for the two stem cell clusters was similar, but response to cytokinin and induction of the RNA interference machinery were unique to the transition cells. Overall, our single-cell analysis confirmed that shoot-borne roots arise from differentiated phloem parenchyma and identified a previously uncharacterized cell identity that is formed in the transition from phloem parenchyma to a root meristem.

SHOOTBORNE-ROOTLESS is required for root initiation

To identify potential regulators of transition stem cells, we searched for factors with expression that changed during the development from phloem parenchyma to stem cell and were enriched in transition compared with late-stage

stem cells (FDR < 0.01). This included 128 genes (Fig. 2E), of which five were transcription factors: an AP2/ERF, two MYBs, a C2H2 zinc finger, and an LBD (fig. S7A). Expression of the tomato *WOX11* ortholog *Solyc06g072890* (35) was not detected at all in our dataset, suggesting that its shoot-borne root-specific function may not be conserved. One of the candidates, the LBD gene *Solyc09g066270*, was highly specific to transition cells and had root-specific expression in the tomato transcriptional atlas [(36); Fig. 2, F and G, and fig. S7B]. A transcriptional reporter confirmed this expression pattern (Fig. 2, H and I). *Solyc09g066270* is a class IB LBD (37), and members of this class were previously linked to the regulation of root development downstream of auxin (17). Injection of auxin into tomato internode 1 induced the expression of *Solyc09g066270*. This induction was abolished by cotreatment with auxin and cytokinin (fig. S7C), consistent with the inhibitory effect of prolonged cytokinin treatment on root initiation (13).

To characterize the function of *Solyc09g066270*, we used CRISPR to generate four independent null alleles (Fig. 3A and table S3). Mutants germinated normally, were fertile, and had normal shoot morphology (Fig. 3, B and C). However, all had barren stems and hypocotyls that completely lacked roots, even under flooding conditions that induce root emergence in wild-type (WT) tomato (38) (Fig. 3, D to G). When tomato stems are cut from the main root

system, they readily form shoot-borne roots, but no such wound-induced roots formed in the mutant (Fig. 3, H and I). The hypocotyl has different ontogeny than the stem and is directly derived from embryonic tissue. Most of the wound-induced roots were lost in cut *sbrl* hypocotyls, but a small number of roots could still initiate from callus-like tissue formed at the wound site, indicating that these roots may be under distinct genetic regulation (Fig. 3, J and K, and fig. S8A). In accordance with its function, we named the gene *SHOOTBORNE-ROOTLESS* (*SBRL*). To determine whether the defect in *sbrl* mutants was in root initiation or emergence, we generated *sbrl DR5::VENUS-NLS* plants. We were unable to find *DR5*-expressing stage 1 or aberrant cell divisions in phloem tissue in six individual plants, suggesting that *SBRL* is specifically required for the earliest stage of root initiation (fig. S8, B and C).

Conservation of shoot-borne roots initiation program

The complete loss of shoot-borne roots in *sbrl* was reminiscent of the *rtcs* and *crli* mutations in the distant monocots maize and rice, which are also caused by disruption to class IB LBD genes (21, 22). To determine the evolutionary relationship between these genes, we generated a maximum likelihood tree of 845 class IB genes from 94 plant species [(37); table S4, Fig. 3L, and fig. S9]. This high-resolution analysis revealed that, rather than a single subclass, as

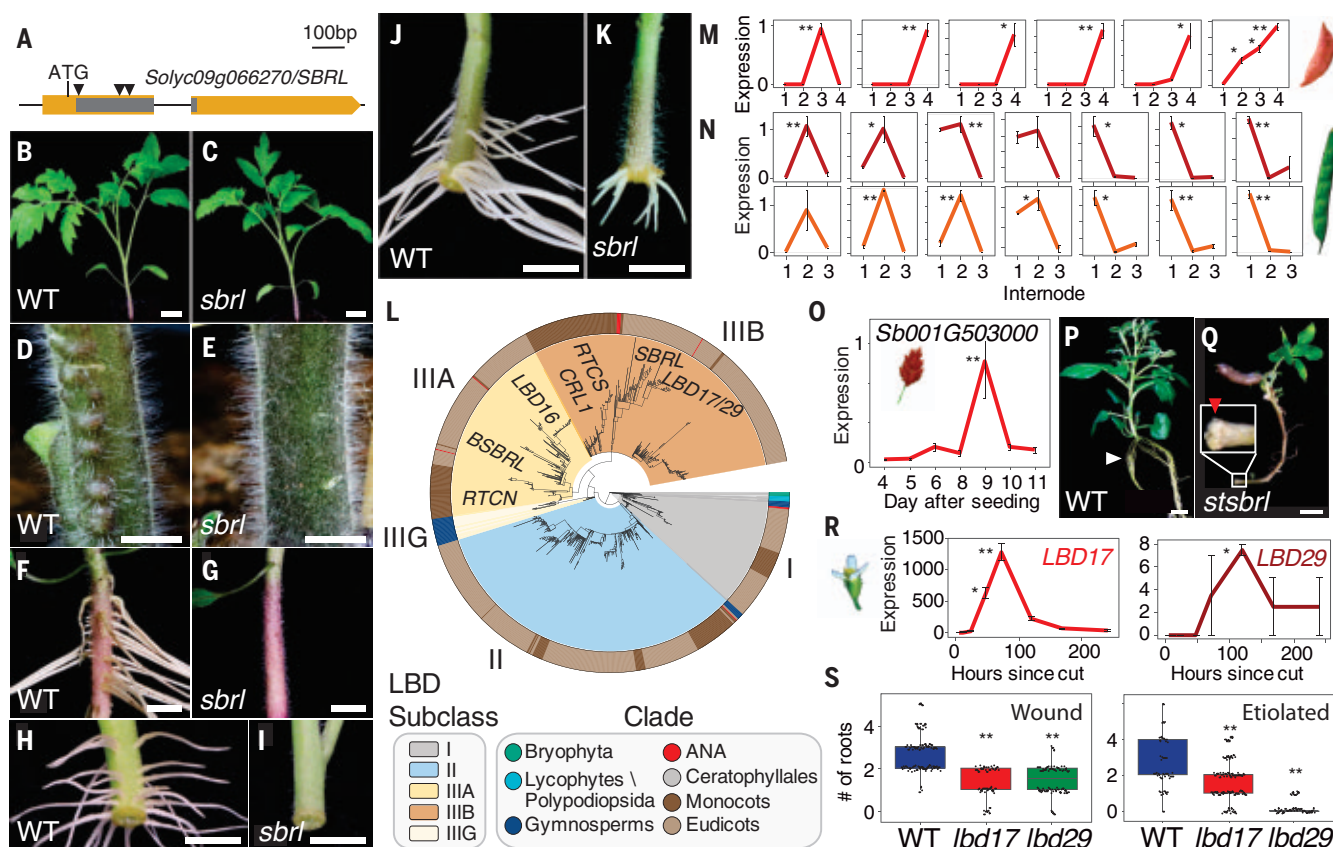


Fig. 3. SBRL regulates shoot-borne root initiation in angiosperms.

(A) Structure of *SBRL*. The LBD is shown in gray. Arrowheads indicate guide RNA (gRNA) targets. (B and C) Four-week-old tomato plants. (D and E) First internode of 8-week-old tomato plants. (F and G) Four-week-old tomato hypocotyls after 1 week of flooding. (H to K) Cut first internode [(H) and (I)] or hypocotyls [(J) and (K)] 1 week after the cut. (L) Maximum likelihood tree of class IB LBDs. Branches with transfer bootstrap expectation < 0.7 were collapsed. See also high-resolution tree in fig S9. (M and N) Expression of the subclass IIIB genes *gl5530* of *I. batatas* (M) and *Pv1G159400* (top) and *Pv7G19500* (bottom) of *P. vulgaris* (N). Each graph shows expression in stem sections of a single plant. In *I. batatas*, shoot-borne roots are apparent on node 5 or 6; in *P. vulgaris*, they are seen on internode 3 (see fig. S11).

(O) Expression of class IIIB gene in the crown root region of *S. bicolor* ($n = 4$ or 5 for each time point). Crown roots appear after day 11 (see fig. S11). (P and Q) WT and *stsbtrl* potato plants. White arrowhead marks shoot-borne roots, and red arrowhead marks the wound callus. *stsbtrl* mutants are slow growing and develop tubers in culture, likely due to systemic effects. (R) Expression of *Arabidopsis* subclass IIIB genes in cut hypocotyls (42). (S) Number of roots formed on *Arabidopsis* hypocotyls after the removal of the root system (left) or induced by etiolation (right) ($n = 95, 53$, and 76 for WT, *lbd17*, and *lbd29* plants, respectively). Error bars indicate SE. Asterisks indicate statistical significant difference from baseline (WT or time 0 hour; * $P < 0.05$; ** $P < 0.001$; Tukey's test). Scale bars in (B) to (K), (P), and (Q), 2 cm.

was previously reported (37), class IB LBDs form five distinct subclasses with subclass-specific protein motifs (fig. S10). Subclass I was found in ferns and all seed plants and likely represents the original member of the class. The moss and lycophytes genes were similar to subclass I but formed an outgroup to the five clades. Subclass II appeared in seed plants. Subclass III was divided into the gymnosperms-only subclass IIIG and the angiosperm-specific subclasses IIIA and IIIB. *SBRL*, *RTCS*, and *CRL1* were all classified as subclass IIIB (Fig. 3L).

Monocots and dicots are separated by ~150 million years (39), and both their vasculature anatomy and shoot-borne root physiology differ. That a mutation in a single subclass IIIB gene led to the loss of shoot-borne roots in all three species raised the hypothesis that the genetic

regulation of these roots' initiation may be deeply conserved in plants. We tested whether the expression of subclass IIIB genes were induced during natural shoot-borne root initiation in two other dicots: sweet potato (*Ipomoea batatas*) and white bean (*Phaseolus vulgaris*). Shoot-borne root initiation could not be synchronized in these species, so we took advantage of the fact that roots formed a developmental gradient along the stem (fig. S11, A to N) and sampled the different stem sections of individual plants. Quantitative reverse transcription polymerase chain reaction (qRT-PCR) analysis showed that, in all cases, class IIIB genes were induced just before the morphological appearance of root meristems (Fig. 3, M and N). To test whether these expression patterns were conserved within monocots, we tested the expression of class IIIB genes during

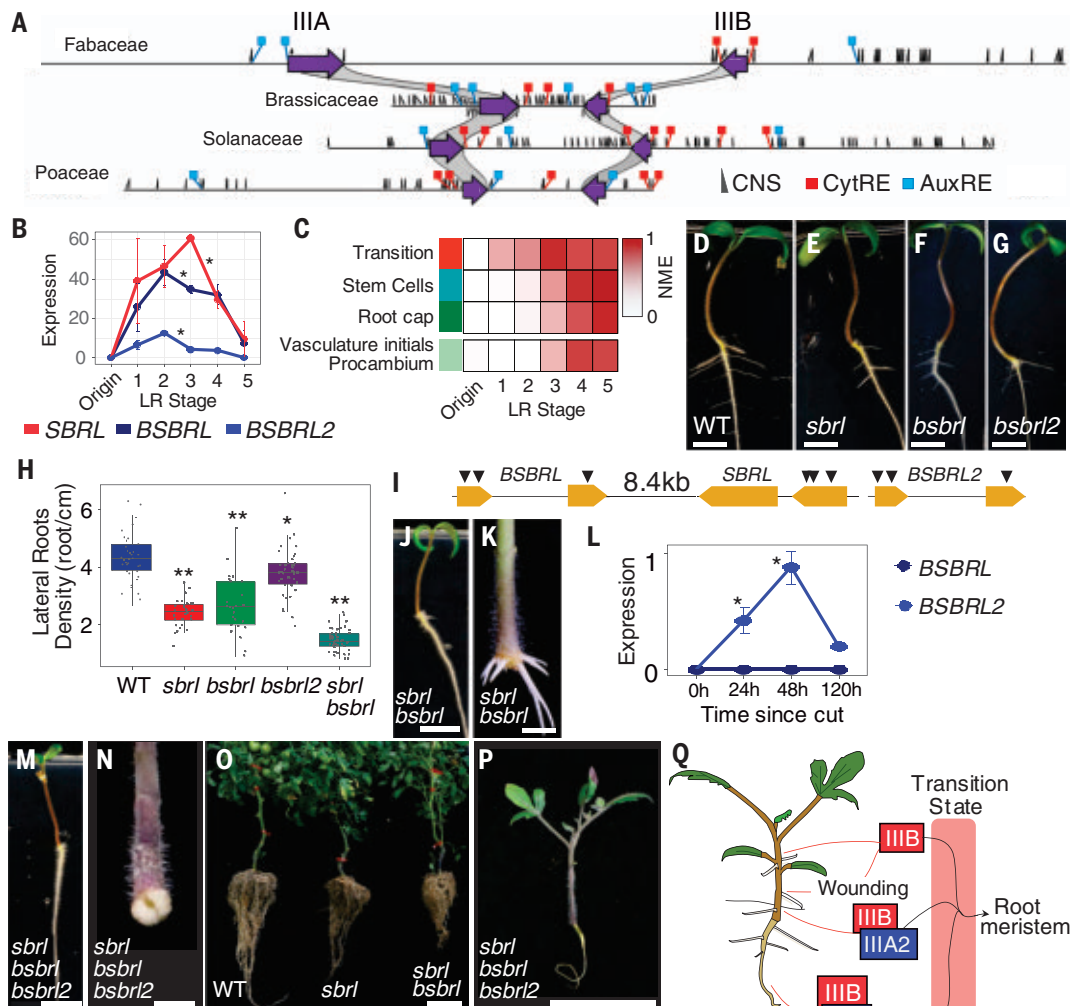
the initiation of *Sorghum bicolor* shoot-borne crown roots. As in dicots, a transient expression of this gene was detected before the morphological appearance of crown roots (Fig. 3O and fig. S11, O to R).

To determine whether the function of subclass IIIB is conserved, we generated CRISPR mutants in the potato (*Solanum tuberosum*) ortholog of *SBRL*, *StSBRL* (table S3). Potato readily generates shoot-borne roots when propagated in culture, but three independently derived CRISPR-homozygous mutants failed to form roots (Fig. 3, P and Q). *Arabidopsis* lacks elongated internodes but can form a few roots on its hypocotyl when it is cut from the main root system or when etiolated seedlings are exposed to light (40, 41). Two close *SBRL Arabidopsis* homologs resulting from a Brassicaceae-specific duplication (*LBD17/29*)

Fig. 4. A conserved superlocus regulates lateral root initiation.

(A) Synteny and cis-regulatory sequence conservation in the *SBRL-BSBRL* superlocus. Black triangles mark conserved noncoding sequences. Red and blue squares mark conserved cytokinin and auxin response elements, respectively (CytRE: TGATTA; AuxRE: TGTCTC/CC/GG). (B) Expression of subclass IIIA/IIIB LBDs during tomato lateral root development. (C) Average expression of tissue identity markers during lateral root development. (D to G) Ten-day-old WT (D) and mutant [(E) to (G)] tomato seedlings. (H) Lateral root density in 10-day-old tomato seedlings ($n = 50, 30, 25, 40,$ and 50 for WT, *sbri*, *bsbri*, *bsbri2*, and *sbri bsbri*, respectively). (I) Gene structure of the *SBRL-BSBRL* superlocus and *BSBRL2*. Arrowheads mark gRNA targets. (J and K) Ten-day-old seedling (J) and cut hypocotyl 10 days after the cut (K) of *sbri bsbri* double mutants. (L) qRT-PCR expression of subclass IIIA genes during wound-induced root initiation on *sbri* hypocotyl ($n = 5$). (M and N) Ten-day-old seedling (M) and cut hypocotyl 10 days after the cut (N) of *sbri bsbri bsbri2* triple mutants. (O and P) Three-month-old pot-grown tomato plants. (Q) Model for the initiation of different root types in angiosperms.

Error bars indicate SE. Asterisks indicate statistically significant difference from baseline (WT or time 0 hours; * $P < 0.05$; ** $P < 0.001$). Data in (H) and (L) were analyzed with Tukey's test; data in (B) were analyzed by Welch's test. Scale bars: (D) to (G), (J), (K), (M), and (N), 1 cm; (O) and (P), 10 cm.



were transiently induced in the hypocotyl after removal of the root system [Fig. 3R; (42)]. Both CRISPR-generated null *lbd17* and *lbd29* mutants had reduced number of roots on cut hypocotyl. Similarly, both mutants exhibited a reduction in the number of roots developed on the hypocotyls of etiolated seedlings. However, *lbd29* mutants had a more significant reduction in the number of these roots (Fig. 3S and table S3; $P < 0.001$; Tukey's honestly significant difference), suggesting subfunctionalization of these paralogs. Finally, our hypothesis is supported by the evolutionary retention of subclass IIIB genes, because they were lacking only in three angiosperm species, two carnivorous plants, *Aldrovanda vesiculosa* and *Utricularia gibba*, and the water plant *Ceratophyllum demersum* (table S4). Common to all three is that they lost their roots during evolution. Taken together, our data indicate that the initiation program of shoot-borne

roots and its specific regulation by subclass IIIB LBDs is deeply conserved in angiosperms.

Deep conservation of an LBD superlocus

During the assembly of the phylogenetic tree, we observed that subclass IIIB genes were almost always located immediately next to a closely related subclass IIIA gene in a single superlocus that exists already in basal-diverging angiosperms (fig. S13 and table S4). Cis-regulatory conservation analysis of 80 plant species from four families using the Conservatory algorithm (43), revealed broad conservation of noncoding regions within the locus, including multiple auxin and cytokinin response elements [Fig. 4A and table S5; (28)], supporting the existence of a conserved regulatory program for the entire locus. To test whether the function of this regulatory sequence is conserved, we constructed a dual reporter of the tomato regulatory sequences of *SBRL* and its

syntenic subclass IIIA gene *BROTHER OF SBRL* (*BSBRL*; *pBSBRL:mNeonGreen-NLS-BSBRLterm* *pBSBRL:mScarlet-NLS-SBRLterm*) and introduced it into *Arabidopsis*. Despite these species having diverged ~120 million years ago (39), the tomato regulatory sequence was sufficient to drive *mScarlet* expression in root primordia that formed on the *Arabidopsis* hypocotyl after removal of the root system (fig. S12, A to I).

The sequence similarity of subclass IIIA and IIIB genes suggests that they perform similar functions, but neither *BSBRL* nor its Solanaceae-specific duplication *BSBRL2* were detected in our single-cell expression dataset. *RTCN* and *LBD16*, the maize and *Arabidopsis* subclass IIIA genes (table S4), respectively, were previously linked to the regulation of lateral root development (17), suggesting that, similar to subclass IIIB function in shoot-borne roots, subclass IIIA genes may play a conserved role in lateral root initiation. To test

this hypothesis, we generated a transcriptional time series of tomato lateral root initiation (Fig. 1, Q to V, and fig. S14A). Both subclass IIIA and IIIB genes were transiently induced in initiating lateral roots, an expression pattern that was conserved in *I. batatas*, *P. vulgaris*, and *S. bicolor* (Fig. 4B and fig. S14, B to H). Furthermore, in *Arabidopsis*, the tomato regulatory sequence drove the transient coinduction of both markers in lateral root primordia. Some ectopic expression was observed in these lines, but because of technical limitations, only a subset of the conserved noncoding region in the 34-kb locus are present in our reporter (fig. S12, J to U). Regardless, these results confirm that the transient expression of subclass IIIA/IIIB gene in lateral root primordia and the core regulatory code driving it are deeply conserved.

To test whether the transient activation of subclass IIIA/IIIB LBD occurs within the context of a transition identity, we used the average expression of markers for the different shoot-borne root identities (table S2) to map the activation of each identity during lateral root development. Transition stem cell markers were the first to be induced, followed by markers of root cap, stem cells, and vasculature initials. This is consistent with the late acquisition of mature root cell identities that was recently reported in an analysis of *Arabidopsis* lateral root initiation (44). The sequence of identity transitions recapitulated that of shoot-borne roots, suggesting that subclass IIIA/IIIB may mediate similar processes in both cases (Fig. 4C).

Root-type-specific regulation by LBD genes

To test the functional role of subclass IIIA genes, we generated CRISPR mutants for tomato *bsb1* and *bsb2*. Both these and *sb1* mutants exhibited a mild but significant reduction in the number of lateral roots, as did mutants of the orthologous genes in *Arabidopsis* (Fig. 4, D to H; and fig. S14I; and table S3). By contrast, stems of both the *bsb1* and *bsb2* mutants had normal shoot-borne root formation (fig. S14, J and K), and the number of roots forming on cut stems was not significantly different from that of WT (19 ± 1.4 , 16.3 ± 3 , and 19.4 ± 2.72 roots for WT, *bsb1*, and *bsb2*, respectively; $n = 6$). To test whether the genes play a redundant function in lateral root initiation, we used a six-guide multiplex CRISPR to target the entire *SBRL-BSBRL* superlocus and examined four independently derived alleles (Fig. 4I and table S3). All *sb1 bsb1* double mutants completely lacked shoot-borne roots and exhibited a significant reduction in the number of lateral roots, whereas the shoot remained unaffected (Fig. 4, H and J). Cut hypocotyl of the double mutant could still produce wound-induced roots (Fig. 4K). Time series expression analysis of these wound-induced hypocotyl roots in *sb1* mutants revealed that the duplicated subclass IIIA gene *BSBRL2*, but

not *BSBRL*, was transiently induced in this root type (Fig. 4L). To test whether these wound-induced roots are subclass IIIA/IIIB dependent, we generated a triple *sb1 bsb1 bsb2* mutant. Although slow to germinate, these plants formed normal primary embryonic roots (Fig. 4M; germinated at 2.6 ± 0.7 and 6.6 ± 1.1 days after sowing for WT and the triple mutant, respectively; $n = 49$ and 22). No wound-induced roots could form on cut hypocotyls of the triple mutant, with only callus-like cell proliferation apparent at the cut site (Fig. 4N). Furthermore, whereas the single and double *sb1 bsb1* mutants could still develop a substantial branched root system when grown in soil (Fig. 4O), no postembryonic roots at all were developed in plants lacking the three subclass IIIA/IIIB genes, either when grown on plates or in soil (Fig. 4, M and P). Our data show that subclass IIIA/IIIB genes, which appeared in early angiosperms, are required for the initiation of postembryonic roots, with a conserved program driving individual paralogs to control root initiation in different developmental contexts.

It has been hypothesized that roots forming in different contexts differ in their early ontogeny but converge on a similar genetic program (14). Indeed, we show here that lateral and shoot-borne roots differ in terms of the number of initial cells involved and their hormonal dynamics. However, the data presented suggest a different model in which a common LBD-associated transition identity is shared among all root initiation events. We propose that the regulation of this common state by root-type-specific subclass IIIA/IIIB genes allows the specialization of different root types and thus is responsible for the diversity in root systems found in angiosperms (Fig. 4Q). Consistently, the initiation of nodules, a legume-specific lateral root-derived structure specialized for rhizobia interaction, is controlled by a legume-specific duplication of a subclass IIIA gene (45, 46). The specific function of these genes and their conserved cis-regulatory program make them a prime target for the custom design of root system architectural traits.

Methods summary

Tomato [*S. lycopersicum* cultivar (cv) M82] seeds were germinated on soil, grown under 16-hour/8-hour light/dark conditions at 24°C for 6 weeks, and then transplanted to 10-liter pots in climate-controlled greenhouses (natural day length, 25°/20°C day/night temperature). *P. vulgaris* and *S. bicolor* were germinated in a closed, moist chamber at room temperature, and 10-day-old seedlings were transferred to 5-liter pots in greenhouses. *I. batatas* cv Georgia Jet was grown from tubers in water at room temperature under ambient light. Seeds of *Arabidopsis* (Col-0) were grown on agar medium plates (0.5× Murashige and Skoog containing 0.5% sucrose and 0.8% agar), strati-

fied for 3 days at 4°C in the dark, and transferred to a 16-/8-hour light/dark, 21°C growth chamber. CRISPR constructs were performed using plant codon-optimized Cas9 with up to six guide RNAs. Transgenic plants were created by cotyledon transformation for tomato, leaf explant transformation for *S. tuberosum* cv. Désirée, and floral dipping for *Arabidopsis*.

For single-cell analysis, cells from tomato internode 1 hand-dissected sections were dissociated in cell wall digestion solution for up to 1 hour, followed by cell separation using FACS into a 96-well plates. Collected RNA from 16 biological replicates was amplified, sequenced, and aligned to the ITAG4 genome with extended 3' untranslated regions. Data normalization, scaling, and principal components analysis was performed with Seurat version 3 software using the default parameters. After batch and stage correction clusters were identified using the Louvain algorithm with multilevel refinement. Pseudotime trajectory analysis was performed using monocle3 (34) on cells from the parenchyma, stem cells, and root cap clusters. Identity classification were performed using ICI as previously described (32). GO term enrichment was performed using the goseq R package. GO terms with $P < 0.05$, as determined by the hypergeometric test, were considered significant.

In situ hybridization was performed using first internode of 4-week-old tomato plants. Antisense digoxigenin-labeled probes of SIWOX4 (Solyc04g078650) and the negative control H4 (Solyc04g011390), the expression of which was confined to the G₁/S phase, were produced by in vitro transcription.

For the phylogenetic analysis, class IB sequences were identified by searching the proteomes of all species for the canonical LBD class IB sequence (37). BLASTX was used to identify unannotated LBD transcripts. Protein sequences were aligned using MUSCLE, and the tree was constructed using IQ-tree2 with automatic model detection and 1000 bootstrap replicates. Conserved noncoding sequences were identified using Conservatory as described previously (43).

Transcriptional developmental series of tomato lateral root development was collected by manually dissecting 0.5-mm root slices from *DR5:3xVENUS-NLS* plants grown on agar plates. RNA was extracted from slices, followed by amplification and library preparation using the QuantSeq 3' mRNA-Seq Library Prep Kit.

REFERENCE AND NOTES

1. J. J. Petricka, C. M. Winter, P. N. Benfey, Control of *Arabidopsis* root development. *Annu. Rev. Plant Biol.* **63**, 563–590 (2012). doi: [10.1146/annurev-arplant-042811-105501](https://doi.org/10.1146/annurev-arplant-042811-105501); pmid: [22404466](https://pubmed.ncbi.nlm.nih.gov/22404466/)
2. C. I. L. Peris, E. H. Rademacher, D. Weijers, Green beginnings - pattern formation in the early plant embryo. *Curr. Top. Dev. Biol.* **91**, 1–27 (2010). doi: [10.1016/S0070-2153\(10\)91001-6](https://doi.org/10.1016/S0070-2153(10)91001-6); pmid: [20705177](https://pubmed.ncbi.nlm.nih.gov/20705177/)

3. K. Sugimoto, S. P. Gordon, E. M. Meyerowitz, Regeneration in plants and animals: Dedifferentiation, transdifferentiation, or just differentiation? *Trends Cell Biol.* **21**, 212–218 (2011). doi: [10.1016/j.tcb.2010.12.004](https://doi.org/10.1016/j.tcb.2010.12.004); pmid: 21236679
4. G. Wachsman, J. Zhang, M. A. Moreno-Risueno, C. T. Anderson, P. N. Benfey, Cell wall remodeling and vesicle trafficking mediate the root clock in *Arabidopsis*. *Science* **370**, 819–823 (2020). doi: [10.1126/science.abb7250](https://doi.org/10.1126/science.abb7250); pmid: 33184208
5. W. Xuan *et al.*, Cyclic programmed cell death stimulates hormone signaling and root development in *Arabidopsis*. *Science* **351**, 384–387 (2016). doi: [10.1126/science.aad2776](https://doi.org/10.1126/science.aad2776); pmid: 26798015
6. T. van den Berg *et al.*, A reflux-and-growth mechanism explains oscillatory patterning of lateral root branching sites. *Dev. Cell* **56**, 2176–2191.e10 (2021). doi: [10.1016/j.devcel.2021.07.005](https://doi.org/10.1016/j.devcel.2021.07.005); pmid: 34343477
7. I. De Smet *et al.*, Auxin-dependent regulation of lateral root positioning in the basal meristem of *Arabidopsis*. *Development* **134**, 681–690 (2007). doi: [10.1242/dev.02753](https://doi.org/10.1242/dev.02753); pmid: 17215297
8. M. A. Moreno-Risueno *et al.*, Oscillating gene expression determines competence for periodic *Arabidopsis* root branching. *Science* **329**, 1306–1311 (2010). doi: [10.1126/science.1191937](https://doi.org/10.1126/science.1191937); pmid: 20829477
9. A. J. Dickinson *et al.*, A plant lipocalin promotes retinal-mediated oscillatory lateral root initiation. *Science* **373**, 1532–1536 (2021). doi: [10.1126/science.abf7461](https://doi.org/10.1126/science.abf7461); pmid: 34446443
10. K. Esau, *Anatomy of Seed Plants* (Wiley, 1977).
11. A. J. Hetherington, L. Dolan, Evolution: Diversification of angiosperm rooting systems in the Early Cretaceous. *Curr. Biol.* **29**, R1081–R1083 (2019). doi: [10.1016/j.cub.2019.08.030](https://doi.org/10.1016/j.cub.2019.08.030); pmid: 31639353
12. P. Groff, D. R. Kaplan, The relation of root systems to shoot systems in vascular plants. *Bot. Rev.* **54**, 387–422 (1988). doi: [10.1007/BF02858417](https://doi.org/10.1007/BF02858417)
13. C. Bellini, D. I. I. Pacurar, I. Perrone, Adventitious roots and lateral roots: Similarities and differences. *Annu. Rev. Plant Biol.* **65**, 639–666 (2014). doi: [10.1146/annurev-arplant-050213-035645](https://doi.org/10.1146/annurev-arplant-050213-035645); pmid: 24555710
14. K. D. Birnbaum, How many ways are there to make a root? *Curr. Opin. Plant Biol.* **34**, 61–67 (2016). doi: [10.1016/j.pbi.2016.10.001](https://doi.org/10.1016/j.pbi.2016.10.001); pmid: 27780106
15. L. Chang, E. Ramireddy, T. Schmittling, Cytokinin as a positional cue regulating lateral root spacing in *Arabidopsis*. *J. Exp. Bot.* **66**, 4759–4768 (2015). doi: [10.1093/jxb/erv252](https://doi.org/10.1093/jxb/erv252); pmid: 26019251
16. A. Bielach *et al.*, Spatiotemporal regulation of lateral root organogenesis in *Arabidopsis* by cytokinin. *Plant Cell* **24**, 3967–3981 (2012). doi: [10.1105/tpc.112.103044](https://doi.org/10.1105/tpc.112.103044); pmid: 23054471
17. J. Lavenus *et al.*, Lateral root development in *Arabidopsis*: Fifty shades of auxin. *Trends Plant Sci.* **18**, 450–458 (2013). doi: [10.1016/j.tplants.2013.04.006](https://doi.org/10.1016/j.tplants.2013.04.006); pmid: 23701908
18. C. Galinha *et al.*, PLETHORA proteins as dose-dependent master regulators of *Arabidopsis* root development. *Nature* **449**, 1053–1057 (2007). doi: [10.1038/nature06206](https://doi.org/10.1038/nature06206); pmid: 17960244
19. Y. Du, B. Scheres, Lateral root formation and the multiple roles of auxin. *J. Exp. Bot.* **69**, 155–167 (2018). doi: [10.1093/jxb/erx223](https://doi.org/10.1093/jxb/erx223); pmid: 28992266
20. H. Hofhuis *et al.*, Phyllotaxis and rhizotaxis in *Arabidopsis* are modified by three PLETHORA transcription factors. *Curr. Biol.* **23**, 956–962 (2013). doi: [10.1016/j.cub.2013.04.048](https://doi.org/10.1016/j.cub.2013.04.048); pmid: 23684976
21. G. Taramino *et al.*, The maize (*Zea mays* L.) RTCS gene encodes a LOB domain protein that is a key regulator of embryonic seminal and post-embryonic shoot-borne root initiation. *Plant J.* **50**, 649–659 (2007). doi: [10.1111/j.1365-3113.2007.03075.x](https://doi.org/10.1111/j.1365-3113.2007.03075.x); pmid: 17425722
22. Y. Inukai *et al.*, Crown rootless1, which is essential for crown root formation in rice, is a target of an AUXIN RESPONSE FACTOR in auxin signaling. *Plant Cell* **17**, 1387–1396 (2005). doi: [10.1105/tpc.105.030981](https://doi.org/10.1105/tpc.105.030981); pmid: 15829602
23. H. Liu *et al.*, ARL1, a LOB-domain protein required for adventitious root formation in rice. *Plant J.* **43**, 47–56 (2005). doi: [10.1111/j.1365-3113.2005.02434.x](https://doi.org/10.1111/j.1365-3113.2005.02434.x); pmid: 15960615
24. Y. Kitomi *et al.*, The auxin responsive AP2/ERF transcription factor CROWN ROOTLESS5 is involved in crown root initiation in rice through the induction of OsRR1, a type-A response regulator of cytokinin signaling. *Plant J.* **67**, 472–484 (2011). doi: [10.1111/j.1365-3113.2011.04610.x](https://doi.org/10.1111/j.1365-3113.2011.04610.x); pmid: 21481033
25. Y. Zhao, Y. Hu, M. Dai, L. Huang, D.-X. Zhou, The WUSCHEL-related homeobox gene WOX11 is required to activate shoot-borne crown root development in rice. *Plant Cell* **21**, 736–748 (2009). doi: [10.1105/tpc.108.061655](https://doi.org/10.1105/tpc.108.061655); pmid: 19258439
26. T. Ulmasov, Z. B. Liu, G. Hagen, T. J. Guilfoyle, Composite structure of auxin response elements. *Plant Cell* **7**, 1611–1623 (1995). pmid: 7580254
27. E. Zürcher *et al.*, A robust and sensitive synthetic sensor to monitor the transcriptional output of the cytokinin signaling network in planta. *Plant Physiol.* **161**, 1066–1075 (2013). doi: [10.1104/pp.112.211763](https://doi.org/10.1104/pp.112.211763); pmid: 23355633
28. M. Lieberman-Lazarovich, C. Yahav, A. Israeli, I. Efroni, Deep conservation of cis-element variants regulating plant hormonal responses. *Plant Cell* **31**, 2559–2572 (2019). doi: [10.1105/tpc.19.00129](https://doi.org/10.1105/tpc.19.00129); pmid: 31467248
29. B. Müller, J. Sheen, Cytokinin and auxin interaction in root stem-cell specification during early embryogenesis. *Nature* **453**, 1094–1097 (2008). doi: [10.1038/nature06943](https://doi.org/10.1038/nature06943); pmid: 18463635
30. T. Stuart *et al.*, Comprehensive integration of single-cell data. *Cell* **177**, 1888–1902.e21 (2019). doi: [10.1016/j.cell.2019.05.031](https://doi.org/10.1016/j.cell.2019.05.031); pmid: 31178118
31. K. Kajala *et al.*, Innovation, conservation, and repurposing of gene function in root cell type development. *Cell* **184**, 3333–3348.e19 (2021). doi: [10.1016/j.cell.2021.04.024](https://doi.org/10.1016/j.cell.2021.04.024); pmid: 34010619
32. I. Efroni, P.-L. Ip, T. Nawy, A. Mello, K. D. Birnbaum, Quantification of cell identity from single-cell gene expression profiles. *Genome Biol.* **16**, 9 (2015). doi: [10.1186/s13059-015-0580-x](https://doi.org/10.1186/s13059-015-0580-x); pmid: 25608970
33. J. Ji *et al.*, WOX4 promotes procambial development. *Plant Physiol.* **152**, 1346–1356 (2010). doi: [10.1104/pp.109.149641](https://doi.org/10.1104/pp.109.149641); pmid: 20044450
34. J. Cao *et al.*, The single-cell transcriptional landscape of mammalian organogenesis. *Nature* **566**, 496–502 (2019). doi: [10.1038/s41586-019-0969-x](https://doi.org/10.1038/s41586-019-0969-x); pmid: 30787437
35. C. Wang *et al.*, The WOX family transcriptional regulator SILAM1 controls compound leaf and floral organ development in *Solanum lycopersicum*. *J. Exp. Bot.* **72**, 1822–1835 (2021). doi: [10.1093/jxb/eraa574](https://doi.org/10.1093/jxb/eraa574); pmid: 33277994
36. Tomato Genome Consortium, The tomato genome sequence provides insights into fleshy fruit evolution. *Nature* **485**, 635–641 (2012). doi: [10.1038/nature11119](https://doi.org/10.1038/nature11119); pmid: 22660326
37. A. S. Chanderbali, F. He, P. S. Soltis, D. E. Soltis, Out of the water: Origin and diversification of the LBD gene family. *Mol. Biol. Evol.* **32**, 1996–2000 (2015). doi: [10.1093/molbev/msv080](https://doi.org/10.1093/molbev/msv080); pmid: 25839188
38. M. L. Vidoz, E. Loret, A. Mensuali, A. Alpi, P. Perata, Hormonal interplay during adventitious root formation in flooded tomato plants. *Plant J.* **63**, 551–562 (2010). doi: [10.1111/j.1365-3113.2010.04262.x](https://doi.org/10.1111/j.1365-3113.2010.04262.x); pmid: 20497380
39. S. Kumar, G. Stecher, M. Suleski, S. B. Hedges, TimeTree: A resource for timelines, timetrees, and divergence times. *Mol. Biol. Evol.* **34**, 1812–1819 (2017). doi: [10.1093/molbev/msx116](https://doi.org/10.1093/molbev/msx116); pmid: 28387841
40. P. Sukumar, G. S. Maloney, G. K. Muday, Localized induction of the ATP-binding cassette B19 auxin transporter enhances adventitious root formation in *Arabidopsis*. *Plant Physiol.* **162**, 1392–1405 (2013). doi: [10.1104/pp.113.217174](https://doi.org/10.1104/pp.113.217174); pmid: 23677937
41. C. Sorin *et al.*, Auxin and light control of adventitious rooting in *Arabidopsis* require ARGONAUTE1. *Plant Cell* **17**, 1343–1359 (2005). doi: [10.1105/tpc.105.031625](https://doi.org/10.1105/tpc.105.031625); pmid: 15829601
42. C. W. Melnyk *et al.*, Transcriptome dynamics at *Arabidopsis* graft junctions reveal an intertissue recognition mechanism that activates vascular regeneration. *Proc. Natl. Acad. Sci. U.S.A.* **115**, E2447–E2456 (2018). doi: [10.1073/pnas.1718263115](https://doi.org/10.1073/pnas.1718263115); pmid: 29440499
43. A. Hendelman *et al.*, Conserved pleiotropy of an ancient plant homeobox gene uncovered by cis-regulatory dissection. *Cell* **184**, 1724–1739.e16 (2021). doi: [10.1016/j.cell.2021.02.001](https://doi.org/10.1016/j.cell.2021.02.001); pmid: 33667348
44. L. Serrano-Ron *et al.*, Reconstruction of lateral root formation through single-cell RNA sequencing reveals order of tissue initiation. *Mol. Plant* **14**, 1362–1378 (2021). pmid: 34062316
45. T. Soyano, Y. Shimoda, M. Kawaguchi, M. Hayashi, A shared gene drives lateral root development and root nodule symbiosis pathways in *Lotus*. *Science* **366**, 1021–1023 (2019). doi: [10.1126/science.aax2153](https://doi.org/10.1126/science.aax2153); pmid: 31754003
46. K. Schiessl *et al.*, NODULE INCEPTION recruits the lateral root development program for symbiotic nodule organogenesis in *Medicago truncatula*. *Curr. Biol.* **29**, 3657–3668.e5 (2019). doi: [10.1016/j.cub.2019.09.005](https://doi.org/10.1016/j.cub.2019.09.005); pmid: 31543454

ACKNOWLEDGMENTS

We thank T. Beeckman, Y. Eshed, Z. Lippman, and S. Savaldi-Goldstein for comments and discussions; M. De Martino for setting up the CRISPR system; I. Pri-Tal for tissue culture work; O. Roth for assistance in etiolated seedlings assay; and M. Chemla for assistance in library preparation. **Funding:** I.E. is supported by a Howard Hughes Medical Institute International Research Scholar grant (grant no. 55008730) and the Israeli Science Foundation (grant no. ISF966/17). A.H. is supported by National Science Foundation grant Plant Genome Research Program grant IOS-1546837 to Z.B.L. **Author contributions:** M.O., N.G.-Y., and I.E. conceived and designed the study and performed the experiments. C.Y. performed the shoot-borne root quantification and lateral root RNA-Seq assay. A.H. performed in situ hybridizations. E.S. performed potato transformation. I.E., N.G.-Y., and M.O. wrote the manuscript. **Competing interests:** The authors declare no competing interests. **Data and materials availability:** Raw and processed data are available at the Gene Expression Omnibus (GEO; single-cell data: GSE159055; lateral root transcriptome data: GSE159050). All other data are available in the main paper or the supplementary materials.

SUPPLEMENTARY MATERIALS

science.org/doi/10.1126/science.abf4368

Materials and Methods

Figs. S1 to S14

References (47–68)

Tables S1 to S6

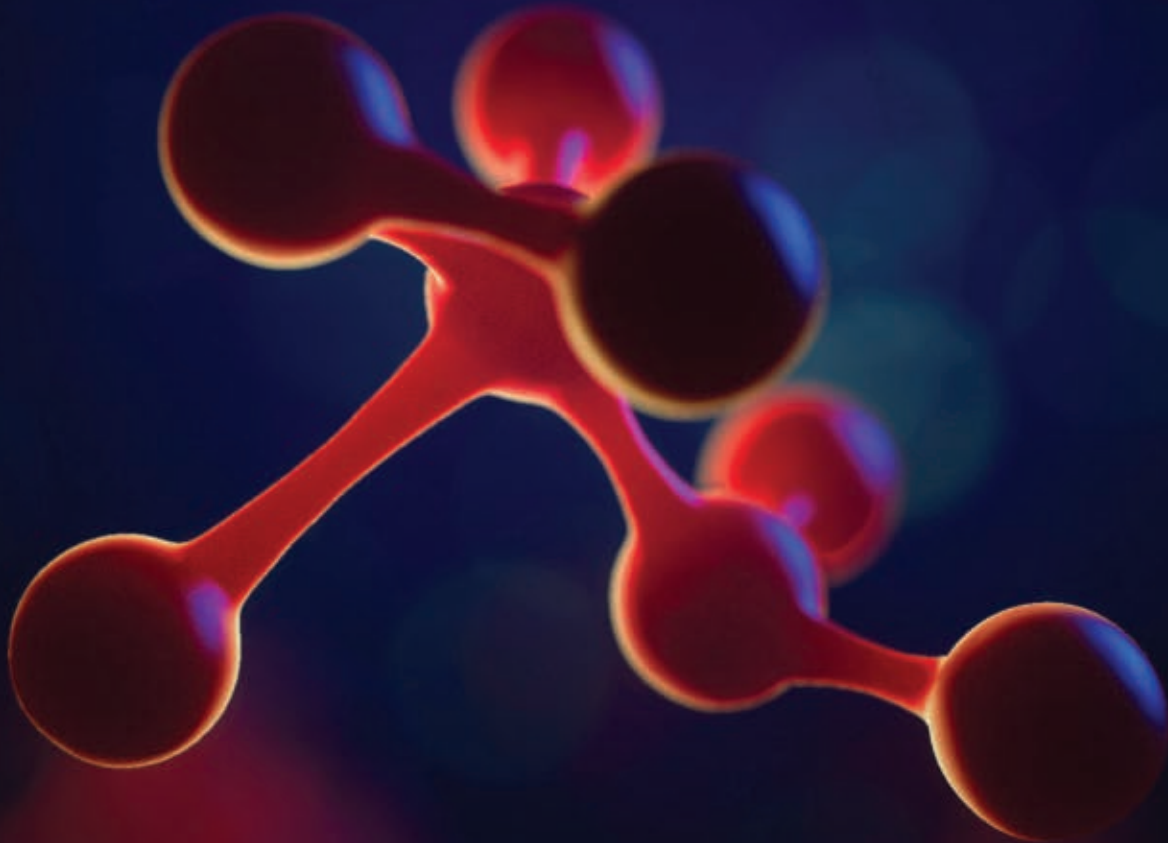
MDAR Reproducibility Checklist

2 November 2020; resubmitted 17 October 2021

Accepted 13 January 2022

[10.1126/science.abf4368](https://doi.org/10.1126/science.abf4368)

Science
JOURNALS 



Publish your research in the Science family of journals

The Science family of journals (*Science*, *Science Advances*, *Science Immunology*, *Science Robotics*, *Science Signaling*, and *Science Translational Medicine*) are among the most highly-regarded journals in the world for quality and selectivity. Our peer-reviewed journals are committed to publishing cutting-edge research, incisive scientific commentary, and insights on what's important to the scientific world at the highest standards.

Submit your research today!

Learn more at **[Science.org/journals](https://www.science.org/journals)**

RESEARCH ARTICLES

NEUROSCIENCE

Rapid eye movement sleep is initiated by basolateral amygdala dopamine signaling in mice

Emi Hasegawa^{1,2}, Ai Miyasaka¹, Katsuyasu Sakurai¹, Yoan Cherasse¹, Yulong Li³, Takeshi Sakurai^{1,2,4*}

The sleep cycle is characterized by alternating non-rapid eye movement (NREM) and rapid eye movement (REM) sleeps. The mechanisms by which this cycle is generated are incompletely understood. We found that a transient increase of dopamine (DA) in the basolateral amygdala (BLA) during NREM sleep terminates NREM sleep and initiates REM sleep. DA acts on dopamine receptor D2 (Drd2)-expressing neurons in the BLA to induce the NREM-to-REM transition. This mechanism also plays a role in cataplectic attacks—a pathological intrusion of REM sleep into wakefulness—in narcoleptics. These results show a critical role of DA signaling in the BLA in initiating REM sleep and provide a neuronal basis for sleep cycle generation.

Sleep-wakefulness states are influenced by noradrenergic neurons in the locus coeruleus, histaminergic neurons in the tuberomammillary nucleus, and serotonergic neurons in the dorsal raphe, all of which share similar firing patterns—with rapid firing during wakefulness, slow and occasional firing during non-rapid eye movement (NREM) sleep, and almost complete cessation of firing during rapid eye movement (REM) sleep (1, 2). However, dopaminergic neurons in the ventral tegmental area (VTA) (DA^{VTA} neurons) were reported to show different firing patterns from those of other monoaminergic neurons (3–5). A recent fiber-photometry study showed that DA^{VTA} neurons exhibited lower activity during NREM sleep than during either wakefulness or REM sleep. The activity of these neurons began to increase before the NREM-to-REM and NREM-to-wakefulness transitions (6). Tracing studies revealed that DA^{VTA} neurons are composed of heterogeneous populations with different input and output organizations (7, 8), which suggests the possible existence of multiple DA^{VTA} neuronal populations with distinct firing patterns across sleep-wakefulness states. In this study, we examined extracellular dopamine (DA) levels across the sleep-wakefulness cycle in several brain regions that receive dense projections of DA^{VTA} neurons, using a G protein-coupled receptor (GPCR) activation-based (GRAB) sensor for DA (GRAB_{DA}) (9) to determine the existence of subpopulations of DA^{VTA} neurons with differential roles in sleep-wakefulness regulation.

DA level in the basolateral amygdala increases before NREM-to-REM sleep transitions

We expressed GRAB_{DA} in the basolateral amygdala (BLA), the nucleus accumbens (NAc), the medial prefrontal cortex (mPFC), or the lateral hypothalamic area (LHA) of mice and implanted optical fibers for photometry to examine the relationship between DA levels and each sleep-wakefulness state transition (Fig. 1 and fig. S1). We found three patterns of DA dynamics during the NREM-to-REM transition. DA levels in the BLA showed a characteristic pattern with a transient increase that started just before each NREM-to-REM transition and a decrease during REM sleep (Fig. 1, A to D). DA elevation started earlier than the NREM-to-REM sleep transition. In the NAc, DA levels also showed an elevation before the NREM-to-REM sleep transition and a fluctuation with a slightly higher mean value during REM sleep (Fig. 1, E to H). The mPFC and LHA shared similar temporal patterns of DA levels, with a robust decrease during REM sleep without a prior increase in DA level (Fig. 1, I to P). Levels of noradrenaline (NA) and serotonin [5-hydroxytryptamine (5-HT)] in the BLA showed completely different patterns from those of DA (fig. S2).

Next, we examined the effect of DA increase in the BLA and NAc during NREM sleep on sleep-wakefulness states. We expressed stabilized step function opsin (SSFO) (10) in DA^{VTA} neurons in *DAT-ires-Cre* mice (Fig. 2, A and H) and implanted optical fibers in the BLA or NAc bilaterally (fig. S3A) for optogenetic stimulation (1-s width). Excitation of DA fibers in the BLA during NREM sleep caused a transition to REM sleep (Fig. 2, B and C). REM sleep started 142.4 ± 33.7 s after stimulation, which was significantly earlier than observed in the control group (Fig. 2C). Excitation of DA fibers in the BLA every 30 min from zeitgeber time 8 (ZT8) to ZT11 robustly increased REM sleep at

the expense of NREM sleep (Fig. 2, D and E, and table S1). The electroencephalography (EEG) power spectrum during each state was not significantly changed by the optogenetic manipulation of DA fibers in the BLA (Fig. 2F). Duration of NREM sleep was shortened because NREM sleep bouts were terminated earlier by the optogenetic stimulation (Fig. 2G).

By contrast, excitation of DA fibers in the NAc during NREM sleep did not cause state transition (Fig. 2, I and J). Shining a light (for 1 s) every 30 min resulted in a slight increase of NREM sleep time at the expense of wakefulness time (Fig. 2, K and L), which is consistent with a previous result that found that excitation of direct pathway neurons in the NAc decreased wakefulness (11). However, this manipulation did not influence REM sleep. Excitation of DA fibers in the mPFC or LHA also did not affect the amount of each state (fig. S4 and table S2).

These observations showed that a transient DA increase in the BLA caused the NREM-to-REM sleep transition. Supporting this, optogenetic inhibition of DA^{VTA} fibers in the BLA lengthened latency to REM sleep and decreased REM sleep amount (Fig. 3, A to E, and table S1) without affecting the EEG power spectrum (Fig. 3F).

Dopamine receptor D2-positive neurons in the BLA trigger NREM-to-REM transition

Complete DA depletion abolished REM sleep in mice, and treatment with a dopamine receptor D2 (Drd2) agonist restored REM sleep (12). Moreover, in rodents, low doses of a Drd2 agonist increased REM sleep, although larger doses of a Drd2 agonist reduced REM sleep, presumably as a result of presynaptic inhibition of DA release (13). These findings suggest the involvement of Drd2 in REM sleep regulation, consistent with the evidence that blockade of Drd2 decreases REM sleep (14). Furthermore, injection of a Drd2 agonist into the amygdala increased REM sleep in rats (15). When considered in conjunction with the fiber-photometry data (Fig. 1), these observations lead us to hypothesize that DA acts on Drd2-positive neurons in the BLA to initiate REM sleep. To examine the effect of DA on Drd2 neurons in the BLA, we performed an electrophysiological study. After expressing SSFO in DA^{VTA} neurons in *Drd2-Cre;DAT-ires-Cre* (Drd2/DAT-Cre) mice, we prepared brain slices and subjected them to whole-cell recordings from Drd2-positive neurons in the BLA (Fig. 4A). Excitation of DA fibers by application of light (1 s) induced long-lasting hyperpolarization, which was blocked by a Drd2 antagonist. This suggests that DA inhibited Drd2 neurons in the BLA through Drd2 (Fig. 4, B to D).

Because DA induced hyperpolarization of Drd2 neurons in the BLA, we next examined whether optogenetic inhibition of these cells

¹International Institute for Integrative Sleep Medicine (WPI-IIS), University of Tsukuba, Tsukuba, Ibaraki 305-8575, Japan.

²Faculty of Medicine, University of Tsukuba, Tsukuba, Ibaraki 305-8575, Japan. ³State Key Laboratory of Membrane Biology, Peking University School of Life Sciences, Beijing 100871, China. ⁴Life Science Center for Tsukuba Advanced Research Alliance (TARA), University of Tsukuba, Tsukuba, Ibaraki 305-8575, Japan.

*Corresponding author. Email: sakurai.takeshi.gf@u.tsukuba.ac.jp

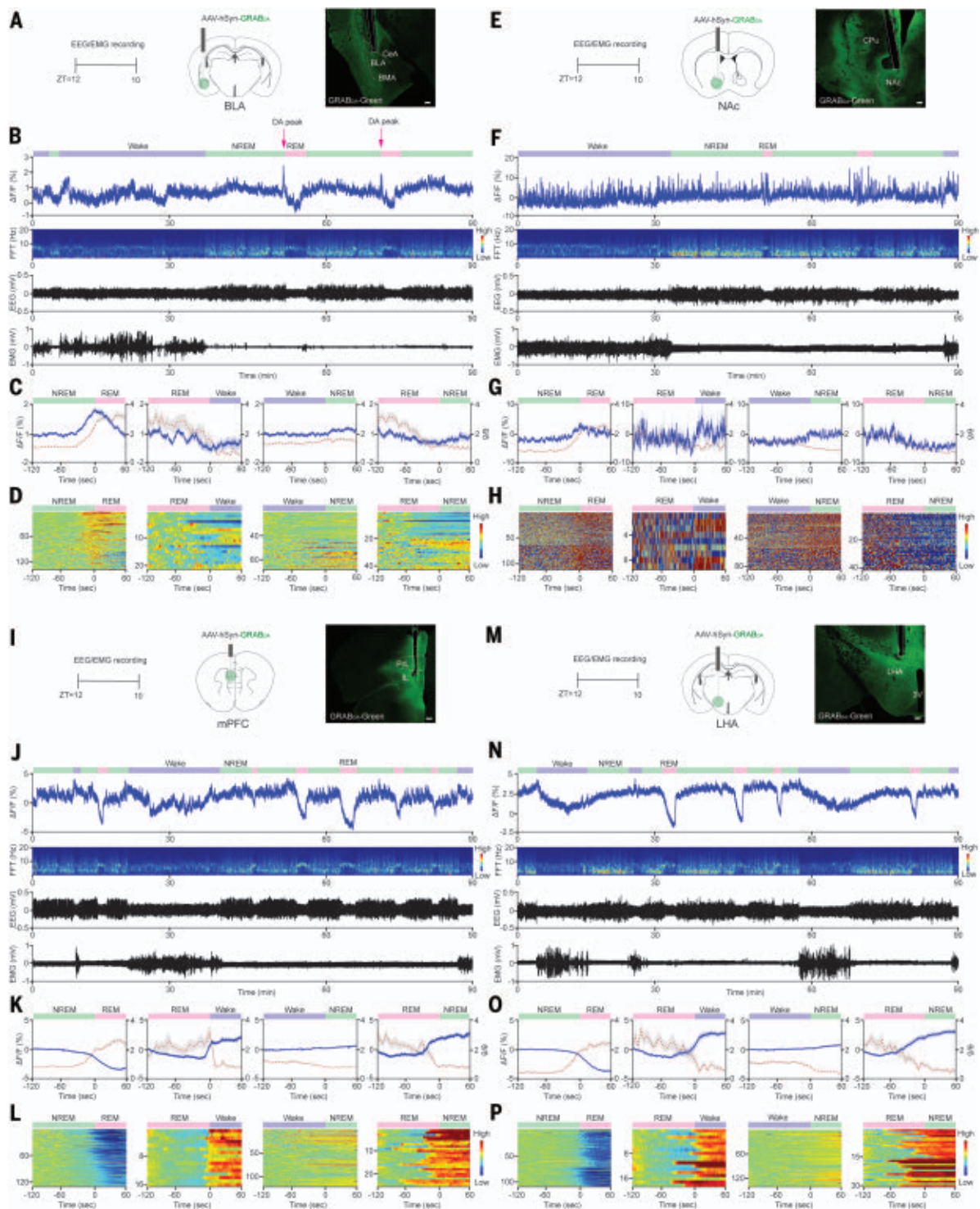


Fig. 1. Temporal changes of DA levels in brain regions across each vigilance state. (A, E, I, and M) (Left) Experimental designs. (Middle) Fiber locations and adeno-associated virus (AAV) injection. (Right) Representative coronal brain sections stained with anti-green fluorescent protein (GFP) (green) antibody. The white lines mark the positions of the optical fibers. Scale bars, 100 μ m. BMA, basomedial amygdala; CPu, caudate putamen; PrL, prelimbic cortex; IL, infralimbic cortex; 3V, third ventricle. (B, F, J, and N) (Top) Representative traces of DA levels in the BLA (B), NAc (F), mPFC (J), and LHA (N) in C57BL/6J mice. Purple, green, and pink bars show wakefulness, NREM sleep, and REM

sleep, respectively. (Middle and bottom) Time-resolved power spectra and waveforms of EEG and electromyography (EMG). $\Delta F/F$, change in fluorescence intensity; FFT, fast Fourier transform. (C, G, K, and O) Temporal changes in DA levels at each transition (blue) and theta/delta ratios (red dotted lines) (averages \pm SEMs). Time is relative to the transition of states. (D, H, L, and P) Heatmaps showing DA level at each transition (3 mice, recorded for 22 hours). Only state transitions where the preceding state lasted >120 s and another state after it lasted >60 s were extracted and converted to data. The numbers of data for each state transition extracted from each mouse are shown in table S6.

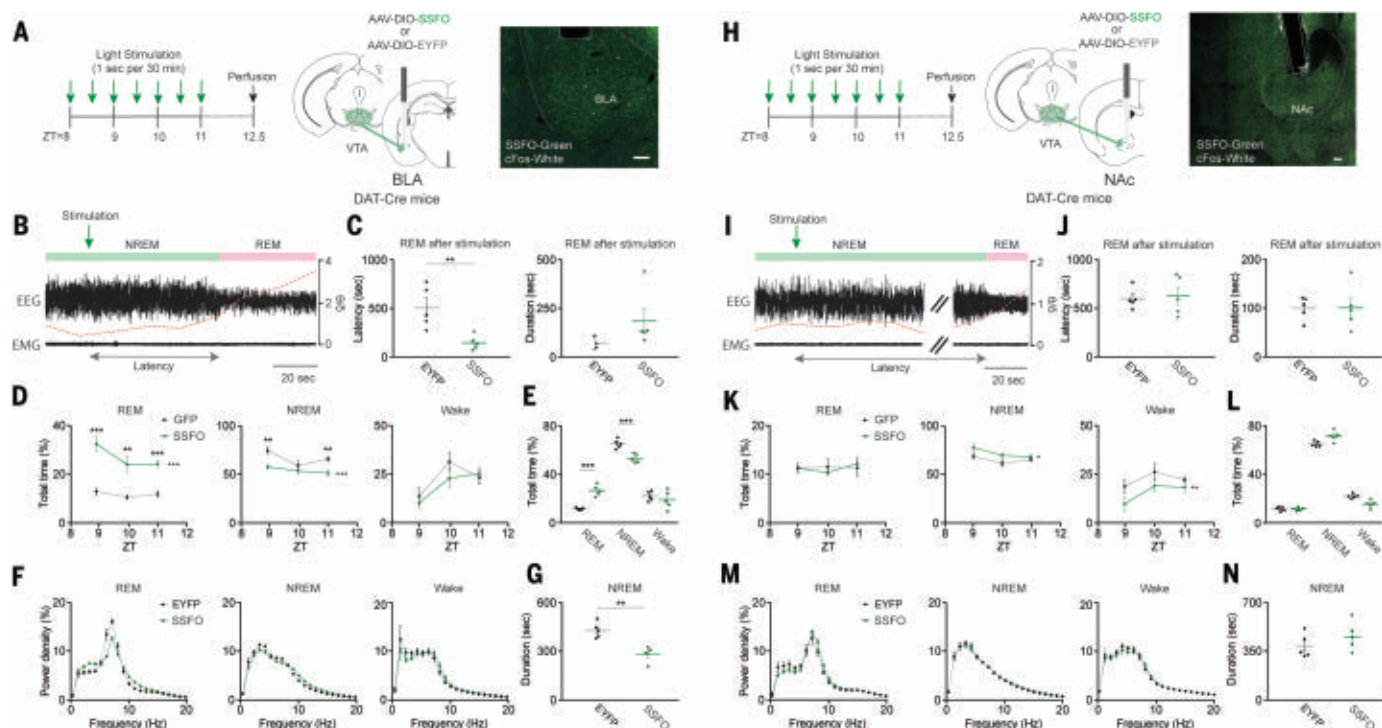


Fig. 2. Optogenetic excitation of DA^{VTA} fibers in the BLA during NREM sleep induces REM sleep. (A and H) (Left) Experimental designs. (Middle) Schematic drawings of fiber placement and AAV injection. (Right) Coronal brain sections stained with anti-GFP (green) and anti-cFos (white) antibodies. The white lines mark the positions of optical fibers. Scale bars, 100 μ m. (B and I) Representative traces of EEG and EMG and theta/delta ratios in *DAT-ires-Cre* mice expressing SSFO in DA^{VTA} neurons and implanted optical fibers in the BLA (B) or NAc (I) (bilateral). Arrows show time of light stimulation. Green and pink bars represent time of NREM and REM sleep, respectively. (C and J) REM latency and duration after first light

stimulation. (D and K) Hourly amounts of REM sleep (REM), NREM sleep (NREM), and wakefulness (wake) with light stimulation in the BLA (D) or NAc (K) for ZT8 to ZT11. (E and L) Total amount of REM sleep (REM), NREM sleep (NREM), and wakefulness (wake) in ZT8 to ZT11. (F and M) Power spectra of EEG frequency during each state in ZT8 to ZT11. (G and N) Duration of NREM in ZT8 to ZT11. Data are from *DAT-ires-Cre* mice expressing SSFO or EYFP in DA^{VTA} neurons with photostimulation in the BLA or NAc (SSFO, $n = 5$, $n = 5$; EYFP, $n = 5$, $n = 5$) [relative to EYFP, * $P < 0.05$, ** $P < 0.01$, *** $P < 0.001$, unpaired t test; *** $P < 0.001$, two-way repeated measures analysis of variance (ANOVA)].

induced REM sleep. We expressed vertebrate low-wavelength opsin (vLWO), which, like *Drd2*, couples to the Gi subclass of G proteins and induces hyperpolarization by light (16) in *Drd2* neurons in the BLA of *Drd2-Cre* mice (Fig. 4E). Whole-cell recordings using slice preparations showed that shining a light pulse (462 nm, 1 Hz, 40 s) caused long-lasting hyperpolarization of enhanced yellow fluorescent protein (EYFP)-positive neurons, similar to the hyperpolarization observed when DA fibers were excited (Fig. 4, F to H). We next implanted optical fibers in the BLA in *Drd2-Cre* mice expressing vLWO and optogenetically inhibited *Drd2* neurons (Fig. 4I). Application of a light pulse during NREM sleep caused a transition to REM sleep (Fig. 4J). REM sleep started 89.2 ± 20.3 s after manipulation, which was significantly earlier than in the control group expressing only EYFP (Fig. 4K). Application of a light pulse every 30 min starting from ZT8 to ZT11 increased the amount of REM sleep and decreased NREM sleep (Fig. 4, L and M, and table S3) without affecting the EEG power spectrum (Fig. 4N). Duration of NREM sleep was shortened

(Fig. 4O). Fos expression was increased in the cell population around EYFP-expressing cells in the BLA but not in EYFP-expressing cells (Fig. 4P), which suggests that inhibition of *Drd2* cells caused disinhibition of BLA neurons. These activated neurons in the amygdala send specific projections to the mesopontine junction regions that are implicated in the REM regulation (fig. S5).

Chemogenetic inhibition of *Drd2* neurons in the BLA of *Drd2-Cre* mice increased REM sleep time and decreased NREM sleep time (Fig. 4, Q to S, and table S4), further supporting the importance of *Drd2* neurons in the BLA in triggering REM sleep. We again observed an increase of Fos-positive neurons in the BLA as well as in the central nucleus of the amygdala (CeA) (Fig. 4T).

Axonal projections by *Drd2* neurons in the BLA were almost exclusively observed in the BLA (fig. S6A), which suggests that *Drd2* neurons in the BLA mainly act inside the BLA. An electrophysiological study also showed that optogenetic inhibition of *Drd2* neurons in the BLA excited neurons other than *Drd2*-positive cells (fig. S6, B to G).

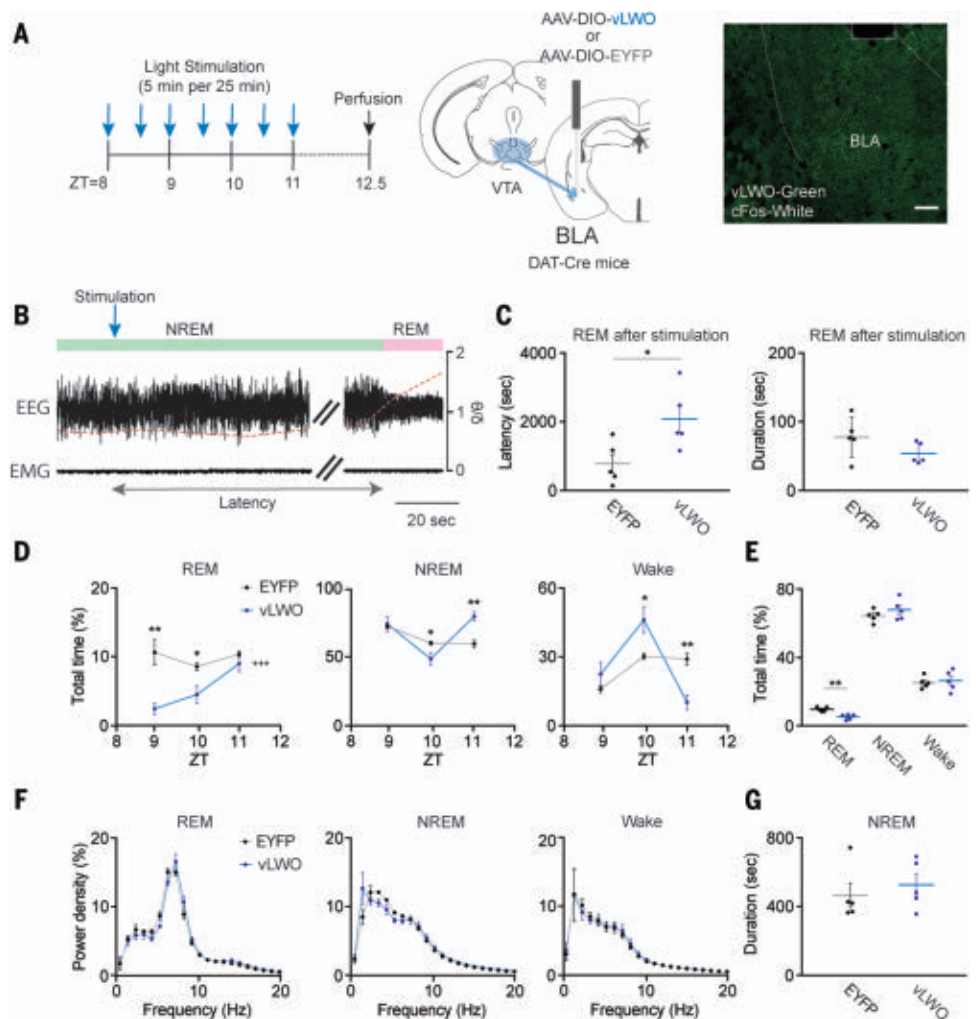
Transient DA increase in the BLA during wakefulness induces cataplexy

We next examined whether DA signaling in the BLA is also involved in the emergence of cataplexy, which is a pathological intrusion of REM sleep into wakefulness. A previous study had shown that *Drd2* agonists or antagonists increased or decreased cataplexy, respectively, in narcoleptic dogs and mice (17–19).

We expressed GRAB_{DA} in the BLA of narcoleptic *orexin-ataxin 3* mice (20) and implanted an optical fiber to examine the relationship between DA level and cataplexy (Fig. 5A and fig. S1C). We fed mice chocolate to increase the number of cataplexy episodes (21). Cataplexy-like episodes (CLEs), characterized by abruptly occurring behavioral arrest (22), were observed in *orexin-ataxin 3* mice (20) but never in wild-type littermates. We observed a transient increase in DA levels while eating chocolate, which was followed by CLEs (Fig. 5B and movie S1). The increment of DA level in the BLA during chocolate feeding in *orexin-ataxin 3* mice (5.8 ± 0.005) was larger than that observed in control mice (1.7 ± 0.002 ; $P < 0.001$, unpaired t test) (Fig. 5, B and C). By contrast,

Fig. 3. Inhibition of DA^{VTA} fibers in the BLA decreases REM sleep. (A) (Left)

Experimental design. (Middle) Fiber placement and AAV injection in the BLA. (Right) Coronal brain section stained with anti-GFP (green) and anti-cFos (white) antibodies in the amygdala. The white line marks the position of the optical fiber. Scale bar, 100 μ m. (B) Representative traces of EEG and EMG and theta/delta ratio in a *DAT-ires-Cre* mouse expressing vLWO in DA^{VTA} neurons and implanted optical fibers in the BLA (bilateral). The blue arrow shows time of light stimulation, and the green and pink bars represent time of NREM and REM sleep, respectively. (C) REM latency and duration after first light stimulation. (D) Amount of REM sleep (REM), NREM sleep (NREM), and wakefulness (wake) per 1 hour with light stimulation in ZT8 to ZT11. (E) Total amount of each state in ZT8 to ZT11. (F) Power spectra of EEG frequency during each state in ZT8 to ZT11. (G) Duration of NREM sleep in ZT8 to ZT11. Data are from *DAT-ires-Cre* mice expressing vLWO or EYFP in DA^{VTA} neurons with photostimulation in the BLA (vLWO, $n = 5$; EYFP, $n = 5$) (relative to EYFP, * $P < 0.05$, ** $P < 0.01$, *** $P < 0.001$, unpaired t test; **** $P < 0.001$, two-way repeated measures ANOVA).



the amplitudes of DA increase in the NAc during chocolate feeding were similar in narcoleptic and control mice (fig. S7).

Next, we expressed SSFO in DA^{VTA} neurons in *DAT-ires-Cre* mice and implanted optical fibers in the VTA for optogenetic excitation during wakefulness (Fig. 5D). We simultaneously monitored DA level in the BLA. Application of laser for 1 s, which was accompanied by Fos expression in SSFO-positive cells in the VTA (Fig. 5D), caused a transient increase in DA level with a similar pattern to that observed during chocolate feeding in narcoleptic mice preceding cataplexy (Fig. 5, B and E). The increase of DA level was followed by CLEs, even in *DAT-ires-Cre* mice in which orexin peptides were produced (movie S2). We next examined the effects of stimulation of DA^{VTA} fibers in the BLA, NAc, mPFC, or LHA (fig. S3D) and found that optogenetic excitation during wakefulness caused CLEs only when optical fibers were implanted in the BLA (fig. S8, A to E).

We next expressed vLWO in *Drd2-Cre* mice and implanted optical fibers in the BLA (Fig. 5F). Optogenetic inhibition by applying a light pulse (1 Hz,

1 min) during wakefulness caused CLEs (Fig. 5, G and H). The EEG power spectrum during the induced CLEs was similar to that observed during cataplexy in *orexin-ataxin 3* mice (Fig. 5H). After optogenetic inhibition, we observed an increase in Fos-positive neurons in the BLA (Fig. 5I). We next injected *AAV-DIO-hM4Di-mCherry* into the BLA of *Drd2-Cre;orexin-ataxin 3* mice (*Drd2/ataxin 3* mice) to examine the effect of chemogenetic inhibition of *Drd2*-positive neurons in the BLA on cataplexy (Fig. 5J). Clozapine-*N*-oxide (CNO) administration increased the total time and number of cataplexy episodes (Fig. 5, K and L, and table S5). Administration of CNO caused an increase in Fos-positive neurons in the BLA and CeA (Fig. 5M). Moreover, optogenetic inhibition of DA^{VTA} fibers in the BLA almost completely abolished the occurrence of CLEs in *DAT-ires-Cre;orexin-ataxin 3* mice (fig. S8, F and G).

Discussion

The amygdala plays a crucial role in processing emotional signals during wakefulness. However, neuroimaging and intracranial recording studies have shown amygdala activation dur-

ing REM sleep in humans (23, 24). We show that a transient increase in DA levels in the BLA during NREM sleep terminates NREM sleep and starts REM sleep. *Drd2*-positive neurons in the BLA play a pivotal role in this process through the disinhibition of BLA neurons. The increment of DA in these peaks showed only a weak correlation with the length of inter-REM intervals that preceded the DA peak as well as the REM sleep duration that followed, which suggests that the DA peak at the transition does not play a major role in the homeostatic regulation of REM sleep (fig. S9).

Retrograde tracing with RetroBeads injected into the BLA and NAc in wild-type mice showed no double-positive cells in the VTA (fig. S10, A to D). Injection of *AAV₂retro-DIO-ChR2-EYFP* into the NAc of *DAT-ires-Cre* mice to label the DA^{VTA} neurons that send innervations to the NAc showed that channelrhodopsin-2 (ChR2)-positive fibers were observed in the NAc and LHA but not in the BLA (fig. S10, E and F). These observations suggest that DA^{VTA} populations sending projections to the BLA and NAc are distinct. DA^{VTA} neurons that send

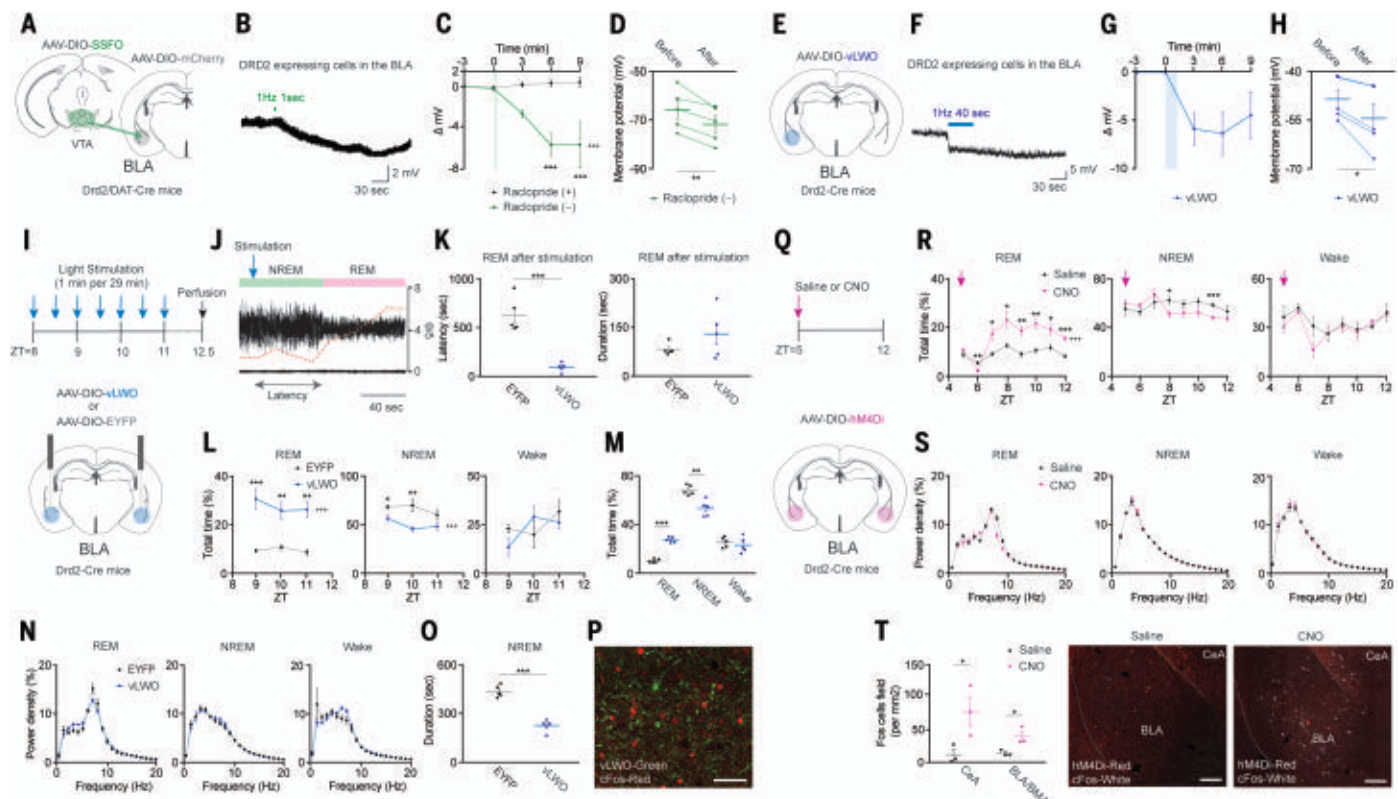


Fig. 4. Drd2-positive neurons in the BLA mediate the NREM-to-REM sleep transition. (A and E) Schematic drawings of experimental design. (B and F) Traces of current clamp recording from Drd2-positive cells in the BLA. Green and blue bars show time of light stimulation of DA^{VTA} axon terminals (B) or Drd2-positive cells (F). (C, D, G, and H) Hyperpolarization of Drd2-positive cells relative to baseline. Before indicates the average for 3 min before light stimulation, and after indicates the average for 3 to 6 min after light stimulation ($^*P < 0.05$, Mann-Whitney test or paired t test; $n = 5$). (B), (C), and (D) were done under the presence of GABA_A and/or raclopride. (I) (Top) Experimental design. (Bottom) Schematic drawing of fiber locations and AAV injection in the BLA. (J) Representative EEG and EMG traces and theta/delta ratio of EEG in Drd2-Cre mice expressing vLWO in Drd2-positive cells in the BLA and implanted optical fibers in the BLA (bilateral). The blue arrow shows time of light stimulation, and green and pink bars represent NREM and REM sleep, respectively. (K) REM latency and duration after first light stimulation. (L) Hourly amount of REM sleep (REM), NREM sleep (NREM), and wakefulness (wake) with light stimulation. (M) Total amount of each state in ZT8 to ZT11. (N) Power

spectra of EEG frequency during each state in ZT8 to ZT11. (O) Duration of NREM sleep in ZT8 to ZT11. Drd2-Cre mice expressed vLWO or EYFP in the amygdala with photostimulation in the BLA (vLWO, $n = 5$; EYFP, $n = 5$) (relative to EYFP, $^*P < 0.05$, $^{**}P < 0.01$, $^{***}P < 0.001$, unpaired t test; $^{+++}P < 0.001$, two-way repeated measures ANOVA). (P) Coronal brain section stained with anti-GFP (green) and anti-cFos (red) antibodies in the amygdala. Scale bar, 100 μ m. (Q) (Top) Experimental design. (Bottom) Schematic drawing of AAV injection in the BLA. (R) Hourly amount of each state after administration of saline or CNO in ZT5 to ZT12. Arrows show the administration of saline or CNO at ZT5 (relative to saline, $^*P < 0.05$, $^{**}P < 0.01$, $^{***}P < 0.001$, paired t test; $^{+++}P < 0.001$, two-way repeated measures ANOVA). (S) Power spectra of EEG frequency during each state in ZT5 to ZT12. (T) (Left) Number of Fos-positive cells in the CeA and the BLA or BMA after administration of saline or CNO (saline, $n = 3$; CNO, $n = 3$) ($^*P < 0.05$, unpaired t test). (Right) Coronal brain sections stained with anti-mCherry (red) and anti-cFos (white) antibodies in the amygdala. Scale bars, 100 μ m. Data are from Drd2 mice expressing hm4Di mCherry ($n = 6$).

innervations to the BLA localize in the dorsal regions, whereas populations that send projections to the NAc were found in the ventral part of the VTA.

In vitro electrophysiological studies suggested that DA- or vLWO-mediated inhibition of Drd2 neurons in the BLA caused long-lasting hyperpolarization (Fig. 4, C and G). This long-lasting hyperpolarization might be a characteristic of this group of neurons when Gi proteins are activated and might be involved in the mechanism that maintains the stability of REM sleep. Mimicking long-lasting inhibition of BLA Drd2 by designer receptors exclusively activated by designer drugs (DREADD) increased REM sleep in wild-type mice and

cataplexy in narcoleptic mice, supporting this hypothesis (Fig. 4, Q and R, and Fig. 5, J and K).

We also found that the DA peak in the BLA preceded cataplectic attacks in narcoleptic mice. Mimicking the DA increase in the BLA induced muscle atonia with behavioral arrests in mice, which were similar to the behaviors observed in cataplexy (Fig. 5, D and E). In this study, we used SSFO for optogenetic excitation of DA^{VTA} neurons because excitation of DA^{VTA} neurons with SSFO by applying a 1-s light pulse caused transient excitation of DA^{VTA} neurons (fig. S11) along with transient DA elevation in the BLA (Fig. 5E), which was similar to the pattern of DA increase before the NREM-to-REM transitions (Fig. 1, A to D). DA

reuptake inhibitors, which are used for the treatment of narcolepsy, had no effect on cataplexy or REM sleep (25), which suggests that transient increase, but not sustained elevation of DA levels, triggers REM sleep or cataplexy.

In narcoleptic patients, cataplexy is often triggered by positive emotion and amygdala activity increases in cataplexy (26), which suggests roles of the amygdala and reward system in cataplexy (27–29). We found that DA levels in the BLA transiently increased before cataplexy attacks in narcoleptic mice but not in wild-type mice (Fig. 5). Positive emotion might induce a transient increase of DA in the BLA in narcoleptics but not in wild types, mimicking the DA dynamics that trigger

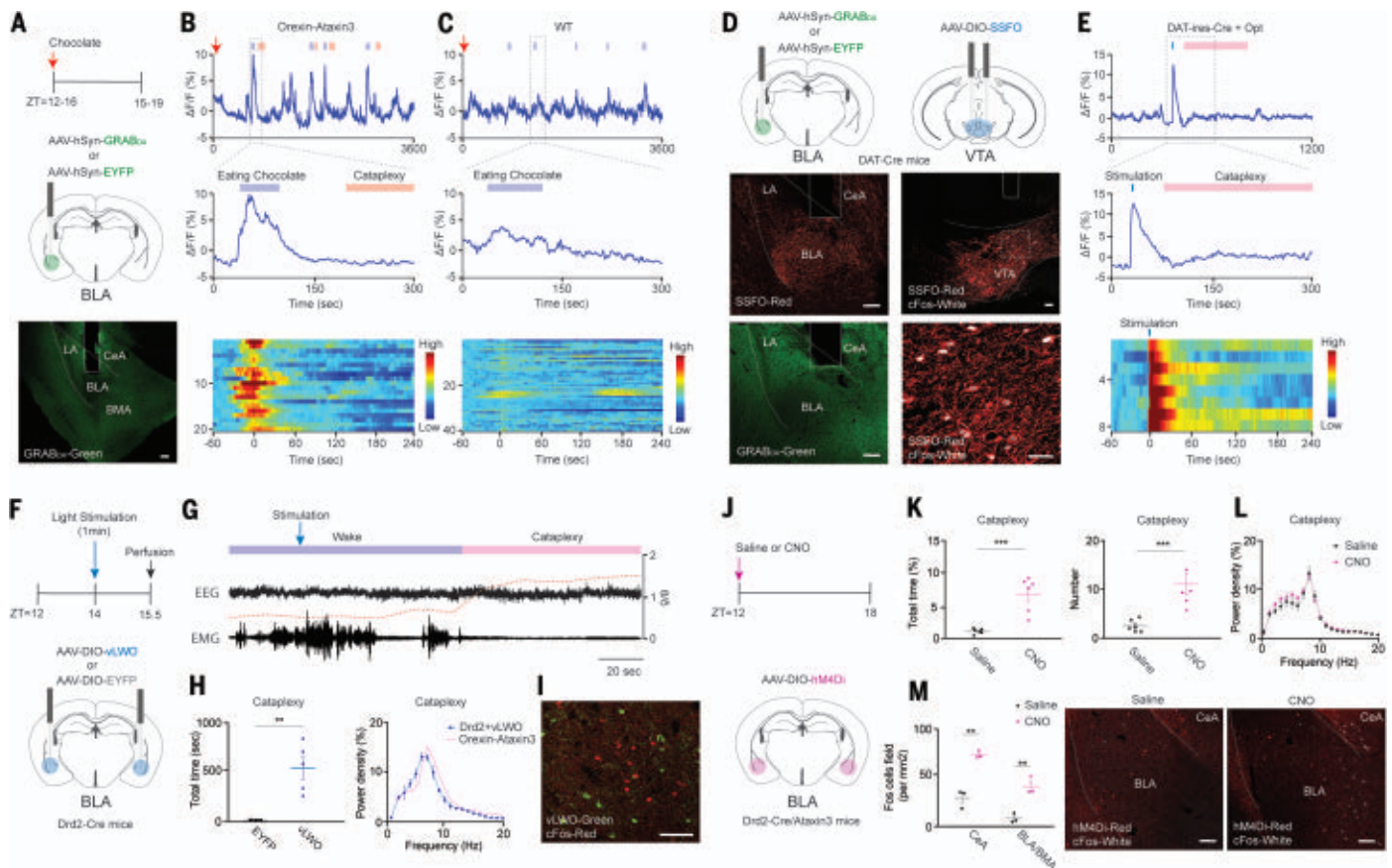


Fig. 5. Transient increase in DA levels in the BLA triggers cataplexy in narcoleptic mice. (A) (Top) Experimental design. Horizontal bar represents time of chocolate feeding. (Middle) Placement of optical fiber and AAV injection. (Bottom) Coronal brain section stained with anti-GFP (green) antibody in the amygdala. The white line marks the position of the optical fiber. Scale bar, 100 μ m. LA, lateral amygdala. (B) (Top) Representative trace of DA level in the BLA in *orexin-ataxin3* mice. Purple and pink bars show times of chocolate feeding and cataplexy, respectively. (Middle) Magnification of time of chocolate feeding and cataplexy. (Bottom) Heatmap showing temporal change of DA levels during chocolate feeding and cataplexy in the BLA in mice ($n = 3$, each recorded three times; total recording number = 20). (C) (Top and middle) Representative traces of DA levels in the BLA in C57BL/6J mice. Purple bars show times of chocolate feeding. (Bottom) Heatmap showing temporal change of DA levels during chocolate feeding in the BLA in C57BL/6J mice (3 mice, each recorded three times, total recording number = 40). (D) (Top) Placement of optical fiber and GRAB_{DA} and SSFO expression in the BLA and VTA. (Middle and bottom) Coronal brain sections double stained with anti-mCherry (red), anti-GFP (green), or anti-cFos (white) antibodies in the BLA and VTA. The white lines show the positions of the fibers. Scale bars, 100 μ m. (E) (Top) Representative trace of DA level in the BLA in a *DAT-ires-Cre* mouse before and after optogenetic excitation. Blue bars show time of light stimulation in *DA^{VTA}* neurons, and pink bars represent time of cataplexy-like episodes. (Middle) Magnification of time of light stimulation and cataplexy. (Bottom) Heatmap showing temporal change of DA levels during cataplexy-like

episode in the BLA after SSFO stimulation in the VTA (*DAT-ires-Cre + Opt*; 3 mice, each recorded two or three times, total recording signal number = 8). (F) (Top) Experimental design. Horizontal bar represents time of light stimulation. (Bottom) Location of AAV injection and fiber implantation. (G) Representative traces of EEG and EMG and theta/delta ratio of EEG in a *Drd2-Cre* mouse expressing vLWO in *Drd2*-positive cells in the BLA and implanted optical fibers in the BLA (bilateral). The blue arrow shows time of light stimulation, and the purple and pink bars represent wakefulness and cataplexy, respectively. (H) (Left) Total amount of cataplexy episodes. *Drd2-Cre* mice expressed vLWO or EYFP in the BLA with photostimulation (vLWO, $n = 5$; EYFP, $n = 5$) (relative to EYFP, $**P < 0.01$, unpaired t test). (Right) Power spectrum of EEG frequency during CLEs evoked by light stimulation compared with that observed during cataplexy in *orexin-ataxin3* mice. (I) Coronal brain section double stained with anti-GFP (green) and anti-cFos (red) antibodies. Scale bar, 100 μ m. (J) (Top) Experimental design. Horizontal bar represents time of saline or CNO administration. (Bottom) Schematic drawing of location of AAV injection. (K) Total amount and number of cataplexy episodes after administration of saline or CNO in ZT12 to ZT18 (relative to saline, $***P < 0.001$, paired t test). (L) Power spectrum of EEG frequency during cataplexy. (M) (Left) Number of Fos-positive cells in the CeA and the BLA or BMA after administration of saline or CNO (saline, $n = 3$; CNO, $n = 3$) ($**P < 0.01$, unpaired t test). (Right) Coronal brain sections double stained with anti-mCherry (Red) and anti-cFos (white) antibodies in the amygdala. Scale bars, 100 μ m. Data are from *Drd2/ataxin3* mice expressing hM4Di mCherry ($n = 6$).

NREM-to-REM transitions. This is consistent with a study that showed an increase in DA levels in narcoleptic dogs only in the amygdala (30). We previously showed that the activity of 5-HT neurons in the dorsal raphe, which are excited by orexin, is involved in the

suppression of cataplexy (31), which suggests that this pathway might inhibit the release of DA in the BLA through 5-HT-mediated inhibition of DA axonal terminals.

Our study shows the importance of transient DA signaling in the BLA in gating REM

sleep by disinhibiting amygdala neurons that send innervations to REM-regulatory regions (fig. S5). This finding sheds light on the mechanism of cataplexy and on our understanding of the pathophysiology of abnormalities in REM sleep, such as REM sleep behavior

disorder and diseases that involve abnormal DA signaling like Parkinson's disease.

REFERENCES AND NOTES

1. T. E. Scammell, E. Arrigoni, J. O. Lipton, *Neuron* **93**, 747–765 (2017).
2. C. B. Saper, T. C. Chou, T. E. Scammell, *Trends Neurosci.* **24**, 726–731 (2001).
3. L. Dahan et al., *Neuropsychopharmacology* **32**, 1232–1241 (2007).
4. J. D. Miller, J. Farber, P. Gatz, H. Roffwarg, D. C. German, *Brain Res.* **273**, 133–141 (1983).
5. J. M. Monti, H. Jantos, *Prog. Brain Res.* **172**, 625–646 (2008).
6. A. Eban-Rothschild, G. Rothschild, W. J. Giardino, J. R. Jones, L. de Lecea, *Nat. Neurosci.* **19**, 1356–1366 (2016).
7. K. T. Beier et al., *Cell* **162**, 622–634 (2015).
8. K. T. Beier et al., *Cell Rep.* **26**, 159–167.e6 (2019).
9. F. Sun et al., *Cell* **174**, 481–496.e19 (2018).
10. O. Yizhar et al., *Nature* **477**, 171–178 (2011).
11. Y. Oishi, M. Lazarus, *Neurosci. Res.* **118**, 66–73 (2017).
12. K. Dzirasa et al., *J. Neurosci.* **26**, 10577–10589 (2006).
13. J. M. Monti, D. Monti, *Sleep Med. Rev.* **11**, 113–133 (2007).
14. M. M. S. Lima et al., *Behav. Brain Res.* **188**, 406–411 (2008).
15. R. Kumar Yadav, B. N. Mallick, *Neuropharmacology* **193**, 108607 (2021).
16. O. A. Masseck et al., *Neuron* **81**, 1263–1273 (2014).
17. C. R. Burgess, G. Tse, L. Gillis, J. H. Peever, *Sleep* **33**, 1295–1304 (2010).
18. S. Nishino et al., *J. Neurosci.* **11**, 2666–2671 (1991).
19. E. Mignot et al., *J. Neurosci.* **13**, 1057–1064 (1993).
20. J. Hara et al., *Neuron* **30**, 345–354 (2001).
21. Y. Oishi et al., *J. Neurosci.* **33**, 9743–9751 (2013).
22. T. E. Scammell, J. T. Willie, C. Guilleminault, J. M. Siegel, International Working Group on Rodent Models of Narcolepsy, *Sleep* **32**, 111–116 (2009).
23. M. Corsi-Cabrera et al., *J. Sleep Res.* **25**, 576–582 (2016).
24. P. Maquet et al., *Nature* **383**, 163–166 (1996).
25. J. P. Wisor et al., *J. Neurosci.* **21**, 1787–1794 (2001).
26. S. Meletti et al., *J. Neurosci.* **35**, 11583–11594 (2015).
27. C. R. Burgess, Y. Oishi, T. Mochizuki, J. H. Peever, T. E. Scammell, *J. Neurosci.* **33**, 9734–9742 (2013).
28. M. S. Reid et al., *Brain Res.* **733**, 83–100 (1996).
29. M. Okura, J. Riehl, E. Mignot, S. Nishino, *Neuropsychopharmacology* **23**, 528–538 (2000).
30. J. D. Miller, K. F. Faulk, S. S. Bowersox, W. C. Dement, *Brain Res.* **509**, 169–171 (1990).
31. E. Hasegawa et al., *Proc. Natl. Acad. Sci. U.S.A.* **114**, E3526–E3535 (2017).

ACKNOWLEDGMENTS

We thank T. Amano and T. Maejima for valuable discussions.

Funding: This work was supported by JSPS KAKENHI Grant-in-Aid for Scientific Research (B) (JP 18H02595) (to T.S.); JSPS KAKENHI Grant-in-Aid for Scientific Research (A) (JP 21H04796) (to T.S.); JSPS KAKENHI Grant-in-Aid for Scientific Research on Innovative Areas, “Widdynamics” (16H06401) (to T.S.); JSPS KAKENHI grant no. JP19K22465 (to T.S.); JST CREST grant no. JPMJCR1655 Japan (to T.S.); AMED grant no. JP21zf0127005 (to T.S.); JSPS KAKENHI Grant-in-Aid for Young Scientists (18K14846) (to E.H.); Naito Memorial Science Grant/Research Grant 2017 (to E.H.); SENSHIN Medical Research Foundation 2017 Young Researcher Grant (to E.H.); and Takeda Science Foundation 2019 (to E.H.).

Author contributions: Conceptualization: E.H. and T.S. Methodology: E.H., T.S., Y.C., A.M., K.S., and Y.L. Funding acquisition: E.H. and T.S. Project administration: E.H. and T.S. Supervision: T.S. Writing: E.H. and T.S. **Competing interests:** The authors declare that they have no competing interests. **Data and materials availability:** All data are available in the main text or the supplementary materials.

SUPPLEMENTARY MATERIALS

science.org/doi/10.1126/science.abl6618
Materials and Methods
Figs. S1 to S11
Tables S1 to S6
References (32–37)
MDAR Reproducibility Checklist
Movies S1 and S2

29 July 2021; accepted 14 January 2022
10.1126/science.abl6618

SYNTHETIC GENOMICS

Transcriptional neighborhoods regulate transcript isoform lengths and expression levels

Aaron N. Brooks^{1,†}, Amanda L. Hughes^{1,†}, Sandra Clauder-Münster¹, Leslie A. Mitchell^{2,§}, Jef D. Boeke^{2,3}, Lars M. Steinmetz^{1,4,5,*}

Sequence features of genes and their flanking regulatory regions are determinants of RNA transcript isoform expression and have been used as context-independent plug-and-play modules in synthetic biology. However, genetic context—including the adjacent transcriptional environment—also influences transcript isoform expression levels and boundaries. We used synthetic yeast strains with stochastically repositioned genes to systematically disentangle the effects of sequence and context. Profiling 120 million full-length transcript molecules across 612 genomic perturbations, we observed sequence-independent alterations to gene expression levels and transcript isoform boundaries that were influenced by neighboring transcription. We identified features of transcriptional context that could predict these alterations and used these features to engineer a synthetic circuit where transcript length was controlled by neighboring transcription. This demonstrates how positional context can be leveraged in synthetic genome engineering.

Gene regulatory sequence features such as promoters and terminators are considered primary drivers of transcript isoform boundaries and expression levels (1–4). In synthetic biology, promoters and terminators are assembled along with coding DNA sequences (CDSs) into transcriptional units (TUs). Promoters and terminators are characterized and distributed as standardized parts. These are used analogously to plug-and-play modules in electronics as if they would function identically in any context (5–7). However, this is not always the case. TUs in eukaryotic genomes exhibit a high degree of interdependence (8) as a result of the physical effects of transcribing neighboring genes (9–11). For example, transcriptional interference between neighboring genes can influence the selection of isoform boundaries and impact expression levels (12–14). Quantifying the extent to which isoform expression and boundaries are driven by factors beyond DNA sequences could improve rational genome design. However, this has been difficult to test systematically as existing technologies cannot achieve the scale required to observe genes in many alternative genetic and transcriptional contexts.

Synthetic yeast genomes create genetic diversity

To overcome this challenge, a synthetic yeast genome (Sc2.0) was designed to encode a Cre-dependent system known as synthetic chro-

mosome rearrangement and modification by LoxP-mediated evolution (SCRaMbLE), which can generate stochastic genomic rearrangements on demand directly in its genome (15). These rearrangements occur at 34 base pair (bp)–loxPsym sites inserted 3 bp downstream of the stop codon of all nonessential CDSs. Upon induction of Cre recombinase, loxPsym sites can recombine in either orientation, producing duplications, deletions, inversions, and translocation events (Fig. 1A). Because of the placement of the loxPsym sites, rearranged CDSs retain their native promoters but can be decoupled from downstream sequences such as 3′-untranslated regions (3′UTRs).

The synthetic yeast chromosome IXR (synIXR) is 91,010 bp in length and contains 43 loxPsym-flanked segments. After SCRaMbLE of synIXR, 64 strains containing 156 deletions, 89 inversions, 94 duplications, and 55 additional complex rearrangements were isolated (16). Notably, these strains do not suffer from gross growth defects (table S1). Altogether, these SCRaMbLE genomes harbor 612 novel (i.e., newly created) junctions formed by juxtaposing genomic segments that are usually separated (Fig. 1A). As some rearrangements occur more than once, there are 363 distinct novel junctions. These novel junctions represent several different types of rearrangements, specifically new convergent and tandem gene pairs; genes with alternative 3′UTRs; and complex juxtapositions of coding sequences, noncoding RNAs (ncRNAs), regulatory elements, and intergenic sequences (fig. S1A) (17). We used this genomic diversity to determine the relative contributions of DNA sequence features versus transcriptional context in establishing RNA isoform boundaries and expression levels.

We profiled the transcriptomes of 64 previously genotyped synIXR SCRaMbLE strains; the parental strain (–SCRaMbLE, JS94), which bears synIXR without rearrangements; and

¹European Molecular Biology Laboratory (EMBL), Genome Biology Unit, 69117 Heidelberg, Germany. ²Institute for Systems Genetics and Department of Biochemistry and Molecular Pharmacology, NYU Langone Health, New York, NY 10016, USA. ³Department of Biomedical Engineering, NYU Tandon School of Engineering, Brooklyn, NY 11201, USA. ⁴Stanford Genome Technology Center, Stanford University, Palo Alto, CA 94304, USA. ⁵Department of Genetics, School of Medicine, Stanford University, Stanford, CA 94305, USA. ***Corresponding author. Email:** lars.steinmetz@stanford.edu

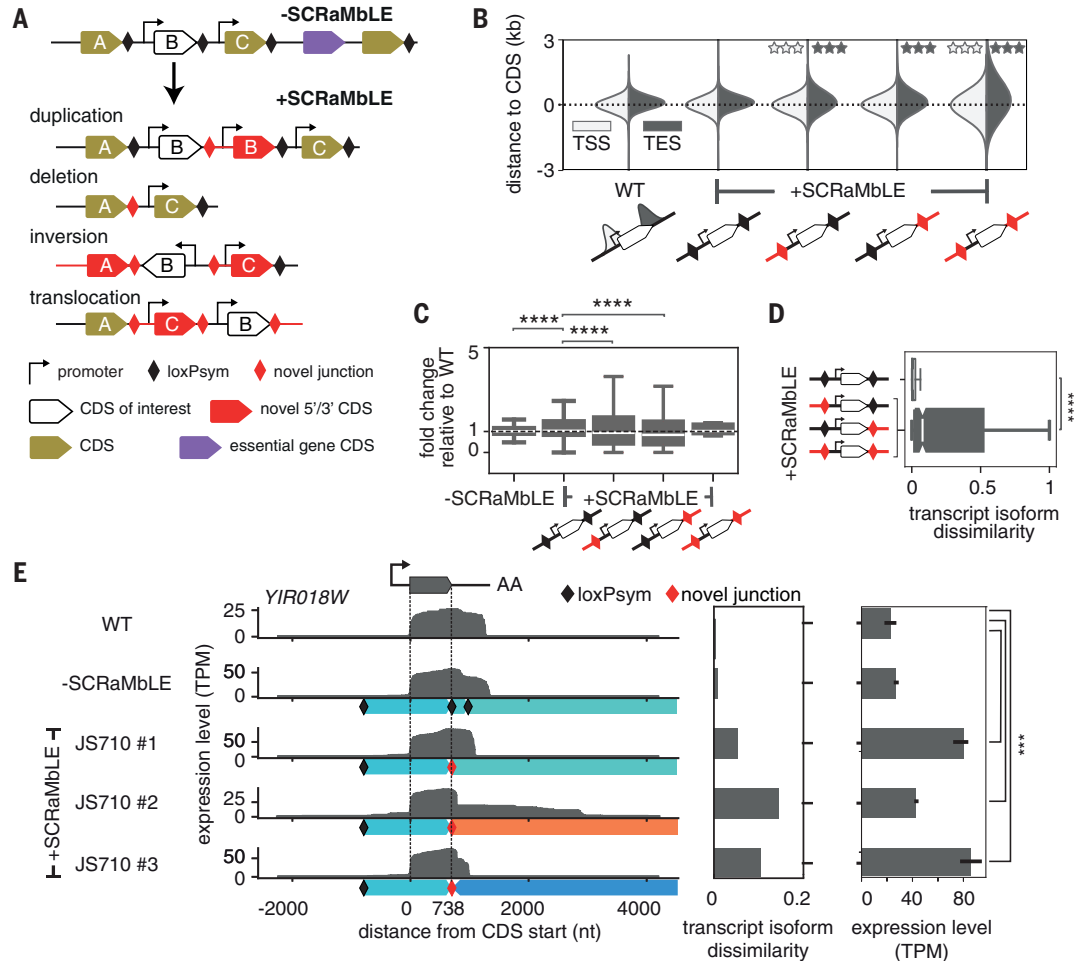
[†]These authors contributed equally to this work.

[§]Present address: Insipix, Inc., Boulder, CO 80301, USA.

[§]Present address: Neochromosome, Inc., New York, NY 11101, USA.

Fig. 1. Genome rearrangement alters transcript isoform expression and boundaries.

(A) Schematic showing SCRaMbLE-induced rearrangements between loxP sites (black diamonds) at the 3' end of all nonessential gene CDSs in the synthetic chromosome, synIXR, inducing multiple possible rearrangements of a CDS ("B" here) with novel junctions (red diamonds). (B) Distributions of TSS (white) and TES (gray) distances from gene CDSs in BY4741 (WT) and +SCRaMbLE strains, divided into rearrangements with novel (red) or native (black) 5' and/or 3' junctions. Stars indicate significant difference in variance from the WT on the basis of Levene's test for equality of variances ($q \leq 0.001$). (C) Distribution of gene expression fold changes compared with WT for the -SCRaMbLE and +SCRaMbLE strains, divided into those with novel (red) or native (black) 5' and/or 3' junctions. (D) Degree of transcript isoform dissimilarity from the WT for genes with novel 5' and/or 3' junctions (red) compared with genes in native arrangements (black) in the SCRaMbLE strains. (E) Transcript expression of the *YIR018W* gene in different contexts: WT (top row), the nonrearranged synIXR strain (-SCRaMbLE, JS94) (second row), and three contexts in a single +SCRaMbLE strain (JS710 no. 1, 2, and 3) (bottom three rows). The left plot shows full-length transcript reads aligned by the CDS (flanked by dotted lines); genomic segments below the read tracks are colored according to their original positions on synIXR as in (16); loxP sites and novel junctions are denoted by black and red diamonds, respectively. The middle plot shows transcript



isoform dissimilarity, calculated as in (D), and the right plot shows Salmon-quantified expression levels from Illumina-stranded mRNA sequencing. TPM, transcripts per million. Bars indicate 95% confidence intervals (CI) on the basis of three biological replicates. Boxplots indicate median and interquartile range (IQR) and whiskers extend to the minimum and maximum values within 1.5 times the IQR. Notches indicate 95% CIs. Asterisks denote significance levels in the Mann-Whitney U test, $***P \leq 1 \times 10^{-3}$, $****P \leq 1 \times 10^{-4}$.

two wild-type (WT) *Saccharomyces cerevisiae* controls using Oxford Nanopore direct RNA sequencing (RNA-seq). This method sequences full-length, native RNA molecules from their polyadenylate [poly(A)] tail without conversion to cDNA (18). Full-length reads span novel junctions and thus allow transcripts to be mapped to their genomic origin in the rearranged genomes (fig. S2A). Additionally, a transcript start site (TSS) and transcript end site (TES) (i.e., the isoform boundaries) can be identified for each RNA molecule. In total, we collected nearly 120 million full-length reads that passed a minimum quality threshold ($Q_{\text{mean}} \geq 6$). Across the genome, we identified 264,899 transcript isoforms that were supported by two or more reads mapping within 25 nucleotides (nt) at both ends (accounting for >77 million reads; tables S2 and S3 and fig. S2, B to F) (17).

To verify that direct RNA-seq accurately reports on transcript TSSs and TESs, we compared the isoforms that we identified on the native chromosomes to 371,087 major transcript isoforms (mTIFs) identified under similar growth conditions in WT *S. cerevisiae* through transcript isoform sequencing (TIF-seq) (19). Isoforms from direct RNA-seq corresponded well [69% of those covering a single open-reading frame (ORF) with mTIFs (fig. S3A)] (17). Notably, we observed a 60% increase in the number of polycistronic isoforms detected with long-read sequencing (4909 isoforms) compared with TIF-seq, particularly in the rearranged genomes, suggesting that direct RNA-seq better captures long RNA species (fig. S3B). To determine whether the direct RNA isoforms that we measured in the SCRaMbLE strains are stable or degraded, we analyzed transcript isoforms in exonuclease

mutants (*rrp6Δ* and *xrn1Δ*) constructed in a representative SCRaMbLE strain background but found no change in isoform abundance (fig. S4). Thus, these isoforms are part of the stable transcriptome in the SCRaMbLE strains.

Genomic rearrangements influence transcript isoform expression

Compared with the WT BY4741, individual SCRaMbLE strains produced variable numbers of transcript isoforms per gene (up to 20 times fewer or more) (fig. S5A). We identified 3228 distinct transcript isoforms generated by 50 genes on synIXR in SCRaMbLE strains compared with the -SCRaMbLE strain. These isoforms were associated with either an altered TSS (in 1313 isoforms), an altered TES (in 2378 isoforms), or simultaneous alterations at both ends (in 2736 isoforms).

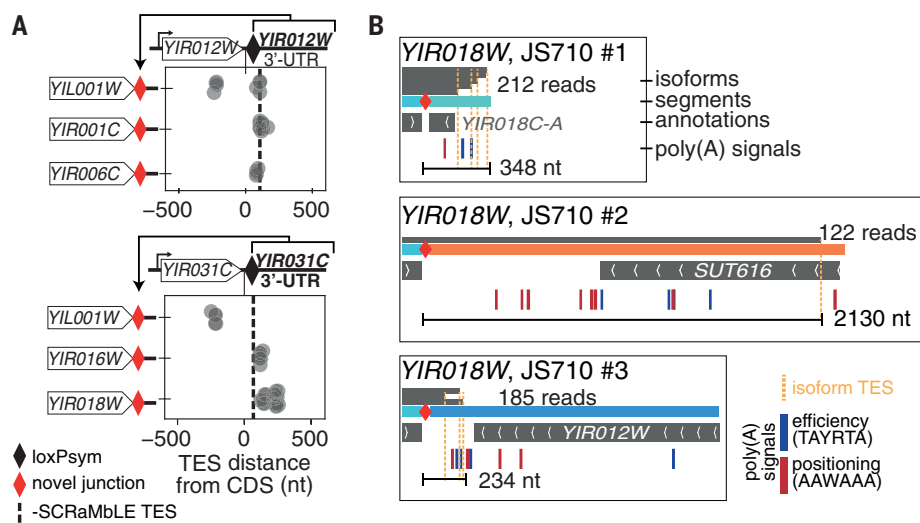


Fig. 2. Isoform boundaries are influenced by factors not encoded in the CDS or 3' UTR sequence.

(A) Examples of two 3'UTRs [from *YIR012W* (top) and *YIR031C* (bottom)] rearranged to the 3' end of three different CDSs (depicted on the left). The positions of all isoform TESs relative to the end of the CDS are plotted for each rearrangement. The TES of the major transcript isoform without rearrangement is indicated by the dashed line. Truncated TESs may indicate an early termination site in the *YIL001W* CDS. (B) 3' ends of *YIR018W* transcript isoforms (stacked gray bars with total read counts indicated) mapped to three rearrangements in the JS710 SCRaMbLE strain (as in Fig. 1E). Rearranged segments are colored according to their original locations on synXLR, as in (16). Annotations and PASs (efficiency and positioning motifs shown in blue and red, respectively) are shown below each context. The longest TES distance and total number of reads supporting the isoforms are indicated for each context. Symbols for degenerate bases in the PAS motifs are as follows: R, A/G; W, A/T; and Y, C/T.

Across all reads, we found that the locations of TSSs and TESs (in relation to their CDSs) were significantly more variable for genes rearranged into novel contexts than genes in their native context (Fig. 1B; Levene's test for equality of variances, $P \leq 0.001$). Although novel 3' junctions affected only TES positioning, novel 5' junctions affected both TSS and TES positioning even though SCRaMbLE maintained the native promoter with its CDS (Fig. 1B). To rule out that the placement of loxPsym sites 3 bp downstream of the stop codon directly affected TES positioning, we measured the change in TES positions between the -SCRaMbLE (loxPsym sites) and WT (no loxPsym sites) strains. This lengthened transcripts by only 34 nt (the length of the loxPsym site) on average (fig. S5B) and had no effect on the variability of transcript boundaries in unrearranged contexts (Fig. 1B). Thus, TES recognition is largely unaffected by the loxPsym site. Unexpectedly, essential genes—which are not flanked by loxPsym sites—also generated a variable number of isoforms across strains, further suggesting that isoforms are responsive to distal changes in their transcriptional neighborhoods (fig. S5A).

Rearrangement of genes into new contexts also affected their expression levels. We used short-read Illumina sequencing for gene expression level quantification and corrected for gene copy number changes resulting from

SCRaMbLE-induced duplications (fig. S6A) (17). On average, expression of genes in novel contexts tended to decrease although it was highly variable (Fig. 1C). For example, there were 18 instances where an unexpressed gene gained detectable expression and 141 cases where gene expression was lost (table S4) (17).

To systematically quantify the changes to the transcription profile of a TU after SCRaMbLE, we computed the cosine similarity of each TU long-read expression profile in every strain compared with that of the WT. We refer to this metric as “similarity”, or “dissimilarity” when we compute its inverse ($1 - \text{cosine similarity}$). This verified that transcript isoforms arising from novel junctions were significantly less similar to the WT than those at native junctions (Fig. 1D; Mann-Whitney U test $P \leq 1 \times 10^{-4}$). For example, the CDS encoding *YIR018W* appears in three different genomic contexts in SCRaMbLE strain JS710, which altered *YIR018W* transcript isoforms and expression levels (Fig. 1E). One context in particular severely disrupted *YIR018W* TESs, leading to 3'UTR extensions of up to 4 kb with little change in expression level (Fig. 1E, JS710 no. 2). Approximately 43% of all rearrangements produced transcript isoforms with less similarity to their native counterparts than this highly extreme rearrangement of *YIR018W*, suggesting that severe transcript isoform disruptions are widespread in SCRaMbLE genomes.

TES alterations are common in SCRaMbLE strains, as reflected by 72 novel polycistronic transcripts and 104 readthrough transcripts (≥ 100 -bp extension), such as *YIR018W*. Because native 3'UTR sequences are decoupled from the CDS by SCRaMbLE, defects in TES recognition could logically arise from the loss or gain of 3'UTR-encoded poly(A) signal (PAS) motifs. If 3'UTR sequences functioned as plug-and-play modules, they would produce the same TES positions when coupled to different CDSs. However, out of all the 3'UTRs that were coupled to multiple different CDSs in the SCRaMbLE strains, only one (*YIR012W*) maintained the TES positioning of the control -SCRaMbLE strain (Fig. 2A). In general, neither the 3'UTR sequence nor the CDS predicted the positioning of TESs (fig. S7A). Densities of PAS positioning and efficiency sequence motifs downstream of CDSs were also insufficient to explain TES positions (fig. S7B). For example, the lengthened *YIR018W* 3'UTR isoform extended through many high-efficiency PASs (Fig. 2B, JS710 no. 2). Thus, a systematic and context-aware assessment of sequence-function relationships could help guide precise engineering of transcription in yeast.

Transcriptional neighborhoods predictably influence transcript isoform boundaries

Rearrangements change not only the genetic sequence but also the transcriptional context surrounding a gene. For example, closer investigation of the *YIR018W* readthrough transcript (Fig. 1E, JS710 no. 2) shows that its context lacks the antisense transcripts present in the WT and two other rearranged contexts that maintain proximal TESs (Fig. 1E). This suggests that neighboring transcription may regulate transcript isoform boundaries and expression levels (fig. S8). To systematically assess this relationship, we extended our cosine similarity metric to quantify transcriptional alterations in flanking regions for every gene, on both strands. Rearrangements that maintained the adjacent transcriptional environment also retained local isoform properties. For example, a rearrangement that replaced the segment downstream of a polycistronic transcript encoding the essential gene *YIR015W* with one containing similar convergent transcription preserved the polycistron (Fig. 3A, first SCRaMbLE row). By contrast, an alternative rearrangement lacking proximal antisense transcription resulted in lengthened TESs and multiple novel downstream polycistronic transcripts (Fig. 3A, second SCRaMbLE row). Similarly, rearrangements that disrupted the upstream transcriptional environment altered the composition and expression of the polycistronic transcript (Fig. 3A, bottom rows).

Across the synthetic genome, TU isoforms became significantly more dissimilar to the WT

as SCRaMbLE induced greater alterations to their transcriptional neighborhoods (Fig. 3B). This relationship was also apparent in the native genome. Paralogs that have maintained similar downstream transcriptional neighborhoods since the yeast whole-genome duplication event ~100 million years ago retained similar transcriptional profiles. Even randomly selected gene pairs with comparable downstream transcriptional neighborhoods generated similar transcript isoforms (Fig. 3, C and D). Together, these results reinforce a link between transcript isoform properties and neighboring transcription both across evolution and throughout the genome.

Our data suggest that both transcriptional neighborhoods and genetic sequences influence isoform boundaries and expression levels. To disentangle these overlapping contributions systematically and genome-wide, we used machine learning. We trained Gradient Boosted Regression Trees (GBRT) to predict TU properties (i.e., expression level changes and TSS and TES distances from gene CDSs) in rearranged contexts using genetic sequence and transcriptional neighborhood features for the predictions (17). Specifically, up- and downstream gene identity and orientation were used as a proxy for sequence features, and properties of the up- and downstream transcriptional environment up to 3 kb away—including gene expression levels, isoform similarity on either strand, and distance to the nearest TU—were used as transcriptional neighborhood features (17). To interpret these models, we computed the predictive value of each feature (Fig. 4A). As expected, upstream features better predicted TSSs and downstream features better predicted TESs, although both contributed equally to predicting expression level changes (Fig. 4A). Notably, models trained only on transcriptional neighborhood features performed comparably to the model trained on all features (Fig. 4B) (17). Thus, changes to isoform boundaries and expression levels in novel genomic contexts are predictable solely from the transcriptional neighborhood. Observations in our dataset support individual associations learned by the GBRT model. For example, placing a TU in a highly expressed region increased its expression (fig. S9A). Likewise, TSS and TES distance from the CDS tended to increase with distance to neighboring 5' and 3' transcription, respectively (fig. S9B).

Engineering TU isoform properties using transcriptional neighborhoods would be impractical if the transcriptional environment (and hence the TU itself) must be measured in each new genetic context. We therefore investigated whether changes to transcriptional neighborhoods in SCRaMbLE strains could be estimated from their transcriptional profiles in the -SCRaMbLE reference strain. Indeed, transcriptional similarities estimated

from the -SCRaMbLE strain correlated with the changes observed in the SCRaMbLE strains (Fig. 4C; Pearson's correlation coefficient (r) = 0.78 and 0.7 for 5' and 3' neighborhoods,

respectively) (17). Thus, transcript isoform properties are predictable from neighboring transcription and can be engineered by modifying the transcriptional neighborhood.

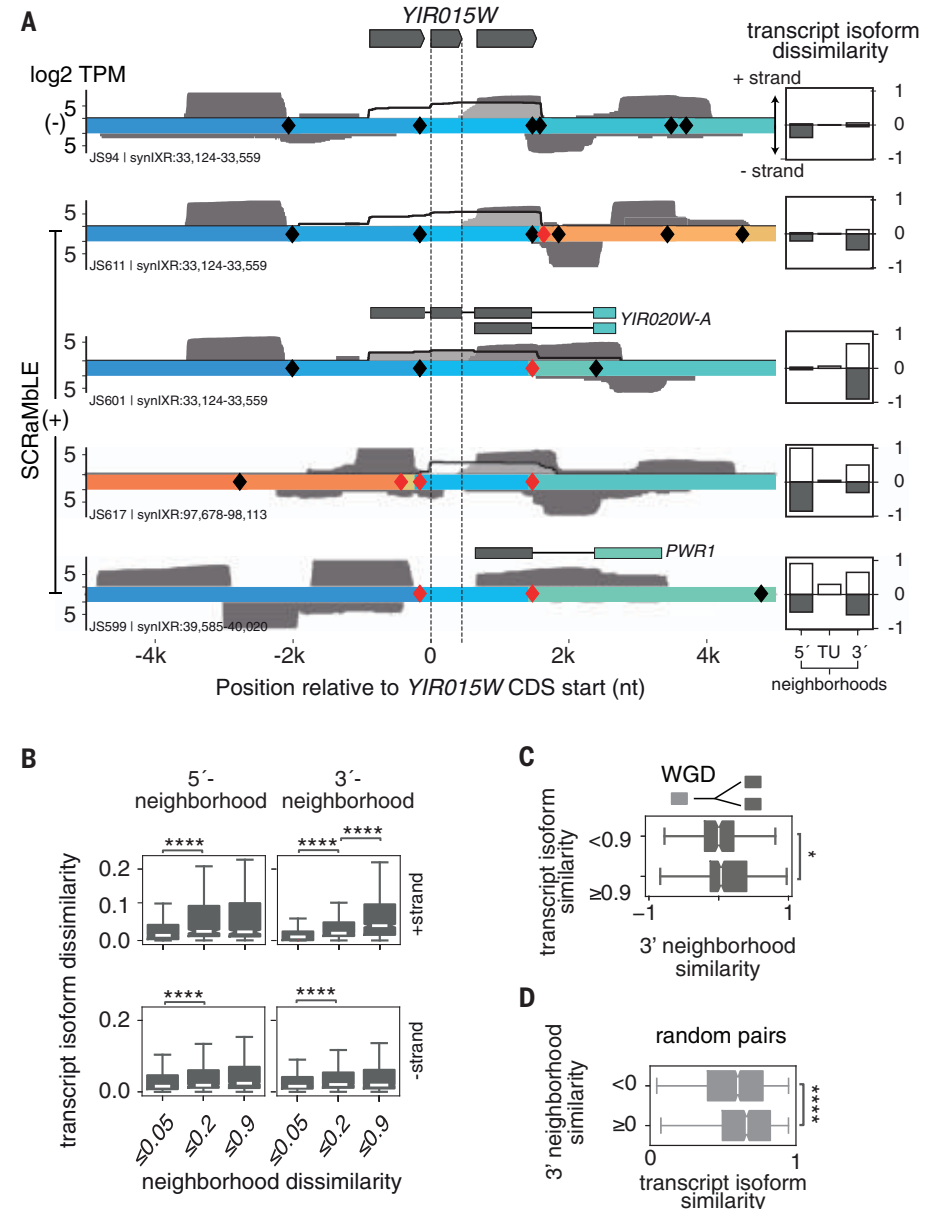


Fig. 3. Transcript isoforms are altered when transcriptional neighborhoods are perturbed. (A) Direct RNA transcript reads covering the essential nuclear ribonuclease P (RNaseP) gene *YIR015W* in -SCRaMbLE and four +SCRaMbLE strains. Reads spanning *YIR015W* CDS are outlined in black with a translucent fill; other reads within a ±5-kb region are solid gray. Sense and antisense reads are located above and below the genomic segment tracks; segments are colored according to their original position on synIXR, as in (16). Gene models show novel polycistronic transcripts incorporating genes from rearranged segments. Quantification of dissimilarity relative to WT expression profiles for each strand (white and gray boxes) in the 5' and 3' regions flanking the TU and for the TU itself are displayed next to each track. Note that k denotes 1000. **(B)** Transcript dissimilarity from the WT is assessed separately in each panel for rearrangements affecting the 5' or 3' transcriptional neighborhood within a 3-kb window on either strand. **(C)** The transcriptional similarities of 3' neighborhoods on both strands are compared for paralogs with more (≥0.9) or less (<0.9) transcript isoform similarity. WGD, whole-genome duplication. **(D)** Transcript isoform similarity of randomly selected gene pairs compared on the basis of the similarity of their downstream transcriptional environment on both strands. Data are represented as the median and IQR with whiskers extending to the minimum and maximum values within 1.5 times the IQR. Notches indicate 95% CIs. Asterisks denote significance levels in the Mann-Whitney *U* test, * $P \leq 0.05$, **** $P \leq 1 \times 10^{-4}$.

Fig. 4. Transcriptional neighborhood predicts transcript isoform expression levels and lengths.

(A) Averaged feature importance scores for models predicting TSS or TES positioning or expression level changes (Δ expn level) for genes in the SCRaMbLE strains learned using Gradient Boosted Regression Trees (GBRT). Stacked bars show the fractional contribution of sequence features and transcriptional features (transcriptional similarity on either strand, expression level fold change, and distance to the nearest isoform) in the 5' and 3' neighborhoods (within 3 kb) for each prediction. The importance of all 5' and 3' features sums to one for each prediction task. (B) Performance of models predicting TSS or TES positioning or Δ expn level trained using genomic features only (sequence), features related to the transcriptional neighborhood only (transcription), or all features (full). Bars indicate 95% CI across all models. MSE, mean squared error. (C) Observed versus predicted (from -SCRaMbLE) flanking transcriptional similarities for rearranged segments and their correlation (Pearson's correlation coefficient, r). Areas of greater density are darker. Because transcript isoform coverage vectors on both strands were used, cosine similarity ranges from -1 to 1.

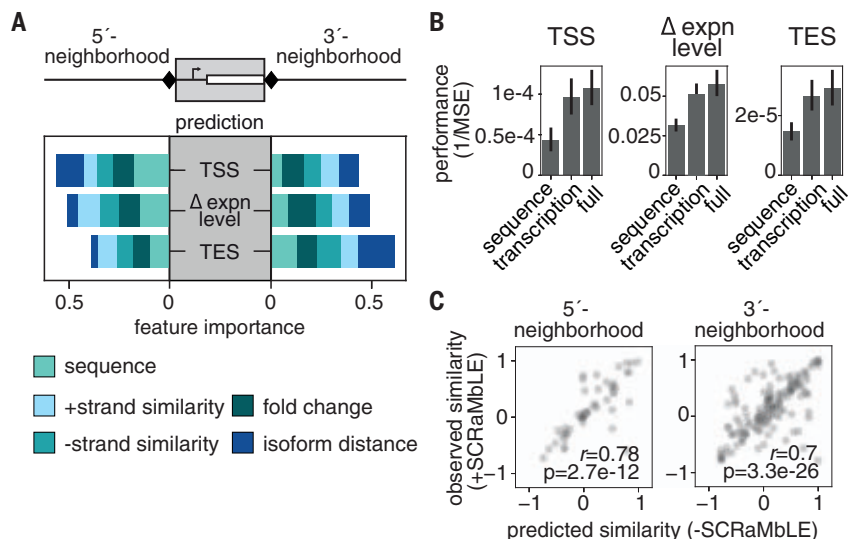
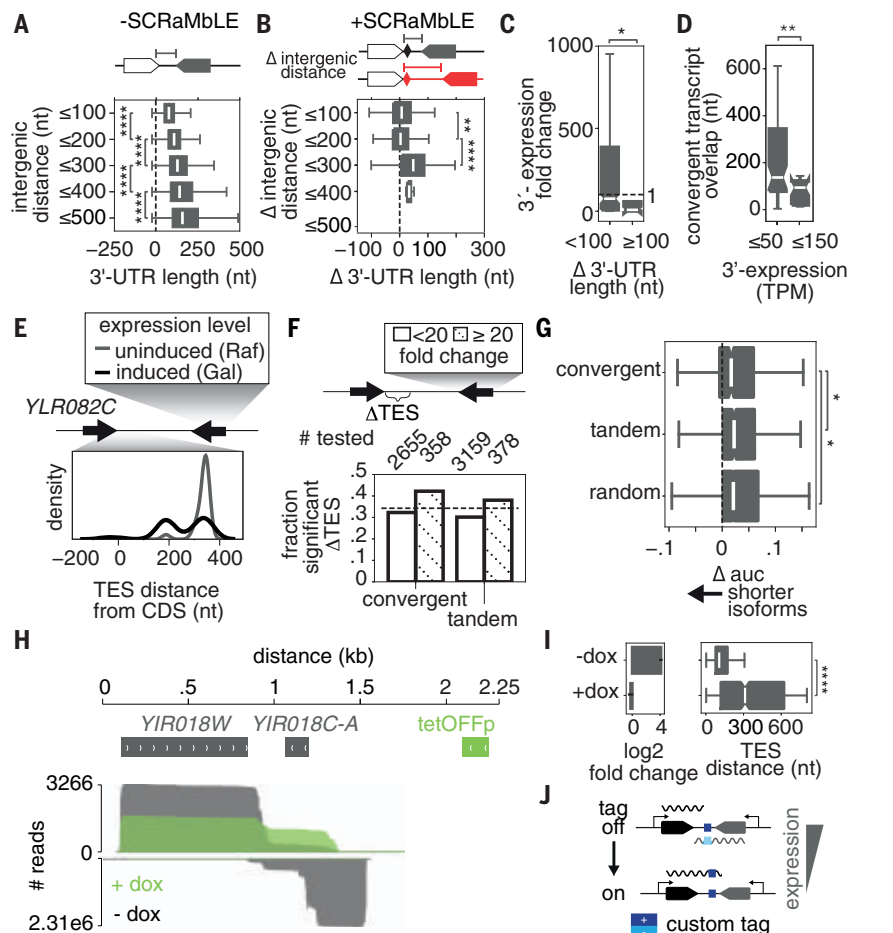


Fig. 5. Neighboring gene expression regulates and can be used to engineer 3' UTR lengths.

(A) 3'UTR lengths of convergent genes binned by 100-bp increments of intergenic distance in the WT genome. (B) Change in 3'UTR lengths of convergent gene pairs plotted by increased (100-bp increments) intergenic distance after SCRaMbLE. (C) Expression fold changes of genes convergent to those with minor (<100 nt) or major (≥ 100 nt) 3'UTR extensions after rearrangement. (D) Length of overlap (nt) between novel convergent transcripts where the downstream member is expressed at a low (≤ 50 TPM) or high (≥ 150 TPM) level. (E) Distribution of *YLR082C* TESs (relative to its CDS) when the convergent gene is overexpressed (Gal, black) or not (Raf, gray). (F) Fraction of genes in convergent and tandem pairs with significantly altered TES positions (Kolmogorov-Smirnov test, $P \leq 0.001$, applied to each gene) when an adjacent gene is overexpressed by a factor of ≥ 20 (hatched) or not (white) after galactose-induced transcription factor (TF) overexpression. Dashed lines indicate the fraction of randomly selected genes with significantly altered TESs in galactose. Numbers of genes tested are indicated above the bars. (G) Change in 3'UTR length distributions for convergent, tandem, and random gene pairs upon TF overexpression in galactose as assessed by the change in the area under the curve (Δ auc) of TES cumulative distributions. Negative values indicate isoform shortening. (H) cDNA sequencing reads aligned to *YIRO18W* (above) and *YIRO18C-A* (below) in a tetracycline-repressible *YIRO18C-A* strain in the absence (gray) and presence (green) of doxycycline. (I) Change in *YIRO18C-A* expression (left), plotted as mean \pm SD, and *YIRO18W* 3' UTR length (right) upon doxycycline-induced inhibition of *YIRO18C-A* expression. (J) The ability to control 3'UTR length by altering convergent gene expression levels could be applied to embed a reversibly expressed, functional sequence tag in transcript 3'UTRs. Only adjacent bins were tested for significance in (A) and (B). Boxplots indicate median and IQR, and whiskers extend to the minimum and maximum values within 1.5 times the IQR. Notches indicate 95% CIs. Asterisks denote significance levels in the Mann-Whitney U test, * $P \leq 0.05$, ** $P \leq 1e-2$, **** $P \leq 1e-4$.



3' UTR lengths can be tuned by convergent transcription

To define principles of neighboring transcriptional cross-talk that could support synthetic genome design, we investigated the relationship between specific features of the model (e.g., intergenic distance and local expression level) and transcript isoform boundaries. There was an increase in 3'UTR lengths as intergenic distance increased across the native yeast genome in our dataset (Fig. 5A) with 3'UTRs of convergently transcribed genes becoming ~25 nt longer for every 100-bp increment of intergenic distance. A similar trend occurred for SCRaMbLE-induced novel convergent gene pairs, although few intergenic distances increased by >300 nt (Fig. 5B). Additionally, 3'UTR lengths were sensitive to downstream expression levels, with decreased levels associated with lengthened 3'UTRs (Fig. 5C). Notably, a significant fraction (34 of 104, hypergeometric P value = 1.2×10^{-7}) of the isoforms extended by ≥ 100 nt were relocated into convergent arrangements with reduced downstream gene expression.

Across the genome, transcripts of convergent genes consistently overlapped by 85 nt on average in our dataset (fig. S10A), consistent with previous observations (20). Even genes rearranged by SCRaMbLE into novel convergent pairs produced transcripts overlapping by 85 nt on average, implying that the process of transcription itself—rather than sequence features—directs the length-restricted interdigitation of convergent 3'UTRs. Reinforcing the observation that transcript length responds to transcriptional context, we found that the overlap length and the fraction of the intergenic space dominated by a transcript increased as the expression level of the convergent transcript decreased (fig. S10, B and C). Additionally, novel convergent gene pairs with a lowly expressed (≤ 50 TPM) downstream gene produced significantly longer overlaps (Fig. 5D).

To confirm that 3'UTR lengths are limited by convergent transcription in the native yeast genome, we measured the effects of perturbing gene expression on isoform boundaries of gene pairs genome-wide. We overexpressed transcription factors (*MSN2*, *GCN4*, *STE12*, *ADRI*, and *HAC1*) in a galactose-inducible manner and mapped the shortening of 3' ends of genes adjacent to those induced by transcription factor overexpression (Fig. 5E) (21). Across all transcription factor overexpression strains, 449 convergent and 502 tandem gene pairs showed a ≥ 20 -fold increase in expression of at least one of their members when grown in galactose (fig. S11). In line with our predictions, 42% of all genes convergent to a gene with a ≥ 20 -fold expression-level increase in galactose had significantly altered TES positioning (Fig. 5F; Kolmogorov-Smirnov test, $P \leq 0.001$, applied to each gene). Convergent genes also had significantly shorter 3'UTR length alterations

when their neighbor was overexpressed than did tandem or random gene pairs (Fig. 5G; the Mann-Whitney U test, $P \leq 0.05$), supporting a role for convergent transcription in limiting 3'UTR length.

Finally, to demonstrate that our model can be applied to genome engineering, we constructed a tetracycline-repressible system to reversibly control a transcript's 3'UTR length by tuning the expression of a downstream, convergent transcript. We chose the *YIRO18W/YIRO18C-A* convergent gene pair, as the length of the *YIRO18W* 3'UTR appeared sensitive to downstream convergent transcription when placed into novel contexts (Fig. 1E and fig. S8). Incorporating a P7xtetO promoter in the BY4741 *YIRO18C-A* locus increased its expression 20-fold and shortened transcript isoforms from the convergent gene, *YIRO18W*. Adding doxycycline to turn off the promoter returned *YIRO18C-A* expression to WT levels and restored *YIRO18W* transcript lengths (Fig. 5, H and I). Because there was no sequence alteration, the 3'UTR alterations resulted solely from transcription changes in the downstream convergent transcript.

Discussion

We show that distal transcription influences local transcript isoform boundaries and expression levels in a predictable manner. Our observations regarding 3'UTR extensions in convergent transcripts suggest that adjacent transcription imposes physical constraints on isoform boundaries. Along with other factors such as PAS motifs, antisense transcription appears to play a role in TES positioning, making convergent genes sensitive to the expression levels of their neighbors. We suggest that convergent transcription may slow RNA polymerase transit thereby affecting TES selection, similar to the regulation of proximal PAS usage by nucleotide availability or mutations that slow RNA polymerase elongation (22).

Relationships between neighboring TUs could be coopted to engineer genomes. For example, the dynamic range of gene expression changes that we observed in rearranged genetic contexts suggests that transcriptional neighborhoods could be exploited to tune expression of TUs by a factor of at least five (Fig. 1C). Furthermore, local gene expression, order, orientation, and/or distance could inform the construction of synthetic circuits that interlink the regulation of neighboring TUs. Specifically, expression could be increased by placing a gene in a highly expressed region, or its TES position could be modulated by altering expression levels or distance of a neighboring convergent transcript. These design principles expand the synthetic biology toolkit and reveal the potential to embed functionalities into a reversibly expressed 3'UTR controlled by

neighboring TU expression, which we term “transcriptional embedding” (Fig. 5J).

We conclude that most yeast DNA sequences do not encode simple plug-and-play properties but have evolved cofunctional relationships that are perturbed outside of their native context. Evaluating the behavior of DNA sequence parts in alternative genomic contexts will provide additional tools to improve rational genome design.

REFERENCES AND NOTES:

1. Z. Guo, F. Sherman, *Mol. Cell. Biol.* **16**, 2772–2776 (1996).
2. F. Ozsolak et al., *Cell* **143**, 1018–1029 (2010).
3. Y. M. Danino, D. Even, D. Ideses, T. Juven-Gershon, *Biochim. Biophys. Acta* **1849**, 1116–1131 (2015).
4. S. Lubliner et al., *Genome Res.* **25**, 1008–1017 (2015).
5. K. A. Curran, A. S. Karim, A. Gupta, H. S. Alper, *Metab. Eng.* **19**, 88–97 (2013).
6. H. Redden, H. S. Alper, *Nat. Commun.* **6**, 7810 (2015).
7. T. Raveh-Sadka et al., *Nat. Genet.* **44**, 743–750 (2012).
8. J. Mellor, R. Woloszczuk, F. S. Howe, *Trends Genet.* **32**, 57–71 (2016).
9. S. Meyer, G. Beslon, *PLoS Comput. Biol.* **10**, e1003785 (2014).
10. S. S. Teves, S. Henikoff, *Nat. Struct. Mol. Biol.* **21**, 88–94 (2014).
11. D. J. Hobson, W. Wei, L. M. Steinmetz, J. Q. Svejstrup, *Mol. Cell* **48**, 365–374 (2012).
12. J. Colin et al., *Mol. Cell* **56**, 667–680 (2014).
13. E. M. Prescott, N. J. Proudfoot, *Proc. Natl. Acad. Sci. U.S.A.* **99**, 8796–8801 (2002).
14. I. H. Greger, N. J. Proudfoot, *EMBO J.* **17**, 4771–4779 (1998).
15. J. S. Dymond et al., *Nature* **477**, 471–476 (2011).
16. Y. Shen et al., *Genome Res.* **26**, 36–49 (2016).
17. See supplementary materials.
18. D. R. Garalde et al., *Nat. Methods* **15**, 201–206 (2018).
19. V. Pelechano, W. Wei, L. M. Steinmetz, *Nature* **497**, 127–131 (2013).
20. T. Nguyen et al., *eLife* **3**, e03635 (2014).
21. R. Sopko et al., *Mol. Cell* **21**, 319–330 (2006).
22. C. Yague-Sanz et al., *Genes Dev.* **34**, 883–897 (2020).
23. A. N. Brooks et al., *Zenodo* (2022); <https://doi.org/10.5281/zenodo.5676293>.

ACKNOWLEDGMENTS

We thank members of the Steinmetz lab, particularly B. Linder, D. Schraivogel, B. Rauscher, M. Bertolini, and K. Fenzl, for useful discussion and helpful comments on the manuscript. We also thank Life Science Editors for assistance with preparing the manuscript. We thank V. Benes, F. Jung, and the EMBL Genomics Core Facility for performing Illumina RNA sequencing. **Funding:** This work was funded by grants from the BMBF (031A460 to L.M.S.) and the Volkswagen Stiftung (94769 to L.M.S.). A.N.B. was supported by a fellowship from the EMBL Interdisciplinary Postdoc (EIPD) program under Marie Skłodowska-Curie Actions COFUND (grant no. 664726). This work was supported in part by NSF grants MCB-161611 and MCB-1445537 to J.D.B. **Author contributions:** Conceptualization: A.N.B., A.L.H., and L.M.S. Methodology: Writing – Original Draft and Visualization: A.N.B. and A.L.H. Software, Data Curation, and Formal Analysis: A.N.B. Investigation: A.L.H. and S.C.M. Writing – Review and Editing: A.N.B., A.L.H., J.D.B., and L.M.S. Resources: L.A.M. and J.D.B. Funding Acquisition and Supervision: A.N.B. and L.M.S. **Competing interests:** L.A.M. is affiliated with Neochromosome, Inc. The other authors declare no competing interests. **Data and materials availability:** Raw data can be downloaded from NCBI SRA (PRJNA664019). Code used to perform analyses can be accessed at git.embl.de/brooks/scramble-transcriptome/. Code and trained GBR models can be accessed at Zenodo (23). A genome browser featuring both long- and short-read alignments is available at <https://apps.embl.de/scramble/>.

SUPPLEMENTARY MATERIALS

science.org/doi/10.1126/science.abg0162
Materials and Methods
Supplementary Text
Figs. S1 to S12
Tables S1 to S7
References (24–41)
MDAR Reproducibility Checklist

4 December 2020; resubmitted 29 July 2021
Accepted 31 January 2022
[10.1126/science.abg0162](https://doi.org/10.1126/science.abg0162)

ULTRACOLD CHEMISTRY

Control of reactive collisions by quantum interference

Hyungmok Son^{1,2*}, Juliana J. Park¹, Yu-Kun Lu¹, Alan O. Jamison³, Tijs Karman⁴, Wolfgang Ketterle¹

In this study, we achieved magnetic control of reactive scattering in an ultracold mixture of ^{23}Na atoms and $^{23}\text{Na}^6\text{Li}$ molecules. In most molecular collisions, particles react or are lost near short range with unity probability, leading to the so-called universal rate. By contrast, the $\text{Na} + \text{NaLi}$ system was shown to have only ~4% loss probability in a fully spin-polarized state. By controlling the phase of the scattering wave function via a Feshbach resonance, we modified the loss rate by more than a factor of 100, from far below to far above the universal limit. The results are explained in analogy with an optical Fabry-Perot resonator by interference of reflections at short and long range. Our work demonstrates quantum control of chemistry by magnetic fields with the full dynamic range predicted by our models.

Advances in cooling atoms and molecules have opened up the field of quantum scattering resonances (1–4) and ultracold chemistry (5, 6). At micro- and nanokelvin temperatures, collisions occur only in the lowest partial wave, and the collisional physics can be reduced to a few well-defined parameters, which, in many systems, are the s-wave scattering length and a two-body loss-rate coefficient. Collisions involving molecules are often much more complex, owing to the strong anisotropic interaction at short range and multiple decay channels including reactions (7–10). One goal of current research is to identify systems that can still be understood with relatively simple models, including the model of universal rate coefficients (11), as well as single-channel and two-channel models. Such systems are most likely to enable researchers to achieve controllable quantum chemistry in which the outcome of reactions is steered by external electromagnetic fields (12, 13).

Collisions in molecular systems can be described by the reflection of the wave function in two regions. At long range, the attractive van der Waals (vdW) potential acts as a highly reflective mirror; owing to quantum reflection in low-temperature scattering (Fig. 1). When the colliding particles are in close proximity, they can again be reflected by the repulsive short-range potential, or they can get lost because of reactions and/or inelastic transfer to other states. These losses can be represented by transmission through the short-range mirror

(Fig. 1). In the universal limit, the transmission is 100%, and the entire incoming flux is lost.

Most ultracold molecular collisions studied thus far have loss-rate coefficients at or close to the universal value (14–25). However, when partial reflection occurs at short range, the resulting loss rate can be higher or lower than the universal value, depending on the interference created by multiple reflection pathways. This fact is analogous to an optical Fabry-Perot interferometer. This optical analog fully captures the results of a single-channel description of reactive molecular collisions (11, 26). We extended the single-channel model by adding a Feshbach resonance as a lossless phase shifter that can tune between constructive and destructive interferences.

Our experimental system, which consists of collisions of triplet ro-vibrational ground-state NaLi with Na near 978 G, is fully described by this Fabry-Perot model. We saw loss rates that exceeded the universal rates by a factor of ~5, tunable via a Feshbach resonance over a range of more than two orders of magnitude. We have also characterized a weaker loss resonance, where the phase shifter was “lossy”—i.e., the closed channel of the Feshbach resonance had a short lifetime and dominated the loss, almost completely spoiling the quality factor of the Fabry-Perot resonator. This resonance has to be described by a two-channel model with the lifetime of the bound state as an additional parameter (27). Our experiment has established $\text{NaLi} + \text{Na}$ as a distinctive system that realizes the full dynamic range of recent models developed to describe reactive collisions involving ultracold molecules (11, 26). Furthermore, to the best of our knowledge, this system is only the second example for which Feshbach resonances between ultracold molecules and atoms have been found (28, 29).

Experimental protocol

A mixture of $\sim 3 \times 10^5$ Na atoms and $\sim 3 \times 10^4$ NaLi molecules in the triplet ro-vibrational

ground state was produced in a 1596-nm one-dimensional (1D) optical lattice created by retro-reflecting the trapping beam. The sample was confined as an array of ~1000 pancake-shaped clouds. The atoms and molecules were both in the upper stretched hyperfine states, where all electron and nuclear spins were aligned along the bias field (30, 31). This spin-polarized mixture was in a chemically stable quartet state. The sample was prepared at a temperature $T_{\text{NaLi}} \approx T_{\text{Na}} \sim T = 1.55 \mu\text{K}$, well within the regime for threshold behavior of collisions, which required the temperature to be much less than the characteristic temperature determined by the vdW potential, $T_{\text{vdW}} = \hbar^2/2\mu k_B r_6^2$ (32) with the vdW length $r_6 = (2\mu C_6/\hbar^2)^{1/4}$, where \hbar is Planck's constant divided by 2π , μ is the reduced mass of NaLi and Na , k_B is the Boltzmann constant, and C_6 is the vdW constant for the atom-molecule potential. With $C_6 = 4026$ in atomic units (33), $T_{\text{vdW}} \approx 500 \mu\text{K}$.

The atom-molecule mixture was initially prepared near the Na-Li Feshbach resonance at 745 G, and then the bias field was ramped to the target value in 15 ms. We determined collisional lifetimes of the atom-molecule mixture by holding the sample for a variable time at the target magnetic field, after which the field was ramped back to 745 G where the remaining molecules were dissociated and detected. The number of dissociated Li or Na atoms in the hyperfine ground state was measured by resonant absorption imaging (30). The hyperfine state of Na atoms from dissociation differed from that of Na atoms in the initial atom-molecule mixture.

Decay curves for the molecules are compared in the inset of Fig. 2, near and far away from the strong atom-molecule Feshbach resonance studied in this work. Our observable $\gamma(B)$ (where γ is the loss rate and B is the magnetic field) is the difference of initial loss rates of NaLi molecules with and without Na atoms. It is obtained by fitting the whole decay curve using the standard differential equations for two-body decay [see supplementary materials (SM)]. The loss in the absence of Na atoms is caused by p-wave reactive collisions between molecules. The measured molecular two-body loss-rate coefficient $\beta = 2.6(7) \times 10^{-12} \text{ (cm}^3/\text{s)}$ ($T_{\text{NaLi}}/\mu\text{K}$) near 980 G is within a factor of 2 of the prediction from the universal loss model (see SM). Single-particle loss due to the vacuum-limited lifetime of >20 s was negligible.

We avoided the need for absolute sodium density measurements by comparing the measured decay rate to the decay rate of the mixture in a nonstretched spin state. Because this mixture collides on a highly reactive doublet potential, the decay was reliably predicted to occur with the s-wave universal rate coefficient, which is well known for our system (33). By

¹MIT-Harvard Center for Ultracold Atoms, Research Laboratory of Electronics, Department of Physics, Massachusetts Institute of Technology, Cambridge, MA 02139, USA. ²Department of Physics, Harvard University, Cambridge, MA 02138, USA. ³Institute for Quantum Computing and Department of Physics and Astronomy, University of Waterloo, Waterloo, Ontario N2L 3G1, Canada. ⁴Institute for Molecules and Materials, Radboud University, Heijendaalseweg 135, 6525 AJ Nijmegen, Netherlands. *Corresponding author. Email: hson@g.harvard.edu

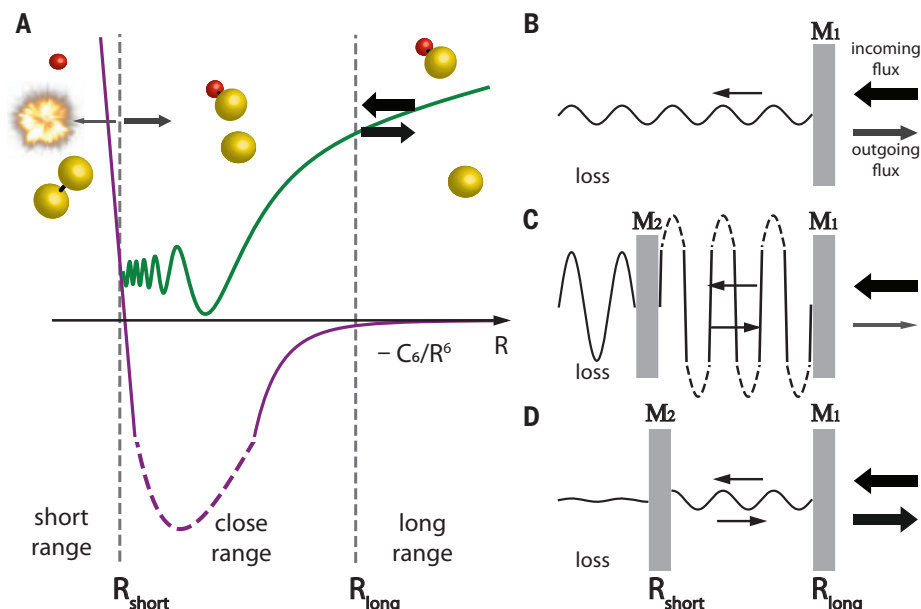


Fig. 1. Fabry-Perot interferometer model for reactive collisions. (A) Collisions between an atom (yellow sphere) and a molecule (yellow and red sphere together) occur in a potential that is the attractive vdW potential $-C_6/R^6$ at long range [$R > R_{\text{long}}$ (where R is the interparticle distance)] and a strongly repulsive potential at short range ($R < R_{\text{short}}$). The scattering dynamics (represented by the wave function in green) can be fully described by quantum reflection off of the vdW potential at $R \sim R_{\text{long}}$ and reflection and transmission at $R \sim R_{\text{short}}$ (11, 26). Loss at close and short range is caused by the coupling of the incoming channel (in our case, a chemically stable quartet state) to a lossy channel (here, a reactive doublet state) and described by a reflectivity of $<100\%$ of the inner mirror. For instance, in the doublet state, a singlet Na_2 molecule (two yellow spheres) can be formed. This situation is fully analogous to an optical Fabry-Perot interferometer with two partially reflective mirrors (M_1 and M_2). Reactive loss is proportional to the flux transmitted through both mirrors. (B) Transmission through mirror M_1 only represents the universal loss. Depending on constructive and destructive interference between multiple reflections, the loss can be highly enhanced [on resonance (C)] or suppressed (D) relative to the universal loss. (C) and (D) are depicted for a reflectivity $|r_2|^2 \sim 0.89$, with 1000-fold loss enhancement between these panels.

comparing datasets taken at different times (see SM), we estimated the uncertainty of the density calibration to be $\sim 40\%$.

We also measured the loss rate of the mixture in the nonstretched spin state by using the measured particle number and temperature, as well as a model for the anharmonic trapping potential. With the measurement, we have confirmed within 30% uncertainty that the rate is indeed the universal rate (see SM). Because we regard the theoretical prediction to be highly reliable, we did not use the experimental density calibration in the analysis reported here.

Fabry-Perot interferometer model

Reactive scattering between molecules and atoms can be matched to the simple picture of an optical Fabry-Perot interferometer with two reflectors, M_1 and M_2 (Fig. 1). Mirror M_1 represents quantum reflection by the long-range vdW potential, and M_2 represents reflection near short range. Inelastic and reactive losses, which occur at close or short range

(Fig. 1), are represented in the Fabry-Perot picture by transmission through the inner reflector M_2 , followed by absorption. For an incoming flux I , the total transmission T_{tot} through both reflectors is given by

$$T_{\text{tot}} = (I \cdot |t_1|^2) \left(\frac{1 - |r_2|^2}{|1 - r_2 r_1 e^{-i\phi}|^2} \right) \equiv (I \cdot |t_1|^2) C \quad (1)$$

r_i and t_i are the amplitude reflection and transmission coefficients for mirror M_i , and ϕ is the round-trip phase, which, in the Fabry-Perot model, can be tuned by the distance between mirrors or the refractive index of the medium. The term $I \cdot |t_1|^2$ is the transmitted flux in the absence of the inner mirror (i.e., $r_2 = 0$) and, for collisions, represents the universal loss. The factor C represents the effect of interference. For later convenience, we characterize the inner reflection by a parameter $0 \leq y \leq 1$: $r_2 = (1 - y)/(1 + y)$, $t_2 = 2\sqrt{y}/(1 + y)$, which is 1 for complete transmission and 0 for complete

reflection. With $r_1 \sim 1$ (quantum reflection approaches unity at low energies), we obtain $C(y, \phi) = 2y/(1 - \cos\phi + y^2(1 + \cos\phi))$. Constructive interference at $\phi = 0$ leads to an enhancement $C = 1/y$, and destructive interference at $\phi = \pi$ leads to a minimum transmission with $C = y$. In the limit of small $y \ll 1$ relevant for our experimental results, the transmission probability for the inner mirror is $\sim 4y$.

In the case of cold collisions, scattering rates are periodic when the close-range potential is modified and new bound states are added to the interparticle potential. Each new bound state results in a resonance and “tunes” the Fabry-Perot interferometer over one full spectral range with the scattering length a varying by $\pm\pi$. In accordance with (11), we defined the normalized scattering length $s = a/\bar{a}$, where $\bar{a} = 0.47799 \cdot r_6$ is the mean scattering length (34). If we substitute $\cos\phi = 1 - 2/(1 + (1 - s)^2)$ (35), we obtain $C(y, s) = y(1 + (1 - s)^2)/(1 + y^2(1 - s)^2)$. This expression exactly reproduces the results of the quantum-defect model used in (11) for the imaginary part of the scattering length, $\beta = \bar{a}C(y, s)$, which is proportional to the zero-temperature loss-rate coefficient. Previous studies (11, 26, 36) already pointed out that their results can be interpreted as an interference effect of multiple reflections between short and long range. The relation between the phase shift ϕ and the parameter s exactly reflects how a short-range phase shift modifies the scattering length (26).

We extended this single-channel model (where s is the normalized background s-wave scattering length without loss, $y = 0$) by adding a Feshbach resonance as a lossless phase shifter for the Fabry-Perot phase

$$s(B) = q \left(1 - \frac{\Delta}{B - B_{\text{res}}} \right) \quad (2)$$

The resonance is at a magnetic field $B = B_{\text{res}}$, q characterizes the background scattering phase far away from the Feshbach resonance, and Δ is the width of the resonance. Tuning the magnetic field across the resonance takes the Fabry-Perot interferometer across a full spectral range and provides tunable interference at fixed low temperature. For finite collision energies, interference has been observed also as a function of collision energy (37).

Results and analysis

The measured loss rates for $\text{Na} + \text{NaLi}$ collisions as a function of magnetic field are shown in Fig. 2. These data, which reveal a resonant enhancement of the loss by more than two orders of magnitude, represent the main result of this paper. Because the ratio of maximum and minimum loss is y^2 in the Fabry-Perot model, this result immediately suggested that

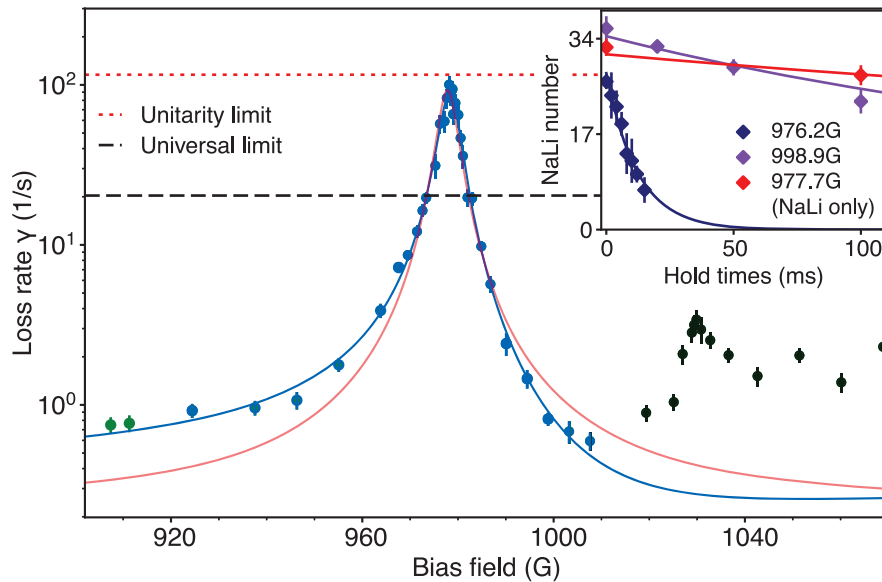


Fig. 2. Observation of Feshbach resonances in Na + NaLi collisions. Observed decay rates are shown as a function of bias field, with 100 Na atoms per pancake-shaped cloud at temperatures of $T_{\text{Na}} = 1.60 \mu\text{K}$ and $T_{\text{NaLi}} = 1.68 \mu\text{K}$, corresponding to an overlap density of $1.1 \times 10^{11} \text{ cm}^{-3}$. Data points taken with different sodium numbers and temperatures were scaled to the same overlap density (see SM). The blue line is a fit of the line shape to the Fabry-Perot contrast function C ; the red line is a Lorentzian fit. Both fits use only the data points represented by blue circles. Green circles were excluded owing to another resonance near 880 G. Black circles show an additional resonance near 1030 G. The red dotted line is the unitarity limit in two dimensions for our experimental conditions. The black dashed line is the universal loss rate. Data points were acquired with 6 to 11 different hold times at each bias field; four to eight measurements at a given hold time were averaged. Error bars indicate 1 SD. The inset shows decay curves of molecules: The dark blue (or red) diamonds are near the strong resonance at 978 G with (or without) Na atoms, and the purple diamonds are off resonance near 1000 G with atoms. Relative to the dark blue diamonds, the overlap density of the purple data is larger by a factor of 2.2. The red line in the inset is a fit for the two-body molecular loss. The dark blue and purple lines are obtained by fitting the standard differential equations of two-body decay processes, including collisions with atoms (see SM).

y has to be < 0.1 . We could fit the asymmetric line shape of the resonance well to the function $C(y, s(B))$ with an overall normalization factor and obtain $y = 0.05$ and $q = 1.61$. However, the observed peak losses were close to the unitarity limit, which provides an upper limit for elastic and inelastic scattering rates. When the scattering length exceeds the de Broglie wavelength $\lambda = 1/k$ (where k is the relative wave number), the elastic cross section in 3D saturates at $4\pi\lambda^2$, whereas the inelastic rate coefficient peaks at $(\hbar/2\mu)\lambda$ (where \hbar is Planck's constant). The observed peak loss rate was close to the unitarity limit, so we had to consider the role of nonzero momentum.

Combining the threshold quantum-defect model for the complex scattering length with a finite momentum S-matrix formulation for the scattering rates, Idziaszek and Julienne (11) obtained the complex scattering length

$$\tilde{a} = \bar{a} \left(s + y \frac{1 + (1-s)^2}{i + y(1-s)} \right) \equiv \alpha - i\beta \quad (3)$$

where α is the real and $\beta = \bar{a}C(y, s(B))$ is the imaginary part of \tilde{a} . The loss-rate coefficient K is given by

$$K = f(k) \frac{2\hbar}{\mu} \beta \quad (4)$$

The function $f(k) = (1 + k^2|\tilde{a}|^2 + 2k\beta)^{-1}$ establishes the unitarity limit for the scattering rates. So far, we have discussed inelastic scattering in three dimensions. However, because our atomic and molecular clouds had the shape of thin pancakes, we were in a 2D regime. Because the vdW length was much smaller than the thickness of the pancakes, the collisions were microscopically 3D and described by the 3D complex scattering length, but additionally, one had to use 2D scattering functions, leading to two effects. First, there is a logarithmic correction of the scattering length. For harmonic axial confinement with frequency ω_{ax} , the correction factor is $l = |1 + (\tilde{a}/\sqrt{\pi}l_0) \ln(B\hbar\omega_{\text{ax}}/\pi k_B T)|^{-2}$, where $B \approx 0.915$ and $l_0 = \sqrt{\hbar/\mu\omega_{\text{ax}}}$ is the associated oscillator length (38, 39). Because Na

and NaLi have different axial confinement frequencies ω_i and masses m_i , we used $\omega_{\text{ax}} = \mu(\omega_{\text{Na}}/m_{\text{Na}} + \omega_{\text{NaLi}}/m_{\text{NaLi}})$ (40). The correction factor l is large only at extremely low temperatures and near confinement-induced resonances (38, 39). In our case, it provided a small shift of the peak loss by ~ 0.3 G. The second modification resulting from the 2D nature of the confinement is in the saturation factor, $f(k)$: In three dimensions, k is obtained from the thermal energy, whereas in two dimensions it is obtained from 2π times the relative kinetic energy of the zero-point motion, $k = \sqrt{\pi}/l_0$. The factor of 2π is a reminder that 2D dynamics cannot be fully captured by adding the zero-point energy to the thermal energy.

Our density calibration used the loss rate for collisions in a Na + NaLi mixture in a nonstretched spin state (see the “Experimental protocol” section). The loss rate is expressed by the imaginary part of the scattering length, β , and for the universal rate, $\beta = \bar{a}$.

For the ratio of the observed loss rate to the loss rate measured for the nonstretched state, we obtain

$$r(B) = f(k)l(\beta/\bar{a}) = \frac{|1 + (\tilde{a}/\sqrt{\pi}l_0) \ln(B\hbar^2/\pi\mu l_0^2 k_B T)|^{-2}}{1 + (\sqrt{\pi}/l_0)^2 |\tilde{a}|^2 + 2(\sqrt{\pi}/l_0)l\beta} \left(\frac{\beta}{\bar{a}} \right) \quad (5)$$

The sodium density and all other factors are common mode and are canceled by taking the ratio. For the calibration measurement, $f(k) = 1$ and $l = 1$, owing to the smallness of the scattering length.

We fit the loss-rate ratio $r(B)$ using four parameters: B_{res} , Δ , q , and y . Because the calibration measurements had uncertainties, we included a fifth fitting parameter in the form of an overall normalization factor, \mathcal{N} . We used an accurate theoretical value of \bar{a} calculated for triplet ground-state NaLi + Na: $\bar{a} = 56.1a_0$ with $\leq 1.5\%$ uncertainty (33). Figure 3 compares the experimental results with the fits. In the figure, we have multiplied $r(B)$ by the constant $2\hbar\bar{a}/\mu$ and divided by the momentum-dependent 2D corrections $f(k)l$ calculated with the parameters of the best fit. In this way, we obtained the zero-temperature 3D loss-rate coefficient, $K_0(B) = (2\hbar/\mu)\beta$, which is a microscopic property of the two-body system Na + NaLi.

The best fit with the single-channel model yielded $B_{\text{res}} = 978.6(1)$ G, $\Delta = 28(2)$ G, $y = 0.0094(47)$, and $q = 1.60(7)$ with $\chi^2_{\text{red}} = 1.23$ [degrees of freedom (dof) = 27]. The normalization factor $\mathcal{N} = 1.32(45)$ was compatible with 1 and therefore was consistent with our calibration method.

Figure 3 also shows a weaker resonance near 1030 G. This resonance could not be explained by the single-channel model (i.e., with a lossless

phase shifter), which predicts that the maximum loss is larger than the universal limit. We therefore extended our model by considering a finite lifetime of the bound state coupled by the Feshbach resonance in the form of a linewidth Γ_b . This extension implied that the phase shifter of the Fabry-Perot resonator was now lossy and prevented the large resonant buildup of wave function inside the interferometer. In this two-channel model, we describe a lossy phase-shifter by

$$s_b(B) = q \left(1 - \frac{\Delta}{B - B_{\text{res}} - i\Gamma_b/2} \right) \quad (6)$$

With Eq. 6, we can express β in the Breit-Wigner form as in (27) (see SM). We assumed that y and q were the same as for the strong resonance because they characterized the same incoming channel, and we used the same normalization factor. We also included a slope and an offset as extra fit parameters to account for other loss channels not covered by our model. We obtained $B_{\text{res}} = 1030.8(7)$ G, $\Delta = 0.21(4)$ G, and $\Gamma_b = 5.38(4)$ G with $\chi^2_{\text{red}} = 2.4$ (dof = 10). The Δ parameter showed that the resonance at 1030 G was two orders of magnitude weaker than the one at 978 G. From the linewidth, we inferred the bound-state lifetime $\tau_b = (\delta\mu\Gamma_b)^{-1} \approx 60$ ns, where the relative magnetic moment between the entrance channel and the closed-channel bound state was $\delta\mu = 2\mu_B$ (where μ_B is the Bohr magneton) assuming a single spin-flip. In our study, the lifetime of a collision complex was obtained from a spectroscopic linewidth, whereas in all previous work on collisions of ultracold molecules, such lifetimes were obtained from a direct time-domain measurement (9, 10). The short lifetime of the bound state suggests that the closed channel has a highly reactive doublet character. Some contribution to Γ_b and y could also come from the 1596-nm trapping light, which can excite collision complexes leading to loss, as observed in other molecular systems (8–10). However, given the small value of y , we expect this effect to be small.

We could also fit the strong resonance to the two-channel model and found $\Gamma_b = 0 \pm 1$ G, confirming that we can regard the strong resonance as a lossless phase shifter. The longer lifetime of the closed channel associated with the strong resonance suggests that it is only weakly coupled to reactive channels. The difference between the two Feshbach resonances is highlighted by examining the total inelastic width, Γ_{inel} , of the resonance (see SM)

$$\Gamma_{\text{inel}} = \Gamma_b + \frac{2yq\Delta}{1 + y^2(q-1)^2} \quad (7)$$

where the first term is the natural linewidth of the bound state itself, and the second term represents the resonantly enhanced decay rate of the incoming channel. The width of the 978-G

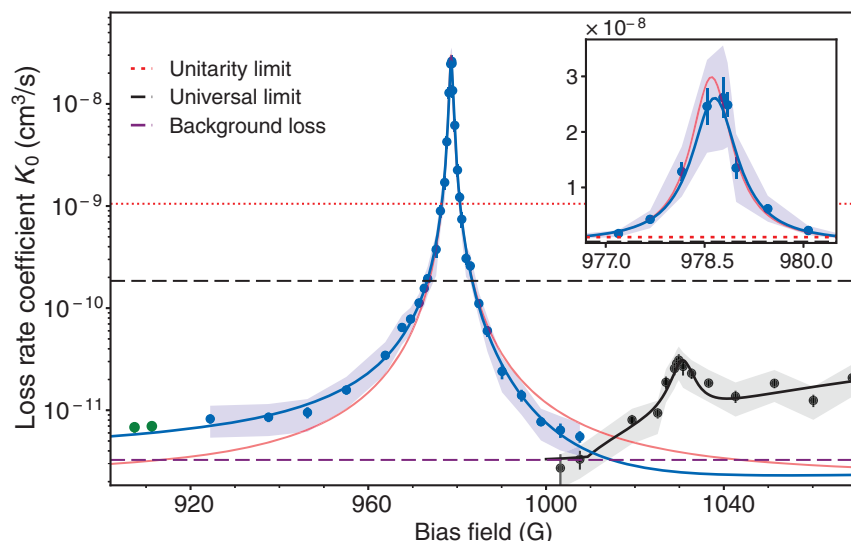


Fig. 3. Zero-temperature loss-rate coefficients K_0 for Na + NaLi collisions. K_0 is the imaginary part of the scattering length times $2h/\mu$. Experimental data points were corrected for nonzero momentum effects, $f(k)$ (see the “Results and analysis” section). The blue line is the best fit based on the single-channel model; the red line is a symmetric Lorentzian fit. For both fits, only blue data points were included. The black line is a fit of the weak resonance using a two-channel model. The two black data points near 1005 G were obtained from the blue points by subtracting the contribution of the wings of the strong resonance. The red dotted line is the unitarity limit in two dimensions, $(h/2\mu)\sqrt{\pi}/l_0$. The black dashed line is the universal limit. The purple dashed line shows the background (open-channel) loss. The shaded area represents the total uncertainty, which is the quadrature sum of the standard deviation and the systematic uncertainty in the density calibration. The inset shows a magnified view of the central part of the figure on a linear scale.

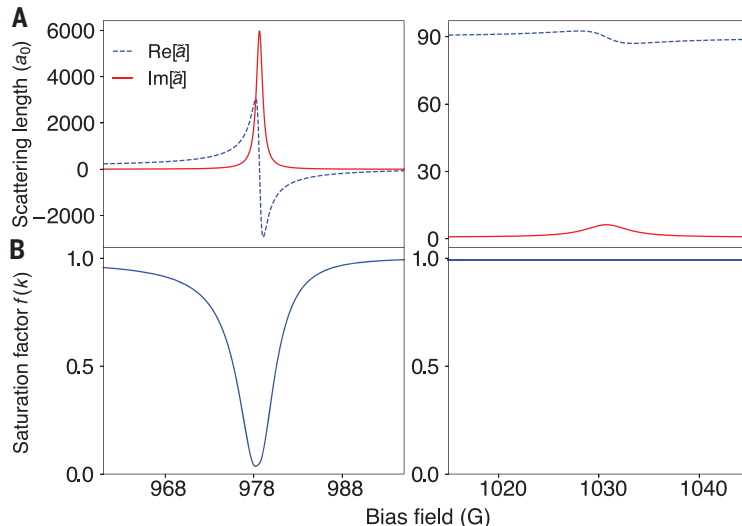


Fig. 4. Complex scattering length and saturation factor calculated from the best-fit results. (A) Real (Re) and imaginary (Im) parts of the scattering lengths \tilde{a} near the strong resonance calculated according to the single-channel model (left plot) and near the weak resonance calculated according to the two-channel model (right plot). (B) Saturation factor $f(k)$ with $k = \sqrt{\pi}/l_0$, where l_0 is the oscillator length for the effective axial confinement frequency. The saturation was negligible for the weak resonance (right plot), whereas $f(k) \sim 0.03$ at the strong resonance (left plot).

resonance was dominated by the open-channel losses at short range (i.e., $y \neq 0$), whereas the weak resonance was limited by the decay rate Γ_b . Equation 7 shows that the y parameter is more easily determined from a strong resonance. By

contrast, the weaker resonance was insensitive to the short-range parameters y and q of the incoming channel. Figure 4 shows the real and imaginary parts of the scattering lengths for the two resonances and illustrates the power

of the simple model: Analysis of the inelastic scattering provides a full description of all s-wave scattering properties, including elastic scattering and momentum dependence. We can also calculate the good-to-bad collision ratio, $k(\alpha^2 + \beta^2)/\beta$, and find that it is maximized away from the resonance (see SM).

Figure 3 shows that the zero-momentum loss rate could be tuned over four orders of magnitude and exceeded the universal limit by a factor of 100, which was reduced by the unitarity limit to a factor of 5 (Fig. 2) [see also (41)].

The quality factor of the Fabry-Perot resonator becomes smaller for nonzero momentum, owing to the lower long-range quantum reflectivity, which has a threshold law of $|r_1| \approx 1 - 2\bar{a}k$. This relation yields $|r_1| \sim 0.93$ using the total (i.e., thermal and zero-point) momentum for k . The resonant enhancement inside the Fabry-Perot resonator is reduced when the transmission of the outer mirror (M_1) is comparable to that of the inner mirror (M_2)—i.e., when $\bar{a}k \sim y$. At this point, the unitarity saturation takes effect and reduces the loss rate from its zero-temperature value shown in Fig. 3.

Discussion

In this study, we have demonstrated the substantial suppression and enhancement of reactive collisions relative to the universal limit, which is possible only if $y \ll 1$, and we have achieved control of chemical reactions via external magnetic fields. An asymmetric line shape can lead to a suppression of inelastic losses below the background loss (42). This suppression was not realized for the results shown in Fig. 3, owing to the neighboring weaker Feshbach resonance.

Our analysis highlights the conditions necessary to observe such a high dynamic range tunability of reactive collisions. The possible contrast is given by $1/y^2$ but is only realized if the Feshbach resonance is sufficiently strong and coupled to a sufficiently long-lived state: $q\Delta/\Gamma_b > 1/y$. This condition for the Feshbach resonance is more difficult to fulfill for smaller values of y , but the Na + NaLi system satisfies this condition for the resonance at 978 G and for several other resonances that we have observed but not yet fully analyzed.

The models for reactive collisions presented here may look rather specialized. However, our two-channel model captures the low-temperature limit of the most general resonance possible for which the complex scattering length is represented by a circle in the complex plane (27, 43) (see SM).

Universal reaction rates are determined only by quantum reflection of the long-range potential and do not provide any information about the “real chemistry” at short range.

Therefore, discovery and characterization of nonuniversal molecular systems are major goals of the field (15–17, 20, 21, 44). However, most of the cases studied exhibited only two- to fourfold deviation from the universal limit, and interpretation of these cases required an accurate density calibration that was not always performed. Some studies showed inelastic rates well below the universal limit, without any resonances (45–47), which can provide only an upper bound for y and leave q undetermined. This work has demonstrated how short-range reflectivity makes it possible to access information about short-range interactions and collisional intermediate complexes. Our analysis showed that suppression of loss below the universal limit could occur for a wide range of parameters, but strong enhancement of loss beyond the universal limit requires fine tuning: an almost lossless Fabry-Perot interferometer tuned to resonance.

In this work, we have experimentally validated a method on the basis of external magnetic fields and quantum interference to realize quantum control of chemistry. Previous studies used microwaves (44, 48) or electric fields (49) to control losses in molecular systems with strong long-range dipolar interactions by modifying the universal rate limit. In our study, we used magnetic fields and quantum interference, without the need for dipolar interactions, to achieve loss-rate coefficients that far exceed the universal limit. All of these methods control one specific decay channel. With the weak resonance, we have also demonstrated that magnetic field can switch between two different mechanisms of reactive scattering, occurring in the chemically stable incoming and the lossy closed channels, respectively.

REFERENCES AND NOTES

1. S. Inouye *et al.*, *Nature* **392**, 151–154 (1998).
2. C. Chin, R. Grimm, P. Julienne, E. Tiesinga, *Rev. Mod. Phys.* **82**, 1225–1286 (2010).
3. A. B. Henson, S. Gersten, Y. Shagam, J. Narevicius, E. Narevicius, *Science* **338**, 234–238 (2012).
4. T. de Jongh *et al.*, *Science* **368**, 626–630 (2010).
5. L. D. Carr, D. DeMille, R. V. Krems, J. Ye, *New J. Phys.* **11**, 055049 (2009).
6. Y. Liu *et al.*, *Nature* **593**, 379–384 (2021).
7. M. Mayle, B. P. Ruzic, J. L. Bohn, *Phys. Rev. A* **85**, 062712 (2012).
8. A. Christenian, M. W. Zwiernlein, G. C. Groenenboom, T. Karman, *Phys. Rev. Lett.* **123**, 123402 (2019).
9. P. D. Gregory, J. A. Blackmore, S. L. Bromley, S. L. Cornish, *Phys. Rev. Lett.* **124**, 163402 (2020).
10. Y. Liu *et al.*, *Nat. Phys.* **16**, 1132–1136 (2020).
11. Z. Idziaszek, P. S. Julienne, *Phys. Rev. Lett.* **104**, 113202 (2010).
12. R. V. Krems, *Int. Rev. Phys. Chem.* **24**, 99–118 (2005).
13. M. T. Bell, T. P. Softley, *Mol. Phys.* **107**, 99–132 (2009).
14. S. Ospelkaus *et al.*, *Science* **327**, 853–857 (2010).
15. J. W. Park, S. A. Will, M. W. Zwiernlein, *Phys. Rev. Lett.* **114**, 205302 (2015).
16. X. Ye, M. Guo, M. L. González-Martínez, G. Quémener, D. Wang, *Sci. Adv.* **4**, eaag0083 (2018).
17. P. D. Gregory *et al.*, *Nat. Commun.* **10**, 3104 (2019).
18. T. Takekoshi *et al.*, *Phys. Rev. Lett.* **113**, 205301 (2014).
19. L. W. Cheuk *et al.*, *Phys. Rev. Lett.* **125**, 043401 (2020).

20. B. Drews, M. Deiß, K. Jachymski, Z. Idziaszek, J. Hecker Denschlag, *Nat. Commun.* **8**, 14854 (2017).
21. G. Poloviy, E. Frieling, D. Uhland, J. Schmidt, K. W. Madison, *Phys. Rev. A* **102**, 013310 (2020).
22. E. R. Hudson, N. B. Gilroy, S. Kotochigova, J. M. Sage, D. DeMille, *Phys. Rev. Lett.* **100**, 203201 (2008).
23. N. Zahzam, T. Vogt, M. Mudrich, D. Comparat, P. Pillet, *Phys. Rev. Lett.* **96**, 023202 (2006).
24. P. Staunum, S. D. Kraft, J. Lange, R. Wester, M. Weidemüller, *Phys. Rev. Lett.* **96**, 023201 (2006).
25. J. Deiglmayr *et al.*, *J. Phys. Conf. Ser.* **264**, 012014 (2011).
26. M. D. Frye, P. S. Julienne, J. M. Hutson, *New J. Phys.* **17**, 045019 (2015).
27. J. M. Hutson, *New J. Phys.* **9**, 152 (2007).
28. X.-Y. Wang *et al.*, *New J. Phys.* **23**, 115010 (2021).
29. H. Yang *et al.*, arXiv:2104.11424 [physics.atom-ph] (2021).
30. H. Son, J. J. Park, W. Ketterle, A. O. Jamison, *Nature* **580**, 197–200 (2020).
31. T. M. Rvachov *et al.*, *Phys. Rev. Lett.* **119**, 143001 (2017).
32. B. Gao, *Phys. Rev. Lett.* **105**, 263203 (2010).
33. R. Hermsmeider, J. Klos, S. Kotochigova, T. V. Tscherbil, *Phys. Rev. Lett.* **127**, 103402 (2021).
34. G. F. Gribakin, V. V. Flambaum, *Phys. Rev. A* **48**, 546–553 (1993).
35. This expression is equivalent to $\tan(\phi/2) = 1/(1 - s)$, which is also given in (26).
36. Y.-P. Bai, J.-L. Li, G.-R. Wang, S.-L. Cong, *Phys. Rev. A* **100**, 012705 (2019).
37. Y. Xie *et al.*, *Science* **368**, 767–771 (2020).
38. D. S. Petrov, G. V. Shlyapnikov, *Phys. Rev. A* **64**, 012706 (2001).
39. Z. Idziaszek, K. Jachymski, P. S. Julienne, *New J. Phys.* **17**, 035007 (2015).
40. Although the relative motion is no longer a simple harmonic oscillator, the expression for ω_{ax} provides the correct kinetic energy $\hbar\omega_{\text{ax}}/4$ of the relative motion.
41. In (50), Yang *et al.* mention a resonant loss rate two to three times the universal limit. However, this is based on an estimate for the universal limit and an unspecified density calibration. Our weak resonance shows that it is easily possible to observe Feshbach resonances that do not exceed the universal limit.
42. J. M. Hutson, M. Beyene, M. L. González-Martínez, *Phys. Rev. Lett.* **103**, 163201 (2009).
43. R. A. Rowlands, M. L. González-Martínez, J. M. Hutson, arXiv:0707.4397 [physics.chem-ph] (2007).
44. L. Anderegg *et al.*, *Science* **373**, 779–782 (2021).
45. S. Jurgilas *et al.*, *Phys. Rev. Lett.* **126**, 153401 (2021).
46. K. K. Voges *et al.*, *Phys. Rev. Lett.* **125**, 083401 (2020).
47. T. T. Wang, M.-S. Heo, T. M. Rvachov, D. A. Cotta, W. Ketterle, *Phys. Rev. Lett.* **110**, 173203 (2013).
48. Z. Z. Yan *et al.*, *Phys. Rev. Lett.* **125**, 063401 (2020).
49. K. Matsuda *et al.*, *Science* **370**, 1324–1327 (2020).
50. H. Yang *et al.*, *Science* **363**, 261–264 (2019).
51. H. Son *et al.*, Data of: Control of reactive collisions by quantum interference, version 1, Zenodo (2021); <https://doi.org/10.5281/zenodo.5797536>.

ACKNOWLEDGMENTS

We thank D. Petrov, P. Julienne, K. Jachymski, and T. Tscherbil for valuable discussions. **Funding:** We acknowledge support from the NSF through the Center for Ultracold Atoms (grant no. 1506369) and from the Air Force Office of Scientific Research (MURI, grant no. FA9550-21-1-0069). Some of the analysis was performed by W.K. at the Aspen Center for Physics, which is supported by the NSF (grant PHY-1607611). H.S. and J.J.P. acknowledge additional support from the Samsung Scholarship. **Author contributions:** H.S. and J.J.P. carried out the experimental work. All authors contributed to the development of models, data analysis, and writing the manuscript. **Competing interests:** None declared. **Data and materials availability:** All data needed to evaluate the conclusions in the paper are present in the main paper or the supplementary materials. All data presented in this paper are deposited at Zenodo (51).

SUPPLEMENTARY MATERIALS

science.org/doi/10.1126/science.abl7257
Supplementary Text
Figs. S1 and S2
References (52–57)

5 September 2021; accepted 23 December 2021
10.1126/science.abl7257

ASTEROIDS

Pebbles and sand on asteroid (162173) Ryugu: In situ observation and particles returned to Earth

S. Tachibana^{1,2*}, H. Sawada², R. Okazaki³, Y. Takano⁴, K. Sakamoto^{1,2}, Y. N. Miura⁵, C. Okamoto^{6†}, H. Yano², S. Yamanouchi³, P. Michel⁷, Y. Zhang⁷, S. Schwartz^{8,9}, F. Thillet^{7,†}, H. Yurimoto¹⁰, T. Nakamura¹¹, T. Noguchi^{3,12}, H. Yabuta¹³, H. Naraoka³, A. Tsuchiyama^{14,15}, N. Imae¹⁶, K. Kurosawa¹⁷, A. M. Nakamura⁶, K. Ogawa¹⁸, S. Sugita¹, T. Morota¹, R. Honda¹⁹, S. Kameda²⁰, E. Tatsumi^{1,21}, Y. Cho¹, K. Yoshioka¹, Y. Yokota², M. Hayakawa², M. Matsuoka^{2,§}, N. Sakatani²⁰, M. Yamada¹⁷, T. Kouyama²², H. Suzuki²³, C. Honda²⁴, T. Yoshimitsu², T. Kubota², H. Demura²⁴, T. Yada², M. Nishimura², K. Yogata², A. Nakato², M. Yoshitake², A. I. Suzuki^{25,26}, S. Furuya^{1,2}, K. Hatake²⁵, A. Miyazaki², K. Kumagai²⁵, T. Okada², M. Abe^{2,27}, T. Usui², T. R. Ireland²⁸, M. Fujimoto², T. Yamada², M. Arakawa⁶, H. C. Connolly Jr.^{29,8}, A. Fujii², S. Hasegawa², N. Hirata²⁴, N. Hirata⁶, C. Hirose³⁰, S. Hosoda², Y. Iijima^{2,†}, H. Ikeda², M. Ishiguro³¹, Y. Ishihara¹⁸, T. Iwata^{2,27}, S. Kikuchi^{2,17}, K. Kitazato²⁴, D. S. Lauretta⁸, G. Libourel⁷, B. Marty³², K. Matsumoto^{33,34}, T. Michikami³⁵, Y. Mimasu², A. Miura^{2,27}, O. Mori², K. Nakamura-Messenger³⁶, N. Namiki^{33,34}, A. N. Nguyen³⁶, L. R. Nittler³⁷, H. Noda^{33,34}, R. Noguchi^{2,38}, N. Ogawa¹⁸, G. Ono³⁰, M. Ozaki^{2,27}, H. Senshu¹⁷, T. Shimada¹⁸, Y. Shimaki², K. Shirai², S. Soldini³⁹, T. Takahashi⁴⁰, Y. Takei^{2,30}, H. Takeuchi^{2,27}, R. Tsukizaki², K. Wada¹⁷, Y. Yamamoto^{2,27}, K. Yoshikawa³⁰, K. Yumoto¹, M. E. Zolensky³⁶, S. Nakazawa², F. Terui^{2,¶}, S. Tanaka^{2,27}, T. Saiki², M. Yoshikawa^{2,27}, S. Watanabe⁴¹, Y. Tsuda^{2,42}

The Hayabusa2 spacecraft investigated the C-type (carbonaceous) asteroid (162173) Ryugu. The mission performed two landing operations to collect samples of surface and subsurface material, the latter exposed by an artificial impact. We present images of the second touchdown site, finding that ejecta from the impact crater was present at the sample location. Surface pebbles at both landing sites show morphological variations ranging from rugged to smooth, similar to Ryugu's boulders, and shapes from quasi-spherical to flattened. The samples were returned to Earth on 6 December 2020. We describe the morphology of >5 grams of returned pebbles and sand. Their diverse color, shape, and structure are consistent with the observed materials of Ryugu; we conclude that they are a representative sample of the asteroid.

Asteroids are small celestial bodies in the Solar System that are left over from the planet formation process. The C-type (carbonaceous) group of asteroids appear to be related to carbonaceous chondrite meteorites, which are known to contain hydrated silicates and organic matter (*1*). Such hydrated asteroids could have delivered water and organic molecules to Earth during or after its formation. Samples from C-type asteroids

are predicted to contain a record of Solar System evolution (*1*). Evidence for ongoing activity on an asteroid surface, including movement and ejection of particles, has previously been inferred from analysis of particles returned to Earth from the S-type (stony) asteroid (25143) Itokawa (*2, 3*).

The Hayabusa2 spacecraft investigated the C-type near-Earth asteroid (162173) Ryugu from June 2018 to November 2019, with the goal

of determining its physical and compositional properties, collecting samples, and returning them to Earth. Ryugu is a “spinning top”-shaped rubble pile, with a mean radius of 448 ± 2 m (*4, 5*). The surface is ubiquitously dark, with variations in reflectance spectra that are due to mixing of bluish and reddish materials (*5, 6*). Some bright boulders are present, which could be related to spectroscopically similar S-type asteroids (*7*). The reddish color is thought to have been produced by surface alteration and space weathering of originally bluish materials during the past 10^6 to 10^7 years (*6*). Hydrous silicates are present across the surface (*8*) but are less abundant than in hydrated carbonaceous chondrites (*8*) or the B-type (bluish and spectroscopically similar to C-type) asteroid (101955) Bennu (*9, 10*). This could be due to dehydration of originally hydrous silicates or minimal aqueous alteration of Ryugu's parent planetesimal (the original body in the early Solar System from which Ryugu formed) (*5, 8*).

Hayabusa2 dropped the Mobile Asteroid Surface Scout (MASCOT) lander onto Ryugu, which showed that the surface is not covered with fine regolith (*11*). A ~3-cm pebble observed by using MASCOT had a thermal inertia of $\sim 280 \text{ J m}^{-2} \text{ K}^{-1} \text{ s}^{-1/2}$, which is much lower than the thermal inertia of chondrites (*12*). This low thermal inertia indicates that the pebble had a high porosity, implying a low tensile strength of a few hundred kilopascals (*12*). Similarly low thermal inertia ($\sim 300 \text{ J m}^{-2} \text{ K}^{-1} \text{ s}^{-1/2}$) was measured for several large (>10 m) boulders and their surroundings (*13*). An artificial impact experiment was performed by using Hayabusa2's Small Carry-on Impactor (SCI), which showed that Ryugu's surface is composed of a cohesionless material, at least in part (*14*). Infrared observations of the SCI-made crater have shown that the subsurface material has spectral properties

¹UTokyo Organization for Planetary and Space Science—Department of Earth and Planetary Science, The University of Tokyo, Tokyo 113-0033, Japan. ²Institute of Space and Astronautical Science, Japan Aerospace Exploration Agency (JAXA), Sagami-hara 252-5210, Japan. ³Department of Earth and Planetary Sciences, Kyushu University, Fukuoka 812-8581, Japan.

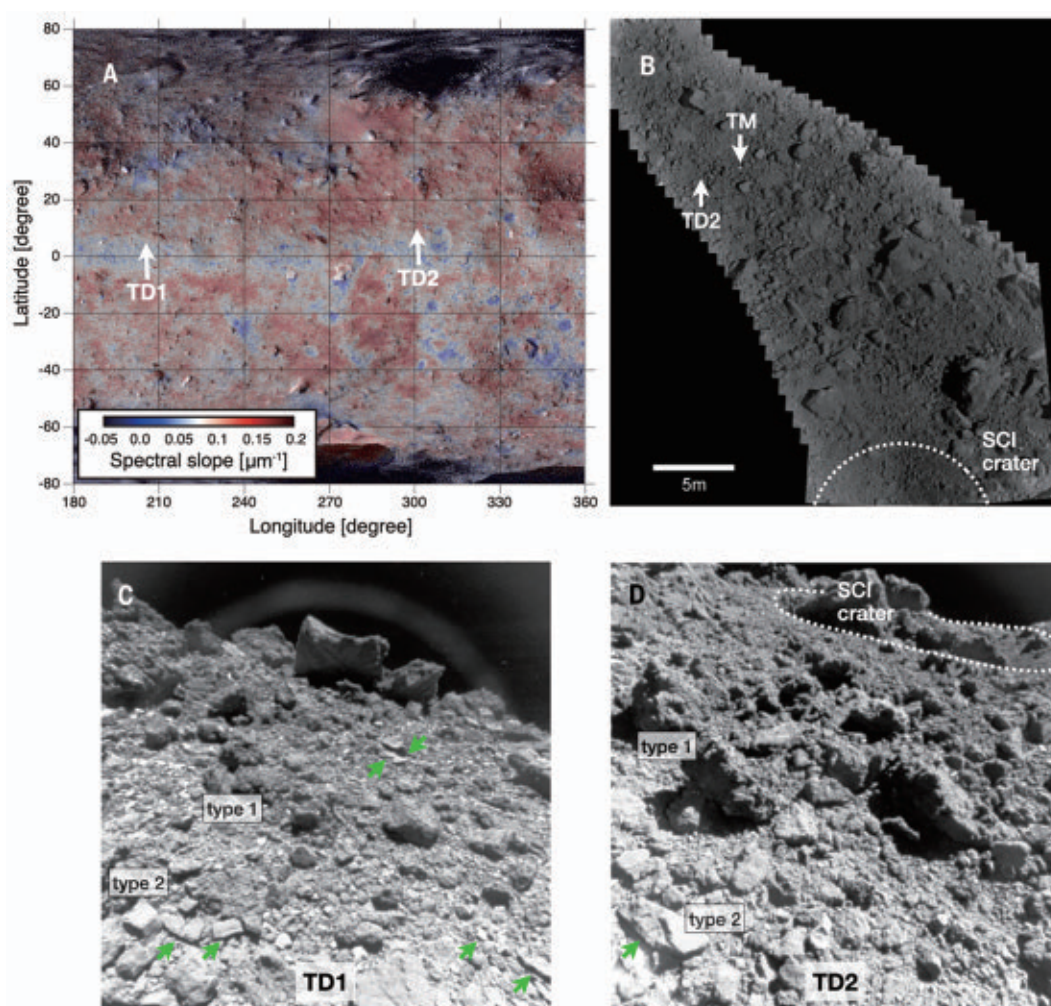
⁴Biogeochemistry Research Center, Japan Agency for Marine-Earth Science and Technology, Kanagawa 237-0061, Japan. ⁵Earthquake Research Institute, The University of Tokyo, Tokyo 113-0032, Japan. ⁶Department of Planetology, Kobe University, Kobe 657-8501, Japan. ⁷Université Côte d'Azur, Observatoire de la Côte d'Azur, Centre national de la recherche scientifique, Laboratoire Lagrange, F-06304 Nice CEDEX 4, France. ⁸Lunar and Planetary Laboratory, University of Arizona, Tucson, AZ 85705, USA. ⁹Planetary Science Institute, Tucson, AZ 85719, USA.

¹⁰Department of Earth and Planetary Sciences, Hokkaido University, Sapporo 060-0810, Japan. ¹¹Department of Earth Sciences, Tohoku University, Sendai 980-8578, Japan. ¹²Division of Earth and Planetary Sciences, Kyoto University, Kyoto, Japan. ¹³Department of Earth and Planetary Systems Science, Hiroshima University, Higashi-Hiroshima 739-8526, Japan. ¹⁴Research Organization of Science and Technology, Ritsumeikan University, Kusatsu 525-8577, Japan. ¹⁵Guangzhou Institute of Geochemistry, Chinese Academy of Sciences, Guangzhou 510640, China.

¹⁶Polar Science Resources Center, National Institute of Polar Research, Tokyo 190-8518, Japan. ¹⁷Planetary Exploration Research Center, Chiba Institute of Technology, Narashino 275-0016, Japan. ¹⁸JAXA Space Exploration Center, JAXA, Sagami-hara 252-5210, Japan. ¹⁹Department of Information Science, Kochi University, Kochi 780-8520, Japan. ²⁰Department of Physics, Rikkyo University, Tokyo 171-8501, Japan. ²¹Instituto de Astrofísica de Canarias, University of La Laguna, E-38205 Tenerife, Spain. ²²Information Technology and Human Factors, National Institute of Advanced Industrial Science and Technology, Tokyo 135-0064, Japan. ²³Department of Physics, Meiji University, Kawasaki 214-8571, Japan. ²⁴Aizu Research Center for Space Informatics, University of Aizu, Aizu-Wakamatsu 965-8580, Japan. ²⁵Marine Works Japan Ltd., Yokosuka 237-0063, Japan. ²⁶Department of Economics, Toyo University, Tokyo 112-8606, Japan. ²⁷Department of Space and Astronautical Science, The Graduate University for Advanced Studies, SOKENDAI, Hayama 240-0193, Japan. ²⁸School of Earth and Environmental Sciences, The University of Queensland, St Lucia, Queensland 4072, Australia. ²⁹Department of Geology, Rowan University, Glassboro, NJ 08028, USA. ³⁰Research and Development Directorate, JAXA, Sagami-hara 252-5210, Japan. ³¹Department of Physics and Astronomy, Seoul National University, Seoul 08826, Korea. ³²Université de Lorraine, Centre national de la recherche scientifique, Centre de Recherches Pétrographiques et Géochimiques, F-54000 Nancy, France. ³³National Astronomical Observatory of Japan, Mitaka 181-8588, Japan. ³⁴Department of Astronomical Science, The Graduate University for Advanced Studies, SOKENDAI, Hayama 240-0193, Japan. ³⁵Department of Mechanical Engineering, Kindai University, Higashi-Hiroshima 739-2116, Japan. ³⁶NASA Johnson Space Center, Houston, TX 77058, USA. ³⁷Carnegie Institution for Science, Washington, DC 20015, USA. ³⁸Department of Science, Niigata University, Niigata 950-2181, Japan. ³⁹Department of Mechanical, Materials and Aerospace Engineering, University of Liverpool, Liverpool L69 3BX, UK. ⁴⁰NEC Corporation, Tokyo 183-8501, Japan. ⁴¹Department of Earth and Environmental Sciences, Nagoya University, Nagoya 464-8601, Japan. ⁴²Department of Aeronautics and Astronautics, The University of Tokyo, Tokyo 113-0033, Japan.

*Corresponding author. Email: tachi@eps.s.u-tokyo.ac.jp †Deceased. ‡Present address: CS Group, 31506 Toulouse CEDEX 5, France. §Present address: Laboratoire d'Études Spatiales et d'Instrumentation en Astrophysique, Observatoire de Paris, 92195 Meudon, France. ¶Present address: Department of Mechanical Engineering, Kanagawa Institute of Technology, Kanagawa 243-0292, Japan.

Fig. 1. Hayabusa2 touchdown locations and Ryugu surface properties. (A) Global map of the spectral slope, which is indicated by the color bar, superimposed on a v-band image map. The spectral slope is measured between the b-band (0.48 μm) and the x-band (0.86 μm) (5, 6). The white arrows indicate the locations of the first touchdown (TD1) and the second touchdown (TD2). (B) Composite map of the TD2 site, assembled from images taken by a wide-angle optical navigation camera (ONC-W1). Also visible are the locations of a target marker (arrow labeled TM) that was used for spacecraft navigation and the crater produced by the SCI experiment (dotted arc, diameter of ~ 18 m) (19). (C and D) Images of the areas surrounding the TD1 and TD2 sites, respectively, taken by another wide-angle optical navigation camera (ONC-W2). Examples of flattened boulders and pebbles are indicated with green arrows. Labels indicate type 1 and type 2 boulders, which have rugged and smooth surfaces, respectively (5). The SCI crater (14) is visible (dotted ellipse) in the image of the TD2 site. The arch-like feature above the surface in (C) is an artifact.



similar to, but distinct from, those of the surface (15). The crater and excavated material have a slightly higher abundance of hydrated silicates, reflecting the extent of aqueous alteration that occurred on Ryugu's parent planetesimal (15).

Sample-collection operations

Hayabusa2 made its first landing [designated touchdown one (TD1)] on 2019 February 21, during which it collected samples of the surface (6). The second landing (TD2) occurred on 2019 July 11, close to the crater made by the SCI, to collect impact ejecta, i.e., subsurface samples (Fig. 1). The two landing locations appeared similar in remote imaging, being covered with boulders and pebbles (Fig. 1). The two types of boulder commonly observed on Ryugu's surface [rugged type 1 and smooth type 2 (5)] are found at both locations. In both landing operations, a 5-g tantalum projectile was fired through the sampler horn at $\sim 300 \pm 30 \text{ m s}^{-1}$ (1, 16, 17) when the horn touched the surface, lifting material into the collector.

The TD2 location hosts fine particle aggregates, observed on the surface of a smooth type 2 boulder (Fig. 2A), which were not identified in proximity images of TD1 or other surface locations (6). These particles did not strongly adhere to the boulder, being blown off by the subsequent ascent thruster firing (Fig. 2B). We infer that the fine particles are geologically recent and, most likely, ejecta from the SCI crater. Images of the impact event show that part of the ejecta curtain fell back on Ryugu's surface, with simulations predicting that the TD2 site was covered with SCI ejecta excavated from a depth of ~ 1 m below the surface (18, 19). The estimated sizes of ejecta particles range from 1 mm to several decimeters (18). This is consistent with the observed particles on the boulder (Fig. 3). We conclude that the TD2 sample location was covered with ejecta excavated from Ryugu's subsurface by the SCI experiment. Sample-collection analog experiments that were performed in Earth gravity indicate that $\sim 50\%$ of the collected particles were taken from depths < 1.5 mm from the surface (fig. S3) (20). Collection under microgravity

should access greater depths; nevertheless, we expect the samples collected during TD2 to include some SCI ejecta. Spectroscopy of the SCI crater and its surroundings revealed only small differences (15), so the identification of subsurface materials in the collected sample requires other analysis methods.

During both landings, the motions of particles kicked up by the sample projectiles and thruster firings were observed with a small monitor camera head (CAM-H) (Fig. 3 and movie S1) (20). One second after the projectile firing at TD1, ~ 10 particles were identified beneath or nearby the sampler horn (Fig. 3C). After another second, the number of particles increased to ~ 20 in the next image (Fig. 3D), of which 3 particles were moving toward CAM-H. We estimate the ejection angle and velocity of these particles as $\sim 50^\circ$ to 60° and 1 to 2 m s^{-1} , respectively (20). Their ejection angle is within the range measured in projectile experiments in Earth gravity (40° to 60° ; fig. S2) (20) and consistent with the most frequent angle range (48° to 54°) in the Hayabusa2 sampling simulations (21). We conclude that these particles

are ejecta produced by the projectile impact. The ejected particles identified near the rocket coupling ring (an assembly used during the spacecraft launch) were centimeter-sized (Fig. 3). Centimeter-sized pebbles were also found in proximity images of the TD1 site (6) and at different surface locations observed by the lander MASCOT (17) and the MINERVA-II (Micro Nano Experimental Robot Vehicle for Asteroid 2) Rover-1A (Fig. 2). The data from MINERVA-II Rover-1A also showed centimeter-sized particles that were disturbed by its hop across the surface (Fig. 2D) (20). This suggests that centimeter-sized pebbles, which do not strongly adhere to larger cobbles and boulders, are present over the surface of Ryugu.

We estimate the total mass of the three ejecta particles observed in Fig. 3 as 0.3 to 3 g, assuming spherical particles with a diameter of 0.5 to 1 cm and bulk density of $\sim 2 \text{ g cm}^{-3}$. If all the ejecta particles in Fig. 3 (~ 20 in number) have the same ejection velocity as the three particles observed moving toward CAM-H, the total amount of ejecta with an ejection velocity of $\sim 1 \text{ m s}^{-1}$ would be ~ 2 to 20 g. Numerical simulations of the Hayabusa2 sample process, which assume a cohesionless granular bed consisting of grains with an average diameter of 0.5 cm, predicted that the total ejecta mass is about an order of magnitude larger than the mass of ejecta with a velocity of $\sim 1 \text{ m s}^{-1}$ (27). We therefore estimate the total ejecta mass as 20 to 200 g. The simulations also predicted that $\sim 0.5\%$ of the total ejecta particles are retained in the sample catcher, which is located above the sampler horn (27). This leads to an estimated total collected mass of 0.1 to 1 g for TD1, which meets the 0.1-g requirement for returned sample analysis (1, 16). Laboratory experiments conducted under Earth gravity by using 1-mm glass spherules with little cohesion force showed that 150 to 250 mg of samples can be collected after projectile firing (fig. S1) (20), which was expected to be increased up to an order of magnitude under microgravity conditions (16). Because the surface materials on Ryugu are not strongly held to the surface by cohesive forces (14), we regard this experiment as an appropriate analog of the sample-collection operation on Ryugu.

In the CAM-H images taken during TD2 (Fig. 3 and movies S2 and S3), dust-like ejecta appear from beneath the sampler horn (Fig. 3), followed by the ejection of numerous larger particles, which is likely due to the projectile firing. We interpret this dust as ejecta with slow velocities or originating from deeper into the surface that did not enter the sampler horn. Three particles visible in Fig. 3 are ~ 1 to 2 cm in diameter, which suggests that loosely packed, movable, centimeter-sized pebbles were present at the TD2 location. The CAM-H images suggest that the amount of material collected

during TD2 was similar to the amount collected during TD1.

Spacecraft ascent

CAM-H continued to take images of flying particles during the ascent after the two landing operations (Fig. 4). Flying particles are visible as objects moving relative to the surface in multiple sequential images (movies S1 and S2). Because no such flying particles were observed during the spacecraft descent, we interpret these particles as ejecta either due to the projectile impact or lifted by the spacecraft thruster firing. Images from a wide-angle optical navigation camera showed boulders moving on the surface because of the thruster operation during TD1 (6), so we infer that the thruster triggered the ejection of most of the

pebbles as well. Numerous millimeter-sized particles were also observed during the TD2 ascent operation (Fig. 4), which indicates the presence of more small particles at the TD2 location than at the TD1 location, which were presumably the SCI ejecta.

The flying pebbles show two morphological types: rugged particles and particles with smooth faces (Fig. 4 and fig. S4). These two types are consistent with the morphological variations that were observed within surface boulders observed by the spacecraft (5) and the MASCOT lander (17). We determined the three-dimensional shapes of flying pebbles for those visible in multiple two-dimensional projections (from different angles) in the CAM-H images. We define L and I as the maximum and minimum caliper

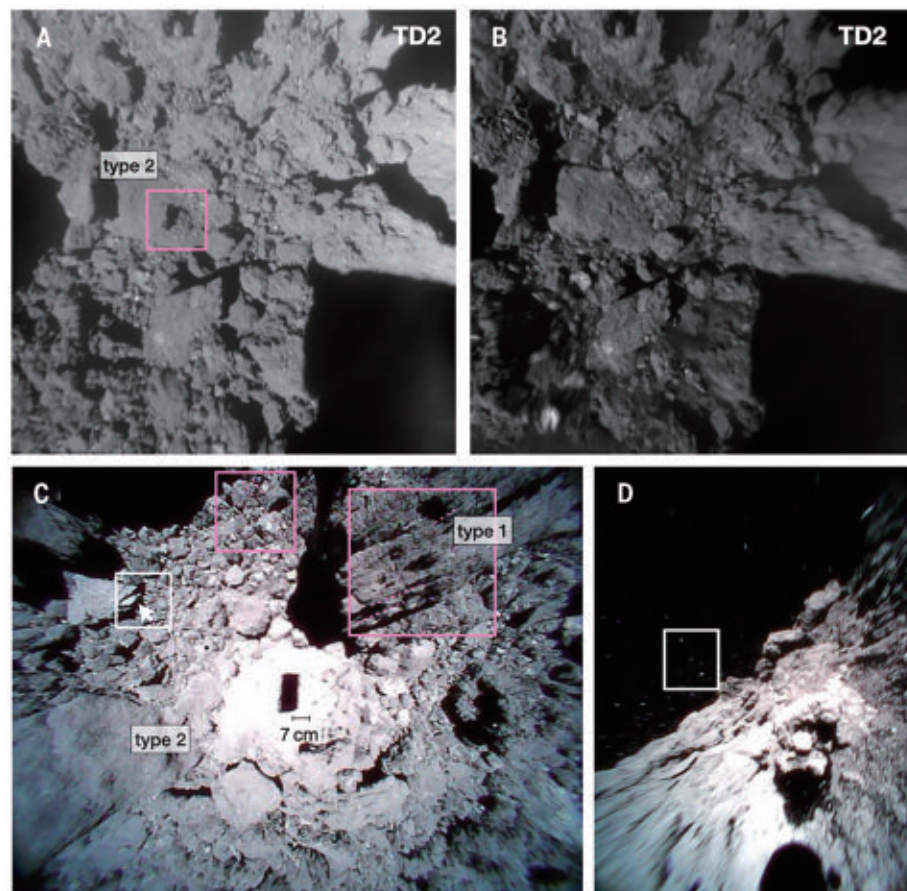


Fig. 2. Pebbles and boulders observed on Ryugu's surface. (A) ONC-W1 image taken 2 s before TD2. Fine particles are visible (within the pink box, which measures ~ 20 by 20 cm) on the surface of a smooth type 2 boulder (5). (B) Same area as shown in (A), taken during the ascent after TD2. The fine particles on the smooth type 2 boulder were blown off by the thruster firing. (C) Image of the surface taken by the MINERVA-II Rover-1A during its hopping operation on 2018 September 28. The shadow of the rover (~ 7 cm long) is visible in the center of the image. Numerous decimeter- to centimeter-sized pebbles are visible. Boulders with layered structure (pink boxes with layers indicated by dotted lines) are observed, along with a boulder from which a flattened piece seems to be peeling (arrow in the white box). Both type 1 and type 2 boulders are present in this region (labeled). (D) Image taken during a hop of MINERVA-II Rover-1A on 2018 October 16. Ejected centimeter-sized pebbles are visible within the white box.

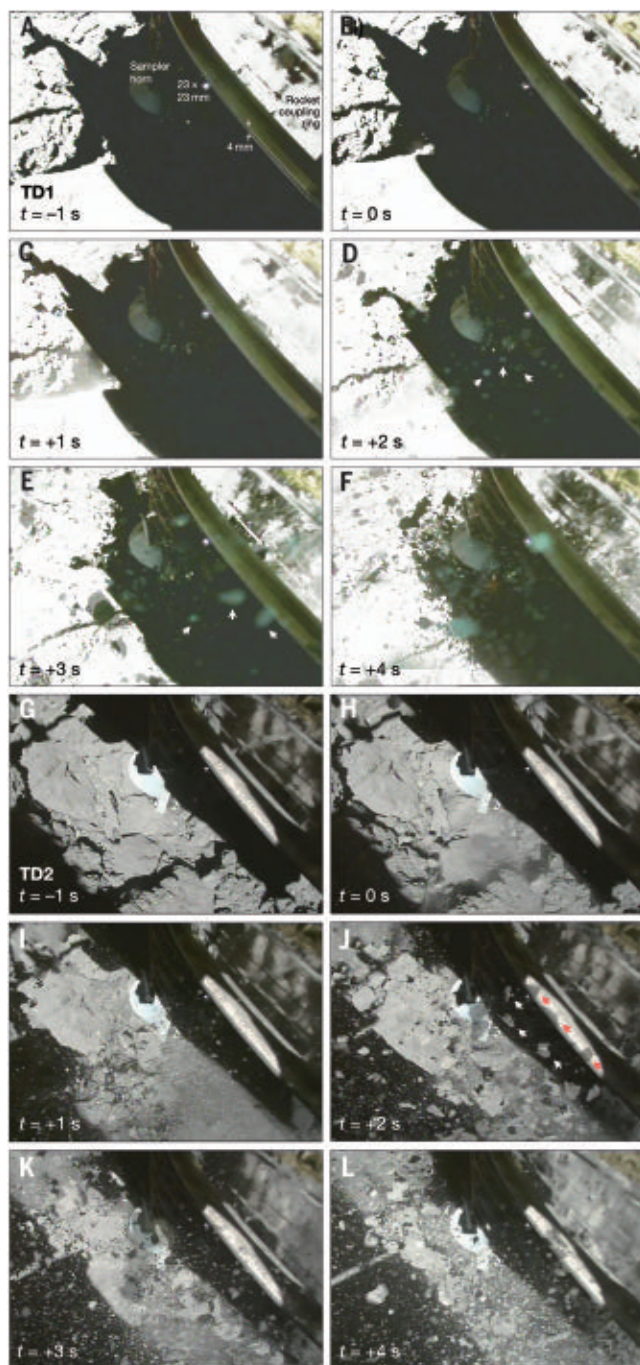


Fig. 3. CAM-H images of the TD1 and TD2 sample acquisition processes. (A to F) TD1 operation. The lower left of each panel indicates the time t from projectile firing, ranging from -1 to $+4$ s. Ejecta particles are visible after $t = 0$. A reflection plate for a laser range finder (23 mm by 23 mm) on the sampler horn and the rim of the rocket coupling ring (4 mm; distance between arrows) are labeled as size references. The white arrows in (D) and (E) indicate the same group of particles moving toward CAM-H. (G to L) Equivalent images of TD2. Three particles, indicated with white arrows in (J), are also seen as mirror images reflected on the rocket coupling ring (red arrows).

lengths—the distance between two parallel lines tangential to the surface—of the maximum-area projection of each particle and S as the smallest dimension measured in the minimum-area projection (fig. S5) (20, 22). The shortest axis

to longest axis (S/L) and intermediate axis to longest axis (I/L) ratios of the particles (Fig. 4 and tables S1 and S2) show that there is a fraction of elongated block-like flat particles on the surface. The 67 particles have a bimodal

distribution centered at (S/L , I/L) of (0.53, 0.69) and (0.35, 0.48) (Fig. 5), which means that two shape types are present in the population of surface pebbles, which we refer to as “subequant” and “elongated block” (23). Pebbles and small boulders with a shape that is both elongated and flat are found at both landing locations (Fig. 1). This suggests that the bimodal distribution of pebble shapes is indigenous to Ryugu’s surface. However, because such a bimodal distribution is not found for boulders larger than 5 m (24), we conclude that this shape variation results from boulder fragmentation or foliation (Fig. 2) (5). This elongated and flat morphology is not typical among clasts (embedded fragments) in carbonaceous chondrite meteorites but is similar to the texture of clasts in shocked hydrated carbonaceous chondrites (25–28). Some of the latter show a high density of parallel fractures that formed because of sudden volatile loss during the release of shock pressure (28).

During the TD1 ascent operation, CAM-H observed a centimeter-sized pebble that passed between the camera and the rocket coupling ring (Fig. 4, C and D). The pebble hit the spacecraft; then 4 s later, a smaller particle (~ 4 mm in size) appeared from the spacecraft side (Fig. 4E). Because no other particles coming from the spacecraft side were observed during the TD1 and TD2 operations, the ~ 4 -mm-sized particle is likely to be a fragment of this centimeter-sized pebble that resulted from its impact with the spacecraft. The CAM-H images from the ascending spacecraft (~ 1 m s $^{-1}$) suggest that the relative velocity of the pebble to the spacecraft was ~ 0.1 m s $^{-1}$. Because fragmentation of typical carbonaceous chondrite material requires an impact velocity of >1 m s $^{-1}$ (20, 29), this implies that the tensile strength of the pebble is much lower than that of typical chondrites (fig. S6) (17, 20). The highly porous material identified on the surface (30) could be of similar composition to the fragile pebble. Alternatively, the pebble might have contained a crack (or cracks), such as the one that was observed on a boulder by the MINERVA-II Rover-1A (Fig. 2).

Samples returned to Earth

Hayabusa2 left Ryugu in November 2019. On 6 December 2020, the reentry capsule containing the samples was delivered to Woomera, South Australia. After transfer to a clean room, the sample chambers were opened and found to contain ~ 5 g of material (31). This is ~ 50 times more than the mission minimum requirement of 0.1 g (1, 16). The samples recovered from chamber A (24 cm 3) of the sample catcher, which was used for the storage of TD1 samples, weigh ~ 3 g. This mass is consistent with the estimate above based on CAM-H images. We therefore conclude that the sample in

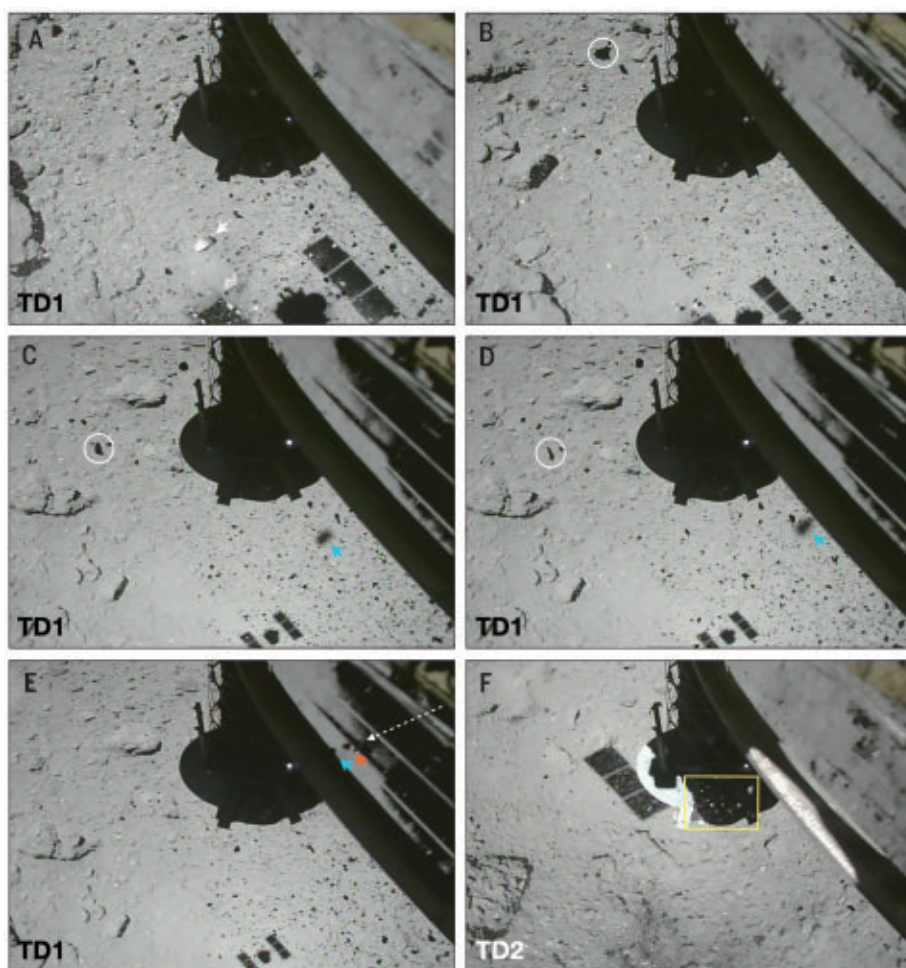


Fig. 4. CAM-H images of flying particles during the ascent operations. (A) Particle with smooth faces indicated with a white arrow. (B) Rugged particle indicated with a white circle. (C and D) Flat particle (white circle) and particle that appears to have hit the spacecraft (blue arrow). (E) Particle coming from the spacecraft side indicated with a blue arrow. Its mirror image is seen on the rocket coupling ring (red arrow). The particle's direction of movement is shown with a white dotted arrow. (F) Millimeter-sized particles (within the yellow box) observed after TD2. Movies S1 and S2 show the full footage of these operations, in which the particle movements are visible. (A) to (E) are from TD1, and (F) is from TD2.

chamber A was lifted by the projectile firing, which worked efficiently to collect asteroid surface regolith. This is unlike the particles returned from the asteroid Itokawa by the original Hayabusa spacecraft, as its projectile failed to fire, which complicated interpretation of the samples (2). Chamber C (12 cm³) of the sample catcher, which was used for samples from TD2, contained ~2 g. This is also consistent with the estimate above from the CAM-H images, which suggests that chamber C samples are also the ejecta from the projectile firing. Unlike TD1, the TD2 sample likely includes material from the subsurface that was excavated by the SCI impact.

We compare the properties of the returned particles to the constraints derived above from the sample collection images. In both chambers

of the sample container, millimeter-sized sand and nearly centimeter-sized pebbles were found, along with submillimeter-sized fine powder. The grain size variation is consistent with expectations derived from the surface observation by the MASCOT lander (11), MINERVA-II rovers, Hayabusa2 cameras (Figs. 2 to 4), and polarimetric observations from Earth (32). All the particles in the two chambers appeared black (Fig. 6), which is consistent with the color and albedo of Ryugu's boulders (5, 6). The sizes of the collected particles are consistent with the ejecta observed during each landing operation (Fig. 3). The largest grains from chamber A are ~5 mm in size, whereas there are three pebbles larger than 5 mm from chamber C (Fig. 6 and table S3). The longest dimension of the largest pebble in chamber C is 10.3 mm, which is close to the maximum size obtainable by the Hay-

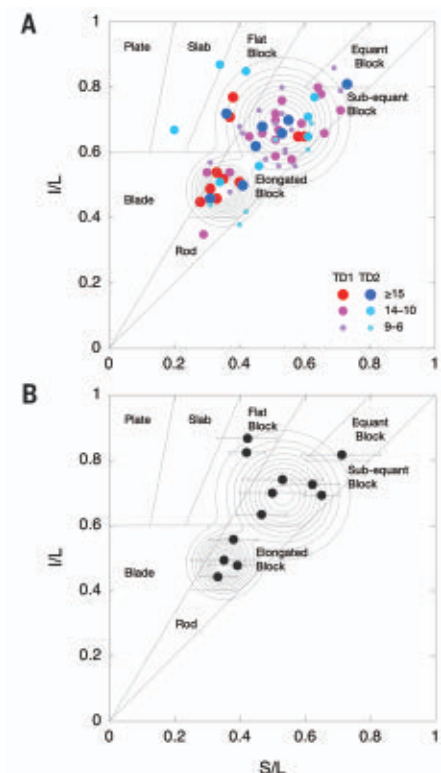


Fig. 5. Shape parameters of flying particles observed during touchdown operations and particles returned to Earth. (A) Properties of particles observed during TD1 and TD2 operations. S/L is the ratio of the shortest axis to the longest axis, and I/L is the ratio of the intermediate axis to the longest axis (25). Contours indicate the probability distribution function of 67 particles, assuming a bimodal distribution (25). (B) Properties of returned samples, six particles each from chambers A and C (25), overlain on the same contours from (A). The distribution is similar. Data for all the particles in both panels are listed in tables S1 to S3.

abusa2 sampler (16, 21). The presence of these large pebbles in chamber C, despite the smaller total mass, can be explained either by projectile destruction of a larger rock or the scoop-up component of the sampler horn, which was designed to pick up surface pebbles (16). Millimeter-sized fine grains and submillimeter-sized sand particles were also found in chamber C, which are likely to include subsurface material, as observed on a boulder (Fig. 2A). Chamber B, which was not used for either landing operation, is located between chambers A and C. A small number of fine particles (smaller than 1 mm) were found in this chamber. This shows that no extensive mixing of particles occurred through the gaps between the chambers during the return to Earth or capsule recovery (16). We are therefore confident that the pebbles and sand in chambers A

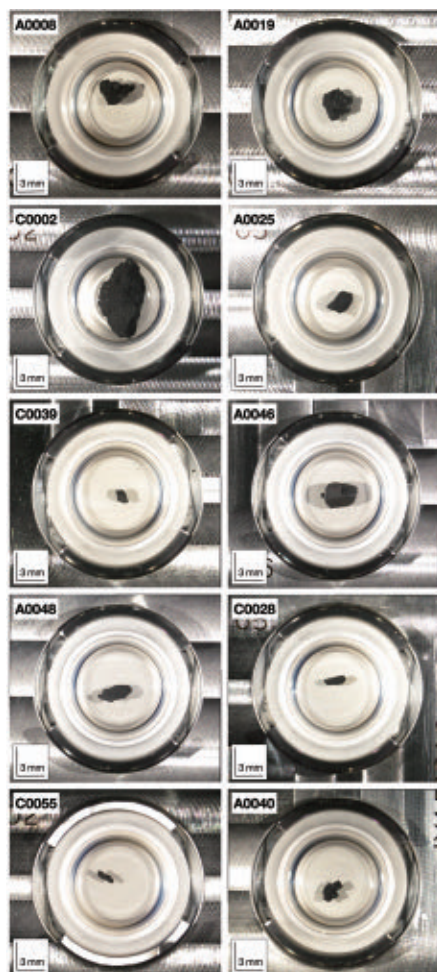


Fig. 6. Microscope images of particles returned to Earth inside the sample container. Particles cataloged as A0008, A0019, A0046, A0048, A0069, and A0083 are from chamber A of the sample container used for TD1. C0002, C0004, C0013, C0019, C0028, and C0055 are from chamber C of the sample container used for TD2. The particles A0008, A0019, A0069, A0083, and C0002 have rugged surfaces, whereas A0046 and C0019 have smooth surfaces. The particles A0048, C0028, and C0055 show elongated blocklike morphologies. Particles were mounted on individual sample holders in a nitrogen atmosphere and are lit from the left and right simultaneously.

and C are the samples acquired in the TD1 and TD2 operations, respectively.

More than 200 pebbles (1 to 10 mm in size) from chambers A and C were individually removed and observed under an optical microscope (Fig. 6). These pebbles show morphological variations: Grains with rugged surface and with smooth surfaces are observed (Fig. 6), which is consistent with the flying pebbles observed during the TD1 and TD2 operations. Although only a few particles have been measured, the elongated block-like pebbles in the collected

sample (Fig. 6) have S/L and I/L ratios (Fig. 5B) that are consistent with those of the flying particles observed at Ryugu (Fig. 5A).

Many returned particles feature curved and straight cracks. Pebbles with a smooth surface could be fragments of particles with straight cracks, possibly formed by shock or thermal fatigue (33). The common presence of cracks in returned pebbles implies that the small thermal inertia of surface boulders (12, 13) is probably due, at least in part, to cracks or fractures in their interior. Microcracks or microporosity could also be responsible for the low thermal inertia.

The color, shape, surface morphology, and structure of the returned pebbles and sand match those of Ryugu's surface material observed from the spacecraft. We therefore conclude that the pebbles and sand inside chambers A and C are representative samples of Ryugu at two surface sites, without substantial alteration during the sample collection and return to Earth. The variations in physical properties among the pebbles and sand, which were not expected before spacecraft arrival at the asteroid, reflect the geological history of Ryugu (1).

REFERENCES AND NOTES

1. S. Tachibana *et al.*, *Geochim. J.* **48**, 571–587 (2014).
2. A. Tsuchiyama *et al.*, *Science* **333**, 1125–1128 (2011).
3. K. Nagao *et al.*, *Science* **333**, 1128–1131 (2011).
4. S. Watanabe *et al.*, *Science* **364**, 268–272 (2019).
5. S. Sugita *et al.*, *Science* **364**, 252 (2019).
6. T. Morota *et al.*, *Science* **368**, 654–659 (2020).
7. E. Tatsumi *et al.*, *Nat. Astron.* **5**, 39–45 (2021).
8. K. Kitazato *et al.*, *Science* **364**, 272–275 (2019).
9. D. S. Lauretta *et al.*, *Nature* **568**, 55–60 (2019).
10. V. E. Hamilton *et al.*, *Nat. Astron.* **3**, 332–340 (2019).
11. R. Jaumann *et al.*, *Science* **365**, 817–820 (2019).
12. M. Grott *et al.*, *Nat. Astron.* **3**, 971–976 (2019).
13. T. Okada *et al.*, *Nature* **579**, 518–522 (2020).
14. M. Arakawa *et al.*, *Science* **368**, 67–71 (2020).
15. K. Kitazato *et al.*, *Nat. Astron.* **5**, 246–250 (2021).
16. H. Sawada *et al.*, *Space Sci. Rev.* **208**, 81–106 (2017).
17. R. Okazaki *et al.*, *Space Sci. Rev.* **208**, 107–124 (2017).
18. K. Wada *et al.*, *Astron. Astrophys.* **647**, A43 (2021).
19. R. Honda *et al.*, *Icarus* **366**, 114530 (2021).
20. Materials and methods are available as supplementary materials.
21. F. Thuillet, P. Michel, S. Tachibana, R.-L. Ballouz, S. R. Schwartz, *Mon. Not. R. Astron. Soc.* **491**, 153–177 (2019).
22. G. H. Bagheri, C. Bonadonna, I. Manzella, P. Vonlanthen, *Powder Technol.* **270**, 141–153 (2015).
23. S. J. Blott, K. Pye, *Sedimentology* **55**, 31–63 (2008).
24. T. Michikami *et al.*, *Icarus* **331**, 179–191 (2019).
25. M. E. Zolensky *et al.*, *Geochim. Cosmochim. Acta* **61**, 5099–5115 (1997).
26. A. E. Rubin, *Geochim. Cosmochim. Acta* **90**, 181–194 (2012).
27. R. D. Hanna, R. A. Ketcham, M. E. Zolensky, W. M. Behr, *Geochim. Cosmochim. Acta* **171**, 256–282 (2015).
28. T. Nakamura *et al.*, Irradiation-energy dependence of the spectral changes of hydrous C-type asteroids based on 4 keV and 20 keV He exposure experiments of Murchison CM chondrite, 51st Lunar and Planetary Science Conference, 16 to 20 March 2020, The Woodlands, TX, Abstract 1310.
29. M. Setoh, A. M. Nakamura, N. Hirata, K. Hiraoka, M. Arakawa, *Earth Planets Space* **59**, 319–324 (2007).
30. N. Sakatani *et al.*, *Nat. Astron.* **5**, 766–774 (2021).
31. T. Yada *et al.*, *Nat. Astron.* 10.1038/s41550-021-01550-6 (2021).
32. D. Kuroda *et al.*, *Astrophys. J. Lett.* **911**, L24 (2021).
33. G. Libourel *et al.*, *Mon. Not. R. Astron. Soc.* **500**, 1905–1920 (2021).

ACKNOWLEDGMENTS

Hayabusa2 was developed and built under the leadership of JAXA, with contributions from the German Aerospace Center and the Centre National d'Études Spatiales (CNES) and in collaboration with NASA and other universities, institutes, and companies in Japan. The sampler system was developed by JAXA, The University of Tokyo, Hokkaido University, Kyushu University, Japan Agency for Marine-Earth Science and Technology, and other universities, institutes, and companies in Japan. **Funding:** S. Tachibana acknowledges JSPS KAKENHI Grant (JP 20H05846), S.W. acknowledges JSPS KAKENHI Grant (17H06459 and 19H01951), P.M., B.M., Y.Z., F. Thuillet, and G.L. acknowledge the French space agency CNES. P.M. and Y.Z. acknowledge funding from the European Union's Horizon 2020 research and innovation program under grant agreement no. 870377 (project NEO-MAPP), from the Université Côte d'Azur "Individual grants for young researchers" program and from Academies of Excellence: Complex Systems and Space, Environment, Risk, and Resilience, part of the IDEX JEDI of Université Côte d'Azur. B.M. acknowledges funding from the European Research Council (grant agreement no. 695618). **Author contributions:** S. Tachibana, coordinated coauthor contributions; led the sampler development with H. Sawada; performed data analyses, and interpretations; and wrote the paper, with contributions from H. Sawada, R.O., Y. Takano, K. Sakamoto, and H. Yano. Sampler development and operation: H. Sawada, R.O., Y. Takano, K. Sakamoto, Y.N.M., C.O., H. Yano, S.Y., T. Noguchi, T. Nakamura, A.T., N.I., K. Kurosawa, and A.M.N.; CAM-H operation: H. Sawada and K.O.; ONC data acquisition and reduction: S. Sugita, R.H., T. Morota, Y. Iijima, S. Kameda, H. Sawada, E.T., C. Honda, Y. Yokota, M. Yamada, T. Kouyama, N.S., K.O., H. Suzuki, K. Yoshioka, M.H., Y.C., M.I., A. Miura, and M.M.; MINERVA-II rovers operation: T. Yoshimitsu, T. Kubota, and H.D.; capsule retrieval operation and curation: S.N., M.F., T. Yamada, T.R.I., H. Sawada, R.O., K. Sakamoto, Y. Takano, Y.N.M., H. Yano, M.N., K. Yagata, A.N., M. Yoshitake, A.I.S., S.F., K.H., A. Miyazaki, K. Kumagai, T.O., M. Abe, H. Yurimoto, T.U., and K.N.-M.; landing site characterization: Y. Tsuda, S.W., T. Saiki, S. Kikuchi, N.O., Y. Yamamoto, Y.S., K. Shirai, N.H. (Kobe), K.O., K. Kitazato, N.H. (Aizu), K.W., H. Yabuta, Y. Ishihara, R.N., T. Morota, N.S., K.M., H. Senshu, R.H., E.T., Y. Yokota, C. Honda, T. Michikami, M.M., and A.M.; interpretation and writing contribution: S. Sugita, Y. Takano, P.M., Y.Z., S. Schwarz, F. Thuillet, H. Yurimoto, T. Nakamura, T. Noguchi, H. Yabuta, H. Naraoka, A.M.N., K. Kitazato, T. Morota, T. Michikami, S. Kameda, E.T., T. Yoshimitsu, T. Yada, T.O., T.U., T.R.I., M.F., H.C.C., S. Hasegawa, D.S.L., G.L., B.M., A.N.N., L.R.N., K.W., K. Yumoto, M.E.Z.; spacecraft science operations: S. Tanaka, M. Yoshikawa, T.I., Y. Yamamoto, K.M., M. H., T.O., R.N., Y.S., N.S., H.N., M.M., H. Yano, R.T., M.O., F. Terui, N.O., H. Sawada, S. Kikuchi, H.T., G.O., Y.M., K. Yoshikawa, T.T., Y. Takei, A.F., C. Hirose, S.N., S. Hosoda, O.M., T. Shimada, S. Soldini, T. Saiki, S.W., and Y. Tsuda; project administration: S.W., M. Yoshikawa, S. Tachibana, K. Kitazato, S. Sugita, T.O., N.N., M. Arakawa, M. Abe, H.I., S. Tanaka, S.N., F.T., T. Saiki, and Y. Tsuda. All authors discussed the results and commented on the manuscript. **Competing interests:** The authors declare no competing interests. **Data and materials availability:** All images and data used in this study are available at the JAXA Data Archives and Transmission System (DARTS) at www.darts.isas.jaxa.jp/pub/hayabusa2/paper/sample/ Tachibana, 2022/. Other data from the mission are available at the DARTS archive www.darts.isas.jaxa.jp/planet/project/hayabusa2/ and on the Small Bodies Node of the NASA Planetary Data System https://pds-smallbodies.astro.umd.edu/data_sb/missions/hayabusa2/. The samples of Ryugu are curated by the JAXA Astromaterials Science Research Group; distribution for analysis is through an Announcement of Opportunity available at <https://jaxa-ryugu-sample-a.o.net>. Our particle size and shape measurements are listed in tables S1 to S3.

SUPPLEMENTARY MATERIALS

science.org/doi/10.1126/science.abj8624
Materials and Methods
Figs. S1 to S7
Tables S1 to S3
References (34–41)
Movies S1 to S4
7 June 2021; accepted 25 January 2022
Published online 10 February 2022
10.1126/science.abj8624

REPORTS

TOPOLOGICAL PHYSICS

A synthetic monopole source of Kalb-Ramond field in diamond

Mo Chen (陈墨)^{1,2,†}, Changhao Li^{1,3,‡}, Giandomenico Palumbo^{4,5}, Yan-Qing Zhu^{4,§}, Nathan Goldman⁴, Paola Cappellaro^{1,3,6,*}

Magnetic monopoles play a central role in areas of physics that range from electromagnetism to topological matter. String theory promotes conventional vector gauge fields of electrodynamics to tensor gauge fields and predicts the existence of more exotic tensor monopoles. Here, we report the synthesis of a tensor monopole in a four-dimensional parameter space defined by the spin degrees of freedom of a single solid-state defect in diamond. Using two complementary methods, we characterized the tensor monopole by measuring its quantized topological charge and its emanating Kalb-Ramond field. By introducing a fictitious external field that breaks chiral symmetry, we further observed an intriguing spectral transition, characterized by spectral rings protected by mirror symmetries. Our work demonstrates the possibility of emulating exotic topological structures inspired by string theory.

Our current understanding of fundamental physical phenomena relies on two main pillars: general relativity and quantum field theory. Their mutual incompatibility, however, poses critical limitations to the formulation of a unifying theory of all fundamental interactions. String theory proposes a powerful and elegant formalism to unify gravitational and quantum phenomena, providing a concrete route to quantum gravity (1). Within this scenario, conventional point-like particles are replaced with extended objects, such as

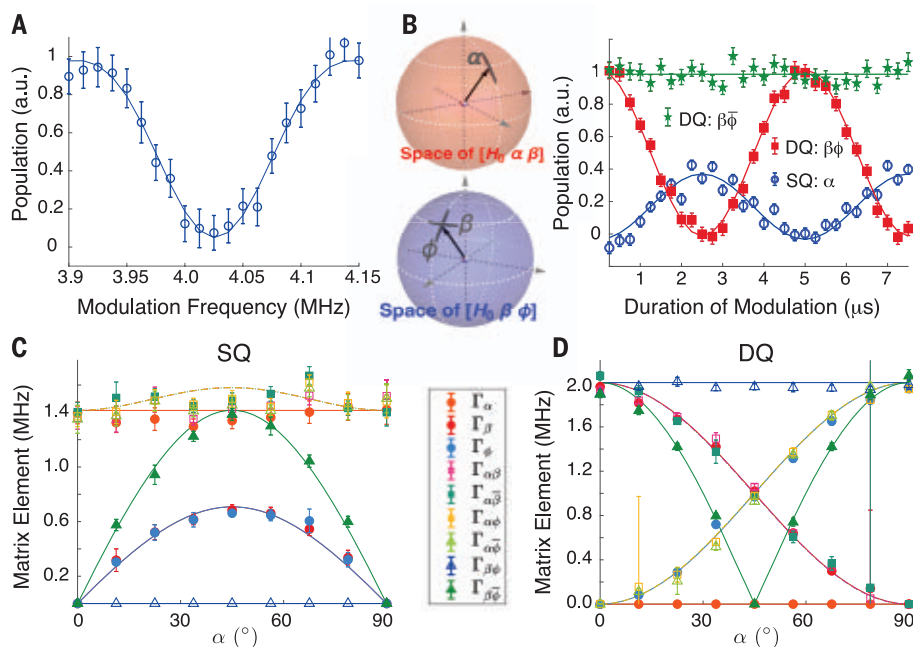
closed and open strings, and conventional vector gauge fields are promoted to tensor Kalb-Ramond (KR) gauge fields (2, 3). In direct analogy with the Dirac monopole (4), tensor gauge fields can emanate from point-like defects called tensor monopoles. In four spatial dimensions, the tensor monopole charge is quantized according to the topological Dixmier-Douady (DD) invariant (5–7), which generalizes the Chern number associated with the Dirac monopole.

Experimental evidence of magnetic monopoles is still lacking in high-energy physics experi-

ments. However, synthetic monopoles associated with effective gauge fields have recently been detected in ultracold matter (8–13). Additionally, momentum-space monopoles play a central role in topological matter, such as in characterizing three-dimensional (3D) Weyl semimetals. Recently, the notions of tensor monopoles and DD invariants were shown to arise in 3D chiral topological insulators (14, 15) and in higher-order topological insulators (16).

In this work, we exploited the high controllability of engineered quantum three-level (qutrit) systems to reveal exotic gauge structures, originally introduced in the context of string theory (2, 3). We considered the spin triplet ground state of a single nitrogen-vacancy (NV) center in diamond, which can be mapped

Fig. 1. Parametric modulations. (A) Determining the resonance condition for parametric modulation. We fixed $\tau = 7.5 \mu\text{s}$, $(m_\alpha, m_\beta, m_\phi) = (0, 1/30, 1/30)$, and swept the modulation frequency around 4 MHz to find $\omega_r = 2H_0$. (B) Examples of coherent Rabi oscillations under parametric modulations, for the engineered Hamiltonian at $(\alpha_0 = \pi/4, \beta_0 = \phi_0 = 0)$. The measured Rabi frequencies are used to calculate the matrix elements $\Gamma_{-m}^{u(v)}$ [shown in (C) and (D)]. To extract the diagonal components of the metric tensor, we used a single-parameter modulation—as shown by the blue curve, for example—representing the SQ transition ($\omega = \omega_r/2$) for α modulation. Owing to chiral symmetry, $|\Gamma_{-0}^{u(v)}| = |\Gamma_{+0}^{u(v)}|$. We therefore measured the population in the first excited state $|\mu_0\rangle$, which gives half contrast (20). The other two curves represent two-parameter modulations resonant with the DQ transition ($\omega = \omega_r$) and possess full contrast. Illustrations of the relevant single- and two-parameter modulations in the Bloch sphere representation are provided at left. (C) Matrix elements $|\Gamma_{-0}^{u(v)}|$ measured for SQ transitions at $\omega = \omega_r/2$. Many matrix elements are expected from theory to coincide, and thus their measured values overlap at $\sqrt{2}$ MHz. (D) Matrix elements $|\Gamma_{-+}^{u(v)}|$ measured for DQ transitions at $\omega = \omega_r$. Markers are experimental data, and solid lines are fits in (A) and (B) and theory in (C) and (D) (20).



¹Research Laboratory of Electronics, Massachusetts Institute of Technology, Cambridge, MA 02139, USA. ²Department of Mechanical Engineering, Massachusetts Institute of Technology, Cambridge, MA 02139, USA. ³Department of Nuclear Science and Engineering, Massachusetts Institute of Technology, Cambridge, MA 02139, USA. ⁴Center for Nonlinear Phenomena and Complex Systems, Université Libre de Bruxelles, CP 231, Campus Plaine, B-1050 Brussels, Belgium. ⁵School of Theoretical Physics, Dublin Institute for Advanced Studies, 10 Burlington Road, Dublin 4, Ireland. ⁶Department of Physics, Massachusetts Institute of Technology, Cambridge, MA 02139, USA.

*Corresponding author. Email: pcappell@mit.edu

†Present address: Institute for Quantum Information and Matter and Thomas J. Watson, Sr., Laboratory of Applied Physics, California Institute of Technology, Pasadena, CA 91125, USA.

‡These authors contributed equally to this work.

§Present address: Department of Physics and Center of Theoretical and Computational Physics, The University of Hong Kong, Pokfulam Road, Hong Kong, China.

into a three-level Weyl-type Hamiltonian \hat{H}_{4D} (q_x, q_y, q_z, q_w) defined over a 4D parameter space

$$\hat{H}_{4D} = \begin{pmatrix} 0 & q_x - iq_y & 0 \\ q_x + iq_y & 0 & q_z + iq_w \\ 0 & q_z - iq_w & 0 \end{pmatrix} \quad (1)$$

Here, the parameters $\mathbf{q} = (q_x, q_y, q_z, q_w)$ can be expressed in terms of the experimentally controllable parameters (H_0, α, β, ϕ) described below, through $q_x + iq_y = H_0 \cos(\alpha) e^{i\beta}$, $q_z + iq_w = H_0 \sin(\alpha) e^{i\phi}$, where $\alpha \in [0, \pi/2]$ and $\beta, \phi \in [0, 2\pi)$. This Hamiltonian hosts a threefold degenerate point in the spectrum, located at the origin $\mathbf{q} = 0$. This singularity is topologically protected by chiral symmetry $\{\hat{H}_{4D}, U\} = 0$, where $U = \text{diag}(1, -1, 1)$, and is a good candidate for a synthetic monopole source of tensor gauge field, as we explain below.

A nodal point in a 3D parameter space is associated with an effective Dirac monopole (12–14). In this scenario, the Berry-curvature field emanates radially from the node, and its flux through a two-sphere enclosing it is quantized, characterized by the Chern number (17). In 4D space, the topological charge associated with a nodal point is provided by a similar invariant, which now involves the flux of a radial three-form curvature over a three-sphere that surrounds the node (14). The three-form curvature $\mathcal{H}_{\mu\nu\lambda}$ is well known in the context of p-form electromagnetism (3), where it derives from a two-form gauge field: the Abelian and antisymmetric KR field $B_{\mu\nu}$ (2)

$$\mathcal{H}_{\mu\nu\lambda} = \partial_\mu B_{\nu\lambda} + \partial_\nu B_{\lambda\mu} + \partial_\lambda B_{\mu\nu} \quad (2)$$

This KR field plays an important role in string theory because it naturally couples to extended objects (2, 3).

Similarly to monopoles associated with vector gauge fields in 3D space, the tensor KR field $B_{\mu\nu}$ gives rise to tensor monopoles with distinct topological properties (5–7, 14–16). These exotic monopoles are point-like sources of the generalized “magnetic” field $\mathcal{H}_{\mu\nu\lambda}$, and their topological charge is obtained by measuring the corresponding flux over a three-sphere surrounding them

$$\mathcal{D}\mathcal{D} = \frac{1}{2\pi^2} \int_{S^3} \mathcal{H}_{\mu\nu\lambda} dq^\mu \wedge dq^\nu \wedge dq^\lambda \quad (3)$$

This topological invariant is known as the $\mathcal{D}\mathcal{D}$ invariant (5–7, 14–16) and generalizes the well-known Chern number. The field $\mathcal{H}_{\mu\nu\lambda}$ radially emanates from the singularity in 4D space, hence providing an observable and unambiguous signature of tensor monopoles.

We next explored how these exotic gauge structures can be measured in engineered systems. First, the KR field $B_{\mu\nu}$ in Eq. 2 can be reconstructed from the eigenstates of the Hamiltonian in Eq. 1 (14, 15). Although state

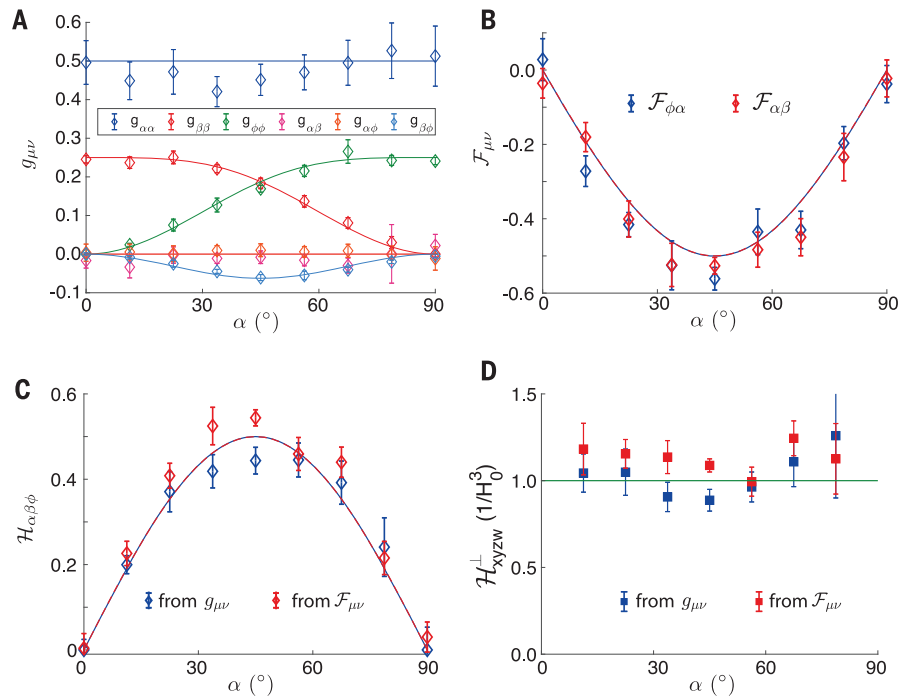


Fig. 2. Revealing the tensor monopole. (A) Independent components of the metric tensor $g_{\mu\nu}$ measured as a function of α . (B) Non-zero components of Berry curvature $\mathcal{F}_{\mu\nu}$ measured as a function of α . (C) Generalized three-form curvature $\mathcal{H}_{\alpha\beta\phi}$ with respect to α , reconstructed from the measured metric tensor $g_{\mu\nu}$ in (A) and the Berry curvature $\mathcal{F}_{\mu\nu}$ in (B). These complementary measurements yield topological invariant $\mathcal{D}\mathcal{D}_{\text{exp},g} = 0.99(3)$ and $\mathcal{D}\mathcal{D}_{\text{exp},\mathcal{F}} = 1.11(3)$, revealing the existence of a tensor monopole within the hypersphere. (D) Radial field component \mathcal{H}_{xyzw}^\perp extracted from the quantum metric in (A) and Berry curvature in (B), showing the characteristic inverse-cube dependence on the radial coordinate. Markers are experimental data, and solid lines are theory (20). The error bars are propagated from fitting errors of resonant frequencies and Rabi oscillations.

tomography could be performed to reconstruct these states and the related tensor fields, this approach is resource intensive. We provide two alternative methods to experimentally measure the curvature $\mathcal{H}_{\mu\nu\lambda}$. The first approach builds on a relation between the three-form curvature and the Fubini-Study quantum metric $g_{\mu\nu}$ (14, 15)

$$\mathcal{H}_{\mu\nu\lambda} = \epsilon_{\mu\nu\lambda} \left[4\sqrt{\det(g_{\mu\nu})} \right] \quad (4)$$

where $\epsilon_{\mu\nu\lambda}$ is the Levi-Civita symbol, and $\bar{\mu}, \bar{\nu} = \{q_x, q_y, q_z\}$ for \mathcal{H}_{xyz} (and similarly for the other components). The metric tensor $g_{\mu\nu}$, which defines the distance between nearby states $|u(\mathbf{q})\rangle, |u(\mathbf{q} + d\mathbf{q})\rangle$ (12, 13, 18–20), thus allows for a measurement of the tensor monopole field. The second approach builds on our experimental parametrization (H_0, α, β, ϕ), which expresses the three-form curvature in Eq. 2 as (20)

$$\mathcal{H}_{\alpha\beta\phi} = -\frac{1}{2} (\mathcal{F}_{\alpha\beta} + \mathcal{F}_{\phi\alpha}) \quad (5)$$

where $\mathcal{F}_{\mu\nu}$ is the standard (2-form) Berry curvature. We will refer to the latter as the Berry curvature, not to be confused with the three-form curvature $\mathcal{H}_{\mu\nu\lambda}$. Both the metric tensor

$g_{\mu\nu}$ in Eq. 4 and the Berry curvature $\mathcal{F}_{\mu\nu}$ in Eq. 5 can be experimentally extracted from spectroscopic responses upon modulating the parameters μ, ν (12, 13, 18, 20).

In our experiment, we exploited these two different probes of the three-form curvature to demonstrate two distinct signatures of the tensor monopole field: its quantized topological charge and its characteristic radial behavior in 4D parameter space.

To synthesize the 4D Hamiltonian in Eq. 1, we used the ground triplet states of a single NV center in diamond at room temperature (fig. S4). An external magnetic field, $B = 490$ G, is applied along the NV axis to lift the degeneracy between the qutrit spin states $|\pm 1\rangle$. At this magnetic field, optical illumination of a 532-nm laser polarizes both the NV electronic spin and the native ^{14}N nuclear spin through polarization transfer in the excited state (21). Hence, we can neglect the nuclear spin part of the Hamiltonian in the analysis: We applied a dual-frequency microwave pulse (22), on resonance with the $|0\rangle \leftrightarrow |\pm 1\rangle$ transitions. In the doubly rotating frame, and upon the rotating wave approximation, we reproduced the minimal tensor monopole model in Eq. 1, where β, ϕ are the phases of the

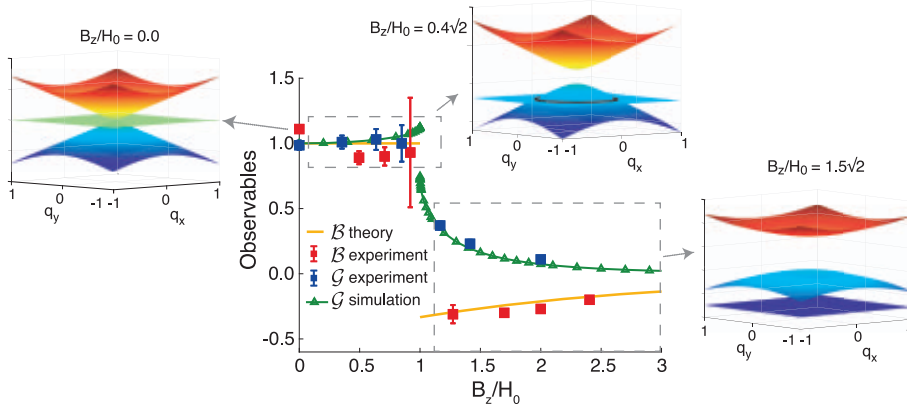


Fig. 3. Spectral transition triggered by an external field. The central plot shows experimental data (blue squares) and numerical simulation (green triangles) (20) of the experimental observable \mathcal{G} based on the metric tensor, experimental data (red squares), and analytical result (yellow line) of the observable \mathcal{B} based on the Berry curvature (20). Both observables show a sudden change at $B_z = H_0$, when the spectral rings cross the boundary of the integration hypersphere. The experimental observables \mathcal{G} , \mathcal{B} correspond to the \mathcal{DD} invariant when $B_z = 0$ and chiral symmetry is preserved. (Insets) Three representative energy spectra as the longitudinal field B_z increases ($q_z = q_w = 0$). The external field splits the triply degenerate Weyl node (left) into doubly degenerate spectral rings (middle). As the field further increases, the system becomes gapped in the enclosed integration hypersphere (right).

two microwave tones, and $H_0 \cos \alpha$, $H_0 \sin \alpha$ are their corresponding microwave amplitudes (20).

This Hamiltonian has three eigenstates $|u_{\{-,0,+\}}\rangle$, with eigenvalues $\{\epsilon_-, \epsilon_0, \epsilon_+\}$ in ascending order. Precise modulations of the microwave frequencies, amplitudes, and phases grant us full access to the 4D parameter space spanned by $(H_0, \alpha, \beta, \phi)$. Using this parametrization, the system is rotationally symmetric about β, ϕ . Therefore, the measurable geometric quantities (the metric tensor and Berry curvature) are independent of β, ϕ

$$g + i\frac{\mathcal{F}}{2} = \begin{pmatrix} \frac{1}{2} & \frac{i\sin(2\alpha)}{4} & -\frac{i\sin(2\alpha)}{4} \\ -\frac{i\sin(2\alpha)}{4} & \frac{\cos^2\alpha[2 - \cos^2(\alpha)]}{4} & -\frac{\sin^2(2\alpha)}{16} \\ \frac{i\sin(2\alpha)}{4} & -\frac{\sin^2(2\alpha)}{16} & \frac{\sin^2\alpha[2 - \sin^2(\alpha)]}{4} \end{pmatrix} \quad (6)$$

As a demonstration of our engineered system, we initialized the NV in the $|0\rangle$ state and let it evolve under the target Hamiltonian (with $\beta = \phi = 0$). We further chose the microwave amplitudes so that the parameters span a hypersphere with fixed radius $H_0 = 2$ MHz, which encloses the tensor monopole at the origin. For various values of α , the resulting dynamics of all three states show excellent agreement with theory (fig. S6).

We next measured the quantum metric tensor and Berry curvature using weak modulations of the parameters $\mu, \nu \in \{\alpha, \beta, \phi\}$ (12, 13, 18). Considering the modulations $\mu(t) = \mu_0 + m_\mu \sin(\omega t + \gamma)$, $\nu(t) = \nu_0 + m_\nu \sin(\omega t)$, with $m_\mu, m_\nu \ll 1$, the Hamiltonian takes the form

$$\hat{H} \approx \hat{H}(\alpha_0, \beta_0, \phi_0) + m_\mu \partial_\mu \hat{H} \sin(\omega t + \gamma) + m_\nu \partial_\nu \hat{H} \sin(\omega t) \quad (7)$$

When $\gamma = 0$, we linearly modulated μ, ν and extracted the metric tensor, while we set $\gamma = \pi/2$ to elliptically modulate μ, ν and extract the Berry curvature, as outlined below.

The parametric modulations coherently drive Rabi oscillations between $|u_-\rangle \leftrightarrow |u_0\rangle$ and $|u_-\rangle \leftrightarrow |u_+\rangle$ when the modulation frequency is tuned on resonance with the energy gap between ground and excited state, $\omega = \epsilon_0 - \epsilon_-$ and $\omega = \epsilon_+ - \epsilon_-$, respectively. We call the transitions $|u_\pm\rangle \leftrightarrow |u_0\rangle$ “single quantum (SQ) transitions” and the transition $|u_-\rangle \leftrightarrow |u_+\rangle$ “double quantum (DQ) transition,” following the change in quantum number. Their Rabi frequencies are directly related to the transition matrix elements when varying one Hamiltonian parameter, $\Gamma_{-,n}^\mu = |\langle u_- | \partial_\mu \hat{H} | n \rangle|$, or when modulating two parameters, either linearly, $\Gamma_{-,n}^{\mu,\nu} = \langle u_- | \partial_\mu \hat{H} \pm \partial_\nu \hat{H} | n \rangle$ or elliptically, $\Gamma_{-,n}^{\mu,\pm\nu} = \langle u_- | \partial_\mu \hat{H} \pm i \partial_\nu \hat{H} | n \rangle$, where $m_\mu = \pm m_\nu$ (20). Here, the subscript for the matrix element, $\{-, n\}$, stands for the transition between eigenstates $|u_-\rangle \leftrightarrow |n\rangle$. Last, we reconstructed the quantum metric tensor and Berry curvature from the relations (12, 20)

$$g_{\mu\mu} = \sum_{n=-1} \frac{(\Gamma_{-,n}^\mu)^2}{(\epsilon_- - \epsilon_n)^2}$$

$$g_{\mu\nu} = \sum_{n=-1} \frac{[(\Gamma_{-,n}^{\mu,\nu})^2 - (\Gamma_{-,n}^{\mu-\nu})^2]}{4(\epsilon_- - \epsilon_n)^2} \quad (\text{linear}) \quad (8)$$

$$\mathcal{F}_{\mu\nu} = \sum_{n=-1} \frac{[(\Gamma_{-,n}^{\mu,\nu})^2 - (\Gamma_{-,n}^{\mu-\nu})^2]}{2(\epsilon_- - \epsilon_n)^2} \quad (\text{elliptical})$$

To measure the quantum metric tensor and Berry curvature in the experiment, we first initialized the NV in the $|m_s = 0\rangle$ state and coherently drove it to the ground eigenstate $|u_-\rangle$ of the Weyl-type Hamiltonian with two microwave pulses. The system was then subjected to the linear and elliptical parametric modulations in Eq. 7, which resonantly drive Rabi oscillations between eigenstates. Last, either the $|u_-\rangle$ or $|u_0\rangle$ state was mapped back to $|0\rangle$ with microwave pulses and optically read out (20).

We began our measurements by precisely determining the resonant frequency $\omega_r = \epsilon_+ - \epsilon_- = 2(\epsilon_0 - \epsilon_-)$. As shown in Fig. 1A, we fixed the time and swept the modulation frequency ω to find the resonance condition. A very weak modulation amplitude reduces power broadening and improves the precision in estimating ω_r .

We then measured the coherent Rabi oscillations under linear and elliptical parametric modulations at the calibrated $\omega = \frac{\omega_r}{2}$ and ω_r for SQ and DQ transitions, respectively. Examples of SQ and DQ Rabi curves for the quantum-metric measurements are shown in Fig. 1B and figs. S8 to S12, including both single- and two-parameter modulations for extracting the diagonal and off-diagonal components. No decoherence effect was observed in these parametric modulations owing to the long coherence time of the NV center. For every combination of modulations μ and ν , we measured both the SQ and DQ Rabi frequencies and recovered the matrix elements $\Gamma_{-,n}^\mu$ and $\Gamma_{-,n}^{\mu,\pm\nu}$, respectively. All measured matrix elements Γ are plotted in Fig. 1, C and D, for the quantum-metric tensor and in fig. S14 for the Berry curvature, showing good agreement with theoretical predictions.

As the main results of this work, we reconstructed both the quantum metric and the Berry curvature of our 4D setting and used them as two complementary approaches to determine the three-form curvature $\mathcal{H}_{\mu\nu\lambda}$ and its related monopole charge (\mathcal{DD} invariant).

The independent components of the metric tensor, reconstructed by using Eq. 8, are shown in Fig. 2A. The excellent agreement between theory and experiment demonstrates an exquisite control over the 4D Weyl-type Hamiltonian in Eq. 1, providing precise information about the quantum geometry of the ground-state manifold.

Using Eq. 4, we then connected the metric tensor to the three-form curvature, a generalized “magnetic” field predicted to emanate from nodal points in 4D space. The measured three-form curvature $\mathcal{H}_{\alpha\beta\phi}$ is shown in Fig. 2C. Using these experimental data, we obtained the quantization of the generalized “magnetic” flux over the three-sphere

$$\mathcal{DD}_{\text{exp},g} = \frac{1}{2\pi^2} \int_0^\pi d\alpha \int_0^{2\pi} d\beta \int_0^{2\pi} d\phi \mathcal{H}_{\alpha\beta\phi} = 0.99(3) \quad (9)$$

which provides an estimation of the \mathcal{DD} invariant in Eq. 3 and signals the presence of the tensor monopole at the center of our parameter space.

Alternatively, one can identify the tensor monopole through the Berry curvatures, $\mathcal{F}_{\mu\nu}$, using Eq. 5. We show the Berry curvature measured through elliptical parametric modulations in Fig. 2B and the reconstructed three-form curvature in Fig. 2C. This second approach, which is complementary to the metric-tensor measurement, further confirms the existence of the tensor monopole through the measurement of its quantized charge

$$\mathcal{DD}_{\text{exp},\mathcal{F}} = \frac{1}{2\pi^2} \int_0^{\frac{\pi}{2}} d\alpha \int_0^{2\pi} d\beta \int_0^{2\pi} d\phi \mathcal{H}_{\alpha\beta\phi} = 1.11(3) \quad (10)$$

Besides its topological charge, the 4D tensor monopole is also fully characterized by its field distribution (6, 14, 20)

$$\mathcal{H}_{\mu\nu\lambda}(\mathbf{q}) = \epsilon_{\mu\nu\lambda\gamma} q_\gamma / (q_x^2 + q_y^2 + q_z^2 + q_w^2)^2 \quad (11)$$

which reflects that the curvature field radially emanates from the topological defect in 4D parameter space. As a consequence, the monopole field has a characteristic inverse-cube dependence on the radial coordinate, $\mathcal{H} \sim (1/H_0)^3$. We have verified this additional signature of the tensor monopole through the experimental determination of the three-form curvature distribution (Fig. 2D). Together, the measurement of the quantized topological charge (\mathcal{DD} invariant) and the characteristic radial behavior of a monopole field fully confirm the existence of a tensor monopole in our synthetic 4D parameter space.

We further explored a spectral transition that can be induced by adding a longitudinal field to the Weyl-type Hamiltonian (23)

$$\hat{H}_{ST} = \hat{H}_{4D} + \text{diag}(B_z, 0, -B_z)/\sqrt{2} \quad (12)$$

The field is realized by detuning the dual-frequency microwave driving by equal and opposite amounts. The field breaks the chiral symmetry but preserves mirror symmetries: $M_1 \hat{H}_{ST}(q_x, q_y, q_z, q_w) M_1^{-1} = \hat{H}_{ST}(-q_x, -q_y, q_z, -q_w)$, $M_2 \hat{H}_{ST}(q_x, q_y, q_z, q_w) M_2^{-1} = \hat{H}_{ST}(q_x, q_y, -q_z, -q_w)$, with $M_1 = \text{diag}(-1, 1, 1)$, $M_2 = \text{diag}(1, 1, -1)$, keeping the Hamiltonian gapless.

Upon application of the field, the system undergoes a topological spectral transition from the 4D Weyl-like structure. The new symmetry-protected energy spectrum features a pair of doubly degenerate surfaces in the $\beta - \phi$ space along $[\alpha = 0(\pi/2), B_z = H_0]$. The spectrum has a more intuitive description in cartesian coordinates, (q_x, q_y, q_z, q_w) , where the field gives rise to two spectral rings in the

$q_x - q_y$ and $q_z - q_w$ space along $q_z = q_w = 0$ and $q_x = q_y = 0$, respectively, with radius B_z (Fig. 3). We identified signatures of the spectral rings using two observables inspired by the tensor-monopole measurements, $\mathcal{G} = 8 \int \epsilon_{\mu\nu\lambda} \sqrt{\det g_{\mu\nu}} d\alpha$ and $\mathcal{B} = -\int (\mathcal{F}_{\alpha\beta} + \mathcal{F}_{\phi\alpha}) d\alpha$. They represent integration over a hyperspherical surface with radius H_0 when viewed in the cartesian coordinate and converge to the \mathcal{DD} invariant when $B_z = 0$.

As the field strength B_z increases, the two spectral rings expand from the origin and cross the boundary of our integration hypersphere at $B_z = H_0$. For various B_z , we performed linear and elliptical parametric modulations to reconstruct the metric tensor (figs. S15 to S20) and the Berry curvature (figs. S21 to S27), from which we obtained \mathcal{G} , \mathcal{B} . We observed a sharp change in both experimental observables \mathcal{G} , \mathcal{B} at $B_z = H_0$, signaling the topological spectral ring (Fig. 3). The results are in agreement with the simulation for \mathcal{G} and analytical form for \mathcal{B} (20),

$$\mathcal{B} = \begin{cases} 1, & B_z < H_0 \\ -\frac{1}{2} \left(1 - \frac{B_z}{\sqrt{B_z^2 + 8H_0^2}} \right), & \text{otherwise} \end{cases} \quad (13)$$

These results reveal that exotic spectral transitions can be simulated in our system upon increasing B_z while keeping H_0 fixed (restricting ourselves to a hypersphere in parameter space): From the Weyl-type nodes ($B_z = 0$) to topological spectral rings ($B_z < H_0$), characterized by a robust \mathcal{B} index, and eventually to a gapped spectrum ($B_z > H_0$).

Our precise control over the Weyl-type Hamiltonian illustrates the potential offered by solid-state qudits in the realm of quantum simulation. Interesting perspectives include the fate of tensor monopoles upon coupling the system to other spins or qubits (10) and the study of non-Abelian structures induced by spectral degeneracies and tensor fields (24).

The Hamiltonian $\hat{H}_{4D}(\mathbf{q})$ in Eq. 1 further suggests that the physics of tensor monopoles could be investigated in systems of particles moving on a 4D lattice, where \mathbf{q} would represent the corresponding crystal momenta. Such 4D Weyl lattice systems have been recently proposed (15, 25) and could be realized in quantum-engineered systems, extending the 3D lattice where particles lie with a synthetic dimension (26, 27). 4D Weyl many-body settings are particularly intriguing because they would enable studying the effects of interactions in systems in which quasiparticles are effectively coupled to higher-form fields (28).

Note added in proof: During the preparation of this manuscript, we noticed another experimental work that describes the observation

of the tensor monopole by using superconducting circuits (29).

REFERENCES AND NOTES

1. B. Zwiebach, *A First Course in String Theory* (Cambridge Univ. Press, 2004).
2. M. Kalb, P. Ramond, *Phys. Rev. D Part. Fields* **9**, 2273–2284 (1974).
3. M. Henneaux, C. Teitelboim, *Found. Phys.* **16**, 593–617 (1986).
4. P. A. M. Dirac, *Proc. R. Soc. London A* **133**, 60–72 (1931).
5. P. Bouwknegt, V. Mathai, *J. High Energy Phys.* **2000**, 007 (2000).
6. R. I. Nepomechie, *Phys. Rev. D Part. Fields* **31**, 1921–1924 (1985).
7. P. Orland, *Nucl. Phys. B* **205**, 107–118 (1982).
8. M. D. Schroer et al., *Phys. Rev. Lett.* **113**, 050402 (2014).
9. M. W. Ray, E. Ruokokoski, S. Kandel, M. Möttönen, D. S. Hall, *Nature* **505**, 657–660 (2014).
10. P. Roushan et al., *Nature* **515**, 241–244 (2014).
11. S. Sugawa, F. Salces-Carcoba, A. R. Perry, Y. Yue, I. B. Spielman, *Science* **360**, 1429–1434 (2018).
12. M. Yu et al., *Natl. Sci. Rev.* **7**, 254–260 (2020).
13. X. Tan et al., *Phys. Rev. Lett.* **122**, 210401 (2019).
14. G. Palumbo, N. Goldman, *Phys. Rev. Lett.* **121**, 170401 (2018).
15. G. Palumbo, N. Goldman, *Phys. Rev. B* **99**, 045154 (2019).
16. O. Dubinkin, A. Rasmussen, T. L. Hughes, *Ann. Phys.* **422**, 168297 (2020).
17. T. T. Wu, C. N. Yang, *Phys. Rev. D Part. Fields* **12**, 3845–3857 (1975).
18. T. Ozawa, N. Goldman, *Phys. Rev. B* **97**, 201117 (2018).
19. M. Kolodrubetz, D. Sels, P. Mehta, A. Polkovnikov, *Phys. Rep.* **697**, 1–87 (2017).
20. Materials and methods are available as supplementary materials.
21. V. Jacques et al., *Phys. Rev. Lett.* **102**, 057403 (2009).
22. H. J. Mamin et al., *Phys. Rev. Lett.* **113**, 030803 (2014).
23. The more conventional phase transition that is induced by translating the hypersphere is described in (20).
24. G. Palumbo, *Phys. Rev. Lett.* **126**, 246801 (2021).
25. Y.-Q. Zhu, N. Goldman, G. Palumbo, *Phys. Rev. B* **102**, 081109 (2020).
26. Y. Wang, H. M. Price, B. Zhang, Y. D. Chong, *Nat. Commun.* **11**, 2356 (2020).
27. T. Ozawa, H. M. Price, *Nat. Rev. Phys.* **1**, 349–357 (2019).
28. T. Manovitz, Y. Shapira, N. Akerman, A. Stern, R. Ozeri, *PRX Quantum* **1**, 020303 (2020).
29. X. Tan et al., *Phys. Rev. Lett.* **126**, 017702 (2021).
30. C. Li, Data and code for figures in paper “A synthetic monopole source of Kalb-Ramond field in diamond,” *Harvard Dataverse* (2021).

ACKNOWLEDGMENTS

M.C., C.L., and P.C. thank M. Li for helpful discussions. **Funding:** This work is supported in part by NSF grant PHY1734011. Work in Brussels is supported by the Fonds De La Recherche Scientifique (FRS-FNRS) Belgium and the ERC Starting Grant TopoCold. **Author contributions:** M.C. and C.L. designed and performed the experiments and analyzed the data, with assistance from P.C. and input of N.G. on the quantum-metric measurement. M.C., C.L., and P.C. discussed and interpreted the results, ran simulations, and developed the analytical model that describes the spectral transition. M.C., C.L., and G.P. analyzed the symmetries and spectral structures of the model, with inputs from all authors. All authors contributed to the writing of the manuscript. P.C. supervised the overall project. **Competing interests:** The authors declare no conflicts of interest. **Data and materials availability:** The data and software code for generating the figures presented in the main text and supplementary materials are available at Harvard Dataverse (30).

SUPPLEMENTARY MATERIALS

science.org/doi/10.1126/science.abe6437

Materials and Methods

Figs. S1 to S27

Table S1

References (31–35)

3 September 2020; resubmitted 16 June 2021

Accepted 14 January 2022

10.1126/science.abe6437

CATALYSIS

Elongation and branching of α -olefins by two ethylene molecules

Thomas Dietel, Fabian Lukas, Winfried P. Kretschmer, Rhett Kempe*

α -Olefins are important starting materials for the production of plastics, pharmaceuticals, and fine and bulk chemicals. However, the selective synthesis of α -olefins from ethylene, a highly abundant and inexpensive feedstock, is restricted, and thus a broadly applicable selective α -olefin synthesis using ethylene is highly desirable. Here, we report the catalytic reaction of an α -olefin with two ethylene molecules. The first ethylene molecule forms a 4-ethyl branch and the second a new terminal carbon-carbon double bond (C2 elongation). The key to this reaction is the development of a highly active and stable molecular titanium catalyst that undergoes extremely fast β -hydride elimination and transfer.

α -Olefins are important starting materials for the synthesis of plastics, pharmaceuticals, and bulk and fine chemicals (1, 2). The synthesis of α -olefins from ethylene, an abundantly available and inexpensive feedstock, is carried out in megaton scale annually and represents one of the most important applications of homogeneous catalysis (1, 2). The selective synthesis of α -olefins from this attractive feedstock is restricted to three α -olefins: 1-butene, 1-hexene, and 1-octene (3, 4). Other synthetic protocols give rise to distributions of α -olefins that must be separated, and the demand for a specific α -olefin rarely matches its proportion in the product distribution. A broadly applicable α -olefin elongation reaction in which α -olefins become selectively elongated by ethylene would be highly desirable. If the reaction were successively applicable, meaning that the elongated α -olefin could undergo a further elongation of the same kind, a very large number of α -olefins would be accessible. Moreover, the selective introduction of branches is attractive for the synthesis of synthetic lubricants (5). Furthermore, branched α -olefins are applied as monomers for the synthesis of highly transparent plastics and as membranes for gas separation (6). Selectively branched α -olefins could also be of interest for functionalization chemistry such as hydroformylation, a large-scale reaction (1, 2).

We recently introduced a broadly tunable synthesis of linear α -olefins (7) and report here on the catalytic reaction of an α -olefin with two ethylene molecules. One of the two ethylene molecules forms a 4-ethyl branch and the other a new terminal C-C double bond rendering the initial olefin C2-elongated. Many linear α -olefins, including long-chain examples such as 1-hexadecene, can undergo this re-

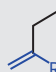
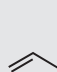
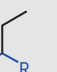
action. Elongation of 4-ethyldec-1-ene, the elongation and branching product of 1-octene, indicates that branched aliphatic α -olefins can be elongated and that successive elongation is possible. Additionally, aromatic and cyclic olefins, such as styrene and bicyclo[2.2.1]hept-2-ene, have been modified successfully. The key to our olefin elongation reaction is the development of a highly active, long-term stable and selective catalyst. The catalyst can mediate C-C coupling at rates observed for highly active enzymes (catalyzing other reactions). Ethylene consumption studies indicate the stability of this catalyst without substantial loss of its high activity for at least 3 hours. At that point, our reactor is completely filled, and we have to stop the reaction. The catalyst has a high α -olefin incorporation rate, undergoes extremely fast β -hydride elimination and transfer, and is based on titanium, the second-most abundant transition metal of Earth's crust.

Co-trimerization of linear α -olefins and ethylene with catalysts that induce selective tri-

merization of ethylene via metallacyclopentane intermediates (4, 8) has been investigated experimentally (9, 10) and theoretically (11). These investigations indicate that selective co-trimerization is difficult to accomplish in such a mechanistic scenario. We concluded that a different mechanism, for example, a Cossee-Arlman mechanism (12, 13), could be an alternative and surmised that a catalyst that produces Schulz-Flory distributions (14–16) with a very small chain-growth probability (α -value) might be suitable if a high α -olefin incorporation rate is observed. Then, α -olefin insertion could be followed by ethylene insertion and, subsequently, β -H elimination and transfer to ethylene. Such a reaction mechanism is also advantageous with regard to by-product formation. The dominant by-product, 1-butene, is a gas under normal conditions and can be separated easily from the liquid α -olefin elongation products.

We have a long-standing interest in the coordination chemistry of aminopyridinato ligands (17) and previously introduced imidazolidiniminato ligands into olefin polymerization (18). Here, we observed that coordinating both ligands to titanium can result in a highly active catalyst that is able to produce Schulz-Flory distributions with a very small α -value (Fig. 1). The organotitanium precursor (compound 1; Fig. 1, A and B) is the key to synthesizing aminopyridinato-imidazolidiniminato titanium dialkyl complexes. In addition, the order of introducing the two ligands and the distinct synthetic protocols, toluene and salt elimination, proved crucial (Fig. 1A). Nuclear magnetic resonance (NMR) tube experiments revealed that 3 reacts with anilinium borate to eliminate toluene and cleanly form the cationic species 4 (Fig. 1A and figs. S7 to S9). Investigation of the ethylene dimerization

Table 1. Elongation and branching of linear α -olefins. Reaction conditions are as follows: $T = 15^\circ\text{C}$; $t = 15$ min; $P_{\text{eth}} = 1.0$ bar; precatalyst is $n_3 = 0.05$ μmol ; $n_{\alpha\text{-olefin}} = 50$ mmol; ammonium borate activator is $[\text{R}_2\text{N}(\text{CH}_3)\text{H}]^+[\text{B}(\text{C}_6\text{F}_5)_4]^-$ ($\text{R} = \text{C}_{16}\text{H}_{33}$ to $\text{C}_{18}\text{H}_{37}$); $\text{Ti/B} = 1/1.1$; scavenger is 300 μmol TIBA; solvent is cumene or toluene; and $V = 15$ ml. SDs are given in parentheses. Three independent runs were carried out and averaged for each α -olefin. The TOFs and the selectivity were calculated based on co-oligomerization products.

Entry	α -Olefin	V_{eth} (liters)	Selectivity (mol %)			TOF ($\times 10^6 \text{ h}^{-1}$)
						
1	1-hexene	1.2 (0.2)	19 (0.3)	73 (0.2)	5 (0.1)	1.4 (0.009)
2	1-octene	1.0 (0.1)	19 (0.4)	73 (0.1)	5 (0.2)	1.4 (0.001)
3	1-decene	1.0 (0.1)	19 (0.0)	73 (0.2)	4 (0.2)	1.3 (0.014)
4	1-dodecene	0.8 (0.0)	20 (0.6)	73 (0.2)	4 (0.2)	1.2 (0.011)
5	1-tetradecene	0.5 (0.1)	21 (0.2)	72 (0.1)	4 (0.1)	0.9 (0.009)
6	1-hexadecene	0.2 (0.0)	20 (0.0)	73 (0.2)	4 (0.1)	0.8 (0.006)

Lehrstuhl für Anorganische Chemie II – Katalysatordesign, Sustainable Chemistry Centre, Universität Bayreuth, 95440 Bayreuth, Germany.

*Corresponding author. Email: kempe@uni-bayreuth.de

activity of **3** after treatment with ammonium borate (Fig. 1C) revealed an increase of the α -value or a decrease of the 1-butene selectivity with increasing temperature. Ethylene oligomerization catalysts usually show a decrease of the α -value with increasing temperature (19–21). Catalysts with an inverse temperature dependence of the α -value are reported as

well (22, 23). 1-Butene selectivity greater than 90 mol % has been observed below 20°C. Turn-over frequencies (TOFs) of greater than 5 million per hour have been observed for all six runs (Fig. 1C), with a maximum of 4800 s⁻¹ bar⁻¹ at 30°C. This is an extremely high TOF. The TOF is in the range between 10⁻² and 10² s⁻¹ for most relevant industrial applications.

TOFs between 10³ and 10⁷ s⁻¹ were recorded for highly active enzymes as catalysts (24). Very high TOFs for ethylene dimerization have been achieved with vanadium-based catalysts (25), for instance, 370 s⁻¹ bar⁻¹ (26). The catalyst system based on **3** is also long-term stable. We carried out a 3-hour run to demonstrate it. The ethylene consumption over time

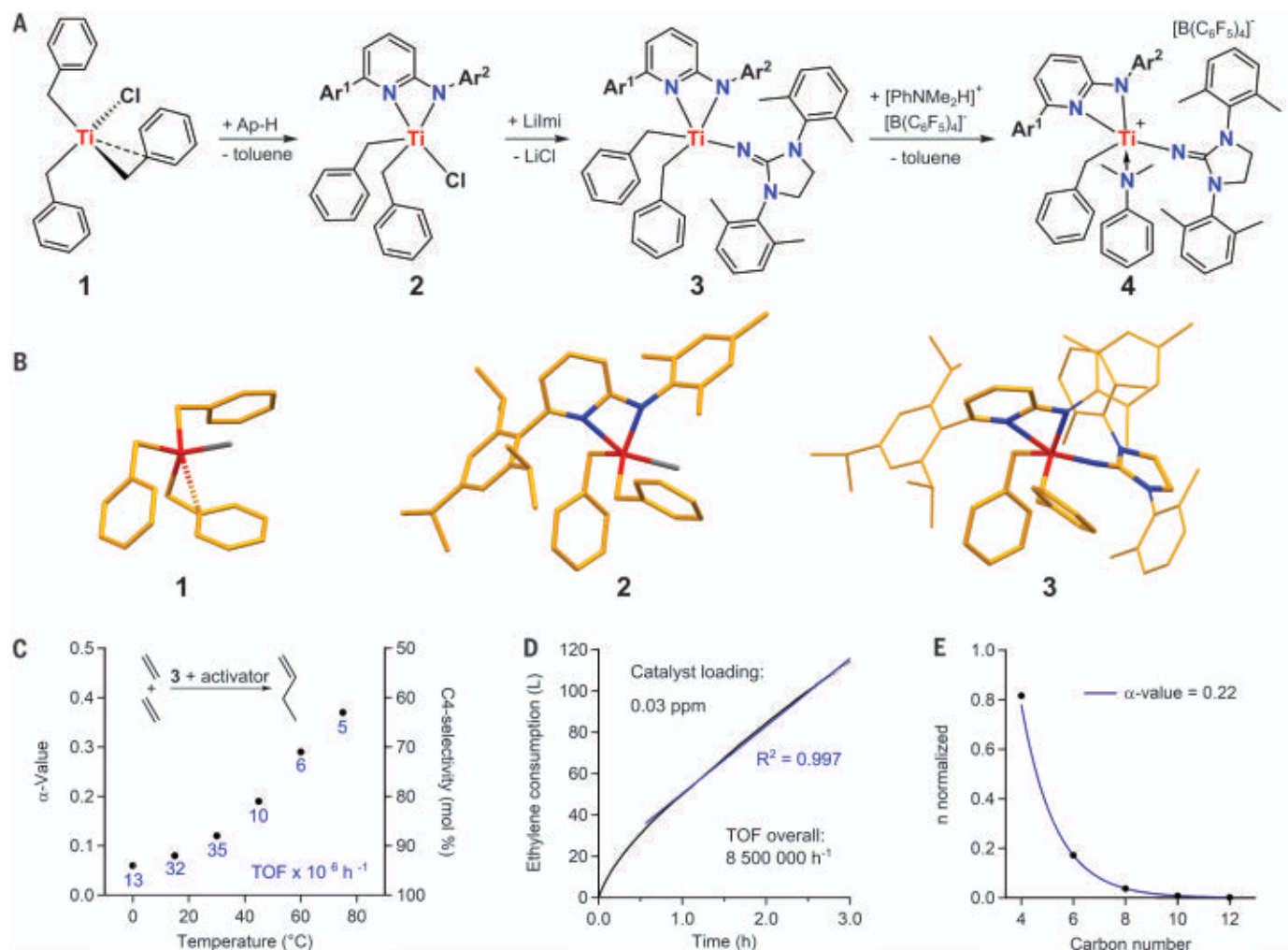


Fig. 1. Catalyst synthesis and selective 1-butene formation. (A) Synthesis of **4** starting from the titanium precursor **1**. After a toluene elimination yielding **2**, a salt metathesis reaction is carried out [Ap-H, *N*-mesityl-6-(2,4,6-triisopropylphenyl)pyridin-2-amine; LiImi, lithium salt of 1,3-bis(2,6-dimethylphenyl)imidazolidin-2-imine]. Compound **3** reacts with *N,N*-dimethylanilinium tetrakis(pentafluorophenyl)borate to form the cationic complex **4**. Ar¹, 2,4,6-triisopropylphenyl; Ar², 2,4,6-trimethylphenyl. (B) Molecular structures of compounds **1** to **3**, as determined by x-ray crystallography. Color coding is as follows: C, orange; Cl, gray; N, blue; and Ti, red. (C) Plot of the temperature dependence of the chain-growth probability [α -value: $\alpha = n_{C+2}/n_C$, with C being the carbon number of the α -olefins obtained (and determined as $n_{\text{octene}}/n_{\text{hexene}}$)] and the TOF obtained with the precatalyst **3** after activation with an ammonium borate cocatalyst. The TOF was calculated based on ethylene consumption. The α -value increases with increasing temperature. Selective 1-butene formation >90% is possible below 20°C. The activity is extremely high and has an optimum at around 30°C. Conditions are as follows: ethylene pressure (P_{eth}) = 2.0 bar; time (t) = 15 min;

precatalyst is $n_3 = 0.05 \mu\text{mol}$; ammonium borate activator is $[\text{R}_2\text{N}(\text{CH}_3)\text{H}]^+[\text{B}(\text{C}_6\text{F}_5)_4]^-$ ($\text{R} = \text{C}_{16}\text{H}_{33}$ to $\text{C}_{18}\text{H}_{37}$); Ti/B = 1/1.1; toluene volume (V_{toluene}) = 150 ml; and scavenger is 300 μmol triisobutylaluminum (TIBA). (D) Plot of the ethylene consumption (black, data points) of a 3-hour run to demonstrate the combination of high activity and long-term stability of the catalyst system based on **3**. At the end of the reaction, the 300-ml reactor that was used is completely filled (fig. S20 and safety note there); the catalyst loading corresponds to about 0.03 parts per million (ppm). The ethylene consumption is constant for more than 2 hours, as shown by a linear fit (blue) that indicates a negligible catalyst decomposition over multiple hours (R^2 , coefficient of determination). Conditions are as follows: $P_{\text{eth}} = 4.0$ bar; temperature (T) = 15°C; precatalyst is $n_3 = 0.2 \mu\text{mol}$; ammonium borate activator is $[\text{R}_2\text{N}(\text{CH}_3)\text{H}]^+[\text{B}(\text{C}_6\text{F}_5)_4]^-$ ($\text{R} = \text{C}_{16}\text{H}_{33}$ to $\text{C}_{18}\text{H}_{37}$); Ti/B = 1/1.1; $V_{\text{toluene}} = 30$ ml; and scavenger is 300 μmol TIBA. (E) Observed (black) and simulated (blue) Schulz-Flory distribution to confirm a Cossee-Arlman-type mechanism. Conditions are as listed for (C) except for $T = 40^\circ\text{C}$, $P_{\text{eth}} = 7$ bar, and $t = 1$ min.

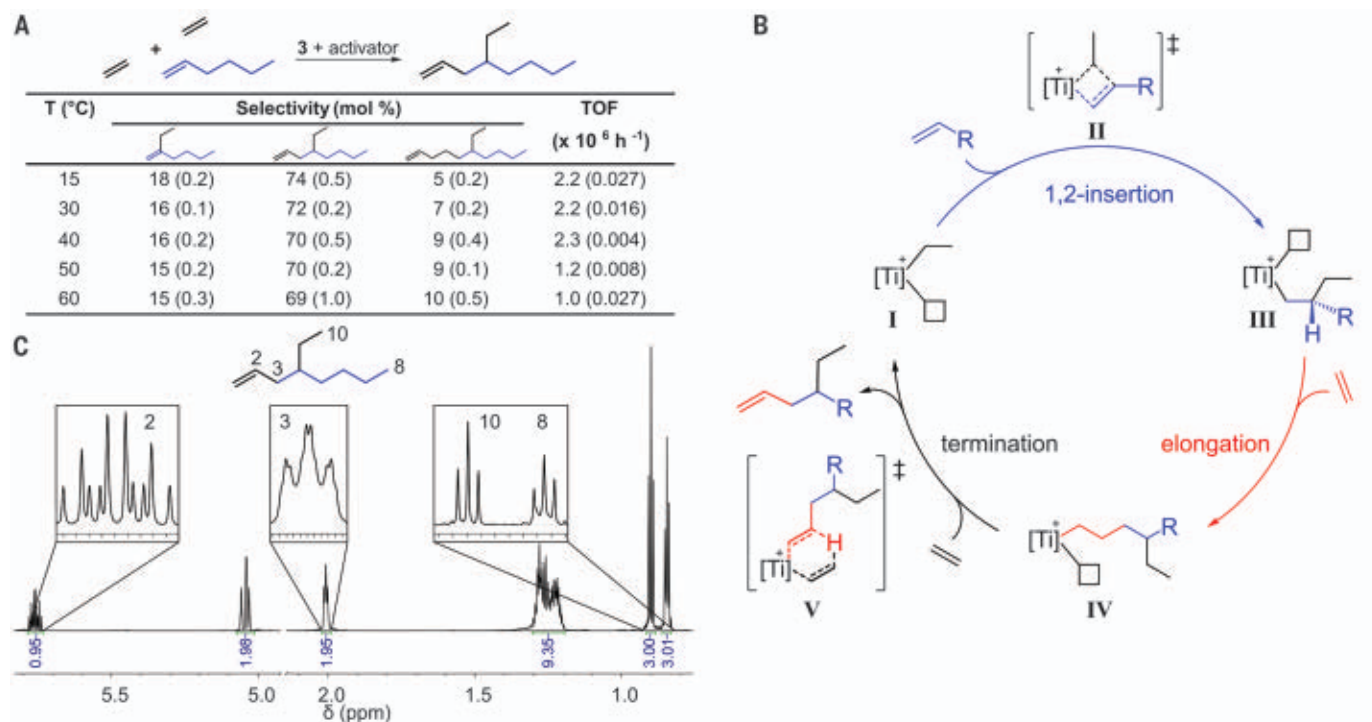


Fig. 2. Catalytic reaction of α -olefins and ethylene. (A) Temperature dependence of the selectivity of liquid co-oligomerization products of 1-hexene with ethylene. The 1-butene co-product can be boiled off easily at the end of the reaction. All runs were carried out three times to confirm reproducibility and determine a standard deviation (SD), which is given in parentheses. The TOFs were calculated based on the formation of liquid products only. Conditions are as

follows: $P_{\text{eth}} = 1.0$ bar; $t = 15$ min; precatalyst is $n_3 = 0.05$ μmol ; ammonium borate activator is $[\text{R}_2\text{N}(\text{CH}_3)\text{H}]^+[\text{B}(\text{C}_6\text{F}_5)_4]^-$ ($\text{R} = \text{C}_{16}\text{H}_{33}$ to $\text{C}_{18}\text{H}_{37}$); $\text{Ti}/\text{B} = 1/1.1$; $V_{\text{C}_6} = 30$ ml; and scavenger is 300 μmol TIBA. (B) Proposed mechanism of the reaction of α -olefins with two ethylene molecules. ‡, transition state. (C) The 1-GHz ^1H NMR spectrum of 4-ethyldec-1-ene, the elongation and branching product of 1-hexene. Insets show multiplets of key signals.

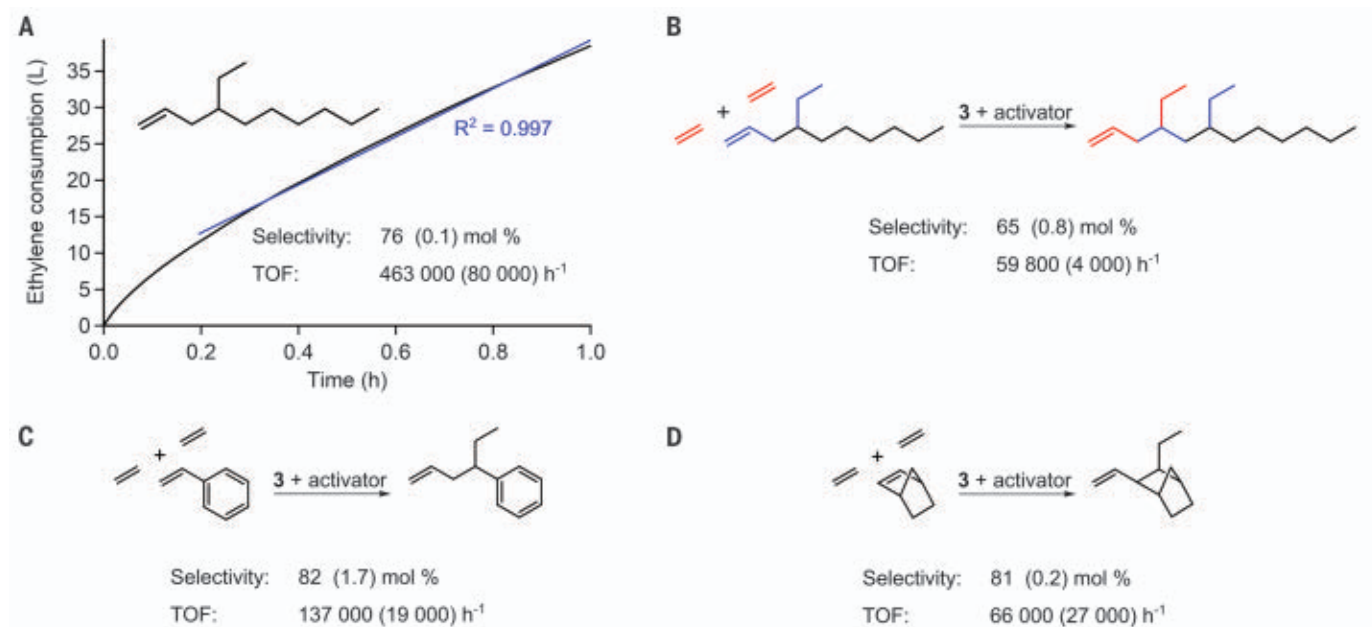


Fig. 3. Elongation and branching of α -olefins. (A) A run for the multigram synthesis of 4-ethyldec-1-ene of 1 hour (300-ml reactor). A combination of two runs and a single simple distillation gave rise to 18 g of product with a purity >96%. The constant ethylene flow (black) for more than 30 min was confirmed by a linear fit (blue). (B) Elongation and branching of an already elongated product. 4-Ethyldec-1-ene, the elongation and branching product of 1-octene, has been further elongated to form 4,6-diethyldec-1-ene with a selectivity of 65 mol %

for the liquid products ($V_{\text{olefin}} = 1.2$ ml; $V_{\text{toluene}} = 2$ ml). (C) Elongation and branching of styrene ($V_{\text{styrene}} = 15$ ml). (D) Elongation and branching of bicyclo [2.2.1]hept-2-ene ($P_{\text{eth}} = 4.0$ bar; 100 mg olefin; $V_{\text{toluene}} = 6.5$ ml). Selectivity (co-oligomerization products) and TOF (product only) were calculated by averaging three experiments for (A), (C), and (D) and two experiments for (B). SDs are given in parentheses. Standard conditions (see Table 1) and modifications listed above were applied.

is shown in Fig. 1D. After a small initial decrease of the ethylene consumption, a linear profile indicates almost no catalyst decay. We had to stop the experiment after 3 hours because our 300-ml reactor was completely filled (fig. S20 and safety note there). The Schulz-Flory olefin product distributions obtained in a run at 40°C with 7-bar ethylene pressure indicate a Cossee-Arlman-type mechanism (Fig. 1E). Activity, selectivity, and long-term stability is only observed if both N-ligands are present. Variation of substituents of the two N-ligands did not result in catalysts with a lower α -value. With a highly active, selective, and long-term stable catalyst in hand, we explored the scope of α -olefin incorporation (Fig. 2).

α -Olefin elongation and branching was investigated using 1-hexene (Fig. 2A). The liquid-product analysis revealed formation of a co-trimerization product (4-ethyloct-1-ene) with a selectivity of 74 mol % at 15°C. Furthermore, two main by-products have been identified: 3-methyleneheptane (co-dimerization product, 18 mol %) and 6-ethyldec-1-ene (co-tetramerization product, 5 mol %). The sum of the main product and the two by-products gave 97 mol %, indicating that other liquid by-products are of low relevance. Repeating the experiments indicated good reproducibility. Investigation of the temperature dependence of the selectivity (Fig. 2A) revealed an increase of the co-tetramerization product yield with increasing temperature, similar to the increase of the α -value in the oligomerization of ethylene (Fig. 1C). Assuming a Cossee-Arlman mechanism (27) for the catalyst system based on **3** (Fig. 1, C and E), the proposed reaction sequence that could give rise to the co-trimerization product and the main by-products is shown in Fig. 2B. β -H elimination and transfer to the monomer ethylene is the starting point (intermediate I; Fig. 2B). Our catalyst is essentially inactive in the presence of α -olefins only, and we do not see products indicating other chain-termination reactions. 1,2-Insertion of the α -olefin takes place next, giving rise to only one H atom for the β -H elimination and transfer, which is attached to a tertiary carbon atom and is, therefore, more protected sterically (intermediate III; Fig. 2B) than the two β -H atoms attached to the secondary carbon atom, which is formed after ethylene insertion (intermediate IV; Fig. 2B). The relatively slow β -H elimination and transfer of III forms the co-dimerization product (3-methyleneheptane for 1-hexene and ethylene). The steric protection of the β -H atom and the presence of only one β -H atom could lead to slower β -H elimination and transfer and seems to be the key to reduce co-dimer formation. Further ethylene insertion provides easily accessible β -H atoms (intermediate IV; Fig. 2B) and very fast chain termination can take place to form the elongation and branching product. Further ethylene

insertions give rise to the co-tetramerization product and even longer ethyl branched oligomers at higher temperatures and/or ethylene pressures. Notably, the α -value of this process and that of the linear α -olefin by-product distribution are similar (figs. S30 and S44).

The 1-GHz ^1H NMR spectrum of the co-trimerization product of 1-hexene is shown in Fig. 2C, including the assignments of key resonances. The shifts, multiplicity, and integrals of the signals are in agreement with the structure of the main product, 4-ethyloct-1-ene.

We next investigated the linear α -olefin scope of the elongation and branching reaction. A variety of linear α -olefins (Table 1) were modified. All α -olefins, including long-chain examples such as 1-hexadecene, were elongated and branched with a selectivity of 72 mol % or higher. We carried out the corresponding experiments three times to demonstrate good reproducibility. Multigram-scale synthesis of 4-ethyldec-1-ene, the elongation and branching product of 1-octene, is shown in Fig. 3A. Ethylene consumption studies revealed a slow decrease of the uptake within the first 15 min and a nearly linear uptake for the remaining 45 min (Fig. 3A). A reaction time of 1 hour seemed optimal for a high activity and product selectivity of 76 mol %, as determined by gas chromatography. Three runs were carried out to demonstrate good reproducibility. We combined two of the three runs and obtained 18 g of product with a purity greater than 96% after a single distillation. The isolated olefin was used again for a second elongation and branching to 4,6-diethyldodec-1-ene with a selectivity of 66 mol % (Fig. 3B). This experiment indicates the possibility of the elongation and branching of branched α -olefins. Furthermore, successive elongation and branching is feasible, which offers access to a large number of α -olefins from the existing α -olefin feedstock. The successful elongation and branching of styrene indicates that the reaction is not limited to purely aliphatic α -olefins (28). Using norbornene, we demonstrated that cyclic olefins can also be modified (29). A selectivity of elongation and branching products of greater than 80 mol % (Fig. 3, C and D) was observed for these latter reactions. Considering that only three α -olefins could previously be synthesized selectively from ethylene, our elongation and branching reaction substantially extends the scope of selectively accessible α -olefins from ethylene. Related catalysts might have potential for the selective synthesis of other interesting co-oligomerization products.

REFERENCES AND NOTES

- K. Weissmermel, H.-J. Arpe, *Industrial Organic Chemistry* (Wiley, ed. 4, 2003).
- H. A. Wittcoff, B. G. Reuben, J. S. Plotkin, *Industrial Organic Chemicals* (Wiley, ed. 3, 2013).
- D. S. McGuinness, *Chem. Rev.* **111**, 2321–2341 (2011).
- O. L. Sydora, *Organometallics* **38**, 997–1010 (2019).
- Y. Gao et al., *Nat. Catal.* **2**, 236–242 (2019).
- Z.-X. Low, P. M. Budd, N. B. McKeown, D. A. Patterson, *Chem. Rev.* **118**, 5871–5911 (2018).
- A. Gollwitzer, T. Dietel, W. P. Kretschmer, R. Kempe, *Nat. Commun.* **8**, 1226 (2017).
- O. L. Sydora et al., *ACS Catal.* **2**, 2452–2455 (2012).
- L. H. Do, J. A. Labinger, J. E. Bercaw, *Organometallics* **31**, 5143–5149 (2012).
- Z. Wang et al., *Catal. Sci. Technol.* **11**, 4596–4604 (2021).
- W. J. Van Rensburg et al., *Organometallics* **35**, 972–981 (2016).
- P. Cossee, *J. Catal.* **3**, 80–88 (1964).
- E. J. Arlman, P. Cossee, *J. Catal.* **3**, 99–104 (1964).
- G. V. Schulz, *Z. Phys. Chem. B Chem. Elemproz. Aufbau Mater.* **30**, 379 (1935).
- P. J. Flory, *J. Am. Chem. Soc.* **58**, 1877–1885 (1936).
- C. T. Young, R. von Goetze, A. K. Tomov, F. Zaccaria, G. J. P. Britovsek, *Top. Catal.* **63**, 294–318 (2020).
- R. Kempe, *Angew. Chem. Int. Ed.* **39**, 468–493 (2000).
- W. P. Kretschmer, C. Dijkhuis, A. Meetsma, B. Hessen, J. H. Teuben, *Chem. Commun.* **2002**, 608–609 (2002).
- T. Wiedemann et al., *J. Am. Chem. Soc.* **136**, 2078–2085 (2014).
- J. S. Rogers, R. J. Lachicotte, G. C. Bazan, *J. Am. Chem. Soc.* **122**, 1830–1831 (1999).
- B. L. Small, M. Brookhart, *J. Am. Chem. Soc.* **120**, 7143–7144 (1998).
- Q. Chen et al., *Dalton Trans.* **48**, 8264–8278 (2019).
- W.-H. Sun et al., *Organometallics* **26**, 2720–2734 (2007).
- B. Cornils, W. A. Herrmann, H.-W. Zanthoff, C.-H. Wong, *Catalysis from A to Z: A Concise Encyclopedia* (Wiley, ed. 4, 2013).
- S. Zhang, K. Nomura, *J. Am. Chem. Soc.* **132**, 4960–4965 (2010).
- X.-Y. Tang et al., *Organometallics* **33**, 1053–1060 (2014).
- The Schulz-Flory product distribution in ethylene homo-oligomerization using **3** after activation with ammonium borate and the temperature dependence of the α -value (Fig. 1, C and E) strongly indicate a Cossee-Arlman mechanism.
- K. Kaneda, M. Terasawa, T. Imanaka, S. Teranishi, *Tetrahedron Lett.* **18**, 2957–2958 (1977).
- H. Hagen, W. P. Kretschmer, F. R. van Buren, B. Hessen, D. A. van Oeffelen, *J. Mol. Catal. A Chem.* **248**, 237–247 (2006).

ACKNOWLEDGMENTS

We thank K. Schweimer and the North Bavarian NMR Centre for recording the 1-GHz NMR spectra and A. Goller for support in the lab. **Funding:** We acknowledge financial support from the University of Bayreuth. **Author contributions:** R.K. conceived the concept. W.P.K., T.D., F.L., and R.K. jointly devised the experimental program. W.P.K. supervised the experimental program. W.P.K., T.D., and F.L. synthesized and characterized the catalysts. T.D. and F.L. performed the oligomerization experiments and analyzed the products. All authors jointly wrote the manuscript. **Competing interests:** The authors declare no competing interests. **Data and materials availability:** Crystallographic data for compounds **1** to **3** are available free of charge from the Cambridge Crystallographic Data Centre under references CCDC 2111472, CCDC 2111473, and CCDC 2111475, respectively. All other data are available in the manuscript or the supplementary materials. Correspondence and requests for materials should be addressed to R.K.

SUPPLEMENTARY MATERIALS

science.org/doi/10.1126/science.abm5281
Materials and Methods
Figs. S1 to S62
Tables S1 to S15
References (30–44)

23 September 2021; accepted 14 January 2022
10.1126/science.abm5281

MAGNETISM

Topological magnon band structure of emergent Landau levels in a skyrmion lattice

T. Weber^{1*}, D. M. Fobes², J. Waizner³, P. Steffens¹, G. S. Tucker^{4,5,†}, M. Böhm¹, L. Beddrich^{6,7}, C. Franz^{6,7}, H. Gabold^{6,7}, R. Bewley⁸, D. Voneshen^{8,9}, M. Skoulatos^{6,7}, R. Georgii^{6,7}, G. Ehlers¹⁰, A. Bauer^{6,11}, C. Pfleiderer^{6,11,12}, P. Böni⁶, M. Janoschek^{2,13,14}, M. Garst^{3,15,16,17}

The motion of a spin excitation across topologically nontrivial magnetic order exhibits a deflection that is analogous to the effect of the Lorentz force on an electrically charged particle in an orbital magnetic field. We used polarized inelastic neutron scattering to investigate the propagation of magnons (i.e., bosonic collective spin excitations) in a lattice of skyrmion tubes in manganese silicide. For wave vectors perpendicular to the skyrmion tubes, the magnon spectra are consistent with the formation of finely spaced emergent Landau levels that are characteristic of the fictitious magnetic field used to account for the nontrivial topological winding of the skyrmion lattice. This provides evidence of a topological magnon band structure in reciprocal space, which is borne out of the nontrivial real-space topology of a magnetic order.

In quantum mechanics, the movement of an electrically charged particle perpendicular to a magnetic field results in a Lorentz force that causes an orbital motion at discrete energy values known as Landau levels. The formation of Landau levels is ubiquitous in a wide range of condensed matter systems, causing, for instance, quantum oscillations in metals and quantum Hall phenomena in two-dimensional electron gases, where the latter reflects the formation of topological electronic bands with a finite Chern number. When the spin of a moving particle adiabatically adjusts to the local magnetization, the geometrical properties of a smooth magnetization texture give rise to an emergent magnetic field, B_{em} , and an emergent Lorentz force (1, 2). This raises the question of whether a magnetization texture may generate an analogous cyclotron motion of collective spin

excitations, causing the formation of Landau levels and topological magnon bands.

Studies of thermal and magnon Hall effects in frustrated magnets (3–5), as well as certain tailored systems (6), strongly suggest the existence of topological magnon bands. Microscopic evidence includes spectroscopic surveys (7, 8) and selected band crossings at very high energies far above the low-lying excitations (9, 10). Skyrmion lattices in chiral magnets offer a particularly simple setting to explore these questions (11–16). Owing to the nontrivial topology in these systems, the average emergent magnetic field is a multiple of a flux quantum $|B_{\text{em}}| = s(4\pi\hbar/e)/A_{\text{UC}}$ per area A_{UC} of the skyrmion, where e represents a coupling constant and \hbar is the reduced Planck constant (17). Here, s is the spin of the particle (i.e., $s = 1/2$ for an electron- or hole-like excitation and $s = 1$ for a magnon). Overwhelming evidence of this fictitious magnetic field has been observed for electron- and hole-like excitations (i.e., fermions) in terms of a topological Hall signal and spin transfer torques (18, 19). In contrast, only indirect evidence has been inferred for a fictitious magnetic field acting on magnons (i.e., bosons) from the rotational motion of skyrmion lattice domains (20).

Here, we used polarized inelastic neutron scattering to determine the predicted dispersion and orbital motion of magnons in the skyrmion lattice of MnSi. Neutron and microwave studies of spin excitations in MnSi have been reported for the topologically trivial magnetic phases, namely the helical, conical, and spin-polarized states (21–25) as well as the paramagnetic regime (26–31). This work has revealed, across the entire Brillouin zone, well-defined dispersive, nonreciprocal spin waves and spin fluctuations in the ordered states and the paramagnetic regime, respectively. In comparison, for the topologically nontrivial skyrmion lattice, extensive microwave spectroscopy (32) and exploratory in-

elastic neutron scans (33, 34) have been reported. These experiments provide an important point of reference, but they are limited to the center of the Brillouin zone in the case of microwave spectroscopy, or are at the proof-of-principle stage for inelastic neutron scattering.

Our approach is best introduced by summarizing the key characteristics of the magnon spectra, as illustrated in Fig. 1. In a semiclassical picture, magnons account for the precession of the magnetization around its equilibrium value $\mathbf{M}(\mathbf{r})$, as described locally with the help of the orthogonal unit vectors $\hat{e}_1 \times \hat{e}_2 = \hat{e}_3$ with $\hat{e}_3(\mathbf{r}) = \mathbf{M}(\mathbf{r})/|\mathbf{M}(\mathbf{r})|$. Within this local frame of reference, the motion of magnons is influenced by the vector potential $A_i(\mathbf{r}) = (\hbar/e)\hat{e}_1\hat{e}_2$ given by the spin connection known from differential geometry. The emergent local magnetic field is obtained by $\mathbf{B}_{\text{em}} = \nabla \times \mathbf{A} = (4\pi\hbar/e)\hat{z}\rho_{\text{top}}$. It is directly related to the topological skyrmion charge of the two-dimensional magnetic texture, $\rho_{\text{top}} = (1/4\pi)\hat{e}_3(\partial_x \hat{e}_3 \times \partial_y \hat{e}_3)$, via the Mermin-Ho relation (35). As the integral over a single skyrmion is quantized, $\int_{\text{UC}} d^2\mathbf{r}\rho_{\text{top}} = -1$; this amounts to a magnetic flux of $-(4\pi\hbar/e)$ per skyrmion.

Shown in Fig. 1A is the hexagonal lattice of skyrmion tubes in an applied magnetic field \mathbf{H} and the classical trajectory of a magnon, for which the local magnetization is perpendicular to \mathbf{H} . The band weaving along the trajectory depicts the orientation of the local coordinate system (black arrows), reflecting the accumulated geometric Berry phase $\oint d\mathbf{r}\mathbf{A}$. The associated topological density ρ_{top} is shown in Fig. 1B. Although the integral $\int_{\text{UC}} d^2\mathbf{r}\rho_{\text{top}} = -1$, the density ρ_{top} varies substantially, resulting in a pattern of positive and negative \mathbf{B}_{em} . The associated emergent Lorentz force enables localized cyclotron orbits within the magnetic unit cell, as illustrated in Fig. 1B, where classical trajectories labeled “1” and “2” circulate around a minimum and a maximum of ρ_{top} , respectively.

Magnetic resonance studies that probe the response to a uniform oscillatory magnetic field, \mathbf{H}_{ac} , identified three fundamental magnon modes (36, 37), depicted in Fig. 1, C1 to C3. For \mathbf{H}_{ac} within the skyrmion lattice plane, clockwise (CW) and counterclockwise (CCW) gyrations of the skyrmion core are generated, whereas a breathing mode (BM) develops for \mathbf{H}_{ac} aligned parallel to the skyrmion tubes. Extensive microwave spectroscopy in MnSi, $\text{Fe}_{1-x}\text{Co}_x\text{Si}$, and Cu_2OSeO_3 established universal agreement with theory based on a few material-specific and sample shape-specific parameters (32).

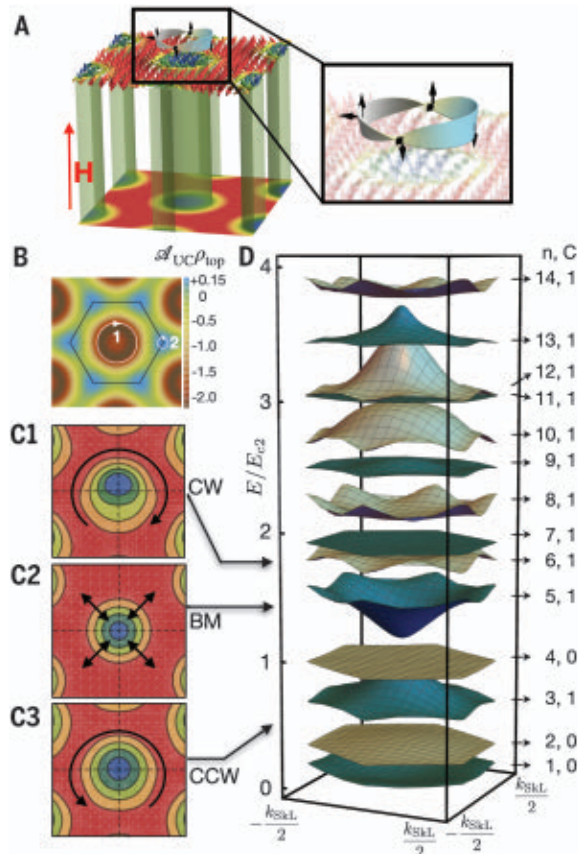
Going beyond this initial work, we calculated the 14 lowest-lying magnon bands of MnSi for momentum transfers \mathbf{q}_{\perp} within the two-dimensional Brillouin zone of the hexagonal skyrmion lattice (SkL) as predicted in (38), where

¹Institut Laue-Langevin, CS 20156, 38042 Grenoble Cedex 9, France. ²Los Alamos National Laboratory, Los Alamos, NM, USA. ³Institut für Theoretische Physik, Universität zu Köln, 50937 Köln, Germany. ⁴Laboratory for Neutron Scattering and Imaging, Paul Scherrer Institute, CH-5232 Villigen, Switzerland. ⁵Laboratory for Quantum Magnetism, École Polytechnique Fédérale de Lausanne, CH-1015 Lausanne, Switzerland. ⁶Physik-Department, Technische Universität München, 85748 Garching, Germany. ⁷MLZ, Technische Universität München, 85748 Garching, Germany. ⁸ISIS Facility, Rutherford Appleton Laboratory, Chilton, Didcot OX11 0QX, UK. ⁹Department of Physics, Royal Holloway University of London, Egham TW20 0EX, UK. ¹⁰Neutron Technologies Division, Oak Ridge National Laboratory, Oak Ridge, TN 37831, USA. ¹¹Centre for Quantum Engineering (ZQE), Technische Universität München, 85748 Garching, Germany. ¹²MCQST, Technische Universität München, 85748 Garching, Germany. ¹³Laboratory for Neutron and Muon Instrumentation (LIN), Paul Scherrer Institute, CH-5232 Villigen, Switzerland. ¹⁴Physik-Institut, Universität Zürich, CH-8057 Zürich, Switzerland. ¹⁵Institut für Theoretische Physik, Technische Universität Dresden, 01062 Dresden, Germany. ¹⁶Institut für Theoretische Festkörperphysik, Karlsruhe Institute of Technology, 76131 Karlsruhe, Germany. ¹⁷Institute for Quantum Materials and Technology, Karlsruhe Institute of Technology, 76131 Karlsruhe, Germany.

*Corresponding author. Email: tweb@ill.fr

[†]Present address: European Spallation Source ERIC, P.O. Box 176, SE-221 00, Lund, Sweden.

Fig. 1. Depiction of emergent Landau levels of magnons and topological magnon bands in a skyrmion lattice. (A) Qualitative depiction of the skyrmion lattice in a magnetic field H . Inset: The classical trajectory of a magnon, illustrating the orientation of the local coordinate system (black arrows) as it tracks the local magnetization and accumulates a Berry phase. (B) Variation of the topological winding density ρ_{top} across the skyrmion lattice, averaging to a winding number of -1 per unit cell area \mathcal{A}_{UC} . Classical trajectories of magnons are denoted 1 and 2 (see text for details). (C1 to C3) Key characteristics of magnons in a skyrmion lattice as observed in microwave spectroscopy. CW, clockwise mode; BM, breathing mode; CCW, counterclockwise mode. (D) Calculated lowest 14 bands in the skyrmion lattice of MnSi within the first Brillouin zone in units $E_{c2} = g\mu_B\mu_0 H_{c2}^{\text{int}}/2$ (38). The dispersive character originates partly in the nonuniform topological winding density ρ_{top} , as illustrated in (B). The band index n and Chern number C are indicated at right. Bands 3, 5, and 6 correspond to the CCW, BM, and CW modes, respectively. The Goldstone mode (GM) corresponds to $n = 1$. The Landau levels represent topological magnon bands with $C = 1$.



k_{SKL} is the magnitude of the reciprocal primitive vectors (Fig. 1D). Noted on the right side are the band index n and the Chern number C . Bands 3, 5, and 6 represent the CCW, BM, and CW modes, respectively. Bands with nonzero Chern numbers are topologically nontrivial.

The associated magnon band structure for \mathbf{q}_{\perp} exhibits a nontrivial topology that is directly linked to the nontrivial real-space topology of the skyrmion lattice. For higher magnon energies, $E \gg E_{c2}$ (where $E_{c2} = g\mu_0\mu_B H_{c2}^{\text{int}}$ represents the energy associated with the internal critical field separating the conical and field-polarized phases), the spin wave equation may be approximated by a Schrödinger equation for the Hamiltonian $\mathcal{H} = (\mathbf{p} + e\mathbf{A})^2/2m$. Here, \mathbf{A} and m are the emergent vector potential and the magnon mass, respectively, obeying $\hbar^2 k_h^2/(2m) = E_{c2}$, where k_h is the helix wave vector. For a topologically trivial texture, the vector potential may be removed by a gauge transformation resulting in the free magnon dispersion $E(\mathbf{q}_{\perp}) = \hbar^2 \mathbf{q}_{\perp}^2/(2m)$.

In contrast, magnons in the skyrmion lattice are expected to form emergent Landau levels with a characteristic cyclotron energy $E_{\text{cycl}} =$

$\hbar e|B_{\text{em}}|/m$. Using $\mathcal{A}_{\text{UC}} = \sqrt{3}a^2/2$ for the area of the magnetic unit cell with lattice constant $a = 4\pi/(\sqrt{3}k_{\text{SKL}})$, this amounts to $E_{\text{cycl}}/E_{c2} = (\sqrt{3}/\pi)(k_{\text{SKL}}/k_h)^2 \approx \sqrt{3}/\pi$. Because each skyrmion contributes two flux quanta, an average density of $2\pi/\sqrt{3} \approx 3.6$ states per E_{c2} is expected for each q_{\perp} . For MnSi with $E_{c2} = 37 \mu\text{eV}$ at 28.5 K, this approximately corresponds to one magnon band per 10 μeV , where the relatively flat dispersion of most bands at higher energies and their finite Chern number stem from the emergent magnetic flux $\mathbf{B}_{\text{em}} = \nabla \times \mathbf{A}$ and thus ρ_{top} shown in Fig. 1B. For low energy, the scalar potential cannot be neglected, resulting in additional, topologically trivial bands.

Polarized inelastic neutron scattering is uniquely suited to verifying the predicted excitation spectra (Fig. 1D) as well as their specific character over a wide range of momentum transfers and excitation energies. In principle, this requires, however, a momentum and energy resolution much better than k_h and the spacing of the Landau levels, respectively, as well as the identification of unambiguous characteristics accessible at low resolution. To satisfy these requirements for MnSi, which are beyond the individual

limits of present-day neutron spectrometers, we combined the information inferred from three different neutron scattering methods. Shown in Figs. 2, 3, and 4 are the experimentally observed spectra alongside the beamline-specific theoretical predictions [see (17) for details]. We began by surveying the spectra recorded by means of unpolarized, time-of-flight (ToF) spectroscopy (Fig. 2, A1 and A2). Then, the distribution of excitation energies and scattering intensities across a large number of positions in parameter space was determined with cold, high-resolution, polarized triple-axis spectroscopy (TAS) (Fig. 2, B1 to D2, and Fig. 4). Finally, selected individual Landau levels were resolved by means of so-called modulation of intensity by zero effort (MIEZE), a type of neutron spin-echo spectroscopy (Fig. 3).

Owing to its incommensurate, multi- k nature, the magnon spectra and the magnetic response tensor of the skyrmion lattice could not be computed in spin wave simulation packages such as SpinW. We therefore developed the necessary simulation tools. Details of the procedures on all software tools are given in (17). The source code is provided at the repository given in (39). The results of our theoretical calculations are shown on the right side of Figs. 2, 3, and 4, where the bottom and top axes denote energies equivalently in units of meV and E_{c2} , and the left and right axes denote momentum transfers equivalently in reciprocal lattice units (rlu) and helical modulation lengths k_h [see (17) for material-specific parameters]. Shown in thin gray lines are the calculated quantitative magnon spectra $E(\mathbf{q})$, whereas the magnetic response tensor $\chi''_{ij}(\mathbf{q}, E)$ is shown in color shading. The latter is related by means of the fluctuation-dissipation theorem (eq. S20) to the magnetic dynamic structure factor $S_{ij}(\mathbf{q}, E)$ measured experimentally. The red and blue shading refers to spin-flip (SF) scattering of a polarized beam corresponding purely to either SF(+ -) or SF(- +) processes, respectively. Shown in black and green shading is SF scattering of an unpolarized beam, resulting in a mixed character [(+ -), (- +)] and non-spin-flip (NSF) scattering [(+ +), (- -)], respectively (17).

To unambiguously identify the salient features of the excitation spectra, we determined the magnon spectra in the skyrmion lattice plane (Figs. 2 and 3) where they exhibit the emergent Landau levels. In addition, spectra for momentum transfers parallel to the skyrmion tubes were recorded (Fig. 4), which display the characteristics of conventional nonreciprocal magnons akin those observed in the topologically trivial phases (21–25, 33, 34). The scattering geometries were chosen carefully to further distinguish nuclear and magnetic scattering (17). Namely the ToF and TAS measurements were performed in the ($hk0$) scattering

plane in the vicinity of the nuclear [110] Bragg reflection (i.e., $\mathbf{G}_{[110]} = [110]$; see the schematic depictions in Figs. 2, 3, and 4). Accordingly, the associated theoretical predictions shown in Figs. 2, 3, and 4 were calculated for a projection onto the subspace perpendicular to the nuclear Bragg vector $\mathbf{G}_{[110]}$.

We begin with the magnon spectra in the skyrmion lattice plane, where the emergent Landau levels are expected. For the unpolarized ToF surveys, the magnetic field \mathbf{H} was parallel to [001] and therefore perpendicular to both $\mathbf{G}_{[110]}$ and the scattering plane, as depicted in Fig. 2A1. This is denoted as setup 1. Because the magnetic satellites were located within the scattering plane, the NSF and SF scattering contained both nuclear and magnetic contributions, additionally motivating TAS. Typical magnon spectra for \mathbf{q}_\perp perpendicular to \mathbf{H} recorded with ToF spectroscopy are shown in Fig. 2A1 and fig. S3. The scattering intensity is presented in yellow/blue shading. Black lines represent the calculated magnetic response tensor, $\chi''_{ij}(\mathbf{q}, E)$, where the line thickness reflects the spectral weight. The intensity compares well with the calculated spectra again shown in Fig. 2A2 as explicitly demonstrated in fig. S6, which is a color-shaded depiction of the calculated dynamic structure factor with a convolution of the ToF resolution.

The calculated spectra for wave vectors perpendicular to the skyrmion tubes, \mathbf{q}_\perp , shown in Fig. 2A2 as gray lines, display the Landau levels stemming from the nontrivial topology of the skyrmion lattice; the calculated magnetic response tensor is shown as black lines, as in Fig. 2A1. The weak dispersion of the Landau levels is caused by variations in \mathbf{B}_{em} as well as the magnon potential. Because the Landau level wave functions of magnons for \mathbf{q}_\perp are distinctly different from the plane wave function of the neutron, the spectral weight at elevated energies gets distributed across a wide range of magnon bands. Thus, a broad distribution of spectral weight, as compared to the well-defined magnon branches along the skyrmion tubes shown in Fig. 4, represents a key signature of the nontrivial topology.

For a quantitative comparison between theory and experiment, and to keep track of spin-flip versus non-spin-flip processes with respect to incoherent and nuclear scattering, we performed high-resolution polarized TAS. Because the predicted spacing of the Landau levels of $\sim 10 \mu\text{eV}$ is well below the resolution of state-of-the-art TAS, we used a setup in which the magnetic field \mathbf{H} was parallel to \mathbf{G} (i.e., $\mathbf{H}_{[110]}$ along [110]) such that the skyrmion lattice stabilized perpendicular to $\mathbf{H}_{[110]}$ with a pair of its satellites parallel to a [110]. This is referred to as setup 2. The polarization \mathbf{P} is aligned adiabatically with $\mathbf{H}_{[110]}$ and hence \mathbf{G} , and thus the SF and NSF scattering were purely magnetic and nuclear, respectively.

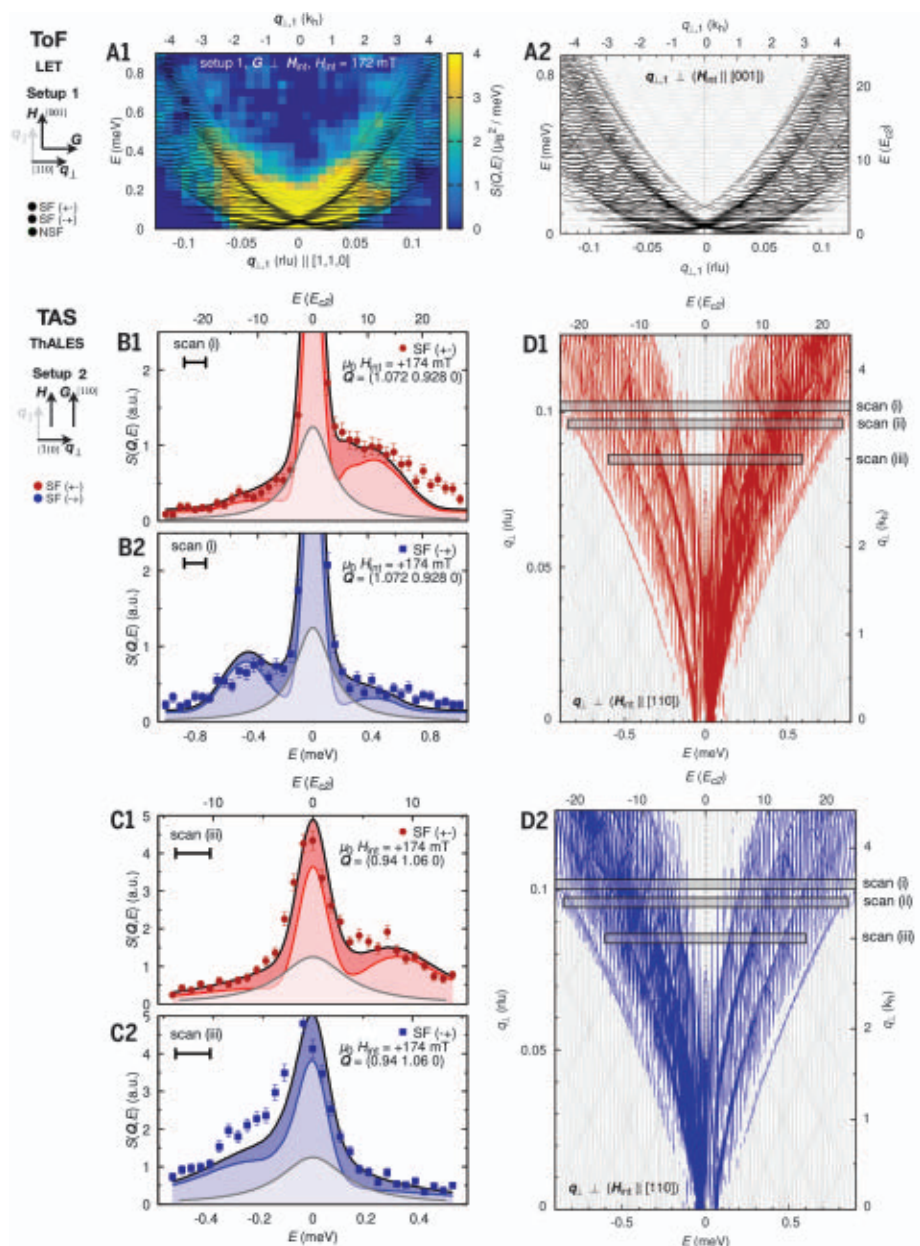


Fig. 2. Magnon spectra of MnSi for momentum transfers perpendicular to the skyrmion lattice tubes.

Left: Experimental data. Right: Quantitative calculations of the magnon spectra. Thin gray lines represent the magnon spectra $E(\mathbf{q})$; black, red, and blue lines represent the magnetic response tensor, $\chi''_{ij}(\mathbf{q}, E)$. The line thickness of the latter reflects the spectral weight. Colors red/blue and green denote spin-flip and non-spin-flip processes, SF and NSF, respectively. Energy and momentum transfers are provided in two corresponding scales. (A1) ToF scattering intensity for momentum transfers $\mathbf{q}_{\perp} \parallel [1,1,0]$. The color shading represents the experimental scattering intensity. Black lines represent the calculated magnetic response tensor shown also in (A2) (see fig. S6B for the calculated dynamic structure factor as convoluted with the instrumental resolution). (A2) Calculated excitation spectra (gray) and magnetic response tensor (black). (B1, B2, C1, and C2) Polarized TAS intensities for selected momentum transfers and field values. Curves shown in red and blue shading represent the sum of the calculated dynamic structure factor convoluted with the instrumental resolution (light-red/blue shading) and a quasi-elastic (QE) contribution attributed to longitudinal fluctuations (gray shading) (17). The same quantitative scaling factor and the same QE contribution was used for all TAS data shown in the main text and (17) for momentum transfers perpendicular and transverse to the skyrmion lattice \mathbf{q}_\perp and \mathbf{q}_\parallel , respectively. (D1 and D2) Calculated magnon spectra and magnetic response tensors. The location of experimental scans shown in (B) and (C) is marked by gray boxes [see figs. S10 and S17 for further data including those of scan (ii)].

Typical energy scans at various values of q_{\perp} are shown in Fig. 2, B1, B2, C1, and C2. The corresponding calculated magnon spectra as well as the magnetic response tensor are shown in Fig. 2, D1 and D2, where the gray shaded boxes denote the parameter range of the energy scans (i), (ii), and (iii) [see figs. S10 and S17 for further data, including those of scan (ii)]. For ease of comparison with the TAS data, the calculated spectra (Fig. 2, D1 and D2) are shown as a function of energy.

A quantitative comparison of the energy dependence of our TAS data with theory is shown in Fig. 2, B1, B2, C1, and C2. Here, the light-red and light-blue shading denote magnetic SF (+ -) and SF (- +) scattering, respectively; the light-gray shaded areas denote a quasi-elastic (QE) contribution; and the red and blue shading denote the sum of the magnon spectral weight and the QE contribution. For the magnon spectra, we convoluted the dynamic structure factor $S_{ij}(\mathbf{q}, E)$ with the instrumental resolution, taking into account incoherent magnetic scattering (for clarity, the incoherent NSF scattering is not shown; see figs. S10 to S12, S16, and S17 for depictions that display the incoherent NSF scattering). Scaling simultaneously all TAS data (i.e., those recorded for momentum transfers q_{\perp} and q_{\parallel}) by the same constant (see Fig. 2, Fig. 4, and figs. S10 to S13, S16, and S17), the energy dependence of the SF scattering due to magnons (Fig. 2, B1 and C2) is already in reasonable quantitative agreement with experiment. This agreement improves further after adding a small QE Gaussian contribution with a linewidth $\Gamma_e \approx 120 \mu\text{eV}$. The weight of this QE scattering is essentially identical in all of the TAS data, where small differences may be attributed to the instrumental resolution. We find that the QE scattering is in good qualitative agreement with longitudinal excitations, as shown theoretically in (17). It is therefore not included in the model of the magnon spectra, which represent transverse spin excitations. In Figs. 2 and 4, we show that the quantitative agreement between $S_{ij}(\mathbf{q}, E)$ and experiment is good. Notably, the sum of the magnon spectra encoded in $S_{ij}(\mathbf{q}, E)$ (red and blue solid lines) and the QE scattering (gray line) indicated in red and blue shading quantitatively agrees with the data points. Unfortunately, a similarly accurate comparison between experiment and theory taking into account the instrumental resolution is technically inaccessible for the ToF and the MIEZE data.

We resolved the lowest-lying Landau level using MIEZE neutron spin-echo spectroscopy. For the MIEZE measurements, a polarized small-angle neutron scattering configuration without polarization analysis was used, where \mathbf{H} was parallel to the incident neutron beam. This is denoted as setup 3 (17). Probing the intermediate scattering function $S(\mathbf{q}, \tau)$ (i.e.,

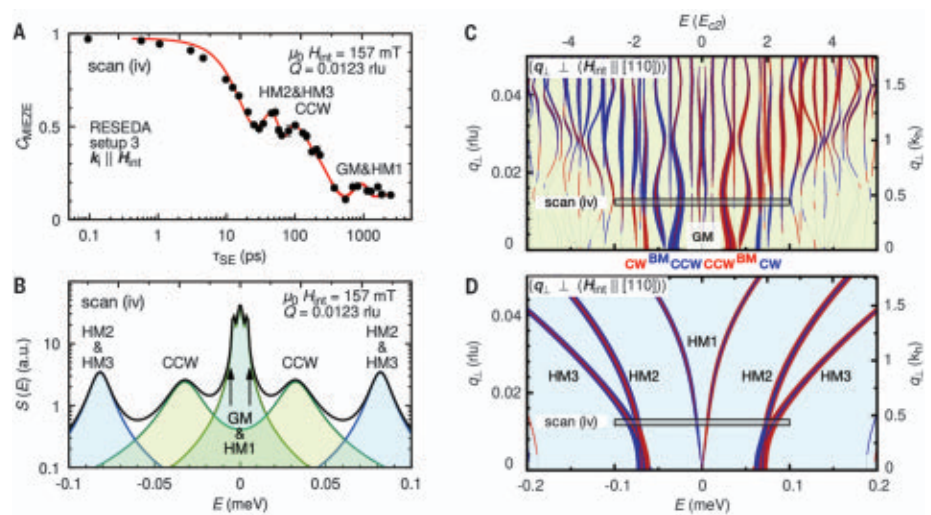


Fig. 3. Neutron scattering intensity and calculated magnon spectra in MnSi in the skyrmion lattice and conical phase at very low energies. MIEZE data were recorded with setup 3 (17). **(A)** MIEZE contrast, C_{MIEZE} , representing the intermediate scattering function, $S(\mathbf{q}, \tau)$, observed in neutron spin-echo spectroscopy at $|\mathbf{q}| = 0.0123 \text{ rlu}$, for a large volume fraction of skyrmion phase and a small coexistent volume fraction of conical phase. The red line represents the Fourier transform of the dynamic structure factor shown in (B). **(B)** Dynamic structure factor, $S(\mathbf{q}, E)$, of the calculated magnon spectra (table S4 and figs. S21 and S22) taking into account linewidths such that the Fourier transform (red line) matches the data in (A). **(C)** Calculated magnon spectra $E(\mathbf{q})$ (gray lines) and spectral weight of the magnetic response tensor $\chi''_{ij}(\mathbf{q}, E)$ in the skyrmion lattice. **(D)** Calculated magnon spectra $E(\mathbf{q})$ and spectral weight of the magnetic response tensor $\chi''_{ij}(\mathbf{q}, E)$ in the conical phase. In (C) and (D), color shaded lines represent $\chi''_{ij}(\mathbf{q}, E)$ in setup 2 used for polarized TAS, where red and blue denote the two spin-flip processes, SF(+ -) and SF(- +), respectively. Energy and momentum transfers are provided in two corresponding scales. The gray-shaded box marked scan (iv) denotes the parameter range where the MIEZE data were recorded. CW, clockwise mode; CCW, counterclockwise mode; BM, breathing mode; GM, Goldstone mode; HM1 to HM3, helimagnons of the conical state.

the time dependence rather than the frequency dependence of the spin correlations), MIEZE allowed simultaneous detection of several excitations with very high resolution (40).

Shown in Fig. 3A is the MIEZE contrast equivalent to $S(\mathbf{q}, \tau)$, where the oscillatory decay is characteristic of several damped propagating excitations (40). The associated dynamic structure factor, $S(\mathbf{q}, E)$, with resonance energies and estimated linewidths is shown in Fig. 3B. Its Fourier transform with respect to energy, $S(\mathbf{q}, \tau)$, matches the experimental data well (Fig. 3A, red curve). To obtain the strongest elastic and thus inelastic intensity of the skyrmion lattice, we chose a sample temperature for the MIEZE experiment for which the skyrmion phase coexisted with a small volume fraction of conical phase, as independently confirmed in TAS measurements (17). Calculated magnon spectra for these coexisting skyrmion lattice and conical phases are shown in Fig. 3, C and D.

Focusing on the zone center, the calculated spectra in the skyrmion lattice (Fig. 3C) reproduce the energies and spectroscopic weights of the CW, CCW, and BM modes in excellent quantitative agreement with microwave spectroscopy (32). Further, the excitation spectrum of the conical phase for the same field strength

(Fig. 3D) reveals that the excitation energies of the lowest-lying helimagnons (HM1, HM2, and HM3) differ suitably from the excitation energies of the skyrmion lattice. Thus, the presence of a small volume of conical phase not only confirmed the existence of the lowest-lying Landau level, but provided an important test of the validity of the MIEZE spectroscopy.

For a direct comparison with experiment, the calculated MIEZE intensities for the skyrmion lattice and conical state, denoted scan (iv) in Fig. 3, C and D, were evaluated numerically for setup 3 (see table S4). Starting at the lowest energy, the Goldstone mode (GM) of the skyrmion lattice ($n = 1$) is predicted to exist at energies similar to those of HM1. This is followed by the CCW mode ($n = 3$) at $\sim 24 \mu\text{eV}$ and an excitation of the skyrmion lattice at $\sim 53 \mu\text{eV}$ that is too weak to be seen experimentally (the BM and CW modes are also too weak to be seen). The next two helimagnons of the conical phase (HM2 and HM3) are expected at $\sim 64.5 \mu\text{eV}$ and $\sim 72.5 \mu\text{eV}$.

As shown by the red line in Fig. 3A, these predictions compare well with the three magnon modes that may be discerned in our data: (i) an excitation at $E_1 = 4 \mu\text{eV}$ that may be attributed to the GM and HM1 with a linewidth $\Gamma_1 = 0.55 \mu\text{eV}$, (ii) an excitation at $E_2 = 30 \mu\text{eV}$

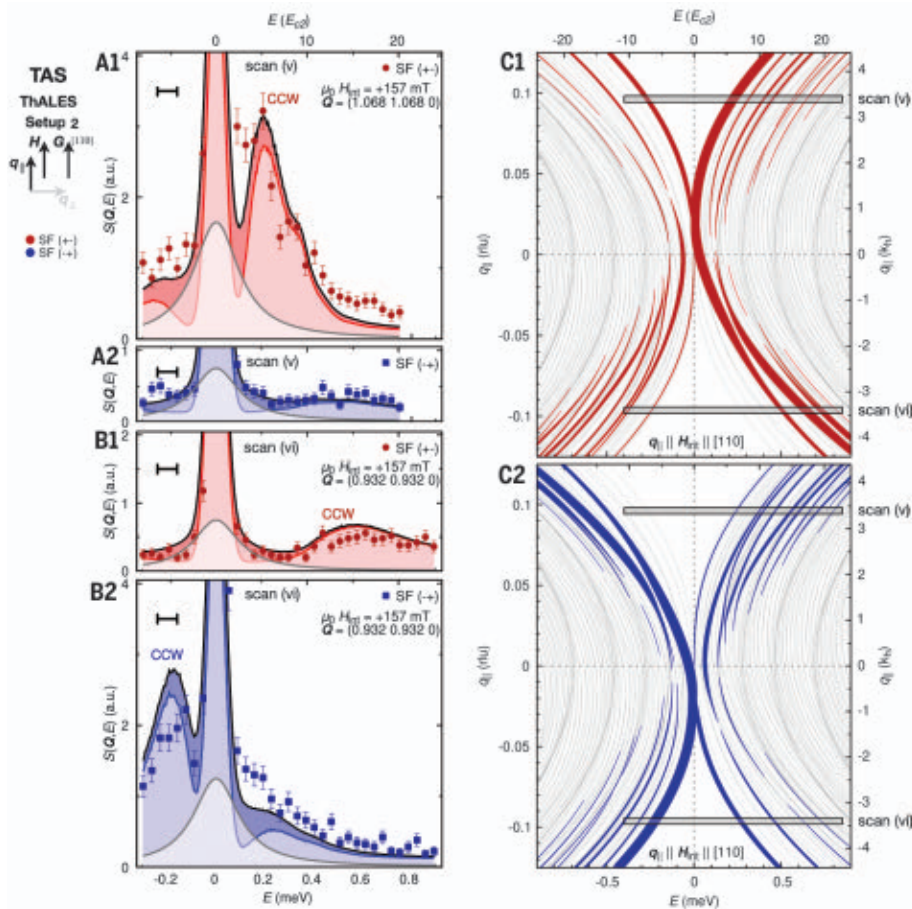


Fig. 4. Polarized neutron scattering intensity and calculated magnon spectra of MnSi for momentum transfers parallel to the skyrmion lattice tubes. Left: Experimental data. Right: Calculations of the magnon spectra. Thin gray lines represent the magnon spectra $E(\mathbf{q})$; red and blue shaded lines denote the magnetic response tensor, $\chi''_{ij}(\mathbf{q}, E)$, for the two spin-flip scattering processes. The line thickness of the magnetic response tensor reflects the spectral weight. Energy and momentum transfers are provided in two corresponding scales. (**A1**, **A2**, **B1**, and **B2**) Polarized TAS intensities for selected momentum transfers and field values chosen to highlight well-defined, dispersive, nonreciprocal magnons. Curves shown in red and blue shading represent the sum of the calculated dynamic structure factor convoluted with the instrumental resolution (light-red/blue shading) and a quasi-elastic (QE) contribution attributed to longitudinal fluctuations (gray shading) (17). The same quantitative scaling factor and the same QE contribution was used for all TAS data shown in the main text and (17), for momentum transfers perpendicular and transverse to the skyrmion lattice \mathbf{q}_\perp and \mathbf{q}_\parallel , respectively. (**C1** and **C2**) Calculated magnon spectra. The location of the experimental data shown in (A) and (B) is marked by gray boxes (see figs. S10 to S13 and S16 for further data).

that may be attributed to the CCW magnon with a linewidth $\Gamma_2 = 10 \mu\text{eV}$, and (iii) an excitation at $E_3 = 80 \mu\text{eV}$ that may be attributed to HM2 and HM3 with a linewidth $\Gamma_3 = 6 \mu\text{eV}$. Thus, the predicted energies of the most intense excitations are in excellent agreement with experiment. The GM is thereby topologically trivial ($C = 0$), whereas the CCW mode, $n = 3$, is topologically nontrivial with $C = +1$.

In contrast to the skyrmion lattice plane, the spectra for momentum transfers along the skyrmion tubes, \mathbf{q}_\parallel , are not sensitive to \mathbf{B}_{em} , where typical polarized TAS intensities using setup 2 are shown in Fig. 4 (see figs. S10 to S13 and S16 for further data and the associated

NSF intensities, representing purely incoherent nuclear scattering). In excellent agreement with the calculated spectra shown in Fig. 4, C1 and C2, the TAS exhibits pronounced maxima with substantial weight. A detailed inspection of the calculated spectra (17) allows these maxima to be attributed to the CCW mode, previously identified at the zone center using microwaves (32). These are conventional, topologically trivial, strongly dispersive spin wave branches.

Moreover, using setup 2, polarized TAS allowed us to discern pronounced individual modes that are clearly nonreciprocal [i.e., $E(-\mathbf{q}_\parallel) \neq E(\mathbf{q}_\parallel)$]. Namely for wave vectors

parallel and antiparallel to \mathbf{H} , the structure factor exhibited a pronounced nonreciprocity [i.e., $S_{ij}(\mathbf{q}, E) \neq S_{ij}(-\mathbf{q}, E)$] already evident in Fig. 4, C1 and C2. Here Fig. 4, A1 and B1, display the same scans under inversion of momentum transfer for the same field orientation (the same applies to the scans shown in Fig. 4, A2 and B2). Related data under field inversion are presented in figs. S13 and S16. This well-known nonreciprocity originates in the combination of Dzyaloshinskii-Moriya and dipolar interactions as discussed in (47); it is characteristic for chiral materials (42). In MnSi it was previously observed in the field-polarized (22, 24) and conical phases (34), as well as in the paramagnetic regime (26).

The topological magnon bands in the skyrmion lattice of MnSi we report here are highly unusual in several ways. First, the connection between the nontrivial topological winding in real space and the topological magnon bands in reciprocal space may be quantitatively captured within a universal framework based on three material-specific parameters: the energy separating the conical and field-polarized state, E_c ; the helical wave vector, k_h ; and the susceptibility in the conical state, $\chi_{\text{con}}^{\text{int}}$ (17). Second, the Landau levels and topological band structure are observed starting at the lowest-lying states up to high energies. Third, we expect contributions to the thermal Hall effect, which, however, will not be quantized given the bosonic character of the magnons. Fourth, an intimate analogy exists between quantum Hall phenomena and the emergent Lorentz force, Landau levels, and the topological magnon band structure caused by the nontrivial real-space topology of skyrmion lattices in chiral magnets. On the basis of the bulk/boundary correspondence, our observations in the bulk imply the existence of chiral edge states that may be technologically useful—for instance, as a directional coupler for quantum technologies.

REFERENCES AND NOTES

- G. E. Volovik, *J. Phys. C* **20**, L83–L87 (1987).
- P. Bruno, V. K. Dugaev, M. Taillefumier, *Phys. Rev. Lett.* **93**, 096806 (2004).
- C. Strohm, G. L. J. A. Rikken, P. Wyder, *Phys. Rev. Lett.* **95**, 155901 (2005).
- H. Katsura, N. Nagaosa, P. A. Lee, *Phys. Rev. Lett.* **104**, 066403 (2010).
- Y. Onose et al., *Science* **329**, 297–299 (2010).
- R. Shindou, R. Matsumoto, S. Murakami, J.-i. Ohe, *Phys. Rev. B* **87**, 174427 (2013).
- R. Chisnell et al., *Phys. Rev. Lett.* **115**, 147201 (2015).
- B. Yuan et al., *Phys. Rev. X* **10**, 011062 (2020).
- W. Yao et al., *Nat. Phys.* **14**, 1011–1015 (2018).
- L.-C. Zhang et al., *Phys. Rev. Res.* **2**, 013063 (2020).
- B. Binz, A. Vishwanath, *Physica B* **403**, 1336–1340 (2008).
- K. A. van Hoogdalem, Y. Tserkovnyak, D. Loss, *Phys. Rev. B* **87**, 024402 (2013).
- J. Iwasaki, A. J. Beekman, N. Nagaosa, *Phys. Rev. B* **89**, 064412 (2014).
- B. Göbel, A. Mook, J. Henk, I. Mertig, *Eur. Phys. J. B* **91**, 179 (2018).
- A. Roldán-Molina, A. Nunez, J. Fernández-Rossier, *New J. Phys.* **18**, 045015 (2016).
- A. Mook, B. Göbel, J. Henk, I. Mertig, *Phys. Rev. B* **95**, 020401 (2017).

17. See supplementary materials.
18. A. Neubauer *et al.*, *Phys. Rev. Lett.* **102**, 186602 (2009).
19. F. Jonietz *et al.*, *Science* **330**, 1648–1651 (2010).
20. M. Mochizuki *et al.*, *Nat. Mater.* **13**, 241–246 (2014).
21. M. Janoschek *et al.*, *Phys. Rev. B* **81**, 214436 (2010).
22. S. V. Grigoriev *et al.*, *Phys. Rev. B* **92**, 220415 (2015).
23. M. Kugler *et al.*, *Phys. Rev. Lett.* **115**, 097203 (2015).
24. T. J. Sato *et al.*, *Phys. Rev. B* **94**, 144420 (2016).
25. T. Weber *et al.*, *Phys. Rev. B* **100**, 060404 (2019).
26. B. Roessli, P. Böni, W. E. Fischer, Y. Endoh, *Phys. Rev. Lett.* **88**, 237204 (2002).
27. C. Pappas *et al.*, *Phys. Rev. Lett.* **102**, 197202 (2009).
28. M. Janoschek *et al.*, *Phys. Rev. B* **87**, 134407 (2013).
29. J. Kindervater *et al.*, *Phys. Rev. B* **89**, 180408 (2014).
30. C. Pappas *et al.*, *Phys. Rev. Lett.* **119**, 047203 (2017).
31. J. Kindervater *et al.*, *Phys. Rev. X* **9**, 041059 (2019).
32. T. Schwarze *et al.*, *Nat. Mater.* **14**, 478–483 (2015).
33. M. Janoschek, F. Jonietz, P. Link, C. Pfeleiderer, P. Böni, *J. Phys. Conf. Ser.* **200**, 032026 (2010).
34. T. Weber *et al.*, *AIP Adv.* **8**, 101328 (2018).
35. N. D. Mermin, T.-L. Ho, *Phys. Rev. Lett.* **36**, 594–597 (1976).
36. M. Mochizuki, *Phys. Rev. Lett.* **108**, 017601 (2012).
37. Y. Okamura *et al.*, *Nat. Commun.* **4**, 2391 (2013).
38. M. Garst, J. Waizner, D. Grundler, *J. Phys. D* **50**, 293002 (2017).
39. T. Weber, Spin wave simulation code for “Topological magnon band structure of emergent Landau levels in a skyrmion lattice”, Zenodo repository: <http://doi.org/10.5281/zenodo.5718363>
40. C. Franz *et al.*, *J. Phys. Soc. Jpn.* **88**, 081002 (2019).
41. S. Seki *et al.*, *Nat. Commun.* **11**, 256 (2020).
42. Y. Tokura, N. Nagaosa, *Nat. Commun.* **9**, 3740 (2018).
43. T. Weber *et al.*, Raw data for “Topological magnon band structure of emergent Landau levels in a skyrmion lattice”, Zenodo repository: <http://doi.org/10.5281/zenodo.5718313>.

ACKNOWLEDGMENTS

We thank the staff at the Institute Laue Langevin, Heinz Maier-Leibnitz Zentrum, ISIS Neutron and Muon Source, Paul Scherrer Institut, the spallation neutron source at Oak Ridge National Laboratory, E. Villard, P. Chevalier, and J. Frank for support; J. Locatelli for the instrument control system; the ILL cluster computing facility for IT support; and M. Kugler for initial implementation of the model and support in early experiments. **Funding:** Supported by the DFG in the framework of TRR80 (project EI, project-id 107745057), SPP 2137 (Skyrmionics) under grant PF393/19 (project-id 403191981), ERC Advanced Grants 291079 (TOPFIT) and 788031 (ExQSiD), and Germany’s excellence strategy EXC-2111 390814868 (A.B. and C.P.); DFG grant GE 971/5-1 (R.G.); the DFG in the framework of SFB 1143 (project A07; project-id 247310070), as well as grants GA 1072/5-1 (project-id 270344603) and GA 1072/6-1 (project-id 324327023) (M.G.); and the LANL Directed Research and Development program via the Directed Research project “A New Approach to Mesoscale Functionality: Emergent Tunable Superlattices (20150082DR)” (D.M.F. and M.J.). Early work by M.G. and J.W. on the spin wave theory was supported by the Institute for Materials Science at Los Alamos (RR2015). This research used resources at the Spallation Neutron Source, a DOE Office of Science User Facility operated by the Oak Ridge National Laboratory. The datasets collected at LET have the DOIs 10.5286/ISIS.E.RB1620412 and 10.5286/ISIS.E.RB1720033. The datasets collected at the ILL have the DOIs 10.5291/ILL-DATA-INTER-413, 10.5291/ILL-DATA-INTER-436, 10.5291/ILL-DATA-INTER-477, 10.5291/ILL-DATA-4-01-1597, and 10.5291/ILL-DATA-4-01-1621. Data recorded at RESEDA were collected under proposal P00745-01. Additional datasets (not shown) were collected at MIRA (proposals 13511 and 15633) MLZ, Garching, Germany; TASP (proposals 20181324 and 20151888) at PSI, Villigen, Switzerland; and CNCS at SNS Oak Ridge, USA. **Author contributions:** T.W., D.M.F., and M.J. proposed and designed the ToF and TAS experiments. T.W. proposed and designed the polarized TAS experiments. C.P. proposed the MIEZE experiment. A.B. grew the single crystal denoted sample 1. T.W., D.M.F., L.B., C.F., H.G., and M.J. performed the experiments. P.S., G.S.T., M.B., R.B., D.V., C.F., M.S., and R.G. supported the experiments at neutron spectrometers under their responsibility. T.W., C.P., P.B., M.J., and M.G. conceived the interpretation. J.W. and M.G. performed the theoretical calculations. T.W., D.M.F., L.B., H.G., and C.F. performed the data analysis. T.W. and M.G. implemented the theoretical skyrmion model for use with TAS resolution convolution. T.W., C.P., P.B., and M.G. wrote the manuscript with input from all authors. All authors discussed the results and reviewed the manuscript. **Competing interests:** The authors declare that they have no competing interests. **Data and materials availability:** The computer code for the spin wave simulations used in this paper can be found at the repository given in (39). All data needed to evaluate

the conclusions in the paper are present in the paper and/or the supplementary materials and available at the repository given in (43).

SUPPLEMENTARY MATERIALS

science.org/doi/10.1126/science.abe4441

Materials and Methods

Supplementary Text

Figs. S1 to S22

Tables S1 to S4

References (44–80)

21 August 2020; resubmitted 30 April 2021

Accepted 31 January 2022

10.1126/science.abe4441

QUANTUM OPTICS

Breakdown of topological protection by cavity vacuum fields in the integer quantum Hall effect

Felice Appugliese^{1*}, Josefine Enkner¹, Gian Lorenzo Paravicini-Bagliani^{1†}, Mattias Beck¹, Christian Reichl², Werner Wegscheider², Giacomo Scalari¹, Cristiano Ciuti³, Jérôme Faist^{1*}

The prospect of controlling the electronic properties of materials via the vacuum fields of cavity electromagnetic resonators is emerging as one of the frontiers of condensed matter physics. We found that the enhancement of vacuum field fluctuations in subwavelength split-ring resonators strongly affects one of the most paradigmatic quantum protectorates, the quantum Hall electron transport in high-mobility two-dimensional electron gases. The observed breakdown of the topological protection of the integer quantum Hall effect is interpreted in terms of a long-range cavity-mediated electron hopping where the anti-resonant terms of the light-matter coupling Hamiltonian develop into a finite resistivity induced by the vacuum fluctuations. Our experimental platform can be used for any two-dimensional material and provides a route to manipulate electron phases in matter by means of vacuum-field engineering.

An intriguing aspect of quantum field theories is the description of empty space as permeated by electromagnetic vacuum fluctuations. Energy conservation forbids any process that would lead to net energy extraction from such states, thus implying that such vacuum fields cannot be detected by direct absorption. Nonetheless, there is much experimental evidence of their existence: Spontaneous emission, the Lamb shift, and the Casimir effect can only be explained by invoking the role of vacuum fields (1). More recently, technological developments of both laser sources and optical nanocavities in the strong light-matter coupling offer a new perspective about vacuum fields, one in which those fluctuations can be sensed directly (2, 3) and used to engineer new properties of matter (4–7) without illumination. Polaritons, optical excitations in the strong light-matter coupling regime, can also be used as sensitive probes of many-body states such as fractional quantum Hall states (8) and Wigner crystals (9). Confining the light on a strongly subwavelength scale is a key element that enabled the achievement of record high interaction strengths (10–13) in

which the anti-resonant terms of light-matter coupling play an important role (14). Cavity-controlled superconductivity (15, 16), long-range ferroelectric order (17, 18), and cavity-mediated superradiance (4), all exploiting the coupling of electrons or dipoles to vacuum fields, have recently been investigated. Experimentally, however, unambiguous identification of modified equilibrium properties of solid-state quantum phases of matter (19) through vacuum fields remains an open challenge.

We recently demonstrated the role of Landau polaritons (20) in controlling the DC bulk magnetotransport (21) in a semiconductor electronic gas, even in the absence of external illumination. The amplitude of the Shubnikov-de Haas oscillations was modified by the presence of a terahertz resonator embedding the Hall bar. However, because a change in the shape of the oscillations in DC magnetoresistivity is sensitively linked to variations of scattering processes, the phenomenology is not universal and every sample is unique. Here, we investigated transport in the integer quantum Hall regime, where the topological protection of the edge currents results in a quantized resistance and where the effect of vacuum fields can be unambiguously revealed.

At low magnetic fields, it is possible to describe transport in the presence of impurity scattering only as a broadening of the Landau levels’ density of states. In the high-magnetic field regime, the random impurity potential instead causes the localization of electrons.

¹Institute of Quantum Electronics, ETH Zürich, Zürich 8093, Switzerland. ²Laboratory for Solid State Physics, ETH Zürich, Zürich 8093, Switzerland. ³CNRS, Laboratoire Matériaux et Phénomènes Quantiques, Université de Paris, F-75013 Paris, France.

*Corresponding author. Email: felicea@phys.ethz.ch (F.A.); jerome.faist@phys.ethz.ch (J.F.)

†Present address: CNRS, ISIS, University of Strasbourg, 67000 Strasbourg, France.

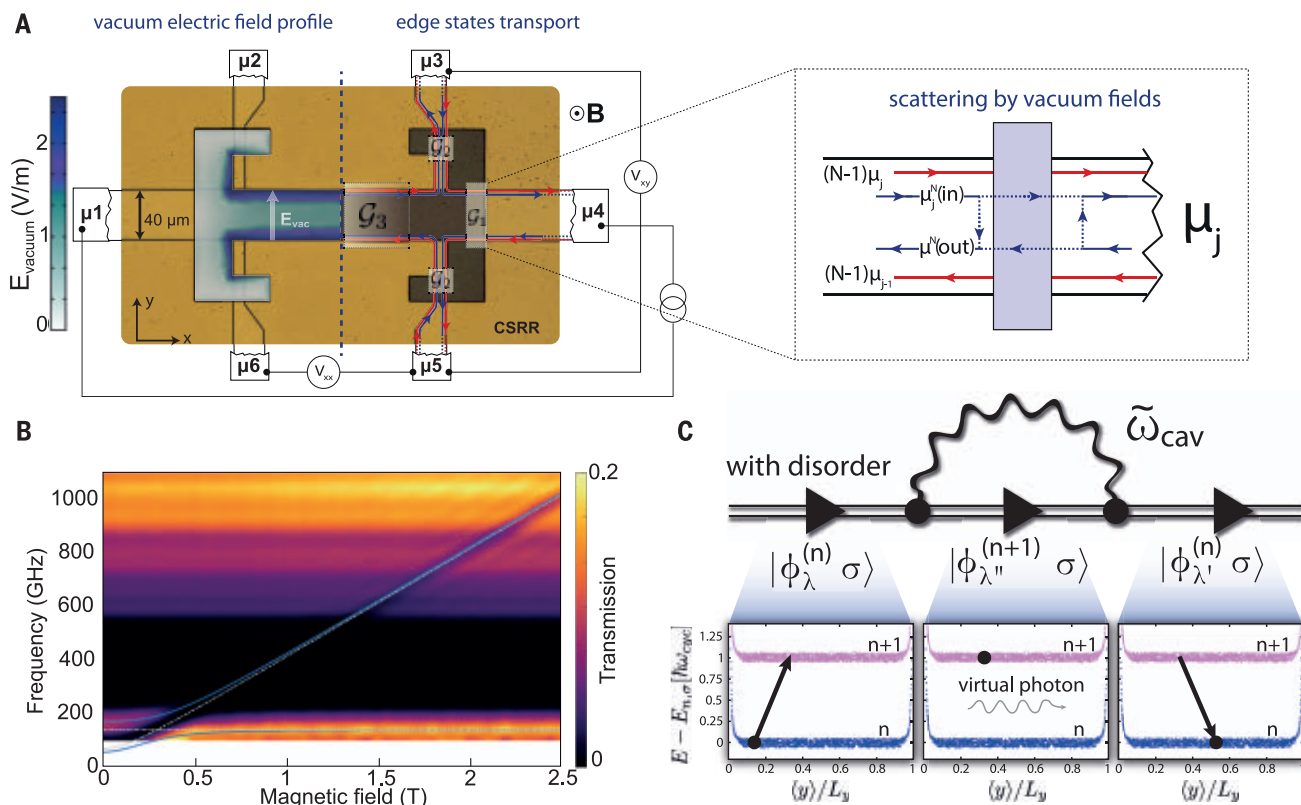


Fig. 1. Description of the experimental geometry and the cavity-mediated electron hopping process. (A) Rendering of a complementary split-ring resonator embedding a Hall bar shown with its electrical contacts (whose chemical potentials are indicated as μ_1 to μ_6). The complementary split ring resonator (CSSR) is defined by a cutout in a metallic gold layer; the 2D electron gas is inserted within the region without metal. Without illumination, at low temperatures and in the linear transport regime, only vacuum fields of the confined electromagnetic modes can affect the electronic transport. The edge conduction channels for the 2D electron gas are also

sketched. (B) Free-space terahertz time-domain spectroscopy transmission measurement performed on a resonator embedding a Hall bar. The polaritonic anticrossing dispersion is clearly visible. The normalized coupling strength is 30%, which shows that the electrons are ultrastrongly coupled to the cavity photons. (C) Top: Schematic representation of a cavity-mediated electron hopping process resulting from the resonator vacuum fields. Bottom: Diagrammatic representation of the same cavity-mediated hopping process (the electron spin σ is conserved), where the indices λ , λ' , λ'' denote disordered eigenstates.

When the Fermi energy lies around a minimum between consecutive Landau levels, both the longitudinal magnetoconductivity σ_{xx} and magnetoresistivity ρ_{xx} simultaneously vanish. In order to describe this nontrivial effect, it is necessary to consider the role of the states at the sample edge.

The simplest picture that best describes the physics of this regime is built on the work of Büttiker (22). The key point is that the bulk is construed as an insulator (because electrons are localized in a fluctuating spatial potential) while the edges are conductors. The current flows through a discrete number of one-dimensional (1D) edge channels from one contact to the next, each of them contributing e^2/h to the conductance and exhibiting zero longitudinal resistance. This system is a prototypical topological insulator (19), where the edge currents are chiral, traveling in opposite directions at the two opposite edges of the sample. As a result, an electron in an edge channel cannot backscatter unless it is scattered on the other edge of the sample. This is true for potentials

that vary slowly over a cyclotron radius but rapidly over the sample dimensions. The impurity potential can be strong, but it still does not produce backscattering when it is short-range (22). For this reason, the topological protection of the quantum Hall effect is robust against local perturbations such as a static disorder. A change in the integer quantum Hall phenomenology can only be explained by invoking the nonlocal nature of the vacuum field associated to a given resonator mode.

Here, we report experimental results that reveal modifications of the integer quantum Hall effect in Hall bars immersed in an electronic resonator where the vacuum field fluctuations are enhanced by their confinement into a strongly subwavelength volume. The geometry of our experiment (21) (Fig. 1A) is a Hall bar of width 40 μm , fabricated on a high-mobility 2D electron gas (23), located in the spatial gap of a complementary metallic resonator (24, 25) with a resonance at 140 GHz. The longitudinal and Hall transverse resistances are measured within the gap of the

resonator. The geometry of the resonator is such that the vacuum field fluctuations $\mathcal{E} = \sqrt{\hbar\omega_{\text{cav}}/2\epsilon_0\epsilon_s V_{\text{eff}}} = 1 \text{ V/m}$ (where \hbar is the Planck constant divided by 2π , ω_{cav} is the cavity mode angular frequency, ϵ_0 is the vacuum permittivity, $\epsilon_s = 13$ is the relative permittivity of GaAs, and $V_{\text{eff}} = 2.72 \times 10^5 \mu\text{m}^3$ is the effective cavity volume) are strongly enhanced relative to the free space, where the amplitude would be on the order of $\mathcal{E} = 0.065 \text{ V/m}$ in that frequency range. This vacuum field, for the lowest-frequency resonance, is fairly homogeneous in the center of the resonator but increases toward the edges. In optical characterization experiments done on an array of such cavities on a Hall bar (21, 26), we observed well-defined Landau polaritons with a light-matter collective Rabi frequency $\tilde{\Omega}_R \approx 0.3\omega_{\text{cav}}$ (Fig. 1B). The resonance between the cavity and the cyclotron frequency occurs at a magnetic field $B \approx 0.3 \text{ T}$. Comparison of the optical spectroscopy performed on arrays and single resonators shows essentially no changes (23).

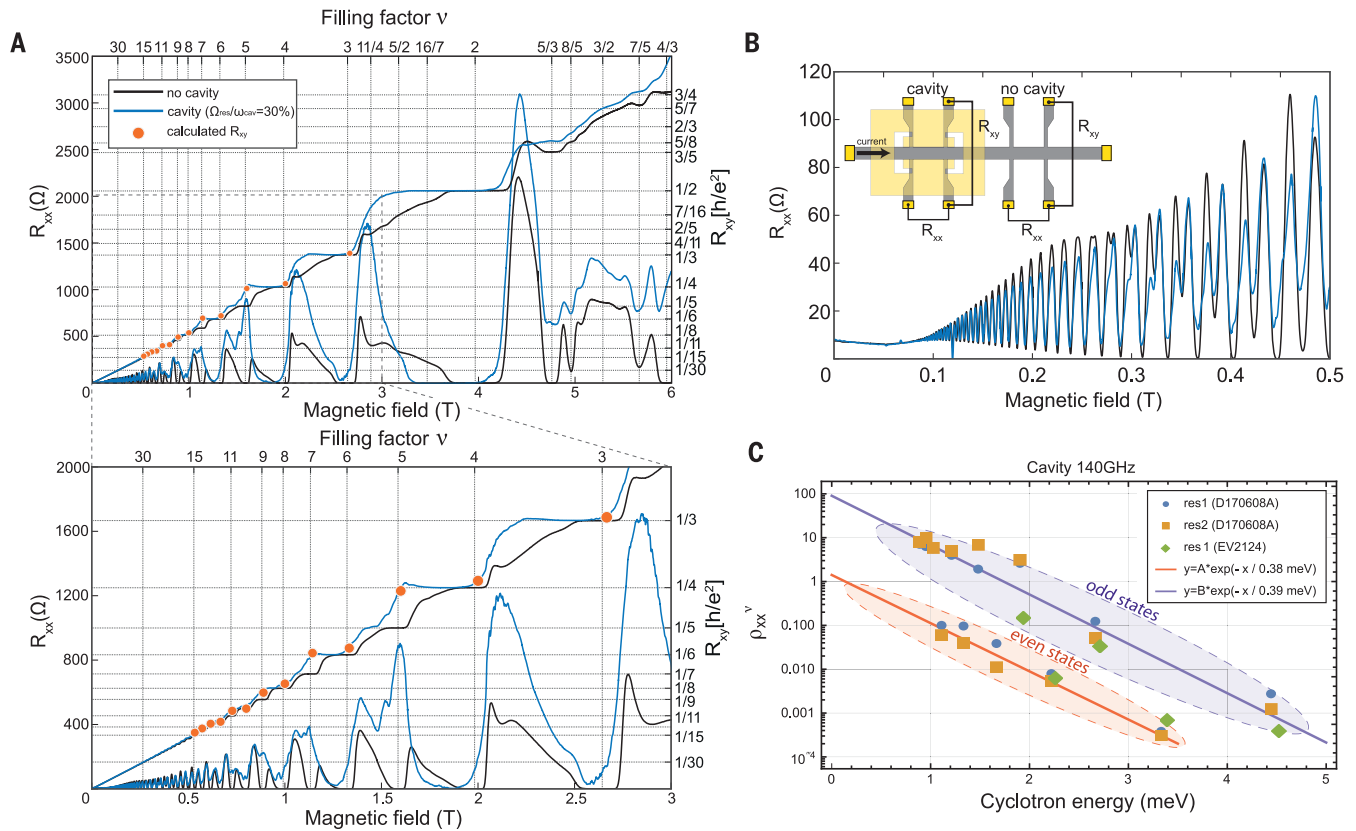


Fig. 2. Breakdown of the quantum Hall effect by vacuum fluctuations.

(A) Longitudinal and transverse resistances for a reference Hall bar (black lines) and for a cavity-embedded Hall bar (blue lines). The calculated transverse resistance (orange dots) computed from the measured longitudinal resistance is overlaid. The prediction is in excellent agreement with the measured transverse resistance (blue curves). For the reference sample with no cavity, the longitudinal resistance is

negligible. (B) Magnetic field region from 0 to 0.5 T, reproduced for better visibility, showing that both the longitudinal and transverse resistances with and without cavity converge to the same value in the limit of zero magnetic field. Inset: Schematic drawing of the electrical configuration allowing the comparison of the resonator and the reference Hall bars. (C) The extracted resistivity ρ_{xx}^v as a function of cyclotron energy for two different samples having very similar densities.

The electron transport in the integer quantum Hall effect proceeds via edge states that are protected against backscattering by the lifting of the time-reversal symmetry provided by the magnetic field (Fig. 1A). As shown in a recent study (27), in the presence of disorder a cavity-mediated long-range hopping can be achieved via the exchange of a virtual cavity photon (Fig. 1C). For an electron occupying a disordered eigenstate $|\phi_{\lambda}^{(n)}\rangle$ in the n th Landau band, the coupling to another disordered eigenstate $|\phi_{\lambda'}^{(n)}\rangle$ in the same Landau band occurs via light-matter coupling to an intermediate state, consisting of an electron in the state $|\phi_{\lambda'}^{(n+1)}\rangle$ in the $(n+1)$ th band with the same spin and one cavity photon. At the lowest order in perturbation theory, the effective coupling between disordered states λ and λ' in the same n th Landau band is given by the expression

$$\tilde{g}_{\lambda,\lambda'}^{(n)} = \sum_{\lambda''} \frac{\tilde{g}_{\lambda,\lambda''}^{(n,n+1)} \tilde{g}_{\lambda'',\lambda'}^{(n,n+1)*}}{\epsilon_{n,\lambda} - \epsilon_{n+1,\lambda''} - \hbar\omega_{\text{cav}}} \quad (1)$$

and can be construed as a cavity-mediated hopping. Note that this intermediate virtual process is due to the counterrotating terms of the light-matter interaction and is quantified by the single-electron vacuum Rabi frequency $\tilde{g}_{\lambda,\lambda'}^{(n,n+1)}$, as detailed in (27). The number of intermediate states is equal to the Landau degeneracy $N_{\text{deg}} = N_{\text{el}}/\nu$, where N_{el} is the number of electrons and ν is the filling factor. The denominator of the expression represents the energy penalty associated to the excitation of the virtual intermediate state described above. Such cavity-mediated hopping involves all the disordered eigenstates, affecting both edge and bulk states. For the quantitative impact of the process, a crucial role is played by the collective vacuum Rabi frequency $\tilde{\Omega}_R = \tilde{g}\sqrt{N_{\text{el}}}$, where the tilde indicates the diamagnetic renormalization (27). Given the anti-resonant nature of the process, additional electromagnetic modes with higher frequencies, such as those that can be observed in Fig. 1B, can contribute in the same qualitative way and reinforce quantitatively the effective cavity-mediated hopping. In addition, the strong elec-

tromagnetic field gradients present at the edge of the metal resonator, as apparent in Fig. 1A, play a role similar to that of impurity disorder in enabling cavity-mediated hopping (27).

The transverse and longitudinal magneto-resistances of a reference sample and of a Hall bar coupled to a cavity are compared in Fig. 2. The reference sample and the cavity-coupled one are fabricated on the same chip and share the same source and drain (23). The sample exhibits a mobility of $16 \times 10^6 \text{ cm}^2 \text{ V}^{-1} \text{ s}^{-1}$ and a density of $2 \times 10^{11} \text{ cm}^{-2}$ and is kept in the dark in a dilution fridge at the nominal temperature of 10 mK; the electron temperature is estimated to be close to 50 mK. Both samples are measured in the same cooling run and are physically located on the same chip. Indeed, identifying unambiguously the effects of vacuum fluctuations experimentally requires that other possible effects be ruled out. [See (23) for details of the precautions taken during sample fabrication and measurement to avoid unwanted artifacts.]

For the reference sample (no cavity), all the integer quantum Hall plateaus are well

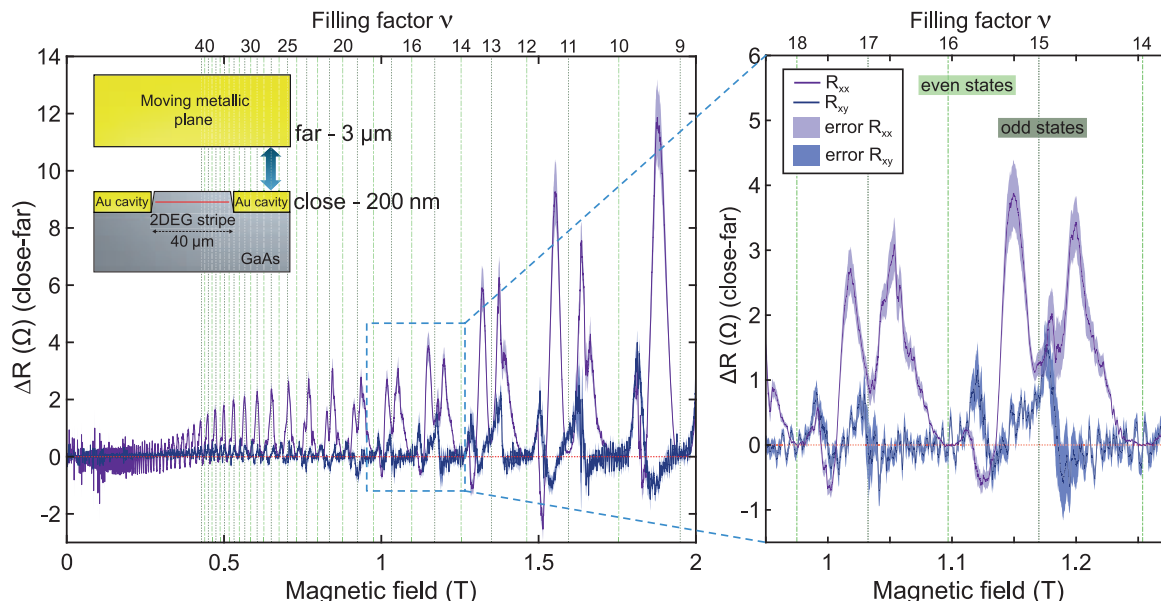


Fig. 3. Modifying the cavity vacuum fields in situ by a metallic tip. Differential longitudinal and transverse resistances are shown for the resonator at 140 GHz with the tip 200 nm and 3 μm away from the surface. Inset: A pictorial representation of the tip brought into the near field of the complementary split ring resonator.

developed, showing zero longitudinal resistance down to $\nu = 11$. By contrast, the cavity-coupled sample displays deviations from the integer quantization, which are especially strong for all the odd plateaus. As expected from the anti-resonant origin of cavity-mediated electron hopping, the modifications of the quantized transport occur on a very wide magnetic field range starting from $B \approx 0.25$ T. At the same time (Fig. 2B, inset), it is important to note that the resistance in the limit of vanishing magnetic field is essentially unchanged by the cavity and that the transport features associated with the fractional quantum Hall regime are only weakly affected. This is an important sanity check because it shows that the mobility and overall quality of the sample are unchanged by the complementary resonator (indeed, the metallic gold layer defining the resonator is deposited around the Hall bar and spatially separated from it) and are also remarkable because the fractional quantum Hall features are usually the most fragile with respect to perturbations (28). This is consistent with the fact that fractional Hall excitations couple extremely weakly to electromagnetic fields. Indeed, a consequence of Kohn's theorem (29) is that for a spatially homogeneous electric field and no disorder, light couples only to the center-of-mass motion of the electrons, which is not affected by the electron-electron interactions responsible for the fractional quantum Hall states. Note also that for moderate magnetic fields ($0.1 < B < 0.25$ T), the cavity sample displays a reduction of the amplitude of Shubnikov-de Haas oscillations with respect to the reference sample, as already evidenced and discussed in our previous study (21) (Fig. 2B, inset).

The experiments shown in Fig. 2 were repeated for a number of temperatures up to 1 K, which allowed us to extract the activation energies of the main transport features. The results (23) confirm the relative immunity toward vacuum fluctuations of the fractional quantum Hall features as compared to the integer ones.

Our experiments revealed that vacuum fluctuations, having been strongly enhanced in the gap of a metallic resonator, generate a long-range hopping that breaks the quantization of the resistance. The quantitative characterization of this phenomenon can be conveniently performed by adopting the formalism based on the Landauer-Büttiker edge state picture at integer filling factors (30). As shown schematically in Fig. 1A, in this theoretical framework, the deviation from quantization is interpreted by a finite transmission t_i of the highest populated edge state of section i of the conductor due to scattering of a fraction $(1 - t_i)$ to the other edge. The strength of the scattering for the edge state ν is related to the length L_i and the width w_i of the conductor, and to resistivity ρ_{xx}^ν , by the relation $t_i = 1/[1 + \rho_{xx}^\nu (L_i/w_i)]$. This model was successfully used to explain how the longitudinal resistance in the region between quantized plateaus depends on the geometry of the voltage probes (30).

In our case, we interpret ρ_{xx}^ν as the “resistivity” originating from the vacuum fluctuations, which concerns only the fraction of the conductor exposed to this field. Such an interpretation, however, requires that the rest of the conductor is in the quantum Hall regime, and as a result this analysis is only

performed in the middle of a quantum Hall plateau.

We implemented and solved the model in the case of a standard Hall bar with six contacts (23). The experimental inputs are the three length-to-width ratios describing the interaction of the vacuum field with the current, voltage probes as well as the main part of the Hall bar (designated \mathcal{G}_1 , \mathcal{G}_2 , and \mathcal{G}_3 , respectively, in Fig. 1A). Using these parameters, the measured values of the longitudinal resistances for the cavity sample are used to fit the relevant value of ρ_{xx}^ν , whereas the predicted values of the corresponding R_{xy} , calculated with our model, are displayed along with the experimental data in Fig. 2A.

The magnetic field values are chosen in the middle of the plateau measured on the reference sample. The impressive quantitative agreement between theory (orange points) and experiment (blue lines) for the Hall resistance is an indication that this model captures well the physics of our experiments and also has predictive power. The value of ρ_{xx}^ν is displayed as a function of the cyclotron energy of the corresponding plateau in Fig. 2C for values of the magnetic field corresponding to the center of the plateaus of the reference sample. The data align according to two groups of points. As is already obvious from the transverse and longitudinal Hall resistance data shown in Fig. 2, the values of ρ_{xx}^ν for odd plateaus are larger (by about two orders of magnitude) than the ones for even plateaus. However, both groups of points show a striking exponential dependence on the cyclotron energy, with a similar slope of ~ 0.4 meV. This observed overall exponential dependence on

the cyclotron energy is consistent with our model for the scattering because the latter involves the overlap between electronic wave functions, whose area naturally scales with the square of the magnetic length l_B^2 and therefore as $1/B$. As a result, the dependence on magnetic field is indeed expected to be the same for the even and odd plateaus, although their overall strengths differ because the Fermi energy is closer to the center of the broadened Landau band for the odd plateaus (27). Indeed, the Zeeman gap is $\sim 20\%$ of the cyclotron gap (19).

To further illustrate the consistency of the results, we report in Fig. 2C another set of data for ρ_{xx}^v taken from a different resonator on the same heterostructure material, having the same shape but with a different geometry of the voltage leads (blue dots). The results, although not identical, still exhibit the same behavior. Finally, on the same graph we also report the measured data for an identical resonator fabricated on a third high-mobility 2D electron gas (EV2124) with the same electron density but grown in a different molecular beam epitaxy reactor and exhibiting a mobility reduced by a factor of 8. Here again, comparable values are obtained, hence the scattering mechanism has a moderate dependence on the disorder.

The very strong increase of the cavity-mediated hopping as the Fermi energy is brought closer to the center of the Landau level, predicted theoretically (27), explains the strong difference in measured scattering rate between odd and even plateaus. Because our measurements of cavity-mediated hopping are performed with the chemical potential lying in the middle between the spin-split Landau bands, a modification of the relative magnitude of the Zeeman splitting with respect to the cyclotron energy should lead to a strong decrease of the cavity-mediated hopping as the Fermi energy is displaced farther away from the bulk Landau band. Such behavior has been tested experimentally by measuring the sample in a tilted field configuration (23).

As predicted by Eq. 1, cavity-mediated hopping is expected to increase strongly with the normalized light-matter coupling strength $\tilde{\Omega}_R/\omega_{\text{cav}}$. We investigated this dependence by designing a series of three cavities with the fundamental mode having the same frequency, but exhibiting different coupling strengths $\tilde{\Omega}_R/\omega_{\text{cav}} = 0.17, 0.2$, and 0.22 (23). As expected, a strong increase of the resistance is observed as a function of the light-matter coupling strength Ω_R , further demonstrating that the scattering originates from the coupling to the vacuum fields.

Finally, another possibility to study the dependence of the cavity-mediated hopping on the coupling is to modify the field distribution of the resonator modes inside the gap. Doing this in situ by approaching a metallic “tip” has

the advantage that, unlike the previous experiment, the experiment does not rely on comparing the transport data between different physical samples. We implemented this idea by approaching, in a controlled and repeatable way, a plane metallic surface in close proximity to the sample during the measurement of the magnetotransport (Fig. 3). Although the clear advantage of this experiment is that no reference sample is needed, it is difficult to exactly quantify the effect of the metallic plate on the light-matter coupling because it changes the local field profile and gradients in a non-trivial way. In Fig. 3 we plot the difference in the longitudinal and transverse Hall resistances when a piezoelectric positioner brings a gold metallic plane in close proximity to the resonator (200 nm) or farther away (3 μm) while the sample is kept at the base temperature. To achieve a better signal/noise ratio and to ensure that the changes were reproducible, we repeated the experiment 60 times. The averaged traces are shown in Fig. 3. Overall, the results show an increase of the cavity-induced scattering as the metallic plate is brought in proximity to the resonator. This shows that the dominant mechanism is the increase of the field gradients as the gap is reduced, rather than a change of the coupling strength Ω_R , as the latter would decrease with the gap.

Our results show that the vacuum field in a deeply subwavelength electromagnetic resonator produces a breakdown of the topological protection of the integer quantum Hall effect. The strong effect reported here on the quantum Hall plateaus and longitudinal resistance is such that one can legitimately wonder whether the much weaker vacuum fluctuations in free space might be what ultimately limits the extreme metrological precision of quantum Hall resistance standards. We note also that an additional vacuum field-induced mechanism for the breakdown of the topological quantization of conductance was recently proposed (31). The results of the present work demonstrate that vacuum field fluctuations can have a strong effect on transport even on topologically protected states. This is shown here in the case of the quantum Hall effect, but these results might have implications for a larger class of topologically protected states (32). An interesting possibility is the engineering of photon modes with larger field gradients, which would allow electromagnetic vacuum fields to be coupled more efficiently to fractional quantum Hall phases and would enable the study of cavity-mediated electron-electron interactions.

REFERENCES AND NOTES

1. P. Milonni, *The Quantum Vacuum: An Introduction to Quantum Electrodynamics* (Academic Press, 1994).
2. C. Riek et al., *Science* **350**, 420–423 (2015).

3. I.-C. Benea-Chelmus, F. F. Settembrini, G. Scalari, J. Faist, *Nature* **568**, 202–206 (2019).
4. F. J. Garcia-Vidal, C. Ciuti, T. W. Ebbesen, *Science* **373**, eabd0336 (2021).
5. H. Hübener et al., *Nat. Mater.* **20**, 438–442 (2021).
6. E. Orgiu et al., *Nat. Mater.* **14**, 1123–1129 (2015).
7. P. Bhatt, K. Kaur, J. George, *ACS Nano* **15**, 13616–13622 (2021).
8. S. Smolka et al., *Science* **346**, 332–335 (2014).
9. T. Smoleński et al., *Nature* **595**, 53–57 (2021).
10. Y. Todorov et al., *Phys. Rev. Lett.* **105**, 196402 (2010).
11. G. Scalari et al., *Science* **335**, 1323–1326 (2012).
12. P. Forn-Díaz, L. Lamata, E. Rico, J. Kono, E. Solano, *Rev. Mod. Phys.* **91**, 025005 (2019).
13. A. F. Kockum, A. Miranowicz, S. D. Liberato, S. Savasta, F. Nori, *Nat. Rev. Phys.* **1**, 19–40 (2019).
14. C. Ciuti, G. Bastard, I. Carusotto, *Phys. Rev. B* **72**, 115303 (2005).
15. F. Schlawin, A. Cavalleri, D. Jaksch, *Phys. Rev. Lett.* **122**, 133602 (2019).
16. A. Thomas et al., arXiv 1911.01459 (2019).
17. Y. Ashida et al., *Phys. Rev. X* **10**, 041027 (2020).
18. A. Thomas et al., *Nano Lett.* **21**, 4365–4370 (2021).
19. S. M. Girvin, K. Yang, *Modern Condensed Matter Physics* (Cambridge Univ. Press, 2019).
20. N. Bartolo, C. Ciuti, *Phys. Rev. B* **98**, 205301 (2018).
21. G. L. Paravicini-Bagliani et al., *Nat. Phys.* **15**, 186–190 (2018).
22. M. Büttiker, *Phys. Rev. B* **38**, 9375–9389 (1988).
23. See supplementary materials.
24. H.-T. Chen et al., *Opt. Express* **15**, 1084–1095 (2007).
25. C. Maissen et al., *Phys. Rev. B* **90**, 205309 (2014).
26. G. L. Paravicini-Bagliani et al., *Phys. Rev. B* **95**, 205304 (2017).
27. C. Ciuti, *Phys. Rev. B* **104**, 155307 (2021).
28. H. L. Stormer, D. C. Tsui, A. C. Gossard, *Rev. Mod. Phys.* **71**, S298–S305 (1999).
29. W. Kohn, *Phys. Rev.* **123**, 1242–1244 (1961).
30. P. L. McEuen et al., *Phys. Rev. Lett.* **64**, 2062–2065 (1990).
31. V. Rokaj et al., arXiv 2109.15075 (2021).
32. R. M. Lutchyn et al., *Nat. Rev. Mater.* **3**, 52–68 (2018).
33. F. Appugliese, ETH Research Collection entry www.research-collection.ethz.ch/handle/20.500.11850/519837 (2021).

ACKNOWLEDGMENTS

We thank J. Andberger for help in the initial stage of the project, P. Märki for technical support, and A. Imamoglu for discussions. **Funding:** Supported by the ERC Advanced grant Quantum Metamaterials in the Ultra Strong Coupling Regime (MUSiC) (grant 340975); the Swiss National Science Foundation (SNF) through the National Centre of Competence in Research Quantum Science and Technology (NCCR QSIT) as well as from the individual grant 200020_192330; and ANR project TRIANGLE (ANR-20-CE47-0011) and FET FLAGSHIP Project PhoQuS (grant agreement 820392) (C.C.). **Author contributions:** F.A. performed measurements, fabricated samples, analyzed the data, and wrote the paper; J.E. performed measurements, fabricated samples, contributed to data analysis, and wrote the paper. G.L.P.-B. performed early measurements and analyzed early results; C.R. and W.W. grew the epitaxial 2DEGs D and F; M.B. grew the epitaxial 2DEG EV; G.S. supported and designed experiments, setups, and samples and wrote the paper; C.C. developed the theory of cavity-induced electron hopping and wrote the paper; J.F. designed the experiments, analyzed the data, developed the model of the effect of the vacuum field on the resistance quantization, supervised the whole work, and wrote the paper. **Competing interests:** The authors declare no competing interests. **Data and materials availability:** Data that support the findings of this article and codes are available in the ETH Research Collection (33).

SUPPLEMENTARY MATERIALS

science.org/doi/10.1126/science.abl5818
Materials and Methods
Supplementary Text
Figs. S1 to S14
Tables S1 and S2
References (34–38)

23 July 2021; accepted 20 December 2021
10.1126/science.abl5818

MOLECULAR KNOTS

Vernier template synthesis of molecular knots

Zoe Ashbridge¹, Elisabeth Kreidt¹, Lucian Pirvu¹, Fredrik Schauffelberger¹, Joakim Halldin Stenlid^{2,3}, Frank Abild-Pedersen³, David A. Leigh^{1,4*}

Molecular knots are often prepared using metal helicates to cross the strands. We found that coordinatively mismatching oligodentate ligands and metal ions provides a more effective way to synthesize larger knots using Vernier templating. Strands composed of different numbers of tridentate 2,6-pyridinedicarboxamide groups fold around nine-coordinate lanthanide (III) ions to generate strand-entangled complexes with the lowest common multiple of coordination sites for the ligand strands and metal ions. Ring-closing olefin metathesis then completes the knots. A 3:2 (ditopic strand:metal) Vernier assembly produces $+3_1\#+3_1$ and $-3_1\#-3_1$ granny knots. Vernier complexes of 3:4 (tetrapotic strand:metal) stoichiometry selectively form a 378-atom-long trefoil-of-trefoils triskelion knot with 12 alternating strand crossings or, by using opposing stereochemistry at the terminus of the strand, an inverted-core triskelion knot with six alternating and six nonalternating strand crossings.

Entangling molecular strands that have robust backbones has two important consequences: (i) strand-crossing regions cannot pass through each other, blocking pathways to particular conformations and altering strand dynamics, and (ii) the structure becomes nontrivial in topological terms (i.e., each crossing can be over or under with respect to others), imparting additional stereochemical complexity (1, 2). Consequently, systematic strand entanglements affect the characteristics and function of DNA (3), RNA (4), and proteins (5). Synthetic molecular knots with relatively simple topologies (6–31), e.g., trefoils (three crossings) and pentafoils (five crossings), show promising properties for anion binding (6, 7), membrane transport (8), catalysis (9, 10), materials (11), nanotherapeutics (12), and the kinetic stabilization of supramolecular structures (13). Examples of extended periodic entanglements, such as two-dimensional (2D) molecularly woven polymers (32–34), 3D woven covalent organic frameworks (35, 36), and polycatenanes (37), have also been described. The use of circular (16, 17) metal helicates offers a route to rotationally symmetric topologies with up to nine crossings. However, the internal angle between building blocks increases with cyclic array size, which can prove difficult to reconcile with normal bond angles and conformations, and to date, the only known circular helicates with more than six crossings have been derived from DNA or peptides. Accordingly, there are no strategies for synthesizing branched or extended arrays of the systematic molecular

entanglements necessary for larger knotted structures and assemblies (2).

Vernier complexes (38–45) are formed when the number of binding sites on one component of a supramolecular complex is not an integer multiple of the number of complementary binding sites on another (Fig. 1). The mismatch favors an assembly that has a number of binding sites equal to the lowest common multiple of the numbers of sites on both components. Vernier templating has been used to form discrete multicomponent assemblies of precise size and composition from much simpler building blocks (38–44), including linear duplexes (39, 40, 44, 45) and very large (156- to 312-atom-long loop) but topologically trivial macrocycles (41–43). Trefoil knots have previously been synthesized through the coordination of a lanthanide (III) ion to a single tritopic ligand strand incorporating three covalently tethered 2,6-pyridinedicarboxamide (pdc) (46, 47) binding sites (10, 13, 48). We reasoned that combining lanthanide ions with ligand strands containing a mismatched number of pdc sites, e.g., ditopic or tetrapotic strands, might generate discrete, large-but-finite extended structures (Fig. 1). However, it was unclear whether such relatively weakly binding, coordinatively mismatched strands would be able to pay the entropic cost of forming a single, discrete multicomponent complex, particularly one requiring ordered entanglements. Furthermore, although point chirality of the pdc units controls the topological chirality of trefoil knots when folding a single ligand strand (Fig. 1A) (10, 13, 48), it would be more demanding to do so with multiple strands entwined around and between multiple metal ions.

Ditopic ligand strand ($(R)_4\text{-L1}$), where (R)₄ refers to the four (R)-configured asymmetric centers of the two pdc units, was synthesized as described in the supplementary materials (section 4). Three molar equivalents of (R)₄-L1 were treated with two molar equivalents

of $\text{Lu}(\text{CF}_3\text{SO}_3)_3$ at 80°C in MeCN (Fig. 2A). A 3:2 strand:metal ion Vernier complex $((R)_4\text{-L1})_3\cdot[\text{Lu}]_2$ formed gradually over 3 days, as evidenced by electrospray ionization mass spectrometry (ESI-MS, m/z $((R)_4\text{-L1})_3\cdot[\text{Lu}]_2$ $[\text{CF}_3\text{SO}_3]_3^{3+}$ 1554.9, etc.; fig. S78) and ¹H nuclear magnetic resonance (NMR) spectroscopy (Fig. 2C). Compared with the folding of an overhand trefoil knot (10, 48), the formation of an open granny knot complex would likely require considerably more miscoordinated and misfolded intermediates to be unraveled and error corrected during the thermodynamically controlled assembly process. This complexity is reflected in the approximately sixfold increase in reaction time necessary to form $((R)_4\text{-L1})_3\cdot[\text{Lu}]_2$ compared with open trefoil knots tied by Ln-coordinated entangling of a single strand (10, 11, 13, 48).

The ¹H NMR spectrum of $((R)_4\text{-L1})_3\cdot[\text{Lu}]_2$ shows distinctive features characteristic of an entangled geometry (10, 11, 13, 48), such as a large upfield shift of the pyridine protons H_A and H_B caused by the shielding effects of enforced proximity to the electron-rich naphthol groups (Fig. 2C). Two sets of strand signals in a 2:1 ratio, e.g., H_A at 6.0 and 7.0 ppm, result from the structure of the Vernier assembly. Pyridine protons (e.g., H_A) of the two wrapping strands of the open knot (blue and orange strands in Fig. 2C) are less shielded than those of the wrapped strand (green), likely because of the increased conformational freedom at the strands' termini and the different pinching effect of the glycol linker (48). The substantial diastereotopic splitting of H_B and H_D indicate that protons in the open granny knot experience a stronger influence of the chiral environment than the symmetrical (other than the point-chiral centers) uncoordinated strands. Diffusion-ordered spectroscopy (DOSY) confirmed that a single species was present at the end of the Vernier assembly process (fig. S64).

The Vernier complex $((R)_4\text{-L1})_3\cdot[\text{Lu}]_2$ has six pendant terminal alkenes positioned for three sets of ring-closing olefin metathesis (RCM). Upon the addition of a Hoveyda-Grubbs second-generation catalyst (49) to $((R)_4\text{-L1})_3\cdot[\text{Lu}]_2$ in $\text{CH}_2\text{Cl}_2/\text{CH}_3\text{NO}_2$ (1:1, v/v) at 50°C, the closed-loop granny knot $(\Lambda_2)\text{-1}\cdot[\text{Lu}]_2$ formed as a single diastereomer (Fig. 2A). The mass spectrum of $(\Lambda_2)\text{-1}\cdot[\text{Lu}]_2$ confirmed the loss of three molecules of ethene from $((R)_4\text{-L1})_3\cdot[\text{Lu}]_2$ (m/z $(\Lambda_2)\text{-1}\cdot[\text{Lu}]_2$ $[\text{CF}_3\text{SO}_3]_3^{5+}$ 826.8, etc.; fig. S80), with good correlation between the calculated and the observed isotope distributions (Fig. 2F). The ¹H NMR spectrum of $(\Lambda_2)\text{-1}\cdot[\text{Lu}]_2$ (Fig. 2D) is consistent with the increased conformational restriction of the closed-loop knot and greater similarity of connections between the pdc environments.

The metal-coordinated granny knot $(\Lambda_2)\text{-1}\cdot[\text{Lu}]_2$ was treated with tetraethylammonium

¹Department of Chemistry, University of Manchester, Oxford Road, Manchester M13 9PL, UK. ²SUNCAT Center for Interface Science and Catalysis, Department of Chemical Engineering, Stanford University, Stanford, CA 94305, USA.

³SUNCAT Center for Interface Science and Catalysis, SLAC National Accelerator Laboratory, Menlo Park, CA 94025, USA. ⁴School of Chemistry and Molecular Engineering, East China Normal University, Shanghai 200062, China.

*Corresponding author. Email: david.leigh@manchester.ac.uk

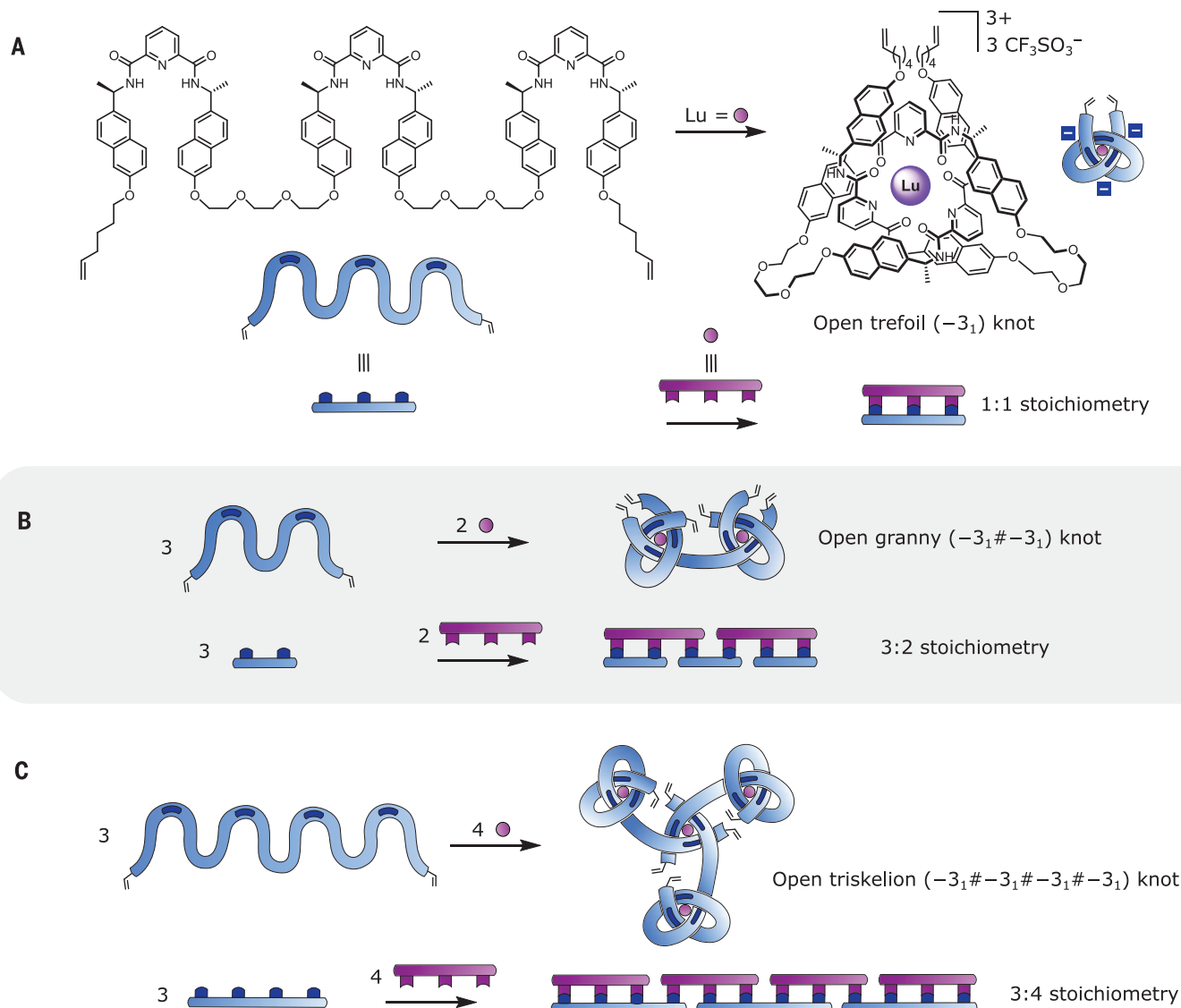


Fig. 1. Vernier template strategy for the synthesis of large molecular knots with extended arrays of entanglements. Discrete supramolecular assemblies produced by (nine-coordinate) lanthanide (III) ions (purple) binding to (tridentate) pdc sites (dark blue bars) in ligand strands (light blue). The mechanical stereochemistry of the strand crossings is programmed by the chirality of the pdc groups [dark blue bars indicate (*R*)-configured chiral centers; red bars in other figures indicate (*S*)-configuration]. The minus signs

in the blue squares refer to the stereochemistry of the strand crossing formed, not to charges. **(A)** A 1:1 ratio of a single tritopic (i.e., three pdc sites) ligand to lutetium (III) ions generates a -3_1 overhand (open trefoil) knot (10). **(B)** A 3:2 ratio of ditopic ligand to metal ions gives a $-3_1\#-3_1$ open granny knot. **(C)** A 3:4 ratio of tetratopic ligand to metal ions gives a $-3_1\#-3_1\#-3_1\#-3_1$ open triskelion knot. Diagrams of the analogous linear Vernier complexes are shown below each knot.

fluoride (Et_4NF), and the resulting demetalated knot was isolated by size-exclusion chromatography to give $(\Lambda_2)\text{-1}$ in 14% yield over three steps. The ^1H NMR spectrum of granny knot $(\Lambda_2)\text{-1}$ is broad (Fig. 2E), consistent with chain reptation (50) in a tightly knotted compound (17), with the spectrum becoming less broadened at elevated temperatures (fig. S72). The matrix-assisted laser desorption/ionization-time-of-flight (MALDI-TOF) mass spectrum confirmed the metal-free knot to be a single species of the expected molecular mass, confirming that the three starting organic building

blocks of $(R)_4\text{-1}$ had been incorporated into one continuous closed-loop strand (fig. S82). The metal-coordinated granny knot $(\Lambda_2)\text{-1}\cdot[\text{Lu}]_2$ could subsequently be reformed by treating $(\Lambda_2)\text{-1}$ with $\text{Lu}(\text{CF}_3\text{SO}_3)_3$ at 80°C in MeCN for 16 hours (supplementary materials, section 6.3, and fig. S21). The enantiomeric granny knot $(\Lambda_2)\text{-1}$ was prepared in analogous fashion from building block $(S)_4\text{-1}$ (supplementary materials, section 6.4). Circular dichroism (CD) spectroscopy confirmed that the Vernier template syntheses of $(\Lambda_2)\text{-1}\cdot[\text{Lu}]_2$ and $(\Lambda_2)\text{-1}\cdot[\text{Lu}]_2$ proceeded with complete topological stereo-

selectivity, with their mirror-image chirality shown by the inverted exciton coupling maxima (Fig. 2G).

Encouraged by these results, we explored increasing the topological complexity through the use of tetratopic ligand strands. These ligands set up conditions for a coordinative mismatch with a lowest common multiple of 12. Complexing four lanthanide (III) ions with three tetratopic ligand strands should form a $3_1\#3_1\#3_1\#3_1$ open-knot Vernier complex [the # symbol denotes the connection of tangles, in this case 3_1 , in the nomenclature for

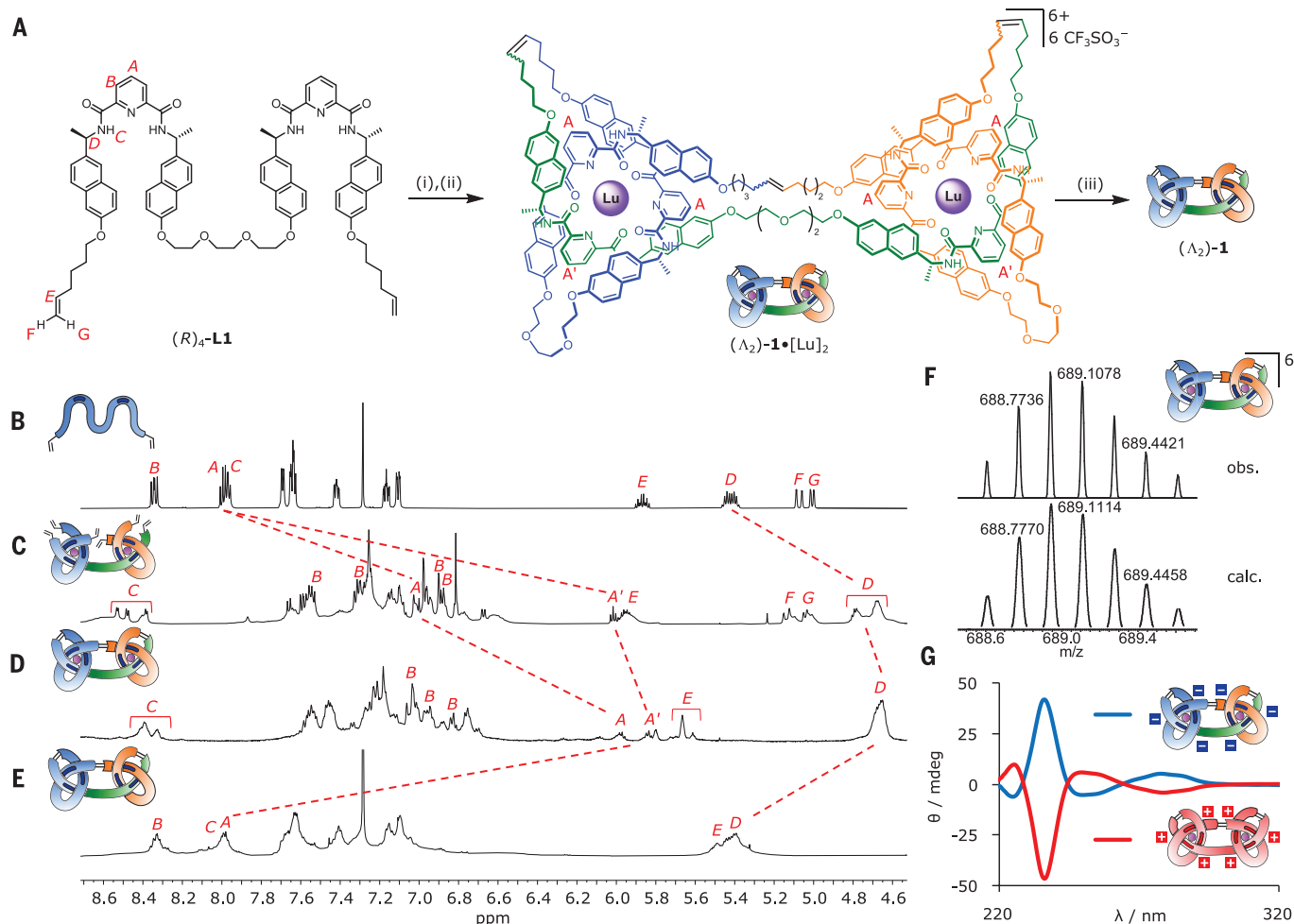


Fig. 2. Vernier (3:2, strand:metal ion) template synthesis of molecular granny knots. (A) Reaction conditions: (i) $\text{Lu}(\text{CF}_3\text{SO}_3)_3$, MeCN, 80°C, 72 hours; (ii) Hoveyda-Grubbs second-generation catalyst, $\text{CH}_2\text{Cl}_2/\text{CH}_3\text{NO}_2$ (1:1, v/v), 50°C, 16 hours; and (iii) Et_4NF , MeCN, room temperature, 1 hour, 14% over three steps. (B to E) Partial ^1H NMR spectra (600 MHz, 298 K) of granny knots and ligand precursor: (B) ditopic ligand $(R)_4\text{-L1}$ (CDCl_3); (C) metal-coordinated open granny knot $((R)_4\text{-L1})_3 \cdot [\text{Lu}]_2$ (CD_3CN); (D) metal-coordinated granny knot $(\Lambda_2)\text{-1} \cdot [\text{Lu}]_2$ (CD_3CN); and (E) organic granny knot $(\Lambda_2)\text{-1}$ (CDCl_3). Selected

spectral assignments correspond to proton labeling in (A). Full assignments can be found in the supplementary materials. (F) High-resolution ESI-MS(+) of closed granny knot $(\Lambda_2)\text{-1} \cdot [\text{Lu}]_2$ comparing the observed spectrum (top) with the calculated isotopic distribution of $[\text{M}-6(\text{CF}_3\text{SO}_3)]^{6+}$ (bottom). (G) Overlaid circular dichroism spectra of granny knots $(\Lambda_2)\text{-1} \cdot [\text{Lu}]_2$ (blue) and $(\Lambda_2)\text{-1} \cdot [\text{Lu}]_2$ (red), (0.05 mM, MeCN), normalized for absorbance. The minus and plus signs in the blue and red squares refer to the stereochemistry of the strand crossings, not to charges.

composite knots (5I)], which could be covalently captured to yield a trefoil-of-trefoils triskelion knot (Fig. 1C). We postulated that this assembly would most likely occur in a stepwise fashion in which a single ligand first folds and entangles around one lanthanide (III) ion, leaving a loose end containing one pdc unit. Several factors (e.g., the entropic cost of lost flexibility of the strand end and stabilizing π -stacking interactions) indicate that the structure with a free pdc site at the strand terminus should be thermodynamically favored over an uncoordinated internal pdc unit; proton NMR confirmed this to be the case (supplementary materials, section 12). Three such intermediates can bind to a fourth lanthanide ion, forming a central trimeric circular helicate, with the resulting Vernier complex fulfilling the coordi-

nation requirements for three ligand strands and four metal ions (Fig. 1C).

Tetrapotic ligand strand $(R)_8\text{-L2}$ was synthesized as detailed in the supplementary materials (section 4). Treatment of $(R)_8\text{-L2}$ with either $\text{Lu}(\text{CF}_3\text{SO}_3)_3$ or $\text{Yb}(\text{CF}_3\text{SO}_3)_3$ in a 3:4 strand:metal ratio at 80°C in MeCN generated the corresponding Vernier open triskelion complexes $((R)_8\text{-L2})_3 \cdot [\text{Lu}/\text{Yb}]_4$ in 7 days (Fig. 3A). The ESI mass spectrum of $((R)_8\text{-L2})_3 \cdot [\text{Lu}]_4$ confirmed a 3:4 ligand-to-metal ratio (m/z $((R)_8\text{-L2})_3 \cdot [\text{Lu}]_4[\text{CF}_3\text{SO}_3]_7^{5+}$ 1865.7, etc.; fig. S84), with good correlation between calculated and observed isotope distributions (Fig. 3B). DOSY showed the Vernier complexes to be single discrete species (fig. S68).

The ^1H NMR spectrum of $((R)_8\text{-L2})_3 \cdot [\text{Lu}]_4$ is broad but shows characteristic upfield shifts

of pyridine protons H_A and H_B upon entanglement (Fig. 4C), similar to those of the open granny knot $((R)_4\text{-L1})_3 \cdot [\text{Lu}]_2$ (Fig. 2C). Both the threefold molecular symmetry of the triskelion complex and the difference in structure between the central and outer entanglement arrays are apparent from the paramagnetic shifts in the ^1H NMR spectrum of $((R)_8\text{-L2})_3 \cdot [\text{Yb}]_4$ (Fig. 3C and supplementary materials, section 15). The pseudocontact shifts of nuclei close to paramagnetic lanthanide ions are highly sensitive to both the relative spatial arrangement of the observed nucleus and the lanthanide, and to the magnetic anisotropy of the lanthanide (which depends on its ligand field) (52, 53). The magnetic anisotropy of a specific lanthanide can be visualized by a tensor, and individual isosurfaces of such a tensor

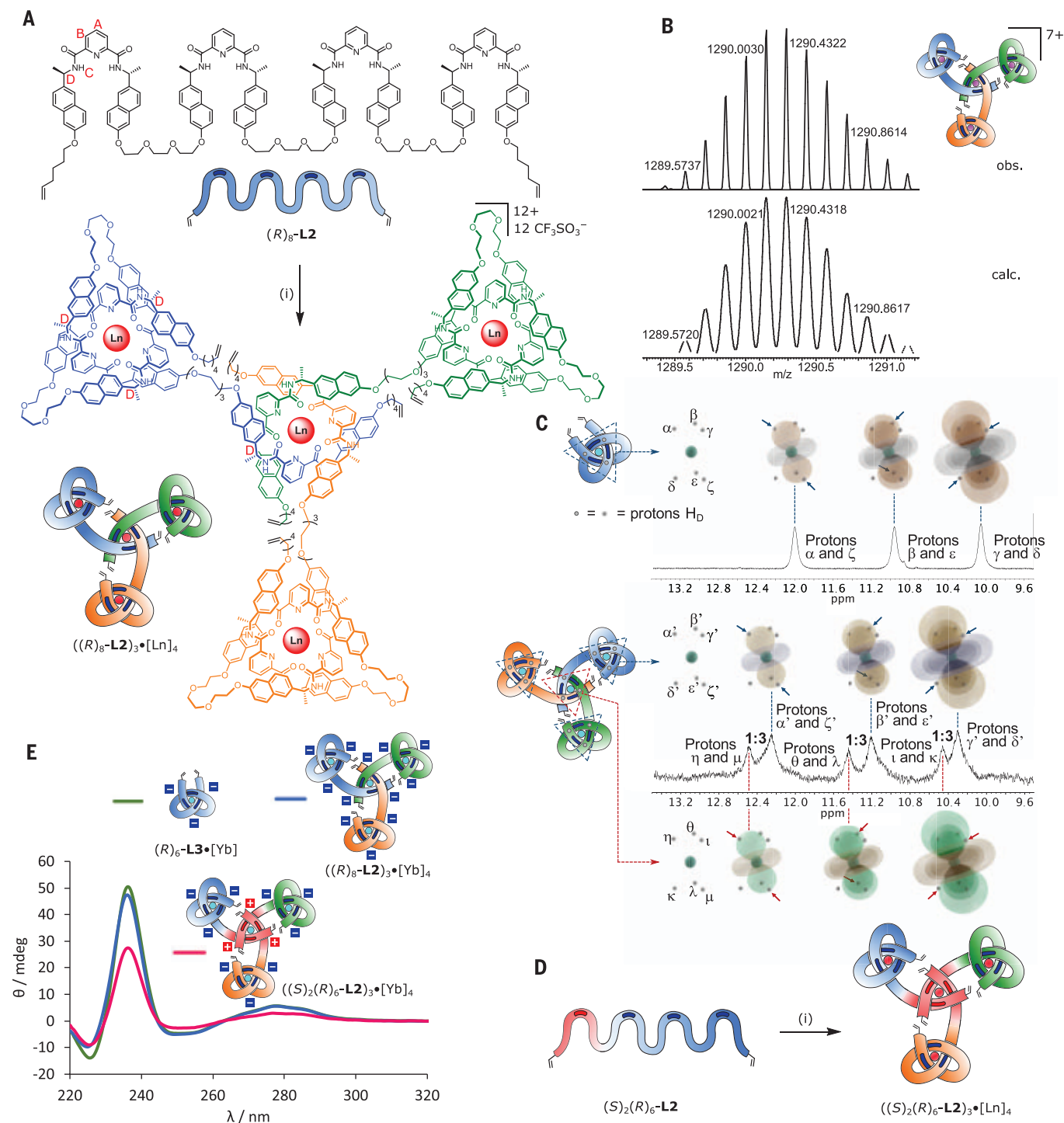


Fig. 3. Vernier (3:4, strand:metal ion) template synthesis of 12-crossing molecular triskelion open-knot complexes. (A) Vernier assembly of triskelion open-knot complex $((R)_8\text{-L2})_3\cdot[\text{Ln}]_4$. Reaction conditions: $\text{Ln}(\text{CF}_3\text{SO}_3)_3$, MeCN, 80°C , 7 days. (B) High-resolution ESI-MS(+) of $((R)_8\text{-L2})_3\cdot[\text{Lu}]_4$ showing the observed distribution (top) and the calculated isotopic distribution (bottom) of $[\text{M}-7(\text{CF}_3\text{SO}_3)]^{7+}$. (C) Partial ^1H NMR spectra (CD_3CN , 600 MHz, 298 K) of open trefoil knot $(R)_6\text{-L3}\cdot[\text{Yb}]$ (top) and open triskelion knot $((R)_8\text{-L2})_3\cdot[\text{Yb}]_4$ (bottom) showing the paramagnetic shifted H_D protons. Protons located on the most compact isoshift surface of the tensor experience the largest shift; protons on the most expanded isoshift surface experience

the smallest shift. The observed pattern for $((R)_8\text{-L2})_3\cdot[\text{Yb}]_4$ reflects the geometry and topology of the complex (supplementary materials, section 8). (D) Vernier assembly of inverted core triskelion open-knot complex $((S)_2(R)_6\text{-L2})_3\cdot[\text{Ln}]_4$. Reaction conditions: $\text{Ln}(\text{CF}_3\text{SO}_3)_3$, MeCN, 80°C , 7 days. (E) Overlaid circular dichroism spectra of Yb(III) triskelion open-knot complexes and inverted core triskelion open-knot and overhand knot: $(R)_6\text{-L3}\cdot[\text{Yb}]$ (green), $((R)_8\text{-L2})_3\cdot[\text{Yb}]_4$ (blue), and $((S)_2(R)_6\text{-L2})_3\cdot[\text{Yb}]_4$ (red). (0.05 mM, MeCN), normalized for absorbance. The minus and plus signs in the blue and red squares refer to the stereochemistry of the strand crossings, not to charges.

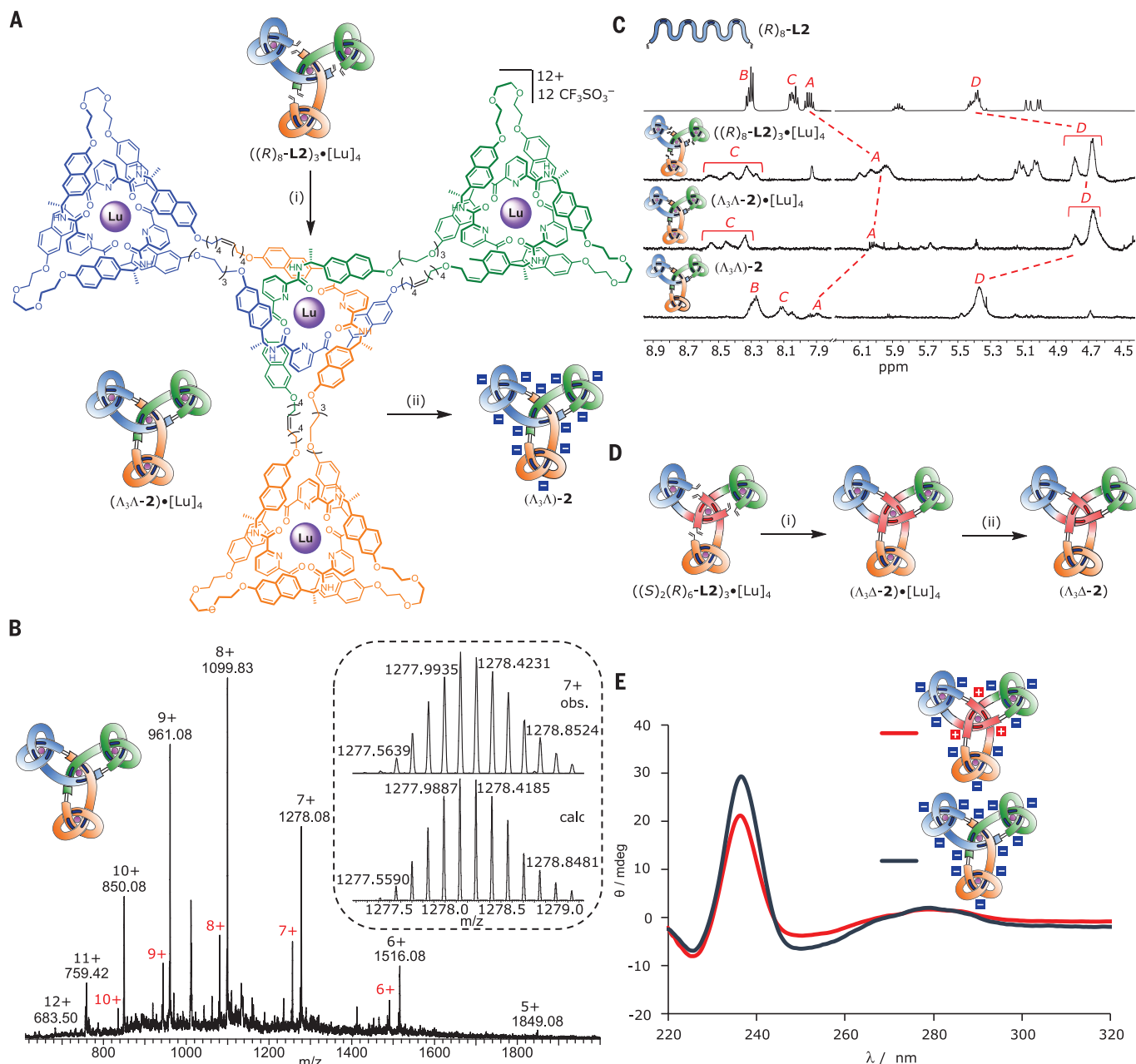


Fig. 4. Formation of closed-loop 12-crossing molecular triskelion knots.

(A) Reaction conditions: (i) Hoveyda-Grubbs second-generation catalyst, $\text{CH}_2\text{Cl}_2/\text{CH}_3\text{NO}_2$ (1:1, v/v), 50°C, 16 hours, and (ii) Et_4NF , MeCN, room temperature, 1 hour, 6% over three steps. **(B)** Low-resolution ESI-MS(+) of closed triskelion knot $(\Lambda_3\Lambda\text{-2}) \cdot [\text{Lu}]_4$, with ions observed either as $[\text{M}-n(\text{CF}_3\text{SO}_3)]^{n+}$ adducts (black) or $[\text{M}-(n+1)(\text{CF}_3\text{SO}_3)+\text{H}]^{n+}$ adducts (red). Inset: Comparison of observed high-resolution spectrum (top) with the calculated isotopic distribution of $[\text{M}-7(\text{CF}_3\text{SO}_3)]^{7+}$ (bottom). **(C)** Partial ^1H NMR spectra (600 MHz, 298 K) of triskelion knot and ligand precursor: $(R)_8\text{-L2}$ (CDCl_3), $((R)_8\text{-L2})_3 \cdot [\text{Lu}]_4$ (MeCN), $(\Lambda_3\Lambda\text{-2}) \cdot [\text{Lu}]_4$

(MeCN), and $(\Lambda_3\Lambda\text{-2}) \cdot [\text{Lu}]_4$ (CDCl_3). Spectral assignments correspond to proton labeling in Fig. 3A. Full assignments can be found in the supplementary materials. **(D)** Reaction conditions: (i) Hoveyda-Grubbs second-generation catalyst, $\text{CH}_2\text{Cl}_2/\text{CH}_3\text{NO}_2$ (1:1, v/v), 50°C, 16 hours, and (ii) Et_4NF , MeCN, room temperature, 1 hour, 8% over three steps. **(E)** Overlaid circular dichroism spectra of remetallated triskelion knots $(\Lambda_3\Lambda\text{-2}) \cdot [\text{Lu}]_4$ (blue) and $(\Lambda_3\Lambda\text{-2}) \cdot [\text{Lu}]_4$ (red) (0.05 mM, MeCN), normalized for absorbance. The minus and plus signs in the blue and red squares refer to the stereochemistry of the strand crossings, not to charges.

relate to certain pseudocontact shifts of nuclei located on these surfaces. Nuclei located on the same isosurface experience the same pseudocontact shift. In a Yb (III)-coordinated control compound (open trefoil complex $(R)_6\text{-L3} \cdot [\text{Yb}]$), the H_D protons bound to the carbon stereocenters, identified by heteronuclear

single quantum coherence correlation (fig. S127), appear as three, equal-intensity, strongly shifted signals (Fig. 3C, top spectrum). This feature indicates that the six H_D protons are located pairwise on three different isosurfaces of the tensor. In the Yb (III) open triskelion complex $((R)_8\text{-L2})_3 \cdot [\text{Yb}]_4$, the H_D protons ap-

pear as two sets of three signals in a 1:3 intensity ratio (Fig. 3C, bottom spectrum), with the most intense set of signals almost coincident with the chemical shifts of those of the open trefoil complex $(R)_6\text{-L3} \cdot [\text{Yb}]$. The 1:3 ratio reflects both the central:outer ratio of metal environments in the open triskelion knot and

the symmetry of the supramolecular Vernier complex. The 1:3 ratio of environments also rules out alternative structures, such as a cyclic tetra-trefoil shield knot (supplementary materials, section 12) or link-like assemblies in which the pdc unit of a strand used to bind the bridging second metal ion is one of the internal sites.

The open-knot Vernier complexes were also characterized by circular dichroism (Fig. 3E). The overall appearance of the CD spectrum of the open triskelion complex $((R)_8\text{-}\mathbf{L2})_3\cdot[\text{Yb}]_4$ (blue) closely resembles that of the Λ -open trefoil complex $(R)_6\text{-}\mathbf{L3}\cdot[\text{Yb}]$ (green), and the spectra are almost identical when normalized for the fourfold number of chromophores in $((R)_8\text{-}\mathbf{L2})_3\cdot[\text{Yb}]_4$. The small differences between the two can be attributed to the different chiral expression of the central entangled feature of $((R)_8\text{-}\mathbf{L2})_3\cdot[\text{Yb}]_4$, which lacks the folded loops of the outer trefoil tangles (48).

Multiple tethered pdc groups cannot assemble around a single lanthanide (III) ion with tethered pdc groups of opposing stereochemistry because of steric clashes (supplementary materials, section 5). Because strand-crossing stereochemistry is governed by the point chirality in the pdc groups, this offers the possibility of a new element of selection and control in assembling Vernier complexes. To explore this, we prepared a diastereomeric ligand strand of $(R)_8\text{-}\mathbf{L2}$ in which one terminal pdc unit had the (S,S) -stereochemistry, namely $(S)_2(R)_6\text{-}\mathbf{L2}$ (supplementary materials, section 4). Treatment of $(S)_2(R)_6\text{-}\mathbf{L2}$ with $\text{Lu}(\text{CF}_3\text{SO}_3)_3$ or $\text{Yb}(\text{CF}_3\text{SO}_3)_3$ in a 3:4 strand:metal ion ratio at 80°C in MeCN generated the corresponding Vernier open inverted core triskelion complexes $((S)_2(R)_6\text{-}\mathbf{L2})_3\cdot[\text{Lu}]_4$ and $((S)_2(R)_8\text{-}\mathbf{L2})_3\cdot[\text{Yb}]_4$ over 7 days (Fig. 3D). Mass spectrometry confirmed the 3:4 ligand-to-metal ratio of the resulting supramolecular structures (fig. S25).

The CD spectrum of $((S)_2(R)_6\text{-}\mathbf{L2})_3\cdot[\text{Yb}]_4$ (Fig. 3E, red) is consistent with the structure being the inverted core triskelion knot with three outer Λ entanglements and a central Δ entanglement. The inverted exciton coupling of the central Δ entanglement compensates for the intensity of the coupling of one of the outer Λ entanglements, leading to an intensity for the inverted core triskelion of approximately half that of the all- Λ open triskelion complex $((R)_8\text{-}\mathbf{L2})_3\cdot[\text{Yb}]_4$ (Fig. 3E, red).

Closure of $((R)_8\text{-}\mathbf{L2})_3\cdot[\text{Lu}]_4$ by RCM, subsequent demetallation by Et_4NF , and size-exclusion chromatography gave the metal-free organic knot $(\Lambda_3\Lambda)\text{-}\mathbf{2}$ in 6% isolated yield over three steps (Fig. 4A) as a single species as determined by DOSY (fig. S70). The broadness of the ^1H NMR spectrum of $(\Lambda_3\Lambda)\text{-}\mathbf{2}$ (Fig. 4C) only reduced noticeably at 348 K (fig. S73), reflecting the degree and congestion of strand entanglement. The most abundant ion in the MALDI-TOF spectrum at m/z 7535 corresponds

to the organic knot (fig. S88). The isolated organic knot could be remetalated by treatment with an excess of $\text{Lu}(\text{CF}_3\text{SO}_3)_3$ over 48 hours in MeCN/ CDCl_3 (4:1, v/v) to form $(\Lambda_3\Lambda)\text{-}\mathbf{2}\cdot[\text{Lu}]_4$ in 92% yield (supplementary materials, section 7.3). ESI-MS of the regenerated $(\Lambda_3\Lambda)\text{-}\mathbf{2}\cdot[\text{Lu}]_4$ shows a pristine spectrum with molecular ion charges ranging from 12+ to 5+ (Fig. 4B). The corresponding inverted core triskelion complex $((S)_2(R)_6\text{-}\mathbf{L2})_3\cdot[\text{Lu}]_4$ was also closed by RCM and demetalated by Et_4NF to give $(\Lambda_3\Delta)\text{-}\mathbf{2}$ (Fig. 4D). The normalized CD spectrum of closed knot $(\Lambda_3\Delta)\text{-}\mathbf{2}\cdot[\text{Lu}]_4$ shows the expected reduction in intensity compared with $(\Lambda_3\Lambda)\text{-}\mathbf{2}\cdot[\text{Lu}]_4$ as a result of the chirality of the central Δ -handed fragment (Fig. 4E and supplementary materials, section 11).

Although the triskelion knot $(\Lambda_3\Lambda)\text{-}\mathbf{2}$ and inverted core triskelion knot $(\Lambda_3\Delta)\text{-}\mathbf{2}$ both have 12 crossings, their topologies are distinctly different. Triskelion knot $(\Lambda_3\Lambda)\text{-}\mathbf{2}$ has 12 alternating crossings, meaning that for each crossing, the thread must formally traverse from one face of the loop to the other and back again; however, $(\Lambda_3\Delta)\text{-}\mathbf{2}$ has six alternating and six nonalternating crossings, the latter crossings achievable by the strand lying across two adjacent sections of the loop. This greatly affects the intrinsic tightness of the isomeric knots, as reflected in their approximate hydrodynamic radii measured by DOSY ($(\Lambda_3\Lambda)\text{-}\mathbf{2}$ 2.03 nm, $(\Lambda_3\Delta)\text{-}\mathbf{2}$ 2.73 nm, CDCl_3 , 298 K; supplementary materials, section 9.2, and table S3).

The C_3 -symmetric triskelion conformation of $(\Lambda_3\Lambda)\text{-}\mathbf{2}\cdot[\text{Lu}]_4$ was calculated to be ~150 kcal/mol more stable than other tangled conformers (supplementary materials, section 14), a symmetry consistent with the 1:3 signal intensities observed for the H_D protons in the ^1H NMR spectrum of $((R)_8\text{-}\mathbf{L2})_3\cdot[\text{Yb}]_4$. The stability was estimated by condensed-phase hybrid density-functional theory calculations [PCM-B3LYP-D3(BJ)/def2-SV(P), with effective core potentials for Lu, using ORCA 4.2.1] on low-energy structures identified by an extensive simulated annealing-based structural search protocol (28) (supplementary materials, section 14). Other than being flexible about the chains that link the trefoil tangles to the central core, the metal-coordinated triskelion knot adopts a well-defined 2D conformation despite being composed of a single continuous self-entangled 1D strand. We note a fundamental similarity to the structure of knitted materials (54), which arise from the systematic self-entanglement of a single 1D strand in a pattern that results in a 2D layer that can adopt complex 3D curvature (like a knitted hat or sweater). This differs from weaving (32–36), which results in the periodic mutual entanglement of multiple 1D strands.

In summary, Vernier template synthesis is a powerful tool for constructing large molecular structures with complex systematic networks of entanglements. Granny knots (six

alternating crossings) were accessed from a 3:2 Vernier complex, and a triskelion knot with 12 alternating crossings and an inverted-core triskelion knot with six alternating and six nonalternating crossings was accessed from 3:4 Vernier complexes. The latter, 378-atom-long closed-loop knots (~40 nm strand length) are among the largest discrete macrocycles synthesized to date, with the added complexity of defined sequences of stereocontrolled strand entanglements, the precise topology affecting the structure and properties of the resulting knots. Both types of triskelion knot topologies are common motifs in extended Hiberno-Saxon knotwork and interlace (55). The ability to synthesize large, hierarchically knotted molecular architectures with precise control of entanglements, crossing stereochemistry, and overall symmetry presents opportunities and research directions for topological molecules and materials.

REFERENCES AND NOTES

- S. D. P. Fielden, D. A. Leigh, S. L. Woltering, *Angew. Chem. Int. Ed.* **56**, 11166–11194 (2017).
- J. F. Stoddart, *Nano Lett.* **20**, 5597–5600 (2020).
- D. Meluzzi, D. E. Smith, G. Arya, *Annu. Rev. Biophys.* **39**, 349–366 (2010).
- M. Zhao, M. T. Woodside, *Nat. Chem. Biol.* **17**, 975–981 (2021).
- N. C. H. Lim, S. E. Jackson, *J. Phys. Condens. Matter* **27**, 354101 (2015).
- J.-F. Ayme et al., *J. Am. Chem. Soc.* **137**, 9812–9815 (2015).
- R. A. Bilbeisi et al., *Chem. Sci.* **7**, 2524–2531 (2016).
- D. P. August et al., *J. Am. Chem. Soc.* **142**, 18859–18865 (2020).
- V. Marcos et al., *Science* **352**, 1555–1559 (2016).
- G. Gil-Ramirez et al., *J. Am. Chem. Soc.* **138**, 13159–13162 (2016).
- N. Katsonis et al., *Nat. Chem.* **12**, 939–944 (2020).
- F. Benyettou et al., *Chem. Sci.* **10**, 5884–5892 (2019).
- D. A. Leigh, L. Pirvu, F. Schaufelberger, D. J. Tetlow, L. Zhang, *Angew. Chem. Int. Ed.* **57**, 10484–10488 (2018).
- C. O. Dietrich-Buchecker, J.-P. Sauvage, *Angew. Chem. Int. Ed.* **28**, 189–192 (1989).
- J.-P. Sauvage, *Angew. Chem. Int. Ed.* **56**, 11080–11093 (2017).
- J.-F. Ayme et al., *Nat. Chem.* **4**, 15–20 (2011).
- J. J. Danon et al., *Science* **355**, 159–162 (2017).
- J. P. Carpenter et al., *Chem* **7**, 1534–1543 (2021).
- Y. Inomata, T. Sawada, M. Fujita, *Chem* **6**, 294–303 (2020).
- Y. Inomata, T. Sawada, M. Fujita, *J. Am. Chem. Soc.* **143**, 16734–16739 (2021).
- H.-N. Zhang, W.-X. Gao, Y.-J. Lin, G.-X. Jin, *J. Am. Chem. Soc.* **141**, 16057–16063 (2019).
- L.-L. Dang, H.-J. Feng, Y.-J. Lin, G.-X. Jin, *J. Am. Chem. Soc.* **142**, 18946–18954 (2020).
- Z. Cui, Y. Lu, X. Gao, H.-J. Feng, G.-X. Jin, *J. Am. Chem. Soc.* **142**, 13667–13671 (2020).
- D. A. Leigh et al., *Nat. Chem.* **13**, 117–122 (2021).
- Y. Segawa et al., *Science* **365**, 272–276 (2019).
- H. Adams et al., *Nature* **411**, 763 (2001).
- P. E. Barran et al., *Angew. Chem. Int. Ed.* **50**, 12280–12284 (2011).
- D. A. Leigh et al., *Nature* **584**, 562–568 (2020).
- J. Brüggenmann et al., *Angew. Chem. Int. Ed.* **46**, 254–259 (2007).
- N. Ponnuswamy, F. B. L. Cougnon, J. M. Clough, G. D. Pantoş, J. K. M. Sanders, *Science* **338**, 783–785 (2012).
- F. B. L. Cougnon, K. Caprice, M. Pupier, A. Bauzá, A. Frontera, *J. Am. Chem. Soc.* **140**, 12442–12450 (2018).
- U. Lewandowska et al., *Nat. Chem.* **9**, 1068–1072 (2017).
- Z. Wang et al., *Nat. Commun.* **8**, 14442 (2017).
- D. P. August et al., *Nature* **588**, 429–435 (2020).
- Y. Liu et al., *Science* **351**, 365–369 (2016).
- Y. Liu et al., *J. Am. Chem. Soc.* **140**, 16015–16019 (2018).
- Q. Wu et al., *Science* **358**, 1434–1439 (2017).
- J. S. Lindsey, *New J. Chem.* **15**, 153–180 (1991).
- T. R. Kelly, R. L. Xie, C. Kraebel Weinreb, T. Bregant, *Tetrahedron Lett.* **39**, 3675–3678 (1998).
- C. A. Hunter, S. Tomas, *J. Am. Chem. Soc.* **128**, 8975–8979 (2006).
- M. C. O'Sullivan et al., *Nature* **469**, 72–75 (2011).

42. D. V. Kondratuk *et al.*, *Angew. Chem. Int. Ed.* **51**, 6696–6699 (2012).
43. D. V. Kondratuk *et al.*, *Chem. Eur. J.* **20**, 12826–12834 (2014).
44. X. Li, C. Hao, C. Tian, P. Wang, C. Mao, *Chem. Commun.* **50**, 6361–6363 (2014).
45. T. Wei, J. H. Jung, T. F. Scott, *J. Am. Chem. Soc.* **137**, 16196–16202 (2015).
46. D. E. Barry, D. F. Caffrey, T. Gunnlaugsson, *Chem. Soc. Rev.* **45**, 3244–3274 (2016).
47. D. E. Barry *et al.*, *Inorg. Chem.* **59**, 2646–2650 (2020).
48. Y. Song *et al.*, *Chem. Sci.* **12**, 1826–1833 (2021).
49. S. B. Garber, J. S. Kingsbury, B. L. Gray, A. H. Hoveyda, *J. Am. Chem. Soc.* **122**, 8168–8179 (2000).
50. P. G. de Gennes, *J. Chem. Phys.* **55**, 572–579 (1971).
51. C. C. Adams, *The Knot Book* (Freeman, 1994).
52. G. Otting, *Annu. Rev. Biophys.* **39**, 387–405 (2010).
53. W.-M. Liu, M. Overhand, M. Ubbink, *Coord. Chem. Rev.* **273–274**, 2–12 (2014).
54. S. G. Markande, E. A. Matsumoto, Knotty knots are tangles on tori. *arXiv:2002.01497v1 [cond-mat.soft]* (2020).
55. R. Megaw, V. Megaw, *Celtic Art: From Its Beginnings to the Book of Kells* (Thames & Hudson, 1989).

ACKNOWLEDGMENTS

We thank the University of Manchester Mass Spectrometry Service Centre (G. Smith and E. Enston) for MALDI-TOF and high-resolution mass spectrometry, the Swedish National Infrastructure for Computing at the National Supercomputer Centre of Linköping University and Stanford University and the Stanford Research Computing Center for computational resources, and J.-F. Lemonnier and S. Borsley for useful discussions. **Funding:** This work was supported by the Engineering and Physical Sciences Research Council (EPSRC grant EP/P027067/1); the European Research Council (ERC advanced grant 786630); Marie Skłodowska-Curie Actions of the European Union (individual postdoctoral fellowship EC 746993 to F.S.); the German Research Foundation (DFG individual postdoctoral fellowship to E.K.); the Knut and Alice Wallenberg Foundation (individual postdoctoral fellowship 2019.0586 to J.H.S.); and the US Department of Energy,

Office of Science, Office of Basic Energy Sciences, Chemical Sciences, Geosciences, and Biosciences Division, Catalysis Science Program to the SUNCAT Center for Interface Science and Catalysis (F.A.-P.). D.A.L. is a Royal Society research professor. **Author contributions:** Z.A., E.K., L.P., and F.S. planned and completed the synthetic work. J.H.S. and F.A.-P. performed computational investigations. D.A.L. directed the research. Z.A., E.K., L.P., F.S., J.H.S., F.A.-P., and D.A.L. analyzed the results and wrote the manuscript. **Competing interests:** The authors declare no competing interests. **Data and materials availability:** All data are available in the main text or the supplementary materials.

SUPPLEMENTARY MATERIALS

science.org/doi/10.1126/science.abm9247
Supplementary Text
Figs. S1 to S128
Tables S1 to S3
References (56–81)
21 October 2021; accepted 1 February 2022
10.1126/science.abm9247

CORONAVIRUS

Broad anti-SARS-CoV-2 antibody immunity induced by heterologous ChAdOx1/mRNA-1273 vaccination

Chengzi I. Kaku^{1,2}, Elizabeth R. Champney¹, Johan Normark³, Marina Garcia⁴, Carl E. Johnson¹, Clas Ahlm³, Wanda Christ⁴, Mrunal Sakharkar¹, Margaret E. Ackerman^{2,5}, Jonas Klingström⁴, Mattias N. E. Forsell³, Laura M. Walker^{1,6*}

Heterologous prime-boost immunization strategies have the potential to augment COVID-19 vaccine efficacy. We longitudinally profiled severe acute respiratory syndrome coronavirus 2 (SARS-CoV-2) spike (S)-specific serological and memory B cell (MBC) responses in individuals who received either homologous (ChAdOx1:ChAdOx1) or heterologous (ChAdOx1:mRNA-1273) prime-boost vaccination. Heterologous messenger RNA (mRNA) booster immunization induced higher serum neutralizing antibody and MBC responses against SARS-CoV-2 variants of concern (VOCs) compared with that of homologous ChAdOx1 boosting. Specificity mapping of circulating B cells revealed that mRNA-1273 boost immunofocused ChAdOx1-primed responses onto epitopes expressed on prefusion-stabilized S. Monoclonal antibodies isolated from mRNA-1273-boosted participants displayed overall higher binding affinities and increased breadth of reactivity against VOCs relative to those isolated from ChAdOx1-boosted individuals. Overall, the results provide molecular insight into the enhanced quality of the B cell response induced after heterologous mRNA booster vaccination.

Multiple safe and effective COVID-19 vaccines have been developed at an unprecedented scale and speed. However, waning vaccine-induced immunity and the emergence of severe acute respiratory syndrome coronavirus 2 (SARS-CoV-2) variants of concern (VOCs) with increased neutralization resistance have limited the effectiveness of currently available vaccines (1–3). An early challenge in vaccine distribution was a halt in ChAdOx1 nCoV-19/AZD1222 (hereafter referred to as ChAdOx1) booster immunization in certain age groups driven by evidence of rare but serious thrombotic events (4, 5). To fully immunize individ-

uals who received a single dose of ChAdOx1 but were not eligible for a ChAdOx1 boost, several countries recommended a switch to heterologous booster vaccination with mRNA-1273 (Moderna) or BNT162b2 (Pfizer/BioNTech). This provided an opportunity to learn that heterologous ChAdOx1/mRNA prime-boost immunization induces higher serum neutralizing antibody titers and confers increased levels of protection relative to homologous ChAdOx1 dosing, but the molecular basis for this difference in immunogenicity remains unknown (6–9).

All currently available COVID-19 vaccines are based on the SARS-CoV-2 spike (S) protein, which plays a key role in viral entry and is the primary target for neutralizing antibodies. The S protein exists on the surface of the virion in a metastable prefusion conformation, and binding of the receptor binding domain (RBD) to angiotensin-converting enzyme 2 (ACE2) triggers shedding of the S1 subunit and transition of the S2 subunit to a highly stable postfusion conformation (10). Early struc-

tural and biochemical studies demonstrated that stabilization of the spike ectodomain through two consecutive proline substitutions in the S2 subunit (S-2P) prevents the transition from the prefusion to postfusion state and leads to enhanced immunogenicity in animal models (11, 12). Several COVID-19 vaccines encode S-2P, so that the protein maintains the prefusion conformation and avoids S1 shedding (for example, mRNA-1273, BNT162b2, and Ad26.COV2.S), whereas others express wild-type (WT) S (for example, ChAdOx1, Sputnik V, and CoronaVac), which likely leads to expression of both pre- and postfusion conformations of S. We comprehensively interrogated serological and circulating B cell responses induced by prime immunization with an adenovirus vector-based vaccine encoding WT S (ChAdOx1) and after a second dose of either ChAdOx1 or an mRNA vaccine expressing S-2P (mRNA-1273).

We recruited 55 health care workers who received either homologous ChAdOx1:ChAdOx1 or heterologous ChAdOx1:mRNA-1273 prime-boost vaccination for blood donation (table S1). None of the volunteers had a documented history of prior SARS-CoV-2 infection. Participants received one dose of ChAdOx1 and, 9 to 12 weeks later, a second dose of either ChAdOx1 ($n = 28$ participants) or mRNA-1273 ($n = 27$ participants). We collected the first blood sample on the day of booster immunization to analyze ChAdOx1-primed immune responses and a second sample 7 to 10 days after the second dose to study the early secondary B cell response induced by homologous or heterologous booster vaccination (Fig. 1A).

We first evaluated serum immunoglobulin G (IgG) binding activity at both sampling time points. All participants mounted weak but detectable SARS-CoV-2 S-specific serum IgG binding responses after the first dose of ChAdOx1, and homologous booster vaccination resulted in a small but significant (4.6-fold) increase in serum IgG binding antibodies (Fig. 1B and

¹Adimab, Lebanon, NH 03766, USA. ²Thayer School of Engineering, Dartmouth College, Hanover, NH 03755, USA.

³Division of Immunology, Department of Clinical Microbiology, Umeå University, Umeå, Sweden. ⁴Centre for Infectious Medicine, Department of Medicine Huddinge, Karolinska Institutet, Stockholm, Sweden. ⁵Geisel School of Medicine, Dartmouth College, Hanover, NH 03755, USA.

⁶Adagio Therapeutics, Waltham, MA 02451, USA.

*Corresponding author. Email: laura.walker@adimab.com

Fig. 1. Serum binding and neutralizing activity after homologous and heterologous prime-boost vaccination.

(A) Immunization and blood draw schedule. (B to G) Serum IgG binding to (B) recombinant SARS-CoV-2 S (1:1 mixture of WT S and S-2P antigens), (C) NTD, (D) RBD, (E) prefusion-stabilized S2, (F) HKU1 S, and (G) OC43 S, as assessed with enzyme-linked immunosorbent assay. Binding of prepandemic donor sera ($n = 17$ donors) is shown for comparison in (F) and (G). Geometric mean AUC values are shown below data points. (H to J) Serum neutralizing activity against (H) authentic SARS-CoV-2 D614G and (I) Beta/B.1.617.2 measured with plaque reduction assay ($n = 27$ or 28 donors from each cohort) and (J) Delta/B.1.617.2 measured with cytopathic effect (CPE)-based colorimetric microneutralization assay ($n = 10$ donors from each cohort). Plotted values represent 50% serum neutralizing titers. Values below the dotted line indicate the percentage of samples with serum neutralizing titers below the limit of detection. (K) Serum neutralizing activity against authentic Omicron/B.1.1.529/BA.1 measured with 100% CPE inhibition ($n = 10$ donors from each cohort). Values below the dotted line indicate the percentage of samples with serum neutralizing titers below the limit of detection. Statistical comparisons between prime and boost were determined by means of Wilcoxon pair-matched rank sum test. Statistical comparisons across groups were determined by means of two-tailed Mann Whitney U test with Bonferroni correction [(B) to (E)] and (H) to (K)] or two-sided Kruskal Wallis test by ranks with subsequent Dunn's multiple comparisons [(F) and (G)]. * $P < 0.05$, ** $P < 0.01$, *** $P < 0.001$, **** $P < 0.0001$. P, Prime; B, Boost; AUC, area under the curve; LOD, limit of detection; ns, nonsignificant. All data are representative of at least two independent experiments.

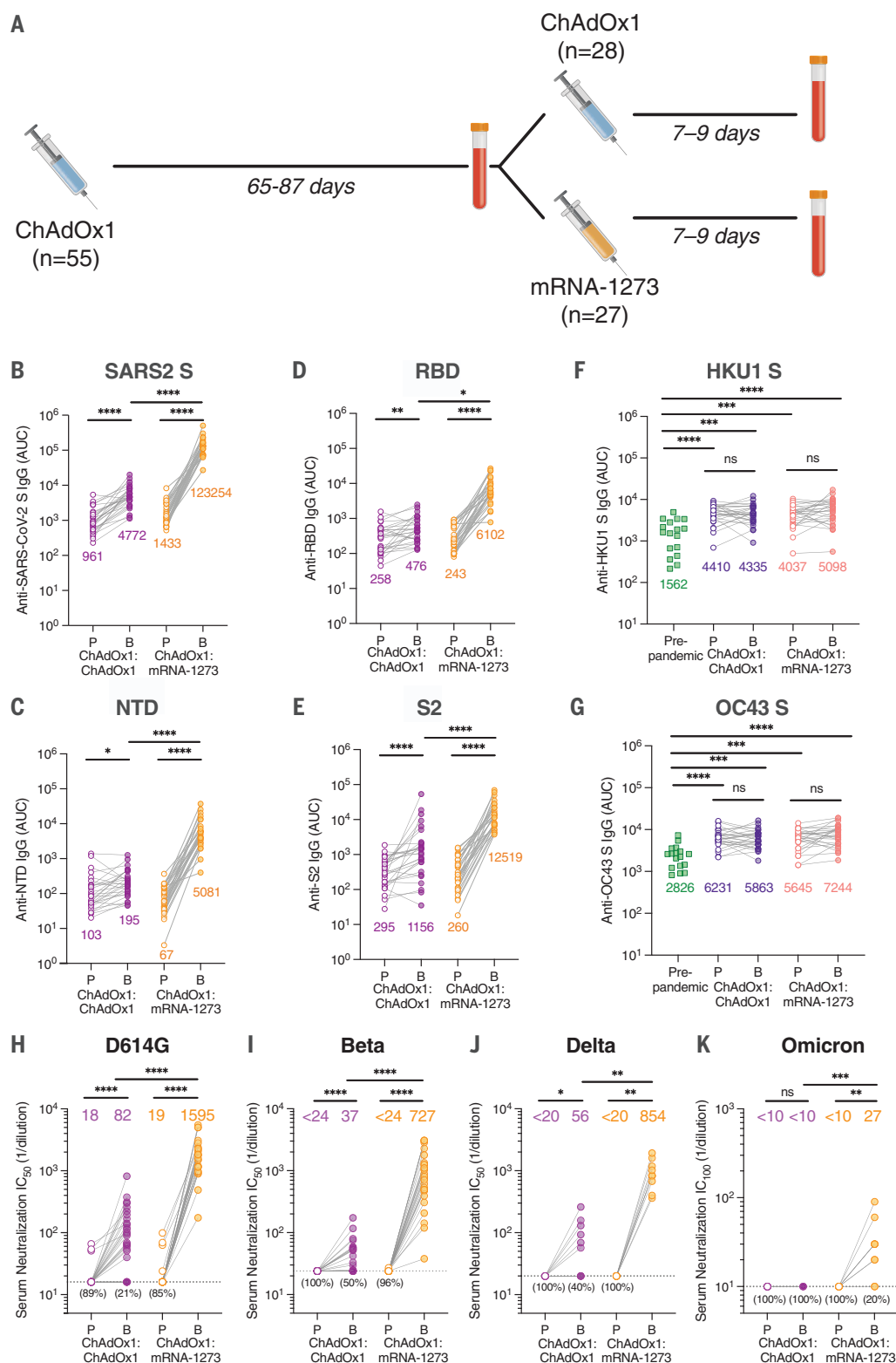


fig. S1). By contrast, heterologous booster vaccination with mRNA-1273 led to a much larger (86-fold) increase in S-specific serum IgG binding responses (Fig. 1B and fig. S1). Correspondingly, ChAdOx1 prime immunization elicited weak serum IgG binding activity to recombinant receptor binding domain (RBD), N-terminal

domain (NTD), and prefusion-stabilized S2 subdomains [geometric mean areas under the curve (AUCs) ranging from 67 to 321], and homologous and heterologous booster immunization enhanced these responses by two- to fourfold and 25- to 77-fold, respectively (Fig. 1, C to E).

Cross-reactive MBCs induced by seasonal β -coronaviruses are activated and expanded after primary SARS-CoV-2 infection and mRNA vaccination (13, 14). To determine whether ChAdOx1:ChAdOx1 and/or ChAdOx1:mRNA-1273 vaccination elicited similar recall responses, we assessed serum IgG binding to recombinant

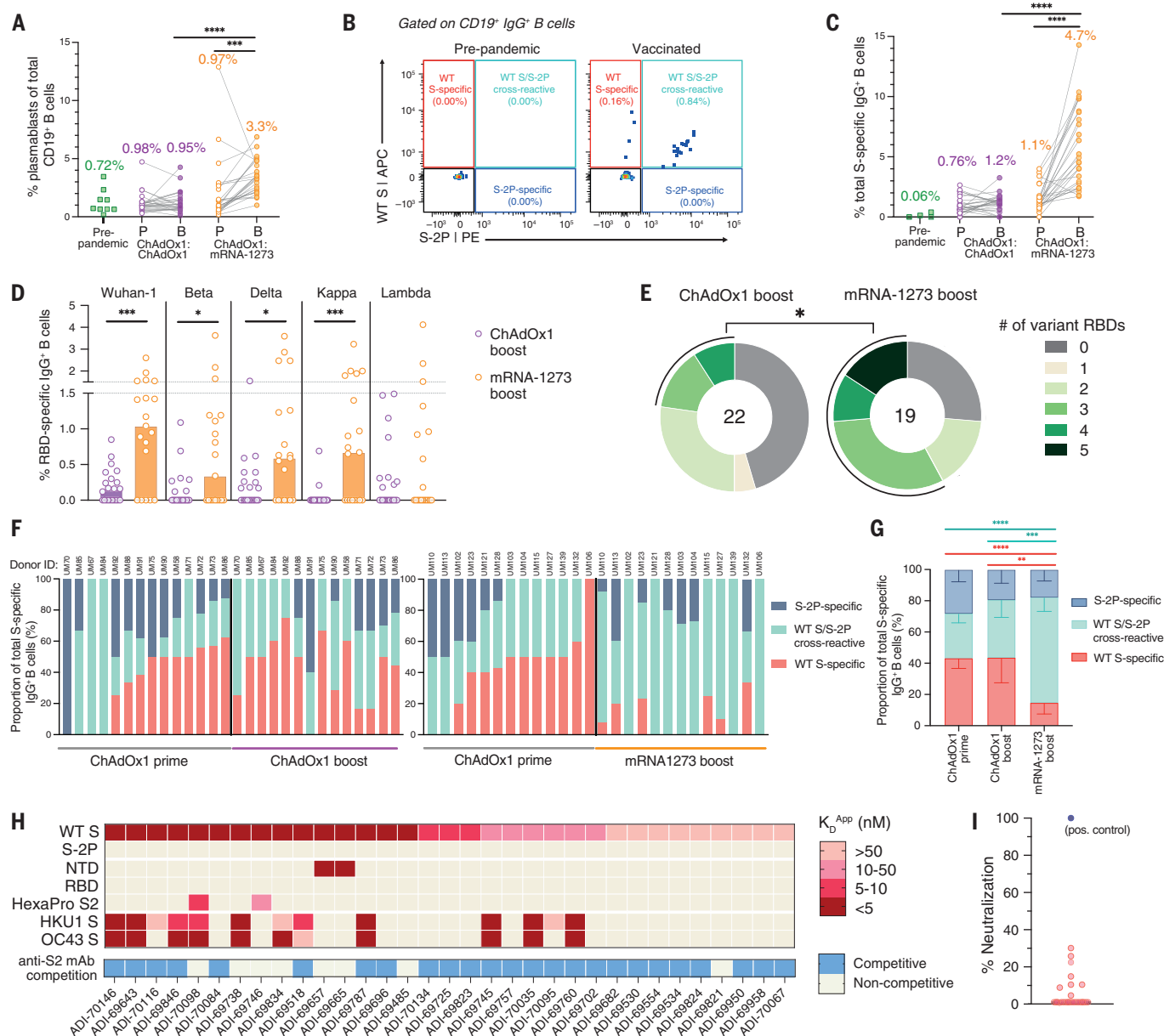


Fig. 2. SARS-CoV-2 S-specific B cell responses induced by homologous and heterologous prime-boost vaccination. (A) Frequencies of plasmablasts (defined as $CD19^+CD20^{-/lo}CD71^+$ cells) among circulating $CD19^+$ B cells after prime and boost vaccination, as determined with flow cytometry. Prepandemic donor samples ($n = 9$ donors) were included for comparison. Median values are shown above data points. (B) Representative fluorescence-activated cell sorting (FACS) gating strategy used for identifying WT S-specific, S-2P-specific, and WT/S-2P cross-reactive IgG^+ B cells. (C) Frequencies of total (WT + S-2P) SARS-CoV-2 S-reactive B cells among circulating IgG^+ B cells, as determined with flow cytometry. Median frequencies are shown above data points. (D) Frequency of circulating IgG^+ B cells reactive with RBDs encoding mutations present in Beta, Delta, Kappa, and Lambda variants. The height of each bar indicates median frequency. (E) Proportion of donors with detectable B cell reactivity with the indicated number of variant RBDs. The total number of donors analyzed is indicated in the center of the pies. Statistical significance was determined by means of Fisher's exact test and calculated according to the proportion of donors with B cells displaying reactivity to ≥ 3 variant RBDs. (F) Proportions of WT S-specific, WT S/S-2P cross-reactive, and S-2P-specific B cells among total S-specific B cells after (left) homologous or (right) heterologous prime-boost

immunization. Donors with S-specific B cell frequencies $< 1\%$ of total IgG^+ B cells at either time point were excluded from this analysis. Donor identification numbers (IDs) are denoted above each bar. (G) Mean proportions of WT S-specific, WT S/S-2P cross-reactive, and S-2P-specific B cells across all donors within each cohort. Error bars indicate 95% confidence intervals. (H) Apparent binding affinities (K_D^{App}) of WT S-specific monoclonal antibodies for WT S, S-2P, prefusion S subdomains (NTD, RBD, and prefusion-stabilized S2), HKU1 S, and OC43 S, as determined with biolayer interferometry (BLI). Competitive binding with an S2-directed antibody (ADI-69962), as determined with a BLI competitive sandwich assay, is indicated below the heatmap. (I) Neutralizing activity of WT S-specific antibodies against MLV-SARS-CoV-2 Wuhan-1 at a concentration of $1 \mu g/ml$. A previously described neutralizing antibody to RBD (ADG-2) was included as a positive control (29). Statistical comparisons between paired prime and boost samples were determined by means of [(A) and (C)] Wilcoxon pair-matched rank sum test. Statistical comparisons between vaccination cohorts were determined by means of [(D) two-sided Mann-Whitney U tests and [(C) and (G)] two-sided Kruskal-Wallis test by ranks with subsequent Dunn's multiple comparisons. * $P < 0.05$, ** $P < 0.01$, *** $P < 0.001$, **** $P < 0.0001$. P, Prime; B, Boost; K_D^{App} , apparent equilibrium constant.

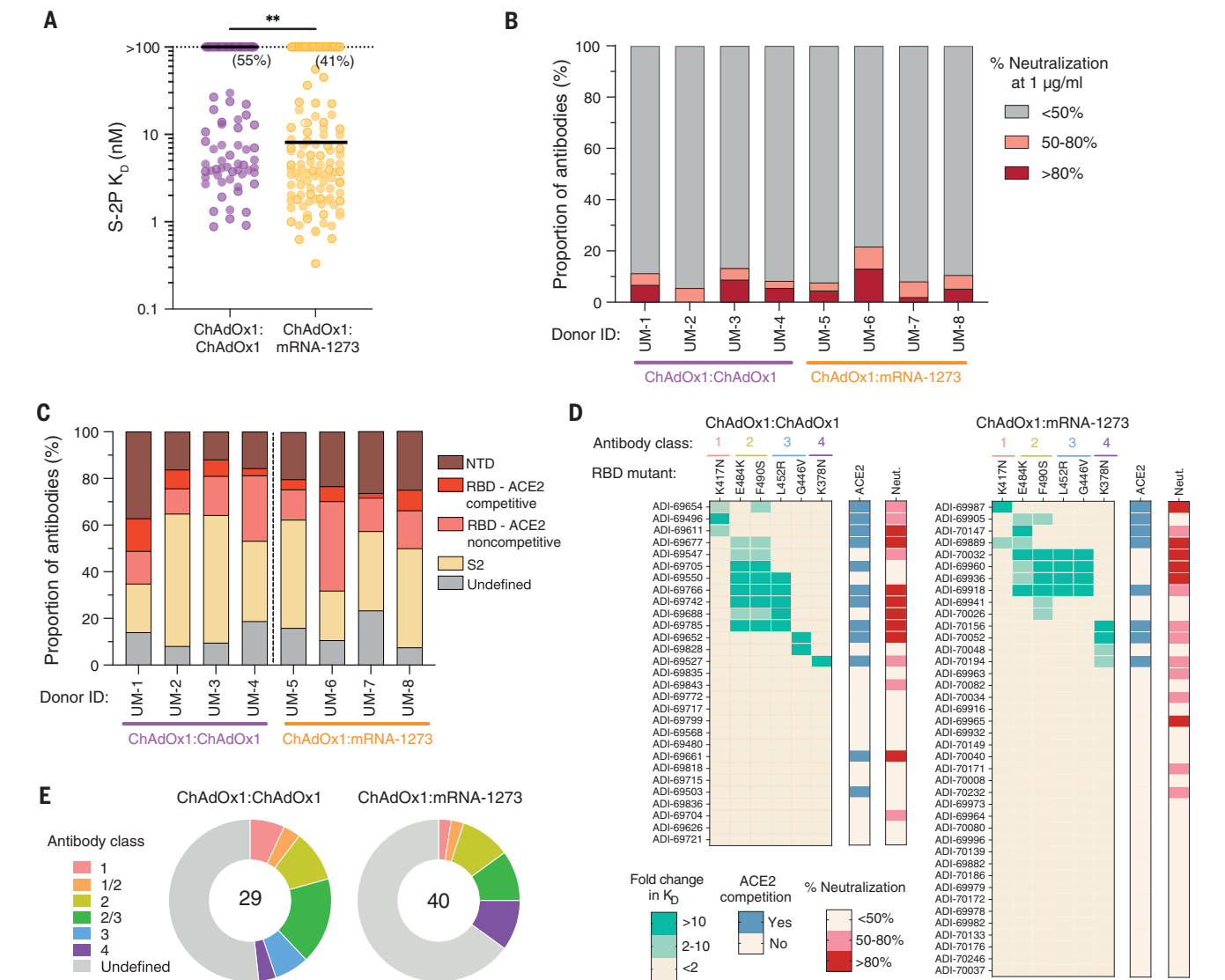


Fig. 3. Binding and neutralization properties of monoclonal antibodies isolated from ChAdOx1- and mRNA-1273-boosted donors. (A) Fab binding affinities for S-2P, as determined with BLI. Antibodies with no detectable monovalent binding activity are excluded, and those with weak binding affinities that could not be fit to a 1:1 binding model are plotted as $K_D > 100$ nM. Black bars indicate medians. Values in parentheses indicate the percentage of antibodies with $K_D > 100$ nM. (B) Proportion of antibodies exhibiting <50%, 50 to 80%, and >80% neutralization activity against MLV-SARS-CoV-2 Wuhan-1 at a concentration of 1 μ g/ml. (C) Proportion of S-2P-reactive antibodies directed to each of the indicated subdomains within prefusion S.

Competitive hACE2 binding was determined by using a BLI-based competition assay. (D) Heatmaps displaying fold change in binding affinity of antibodies to RBD to variant RBDs containing the indicated single point mutations. Competitive hACE2 binding activity and percentage neutralization against MLV-SARS-CoV-2 Wuhan-1 at a concentration of 1 μ g/ml are shown in the bars on the right. (E) Summary of the distribution of antibodies to RBD belonging to each of the indicated classes. The numbers in the center of the pies indicate the total number of antibodies analyzed. Statistical comparisons were made by means of (A) two-sided Mann-Whitney U tests. K_D , equilibrium dissociation constant. $**P < 0.01$.

OC43 and HKU1 S proteins at both sampling time points. At the preboost time point, we detected significantly elevated serum antibody titers to both OC43 and HKU1 relative to pre-pandemic sera samples, suggesting a “back-boosting” of preexisting cross-reactive MBCs induced by seasonal β -CoV infections (Fig. 1, F and G). However, this response was not further amplified after homologous or heterologous booster immunization.

We next evaluated serum neutralizing activity against authentic SARS-CoV-2 D614G, B.1.617.2/Delta, B.1.351/Beta, and B.1.1.529/

Omicron variants at both sampling time points. At the preboost time point, the vast majority of donors (87%) displayed weak or undetectable serum neutralizing activity against SARS-CoV-2 D614G, with 50% neutralization titers ranging from <16 to 66 (Fig. 1H), and none of the donors showed detectable serum neutralization against Beta, Delta, or Omicron (Fig. 1, I to K). Homologous ChAdOx1 booster immunization resulted in an overall 4.6-fold increase in serum neutralizing activity against SARS-CoV-2 D614G (geometric mean titer = 82), but neutralizing titers remained at the

lower limit of detection in 21% (6 of 28) of donors (Fig. 1H). In about half of the individuals, we also observed a small but significant (1.5 to 2.4-fold) rise in serum neutralizing activity against Beta and Delta after ChAdOx1 booster immunization (Fig. 1, I and J), but none of the donor sera exhibited detectable neutralization against Omicron (Fig. 1K). In contrast to the relatively weak serum neutralizing responses observed after two doses of ChAdOx1, heterologous mRNA-1273 booster vaccination significantly enhanced serum neutralizing titers to SARS-CoV-2 D614G, Beta, and Delta in all

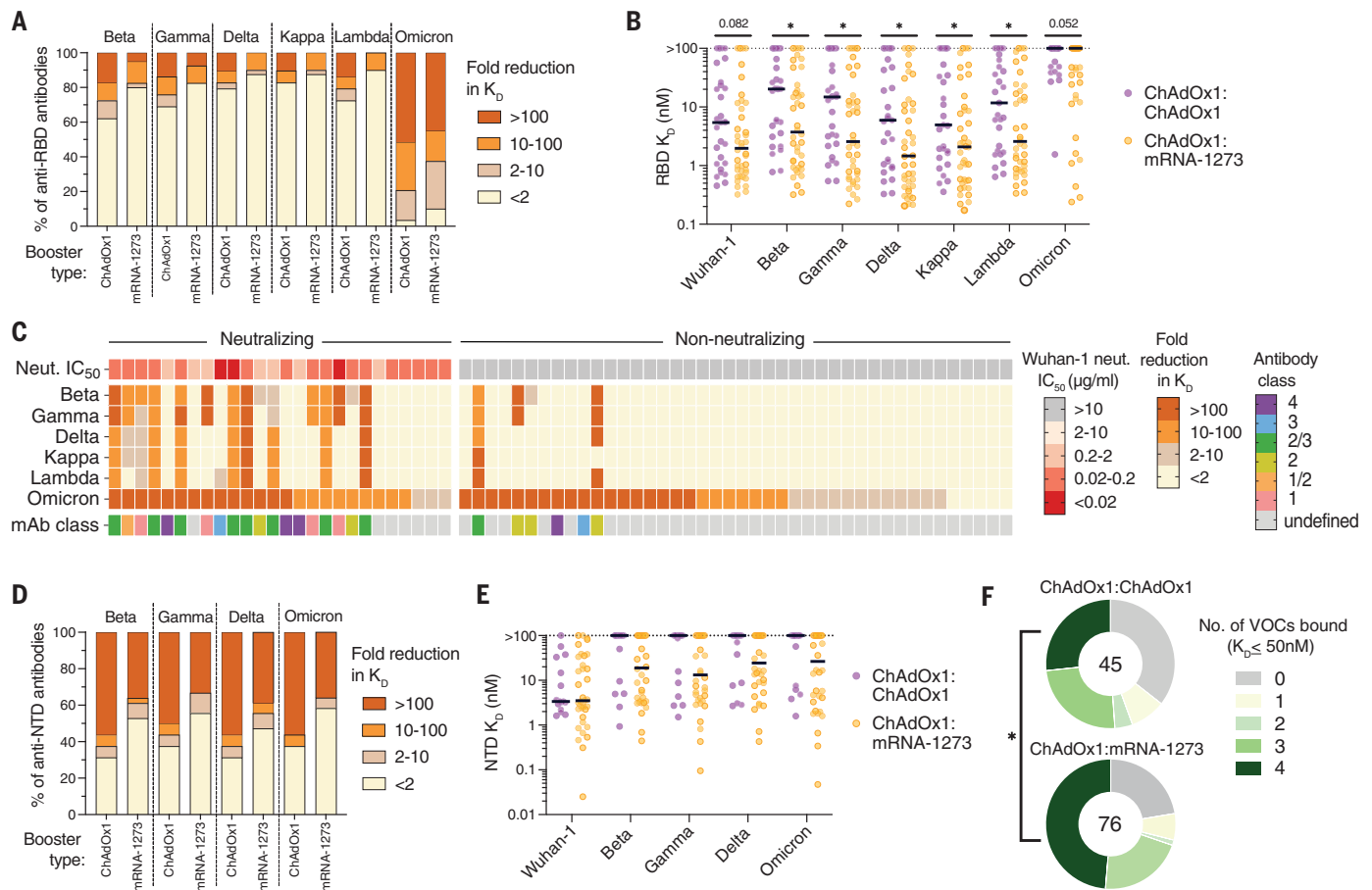


Fig. 4. Breadth of antibody binding to SARS-CoV-2 variants. (A) Proportion of RBD-reactive antibodies with the indicated fold reduction in Fab binding affinity to RBDs incorporating mutations present in the Beta, Gamma, Delta, Kappa, Lambda, and Omicron variants relative to the Wuhan-1 RBD, as determined with a bead-based flow cytometric assay. (B) Fab binding affinities of RBD-directed antibodies to Wuhan-1 and variant RBDs. Antibodies that did not reach half-maximal saturation at the highest concentration tested (100 nM) are shown as $K_D > 100$ nM. Black bars denote medians. (C) Heatmap showing the fold reduction in affinity to variant RBDs compared with the Wuhan-1 RBD among neutralizing and non-neutralizing antibodies to RBD. The top bar indicates the neutralization inhibitory concentration (IC_{50}) of each mAb against MLV-SARS-CoV-2 Wuhan-1. Antibodies that did not reach

50% neutralization at 10 μ g/ml were classified as non-neutralizing. The bottom bar denotes the class of each antibody. (D) Proportion of NTD-directed antibodies with the indicated fold reductions in binding activity to variant NTDs relative to the Wuhan-1 NTD. (E) Fab binding affinities of NTD-directed antibodies to Wuhan-1 and variant NTDs. Antibodies that did not reach half-maximal saturation at 100 nM are shown as $K_D > 100$ nM. Black bars denote medians. (F) Combined proportions of antibodies to RBD and NTD that bound the indicated number of variants of concern (Beta, Gamma, Delta, and Omicron) with $K_D \leq 50$ nM. The number in the center of the pie indicates the total number of antibodies tested. Statistical significance was determined by [(B) and (E)] two-sided Mann-Whitney U tests or (F) Fisher's exact test. K_D , equilibrium dissociation constant; * $P < 0.05$.

donors (geometric mean titers = 1595, 727, and 854 for D614G, Beta, and Delta, respectively) (Fig. 1, H to J). Furthermore, about 80% of donor sera displayed low but detectable neutralizing activity against Omicron, with 100% neutralization titers ranging from <10 to 90 (Fig. 1K). Taken together, heterologous ChAdOx1:mRNA-1273 prime-boost vaccination elicits superior binding and neutralizing antibody responses to SARS-CoV-2 and VOCs relative to homologous ChAdOx1:ChAdOx1 vaccination.

Previous studies of other viral infections have shown that booster vaccination typically induces a rapid and robust antigen-specific plasmablast response that peaks at approximately day 7 after immunization and accounts for a relatively large proportion of peripheral

blood B cells (15, 16). We therefore assessed the frequency of plasmablasts in peripheral blood 7 to 10 days after homologous and heterologous booster vaccination (fig. S2A). Although we observed modest plasmablast expansion in a subset of ChAdOx1-boosted donors, the median frequency of plasmablasts across all donors was not significantly elevated relative to preboost or unpaired prepandemic healthy donor samples (Fig. 2A). By contrast, heterologous booster immunization induced a robust plasmablast response in almost all donors, in which plasmablast frequencies averaged 3% and accounted for up to 7% of all CD19⁺ peripheral blood B cells (Fig. 2A).

We next investigated the magnitude and specificities of the S-specific MBC response induced after both prime and boost immunization.

Because ChAdOx1 encodes WT S, which may elicit B cell responses to both pre- and post-fusion conformations of S, we evaluated B cell responses to both prefusion-stabilized (S-2P) and WT (unstabilized) forms of the S protein (Fig. 2B and fig. S2B). SDS-polyacrylamide gel electrophoresis (SDS-PAGE) analysis revealed that the recombinant WT S preparation used for B cell staining contained both uncleaved and cleaved forms of S, the latter likely representing a mixture of prefusion, post-fusion, and non-native or dissociated forms of S (fig. S3). The frequency of total S (WT + S-2P)-specific IgG⁺ B cells ranged from 0 to 3.7% after ChAdOx1 prime immunization, and homologous booster immunization did not significantly enhance this response in most donors (Fig. 2C). By contrast, mRNA-1273 booster

vaccination induced a robust expansion of S-specific IgG⁺ B cells in most donors, averaging a fourfold increase over the corresponding ChAdOx1 prime-induced responses (Fig. 2C). Similarly, mRNA-1273 booster immunization expanded S-specific IgM⁺CD27⁺ and IgA⁺ MBC cell populations (fig. S4). mRNA-1273 boost also elicited significantly higher-magnitude B cell responses to individual subdomains within prefusion S (RBD, NTD, and prefusion-stabilized S2)—including RBDs that encode mutations found in the Beta, Delta, and Kappa variants—relative to homologous ChAdOx1 boost (Fig. 2D and figs. S5 and S6). Only 23% of ChAdOx1-boostered donors displayed detectable B cell reactivity with ≥ 3 variant RBDs compared with 58% of mRNA-boostered donors (Fig. 2E). Overall, the results suggest that heterologous ChAdOx1:mRNA-1273 prime-boost vaccination induces a more robust B cell response to SARS-CoV-2 and VOCs relative to homologous ChAdOx1:ChAdOx1 immunization.

The use of dual-labeled SARS-CoV-2 S probes for B cell staining allowed us to assess the frequencies and proportions of WT S-specific, WT S/S-2P-reactive, and S-2P-specific B cells induced before and after booster immunization. In the majority of donors (19 of 27), $\geq 30\%$ of the total S-specific IgG⁺ MBC response induced by ChAdOx1 prime immunization was directed toward epitopes expressed only on WT S, with the remaining B cells displaying either specificity for S-2P or cross-reactivity between WT S and S-2P (Fig. 2, F and G). As expected, homologous ChAdOx1 booster vaccination did not significantly modify this response in most donors (Fig. 2, F and G). By contrast, we observed a massive decline in the proportion of circulating WT S-specific B cells after mRNA booster immunization in most donors (Fig. 2, F and G). Correspondingly, booster immunization with mRNA-1273 preferentially expanded WT S/S-2P cross-reactive B cells, increasing from a median frequency of 0.3% before booster immunization to 3.4% after mRNA-1273 boost (fig. S7). Thus, in addition to driving a robust expansion of ChAdOx1 prime-induced B cells, heterologous mRNA-1273 booster immunization redirects the B cell response toward epitopes expressed on prefusion S.

To characterize the specificities and functional properties of the WT S-specific antibodies induced by ChAdOx1 prime immunization, we cloned and expressed 33 monoclonal antibodies from single WT S-specific B cells in five donors. The antibodies used a diversity of variable heavy-chain (VH) and variable light-chain (VL) germline genes, and 28 out of 33 contained somatic mutations, which is consistent with an MBC origin (fig. S8). The avid binding affinities of the antibodies for recombinant WT S ranged from 1 to 36 nM, and none displayed detectable binding to S-2P (Fig. 2H). More than 85% (29 of 33) of the WT

S-specific antibodies failed to bind to recombinant subdomains that compose prefusion S, and 40% displayed reactivity with HKU1 and/or OC43 S, potentially suggesting recognition of conserved epitopes within postfusion S2 (Fig. 2H). Given the lack of availability of recombinant postfusion S antigens, we evaluated this possibility by performing competitive binding assays with an S2-directed antibody (ADI-69962) that targets an epitope expressed on WT S, S-2P, and prefusion-stabilized S2 antigens (fig. S9). Of the WT S-specific antibodies, 76% (25 of 33) showed competitive binding with ADI-69962, suggesting recognition of a distinct antigenic site within the S2 subunit that overlaps with the ADI-69962 epitope but is not expressed on S-2P (Fig. 2H). Consistent with their lack of reactivity with prefusion S, none of the WT S-specific antibodies displayed $>50\%$ neutralizing activity against SARS-CoV-2 Wuhan-1 at a 1 $\mu\text{g}/\text{ml}$ concentration (Fig. 2I). We conclude that a relatively large proportion of the SARS-CoV-2 S-specific B cell response induced by homologous ChAdOx1 prime-boost immunization is composed of non-neutralizing anti-S2 specificities that fail to bind prefusion S.

To determine whether homologous and heterologous booster vaccination regimens induce distinct B cell responses to prefusion S, we obtained 163 and 252 paired VH and VL sequences from single S-2P-reactive B cells from four donors in each cohort after ChAdOx1 or mRNA-1273 booster immunization (table S2). Both booster regimens induced highly diverse B cell responses, with 0 to 8.6% of antibodies belonging to expanded clonal lineages (fig. S10). IGHV3-30 was significantly overrepresented in the S-reactive MBC population in both ChAdOx1 and mRNA-1273-boostered individuals, as observed previously in antibodies isolated from naturally infected and mRNA-vaccinated donors (fig. S11A) (17, 18). The antibodies isolated from both donor cohorts also displayed similar levels of somatic hypermutation (SHM), which ranged from a median of 4 to 7 and 6 to 7 VH nucleotide substitutions for ChAdOx1- and mRNA-1273-boostered donors, respectively (fig. S12A). In seven out of eight donors, $>90\%$ of sequences contained somatic mutations, suggesting that the acute B cell response induced by either booster regimen largely comprised preexisting MBCs primed by ChAdOx1 immunization (fig. S12B). Furthermore, the degree of SHM was comparable with that observed in antibodies previously isolated from SARS-CoV-2 convalescent individuals at a similar time point after infection (approximately 3 months), suggesting that the kinetics of affinity maturation after ChAdOx1 prime immunization may be similar to that of natural infection (fig. S12). Overall, the results demonstrate that the genetic features of S-2P-reactive antibodies induced by homologous

and heterologous booster vaccination are highly similar, with both groups rich in clonally expanded and somatically mutated sequences.

We next measured the binding affinities and neutralizing activities of the isolated S-2P-reactive antibodies. Antibodies isolated from mRNA-boostered donors exhibited overall higher Fab binding affinities [median equilibrium dissociation constant (K_d) = 12 nM] as compared with those isolated from ChAdOx1-boostered donors [median K_d >100 nM] (Fig. 3A). However, only a small subset of binding antibodies isolated from both donor cohorts (6 to 13% and 8 to 21% for ChAdOx1- and mRNA-1273-boostered donors, respectively) displayed $>50\%$ neutralizing activity against SARS-CoV-2 Wuhan-1 at a concentration of 1 $\mu\text{g}/\text{ml}$ (Fig. 3B). Thus, the neutralizing antibody response represents only a minor fraction of the total prefusion S-reactive binding response induced by both homologous and heterologous prime-boost immunization.

To examine how the type of booster immunization affects the B cell immunodominance hierarchy to prefusion S, we evaluated the proportion of S-2P-reactive antibodies directed to the NTD, RBD, and prefusion-stabilized S2 subdomains in each donor from which monoclonal antibodies were isolated. We observed relatively similar proportions of antibodies targeting each subdomain within prefusion S, although S2-directed antibodies dominated the response in a subset of donors in both groups (Fig. 3C). S-2P-reactive antibodies displaying cross-reactivity with OC43 and HKU1 S only comprised about 5% of the S-2P-reactive B cell response elicited by both booster regimens (fig. S13). RBD-directed hACE2-blocking antibodies also represented a small proportion of the S-2P-reactive binding response in both donor cohorts, ranging from 3 to 14% and 2 to 9% in ChAdOx1:ChAdOx1- and ChAdOx1:mRNA-1273-immunized donors, respectively (Fig. 3C). As expected, these rare ACE2-competitive antibodies represented the majority of the neutralizing response, thus explaining the limited number of neutralizing antibodies observed among total S-2P binding antibodies (fig. S14). To further map the epitopes recognized by the RBD-directed antibodies, we evaluated their binding reactivities with recombinant RBDs containing mutations associated with escape from common antibody classes, including K417N (class 1), E484K and F490S (class 2), L452R and G446V (class 3), and K378N (class 4) (19, 20). Both booster regimens induced comparable proportions of antibodies targeting common antigenic sites within the RBD (Fig. 3, D and E). Although homologous ChAdOx1 booster vaccination induces a higher frequency of WT S-specific antibodies compared with that of a heterologous mRNA-1273 boost, both immunization regimens establish similar immunodominance hierarchies to prefusion-stabilized S.

Last, we assessed the RBD- and NTD-directed antibodies isolated from both donor cohorts for reactivity with multiple SARS-CoV-2 VOCs and variants of interest (VOIs). Against pre-Omicron VOCs and VOIs (Beta, Gamma, Delta, Kappa, and Lambda), 41% (12 of 29) of RBD-directed antibodies derived from ChAdOx1-boostered individuals displayed reduced binding activity (greater than twofold) to two or more of these variants as compared with only 20% (8 of 40) of antibodies isolated from mRNA-1273-boostered individuals, suggesting that mRNA-1273 booster vaccination activates a larger proportion of broadly reactive B cells (Fig. 4A and fig. S15A). Furthermore, the mRNA-elicited antibodies bound to both WT and pre-Omicron VOC and VOI RBDs with significantly higher affinities (median K_d = 1.4 to 3.7 nM) relative to the ChAdOx1-induced antibodies (median K_d = 4.9 to 20.3 nM) (Fig. 4B), potentially explaining their increased breadth of binding. However, in contrast to earlier variants, the Omicron variant broadly escaped recognition by RBD-directed antibodies induced by both booster regimens, with 24 of 29 (83%) and 29 of 40 (73%) antibodies derived from ChAdOx1- and mRNA-1273-boostered individuals, respectively, showing significantly reduced binding reactivity (<10% of wild type) to the Omicron RBD (Fig. 4A). Among the 26 neutralizing antibodies identified from both donor cohorts, only three maintained binding to the Omicron RBD within 10-fold of the Wuhan-1 RBD (Fig. 4C). This result is consistent with the large number of mutations within the frequently targeted class 1/2/3 RBD epitopes and provides a molecular explanation for the extensive resistance of this variant to neutralization by convalescent and vaccinee sera (21, 22).

Consistent with the overall increased breadth of recognition by RBD-directed antibodies induced by heterologous booster vaccination, 52 to 58% of NTD-directed antibodies isolated from mRNA-1273-boostered donors retained binding to each of the four VOCs tested (Beta, Gamma, Delta, and Omicron) compared with only 31 to 37% of antibodies isolated from ChAdOx1-boostered donors (Fig. 4D and fig. S15B). Furthermore, the NTD-specific antibodies isolated from mRNA-1273-boostered donors trended toward higher binding affinities across all VOCs tested as compared with antibodies derived from ChAdOx1-boostered donors (Fig. 4E). Overall, a significantly larger fraction of antibodies to RBD and NTD (49%) derived from mRNA-boostered donors retained reactivity (K_d < 50 nM) with all VOC NTDs or RBDs relative to ChAdOx1-boostered donors (26%) (Fig. 4F). Thus, heterologous mRNA-1273 immunization appears to skew the early secondary B cell response toward higher-affinity clones with improved breadth of variant recognition compared with homologous ChAdOx1 immuniza-

tion, although the Omicron variant broadly escapes neutralizing antibodies induced by both booster regimens.

Heterologous ChAdOx1:mRNA-1273 prime-boost immunization induces significantly broader and more potent serum neutralizing antibody and MBC responses against WT SARS-CoV-2 and VOCs relative to homologous ChAdOx1 vaccination, and this difference appears to be driven by both the magnitude and quality of the early secondary B cell response. Expression of WT S by ChAdOx1 appears to distract the B cell response away from neutralizing sites of vulnerability present on prefusion S, and homologous booster vaccination further expands these non-neutralizing specificities. By contrast, heterologous booster immunization with mRNA-1273, which encodes S-2P, redirects the B cell response toward epitopes expressed on prefusion-stabilized S. Furthermore, mRNA-1273 activates B cells with higher affinity for prefusion S and greater breadth of reactivity relative to ChAdOx1. The molecular basis for this difference remains to be determined but could potentially be associated with differences in cell-surface expression of S-2P relative to WT S or the distinct innate immunostimulatory properties of mRNA versus adenoviral particles (23, 24). Last, although heterologous ChAdOx1:mRNA-1273 prime-boost immunization shows superior immunogenicity relative to two-dose ChAdOx1, the B cell response induced by both vaccination regimens is dominated by non-neutralizing antibodies, and the vast majority of neutralizing antibodies fail to recognize the Omicron variant. Although studies in animal models have demonstrated that non-neutralizing antibodies can contribute to protection, serum neutralizing antibody titer strongly correlates with vaccine-induced efficacy against symptomatic COVID-19 in humans (25, 26). Thus, rationally designed immunogens that focus the B cell response on conserved, neutralizing epitopes within the RBD and S2 subunit may enhance the potency, breadth, and durability of protection against SARS-CoV-2, future emerging VOCs, and potentially preeminent β -coronaviruses (27, 28).

REFERENCES AND NOTES

1. L. J. Abu-Raddad, H. Chemaitelly, A. A. Butt, National Study Group for COVID-19 Vaccination, *N. Engl. J. Med.* **385**, 187–189 (2021).
2. S. A. Madhi et al., *N. Engl. J. Med.* **384**, 1885–1898 (2021).
3. C. H. Hansen et al., medRxiv 21267966 [Preprint] (2021).
4. C. R. Simpson et al., *Nat. Med.* **27**, 1290–1297 (2021).
5. J. B. Schulz et al., *Ann. Neurol.* **90**, 627–639 (2021).
6. J. Barros-Martins et al., *Nat. Med.* **27**, 1525–1529 (2021).
7. J. Normark et al., *N. Engl. J. Med.* **385**, 1049–1051 (2021).
8. P. Nordström, M. Ballin, A. Nordström, *Lancet Reg. Health Eur.* **11**, 100249 (2021).
9. A. Rössler, L. Riepler, D. Bante, D. von Laer, J. Kimpel, *N. Engl. J. Med.* *NEJMc2119236* (2022).
10. M. A. Tortorici, D. Veesler, *Adv. Virus Res.* **105**, 93–116 (2019).
11. D. Wrapp et al., *Science* **367**, 1260–1263 (2020).
12. J. Yu et al., *Science* **369**, 806–811 (2020).
13. F. Amanat et al., *Cell* **184**, 3936–3948.e10 (2021).
14. R. C. Brewer et al., *Nat. Immunol.* **23**, 33–39 (2022).
15. M. Mukhamedova et al., *Immunity* **54**, 769–780.e6 (2021).
16. J. Wrammert et al., *Nature* **453**, 667–671 (2008).
17. D. F. Robbiani et al., *Nature* **584**, 437–442 (2020).
18. Z. Wang et al., *Nature* **592**, 616–622 (2021).
19. C. O. Barnes et al., *Nature* **588**, 682–687 (2020).
20. A. J. Greaney et al., *Nat. Commun.* **12**, 4196 (2021).
21. M. McCallum et al., *Science* **375**, XXX (2021).
22. W. Dejnirattai et al., *Cell* **185**, 467–484.e15 (2022).
23. R. Bos et al., *NPJ Vaccines* **5**, 91 (2020).
24. N. Chaudhary, D. Weissman, K. A. Whitehead, *Nat. Rev. Drug Discov.* **20**, 817–838 (2021).
25. D. Li et al., *Cell* **184**, 4203–4219.e32 (2021).
26. D. S. Khoury et al., *Nat. Med.* **27**, 1205–1211 (2021).
27. D. Pinto et al., *Science* **373**, 1109–1116 (2021).
28. A. A. Cohen et al., *Science* **371**, 735–741 (2021).
29. C. G. Rappazzo et al., *Science* **371**, 823–829 (2021).

ACKNOWLEDGMENTS

We thank study nurse I.-L. Persson and personnel at the Clinical Research Center at Umeå University Hospital for support, enrollment of study subjects, and sampling. We also thank L. Vikström, M. Järner, and M. Lagerqvist at Umeå University for processing of samples and A. Edin at Umeå University Hospital for the summary of clinical data. We also acknowledge Parexel for assistance with figure preparation and E. Krauland, J. Nett, and M. Vasquez for helpful comments on the manuscript. All IgGs were sequenced by Adimab's Molecular Core and produced by the High Throughput Expression group. **Funding:** M.N.E.F. is funded by grants from the Swedish Research Council (2020-06235) and from the SciLifeLab National COVID-19 Research Program (VC-2020-0015), financed by the Knut and Alice Wallenberg Foundation. C.A. is funded by the Swedish Research Council (2021-04665). J.N. is a Wallenberg Center for Molecular Medicine Associated Researcher. M.G., W.C., and J.K. are funded by Swedish Research Council (#2020-05782) and SciLifeLab/KAW (#VC-2021-0026). **Author contributions:** L.M.W. and M.N.E.F. conceived and designed the study. C.A. and J.N. are principal investigators for the clinical trial and supervised sample collection. M.G., W.C., and J.K. performed Omicron serum neutralization assays. C.I.K. performed serum and B cell analyses, single B cell sorting, and antibody characterization. C.E.J. produced recombinant IgG antibodies for characterization. E.R.C. designed and performed developability and biolayer interferometry assays. C.I.K. and M.S. developed, designed, and performed pseudovirus neutralization assays. C.I.K. and M.E.A. developed, designed, and performed multiplexed flow cytometry assays. C.I.K., E.R.C. and L.M.W. analyzed the data. C.I.K. and L.M.W. wrote the manuscript, and all authors reviewed and edited the paper. **Competing interests:** C.I.K., E.R.C., C.E.J., M.S., and L.M.W. are employees of Adimab and may hold shares in Adimab. L.M.W. is an employee of Adagio Therapeutics and holds shares in Adagio Therapeutics. J.N., M.G., C.A., W.C., J.K., and M.N.E.F. declare no competing interests. L.M.W., C.I.K., and M.N.E.F. are inventors on a provisional patent application (US patent application no. 63/307,230) describing the SARS-CoV-2 antibodies. **Data and material availability:** Antibody sequences have been deposited in GenBank (accession codes OL697893 to OL698712). All other data are available in the manuscript or supplementary materials. IgGs are available from L.M.W. under a materials transfer agreement (MTA) from Adagio Therapeutics. Requests for clinical samples should be addressed to mattias.forsell@umu.se. Sharing is regulated by the Swedish law of bio banking and requires a collaboration with Umeå University (represented by MNE Forsell) and must comply with EU regulations for GDPR. This work is licensed under a Creative Commons Attribution 4.0 International (CC BY 4.0) license, which permits unrestricted use, distribution, and reproduction in any medium, provided the original work is properly cited. To view a copy of this license, visit <https://creativecommons.org/licenses/by/4.0/>. This license does not apply to figures/photos/artwork or other content included in the article that is credited to a third party; obtain authorization from the rights holder before using such material.

SUPPLEMENTARY MATERIALS

science.org/doi/10.1126/science.abn2866
Materials and Methods
Figs. S1 to S15
Tables S1 and S2
References (30–35)
MDAR Reproducibility Checklist

19 November 2021; accepted 2 February 2022
Published online 10 February 2022
10.1126/science.abn2868

CORONAVIRUS

Structures of the Omicron spike trimer with ACE2 and an anti-Omicron antibody

Wanchao Yin^{1†*}, Youwei Xu^{1†}, Peiyu Xu^{1†}, Xiaodan Cao^{2†}, Canrong Wu^{1†}, Chunyin Gu^{2†}, Xinheng He^{1,3}, Xiaoxi Wang¹, Sijie Huang¹, Qingning Yuan⁴, Kai Wu⁴, Wen Hu⁴, Zifu Huang⁵, Jia Liu², Zongda Wang², Fangfang Jia², Kaiwen Xia², Peipei Liu², Xueping Wang², Bin Song⁶, Jie Zheng⁶, Hualiang Jiang^{3,5,7}, Xi Cheng^{3,5}, Yi Jiang^{1,3,5}, Su-Jun Deng^{2*}, H. Eric Xu^{1,3,7*}

The severe acute respiratory syndrome coronavirus 2 (SARS-CoV-2) Omicron variant has become the dominant infective strain. We report the structures of the Omicron spike trimer on its own and in complex with angiotensin-converting enzyme 2 (ACE2) or an anti-Omicron antibody. Most Omicron mutations are located on the surface of the spike protein and change binding epitopes to many current antibodies. In the ACE2-binding site, compensating mutations strengthen receptor binding domain (RBD) binding to ACE2. Both the RBD and the apo form of the Omicron spike trimer are thermodynamically unstable. An unusual RBD-RBD interaction in the ACE2-spike complex supports the open conformation and further reinforces ACE2 binding to the spike trimer. A broad-spectrum therapeutic antibody, JMB2002, which has completed a phase 1 clinical trial, maintains neutralizing activity against Omicron. JMB2002 binds to RBD differently from other characterized antibodies and inhibits ACE2 binding.

The Omicron variant of severe acute respiratory syndrome coronavirus 2 (SARS-CoV-2), the causative virus of COVID-19, was initially reported in South Africa in November 2021 and quickly became the dominant strain worldwide (*1*). Phylogenetic tree analyses revealed that Omicron evolved independently from previous variants of concerns (VOCs), including the predominant Alpha, Beta, Gamma, and Delta variants (Fig. 1A) (2–5). Compared with the original wild-type (WT) strain of SARS-CoV-2, Omicron has 60 amino acid mutations, of which 37 are in the spike protein, the target of most COVID-19 vaccines and therapeutic antibodies (Fig. 1B). This high variation is reflected in different behavior, with the Omicron variant showing enhanced transmission, antibody evasion, and vaccine resistance (6–8).

To study the mechanism for Omicron's enhanced transmission, we first biochemically characterized the interactions of the SARS-CoV-2 receptor angiotensin-converting enzyme 2 (ACE2) with the trimer of the spike extracellular domain from Omicron and the original WT strain, both of which contain proline

substitutions (2P or 6P) and a mutated furin cleavage site to stabilize the prefusion conformation (*9, 10*). Monomeric human ACE2 bound to Omicron trimeric spike protein with approximately sixfold higher affinity [dissociation constant (K_D) = 2.5 ± 0.6 nM] than the WT spike trimer (K_D = 14.7 ± 4.9 nM). The dimeric human ACE2 bound to Omicron spike trimer (K_D = 0.3 ± 0.2 nM) with approximately ninefold higher avidity than WT (K_D = 2.7 ± 1.4 nM) (Fig. 1, C and D). We then studied the interactions of ACE2 with the monomeric receptor binding domain (RBD) from the Omicron and WT strains. Monomeric human ACE2 bound to immobilized Omicron RBD (K_D = 38.9 ± 10.5 nM) with approximately twofold higher affinity than WT RBD (K_D = 75.5 ± 2.1 nM) (Fig. 1, C and D). The enhanced interaction of Omicron spike and RBD proteins with human ACE2 is consistent with previously published data (*11*) and may contribute to the increased infectivity of the Omicron variant.

To determine the structural basis of the higher affinity of the Omicron spike trimer for ACE2, we solved the structure of the ACE2-Omicron spike trimer complex at a global resolution of 2.77 Å (table S1). Despite an excess of ACE2 (molar ratio of 3.2:1 ACE2 to spike trimer; fig. S1A), we only observed strong density for one ACE2 bound to one RBD from the spike trimer in the open “up” conformation (Fig. 2A and fig. S2). The other two RBDs, with clear density, are in the closed “down” conformation. Particle classification revealed that most of the picked particles (~70%) do not have ACE2 bound. We also determined the structure of this apo Omicron spike trimer at a global resolution of 2.56 Å (fig. S2 and table S1). All three RBDs are in the closed-down conformation and are less visible in the high-

resolution map (2.56 Å; fig. S3A) yet become more visible in lower-resolution maps (4.5 and 6.5 Å; fig. S3, B and C). This contrasts with the clear visibility of the three RBDs in the ACE2-Omicron spike complex in a high-resolution map (2.56 Å; Fig. 2A), indicating that the RBD in the apo form is more dynamic, and ACE2 binding likely stabilizes the conformation of the three RBDs. Thermal shift assays at pH 7.4 revealed that the Omicron and WT RBD have single melting temperatures (T_m s) of 45.7° and 51.0°C, respectively (fig. S1C), indicating that the Omicron RBD is less stable than the WT RBD. By contrast, both the Omicron and WT spike trimer displayed two T_m s (fig. S1D), with the high T_m corresponding to the dissociation of the spike trimer and the low T_m corresponding to unfolding of the RBD. The T_m profile of the WT spike trimer is similar to previous reports (*10, 12*). T_m 1 of both the Omicron and the WT spike trimer is similar to the respective T_m for the isolated RBD (fig. S1, C and D), indicating that the Omicron RBD within the context of the spike trimer remains less stable than the WT RBD. We further confirmed the highly flexible nature of the Omicron RBD by performing hydrogen-deuterium exchange mass spectrometry (HDX), which showed that the Omicron spike trimer has an overall higher rate of HDX (fig. S4), particularly in the RBD region, consistent with its lower thermal stability.

Mapping the 37 mutations onto the up protomer of the ACE2-bound spike trimer revealed that most mutations are located on the surface of the spike protein, with many of them in known epitopes of therapeutic antibodies (Fig. 2B). We grouped the surface mutations into three hotspots (Fig. 2C and table S2). Eight mutations in the N-terminal domain (hotspot I) would affect the structures of the epitopes for a number of antibodies; for example, Δ 143-145 would remove the epitope for the 4A8 antibody (*13*). Fifteen mutations are in the RBD, which contains the ACE2-binding site as well as the epitopes for 90% of antibodies induced by infection or vaccination. Ten of these mutations are in the RBM (hotspot II) and five are near the core structure domain (hotspot III) (Fig. 2C). Hotspot II encompasses the epitopes for therapeutic antibodies AZD1061, REGN10987, and REGN10933, and hotspot III overlaps the epitope for LY-CoV555 (Fig. 2B) (*14–16*).

Local refinement of the ACE2-RBD region produced a high-quality map at 2.57-Å resolution, which allowed unambiguous building of the ACE2-RBD complex (Fig. 3A, table S1, and fig. S2). Although their RBDs differ at 15 residues, the overall structure of the Omicron ACE2-RBD complex is similar to two high-resolution x-ray structures of the WT ACE2-RBD complex [PDB codes: 6LZG and 6MOJ (*17, 18*)], with the α atoms of the

¹The CAS Key Laboratory of Receptor Research, Shanghai Institute of Materia Medica, Chinese Academy of Sciences, Shanghai 201203, China. ²Shanghai Jemincare Pharmaceuticals Co., Ltd., Shanghai 201203, China.

³University of Chinese Academy of Sciences, Beijing 100049, China. ⁴The Shanghai Advanced Electron Microscope Center, Shanghai Institute of Materia Medica, Chinese Academy of Sciences, Shanghai 201203, China. ⁵State Key Laboratory of Drug Research, Shanghai Institute of Materia Medica, Chinese Academy of Sciences, Shanghai 201203, China.

⁶Immunological Disease Research Center, Shanghai Institute of Materia Medica, Chinese Academy of Sciences, Shanghai 201203, China. ⁷School of Life Science and Technology, ShanghaiTech University, 201210 Shanghai, China.

*Corresponding author. Email: wcyin@simm.ac.cn (W.Y.); dengsjun@jemincare.com (S.-J.D.); eric.xu@simm.ac.cn (H.E.X.)

†These authors contributed equally to this work.

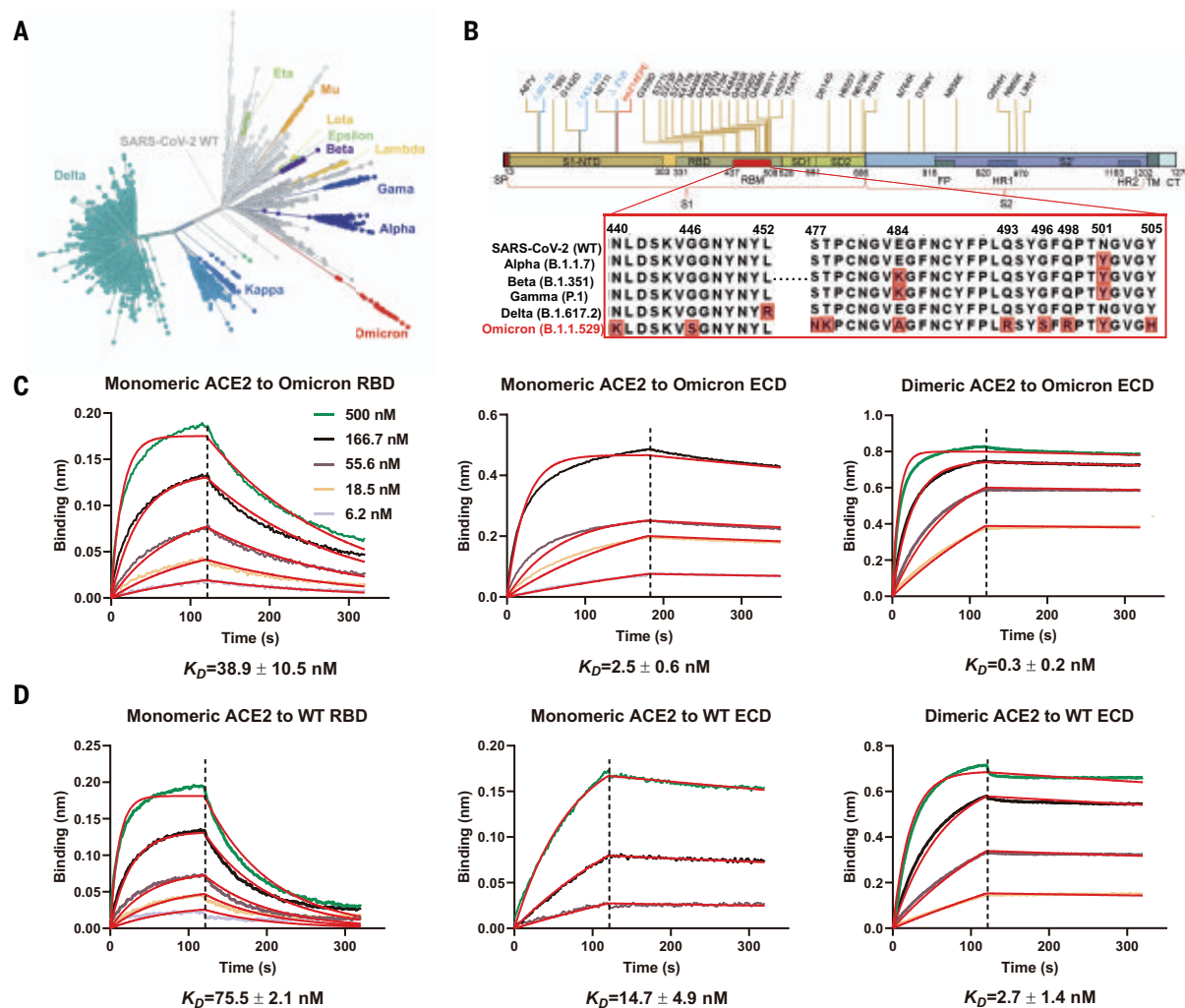


Fig. 1. High-affinity binding of the SARS-CoV-2 Omicron spike protein with human ACE2. (A) Phylogeny of the SARS-CoV-2 variants. VOCs and variants of interest are labeled on the graph; the number of spike protein mutations is positively correlated with the distance from the original strain. (B) Schematic of the Omicron spike protein domain architecture. Mutations of the Omicron spike protein are labeled with different colors (blue for deleting

mutation, red for inserting mutation). Mutations in RBM are compared with WT SARS-CoV-2 and four other VOC strains. SP, signal peptide; RBM, receptor-binding motif; SD1, subdomain 1; SD2, subdomain 2; FP, fusion peptide; HR1, heptad repeat 1; HR2, heptad repeat 2; TM, transmembrane region; CT, cytoplasmic tail. (C and D) Binding of Omicron and WT spike protein trimer and RBD to ACE2 as determined by BLI.

whole RBD deviating by <0.4 Å (Fig. 3B and table S3). We did see local differences at the ACE2-RBD interface: The Omicron RBD forms extra interactions with ACE2, including interactions from RBD mutations S477N, Q493R, Q496S, Q498R, and N501Y to ACE2 (Fig. 3C). In particular, the side chain of S477N forms two extra hydrogen bonds with S19 of ACE2, the Q498R mutation forms two additional hydrogen bonds with Q42 and D38 from ACE2, and the N501Y mutation forms extensive packing interactions with ACE2 residues Y41 and K353. These additional interactions may compensate for the loss of polar interactions between WT RBD and ACE2 caused by RBD mutations K417N and E484A (Fig. 3, C and D), consistent with the enhanced affinity of the Omicron RBD with ACE2 (Fig. 1, C and D).

We observed RBD-RBD interactions from one of the two down RBDs to the up RBD (Fig. 3A), with the interface composed of residues A475 and F486 from the down RBD and residues L368, F374, and T385 from the up RBD (Fig. 3A and fig. S5A). Structure comparison revealed that the RBD-RBD interface is not observed within the WT spike trimer because of movement of a loop (residues 368 to 374) caused by Omicron RBD mutations S371L, S373P, G339D, and S375F, which are in hotspot III (Fig. 2C and fig. S5A). This RBD-RBD interaction may stabilize the up conformation of the RBD that promotes ACE2 binding. In addition, the Omicron mutations S371L, S373P, and S375F are located at the entrance to the fatty acid-binding pocket in the WT RBD (19), and these Omicron mutations distort the pocket

(fig. S5B), thus destabilizing the RBDs in the all closed-down conformation. Consistent with involvement of spike dynamics, ACE2 binds to the Omicron spike trimer with sixfold to ninefold higher avidity than to the WT spike trimer but binds to the Omicron RBD monomer with twofold higher affinity than to WT RBD (Fig. 1, C and D). We suggest that in addition to destabilization of RBDs in the closed conformation, the RBD-RBD interactions that stabilize one RBD in the open up conformation within the spike trimer may act together with the compensating mutations in the ACE2-binding site to contribute to the higher affinity of Omicron, and this likely plays a role in its higher infectivity.

We previously discovered an antibody, JMB2002, that showed potent efficacy against

Fig. 2. Structure of the ACE2-bound Omicron spike trimer complex and epitopes of current antibodies.

(A) Cryo-EM density of the ACE2-Omicron spike trimer complex. (B) Overall structure of the ACE2-Omicron spike trimer complex and locations of the Omicron mutations. Epitope hotspots are highlighted in red circles, with the number of antibodies indicated next to the epitopes. (C) Histogram of epitope corresponding with residue numbers. Each epitope was counted if more than three heavy atoms of the residue were closer than 5 Å with the antibody. The PDB IDs and corresponding epitopes are summarized in table S2 in the supplementary materials.

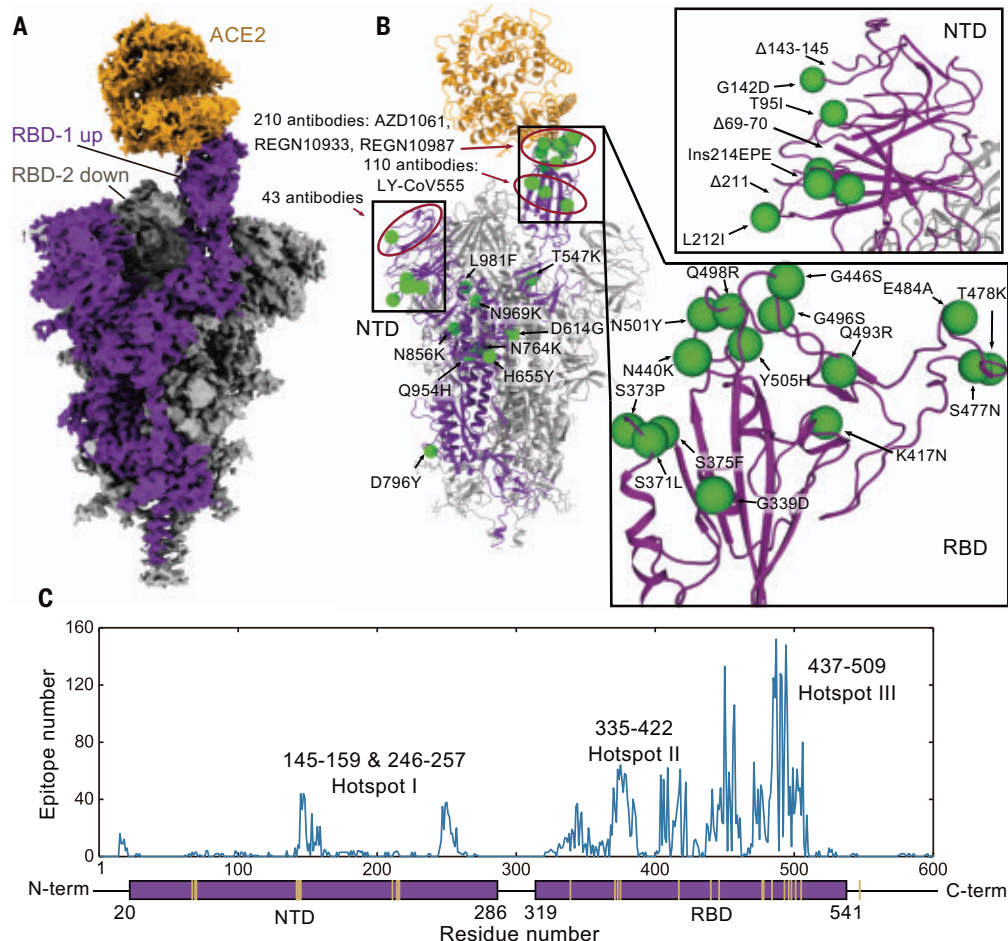
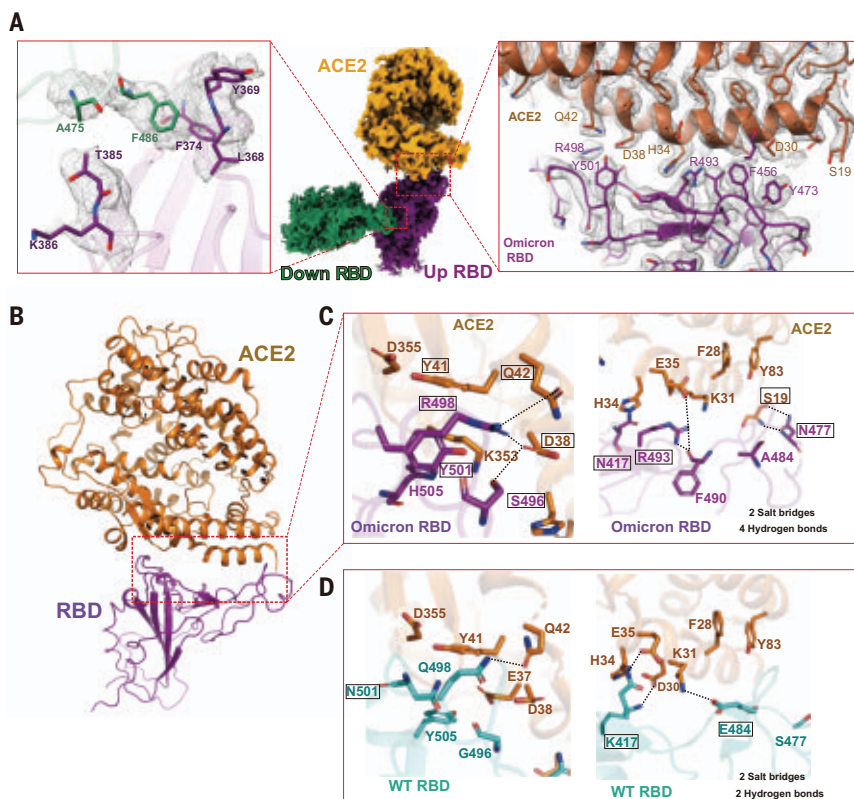


Fig. 3. Structural analysis of Omicron RBD and ACE2.

(A) Cryo-EM density of the Omicron RBD-RBD-ACE2 interface. ACE2 is colored in orange. The ACE2-bound RBD (also called the up RBD) is shown in purple. The down RBD, which directly binds to up RBD, is shown in green. Left panel is a magnified view of the RBD-RBD interaction. Middle panel is an overall cryo-EM density of the down RBD-RBD-ACE2 region. Right panel is the ACE2-RBD-binding interface. Residues are shown in sticks, with the correspondent cryo-EM density represented in mesh. (B) Overall structural model of Omicron RBD-ACE2-bound region. (C) Magnified view of Omicron RBD-ACE2 with hydrogen bond interactions. (D) Detailed hydrogen bond interactions in WT RBD-ACE2 interfaces with the same view as in (B). WT RBD is shown in blue, Omicron RBD in purple, and ACE2 in orange. Hydrogen bond or salt bridge interactions are shown as dotted lines.



the WT SARS-CoV-2 in cell-based models and in a rhesus monkey model (20). JMB2002 has completed a phase 1 clinical trial in healthy donors and was shown to have excellent safety and pharmacokinetic properties and has been approved for a clinical trial in the United States (IND 154745). We evaluated the binding of JMB2002 to WT and Omicron spike trimers. JMB2002 Fab bound the Omicron spike trimer with approximately fourfold increased affinity ($K_D = 3.2 \pm 3.0$ nM) compared with the WT spike trimer ($K_D = 12.2 \pm 11.6$ nM), whereas JMB2002 IgG showed similar avidity for the Omicron spike trimer ($K_D = 0.4 \pm 0.1$ nM) and WT ($K_D = 0.5 \pm 0.3$ nM) (Fig. 4, A to D). Furthermore, JMB2002 was able to directly inhibit the binding of ACE2 to the Omicron spike trimer with a median inhibitory concentration of 1.8 nM (Fig. 4E). In pseudovirus neutralization assays, JMB2002 effectively blocked the entry of the Omicron pseudovirus into human ACE2-expressing cells in addition to blocking the WT pseudovirus (Fig. 4F and fig. S6A). JMB2002 was also able to neutralize a number of VOCs, including variants of Alpha, Beta, and Gamma, but not Delta (fig. S6, B to E).

To reveal the basis of JMB2002 inhibition of Omicron, we solved the structure of the Omicron spike trimer bound to a Fab from JMB2002 at a global resolution of 2.69 Å (Fig. 5A, table S1, and figs. S7 and S8). To stabilize the constant regions of Fab, we used a nanobody that binds to the interface between the variable and constant regions of the light chain (27). The cryo-electron microscopy (cryo-EM) density map reveals the binding of two Fab molecules to two RBDs (one up and one down) of the trimeric spike (Fig. 5, A and B). The overall structure of the spike trimer in the Fab-bound complex is very similar to that of the ACE2-bound complex, with a root mean square difference of 1.0 Å over all Cα atoms of the spike trimer, including the unusual RBD-RBD dimer configuration (fig. S9, A and B).

Within the Fab-spike trimer structure, both Fabs bind to the same region in their respective RBD (Fig. 5, C and D). Local refinement of the Fab-bound RBD structure generated a density map to a resolution of 2.47 Å (figs. S7G and S8D), which provides detailed interactions between Fab and RBD. The Fab-binding site does not overlap with the ACE2-binding site (fig. S9C). However, in the context of the trimer, Fab binding to the down RBD would clash with ACE2 binding to the up RBD (Fig. 5E), consistent with direct inhibition of ACE2 binding to the Omicron spike trimer by JMB2002 (Fig. 4E).

Particle classification also revealed two additional antibody-bound complexes at a global resolution of 2.92 and 3.18 Å, respectively (figs. S7 and S8). One of the two complexes has the

spike trimer with one up RBD bound to one Fab and two down RBDs in the apo state (fig. S8A). The other complex contains the spike trimer with two up RBDs and one down RBD, with each RBD bound to one Fab (fig. S8C). The up-down RBD-RBD interactions within the spike trimer are conserved in these complexes. The diverse configuration and stoichiometry ratio of the spike trimer bound to the antibody further highlight the conformation flexibility of the Omicron spike RBD. The ability of the spike trimer to bind to three Fab molecules provides additional evidence for the potency of JMB2002 against Omicron.

The L452R mutation in the Delta variant is at the center of the binding epitope of JMB2002, and this mutation would clash with Y102 from the heavy chain of the Fab (Fig. 5F), thus pro-

viding an explanation for its loss of potency against the Delta variant. In addition, the binding site of the JMB2002 Fab on the RBD is distinct from the epitopes for previously defined class I to class IV antibodies (Fig. 5G) (22), so JMB2002 represents a new class of antibody against the spike trimer.

In this study, we report biochemical characterization of the Omicron spike trimer and its binding to ACE2. Our data reveal that the Omicron RBD is less stable and more dynamic than the WT RBD, and the Omicron spike trimer has sixfold to ninefold increased affinity for binding to ACE2. We further solved the structures of the Omicron spike trimer in the apo state or bound to ACE2 or an anti-Omicron antibody. The ACE2-bound structure reveals that the Omicron spike trimer contains an unusual

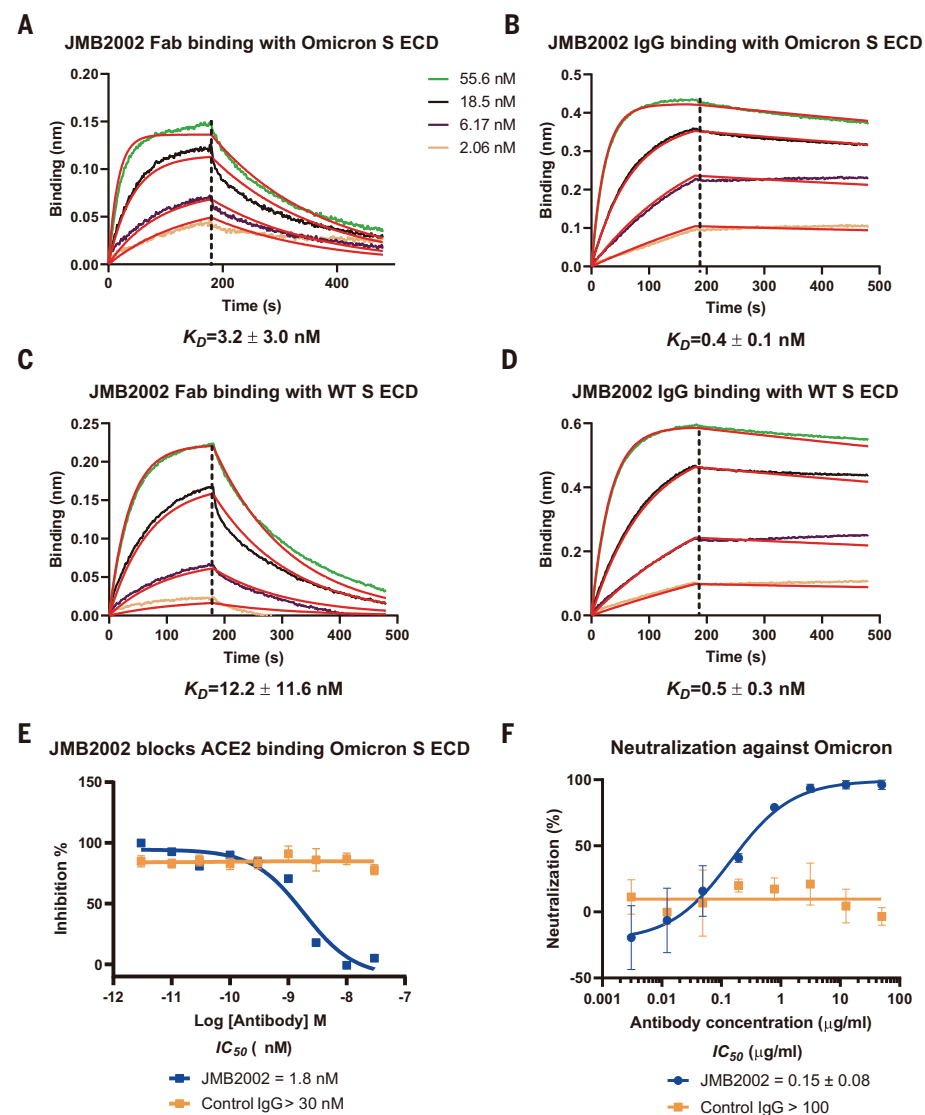
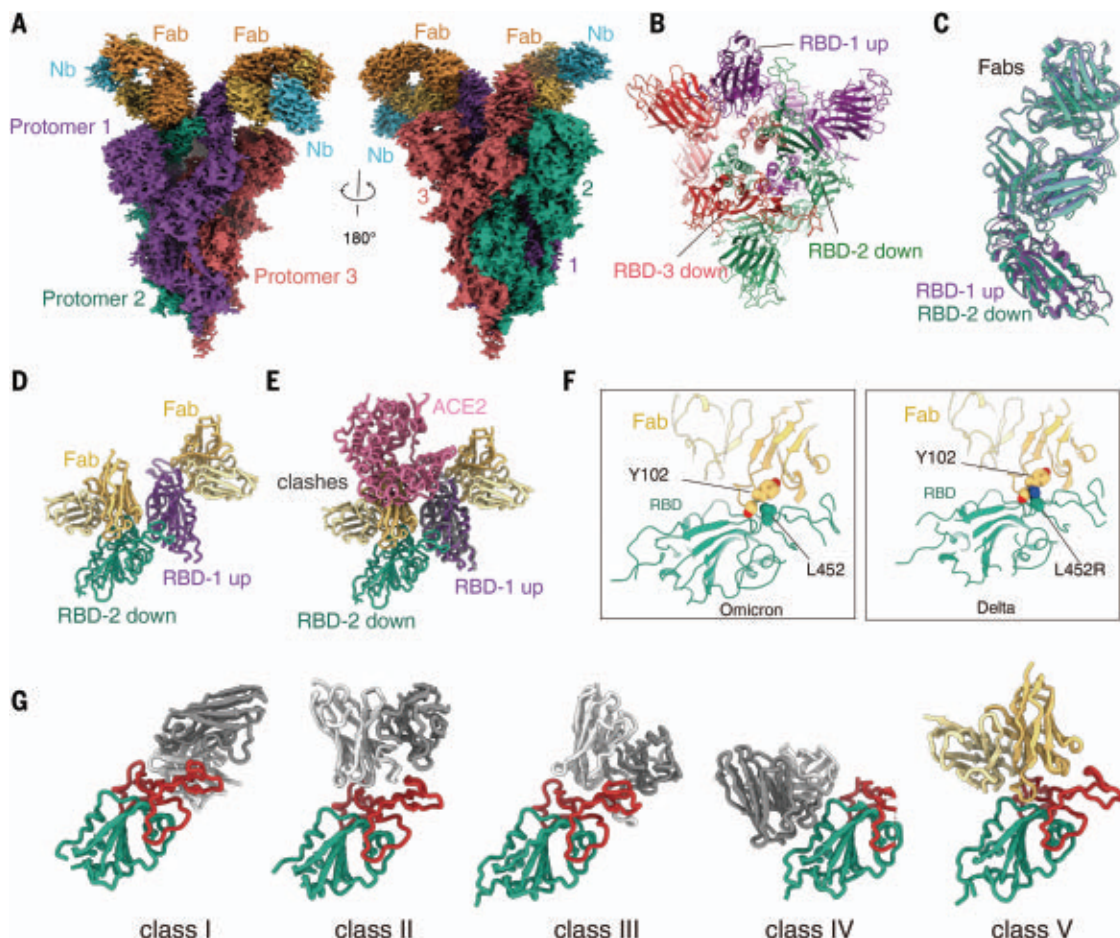


Fig. 4. Inhibition of ACE2 binding to the spike trimer by an anti-Omicron antibody. (A and C) Binding of JMB2002 Fab to the Omicron and WT spike trimer. (B and D) Binding of JMB2002 IgG to the Omicron and WT spike trimer. (E) Direct inhibition of ACE2 binding to the Omicron spike trimer by JMB2002. (F) Inhibition of the pseudovirus of Omicron by JMB2002.

Fig. 5. Structure of the Omicron spike trimer with antibody JMB2002.

(A) Cryo-EM density map of the Fab-bound Omicron spike trimer shown as two front views. (B) Top view of Fab-bound Omicron spike trimer complex model with Fab and nanobody hidden. (C) Superposition of the Fab-bound RBD-1 and RBD-2. (D) Structure of the Fab-bound RBD-1 and RBD-2. (E) Superposition of the ACE2-bound and Fab-bound RBD-1 showing that Fab binding to RBD-2 inhibits ACE2 binding to RBD-1. (F) Left panel, L452 residue from Omicron RBD interacts with Fab. Right panel, the Delta variant L452R mutation blocks the Fab binding. (G) Binding modes of four representative classes of antibody that neutralize SARS-CoV-2. PDB codes: class I, 7CM4; class II, 7CHF; class III, 7K90; and class IV, 6WPS. The JMB2002 Fab in the Omicron S protein structure shows distinct binding modes from the other four classes of antibodies.



RBD-RBD interaction and extra interactions in the ACE2-RBD interface, both of which contribute to the higher affinity of ACE2 to the Omicron spike trimer. Structural analysis of the Omicron spike trimer also provides a mechanistic basis for the ability of Omicron to escape most therapeutic antibodies and reduce the efficacy of vaccinations.

In addition, our structures of antibody-bound Omicron spiker trimer uncover a distinct mode of antibody binding to the spike trimer, in which the unusual RBD-RBD configuration is preserved. The binding epitope of this broad-spectrum antibody is different from previous anti-SARS-CoV-2 antibodies, thus opening a new venue for antibody drug discovery targeting various strains of SARS-CoV-2, including Omicron.

REFERENCES AND NOTES

1. J. Ai et al., *Emerg. Microbes Infect.* **11**, 337–343 (2022).
2. M. Yuan et al., *Science* **373**, 818–823 (2021).
3. Y. Cai et al., *Science* **373**, 642–648 (2021).
4. R. Earnest et al., *medRxiv* 2021.10.06.21264641 [Preprint] (2021). <https://doi.org/10.1101/2021.10.06.21264641>.
5. K. B. Pouwels et al., *Nat. Med.* **27**, 2127–2135 (2021).
6. Y. Cao et al., *Nature* 10.1038/s41586-021-04385-3 (2021).
7. D. Planas et al., *Nature* 10.1038/s41586-021-04389-z (2021).
8. L. Liu et al., *Nature* 10.1038/s41586-021-04388-0 (2021).

9. D. Wrapp et al., *Science* **367**, 1260–1263 (2020).
10. C. L. Hsieh et al., *Science* **369**, 1501–1505 (2020).
11. E. Camerini et al., *Nature* 10.1038/s41586-021-04386-2 (2021).
12. J. Juraszek et al., *Nat. Commun.* **12**, 244 (2021).
13. X. Chi et al., *Science* **369**, 650–655 (2020).
14. J. Hansen et al., *Science* **369**, 1010–1014 (2020).
15. B. E. Jones et al., *Sci. Transl. Med.* **13**, eabf1906 (2021).
16. D. Pinto et al., *Nature* **583**, 290–295 (2020).
17. Q. Wang et al., *Cell* **181**, 894–904.e9 (2020).
18. J. Lan et al., *Nature* **581**, 215–220 (2020).
19. C. Toelzer et al., *Science* **370**, 725–730 (2020).
20. C. Gu et al., *MAbs* **13**, 1930636 (2021).
21. Y. Yan et al., *Science* **373**, 413–419 (2021).
22. S. Kumar, A. Chandele, A. Sharma, *PLOS Pathog.* **17**, e1009885 (2021).

ACKNOWLEDGMENTS

The cryo-EM data were collected at the Shanghai Advanced Electron Microscope Center. **Funding:** This work was partially supported by the Ministry of Science and Technology of China (grant 2018YFA0507002 to H.E.X.); the Shanghai Municipal Science and Technology Major Project (grant 2019SHZDZX02 to H.E.X.); the CAS Strategic Priority Research Program (grant XDB37030103 to H.E.X.); the National Natural Science Foundation of China (grant 32171189 to W.Y., grant 32130022 to H.E.X., grant 31770796 to Y.J., and grant 81902085 to Y.X.); the Youth Innovation Promotion Association of CAS (grant 2021278 to W.Y.); the National Science Fund for Excellent Young Scholars (grant 82122067 to W.Y.); the Key Tasks of LG Laboratory (grant LG202103-03-05 to W.Y. and grant LG202101-01-03 to Y.X.); the Fund of Youth Innovation Promotion Association (grant 2018319 Y8G7011009 to X.C.); the Science and Technology Commission of Shanghai Municipal (grant 20431900100 to H.J.); the Jack Ma

Foundation (grant 2020-CMKYGG-05 to H.J.); the National Science and Technology Major Project (grant 2018ZX09711002 to Y.J.); and the China Postdoctoral Science Foundation (Funded Project E11289R078 to C.W.). **Author contributions:** W.Y. designed the expression constructs, purified the spike complex proteins, screened the cryo-EM conditions, prepared the cryo-EM grids, collected cryo-EM images toward the structures, and participated in figure and manuscript preparation. Y.X. collected cryo-EM images with the help of Q.Y., K.W., and W.H.; performed density map calculations; participated in the model building; and refined the final models with P.X.; Y.X., P.X. and C.W. participated in figure and manuscript preparation. X.W. purified the ACE2 protein. S.H. performed the AlphaScreen assays. H.J. supervised X.C., Z.H., and X.H.; analyzed the molecular dynamics simulations; and participated in figure preparation. J.Z. supervised B.S., detected the HDX data by mass spectrometry, and participated in figure preparation. Y.J. participated in experimental design and manuscript editing. S.D. supervised X.C., C.G., J.L., Z.W., F.J., K.X., P.L., and X.W.; provided the JMB2002 antibodies; performed the function assays for JMB2002 antibodies and spike proteins; and participated in manuscript writing. H.E.X. conceived and supervised the project, analyzed the structures, and wrote the manuscript with inputs from all authors. **Competing interests:** W.Y., Y.X., P.X., C.W., X.H., X.W., S.H., Q.Y., K.W., W.H., Z.H., B.S., J.Z., H.J., X.C., Y.J., and H.E.X. declare no competing interests. X.C., C.G., J.L., Z.W., F.J., K.X., P.L., X.W., and S.-J.D. are employees of Shanghai Jemincare Pharmaceuticals and are developing JMB2002 as a potential anti-Omicron therapeutic. **Data and materials availability:** Density maps and structure coordinates have been deposited with immediate release. The accession numbers for the Electron Microscopy Database and the Protein Data Bank, respectively, are EMD-32679 and PDB ID 7WP9 for the Omicron spike trimer, EMD-32680 and PDB ID 7WPA for the Omicron spike trimer in complex with hACE2, EMD-32681 and PDB ID 7WPB for the local refined reconstruction of the Omicron

spike RBD in complex with hACE2, EMD-32682 and PDB ID 7WPC for local refined reconstruction of a second Omicron spike RBD in complex with RBD-hACE2, EMD-32683 and PDB ID 7WPD for Omicron spike trimer in complex with one JMB2002 Fab, EMD-32684 and PDB ID 7WPE for the Omicron spike trimer in complex with two JMB2002 Fabs, EMD-32685 and PDB ID 7WPF for the Omicron spike trimer in complex with three JMB2002 Fabs, and EMD-32736 and PDB ID 7WRV for local refined reconstruction of the Omicron spike RBD in complex with JMB2002 Fab. Materials are available upon request. This work is licensed under a Creative Commons

Attribution 4.0 International (CC BY 4.0) license, which permits unrestricted use, distribution, and reproduction in any medium, provided the original work is properly cited. To view a copy of this license, visit <https://creativecommons.org/licenses/by/4.0/>. This license does not apply to figures/photos/artwork or other content included in the article that is credited to a third party; obtain authorization from the rights holder before using such material.

SUPPLEMENTARY MATERIALS

science.org/doi/10.1126/science.abn8863

Materials and Methods
Figs. S1 to S10
Tables S1 to S3
References (23–36)
MDAR Reproducibility Checklist

28 December 2021; accepted 2 February 2022
Published online 8 February 2022
10.1126/science.abn8863

EPIGENETICS

Highly enriched BEND3 prevents the premature activation of bivalent genes during differentiation

Jing Zhang^{1†}, Yan Zhang^{1†}, Qinglong You^{1,2†}, Chang Huang¹, Tiantian Zhang¹, Mingzhu Wang³, Tianwei Zhang¹, Xiaocheng Yang^{1,2}, Jun Xiong¹, Yingfeng Li¹, Chao-Pei Liu¹, Zhuqiang Zhang¹, Rui-Ming Xu^{1,2*}, Bing Zhu^{1,2*}

Bivalent genes are ready for activation upon the arrival of developmental cues. Here, we report that BEND3 is a CpG island (CGI)–binding protein that is enriched at regulatory elements. The cocrystal structure of BEND3 in complex with its target DNA reveals the structural basis for its DNA methylation–sensitive binding property. Mouse embryos ablated of *Bend3* died at the pregastrulation stage. *Bend3* null embryonic stem cells (ESCs) exhibited severe defects in differentiation, during which hundreds of CGI-containing bivalent genes were prematurely activated. BEND3 is required for the stable association of polycomb repressive complex 2 (PRC2) at bivalent genes that are highly occupied by BEND3, which suggests a reining function of BEND3 in maintaining high levels of H3K27me3 at these bivalent genes in ESCs to prevent their premature activation in the forthcoming developmental stage.

CpG islands (CGIs) are generally associated with housekeeping genes (1–3). BANP, a DNA methylation–sensitive CGI-binding protein, is required for their activation (4). CGIs are also associated with bivalent genes (5, 6), so we investigated whether and how CGI-associated bivalent genes are regulated by sequence-specific recognition. BEND3 was identified as an unmethylated DNA-binding protein in vitro (7, 8). Chromatin immunoprecipitation sequencing (ChIP-seq) experiments in mouse TT2 embryonic stem cells (ESCs) (9) identified a total of 27,536 BEND3 peaks, with ~51 and 28% of them overlapped with promoters and enhancers, respectively (Fig. 1A).

BEND3 occupancy was heavily biased toward CGI-associated genes (Fig. 1, B to D). Approximately 85% (12,037 of 14,117) of CGI-associated transcription start sites (TSSs) and 81% of CGI-associated enhancers (1246 of 1533) were

bound by BEND3 (Fig. 1, C and D). BEND3 and nonmethylated island (NMI) signals (10) displayed a strong overlap at BEND3 peaks (fig. S1A). Notably, BEND3 occupied active (H3K4me3 only) and bivalent promoters (H3K4me3 and H3K27me3) but not silenced promoters (H3K27me3 only) (Fig. 1E). At enhancers, BEND3 preferentially occupied poised enhancers marked by H3K4me1 and H3K27me3 (Fig. 1F). Notably, 45% of poised enhancer-associated genes are bivalent genes (Fig. 1G) (11–13).

A sequence motif (CCCACGCG) containing two CpG sites (Fig. 2A) was identified as the most enriched motif using the ChIP-seq analysis software HOMER (14). BEND3-bound regions exhibited far lower CpG methylation levels than those at the unbound sites (Fig. 2B).

The binding motif of BANP shares CGCG with the BEND3 motif but differs at flanking regions (Fig. 2A). BANP is enriched at the CGI promoters but not at the CGI enhancers (fig. S1B) (4). Different from BEND3, BANP strongly prefers the active CGI promoters (fig. S1C), which suggests that BEND3 may play a distinct role in regulating bivalent genes.

BEND3 has four BEN domains (fig. S2A), and the *Drosophila* Insv BEN domain is a sequence-specific DNA-binding module (15). In electrophoretic mobility shift assays (EMSAs), only

the fourth BEN domain (BEN4) of BEND3 exhibited binding toward a probe containing the CCCACGCG motif (Fig. 2C).

To understand how BEN4 recognizes its target DNA in a DNA methylation–sensitive manner, we solved a 2.5-Å structure of a selenomethionine-substituted L740→M (L740M) mutant of BEN4 bound to a 16-nucleotide oligomer DNA containing the consensus recognition motif and a 3.5-Å structure of native BEN4 bound to the same DNA. Both structures show a domain-swapped dimer of BEN4 bound to two independent DNA duplexes, with the L740M dimer generated by crystal symmetry (Fig. 2D). Despite the difference in the relative orientation of two protein-DNA modules within each complex and variation in the hinge region connecting the two globular domains, the two structures share a common DNA-binding mode (fig. S2B). We will use the more accurate L740M structure for description henceforth, unless otherwise specified. Each BEN4 monomer features five α helices, α 1 to α 5, and an independent DNA-binding module in BEN4 is formed by α 1 to α 4 from one monomer and a domain-swapped α 5' from the neighboring molecule (Fig. 2D). By contrast, the third BEN domain (BEN3) is monomeric in solution and in the crystal (fig. S2C). BEN3 shares high sequence similarity with BEN4 (fig. S2D), and the overall structure of the BEN3 domain is very similar to that of BEN4 except for the orientation of α 5, which folds back and packs against its N-terminal helices to form a globular domain (fig. S2C). The monomeric BEN3 structure offers insights into the mechanism of dimer formation of BEN4. The dimeric conformation of BEN4 is mediated by its hinge region between α 4 and α 5 (Fig. 2D). A monomeric BEN4 mutant (BEN4-mu) with its hinge region (residues 787 to 792) replaced by the counterpart sequence of BEN3 (residues 621 to 626) can still bind to the consensus motif, but only one DNA molecule can be bound (fig. S2E).

The BEN4 domain interacts with both strands of DNA, with α 5 (residues 791 to 818) occupying the major groove and a segment of the loop between α 3 and α 4 (residues 756 to 771) contacting the minor groove. Detailed protein-DNA contacts involving the consensus sequence are illustrated schematically (Fig. 2E). For the

¹National Laboratory of Biomacromolecules, CAS Center for Excellence in Biomacromolecules, Institute of Biophysics, Chinese Academy of Sciences, Beijing 100101, China. ²College of Life Sciences, University of Chinese Academy of Sciences, Beijing 100049, China. ³Institutes of Physical Science and Information Technology, Anhui University, Hefei 230601, Anhui, China. *Corresponding author. Email: rmxu@ibp.ac.cn (R.-M.X.); zhubing@ibp.ac.cn (B.Z.)

†These authors contributed equally to this work.

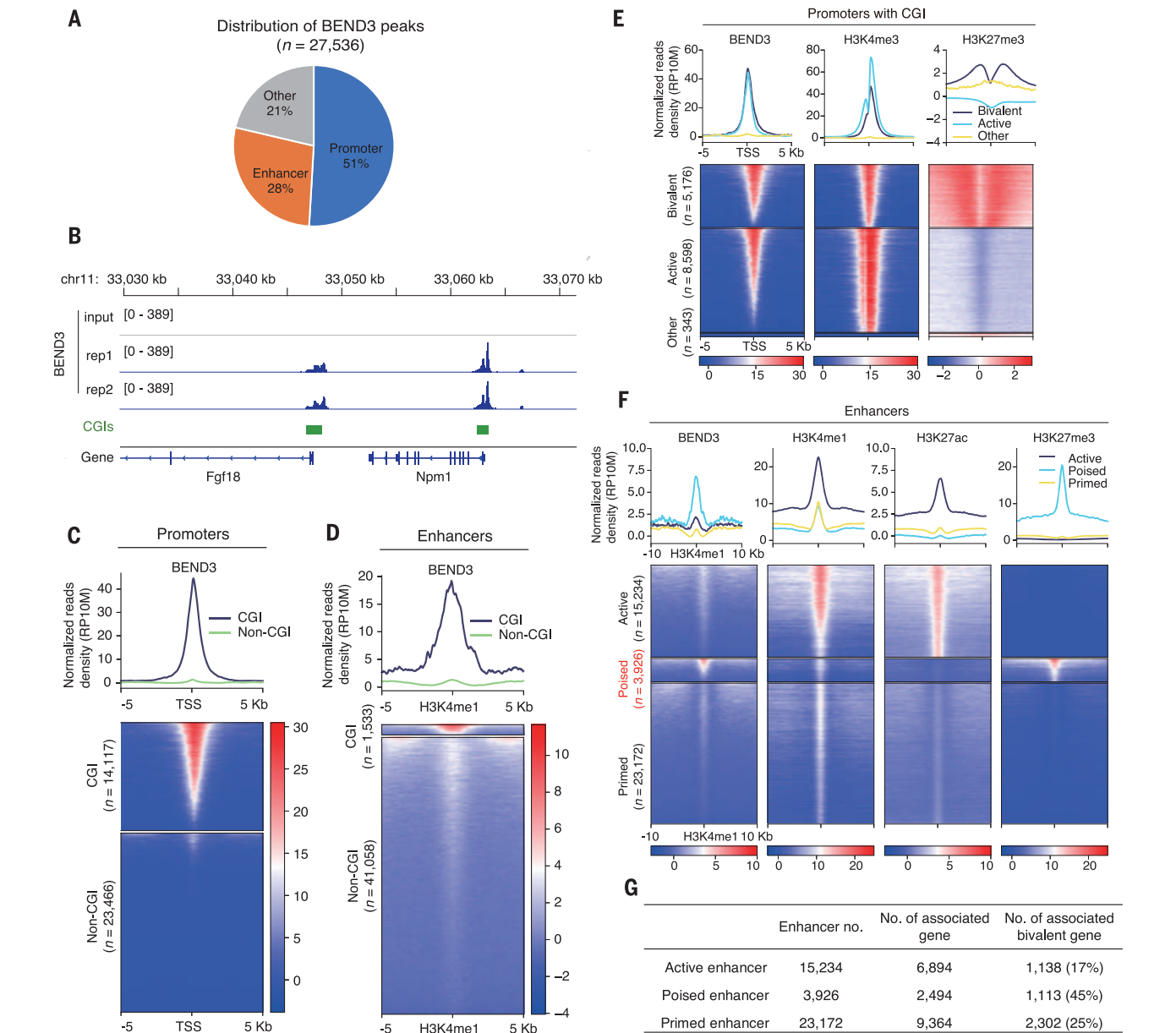


Fig. 1. BEND3 is enriched at CGI promoters and CGI enhancers. (A) Distribution of BEND3 ChIP-seq peaks. (B) Examples of BEND3 ChIP-seq tracks. chr11, chromosome 11. (C) Heatmaps of BEND3 ChIP-seq signals around the TSSs of CGI and non-CGI promoters. (D) Heatmaps of BEND3 ChIP-seq signals surrounding

CGI and non-CGI enhancers. (E) Heatmaps of BEND3 ChIP-seq signals around the TSSs of different types of CGI promoters. (F) Heatmaps of BEND3 ChIP-seq signals surrounding different types of enhancers. (G) The total number of enhancers in each group and the number and percentage of their associated bivalent genes.

top strand, E804 and C(+7) form a key base-specific contact, whereas R808, S732, and N735 contact the sugar-phosphate backbone. For the bottom strand, key base-specific contacts include that between R807 and G(−9) and that between K812 and G(−5) and G(−6), whereas the N759, S761, K766, H795, and K813 contact the sugar-phosphate backbone. Notably, the side chains of E804, R807, and K812 on $\alpha 5$ form base-specific hydrogen bonds in the major groove (Fig. 2F). Mutations of R807 or K812 abolished the DNA-binding activity of BEN4 (Fig. 2G). Moreover, in *Bend3* knockout

(KO) ESCs rescued by a full-length BEND3 R807K-K812E mutant (fig. S2F), the chromatin localization of BEND3 was mostly lost (Fig. 2H), which indicates that BEN4 is the main domain responsible for chromatin localization. We observed a close contact between the guanidino group of R807 and C(−10). Modeling of a 5′-methyl (5′-m) group onto C(−10) introduces a direct clash between 5′-mC(−10) and R807 (Fig. 2I). This is in accordance with the observation that methylation at C(−10) prevented BEN4 from binding its target DNA (Fig. 2J). Within the CCCACGCG motif,

only the first six base pairs are required for base-specific interaction or methylation-sensitive binding to BEND3. We acquired *Bend3*^{+/*tm1a*} mice carrying a recombinant *Bend3*^{*tm1a*} allele with an IRES:LacZ trapping cassette inserted into the third intron (fig. S3A) (16). A *Bend3*^{−/−} allele with all four BEN domains excised was obtained after crossing with *Zp3-Cre* mice. After crossing *Bend3*^{+/*−*} males and females, no *Bend3*^{−/−} pups were born and no *Bend3*^{−/−} embryos were identified at embryonic day 6.5 (E6.5); however, *Bend3*^{−/−} embryos were

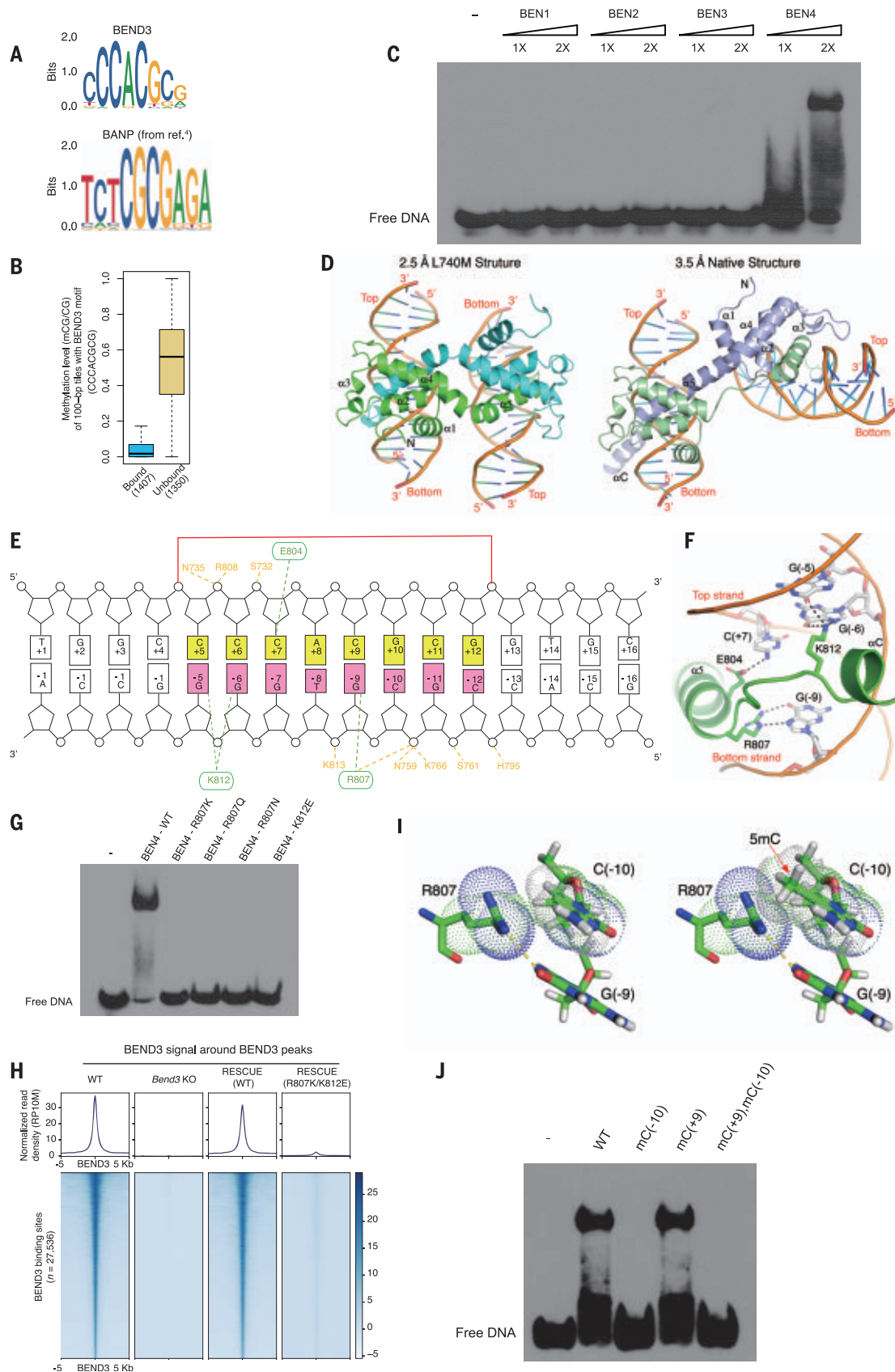
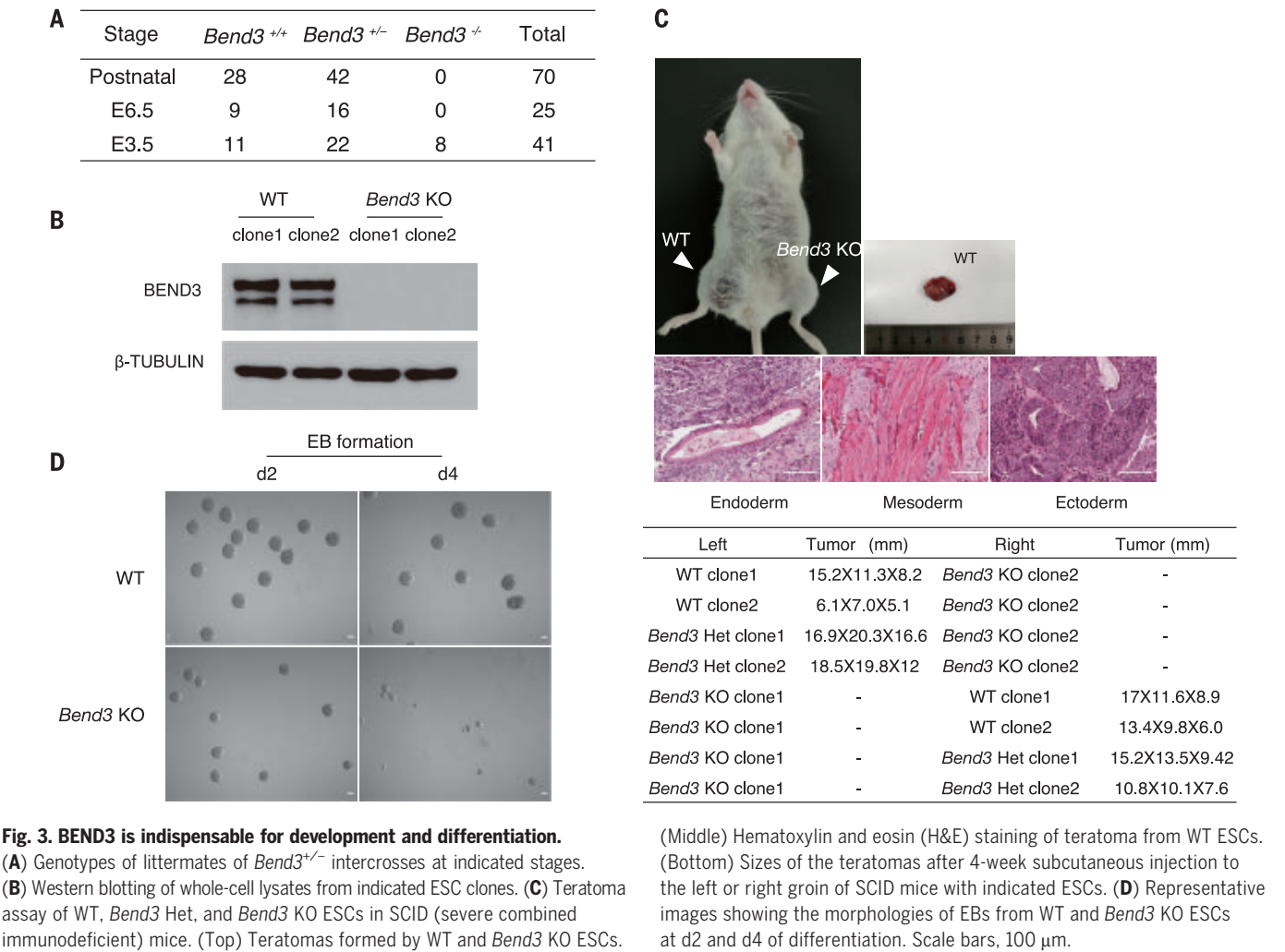


Fig. 2. Sequence-specific recognition of BEND3 and the underlying structure basis.

(A) Top BEND3-binding motif identified by HOMER (top), and the BANP-binding motif from literature (4) (bottom). (B) DNA methylation level of BEND3-bound and BEND3-unbound 100-base pair (bp) tiles containing BEND3-binding motif. (C) EMSA results of the binding of individual recombinant BEN domain with a 16-nucleotide oligomer DNA probe containing BEND3-binding motif. Proteins were added with increasing amount. (D) Structures of the complex containing two BEN4 domains bound to two 16-nucleotide oligomer DNA duplexes. (E) A schematic drawing of BEN4-DNA interaction. (F) A detailed view of BEN4-DNA interaction. (G) EMSA results with BEN4 wild types or mutants. (H) Heatmaps of BEND3 ChIP-seq signals around BEND3-binding sites in WT TT2, *Bend3* KO, and rescued cell lines. (I) Structural explanation for the DNA methylation-sensitive property of BEN4. (J) EMSA results showing methylation at C(-10) blocks BEN4 binding. Single-letter abbreviations for the amino acid residues are as follows: A, Ala; C, Cys; D, Asp; E, Glu; F, Phe; G, Gly; H, His; I, Ile; K, Lys; L, Leu; M, Met; N, Asn; P, Pro; Q, Gln; R, Arg; S, Ser; T, Thr; V, Val; W, Trp; and Y, Tyr.



observed at around the Mendelian ratio at E3.5 (Fig. 3A), which suggests that *Bend3* deletion led to embryonic lethality between E3.5 and E6.5. We derived *Bend3*^{+/+} [wild-type (WT)], *Bend3*^{+/-} (*Bend3* Het), and *Bend3*^{-/-} (*Bend3* KO) ESCs from corresponding blastocysts (Fig. 3B and fig. S3B). *Bend3* KO ESCs appeared to be largely normal in morphology, alkaline phosphatase staining, and expression of self-renewal genes (fig. S3, C to E).

Given the pregastrulation lethal phenotype, BEND3 is likely required for ESC differentiation. In fact, 1 × 10⁶ *Bend3* KO ESCs injected into the groins of immune-deficient mice could not form teratomas (Fig. 3C). Next, we performed embryoid body (EB) formation assay. After hanging drop culture for 2 days, EBs derived from *Bend3* KO ESCs were smaller and gradually shrank as a result of massive cell death (Fig. 3D), which again indicates a critical role of BEND3 in differentiation.

To clarify the molecular mechanism underlying the differentiation defect, we harvested WT, *Bend3* Het, and *Bend3* KO EBs at day 1 (d1), d2, and d3 during differentiation and per-

formed RNA sequencing (RNA-seq) experiments. Principal components analysis (PCA) revealed that the expression profiles of *Bend3* KO cells gradually differed from the control cells during differentiation (Fig. 4A), and the number of dysregulated genes gradually increased as differentiation progressed (Fig. 4B); however, even at d3, only a fraction of BEND3 targets were dysregulated. We noticed that a small group of BEND3 peaks (~5%) exhibited much greater levels of BEND3 signal (Fig. 4C), and they tended to have more BEND3-binding motifs (Fig. 4D). BEND3 is associated with both active and bivalent genes (Fig. 1E). However, gene set enrichment analysis (GSEA) results indicated that bivalent genes that were associated with high levels of BEND3—but not their counterparts among the active genes—were significantly up-regulated in *Bend3* KO EBs at d3 (fig. S4A). These data suggest that BEND3 preferentially attenuates the expression of its top target bivalent genes during differentiation.

To analyze the effect of BEND3 binding on gene expression, we categorized bivalent and

active BEND3 target genes according to the number of BEND3-binding motifs (≥5, 3 to 4, 1 to 2, or 0) of their associated BEND3 peaks and plotted their transcriptional changes upon *Bend3* deletion. Bivalent BEND3 targets with the highest number of BEND3 motifs were up-regulated upon differentiation in *Bend3* KO EBs at d2 and d3, but such a trend was not observed in ESCs or for the active target genes (Fig. 4E and fig. S4, B and C).

Notably, the aberrantly up-regulated genes tended to exhibit some degree of up-regulation in d2 and d3 WT EBs compared with WT ESCs (fig. S4D). We speculated that these genes might be up-regulated during normal differentiation, and the loss of BEND3 accelerated this process. To test this, we performed further analysis using a long-term differentiation (up to d8) dataset from WT J1 ESCs. We focused on BEND3 targets that were bivalent and were aberrantly up-regulated in *Bend3* KO d3 EBs, and we found that these genes were not up-regulated at d2 but were robustly activated at d5 and d8 in WT EBs (fig. S4E). Compared with WT ESCs, only 4% of these genes were

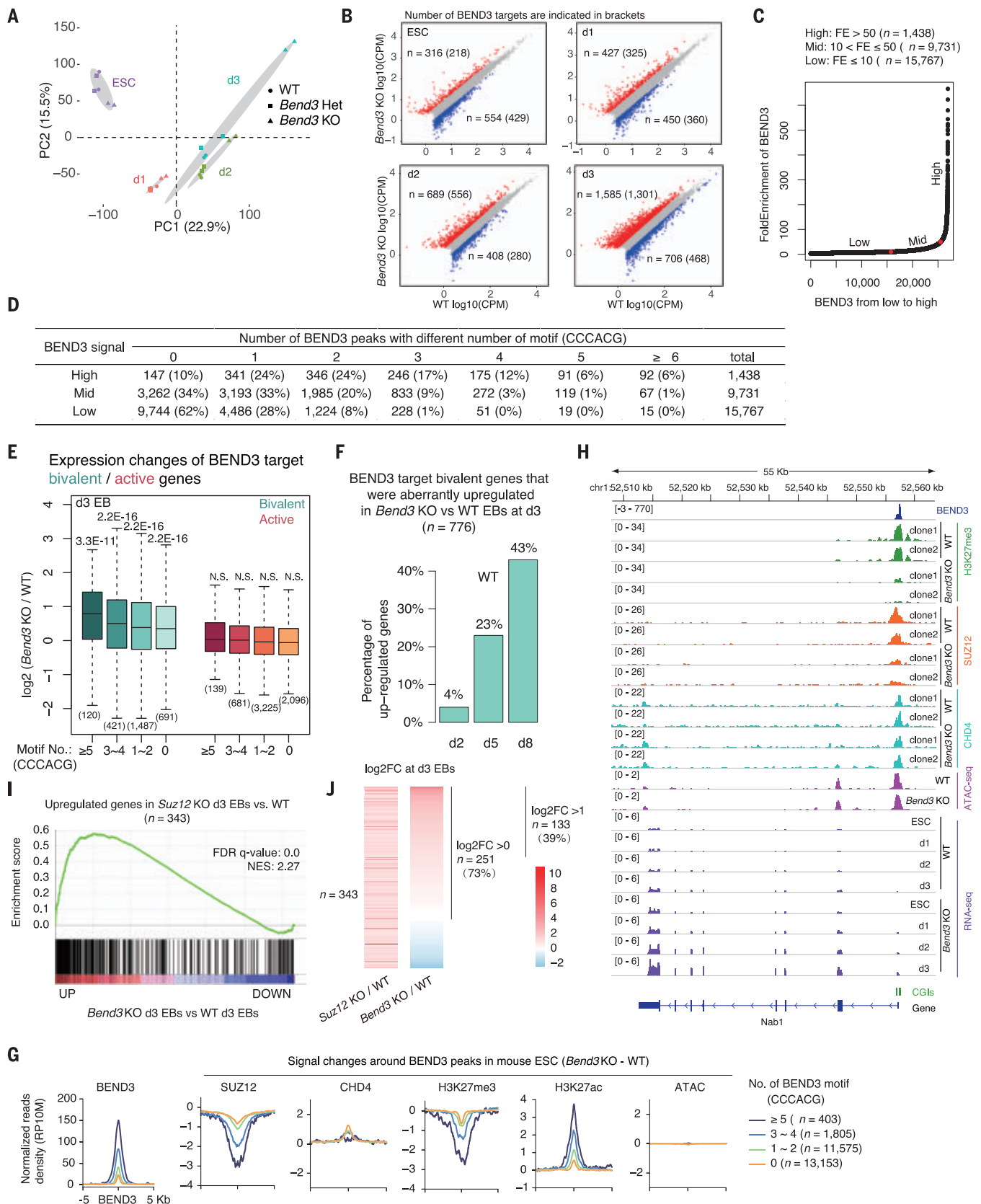


Fig. 4. *Bend3* deletion leads to premature activation of highly occupied bivalent genes during differentiation. (A) PCA results of transcriptomes in WT, *Bend3* Het, and *Bend3* KO ESCs and EBs at d1, d2, and d3. Two clones were

used for each genotype. (B) Scatter plots showing gene expression levels between WT and *Bend3* KO ESCs and EBs at d1, d2, and d3 during differentiation. Significantly dysregulated (fold change > 2; adjusted *P* < 0.05

and $P < 0.01$) genes are labeled in red (up-regulated) or blue (down-regulated). Other genes are labeled in gray. **(C)** Scatter plot showing the fold enrichment (FE) of all BEND3 ChIP-seq peaks ($n = 26,936$) identified in WT ESCs.

(D) Number and percentage of all BEND3 ChIP-seq peaks containing different number of motif (CCCACG). **(E)** Box plots showing the transcriptional changes of BEND3 target bivalent and active genes in d3 EBs. Genes are grouped by the motif number of associated BEND3 peaks at promoters or enhancers, and genes with a read count of >50 in at least one sample of a comparison were kept for analysis. **(F)** Percentage of up-regulated genes in d2, d5, and d8 EBs from J1

ESCs for aberrantly up-regulated BEND3 target bivalent genes in *Bend3* KO d3 EBs. **(G)** Changes of normalized read density of SUZ12, CHD4, H3K27me3, H3K27ac, and chromatin accessibility (ATAC-seq) at four BEND3 peak groups in WT and *Bend3* KO mouse ESCs. **(H)** Snapshots of a representative region strongly occupied by BEND3 showing indicated chromatin features and expression levels. **(I)** GSEA for up-regulated genes in *Suz12* KO d3 EBs with respect to the global transcriptional changes observed in *Bend3* KO d3 EBs. **(J)** The effect of *Bend3* KO on the expression of genes up-regulated in *Suz12* KO d3 EBs. \log_2 FC, \log_2 fold change.

up-regulated in WT d2 EBs, but 23 and 43% of them became up-regulated in WT d5 and d8 EBs, respectively (Fig. 4F).

BEND3 participates in the recruitment of PRC2 to major satellites in cells lacking DNA methylation (17), and BEND3 interacts with the NuRD complex (17, 18). Therefore, we performed ChIP-seq experiments for SUZ12 (a subunit of PRC2) and CHD4 (a subunit of NuRD) in WT and *Bend3* KO ESCs. We found that the SUZ12 signal at the BEND3 peaks was reduced upon the loss of BEND3, the levels of SUZ12 decreased, and the concomitant H3K27me3 reduction correlated with the number of BEND3-binding motifs (Fig. 4, G and H, and fig. S5A). These changes were specific for bivalent targets, especially those that were aberrantly up-regulated in d3 *Bend3* KO EBs, but not for active targets (fig. S5, B and C). We did not observe a loss of CHD4 occupancy or an increase of assay for transposase-accessible chromatin with high-throughput sequencing (ATAC-seq) signal upon *Bend3* deletion, although the increase of H3K27ac accompanied the loss of H3K27me3 (Fig. 4G and fig. S5A).

We next analyzed the expression of genes associated with all of the H3K27me3 peaks that overlapped with BEND3 peaks and exhibited greater than twofold reduction of H3K27me3 signal upon *Bend3* deletion. We found that the loss of H3K27me3 did not lead to immediate activation of these genes in ESCs but caused premature up-regulation during differentiation (fig. S5D).

Finally, we analyzed public transcriptome data from WT and *Suz12* KO EBs (19). GSEA results indicated that genes up-regulated in *Suz12* KO d3 EBs were significantly enriched in genes up-regulated in *Bend3* KO d3 EBs (Fig. 4I). Among 343 genes with greater than twofold up-regulation in *Suz12* KO d3 EBs, 73% (251) of them exhibited increased expression, and 39% (133) of them reached the twofold threshold in *Bend3* KO d3 EBs (Fig. 4J). These results provide further support that BEND3 function is largely PRC2 dependent.

Taken together, our results suggest that BEND3 is required for the optimal association

of PRC2 at bivalent CGIs highly enriched with BEND3. *Bend3* deletion leads to reduced PRC2 and H3K27me3 levels at these genes. This does not immediately activate most of these genes because the differentiation signal and corresponding transcription factors are not yet available; however, the loss of H3K27me3 affects the kinetics of bivalent gene induction upon the arrival of the differentiation signal and causes premature activation and the failure of differentiation. Gene bivalency was observed many years ago (20), but its exact function remains a matter of debate. It is widely expected in priming bivalent genes for faster induction, largely because of the enrichment of H3K4me3. However, MLL2 deletion abolishes H3K4me3 at bivalent genes without affecting their induction kinetics (21). We propose that gene bivalency can prevent premature gene activation during differentiation—an opposite effect of priming—which we refer to as reining.

Not all BEND3 targets are equally affected by *Bend3* deletion, and similar events have been observed for many sequence-specific binding proteins (22–24), likely because of the compounding effect of other sequence-specific binding proteins nearby. Nevertheless, the finding that BEND3 has a stronger effect at its highly occupied targets is notable and reflects a principle coined as “more is different” (25).

REFERENCES AND NOTES

1. F. Larsen, G. Gundersen, R. Lopez, H. Prydz, *Genomics* **13**, 1095–1107 (1992).
2. J. Zhu, F. He, S. Hu, J. Yu, *Trends Genet.* **24**, 481–484 (2008).
3. S. Beck *et al.*, *Nat. Commun.* **5**, 5490 (2014).
4. R. S. Grand *et al.*, *Nature* **596**, 133–137 (2021).
5. T. S. Mikkelsen *et al.*, *Nature* **448**, 553–560 (2007).
6. M. Ku *et al.*, *PLOS Genet.* **4**, e1000242 (2008).
7. J. Xiong *et al.*, *Mol. Cell* **64**, 913–925 (2016).
8. M. Iurlaro *et al.*, *Genome Biol.* **14**, R119 (2013).
9. M. Tachibana *et al.*, *Genes Dev.* **16**, 1779–1791 (2002).
10. H. K. Long *et al.*, *eLife* **2**, e00348 (2013).
11. E. Blanco, M. González-Ramírez, A. Alcaine-Colet, S. Aranda, L. Di Croce, *Trends Genet.* **36**, 118–131 (2020).
12. A. Rada-Iglesias *et al.*, *Nature* **470**, 279–283 (2011).
13. S. Cruz-Molina *et al.*, *Cell Stem Cell* **20**, 689–705.e9 (2017).
14. S. Heinz *et al.*, *Mol. Cell* **38**, 576–589 (2010).
15. Q. Dai *et al.*, *Genes Dev.* **27**, 602–614 (2013).

16. M. C. Birling *et al.*, *Nat. Genet.* **53**, 416–419 (2021).
17. N. Saksouk *et al.*, *Mol. Cell* **56**, 580–594 (2014).
18. K. M. Sathyan, Z. Shen, V. Tripathi, K. V. Prasanth, S. G. Prasanth, *J. Cell Sci.* **124**, 3149–3163 (2011).
19. E. M. Riising *et al.*, *Mol. Cell* **55**, 347–360 (2014).
20. B. E. Bernstein *et al.*, *Cell* **125**, 315–326 (2006).
21. D. Hu *et al.*, *Nat. Struct. Mol. Biol.* **20**, 1093–1097 (2013).
22. D. A. Cusanovich, B. Pavlovic, J. K. Pritchard, Y. Gilad, *PLoS Genet.* **10**, e1004226 (2014).
23. D. Kenzelmann Broz *et al.*, *Genes Dev.* **27**, 1016–1031 (2013).
24. F. Spitz, E. E. Furlong, *Nat. Rev. Genet.* **13**, 613–626 (2012).
25. P. W. Anderson, *Science* **177**, 393–396 (1972).

ACKNOWLEDGMENTS

We thank the staff from the animal center of the Institute of Biophysics for technical assistance. We thank X. Yang and J. Hao from the Pathology Analysis Group of the Institute of Biophysics for assistance with paraffin embedding and histomorphology. We thank beamline scientists at BL17U of the Shanghai Synchrotron Radiation Facility (SSRF) for technical support during data collection. **Funding:** This work was supported by grants from the Chinese Ministry of Science and Technology (2019YFA0801401, 2017YFA0504100, 2019YFA0508900, 2017YFA0504202, and 2016YFA0100400), the China Natural Science Foundation (31771429, 31501059, 31991162, and 31521002), the Chinese Academy of Sciences (XDB37010100, XDB39010100, and QYZDY-SSW-SMC031), and the K. C. Wong educational foundation (GJTD-2020-06). Z.Z. and J.X. are supported by the Youth Innovation Promotion Association (2017133 and 2020097) of the Chinese Academy of Sciences. **Author contributions:** B.Z. and R.-M.X. designed and supervised the project. J.Z. performed most of the experiments. Y.Z. performed the bioinformatics analysis. Q.Y. performed the crystallization experiments. C.H., Tian.Z., M.W., Tian.Z., J.X., X.Y., Y.L., C.-P. L., and Z.Z. assisted in experiments and data analysis. J.Z., Y.Z., Q.Y., R.-M.X., and B.Z. wrote the manuscript, and all the authors read and commented on the manuscript. **Competing interests:** The authors declare no competing interests. **Data and materials availability:** The ChIP-seq, CUT&Tag (cleavage under targets and tagmentation), RNA-seq, ATAC-seq, and T-WGBS datasets have been deposited in BIG GSA (under accession no. CRA004815 and publicly accessible at <https://ngdc.cncb.ac.cn/gsa>). Atomic coordinates and x-ray diffraction data have been deposited in the Protein Data Bank under the accession codes 7V9F, 7V9G, 7V9H, and 7V9I for the BEN4 L740M and native, BEN3, and BEN4-mu structures, respectively. Materials generated in this study will be provided upon request.

SUPPLEMENTARY MATERIALS

science.org/doi/10.1126/science.abm0730
Materials and Methods
Figs. S1 to S7
Tables S1 to S3
References (26–52)
MDAR Reproducibility Checklist

26 August 2021; accepted 2 February 2022
Published online 10 February 2022
10.1126/science.abm0730



Shenzhen Institute of
Advanced Technology
Chinese Academy of Sciences



Established in partnership between the Chinese Academy of Sciences and the Shenzhen Municipal Government, the Shenzhen Institute of Advanced Technology (SIAT) is a newly-created university with an objective to become the world's preeminent institute for emerging science and engineering programs. SIAT is equipped with state-of-art teaching and research facilities and is dedicated to cultivating international, visionary, and interdisciplinary talents while delivering research support to pursue innovation-driven development.

SIAT is located in Shenzhen, also known as the "Silicon Valley of China," a modern, clean, and green city, well-known for its stunning architecture, vibrant economy, and its status as a leading global technology hub. SIAT is seeking applications for faculty positions of all ranks in the following academic programs: Computer Science and Engineering, Bioinformatics, Robotics, Life Sciences, Material Science and Engineering, Biomedical Engineering, Pharmaceutical Sciences, Synthetic Biology, Neurosciences, etc. SIAT seeks individuals with a strong record of scholarship who possess the ability to develop and lead high-quality teaching and research programs. SIAT offers a comprehensive benefits package and is committed to faculty success throughout the academic career trajectory, providing support for ambitious and world-class research projects and innovative, interactive teaching methods.

Further information:

<https://www.siat-sz.edu.cn/>



**YOUR NEXT
BIG SCIENTIFIC
DISCOVERY:
A NEW JOB.**



Find your next job at [ScienceCareers.org](https://www.ScienceCareers.org)

ScienceCareers

FROM THE JOURNAL SCIENCE MAAAS

ETH zürich

Assistant Professor (Tenure Track) of Robotic Materials

→ The Department of Materials
(www.mat.ethz.ch) at ETH Zurich invites applications for the above-mentioned position.

→ The department is searching for excellent candidates to develop a world-leading research program in robotic materials, i.e. new materials whose properties enhance robotic functionality. The candidate will constitute the focus of a strong ETH collaborative network, involving colleagues engaged in robotics and the human-robot interface in other departments. The candidate will have an outstanding research record in materials for robotic actuation and sensing, with a strong focus on applications, ideally in robotics or related technologies. At the assistant professor level, commitment to teaching and the ability to lead a research group are expected.

→ Assistant professorships have been established to promote the careers of younger scientists. ETH Zurich implements a tenure track system equivalent to other top international universities.

→ **Please apply online:**
www.facultyaffairs.ethz.ch

→ Applications should include a curriculum vitae, a list of publications, a statement of future research and teaching interests, a description of the leadership philosophy, and a description of the three most important achievements. The letter of application should be addressed **to the President of ETH Zurich, Prof. Dr. Joël Mesot**. **The closing date for applications is 1 May 2022.** ETH Zurich is an equal opportunity and family friendly employer, values diversity, strives to increase the number of women professors, and is responsive to the needs of dual career couples.



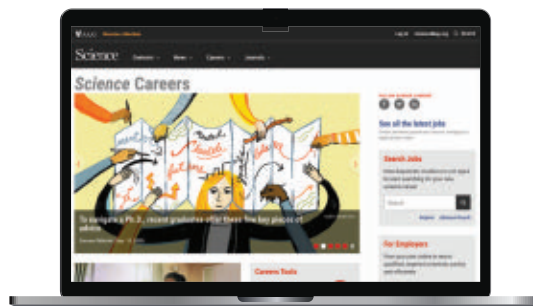
Science Careers helps you advance your career. Learn how !

- Register for a free online account on **ScienceCareers.org**.
- Search hundreds of job postings and find your perfect job.
- Sign up to receive e-mail alerts about job postings that match your criteria.
- Upload your resume into our database and connect with employers.
- Watch one of our many webinars on different career topics such as job searching, networking, and more.
- Download our career booklets, including Career Basics, Careers Beyond the Bench, and Developing Your Skills.
- Complete an interactive, personalized career plan at "my IDP."
- Visit our Employer Profiles to learn more about prospective employers.
- Read relevant career advice articles from our library of thousands.

Visit **ScienceCareers.org**
today — all resources are free

ScienceCareers

FROM THE JOURNAL SCIENCE  AAAS



SCIENCECAREERS.ORG

myIDP:

A career plan customized
for you, by you.



For your career in science, there's only one **Science**

Features in myIDP include:

- Exercises to help you examine your skills, interests, and values.
- A list of 20 scientific career paths with a prediction of which ones best fit your skills and interests.
- A tool for setting strategic goals for the coming year, with optional reminders to keep you on track.
- Articles and resources to guide you through the process.
- Options to save materials online and print them for further review and discussion.
- Ability to select which portion of your IDP you wish to share with advisors, mentors, or others.
- A certificate of completion for users that finish myIDP.



Visit the website and start
planning today!
myIDP.sciencecareers.org

**Science
Careers**
MAAS

In partnership with:



Universität
Rostock



Traditio et Innovatio



Universitätsmedizin
Rostock

The **Rostock University Medical Center** invites, subject to budgetary regulations, at the earliest possible date, applications for a

W3 (Full) Professorship for Immunology

according to the regulations of the "§61 Landeshochschulgesetz Mecklenburg-Vorpommern (LHG M-V)", as a permanent employment. A private-law contract with the University Medical Center will be established describing the terms of your service in research, teaching and patient care. The holder of the professorship becomes the director of the Institute of Immunology.

We are looking for a researcher with an excellent international reputation in immunological research. The successful applicant must be able to represent the entire subject of Immunology in teaching. The research profile is intended to strengthen the faculty's priorities as well as existing research networks. Commitment to the acquisition of further collaborative research projects is expected.

The requirements for the position of §58 Abs. 1 LHG M-V apply. In particular, this includes a completed university degree, doctorate, habilitation or equivalent academic achievements and, if necessary, specialist certification for the subject of immunology as well as university pedagogical aptitude. The prerequisites for acquiring the subject-specific advanced training authorization must be met.

The Rostock University Medical Center is aiming at a sustained academic profile within the framework of the research focus areas "Biomedical Engineering/Biomaterials", "Neurosciences" and "Oncology", and the University profile initiatives "Life, Light and Matter" and "Aging of the Individual and Society", to which the applicant is expected to contribute.

This advertisement is aimed at all people regardless of their gender. The University Medical Center Rostock intends to increase the proportion of women in its scientific staff and therefore particularly invites qualified women to apply, with reference to §7 (3) of the Equality Act of Mecklenburg-Western Pomerania. Women will be given preferential consideration in the case of equivalent qualifications, unless there are compelling reasons for preferring a male competitor. Severely disabled applicants will be given special consideration if they have the same suitability, ability and qualifications.

Applications including a detailed curriculum vitae, a description of the academic career and previous work in research and teaching, a structured list of publications, with indication of the impact factors, five important original papers and a list of previously acquired third-party funding, are to be submitted to the **Dean and Scientific Director of the Rostock University Medical Center, Prof. Dr. med. univ. Emil C. Reisinger, Ernst-Heydemann-Str. 8, 18057 Rostock**, no later than **21.04.2022**.

A completed application form, which can be downloaded from https://www.med.uni-rostock.de/fileadmin/Verwaltung/dekanat/Anlage_Bewerbungsunterlagen_Professuren.pdf must be attached to the documents.

The application costs will not be covered according to the regulatory action of the state of Mecklenburg-Western Pomerania.

www.med.uni-rostock.de

By Yunhe Tong

My writing journey

I grew up in China and was still developing my English skills, so I was nervous when I emailed my Ph.D. supervisor the first draft of a manuscript. One week later, he sent it back full of changes. At first, I was frustrated that my writing required so much editing. But after I took a closer look, I realized where I'd gone astray. He had shortened many of my sentences and commented that I should avoid unnecessarily long and complicated phrases. The advice was counter to what I'd learned when studying for English language proficiency exams. Showing off complex grammar and advanced vocabulary had always brought higher scores, so that's how I approached writing. But I clearly had more lessons left to learn.

I started to learn English when I was 14 years old. I needed to pass a written English exam to be admitted to high school in China, so my teacher had us practice vocabulary and grammar. In later years, I needed to pass other English exams to gain admission to university, and to graduate. Writing wasn't a huge component of them—instead, they consisted mostly of multiple choice questions testing reading comprehension, vocabulary, and grammar.

The first time I needed to write anything substantive in English was during my master's program in China, when I wanted to submit a manuscript to an international journal. I didn't have enough confidence to compose a first draft in English, so I wrote it in Mandarin and used an online translation tool.

The paper was accepted, which gave me a feeling that my strategy worked. But as I read more papers in English and reassessed my own writing, I realized my approach wasn't ideal. The tool had translated my text word for word, creating sentences that were technically correct but sounded unnatural, in part because sentences are structured differently in Mandarin and English.

I knew if I wanted to continue publishing, I would need to write in English directly—and when I moved to the United Kingdom for my Ph.D., I had no choice. Suddenly, I not only had to publish papers in English; I also had to write emails and prepare proposals in that language. (I needed to speak English, too, which was its own challenge—but that's a different story.)

At first, I sometimes sat at my computer all day and only ended up with 200 words of text. I couldn't tell whether my writing was any good. Every time I composed a sentence, I imagined someone laughing at it.



“Every time I composed a sentence, I imagined someone laughing at it.”

One day I'd had enough of writing the same sentence over and over. I decided to write the first draft of a manuscript as quickly as possible. That's when something magical happened: The sentences seemed to flow out of me, and in a few hours I had a rough draft. I had to go back and edit my work later, but it was a relief to have text to work with—and to know that my draft could only get better.

My supervisor's feedback on the draft was another turning point. Without his comments, I wouldn't have figured out that complicated sentences and big words might confuse my readers. He also helped me see the importance of telling a story as clearly as possible, paring down tangential details.

I now think through my simplified message before I start to write. I also try to get a first draft down quickly, doing my best to quiet the perfectionist voice in my head. Then I go back and take a closer look to see whether I can make my sentences more concise and trim any unnecessary details. I've also become more relaxed about editing: Even if I receive a manuscript full of changes again, I will just take it as an opportunity to discover problems I am not aware of. Lately, though, I've noticed that my supervisor has made fewer revisions, which gives me confidence I'm making progress.

It's frustrating to know I will probably never write as well as my supervisor. But I take solace in the fact that writing is hard for many native English speakers, too. It's not like solving a straightforward math problem—there's an art to it, and it can take years of practice. I hope my journey can help others develop writing strategies that work for them. ■

Yunhe Tong is a Ph.D. student at the University of Bristol.

CALL FOR PAPERS



Energy Material Advances

Energy Material Advances is an online-only, Open Access journal published in affiliation with **Beijing Institute of Technology (BIT)** and distributed by the **American Association for the Advancement of Science (AAAS)**. The journal publishes, research articles, review articles, short communications, perspectives, and editorials. *Energy Material Advances* covers multiple fields from cutting-edge material to energy science, investigating theoretical, technological as well as engineering aspects.

Submit your research to *Energy Material Advances* today!

Learn more at spj.sciencemag.org/energymatadv

The Science Partner Journal (SPJ) program was established by the American Association for the Advancement of Science (AAAS), the nonprofit publisher of the *Science* family of journals. The SPJ program features high-quality, online-only, Open Access publications produced in collaboration with international research institutions, foundations, funders and societies. Through these collaborations, AAAS furthers its mission to communicate science broadly and for the benefit of all people by providing top-tier international research organizations with the technology, visibility, and publishing expertise that AAAS is uniquely positioned to offer as the world's largest general science membership society.

Visit us at: spj.sciencemag.org



@SPJournals



@SPJournals



OPEN ACCESS

ARTICLE PROCESSING CHARGES WAIVED UNTIL JULY 2023



EMPOWER
WITH EVIDENCE

AAAS | ANNUAL MEETING

**We Appreciate the Support of the 2022
AAAS Annual Meeting Sponsors!**

Johnson & Johnson

ASU Arizona State
University

Drexel
UNIVERSITY

QUAD
FELLOWSHIP
by Schmidt Futures

Enhance your visibility at the AAAS Annual Meeting! Don't miss your chance to grab the attention of researchers, journalists, policymakers, students, and funding agencies. Get in touch with us for sponsorship and exhibit opportunities during the 2023 AAAS Annual Meeting.

Visit our website for more information:

aaas.org/meetings | [#AAASmtg](https://twitter.com/AAASmtg)